University of Alberta

HEAT TRANSFER IN WASTE-ROCK PILES CONSTRUCTED IN A CONTINUOUS PERMAFROST REGION

by

Hoang Nam Pham

A thesis submitted to the Faculty of Graduate Studies and Research
in partial fulfillment of the requirements for the degree of

Doctor of Philosophy

in

Geotechnical Engineering

Department of Civil and Environmental Engineering

Spring 2013
Edmonton, Alberta

To my parents

Phạm Phúc Hoàn

and

Giả Thị Lang

Abstract

This study is a part of a field experiment constructed at the Diavik Diamond Mine in northern Canada to investigate water flow, geochemical reactions, thermal and gas transport within unsaturated piles of mine waste rock in a continuous permafrost permafrost. Diavik waste rock is categorized by its sulfur content: Type I rock, Type II rock and Type III rock . Three experiment waste-rock piles of 15 m high were constructed to achieve the project objectives. Two uncovered test piles are referred to as Type I test pile (Type I rock) and Type III test pile (Type III rock). The third test pile is covered test pile in which the Type III rock is covered by a layer of 1.5 m till and 3 m Type I rock. Three drill holes of 40 m depth in a 80 m high pile were also instrumented to reexamine the results of the test piles. This thesis focuses on the thermal aspects of the project.

Thermal measurements in the uncovered piles implied the importance of wind on heat transport. Temperatures within the piles were found to decrease with time and permafrost aggradation near the base and in bedrock foundation. At the covered pile, temperatures at and below the till cover were frozen. There was no significant impact of wind on temperatures below the cover and heat influx across the cover was small. Bedrock foundation temperature of the covered pile showed a small cooling trend and less fluctuation compared to bedrock foundation of the uncovered piles. Linear stability analysis for the onset of natural air convection in waste-rock piles with physical properties based on Diavik waste rock was also performed. The results indicate that oxidation can create sufficient temperature gradients (or buoyancy forces) to trigger natural air convection.

Ground temperatures of three 40 m drill hole in the 80 m high full-scale pile showed that conduction was dominated and the pile was cooling. According to numerical simulations, using air convection cover (ACC) the 80 m high pile will be frozen for the next 100 years under a proposed climate warming for the site. Furthermore, numerical simulations also showed that ACC can maintain frozen condition within waste-rock piles even though there was a heat release due to sulfide oxidation. This heat release may create natural air convection within waste-rock piles which aids in its removal.

Acknowledgments

This thesis ends my long journey of achieving a Ph.D. degree and without the helps from my supervisor Dr. David C. Sego, I could have not finished the thesis. He has provided great guidance throughout the research and gone through every page of this thesis to give great comments and suggestions. I would also thank to my co-supervisors Drs. Ward Wilson and Lukas Arenson for valuable instruction and discussion.

Several chapters of this thesis received comments and suggestions from Drs. David Blows, Richard Amos and Marek Stastna of the University of Waterloo, Dr. Leslie Smith of the University of British Columbia, Dr. Morris Flynn of the University of Alberta and Lianna Smith of Rio Tinto, I greatly appreciate that. I would like to express my gratitude to my PhD. committee, Drs. Ania Ulrich, Morris R. Flynn, Jean Côté and N. (Raj) Rajaratnam for spending time to read my work and providing helpful suggestions.

The construction of the test piles and installation of instrument were difficult and these have not been done without brilliant personnel who have involved to the project. We call them the Testpilers and I am indebted to them for their assistance. The research is made possible through funding provided by the Natural Science and Engineering Research Council of Canada, the International Network for Acid Prevention, the Mine Environment Neutral Drainage program, the Canadian Foundation for Innovation and Rio Tinto (Diavik Diamond Mines Inc).

I am grateful to Christine Hereygers and Steve Gamble, at the Geotechnical Centre for great assistance both in field and laboratory work. I would like to thank Mr. Jianfeng Chen for discussion of laboratory work and having great talks about life. During the long period of study and research at the University of Alberta, great talks have been made with my office mates and colleagues of the Geotechnical Group, I greatly appreciate.

Finally, I have received tremendous supports from my parents, my brothers and sisters and Dung Pham and without their encouragements I would have not completed this work. I dedicate this thesis to them.

TABLE OF CONTENTS

LIST OF TABLES

LIST OF FIGURES

CHAPTER 1

Introduction

1.1 Statement of problem

Mining has increased in Canada including in both arctic and subarctic regions and it has produced at around 350 million tonnes of waste rock (Crowe et al., 2000). Waste rock is the overburden rock that has to be excavated to reach ore bodies and waste rock usually contains concentrations of sulfide minerals mainly pyrite (FeS_2) and pyrrhotite ($Fe_{1-x}S$) that are low to extract economically. When the sulfide minerals contained in waste rock are exposed to oxygen and water, these minerals are oxidized to produce Acid Rock Drainage (ARD), which is low pH water. The resulting acidic water causes other metals in waste rock to leach out with the pore water. Without proper treatment methods, the oxidation process can continue for hundreds or even thousands of years (Nordstrom and Alpers, 1999; Moncur et al., 2005). ARD poses a serious threat to the environment of mine and its surrounding regions and it has been considered as one of the largest liability that costs Canadian mining industry several billion Canadian dollars to clean up (MEND, 2001).

The essential components of ARD are sulfide minerals, water and oxygen, therefore eliminating or reducing one or more the essential components can control ARD. The removal of sulfide minerals in waste rock and exclusion of water to the extent that ARD does not occur are not considered practical and economical solutions (Robertson, 1987). Elimination of oxygen to the extent that ARD is reduced significantly requires the placement of a cover system with a layer or layers of soils or other materials having low oxygen diffusivity. Moreover, the rate of oxidation on the waste rock particle surface is catalyzed by bacteria (*Thiobacillus ferrooxidans*) and the reaction rate is temperature-dependent due to bacterial activity (Jaynes et al., 1984b). Under cool or warm temperatures, the reaction rate reduces significantly and follows Arrhenius behavior (Jaynes et al., 1984b).

When potentially acid generating (PAG) waste rock (or reactive waste rock) is stockpiled in permafrost regions, cold temperatures of the ambient environment can induce permafrost (i.e. < 0 °C) within waste rock dumps (piles or stockpiles). The permafrost condi-

tions of the waste rock can eliminate/reduce the oxidation process of sulfide minerals and therefore eliminating/reducing ARD. As a result, the potential ARD is constrained to in the active layer which is the thawed layer near the surface of the waste rock dumps in each summer. Under current mine closure strategies in permafrost regions, the strategies are to develop permafrost within the PAG waste rock by covering PAG waste rock with non-acid generating (NAG) waste rock or soils so that the active layer is constrained within the NAG waste rock layer (MEND1.61.2, 1996).

Under current climate change predictions, Environment Canada indicated that mean winter air temperatures warm between 4 °C at attitude 50 °N and 7 °C at 80 °N by 2100, and the active layer thickness is expected to increase due to the warming (Environment Canada, 1998). The impacts of global warming will be significant in discontinuous permafrost regions as it thickens the active layer, increases sulfide oxidation rates and dissolved metals due to increases in ground temperatures of PAG waste rock. In continuous permafrost regions, the impacts of warming is less evident as global warming may increase ground temperatures. However, ground temperatures will still be under a frozen state (i.e. < 0 °C) and the increase in active layer will not be significant. The use of artificial cooling techniques can compensate for global warming and maintains permafrost in PAG waste rock in waste-rock piles.

One of the artificial cooling techniques is air convective cover (ACC). The ACC technique is modified from a previous proven technique, air convection embankment (ACE), that was developed for the protection of road and railway embankments in "warm permafrost regions" (discontinuous permafrost) of Alaska and northern China (Goering and Kumar, 1996; Goering, 1998; Goering and Kumar, 1999; Binxiang et al., 2007a; Wu et al., 2008; Xu and Goering, 2008b; Li, 2008; Cheng, 2009). The ACC usually contains two layers: the lower layer (or latent heat layer) is low in permeability but high degree of saturation soils or fine fractions of NAG waste rock; and the upper layer (or air convection layer) is made of high permeability coarse rock where the coarse fractions of NAG waste rocks can be a candidate. The properties of the lower layer can decrease oxygen transport to the below PAG waste rock and constrain the active layer within the upper layer through the large latent heat of water of the lower layer. The upper layer with high permeability can utilize natural air convection during winter because of its unstable air-density stratification (cool-heavy air above warm-light air) within this layer. Natural air convection in winter transfers heat more efficiently than conduction in summer. The imbalance heat transfer between summer and winter cools the PAG waste rock below. The ratio of heat transfer though natural air convection during winter to conduction heat transfer during summer can be significant depending on permeability, thickness and the adverse temperature gradient across this layer. The ultimate goal of the ACC is to provide rapid convective cooling to freeze the underlying PAG waste rock to eliminate ARD.

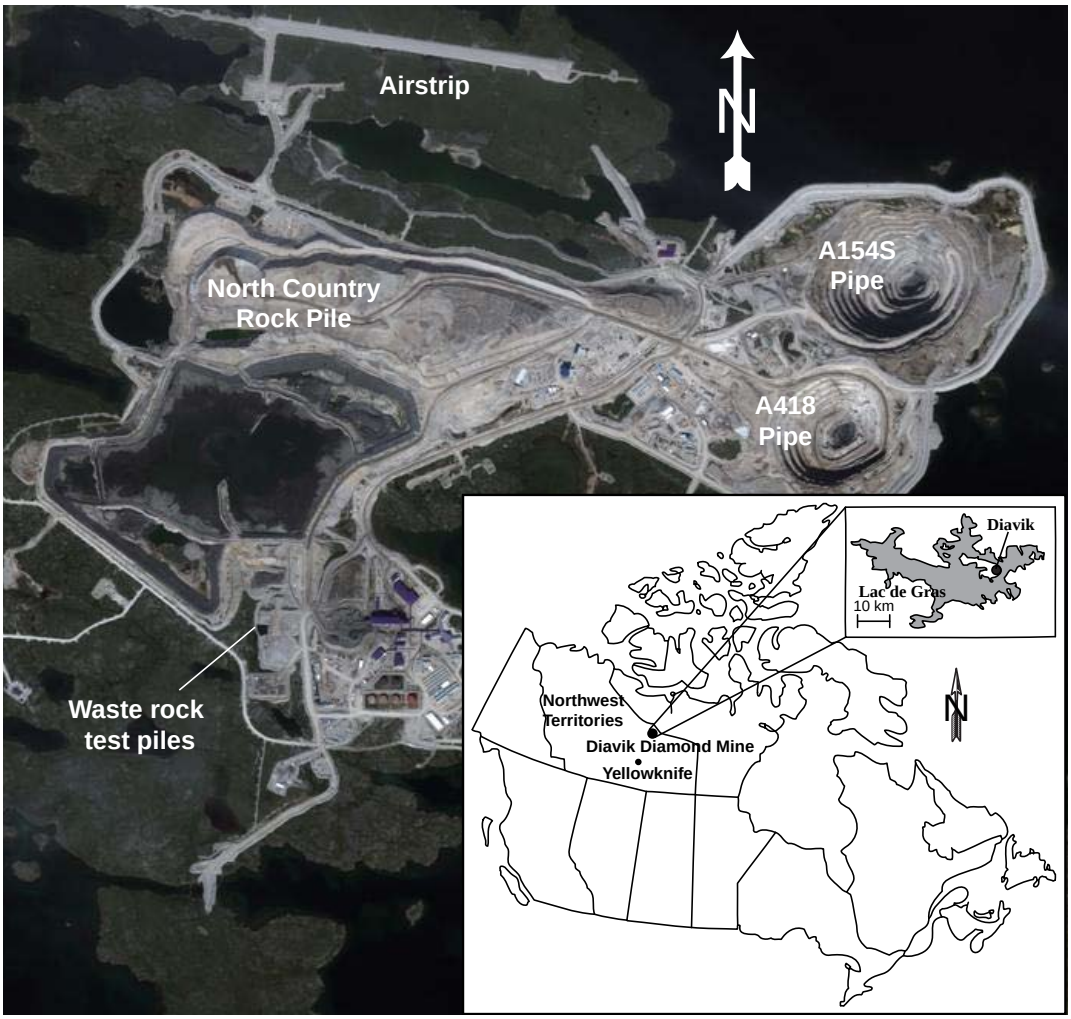

Figure 1.1: Location of Diavik diamond mine.

1.2 Site description and background

The experimental piles (test piles) are located at the Diavik diamond mine which is about 300 kilometers northeast of Yellowknife in the Northwest Territories, Canada (Fig. 1.1). The Diavik diamond mine is an operating open-pit and underground diamond mine that is located on a 20 km^2 island within the lake Lac de Gras. The mine is in a continuous permafrost region of northern Canada with a mean annual air temperature (MAAT) of -9.1 °C over the last decade (between 2000 and 2010) measured at the Diavik weather station. In 2010, a maximum ambient air temperature in July was recorded of 26.1 °C and a minimum ambient air temperature of -37.3 °C occurred in February. Monthly average Relative Humidity (RH) ranged between 71.0 % in June and 88.0 % in October. Total precipitation at the site was 280 mm of which 60 % coming from snow and an average wind speed of 17 m/s (including calm periods) (Environment-Canada, 2008a).

Temperature data of thermistor cables installed at the site indicated that a minimum

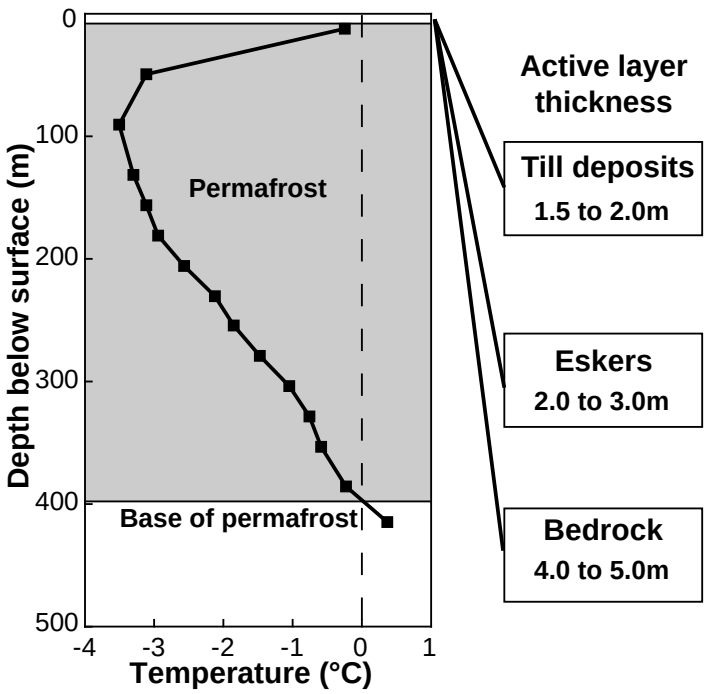

Figure 1.2: Temperature profile at Diavik (data obtained from Mareschal et al. (2004)) and active layer thickness of some typical surfaces.

permafrost temperature reached -3.5 °C at a depth about 100 m and the permafrost thickness was about 400 m (Fig. 1.2). The active layer thickness at the site depends on soil types, which are (DDMI, 2006):

- Till deposits: between 1.5 and 2.0 m;
- Granular deposits: from 2.0 to 3.0 m
- Bedrock: between 4.0 and 5.0 m.
- Poorly-drained areas, high moisture content and vegetation cover: less than 1.0 m.

Due to the traces of pyrrhotite $Fe_{(1-x)}S$ $(x = 0 \text{ to } 0.2)$ and other sulfide minerals in biotite schist, waste rock containing some concentrations of biotite schist is considered as acid-generating potential waste rock. Furthermore, during mining waste rock samples were collected and analyzed for its sulfur contents and based on the concentration of sulfur, waste rock is categorized into groups (DDMI, 2006).

- Type I waste rock: < 0.04 wt % S, no acid-generating potential, used as construction materials.
- Type II waste rock: between 0.04 and 0.08 wt % S, low acid-generating potential due to a low concentration of biotite schist and its production is about 5% of the total volume of waste rock annually.

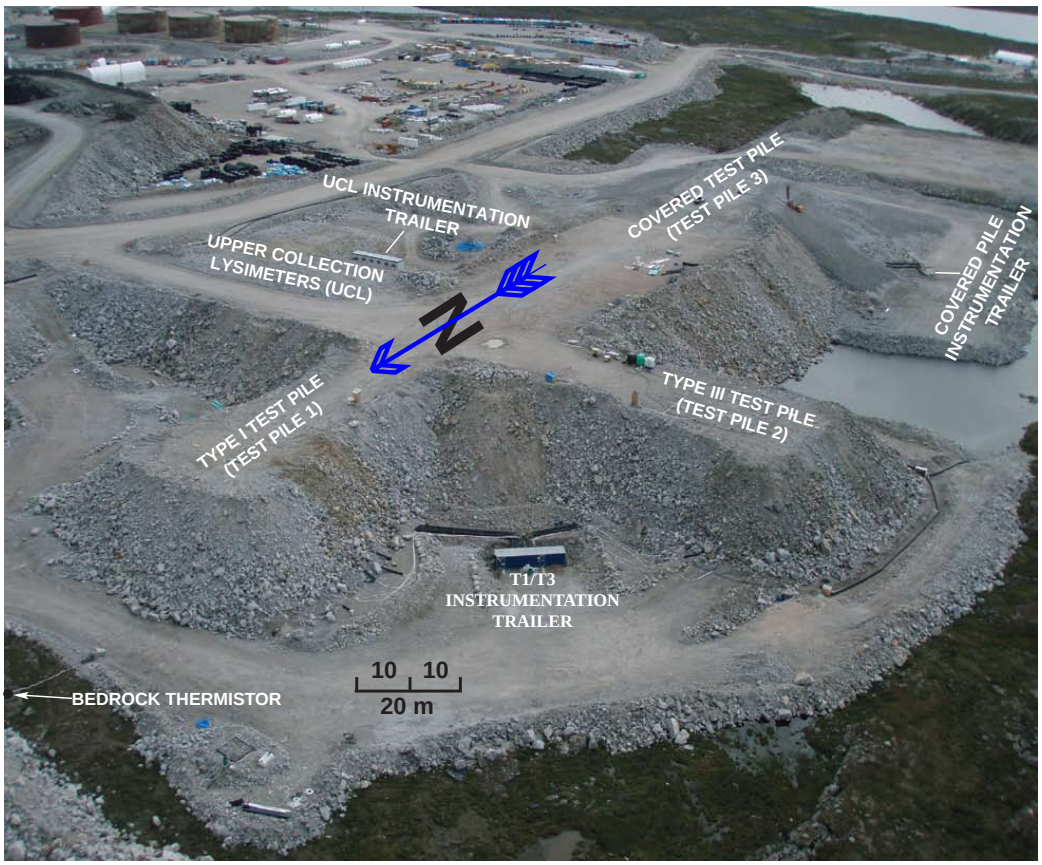

Figure 1.3: Aerial view of the test piles at Diavik diamond mine.

- Type III waste rock: $>$ 0.08 wt % S, potentially acid generating due to a greater concentration of biotite schist, it is the largest by volume of waste rock at the site.

Each waste rock type is stockpiled in a designed storage area and at the end of the mine the permanent stockpiles (rock piles or waste rock dumps) will contain up to 184 Mt of waste rocks covering an area of 3.5 km^2 with 60 to 80 m high, in which 75 % will be Type III waste rock (DDMI, 2006). Under the current closure and reclamation plan, each waste-rock type will have different closure strategies: the Type I waste-rock pile, due to geotechnical stability, will be re-sloped to 18.4°. Similarly, the Type II waste-rock pile will also be re-sloped to 18.4° (3H:1V) however it will be covered by a layer of 4 m Type I waste rock. Finally, the Type III waste-rock pile will be re-contoured to a slope of 18.4°, capped with a layer of 1.5 m till to prevent water and oxygen infiltration as well as acting like a latent heat layer. Above the till, there will be a 3-m layer of Type I waste rock that will retain active layer (DDMI, 2006).

Based on the closure and reclamation plan of Diavik waste rock, three experimental-instrumented waste-rock piles (or test piles) were constructed during the period 2004 – 2007. Two uncovered test piles are referred to as Type I test pile (containing Type I waste rock) and Type III test pile (containing Type III waste rock). Type I and III test piles are

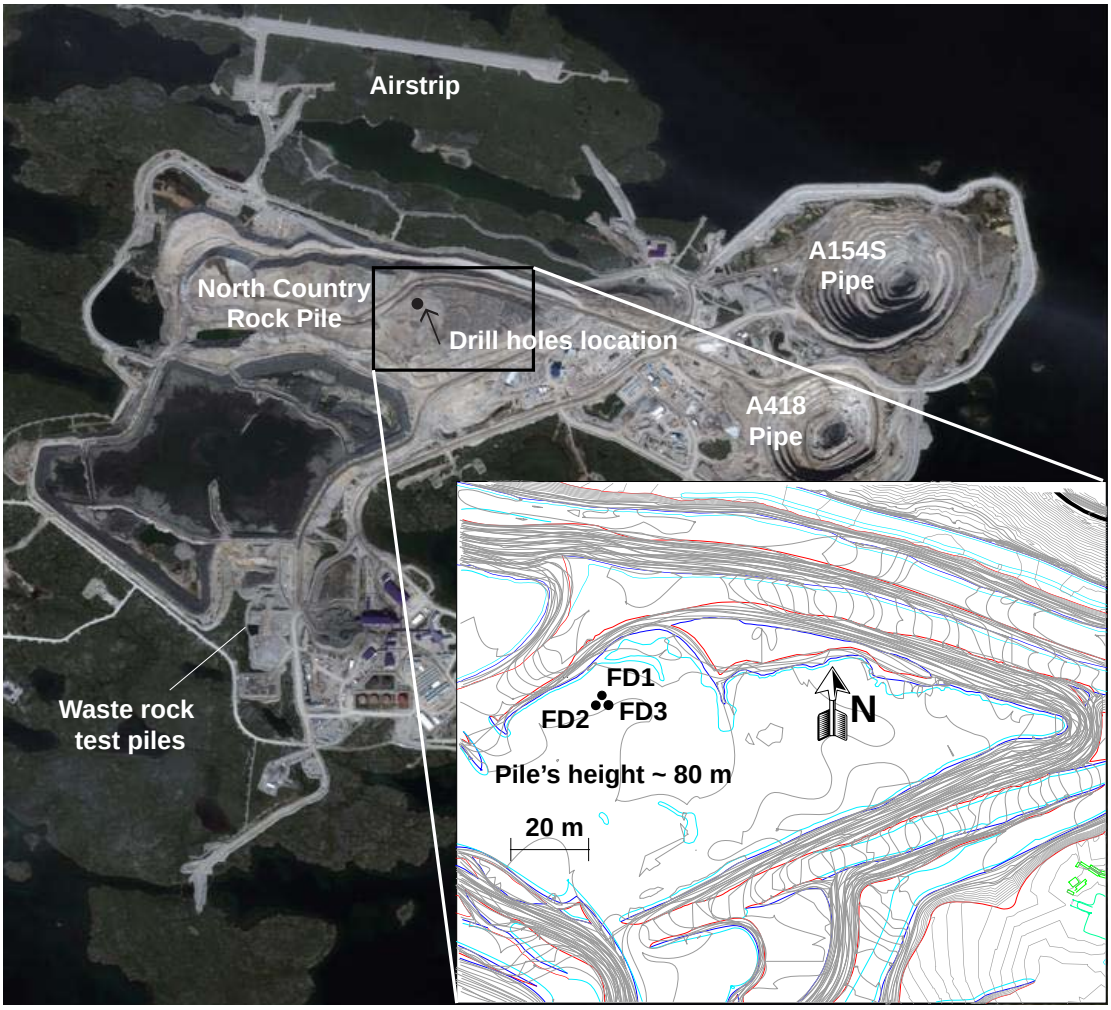

Figure 1.4: Drill holes at the full-scale waste-rock pile at Diavik

15 m high, approximately 20 m × 30 m at the surface, and 50 m × 60 m at the base. The third test pile is a covered test pile which was constructed based on the closure and reclamation plan for Type III waste rock. The covered test pile is also 15 m high, approximately 25 m × 30 m at the surface, and 60 m × 85 m at the base (Fig. 1.3). Along with the experimental data from the test piles, three 8-inch holes spaced at 5 m, FD1 (32.2 m depth), FD2 (30.7 m depth) and FD3 (40.2 m depth), were drilled in May 2010 at a full-scale pile (80 m height) of Type III waste rock to install instruments (Fig. 1.4).

The aims of the test piles project at Diavik diamond mine are to characterize the flow, thermal, and gas transport as well as the geochemical and microbiological processes in low sulfide waste-rock piles in a continuous permafrost environment. Various instruments were installed to measure matrix flow, pore water and bulk pile geochemistry, gas-phase oxygen and carbon dioxide concentrations, temperature evolution, microbiological populations, waste rock permeability to air, and thermal conductivity.

1.3 Objectives and scope of the thesis

Within the scope of the the test piles project at Diavik diamond mine, this research objectives intend to advance the understanding of thermal behaviors of uncovered and covered field experimental waste-rock piles as well as a full-scale waste-rock pile deposited onto a continuous permafrost region of the Canadian Arctic under the current climate condition and projected global warming. The application of ACC for PAG waste rock though numerical simulations is also a focus. To achieve these objectives, this research is divided into three different main tasks including numerical study, laboratory study and field study. The objectives of each task are listed as the followings:

1. Characterization of grain size distribution of waste rock and in-situ measurements of thermal conductivity of waste rock under frozen and thawed states.

2. Investigate and analyze spatial and temporal distribution of thermal regimes of covered and uncovered experimental waste-rock piles as well as a full-scale waste-rock pile.

3. Investigate the significance of wind-induced advection on the thermal regimes of uncovered experimental waste-rock piles.

4. Analyze thermal regime within bedrock foundations with and without experimental waste-rock piles above.

5. Numerical study of thermal evolutions of a full-scale waste-rock piles with and without various closure concepts (including ACC) and proposed climate change.

6. Assume various oxidation rates of sulfide minerals and utilize ACC, numerical simulations are run to examine the effectiveness of ACC of maintaining PAG waste rock frozen.

7. Laboratory and numerical study of natural air convection in porous media are conducted for advancing understanding natural air convective heat transfer.

1.4 Organization of the thesis

The thesis is written under a paper-based format, therefore the materials in introduction and site description sections of each chapter are maybe repeated. With the above objectives, this thesis contains eleven chapters and a brief introduction of each chapter is as the followings:

- Chapter 2 gives a brief introduction of background information and research reviews related to the thesis including: waste rocks and ARD in mining industry, processes creating ARD, basic concepts of permafrost engineering and engineering problems in permafrost regions, potential ARD treatment in permafrost regions, importance of gas transport in thermal and ARD processes, and basic formulations for calculation of thermal related properties.

- Chapter 3 gives the grain size distribution of waste rock at Diavik, theory of thermal conductivity probe is provided and thermal conductivity results of test piles are presented for the period between 2006 and 2010.

- Chapter 4 provides thermal experimental results of the Type III test pile (an uncovered test pile) and bedrock foundations. Calculation of air velocity based on temperature induced and the results of calculated heat budget of the test pile are also presented.

- In Chapter 5, the correlation analyses of measured-internal temperatures to surface temperature, wind and air pressure are conducted. The significant effects of wind-induced advection is recognized.

- Chapter 6 presents the thermal results of the covered test pile and the significant impacts of the cover on thermal regimes of Type III waste rock beneath.

- Chapter 7 gives thermal results from three drill holes up to 40 m on a full-scale waste-rock pile and numerical simulations of thermal evolution with various closure concepts under a proposed global warming.

- Chapter 8 presents a conceptual model for waste-rock piles in continuous permafrost regions including the critical physical and chemical processes related to thermal behaviors.

- In chapter 9, based on the conceptual model in Chapter 9, numerical simulations of thermal behavior of covered and uncovered waste-rock piles were carried out. Furthermore, various closure concepts of PAG waste rock and the effects of wind and sensitivity analyses of permeability were also considered.

- Chapter 10 summarizes and discusses the critical results obtained. Recommendations for further research are also given in this chapter.

- In the Appendices, appendix A gives laboratory results and numerical simulations of natural air convection in porous media of a cylindrical tank heated from below and cooled from above. The results provide advance understanding of natural air convection that will help the design of ACC with more efficiency and economy. Appendix B deals with condition for the onset air convection in a waste-rock pile with and without heat generation due to oxidation of sulfide minerals. Appendix C provides additional field data including temperature and pore-air pressure. Finally, appendix D provides wiring diagrams and programs that are used in the data loggers at the site.

References

Binxiang, S., Lijun, Y., and Xuezu, X. (2007a). Onset and evaluation on winter-time natural convection cooling effectiveness of crushed-rock highway embankment. *Cold Regions Science and Technology*, 48(3):218 – 231.

Cheng, G., W. Q. M. W. (2009). Innovative designs of permafrost roadbed for the Qinghai-Tibet Railway. *Science in China, Series E: Technological Sciences*, 52(2):530–538. cited By (since 1996) 2.

Crowe, A. S., Ptacek, C. J., Rudolph, D. L., and McGregor, R. (2000). Threats to sources of drinking water and aquatic ecosystem health in Canada. Technical report, Environment Canada.

DDMI (2006). Interim Closure and Reclamation Plan. Version 2, September 2006.

Environment-Canada (2008a). Climate Data Online. National Climate Data and Information Archive. Technical report, Environment Canada.

EnvironmentCanada (1998). Climate change impacts on permafrost engineering design. Technical report, Panel on Energy Research and Development (PERD), Environment Canada.

Goering, D. and Kumar, P. (1999). Permeability effects on winter-time natural convection in gravel embankments. In Hutter, K., Wang, Y., and Beer, H., editors, *Advances in Cold-Region Thermal Engineering and Sciences*, volume 533 of *Lecture Notes in Physics*, pages 455–464. Springer Berlin / Heidelberg. 10.1007/BFb0104203.

Goering, D. J. (1998). Experimental investigation of air convection embankments for permafrost-resistant roadway design. In *Seven International Conference on Permafrost*.

Goering, D. J. and Kumar, P. (1996). Winter-time convection in open-graded embankments. *Cold Regions Science and Technology*, 24(1):57–74.

Jaynes, D. B., Rogowski, A. S., and Pionke, H. B. (1984b). Acid mine drainage from reclaimed coal strip mines: 1. Model description. *Water Resour. Res.*, 20:233–242.

Li, G.a, L. N. b. K. J. N. F. Y. W. S. L. B. G. (2008). Study on design optimization of a crushed stone layer with shading board placed on a railway embankment on warm permafrost. *Cold Regions Science and Technology*, 54(1):36–43. cited By (since 1996) 3.

Mareschal, J. C., Nyblade, A., Perry, H. K. C., Jaupart, C., and Bienfait, G. (2004). Heat flow and deep lithospheric thermal structure at Lac de Gras, Slave Province, Canada. *Geophys. Res. Lett.*, 31(12):L12611–.

MEND (2001). List of potential information requirements in metal leaching/acid rock drainage assessment and mitigation work. Technical report, CANMET Mining and Mineral Sciences Laboratories.

MEND1.61.2 (1996). Acid mine drainage in permafrost regions: Issues, control strategies and research requirements. Technical report, Department of Indian and Northern Affairs Canada.

Moncur, M., Ptacek, C., Blowes, D., and Jambor, J. (2005). Release, transport and attenuation of metals from an old tailings impoundment. *Applied Geochemistry*, 20(3):639–659.

Nordstrom, D. K. and Alpers, C. N. (1999). Negative pH, efflorescent mineralogy, and consequences for environmental restoration at the Iron Mountain Superfund site, California. *Proceedings of the National Academy of Sciences of the United States of America*, 96(7):3455–3462.

Robertson, A. M. (1987). Alternative acid mine drainage abatement measures. Technical report, Steffen, Robertson and Kirsten (B.C.) Inc., Vancouver, B.C., Canada.

Wu, Q., Lu, Z., Tingjun, Z., Ma, W., and Liu, Y. (2008). Analysis of cooling effect of crushed rock-based embankment of the Qinghai-Xizang Railway. *Cold Regions Science and Technology*, 53(3):271–282.

Xu, J. and Goering, D. J. (2008b). Experimental validation of passive permafrost cooling systems. *Cold Regions Science and Technology*, 53(3):283–297.

CHAPTER 2

Literature Review

Acid water produced by sulfide oxidation of waste rock has adverse effects on environment and is being resolved in southern regions of Canada in recent years. However, in northern regions, acid generation can be eliminated or reduced by cooling waste rock into a frozen state. One of the effective tools is air convective cover (ACC) in which natural air convection creates an unbalanced heat transfer between summer and winter. The ACC draws more heat from the waste rock during winter and it allows less heat penetration during summer.

There is an extensive body of literature available in the field of permafrost engineering, multiphase heat and mass transfer, and natural air convection in porous media. Therefore, the chapter only provides fundamental information of all the topics related to the works of this thesis. ***Waste-rock piles (waste dumps or stockpiles)*** *and their environmental impacts are presented first. Then a fundamental introduction of permafrost and permafrost engineering follows and later heat transfer mechanism and natural heat convection in porous media are introduced. Finally phase relations and formulation for calculation thermal properties of thawed and frozen soils/waste rock are introduced.*

2.1 Waste-rock piles (waste dumps or stockpiles)

Mining industry in Canada is significant and it provides incomes for a large population, however it also produces about 2-million tonnes of mine wastes (waste rock and tailings) every day (Mining Watch Canada, 2009). Waste rock from open pit or underground mining is usually unsaturated and consists of minerals that are insignificant for further processes (Blight, 2010). Based on grain size characteristics, waste rock is a well-graded material (from boulder down to silt). Furthermore, waste rock is commonly stored in waste-rock piles and these piles can occupy a large land surface. Depending on topography at the dump site, the waste-rock piles can be in the forms of "valley-fill", "side-hill" or "open piles" (heaped in flat regions) (Fig. 2.1) and the methods of constructing waste-rock piles often are "end-dumped" and "layer-dumped" (Blight, 2010). The end-dumping method often results in material segregation along the slope of the dumped face as particle size

usually increases with depth (Van Zyl, 1993). Therefore, stratification and heterogeneity are common in waste-rock piles (Smith et al., 1995; Lefebvre et al., 2001b; Azam et al., 2007).

2.2 Acid rock drainage (ARD)

Acid rock drainage occurs when waste rock containing sulfide minerals is exposed to air and water with the help of bacteria catalysis (*Thiobacillus ferrooxidans*). Oxidation of sulfide minerals in waste rock becomes sulfuric acid which is harmful to the surrounding environment. The chemical changes within waste rock also release heavy metals and other toxic chemicals which are transported by drainage water through waste-rock piles (Nordstrom and Alpers, 1999; Moncur et al., 2005).

Pyrite (FeS_2) is the dominant sulfide minerals in waste rock as a result acid generation reactions are usually described through the oxidation of pyrite (Lowson, 1982; Evangelou, 1995). A simple but widely accepted version of ARD are described by the following:

$$\underbrace{FeS_2}_{\text{pyrite}} + 3.5O_2 + H_2O \Rightarrow Fe^{2+} + 2SO_4^{2-} + 2H^+ \tag{2.1}$$

As a result, hydrogen ions are created and they cause elevated acidity, lowered pH and dissolved metals. In addition, the oxidation reactions are exothermic, producing $1.41\text{x}10^4\,\text{kJ/mole}(FeS_2)$ (or $2.19\text{x}10^4\,\text{kJ/kg}\,(\text{S})$) (Lowson, 1982). The heat release can cause elevated temperatures at highly reactive locations within waste-rock pile. A more completed version of oxidation processes of pyrite were shown by Singer and Stumm (1970); Lowson (1982); Evangelou (1995); Nordstrom and Alpers (1999).

2.3 Permafrost Engineering

2.3.1 Permafrost in the Northern Hemisphere

Permafrost is a ground thermal condition, which is in a frozen state (i.e. $< 0°\text{C}$) for two years or more. Permafrost is widespread and underlaid about 22% of the exposed surface of the earth and about 50% of Canada (Davis, 2001). Permafrost often occurs in high-latitude (close to the poles) and high-altitude (high mountain ranges) regions, where air temperatures are cold and prolonged winter period (Davis, 2001) (Fig. 2.2). Furthermore, the soil or rock layer near the earth's surface in permafrost regions subjected to freeze and thaw each year is called ***"active layer"***. It is also referred to as ***a "seasonally frozen ground"***, ***"seasonal frost"*** or ***"annually thawed layer"*** (Andersland and Ladanyi, 2004)

There are two major groups of permafrost namely: continuous and discontinuous regions. Continuous permafrost zone in which permafrost exists continuously the whole areas below the ground surface except for zones that retain large latent heat such as beneath rivers

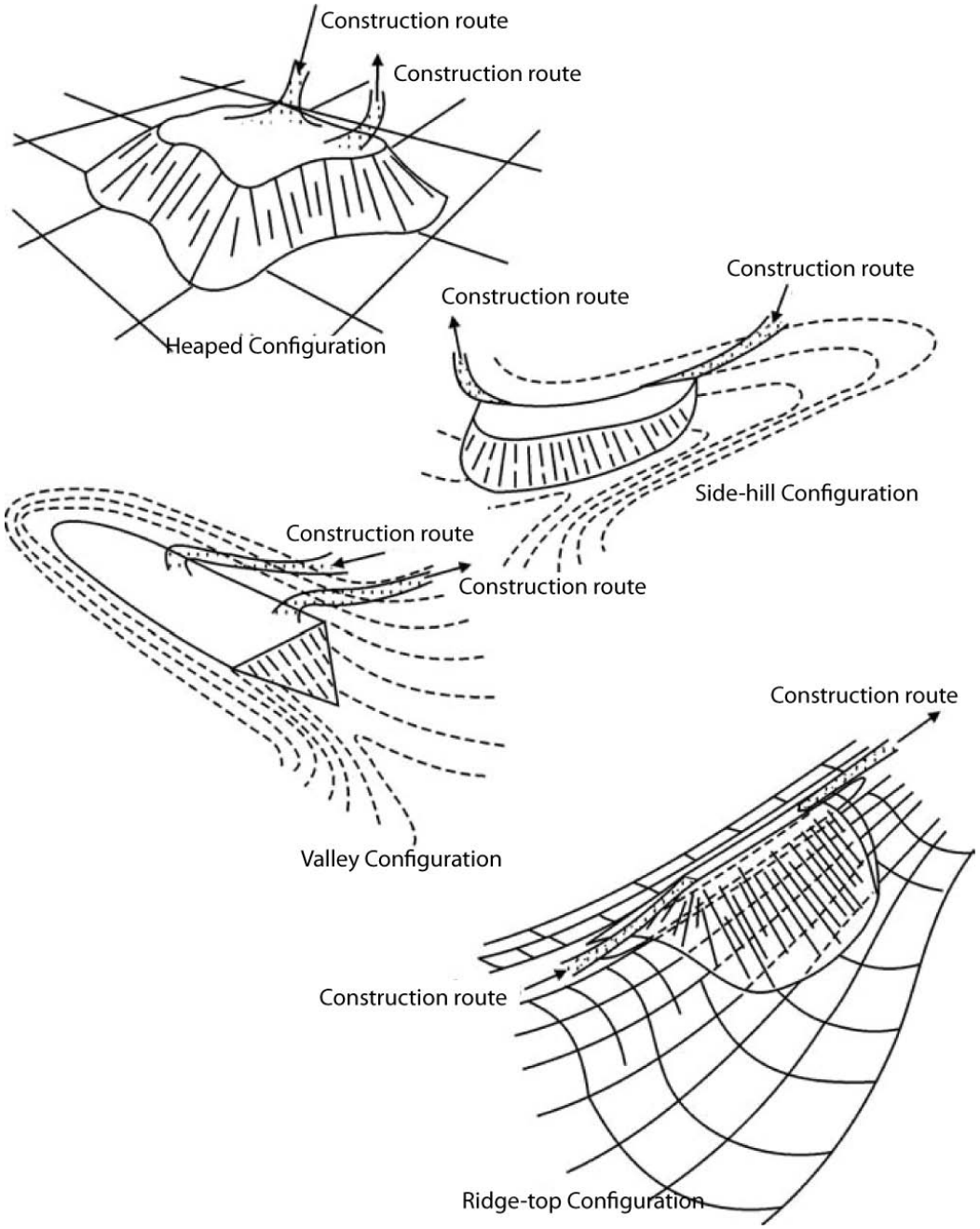

Figure 2.1: Topography dictates the configurations of waste-rock pile (modified from Blight, 2010)

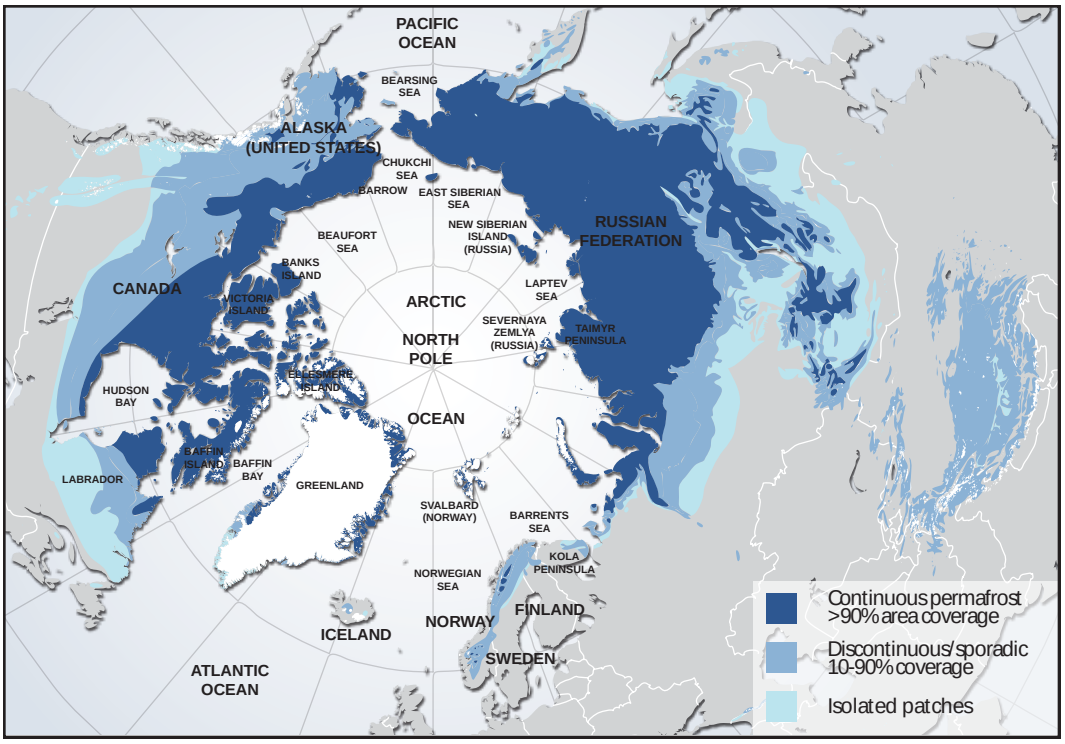

Figure 2.2: Permafrost distribution (modified from Rekacewicz, 2005)

and lakes. Permafrost thickness can be more than 650 m in the far north where the active layer is very thin (less than 0.5m) (Fig. 2.3). Discontinuous permafrost zone in which permafrost underlies some parts of the land area below the surface and the active layer is often thick. Moreover, in areas where soil has high moisture contents and thick vegetation cover permafrost can also exist in small frozen lenses (Geological Survey of Canada, 2007). Geological Survey of Canada (2007) divided permafrost regions by the mean of Mean Annual Air Temperature (MAAT) isotherms:

- Discontinuous permafrost zone: between -1 °C and -7.5 °C isotherms
- Continuous permafrost zone: north of -7.5 °C isotherm

Under this definition, more than 50 % of the ground surface of Canada is occupied by permafrost (Fig. 2.2) and about half of its permafrost regions has MAAT warmer than $-2\,°C$ (Geological Survey of Canada, 2007).

Based on the coldest month of the year, Bates and Bilello (1966) determined the southern boundary of cold regions in northern hemisphere and they further divided the cold regions into smaller groups:

- Region of cold winter: between 0 and -17.8 °C
- Region of very cold winter: between -17.8 and -32.0 °C

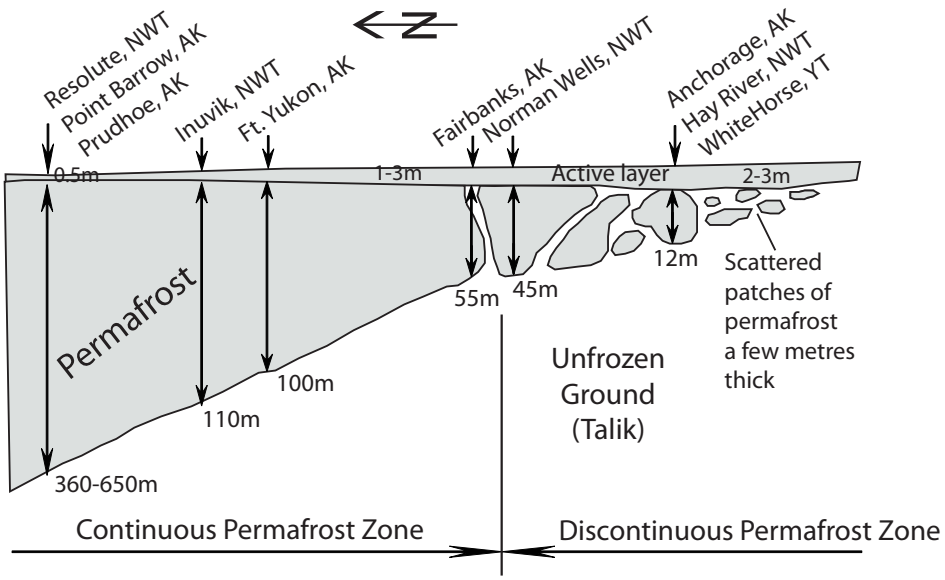

Figure 2.3: Active layer thickness in permafrost regions (modified from Davis, 2001).

- Region of extremely cold winter: between -32 and -62.2 °C

Under an annual thermal cycle in cold regions, heat is extracted from the ground during winter and enters the ground during summer. As a result, this process forms the active layer and a typical temperature profile as shown in Fig. 2.4. The thickness of the active layer changes according to the mean annual surface temperature (MAST), which is lower as one goes north. Mean annual ground temperature (MAGT) usually warms with depth at a rate depending on the upward geothermal gradient (Lunardini, 1981).

2.3.2 Climate change

When climate change and global warming occur, the rise in air temperatures, changes to snow cover thickness and distribution, ground surface disturbances, precipitation and other climatic variables will significantly impact on the subsurface thermal regimes. As a result, the thermal equilibrium between the ambient air and ground changes and heat flux into the ground increases. The warming in continuous permafrost regions will deepen the active layer and elevate subsurface temperatures, however ground temperatures remain below 0 °C. Whereas, in discontinuous permafrost regions where ground temperatures are usually warm (close to 0 °C), an increase in air temperatures can induce more heat into the ground causing permafrost to thaw (Esch and Osterkamp, 1990; Nelson et al., 2003).

Fig. 2.5A shows that in northern Alaska, permafrost temperatures have increased by about 2 °C during the last two decades. The warming of permafrost also occurs in Canada and it was significant in the centre and north of the Mackenzie Valley. However, in the southern Mackenzie Valley the warming was small (Fig. 2.5B).

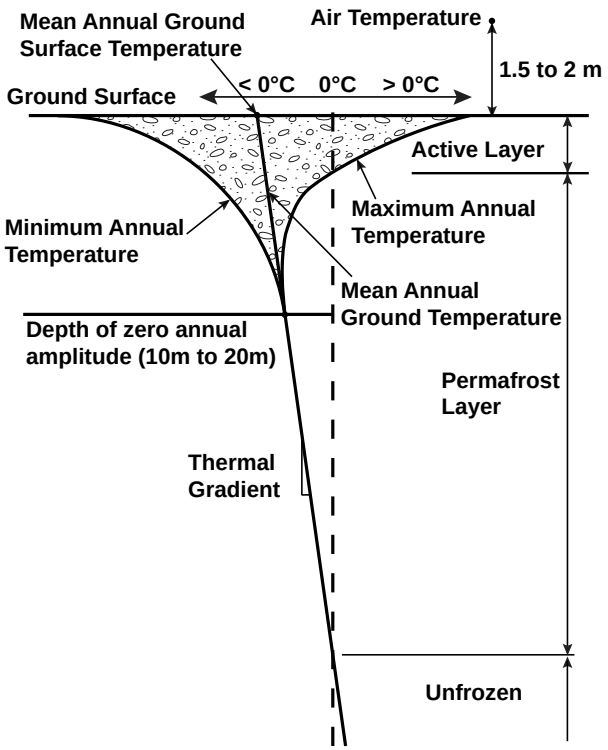

Figure 2.4: Typical temperature profile in permafrost regions (modified from Lunardini, 1981)

2.3.3 Energy balance at the ground surface

Changes in the thermal regime of subsoil in both thawed or frozen states are controlled by the energy transfers at the ground surface. Moreover, these energy transport processes are extremely complex, highly coupled and rapidly changing according to climatic variables and ground conditions (Lunardini, 1981). The energy balance can be written as (Lunardini, 1981)

$$R_n + G + Q_{evap} + Q_{conv} + Q_S = 0 \tag{2.2}$$

Where: R_n is the net radiation, G is the ground surface heat flux, Q_{conv} is the convective (sensible) heat transfer related to the differences of temperature between the surface and ambient air above, Q_{evap} is the latent heat transfer, Q_S is the heat source/sink. Lunardini (1981) provided detailed formulations of calculation for each component.

At a given site numerous measurements are required to determine parameters for each component of the above energy balance. Not only the costs associated with the measurements but also the difficulties to obtain reliable measured values, therefore for the purpose of defining a boundary condition for thermal modeling of subsoil, ground surface temperature (GST) is usually used (Andersland and Ladanyi, 2004). In permafrost engineering, GST is defined as ground temperature at 1 cm depth below the surface. However if the

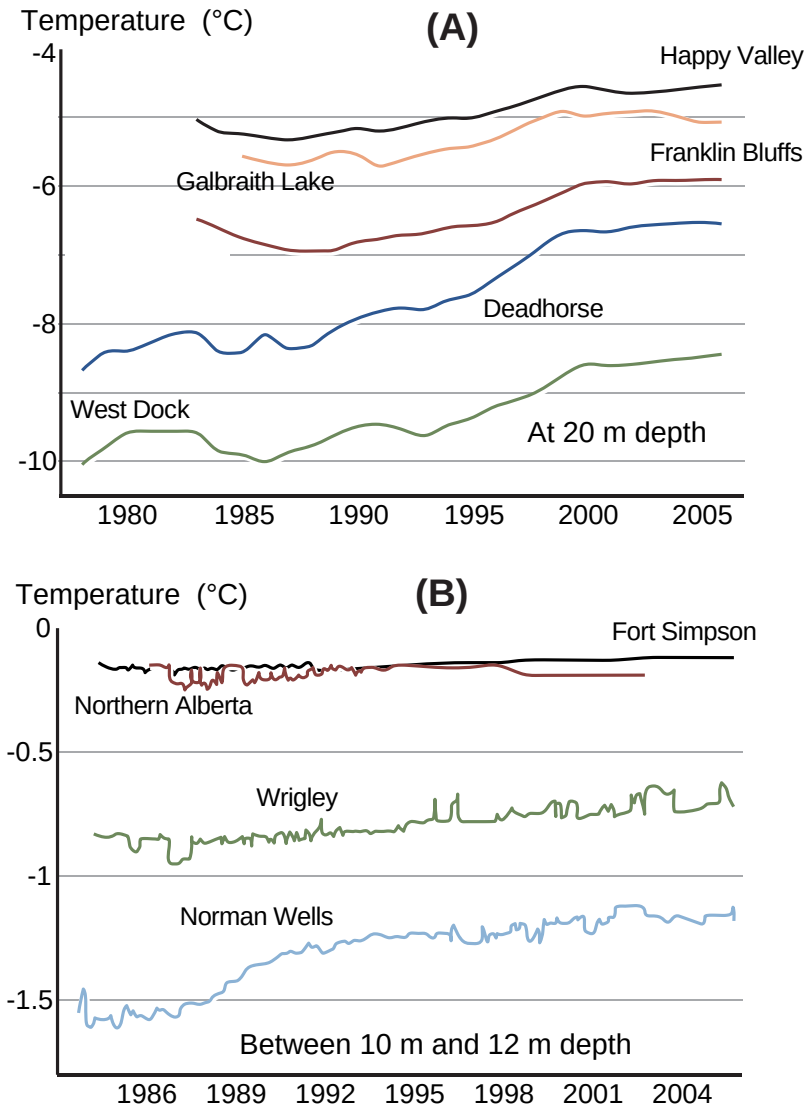

Figure 2.5: Warming permafrost in northern Alaska (A); in Mackenzie Valley (B) (modified from Romanovsky et al., 2007).

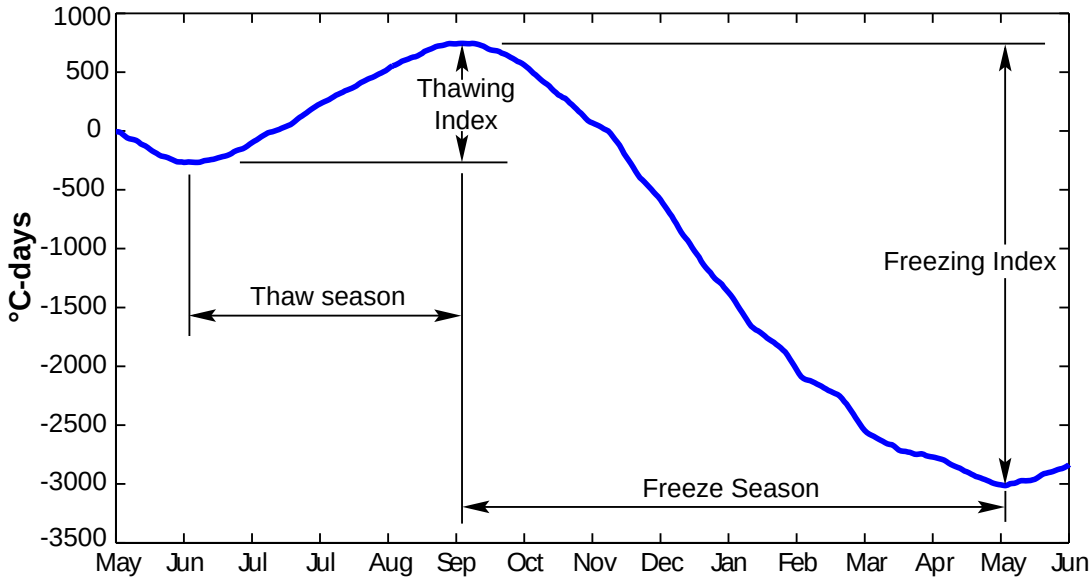

Figure 2.6: Air thawing-freezing indices (°C-days) at Diavik mine site during 2009 - 2010 based on daily average values.

actual measurements of GST is not available, GST is often determined using thawing and freezing indices of air temperature and surface n-factors, which is used to describe to the physical properties of the ground surface such as moisture content, emissivity coefficient, vegetation cover and many others.

2.3.4 Air freezing and thawing indices

Air freezing and thawing indices, I_{af} (°C-days) and I_{at} (°C-days) are an intuitive way to describe the strength of air temperature and are calculated using Eqn. 2.3 and Eqn. 2.4 in which t is time in days and T is air temperature in °C (Lunardini, 1981). The values of air freezing and thawing indices and the seasonal length can be determined by plotting the accumulative values of the mean daily air temperature. This is shown in Fig. 2.6 for the daily mean air temperature at Diavik mine site during 2009 - 2010.

$$I_{af} = \int_{t_0}^{t_1} |T|\,\mathrm{dt},\ T < 0\,^{\circ}\mathrm{C} \tag{2.3}$$

$$I_{at} = \int_{t_0}^{t_1} T\,\mathrm{dt},\ T > 0\,^{\circ}\mathrm{C} \tag{2.4}$$

Fig. 2.7 shows the distribution of air thawing and freezing indices in the northern Canada. Fig. 2.8 shows that as one goes further north, I_{af} increases to about 7000 (°C-days) whereas I_{at} decreases to near 0 (°C-days) at 90 °N.

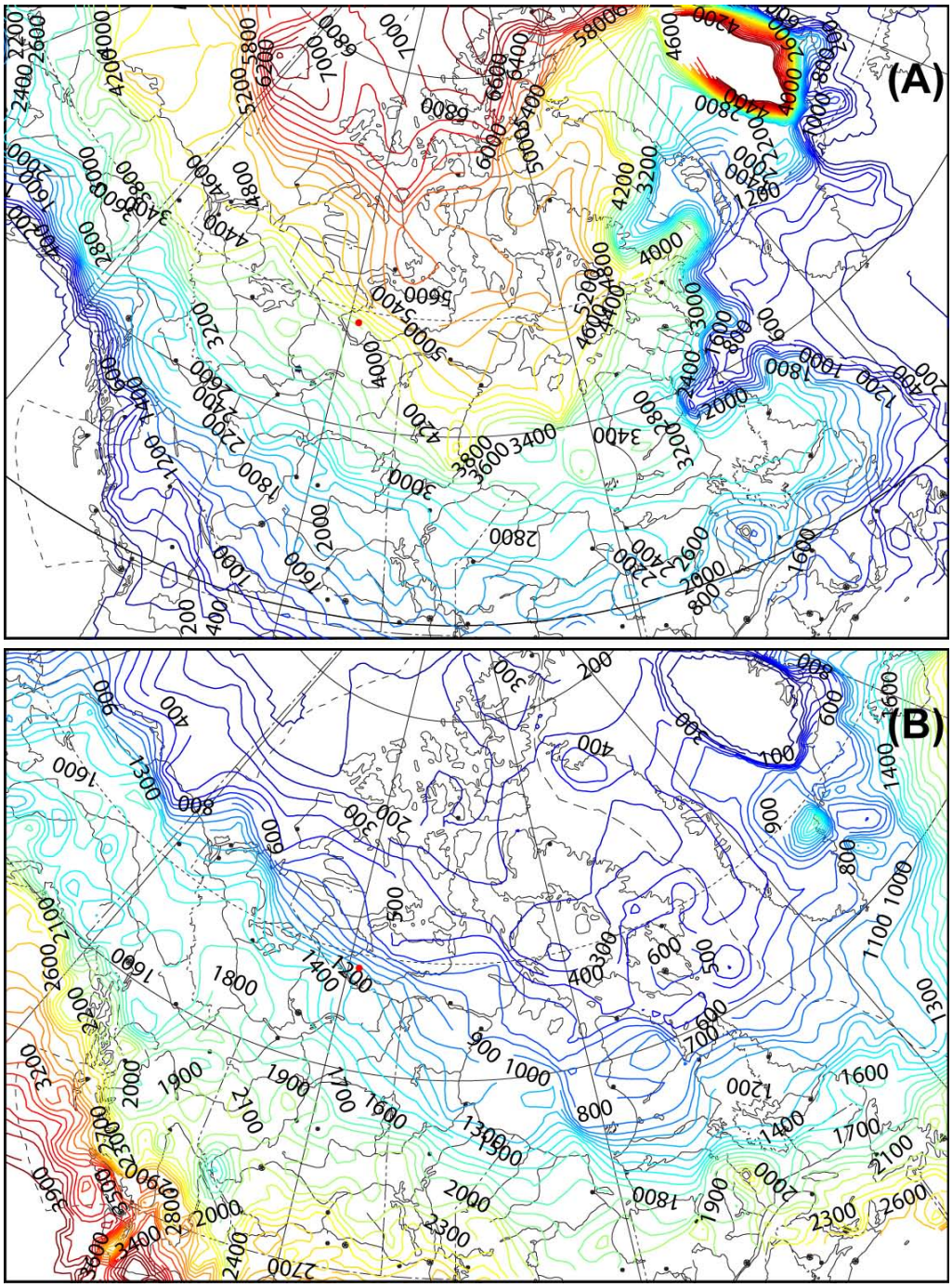

Figure 2.7: Air freezing (A) and thawing (B) indices (°C-days) in the northern Canada, the data was obtained from Zhang (1998).

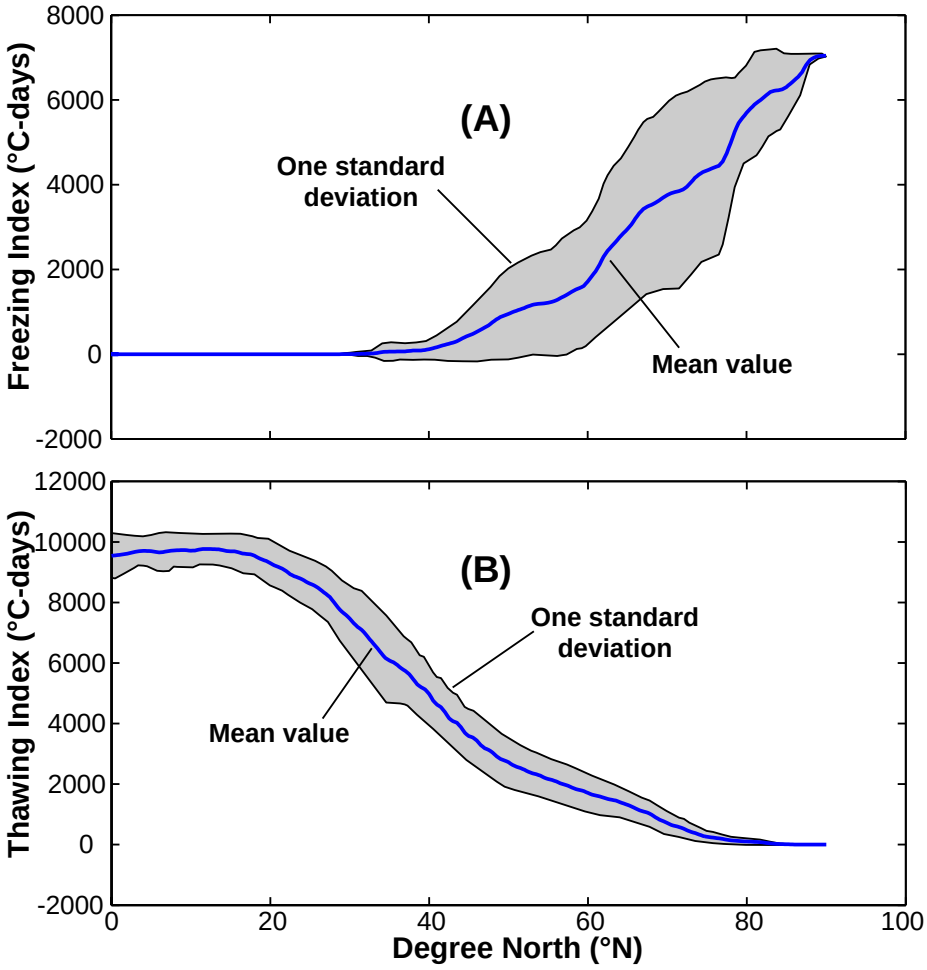

Figure 2.8: Air freezing and thawing indices (°C-days) in the Northern hemisphere, the data was obtained from Zhang (1998).

Table 2.1: Various values of n-factor for some typical surfaces (data from Lunardini, 1981)

Type of surface	Freezing, n_f	Thawing, n_t
Snow	1.00	—
Pavement free of snow and ice	0.90	—
Sand and gravel	0.90	2.00
Turf	0.50	1.00
Spruce trees, brush, moss over peat soil	0.29	0.37
Trees and brush cleared moss over peat soil	0.25	0.73
Vegetation and mineral soil surface	0.33	1.22
Gravel, coarse rock		
Measured values	0.60 - 1.00	1.30 - 2.00
Northern values	0.90 - 0.95	
Asphalt surface		
Measured values	0.29 - 1.00	1.40 - 2.30
Northern values	0.90 - 0.95	
Concrete surface		
Measured values	0.25 - 0.95	1.30 -2.10
Northern values	0.70 - 0.90	

2.3.5 Surface n-factors

Surface n-factors are used to calculate GST indices from air temperature indices and they are determined experimentally for typical ground surfaces (Lunardini, 1981). Surface n-factors are site specific values and they are greatly influenced by climatic, surface and sub-surface conditions of the ground and they may vary throughout a year. By definition, surface n-factors are the ratio between freezing (I_{sf}) or thawing (I_{st}) index of GST to air freezing (I_{af}) or thawing (I_{at}) index as shown in Eqn. 2.5 and Eqn. 2.6.

$$n_f = \frac{I_{sf}}{I_{af}} \tag{2.5}$$

$$n_t = \frac{I_{st}}{I_{at}} \tag{2.6}$$

Table 2.1 lists approximate surface n-factor values for several ground surface types. MAST can be calculated via n_f, n_t, I_{af} and I_{at} as (Smith and Riseborough, 1996)

$$MAST = \frac{n_t I_{at} - n_f I_{af}}{P} \tag{2.7}$$

where $P = 365$ days is the annual period.

2.3.6 Permafrost impacts on infrastructure

In a frozen state soils are impervious and develop high short-term strength; these properties are important and need to be considered when constructing infrastructure on permafrost. However, when the surface conditions are altered by construction activity or climate change more heat may flow into the ground increasing its temperatures. This process may cause permafrost to warm or thaw, and the active layer can become deeper and/or not refreeze (Hinkel et al., 2003; Romanovsky et al., 2003). The thawed ground looses much of its high strength leading to enhanced deformation and therefore the infrastructure built on the surface of this warming or melting permafrost may become unstable. Differential settlement, ice lenses and frost heave are the most common problems associated with construction in permafrost regions. Current engineering practices must account for permafrost and minimize disturbance to the existing thermal regimes when possible (Hinkel et al., 2003).

2.3.7 Permafrost protection for infrastructure

In permafrost regions, maintaining foundation soils under a frozen condition is important due to its high strength and impermeability, especially structures with foundations in fine-grained soils having high ice content or "ice-rich permafrost" soils. Many studies have been conducted to develop techniques that can preserve original thermal condition or promote permafrost aggradation. Esch (1988) reported the method of white paint for road surface to increase surface reflectivity therefore reducing surface temperature. From experimental data at a site in Alaska, MAST reduced from 1.1°C to -0.5°C by white paint (Esch, 1988). Snowsheds are used to prevent snow accumulated on the sides of embankment and promote cold air circulation within during winter; moreover in summer, snowsheds stop direct radiation from the sun to the slopes to warm the embankment. Data from an experiment in Bonanza Creek, Alaska, Zarling and Braley (1986) reported a decrease in MAST of the slopes from 3.9 °C to -2.3 °C (after converted from °F) by using snowsheds. Zarling et al., 1983; Lai et al., 2009 discussed the use of thermosyphons and air ducts in road and railway embankments; both methods prevented permafrost degradation in/below the embankments. Esch, 1987; Feklistov and Rusakov, 1996; Liu and Tian, 2002; Wen et al., 2008 examined the use of foam insulation in roadway and airfield embankments in both continuous and discontinuous permafrost regions. Foam insulation reduces heat penetration into foundation soils and therefore it eliminates thawing permafrost.

Air Convection Embankment (ACE) has been used recently by Goering and Kumar (1996); Goering (1998); Goering and Kumar (1999); Binxiang et al. (2007a); Wu et al. (2008); Xu and Goering (2008b); Li (2008) and Cheng (2009) because of its high cooling effectiveness, simple design and low maintenance costs for protection permafrost beneath road or railway embankments in Fairbanks, Alaska and northern China. The working principle of ACE is that it extracts heat from the ground during winter via natural air convection

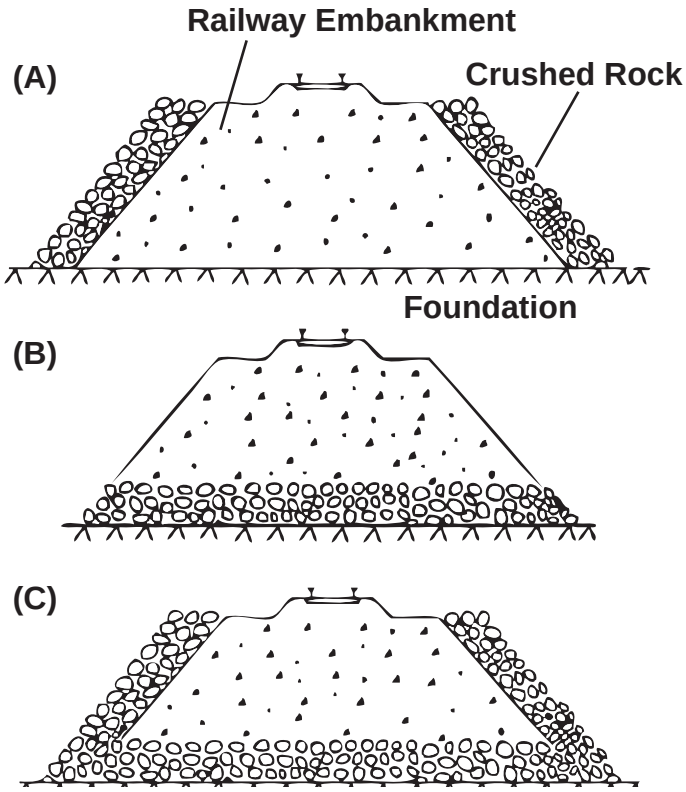

Figure 2.9: Various configurations of ACE for rail roads. (A) "crushed-rock revetment embankment"; (B) "crushed-rock based embankment"; (C) "U-shaped crushed-rock embankment" (modified from Mu et al., 2010).

which can be significant depending on the permeability of ACE. However, during summer heat is transferred into the ground via conduction through an air saturated porous medium having a low thermal conductivity. The imbalance of heat transfer through a year cools the embankment and its foundation soils.

Construction of the Qinghai-Tibet Railway in China provided a remarkable opportunity for researchers to examine cooling effects associated with ACE and other methods for protecting permafrost beneath the railway in a relatively warm permafrost area. Both experimental and numerical studies have been conducted to further understand the theory, to calibrate material properties, as well as, to evaluate long-term maintenance requirements (Liu and Lai, 2005; Zhang et al., 2006; Quan et al., 2006; Sheng et al., 2006; Binxiang et al., 2007a; Wu et al., 2008; Mu et al., 2010; Qin et al., 2010; Sun et al., 2009). Numerical study performed by Liu and Lai (2005) for a "ventilated embankment" combined with a foam layer suggested that the foam layer provided insignificant impacts on the thermal regime of the embankment. Zhang et al. (2006) used numerical modeling to study the performance of air-ducts installed in an embankment and concluded that the foundation of the embankment will remain frozen for the next 50 years under a proposed warming. The study

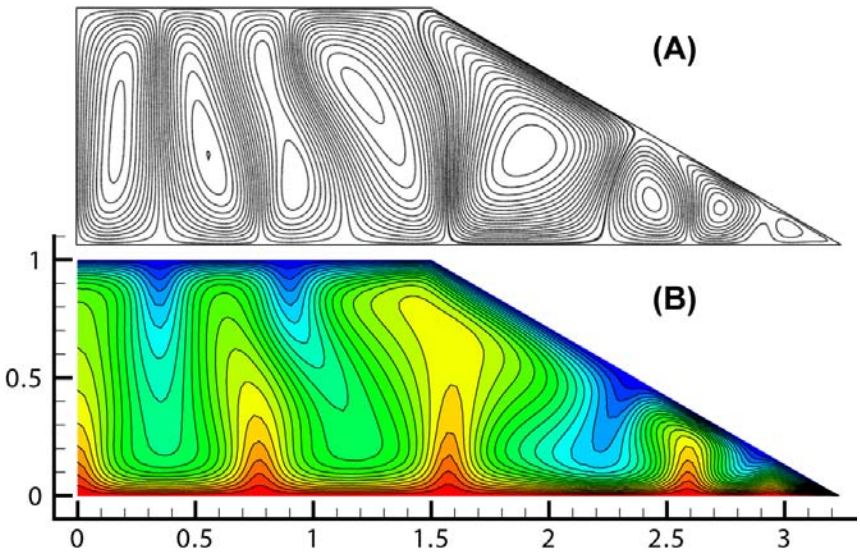

Figure 2.10: Streamlines (A) and Isotherms (B) in an ACE having $Ra = 300$ with closed surface and side slope.

of Quan et al. (2006) found that the use of "sunshade board" installed along the slopes of "a riprap embankment" adequately raised permafrost table and decreased ground temperatures within the foundation. Despite the effectiveness of ACE, Wu et al. (2008) concluded that ACE is only suitable for regions having relatively cold air temperatures. Fig. 2.9 shows various configurations of the Qinghai-Tibet Railway in which the "U-shaped crushed-rock" embankment (Fig. 2.9C) is more effective than the other configurations (Fig. 2.9A and B) (Mu et al., 2010). Fig. 2.10 shows the cooling effects of an embankment at a high Rayleigh number, $Ra = 300$, (calculated through Eqn. 2.8 in Section 2.6) in which cool air sinks to the base and warm air raises to the surface (Fig. 2.10). The alternative cool-sinking and warm-raising air forms convective cells within the embankment to transfer heat vertically from the base.

2.4 ARD in permafrost regions

Mining in permafrost regions of Canada has become important due to the rich natural resources, the increased employment and revenue for the northern peoples. However, ARD is also a major concern to the environment in the permafrost regions which is being affected by climate change and other industrial activities. Therefore, the mining industry must demonstrate that it utilizes the most feasible and environmental friendly technology to eliminate environmental impacts associated with ARD of mine waste and mining activities. In continuous permafrost regions, cold temperatures provides an exceptional mean for the treatment of ARD, that is permafrost encapsulation of reactive waste rock (Arenson and Sego, 2007).

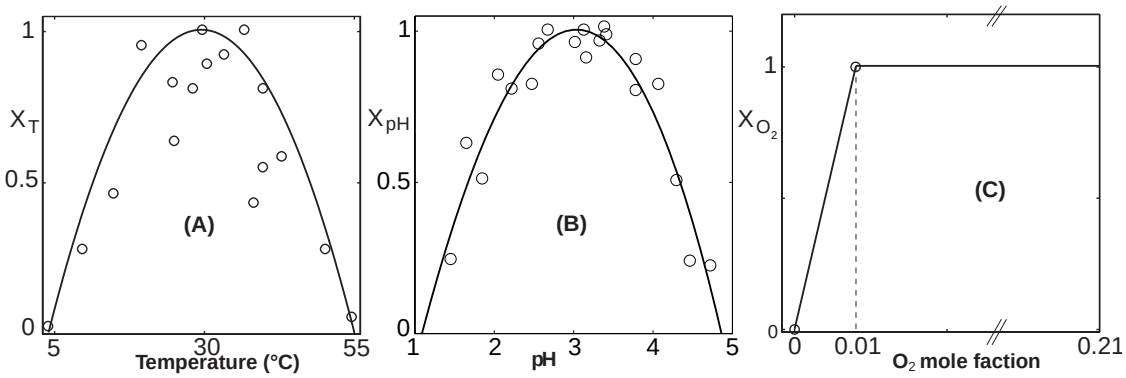

Figure 2.11: The relation between normalized oxidation rate of pyrite with: Temperature (°C) (A), pH (B) and oxygen concentration (C) (modified from Jaynes et al., 1984b).

Oxidation of pyrite is catalyzed by bacteria, which is *Thiobacillus ferrooxidans*, however the population of the bacteria depends on the environment conditions (Lundgren, 1975; Lowson, 1982; Jaynes et al., 1984b). As shown in Fig. 2.11 at temperatures near 0 °C and above 55°C the chemical and biological oxidation of sulfide materials are negligible compared to that at 30 °C. Therefore, if acid potential waste rock is maintained frozen, ARD can be reduced significantly or eliminated. The figure also indicates that pH and oxygen concentration at the oxidation locations can control oxidation rates. In permafrost regions, keeping the reactive waste rock permanently frozen can be achieved by raising the active layer through the waste-rock piles into a soil cover system (insulation cover).

2.4.1 Thermal covers for waste rock in permafrost regions

Waste rock produced by mining is in permafrost regions typically separated into two groups: Potentially Acid Generating (PAG) waste rock that needs to be kept frozen and Non-Acid Generating (NAG) waste rock which can be used as construction materials and may be subjected to freeze and thaw. Interim Closure and Reclamation Plan (ICRP) for the Diavik Diamond Mine presents a closure concept for PAG waste rock using a cover system of two layers including a 1.5-m till layer covered with a 3-m layer of NAG waste rock. Based on numerical models, the prediction was that permafrost will establish in PAG waste rock over the next 25 years after deposit due to the cold climate at the site and the active layer will remain in the cover (NAG waste rock) (Diavik Diamond Mines, 2006).

However, permafrost encapsulation only works efficiently in environments where very cold air temperatures exist and therefore limiting insulation covers (thermal covers) to continuous permafrost regions (Arenson and Sego, 2007). Several insulation cover concepts are shown in Fig. 2.12 and the actual thickness of each layer has to be determined based on site specific conditions. However, the total thickness of the cover may vary between 1.0 and up to 5.0 m which has been used at several mining sites in northern Canada (MEND6.1, 1993). One of the prominent method is Air Convective Cover (ACC) which is based on

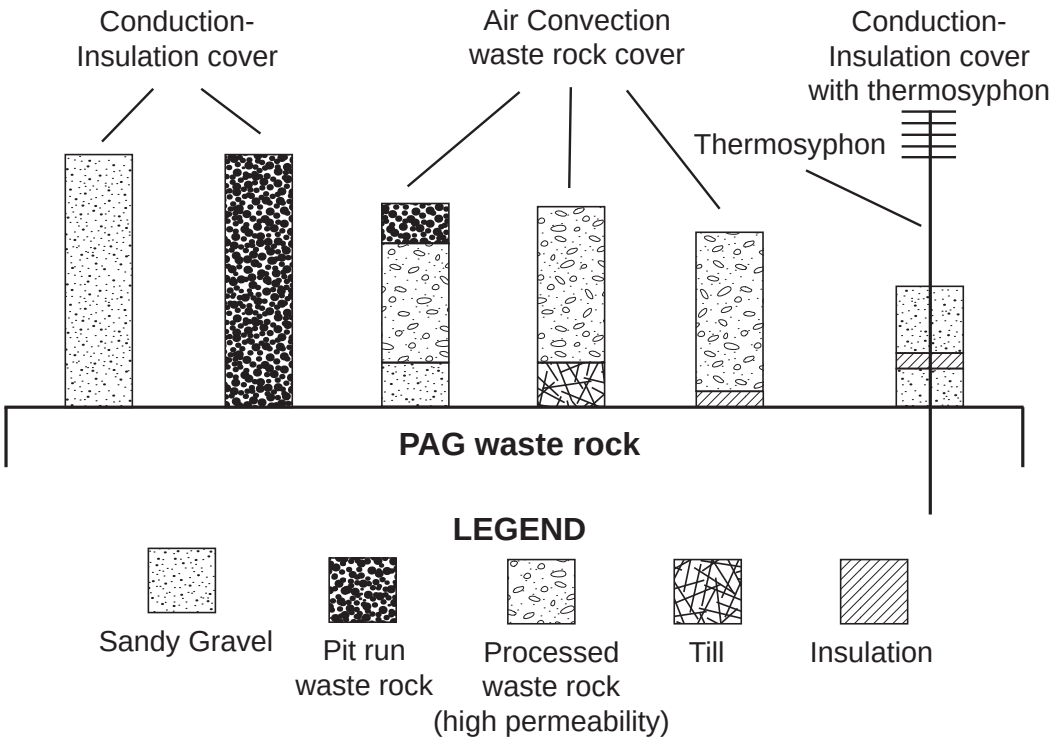

Figure 2.12: Insulation cover concepts for waste rock in permafrost regions (added and modified from MEND6.1, 1993)

ACE (Goering and Kumar, 1996). The main difference between ACC and ACE is that in ACC there is an additional layer of usually low permeability and high moisture (latent heat layer) contain below the high permeability outer layer (Fig. 2.12). This latent heat layer is important as it controls heat penetration and therefore the active layer via latent heat.

2.5 Heat transfer mechanisms in porous medium

Heat transfer through unsaturated/frozen porous waste rock/soils, which include the coexistence of multiphase components such as air, water and ice, under permafrost conditions is complex and three heat transfer/transport modes (conduction, convection and radiation) may be involved.

Conduction is heat transfer in a region where a temperature gradient exists (from high to low temperatures) through vibrational impact of molecules and kinetic impact of molecules (Lunardini, 1981). In porous media, conduction can be complex due to the co-existence of multiphases and the arrangement between them (or texture).

Convection is the transport of heat via a moving fluid in a region having a temperature difference. Due to the associated mass transfer (moving fluid), Lunardini (1981) used the term "energy transport phenomenon" instead of "heat transfer process". There are

two types of convection in a porous medium.

- Forced convection is heat transport in which moving fluid is created by external forces such as wind or pressure variations.
- Free (natural) convection is heat transport in which moving fluid is induced by concentration or temperature gradients, which create density gradients, under a gravity field.

Radiation is heat transfer by electromagnetic radiation when temperature is larger than absolute zero. Within a porous medium, radiation is usually much smaller than conduction or convection and can be neglected (Lunardini, 1981). However in coarse porous materials, such as crushed rock, the radiation between particles can be significant (Côté et al., 2011).

2.6 Natural convection in porous media of single fluid

Theoretical work on natural convection in porous media was initiated by Horton and Rogers Jr. (1945) along with Lapwood (1948) based on the technique developed by Lord Rayleigh (Chandrasekhar, 1961). Nield and Bejan (1999) presented an extensive literature survey focusing on both theoretical and experimental works of convection in porous media (both forced and natural) that have been carried out. Research results were applied to areas such as porous insulation, energy storage, agricultural storage, geothermal reservoirs and other subjects in chemical and mechanical engineering (Bejan and Khair, 1985; Delmas and Wilkes, 1992; Moghtaderi et al., 2000; Binxiang et al., 2005; Helmig et al., 2007a; Domine et al., 2008). In principle, natural fluid convection occurs when an adverse temperature gradient (warm temperature at the bottom and cool temperature at the top) across a porous body is large enough for buoyancy forces to overcome viscous forces in a gravity field (Nield and Bejan, 1999). Fluid in motion at the critical temperature gradient is characterized by stationary convection cells. For the simple case of a single-fluid-saturated porous medium in which Darcy's Law is used to describe the fluid motion and a Boussinesq's approximation of the fluid density; natural convection of fluid in a porous medium is characterized by two nondimensional numbers, namely the Rayleigh and Nusselt numbers (Nield and Bejan, 1999).

2.6.1 Rayleigh number

Rayleigh number Ra is defined as (Nield and Bejan, 1999):

$$Ra = \frac{\rho g \beta K H C_f \Delta T}{\mu \lambda} \tag{2.8}$$

Where ρ is the fluid density, K is the intrinsic permeability of the porous medium, which is independent on the fluid's properties, μ is the fluid dynamic viscosity, g is the gravitational acceleration, β is the coefficient of thermal expansion of the fluid, λ is the effective (bulk) thermal conductivity of the porous medium, ΔT is the temperature difference between the top and bottom surface having a thickness of H, C_f is the volumetric heat capacity of the fluid.

The critical value for the onset of natural convection is $Ra_c = 4\pi^2 = 39.5$ if both boundaries are impermeable in an infinite horizontal porous layer that is heated from below (Nield and Bejan, 1999). Therefore, if the Rayleigh number, Ra, of the fluid-porous medium system calculated though Eqn. 2.8 is less than Ra_c, the heat transfer is dominated by conduction. Straus (1974); Caltagirone (1975); Kimura et al. (1986) reported numerical calculations of natural fluid convection in a rectangle domain filled with a fluid saturated porous medium, impermeable surfaces, insulated lateral walls and heated from below. The following results were obtained:

- For $Ra < 4\pi^2$, heat transfer in the system is dominated by conduction.
- For $4\pi^2 \leq Ra <$ 280 to 400, heat transport is convection via stationary convection cells, the large range of the upper bound is due to the aspect ratios of the domain.
- For $Ra \geq$ 280 to 400, heat transport is convection however a stable convection regime is not reached.

However, the above results are for conducting (constant temperatures) and impermeable surfaces. Depending on given boundary conditions for both mass and heat transfers, the values of Ra_c range between 3 and $4\pi^2$ (Nield and Bejan, 1999). To demonstrate the relation between Ra, the convective flow structures and isotherms, Fig. 2.13 shows the curvature of isotherms and how the fluid velocity increases as Ra increases. In addition, the temperature gradients of the top and bottom boundaries also increase and therefore heat transfer at the boundaries also increases with increasing Ra.

2.6.2 Nusselt number

Nusselt number (Nu) is the other dimensionless number defining the heat transport rate of natural convection. It is the ratio of heat transport with and without convection. Therefore, if there is no natural convection, $Ra \leq Ra_c$, the value of Nu is at a minimum value (i.e. 1); in this case, heat transfer is conduction. When $Ra > Ra_c$, convection initiates and Nu is greater than 1. By using nonlinear theory, Nu can be written as (Nield and Bejan, 1999):

$$Nu = 1 + \sum_{j=1}^{\infty} 2\left(1 - \frac{Ra_{cj}}{Ra}\right) \tag{2.9}$$

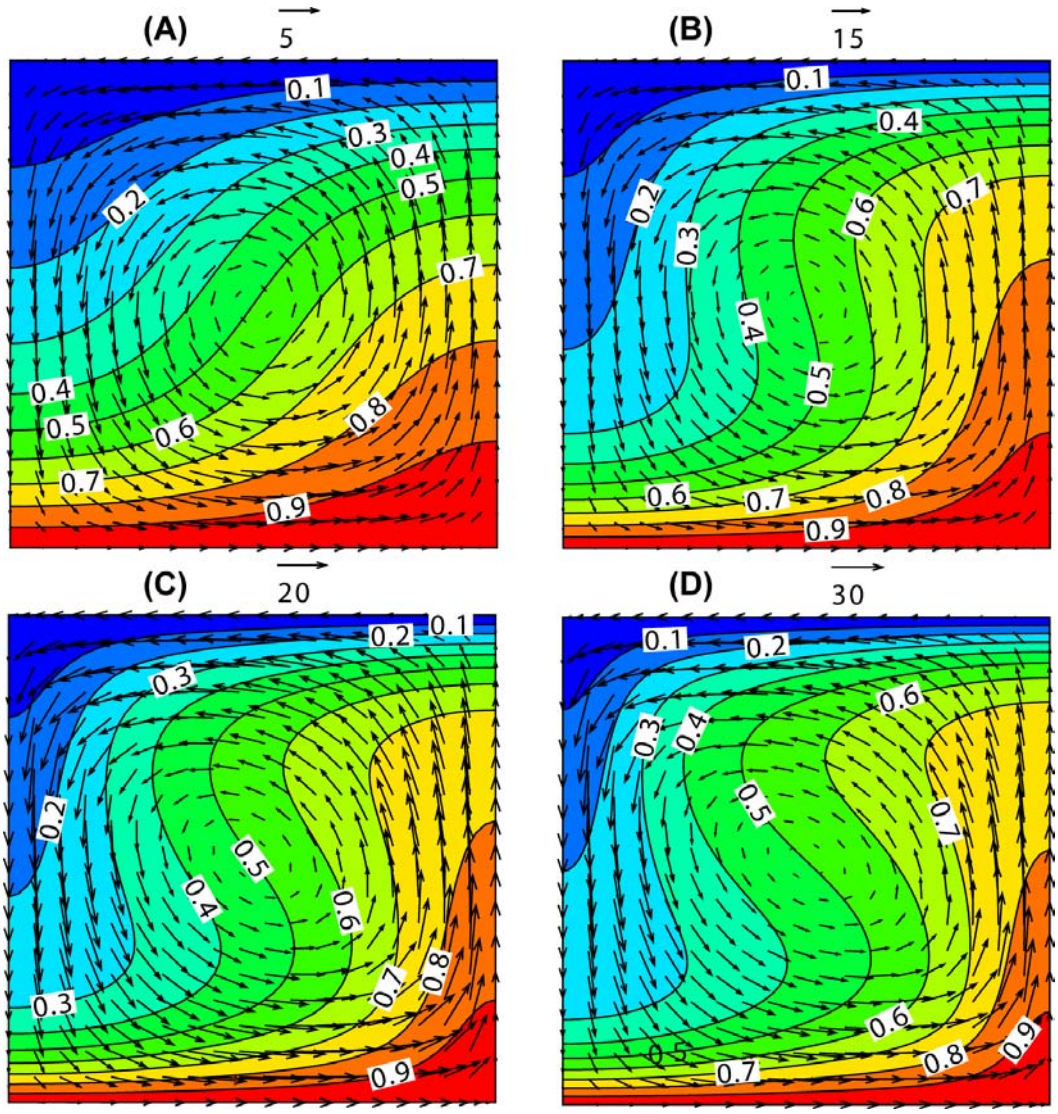

Figure 2.13: Nondimensional isotherms and fluid velocity vectors of a rectangular heated from below with impermeable surfaces at $Ra = 50$ (A), $Ra = 100$ (B) $Ra = 150$ (C) and $Ra = 200$ (D).

Where: $Ra_{cj} = 4j^2\pi^2$, j is an integer, Fig. 2.14A shows the plot of Eqn. 2.9 of mode 1, 2, and 3 in which higher modes resulting in smaller wavelengths (Nield and Bejan, 1999). Experimental and numerical results from several researchers are displayed in Fig. 2.14B.

However, based on experimental results and some of which are shown in Fig. 2.14 B, Wang and Bejan (1987) obtained the $Nu - Ra$ relation based on the Darcy-Forschheimer flow regime and scaling analysis (Eqn. 2.10).

$$Nu = \left\{ \left(\frac{Ra}{40} \right)^{-1.65} + \left[1896.4 \left(Ra\, Pr_p \right)^{1/2} \right]^{-1.65} \right\}^{-1/1.65} \tag{2.10}$$

$$Pr_p = Pr_e \frac{H}{K} \tag{2.11}$$

$$Pr_e = \frac{Pr_f}{c_F} \frac{\lambda_f}{\lambda} \left(\frac{K}{H^2} \right)^{1/2} \tag{2.12}$$

$$Pr_f = \frac{\nu}{\alpha} \tag{2.13}$$

Where Pr_p is the porous medium Prandtl number defined in Eqn. 2.11, Pr_e is an effective Prandtl number as shown in Eqn. 2.12, Pr_f is the fluid Prandtl number (Eqn. 2.13), λ_f and $\lambda = n\lambda_f + (1-n)\lambda_s$ are the fluid and medium thermal (effective) conductivity, n is the porosity of porous medium, λ_s is the thermal conductivity of solids, c_F is the Forschheimer's constant (see formula 1.13 page 10 in Nield and Bejan (1999) for details), ν and α are the kinematic viscosity and thermal diffusivity of the fluid, other parameters were defined in Eqn. 2.8. The relationship Eqn. 2.10 predicts values of Nu that slightly larger than those of Eqn. 2.9 (Nield and Bejan, 1999).

2.7 Importance of convective/advective heat/mass transfer in multiphase porous media

Usually, diffusion/conduction is usually considered to be the main transport mechanism of mass/heat in unsaturated soils or porous media due to its low permeability. However, under some circumstances depending on the geometry of the domain, intrinsic properties of porous materials, internal heat sources and spatial distributions of heat and mass, thermally induced advection/convection may be significant. Furthermore, barometric pressure variations and wind-induced advection are the external forces that can also contribute a significant portion of heat/mass transport through forced convection and soil respiration. However, these mechanisms have just been recognized recently. Zyvoloski (1990) used FEHMN, which is a finite element code for multiphysics phenomena in saturated/unsaturated porous media, to simulate transport processes of the containment of nuclear waste in Yucca Mountain, however due to the highly complex and coupled processes and three-dimensional

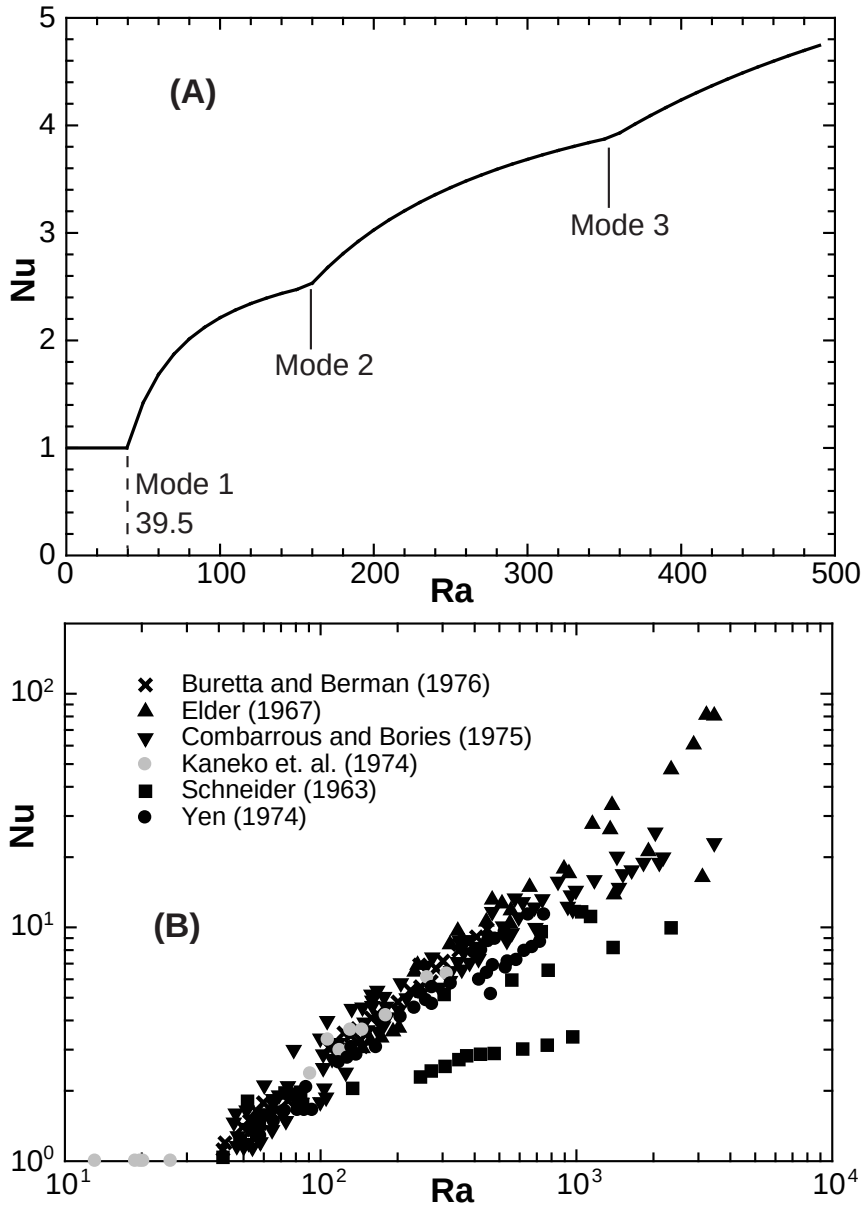

Figure 2.14: The relationship $Nu(Ra)$ described by Eqn. 2.9 (A). Experimental results of Nusselt versus Rayleigh number (B) (data from Sakamoto and Kulacki, 2007).

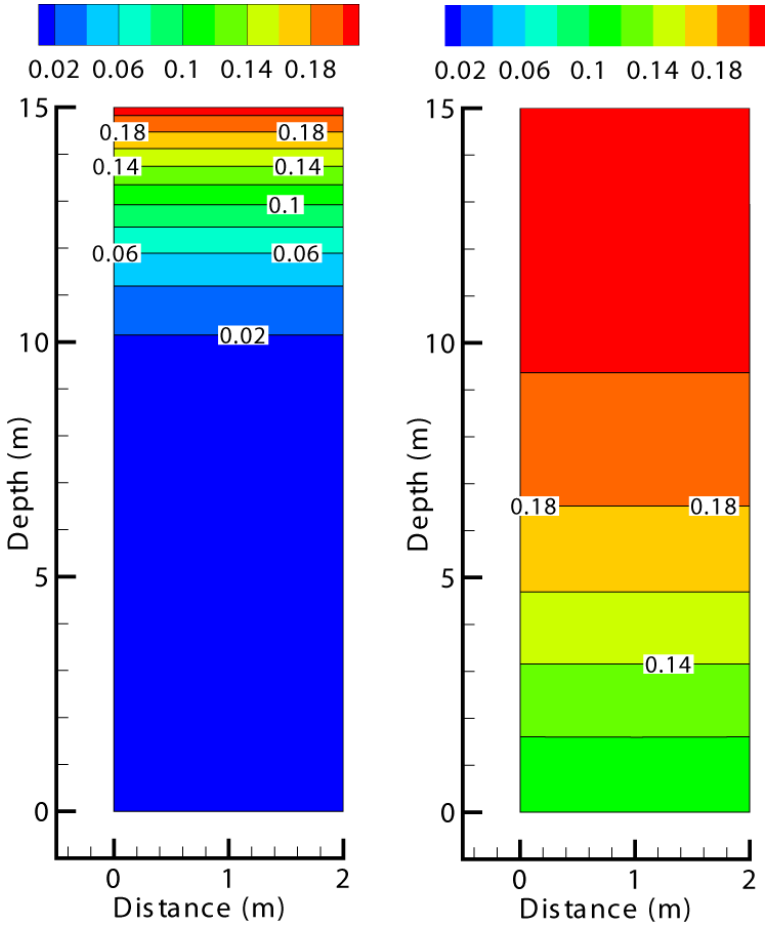

Figure 2.15: Contour of O_2 concentration with depth with (right) and without (left) barometric pumping at the surface at $p_{atm} = 200\sin(2\pi t)(Pa)$

effects, numerical results were not comparable to measured data of temperature and gasflow pattern under some circumstances. Amter et al. (1991) reported numerical simulations to examine the migration of ^{14}C. Their results indicated that air convection cells could be created by a small change of thermal boundary conditions in a relatively large computational domain, width of about 2 km and height of around 500 m. By using numerical modeling, Rose and Guo (1995) concluded that in high permeability unsaturated soils air convection was mainly controlled by buoyancy forces created by temperature gradient and the topographic relief of the dump, which promotes upward air circulation. Wessling (2007) used a numerical approach to examine underground coal fire and showed that permeability must be high ($K \geq 10^{-9}\,\mathrm{m}^2$) to maintain a high oxygen supply via thermally induced convection otherwise convection was so weak.

Massmann and Farrier (1992a); Massman et al. (1997a); Massman (2006a); Neeper (2001, 2002, 2003); Neeper and Stauffer (2005) indicated the impacts of barometric pumping on gas transport in vadose zones (the zones above water table) by using both numerical simulations and analytical analyses. They concluded that the gasflow due to barometric

pumping of the measured range of periods and amplitudes was negligible as the permeability of porous materials in their study was small in the order of $10^{-12}\,m^2$. The permeability of waste rock is about two order of magnitude larger, therefore gasflow due to barometric pumping can be significant. However, the study of this process in waste-rock piles is virtually unavailable in literatures. Fig. 2.15 shows O_2 concentration after 7 days with barometric pressure fluctuations with a period of 1 day. The left figure demonstrates the slow process of O_2 diffusion and the right shows the effectiveness of barometric pumping in the transport of O_2. The studies of multiphase transport processes in unsaturated/fractured rock, which would be used to contain nuclear waste in Yucca Mountain, Nevada were conducted by Tsang and Pruess (1987); Doughty and Pruess (1990, 1991); Huang et al. (1999); Rutqvist et al. (2002); Xu et al. (2008); Tsang et al. (2009). The studies emphasize the importance of gas transport induced by temperature on other processes such as water/vapor and heat transports and they provide not only broad but also deep knowledge of coupled processes occurring in unsaturated/fractured rock, which can be applied for waste-rock piles. Cathles and Apps (1975); Davis and Ritchie (1987); Pantelis and Ritchie (1992); Anne and Pantelis (1997); Moghtaderi et al. (2000); Lefebvre et al. (2001c) presented results of numerical simulations and field data from waste-rock piles. Complex multiphase and multicomponent systems were created including internal heat sources due to ARD and air convection. Natural and forced air convection in these waste-rock piles were significant because of the high permeability of waste rock ($K \geq 10^{-9}\,m^2$). Most of the research on air convection in waste rock focuses on temperature-driven air convection. However, air (gas) density can be varied by the changes of its molar mass via the variations of its components concentrations such as oxygen and/or water vapor, which are common. Furthermore, the heterogeneous nature of waste-rock piles in which there are interbedded layers of fine and coarse rock made the examination of transport processes more complicated (Smith et al., 1995).

2.8 Phase relationships, thermal properties of soil/waste rock

Modeling of heat transfer in soils or waste rock in permafrost regions requires the knowledge of soil thermal properties. Thermal conductivity and heat capacity are the two fundamental thermal properties. Moreover, phase relationships are important to aid the determination of these thermal properties.

2.8.1 Phase relationships

Various volume-mass relationships of unsaturated-frozen soils can be described as (Andersland and Ladanyi, 2004) and schematic diagrams are shown in Fig. 2.16:

- Solid density , ρ_s and dry density, ρ_d

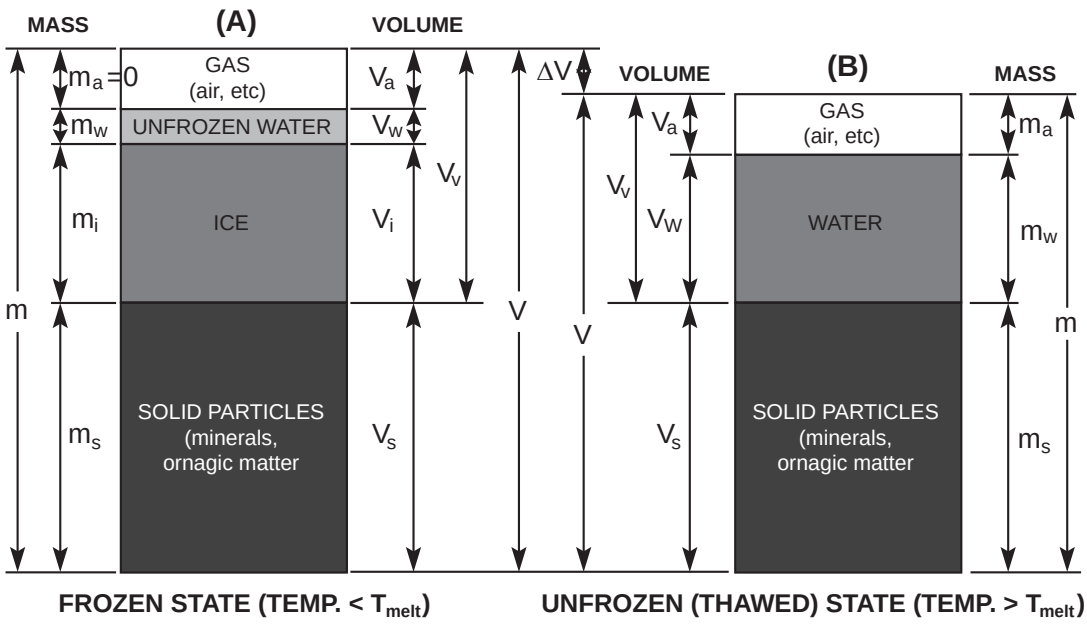

Figure 2.16: Volume-mass relationships (modified from Andersland and Ladanyi, 2004)

$$\text{Solids density} \quad \rho_s = \frac{m_s}{V_s} \tag{2.14}$$

$$\text{Dry density} \quad \rho_d = \frac{m_s}{V} \tag{2.15}$$

- Void ratio, e

$$e = \frac{V_v}{V_s} = \frac{\rho_s}{\rho_d} - 1 \tag{2.16}$$

- Degree of saturation, S_w

$$S_w = \frac{V_w}{V_v} \tag{2.17}$$

Where V_v and V_s are the volume of voids and solids respectively.

- Porosity, n

$$n = \frac{V_v}{V} = \frac{e}{1+e} = 1 - \frac{\rho_s}{\rho_d} \tag{2.18}$$

- Total gravimetric water content, w

$$w = \frac{m_w + m_i}{m_s} = w_w + w_i \tag{2.19}$$

Where w_w is the gravimetric unfrozen water content; w_i is the gravimetric ice water content.

- Bulk density (frozen and unfrozen), ρ

$$\rho = \frac{m}{V} = \frac{m_w + m_i + m_s}{V} = \rho_d (1 + w) \tag{2.20}$$

- Specific gravity of soil solids, G_s

$$G_s = \frac{\rho_s}{\rho_w} \tag{2.21}$$

2.8.2 Thermal conductivity

Effective (bulk) thermal conductivity, λ which has a unit of $\mathrm{W}/(\mathrm{m}\cdot\mathrm{K})$, of a multiphase system like frozen or thawed, unsaturated soils or waste rock is a function of density, porosity, water content (or ice content), the structure of soil particles (or soil's texture) and thermal conductivity of each component. In a frozen state, ice content and unfrozen waster are a function of temperature and this induces an additional challenge when measuring λ. The most common methods used to determine λ are expressed below.

2.8.2.1 Johansen (1975) method

The method expresses λ through normalized thermal conductivity λ_r (Kersten's number) which is a function of dry, λ_{dry}, and saturated, λ_{sat}, thermal conductivity as:

$$\lambda = \left(\lambda_{sat} - \lambda_{dry}\right) \lambda_r + \lambda_{dry} \tag{2.22}$$

Where:
Natural soils

$$\lambda_{dry} = \frac{0.135\rho_d + 64.7}{2700 - 0.947\rho_d}\ \mathrm{W}/(\mathrm{m}\cdot\mathrm{K}) \tag{2.23}$$

Crushed rocks

$$\lambda_{dry} = 0.039\, n^{-2.2}\ \mathrm{W}/(\mathrm{m}\cdot\mathrm{K}) \tag{2.24}$$

Saturated unfrozen soils

$$\lambda_{sat} = 0.57^n \lambda_s^{1-n} \tag{2.25}$$

Saturated frozen soils

$$\lambda_{sat} = 2.2^n \lambda_s^{1-n} 0.269^{w_w} \tag{2.26}$$

Johansen (1975) provided relations between λ_r and the degree of saturation S_w as:
Coarse unfrozen soils

$$\lambda_r = 0.7 \log S_w + 1.0 \tag{2.27}$$

Fine unfrozen soils

$$\lambda_r = \log S_w + 1.0 \tag{2.28}$$

Other types of frozen soil: $\lambda_k = S_w$.

Côté and Konrad (2005a) expanded the Johansen (1975) method and reported more relevant relations between S_w and λ_r for "coarse-base materials". The relations were based on the results of almost 200 tests as the followings.

Unfrozen

$$\lambda_r = \frac{4.7 S_w}{1 + 3.7 S_w} \tag{2.29}$$

Frozen

$$\lambda_r = \frac{1.8 S_w}{1 + 0.8 S_w} \tag{2.30}$$

2.8.2.2 Kersten (1949) method

The method was based on test results of natural soils and crush rock at both frozen (−4 °C) and thaw (+4 °C) conditions. The equations are expressed in SI units as (Farouki, 1981b).

Fine-grain soils (silty clay)

- Unfrozen

$$\lambda = 0.1442 \left[0.9 \log w_w - 0.2\right] \times 10^{0.6243 \rho_d} \tag{2.31}$$

- Frozen

$$\lambda = 0.001442 \times 10^{1.373 \rho_d} + \left(0.01226 \times 10^{0.4994 \rho_d}\right) w_w \tag{2.32}$$

Coarse-gain soils (sandy soils)

- Unfrozen (Fig. 2.17A)

$$\lambda = 0.1442 \left[0.7 \log w_w + 0.4\right] \times 10^{0.6243 \rho_d} \tag{2.33}$$

- Frozen (Fig. 2.17B)

$$\lambda = 0.01096 \times 10^{0.8116 \rho_d} + \left(0.00461 \times 10^{0.9115 \rho_d}\right) w_w \tag{2.34}$$

Care must be taken when applying Kersten (1949) equations to coarse-grain materials due to the discrepancy between measurements and these equations, however these equations give reasonable results for fine-grain soils.

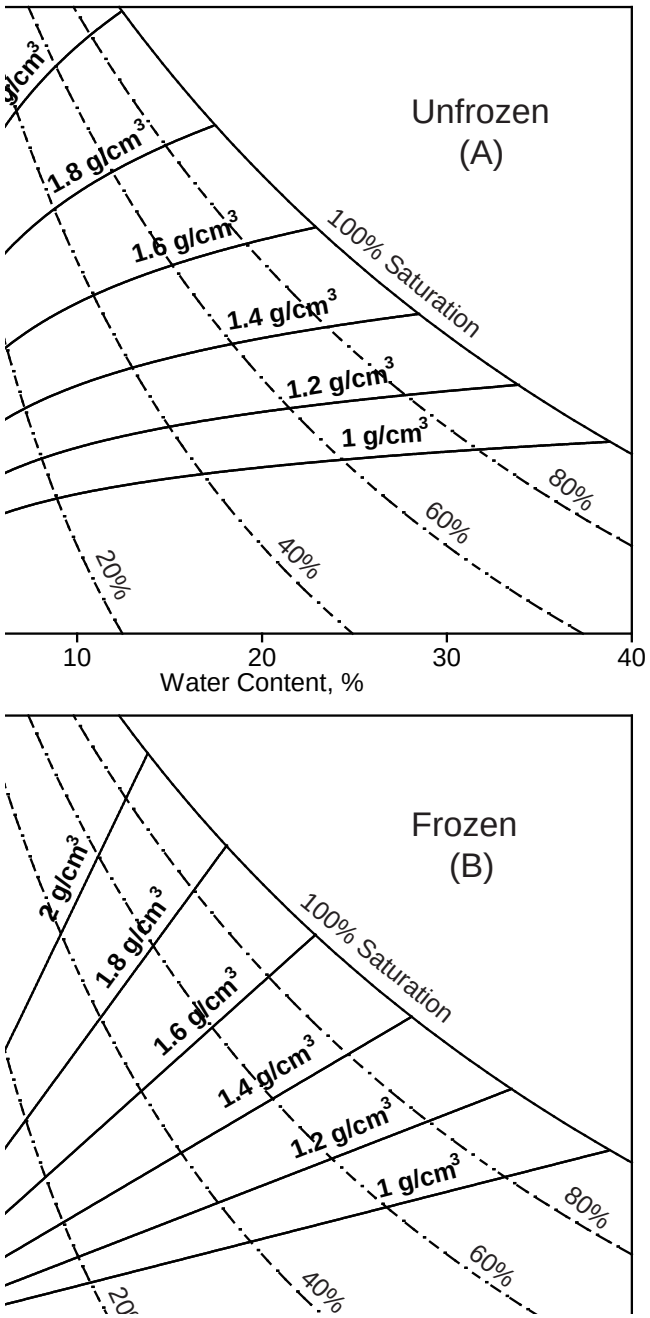

Figure 2.17: Thermal conductivity of unfrozen (A) and frozen (B) sandy soils with specific gravity of soil solid $G_s = 2.65$.

2.8.3 Heat capacity

Heat required to increase temperature of a material by one degree is called heat capacity and heat capacity can be determined through mass or volume. When it is based on mass, it is called specific heat capacity and represented by a lower case c $(\mathrm{J}/(\mathrm{kg}\cdot\mathrm{K}))$. If it is based on volume, it is called volumetric heat capacity with a capital $C = c\rho$ $\left(\mathrm{J}/\left(\mathrm{m}^3\cdot\mathrm{K}\right)\right)$. The volumetric heat capacity of multiphase materials (such as soils or porous media) can be computed by adding the volumetric heat capacity of each component (Lunardini, 1981).

$$C = \sum_{i=1}^{n} C_i \theta_i \quad \left(\mathrm{J}/\left(\mathrm{m}^3\cdot\mathrm{K}\right)\right) \tag{2.35}$$

Where θ_i and C_i are the volume fraction and volumetric heat capacity of component i in soils.

Neglecting air heat capacity, the volumetric heat capacity is defined as:

$$C = \rho_d \left(c_s + c_w w_w + c_i w_i\right) \quad \left(\mathrm{kJ}/\left(\mathrm{m}^3\cdot\mathrm{K}\right)\right) \tag{2.36}$$

Where c_s is the specific heat capacity of solid phase, $c_w = 4184$ and $c_i = 2100$ $\left(\mathrm{kJ}/\left(\mathrm{m}^3\cdot\mathrm{K}\right)\right)$ are the specific heat capacity of water and ice respectively, w_w and w_i are unfrozen water and ice content. During freezing, where pore water in soil changes its phase with temperature, the volumetric heat capacity must include a component accounting for latent heat of fusion at the phase change temperature (i.e. 0 °C). Thus, the apparent volumetric heat capacity of soils accounting for this phase change is defined as (Lunardini, 1981):

$$\overline{C} = C + L_f \rho_d \frac{\partial w_w}{\partial T} \tag{2.37}$$

or

$$\overline{C} = \rho_d \left(c_s + 4184\, w_w + 2100\, w_i + L_f \frac{\partial w_w}{\partial T}\right) \tag{2.38}$$

Where L_f $(\mathrm{kJ}/\mathrm{kg})$ is the latent heat of fusion for water and $\dfrac{\partial w_w}{\partial T}$ is the rate of change of unfrozen water content with temperature.

2.9 Summary

Various aspects of the literature related to research objectives were presented although mathematical details related to multiphase heat and mass transfer and linear stability analysis for the onset of heat convection in porous medium will be discussed later.

Fundamental aspects of permafrost engineering, phase relations, thermal properties of multiphase porous medium, acid rock drainage (ARD) of waste-rock piles and potential mitigated techniques for ARD in continuous permafrost regions were given. A prominent

technique for reducing ARD in waste-rock piles via maintaining permafrost within waste rock is air convective cover (ACC) which is simple in design and has a low long-term cost of maintenance. It is based on the well established theory, proven in laboratory tests and recent success in the protection of permafrost foundation under embankments.

The importance of air convection/advection (due to natural air convection, wind-induced advection and barometric pressure variation) in partially saturated porous media was also discussed as air convection/advection transports both heat and mass. Air convection/advection carries oxygen-rich air into oxidation/combustion sites and therefore it enhances oxidation/combustion rates resulting in high temperatures. Even though there are no heat production due to oxidation or combustion, strong air convection/advection can alter the internal thermal field within a waste-rock pile.

References

Amter, S., Lu, N., and Ross, B. (1991). Thermally driven gas flow beneath Yucca mountain, Nevada. *Multiphase Transport in Porous Media*, HTD-Vol. 186:17–23.

Andersland, O. B. and Ladanyi, B. (2004). *Frozen Ground Engineering*. John Wiley & Sons.

Anne, R. and Pantelis, G. (1997). Coupled natural covection and atmosphere wind forced advection in above ground reacting heaps. In *Inter Conf on CFD in Mineral Processing and Power Generation, CSIRO*.

Arenson, L. and Sego, D. (2007). Protection of mine waste tailing ponds using cold air convection. Assessment and Remediation of Contaminated Sites in Arctic and Cold Climates.

Azam, S., Wilson, G., Herasymuik, G., Nichol, C., and Barbour, L. (2007). Hydrogeological behaviour of an unsaturated waste rock pile: A case study at the Golden Sunlight Mine, Montana, USA. *Bulletin of Engineering Geology and the Environment*, 66(3):259–268.

Bates, R. E. and Bilello, M. A. (1966). Defining the cold regions of the northern hemisphere. Technical report, Cold Regions Research And Engineering Lab Hanover N H.

Bejan, A. and Khair, K. R. (1985). Heat and mass transfer by natural convection in a porous medium. *International Journal of Heat and Mass Transfer*, 28(5):909–918.

Binxiang, S., Lijun, Y., and Xuezu, X. (2007a). Onset and evaluation on winter-time natural convection cooling effectiveness of crushed-rock highway embankment. *Cold Regions Science and Technology*, 48(3):218 – 231.

Binxiang, S., Xuezu, X., Yuanming, L., and Mengxia, F. (2005). Evaluation of fractured rock layer heights in ballast railway embankment based on cooling effect of natural convection in cold regions. *Cold Regions Science and Technology*, 42(2):120 – 144.

Blight, G. (2010). *Geotechnical Engineering for Mine Waste Storage Facilities*. CRC Press.

Caltagirone, J. P. (1975). Thermoconvective Instabilities In A Horizontal Porous Layer. *Journal Of Fluid Mechanics*, 72(NOV25):269–287.

Canada, M. (2009). Two million tonnes a day - a mine waste primer.

Cathles, L. and Apps, J. (1975). A model of the dump leaching process that incorporates oxygen balance, heat balance, and air convection. *Metallurgical and Materials Transactions B*, 6:617–624. 10.1007/BF02913857.

Chandrasekhar, S. (1961). *Hydrodynamic and Hydromagnetic Stability*. Oxford At The Clarendon Press.

Cheng, G., W. Q. M. W. (2009). Innovative designs of permafrost roadbed for the Qinghai-

Tibet Railway. *Science in China, Series E: Technological Sciences*, 52(2):530–538. cited By (since 1996) 2.

Côté, J., Fillion, M.-H., and Konrad, J.-M. (2011). Intrinsic permeability of materials ranging from sand to rock-fill using natural air convection tests. *Canadian Geotechnical Journal*, 48(5):679–690.

Côté, J. and Konrad, J.-M. (2005a). Thermal conductivity of base-course materials. *Canadian Geotechnical Journal*, 42:61–78(18).

Davis, G. B. and Ritchie, A. I. M. (1987). Model of oxidation in pyrite mine wastes: Importance of particle size distribution. *Applied Mathematical Modelling*, 11(6):417–422.

Davis, N. (2001). *Permafrost: A Guide to Frozen Ground in Transition*. University of Alaska Press.

Delmas, A. and Wilkes, K. (1992). Numerical analysis of heat transfer by conduction and natural convection in loose-fill fiberglass insulation–effects of convection on thermal performance. Technical report.

Domine, F., Albert, M., Huthwelker, T., Jacobi, H.-W., Kokhanovsky, A., Lehning, M., Picard, G., and Simpson, W. (2008). Snow physics as relevant to snow photochemistry. *Atmos. Chem. Phys.*, 8(2):171–208.

Doughty, C. and Pruess, K. (1990). Similarity solution for two-phase fluid and heat flow near high-level nuclear waste packages emplaced in porous media. *International Journal of Heat and Mass Transfer*, 33(6):1205 – 1222. Nuclear Waste Deposits;Similarity Solutions;Waste Emplacement;.

Doughty, C. and Pruess, K. (1991). Mathematical model for two-phase water, air, and heat flow around a linear heat source emplaced in a permeable medium. volume 87, pages 256 – 265, Minneapolis, MN, USA. Heat Flow;Linear Heat Source;Nuclear Waste Repository;Numerical Simulator TOUGH2;Similarity Solution;.

Esch, D. and Osterkamp, T. (1990). Cold Regions Engineering: Climatic Warming Concerns for Alaska. *Journal of Cold Regions Engineering*, 4(1):6–14.

Esch, D. C. (1987). Insulation performance beneath roads and airfields in Alaska. Technical report, Transportation Research Record, 1146, Transportation Research Board, Washington, D.C.

Esch, D. C. (1988). Roadway Embankments on Warm Permafrost Problems and Remedial Treatments. In *Permafrost Proceedings, Fifth International Conference*.

Evangelou, V. P. (1995). *Pyrite oxidation and its control (p. 293)*. Boca Raton: CRC Press Inc.

Farouki, O. T. (1981b). *Thermal properties of soils*. United States Army Corps of Engineers, Cold Regions Research and Engineering Laboratory, Hanover, New Hampshire,

USA.

Feklistov, V. N. and Rusakov, N. L. (1996). Application of foam insulation for remediation of degraded permafrost. *Cold Regions Science and Technology*, 24(2):205–212.

Geological Survey of Canada, N. R. C. (2007). Permafrost: Where does it occur?

Goering, D. and Kumar, P. (1999). Permeability effects on winter-time natural convection in gravel embankments. In Hutter, K., Wang, Y., and Beer, H., editors, *Advances in Cold-Region Thermal Engineering and Sciences*, volume 533 of *Lecture Notes in Physics*, pages 455–464. Springer Berlin / Heidelberg. 10.1007/BFb0104203.

Goering, D. J. (1998). Experimental investigation of air convection embankments for permafrost-resistant roadway design. In *Seven International Conference on Permafrost*.

Goering, D. J. and Kumar, P. (1996). Winter-time convection in open-graded embankments. *Cold Regions Science and Technology*, 24(1):57–74.

Helmig, D., Bocquet, F., Cohen, L., and Oltmans, S. (2007a). Ozone uptake to the polar snowpack at Summit, Greenland. *Atmos. Environ.*, 41(24):5061–5076.

Hinkel, K. M., Smith, O., Nelson, F. E., Tucker, W., Parker, W., Vinson, T., Romanovsky, V., and Brigham, L. W. (2003). Climate Change, Permafrost, and Impacts on Civil Infrastructure. Technical report, U.S. Arctic Research Commission.

Horton, C. and Rogers Jr., F. (1945). Convection currents in a porous medium. *Journal of Applied Physics*, 16(6):367–370.

Huang, K., Tsang, Y., and Bodvarsson, G. (1999). Simultaneous inversion of air-injection tests in fractured unsaturated tuff at Yucca Mountain. *WATER RESOURCES RESEARCH*, 35(8):2375–2386.

Jaynes, D. B., Rogowski, A. S., and Pionke, H. B. (1984b). Acid mine drainage from reclaimed coal strip mines: 1. Model description. *Water Resour. Res.*, 20:233–242.

Johansen, O. (1975). *Thermal conductivity of soils*. PhD thesis, Institute for Cold Technology, Norwegian Institute of Technology (NTH).

Kersten, M. (1949). Laboratory research for the determination of the thermal properties of soils. Technical report, University of Minnesota, Engineering Experiment Station, Bulletin No. 28.

Kimura, S., Schubert, G., and Straus, J. M. (1986). Route to chaos in porous-medium thermal convection. *Journal of Fluid Mechanics*, 166:305–324.

Lai, Y., Guo, H., and Dong, Y. (2009). Laboratory investigation on the cooling effect of the embankment with L-shaped thermosyphon and crushed-rock revetment in permafrost regions. *Cold Regions Science and Technology*, 58(3):143–150.

Lapwood, E. R. (1948). Convection of a fluid in a porous medium. *Mathematical Proceed-*

ings of the Cambridge Philosophical Society, 44(04):508–521.

Lefebvre, R., Hockley, D., Smolensky, J., and Gelinas, P. (2001b). Multiphase transfer processes in waste rock piles producing acid mine drainage: 1: Conceptual model and system characterization. *Journal of Contaminant Hydrology*, 52(1-4):137–164.

Lefebvre, R., Hockley, D., Smolensky, J., and Lamontagne, A. (2001c). Multiphase transfer processes in waste rock piles producing acid mine drainage. 2. Applications of numerical simulation. *Journal of contaminant hydrology*, 52(1-4):165–186.

Li, G.a, L. N. b. K. J. N. F. Y. W. S. L. B. G. (2008). Study on design optimization of a crushed stone layer with shading board placed on a railway embankment on warm permafrost. *Cold Regions Science and Technology*, 54(1):36–43. cited By (since 1996) 3.

Liu, J. and Tian, Y. (2002). Numerical studies for the thermal regime of a roadbed with insulation on permafrost. *Cold Regions Science and Technology*, 35(1):1–13.

Liu, Z. and Lai, Y. (2005). Numerical analysis for the ventilated embankment with thermal insulation layer in Qinghai-Tibetan railway. *Cold Regions Science and Technology*, 42(3):177–184.

Lowson, R. T. (1982). Aqueous oxidation of pyrite by molecular oxygen. *Chemical Reviews*, 82(5):461–497.

Lunardini, V. J. (1981). *Heat transfer in cold climates*. Van Nostrand Reinhold Company.

Lundgren, D. (1975). Microbiological problems in strip mine areas: Relationship to the metabolism of Thiobacillus ferrooxidans. pages –.

Massman, W. (2006a). Advective transport of CO_2 in permeable media induced by atmospheric pressure fluctuations: 1. An analytical model. *J. Geophys. Res. G Biogeosci.*, 111(3):–.

Massman, W., Sommerfeld, R., Mosier, A., Zeller, K., Hehn, T., and Rochelle, S. (1997a). A model investigation of turbulence-driven pressure-pumping effects on the rate of diffusion of CO2, N2O, and CH4 through layered snowpacks. *J. Geophys. Res. D Atmos.*, 102(15):18851–18863.

Massmann, J. and Farrier, D. F. (1992a). Effects of atmospheric pressures on gas transport in the vadose zone. *Water Resour. Res.*, 28(3):777–791.

MEND6.1 (1993). Preventing AMD by disposing of reactive tailings in permafrost. Technical report, Mine Environment Neutral Drainage (MEND).

Mines, D. D. (2006). Interim closure and reclamation plan. *Report ICRP Sep2006 Submitted to Wekeezhii Land and Water Board*.

Moghtaderi, B., Dlugogorski, B., and Kennedy, E. (2000). Effects of wind flow on self-heating characteristics of coal stockpiles. *Process Safety and Environmental Protection*,

78(6):445 – 453.

Moncur, M., Ptacek, C., Blowes, D., and Jambor, J. (2005). Release, transport and attenuation of metals from an old tailings impoundment. *Applied Geochemistry*, 20(3):639–659.

Mu, Y., Ma, W., Liu, Y., and Sun, Z. (2010). Monitoring investigation on thermal stability of air-convection crushed-rock embankment. *Cold Regions Science and Technology*, 62(2-3):160–172.

Neeper, D. A. (2001). A model of oscillatory transport in granular soils, with application to barometric pumping and earth tides. *Journal of Contaminant Hydrology*, 48(3-4):237–252.

Neeper, D. A. (2002). Investigation of the vadose zone using barometric pressure cycles. *Journal of Contaminant Hydrology*, 54(1-2):59–80.

Neeper, D. A. (2003). Harmonic analysis of flow in open boreholes due to barometric pressure cycles. *Journal of Contaminant Hydrology*, 60(3-4):135–162.

Neeper, D. A. and Stauffer, P. (2005). Unidirectional gas flow in soil porosity resulting from barometric pressure cycles. *Journal of Contaminant Hydrology*, 78(4):281–289.

Nelson, F. E., Brigham, L. W., Hinkel, K. M., Smith, O., Parker, W., Tucker, W., Romanovsky, V. E., Vinson, T., Shiklomanov, N. I., Cole, D. M., Lee, W., Klene, A. E., and Saxton, A. (2003). Climate Change, Permafrost, and Impacts on Civil Infrastructure. Technical report, U.S. Arctic Research Commission.

Nield, D. and Bejan, A. (1999). *Convection in porous media*. Springer, New York.

Nordstrom, D. K. and Alpers, C. N. (1999). Negative pH, efflorescent mineralogy, and consequences for environmental restoration at the Iron Mountain Superfund site, California. *Proceedings of the National Academy of Sciences of the United States of America*, 96(7):3455–3462.

Pantelis, G. and Ritchie, A. I. M. (1992). Rate-limiting factors in dump leaching of pyritic ores. *Applied Mathematical Modelling*, 16(10):553–560.

Qin, Y., Zhang, J., Li, G., and Qu, G. (2010). Settlement characteristics of unprotected embankment along the Qinghai-Tibet Railway. *Cold Regions Science and Technology*, 60(1):84–91.

Quan, X., Li, N., and Li, G. (2006). A new ripraped-rock slope for high temperature permafrost regions. *Cold Regions Science and Technology*, 45(1):42–50.

Rekacewicz, P. (2005). Permafrost distribution in the Arctic. UNEP/GRID-Arendal Maps and Graphics Library.

Romanovsky, V., Sergueev, D., and Osterkamp, T. (2003). Temporal variations in the active layer and near-surface permafrost temperatures at the long-term observatories in northern Alaska. In Phillips, M., S. S. and Arenson, L. U., editors, *Permafrost*, pages 989–994.

Swets & Zeitlinger, Lisse.

Romanovsky, V. E., Gruber, S., Instanes, A., Jin, H., Marchenko, S. S., Trombotto, D., and Walter, K. M. (2007). Global outlook for Ice and Snow: Frozen Ground. Technical report, United Nations Environment Programme.

Rose, A. W. and Guo, W. (1995). Thermal convection of soil air on hillsides. *Environmental Geology*, 25:258–262. 10.1007/BF00766755.

Rutqvist, J., Wu, Y., Tsang, C., and Bodvarsson, G. (2002). A modeling approach for analysis of coupled multiphase fluid flow, heat transfer, and deformation in fractured porous rock. *INTERNATIONAL JOURNAL OF ROCK MECHANICS AND MINING SCIENCES*, 39(4):429–442.

Sakamoto, H. and Kulacki, F. A. (2007). Buoyancy driven flow in saturated porous media. *J. Heat Transfer*, 129(6):727–734.

Sheng, Y., Wen, Z., Ma, W., Liu, Y., Qi, J., and Wu, J. (2006). Long-term evaluations of insulated road in the Qinghai-Tibetan plateau. *Cold Regions Science and Technology*, 45(1):23–30.

Singer, P. C. and Stumm, W. (1970). Acidic Mine Drainage: The Rate-Determining Step. *Science*, 167(3921):1121–1123.

Smith, L., Lopez, D., Beckie, R., Morin, K., Dawson, R., and Price, W. (1995). Hydrogeology of waste rock dumps. Technical report, Department of Natural Resources Canada, Ottawa, Ontario, Canada.

Smith, M. W. and Riseborough, D. W. (1996). Permafrost monitoring and detection of climate change. *Permafrost Periglac. Process.*, 7(4):301–309.

Straus, J. M. (1974). Large amplitude convection in porous media. *Journal of Fluid Mechanics*, 64(01):51–63.

Sun, B., Yang, L., Liu, Q., Wang, W., and Xu, X. (2009). Numerical analysis for critical thickness of crushed rock revetment layer on Qinghai-Tibet Railway. *Cold Regions Science and Technology*, In Press, Corrected Proof:–.

Tsang, Y. and Pruess, K. (1987). Study of thermally induced convection near a high-level nuclear waste repository in partially saturated fractured tuff. *Water Resources Research*, 23(10):1958–1966.

Tsang, Y. W., Birkholzer, J. T., and Mukhopadhyay, S. (2009). Modeling of thermally driven hydrological processes in partially saturated fractured rock. *Rev. Geophys.*, 47(3):RG3004–.

Van Zyl, D. (1993). Mine waste disposal. In *Geotechnical practice for waste disposal, Edited by David Edwin Daniel*.

Wang, M. and Bejan, A. (1987). Heat transfer correlation for Benard convection in a

fluid saturated porous layer. *International Communications in Heat and Mass Transfer*, 14(6):617 – 626.

Wen, Z., Sheng, Y., Ma, W., and Qi, J. (2008). In situ experimental study on thermal protection effects of the insulation method on warm permafrost. *Cold Regions Science and Technology*, 53(3):369–381.

Wessling, S. (2007). *The investigation of underground coal fires - towards a numerical approach for thermally, hydraulically, and chemically coupled processes*. PhD thesis, University of Munster.

Wu, Q., Lu, Z., Tingjun, Z., Ma, W., and Liu, Y. (2008). Analysis of cooling effect of crushed rock-based embankment of the Qinghai-Xizang Railway. *Cold Regions Science and Technology*, 53(3):271–282.

Xu, J. and Goering, D. J. (2008b). Experimental validation of passive permafrost cooling systems. *Cold Regions Science and Technology*, 53(3):283–297.

Xu, T., Senger, R., and Finsterle, S. (2008). Corrosion-induced gas generation in a nuclear waste repository: Reactive geochemistry and multiphase flow effects. *APPLIED GEOCHEMISTRY*, 23(12):3423–3433.

Zarling, J. P. and Braley, W. A. (1986). Thaw stabilization of roadway embankments constructed over permafrost. Technical report, Rep. No. FHWA-AK-RD-87-20, Federal Highway Administration, Washington, D.C.

Zarling, J. P., Connor, B., and Goering, D. (1983). Air duct systems for roadway stabilization over permafrost areas. In *Interim Study Reports As Presented to the 4th International Conference On Permafrost*.

Zhang, M., Lai, Y., Niu, F., and He, S. (2006). A numerical model of the coupled heat transfer for duct-ventilated embankment under wind action in cold regions and its application. *Cold Regions Science and Technology*, 45(2):103–113.

Zhang, T. (1998). Global annual freezing and thawing indices. Technical report, National Snow and Ice Data Center, Boulder, CO, USA.

Zyvoloski, G. (1990). Simulation of heat transfer in the unsaturated zone. In *International High Level Radioactive Waste Management Conference, Las Vegas, Nevada*.

CHAPTER 3

Thermal conductivity and grain size distribution of waste rock at Diavik

3.1 Introduction

Waste-rock piles pose a potential environmental-related problems consisting of acid rock drainage (ARD), leaching of metals, erosion, slope stability, and others. Waste rock usually consists of a wide ranges of particle sizes as a result of the blasting of the overburden rock consisting of fine particles (silt sizes or smaller, $\leq$0.02 mm) to boulder ($\geq$1 m in diameter). Construction methods can influence the particle size distribution and the heterogeneity of waste-rock piles (Smith et al., 1995; Azam et al., 2007). The most commonly used method is end-dumping that generally creates segregation of materials along the dump face. The regions near and at the toe of waste-rock piles usually consist of coarse rock and have much higher permeability due to traffic compaction (Smith et al., 1995; Azam et al., 2007), which can support air convection/advection created by wind, barometric pumping, and buoyancy forces (Amos et al., 2009a). Meanwhile, the upper surface and the top layers of waste-rock piles consist of fine-grained soils and have much lower permeability (Smith et al., 1995) therefore diffusion of mass and conduction of heat dominate these zones (Lefebvre et al., 2001a). Waste rock can be classified as "rock-like" ($<$20% passing of 2 mm sieve) or "soil-like" ($\geq$20% passing of 2 mm sieve) materials (Dawson and Morgenstern, 1995). As a result, the upper zones of waste-rock piles are more "soil-like" meanwhile the lower zones tend to be more "rock-like".

When a waste-rock pile is constructed in a permafrost region, it is vital to know thermal properties of the waste-rock pile for thermal transports as well as its hydrogeological properties for the determination of water/pollutant transports. Because water/pollutant transports in this waste-rock pile are thermally controlled as freezing waste rock may limit fluid transports to the active layer during summer. However, during winter, ground water flow is generally inactive as the entire waste-rock profile is frozen. Permafrost aggradation in potential-acid generating mine wastes under engineered covers has been suggested by

Robertson (1987); Arenson and Sego (2007) as a solution to control ARD. Moreover, difficulties arise when one tries to obtain undisturbed samples from deep beneath the surface or even at the surface to measure thermal properties. Because any disturbance to the samples may change the physical conditions and therefore the thermal properties. Thus, thermal properties of waste-rock piles are usually determined through in-situ measurements. This chapter presents the results of grain size distribution and in-situ measurements of thermal conductivity in unsaturated waste-rock test piles ("test piles") built at Diavik Diamond Mine Inc. (DDMI).

3.2 Characterization methods

3.2.1 Grain size distribution

Approximately 244 samples of Type I test pile (Chapter 1) and 313 samples of the Type III test pile (Chapter 1) were taken and typical sample weight was 10 kg of waste rock ($\leq$ 100 mm in diameter). The samples were collected for various analyses such as grain size distribution, hydrological properties and bio-chemical-mineralogical parameters. Grain size distribution analysis was done by sieving following the ASTM standard method D422-63 (ASTM, 2007).

3.2.2 Thermal conductivity characterization

3.2.2.1 Probe descriptions and measurement procedures

There are about 35 access lines (made of 3-inch PVC pipe) for thermal conductivity measurements which were installed during construction of the test piles at each face Fig. 3.1 and Fig. 3.2A. The thermal conductivity probe includes: a 1.3 m steel rod (diameter of 6.3 mm), six Teflon discs placed at a 0.23 m interval on the steel bar, eight heating wires (nichrome) formed into four pairs as heat source and foam rings attached to the discs to eliminate airflow within the probe during test. The actual probe and detailed drawing of one section of the probe are showed in Fig. 3.2B and C. Due to a large ratio between the probe length (1.15 m) and the probe diameter (36 mm), the probe is considered as a line heat source (Carslaw and Jaeger, 1959). Three thermistors are attached to the probe, one at the center and one at 0.3 m below and above the center, to determine its temperatures during the test. Thermistor sensors are YSI 44030 type, providing a precision of ±0.1 °C over a range between -80 and +120 °C. Temperatures of these thermistors were recorded every one minute using a Campbell Scientific CR510. The test procedure includes: the probe is lowered down into a test pile through an access line to a given depth and then left for about one hour to achieve thermal equilibrium with the surrounding waste rock. The heating phase is begun by heating the wires for about 11 hours by a voltage of 12 V and this voltage would provide a constant heat source of 7.5 W/m to the probe.

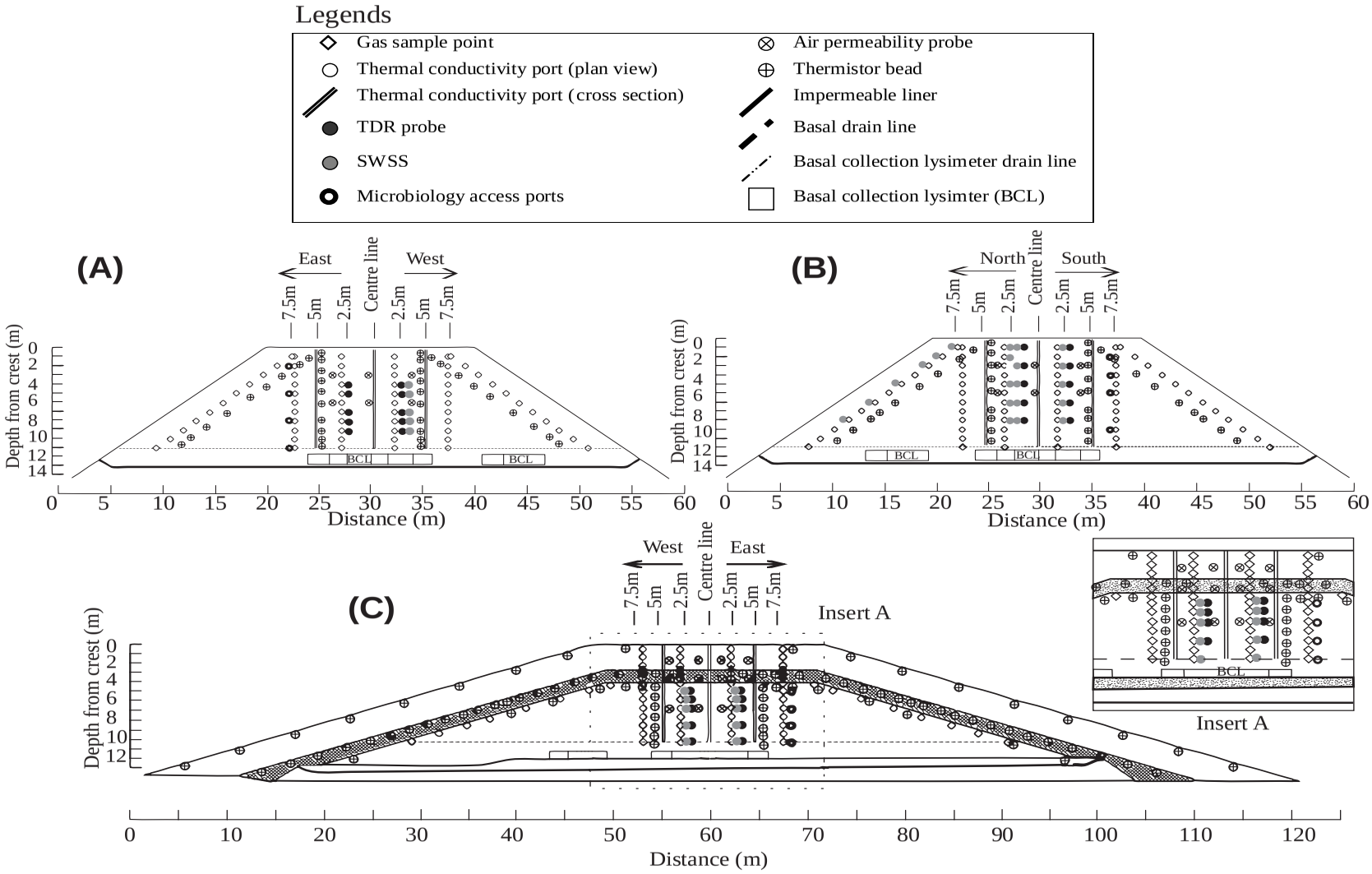

Figure 3.1: Cross sectional view of interior pile instrument distributions and dimensions for the most intensively instrumented faces of (a) Type I pile; (b) Type III pile; and (c) Covered pile (modified from Smith et al., 2012)

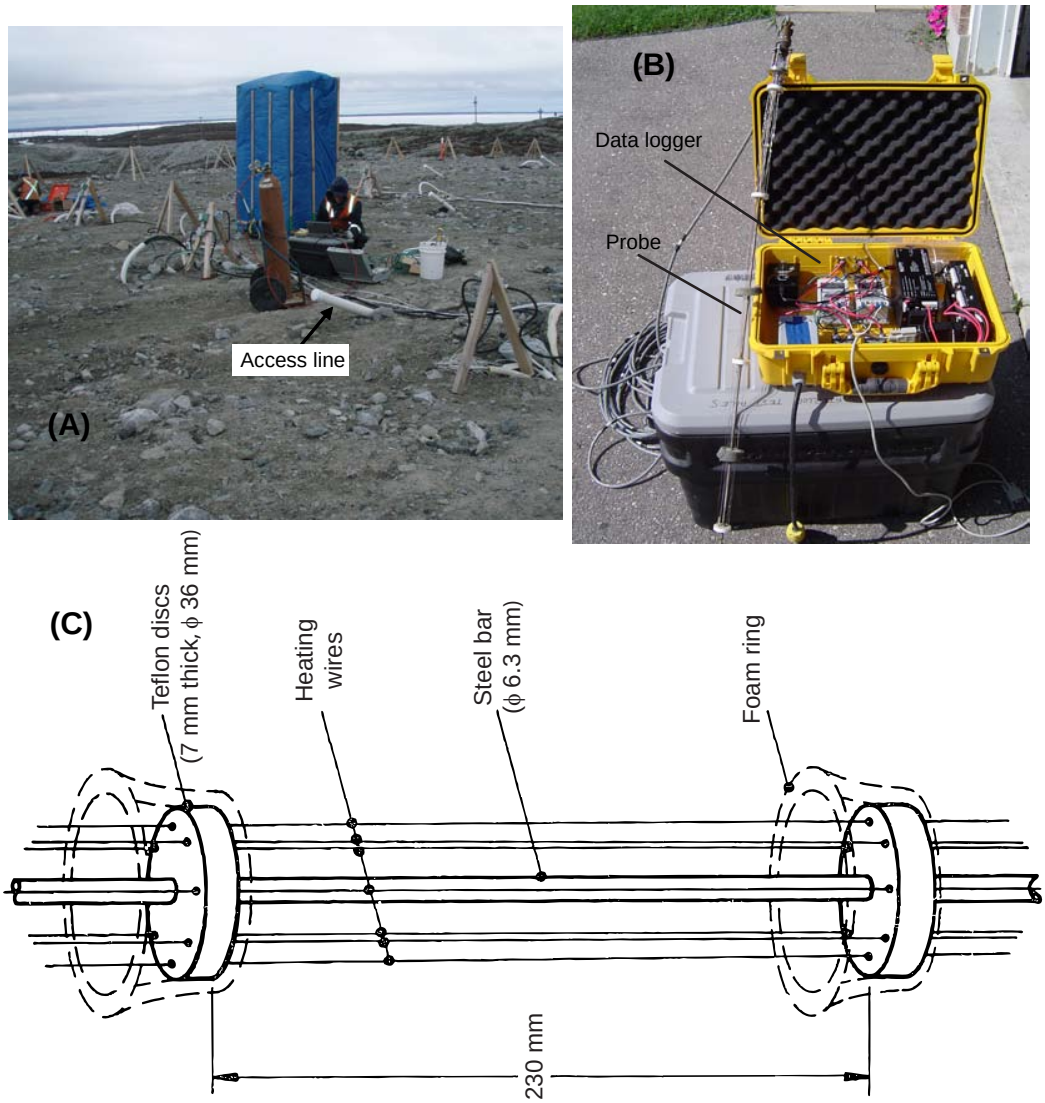

Figure 3.2: Access lines on top of the covered pile (A); actual thermal conductivity probe and data logger (B); a section of thermal conductivity probe (C) (modified from Blackford and Harries, 1985).

3.2.2.2 Continuous line source model

In cylindrical coordinates (θ, r, z), with initial and boundary conditions being only a function of r, heat conduction equation of a homogeneous and isotropic medium can be expressed as:

$$\frac{\partial T}{\partial t} = \kappa \left(\frac{\partial^2 T}{\partial r^2} + \frac{1}{r} \frac{\partial T}{\partial r} \right) \tag{3.1}$$

Where: T is temperature (K), κ is thermal diffusivity (m^2/s), t is time (s), r is the radial distance (m). The thermal diffusivity of waste rock is defined through its effective (bulk or apparent) thermal conductivity λ $(W/(m \cdot K))$ and effective volumetric heat capacity

$C = \rho c$ $\left(\mathrm{J}/\left(\mathrm{m}^3 \cdot \mathrm{K}\right)\right)$ in which c $(\mathrm{J}/(\mathrm{kg} \cdot \mathrm{K}))$ and ρ $\left(\mathrm{kg}/\mathrm{m}^3\right)$ are specific heat capacity and bulk density of waste rock as:

$$\kappa = \frac{\lambda}{\rho c} \tag{3.2}$$

With a constant heat flux of Q (W/m) at $r = 0$, T_o is an initial temperature and a boundary temperature at $r = \infty$, the analytical solution of Eqn. 3.1 at a radius r and time t is described as (Carslaw and Jaeger, 1959):

$$T(r,t) = T_o - \frac{Q}{4\pi\lambda} Ei\left(-\frac{r^2}{4\kappa t}\right) \tag{3.3}$$

The exponential integral function, $-Ei(-x) = \int_x^{\infty} \frac{e^{-u}}{u} \mathrm{d}u$

For small x, Ei is given as

$$Ei(-x) \simeq 0.5772 + \ln x - x + {}^1\!/_4 x^2 + \mathscr{O}(x^3) \tag{3.4}$$

Therefore, for large values of $t \gg {}^{r^2}\!/_{4\kappa}$, Eqn. 3.3 becomes

$$\text{Heating phase:} \quad T(t) = T_o + \frac{Q}{4\pi\lambda}\left(\ln(t) - 0.5772 - \ln\left(\frac{r^2}{4\kappa}\right)\right) \tag{3.5}$$

If the probe temperatures are plotted versus the natural logarithm of time, the effective thermal conductivity can be determined at a given value of Q.

However, when the heat source is turned off at time t_c (cooling phase) and $(t - t_c) \gg \frac{r^2}{4\kappa}$, similarly the solution of Eqn. 3.1 becomes

$$\text{Cooling phase:} \quad T(t) = T_o + \frac{Q}{4\pi\lambda} \ln\left(\frac{t}{t - t_c}\right) \tag{3.6}$$

Again, the slope of the plot of the probe temperatures with time during the cooling phase defines the effective thermal conductivity of waste rock. Thus, the effective thermal conductivity of waste rock can be determined either from the heating (Eqn. 3.5) or cooling phases (Eqn. 3.6). However, the above solutions were developed for an infinite length heat source where the radial heat transfer is valid. An analytical solution for a probe with a finite length-diameter ratio was derived by Blackwell (1956) who found that the error in temperature was about 0.12% for a probe with a length-diameter ratio of 30. The probe described above has the length-diameter ratio of $1150/36 = 32$ therefore the discrepancy between measured and calculated temperatures is significantly small.

3.3 Results and Discussion

3.3.1 Grain size distribution

Fig. 3.3 shows the one standard deviation about mean of grain size distribution for 124 Type I rock samples, 162 Type III rock samples, 30 till samples and 54 Type III rock samples from the covered test pile. The Type I test pile shows the greatest variation in particle size between samples at faces compared to Type III and the Covered test pile. Furthermore, the Type I rock was slightly coarser than the Type III rock placed within the Type III and covered test piles. However, the small change of Type III rock in the covered test pile maybe due to fewer samples obtained for analysis from the covered test pile.

According to Unified Soil Classification System (USCS, ASTM-D2487, 2000), sieve $No.4$ (4.75 mm, the boundary between fine gravel and coarse sand) is used for classification of coarse-grained soils along with the coefficient of curvature C_c (Eqn. 3.7) and the coefficient of uniformity C_u (Eqn. 3.8). If a sample contains more than 50 % materials finer than 4.75 mm, it is classified as sand and the reverse is gravel.

$$C_c = \frac{D_{30}^2}{D_{10}D_{60}} \tag{3.7}$$

$$C_u = \frac{D_{60}}{D_{10}} \tag{3.8}$$

Where D_{10}, D_{30} and D_{60} are the diameter of particle that 10, 30 and 60 % of the material are finer than.

Based on the mean particle size distribution, the Type I and III rocks were classified as well-graded gravel with sand (GW); Type III core of the covered test pile as well-graded gravel with silt and sand (GW-GM); the till material as poorly graded sand with silt and gravel (SP-SM). All the samples ($\leq$ 100 mm) of Type I and III rocks excluded cobble and boulder fractions, thus ASTM-D2487 (2000) suggested to add the words "with cobbles and boulders" to the group names. Hence, Type I and Type III pile can be classified as well-graded gravel with sand, cobbles and boulders (GW): 48 to 72 % fine to coarse, hard, and subangular gravel; 22 to 50 % fine to coarse, hard and subangular sand; 2 to 6 % fines; $C_u >$ 50, $C_c \geq 1.5$. Till material was poorly graded sand with silt and gravel (SP-SM): containing 55 to 58 % fine to coarse sand; 28 - 37 % fine to coarse gravel; 8 to 13 % fines; $C_u = 35.9$, $C_c = 0.5$. Type III from the core of the covered test pile was well-graded gravel with silt, sand, cobbles and boulders (GW-GM): 46 to 66 % fine to coarse, hard, and subangular gravel; 29 to 45 % fine to coarse, hard and subangular sand; 5 to 9 % fines; $C_u = 80.6$, $C_c = 1.6$.

Fig. 3.4 shows the grain size distribution of Type I, Type III and waste rock of other

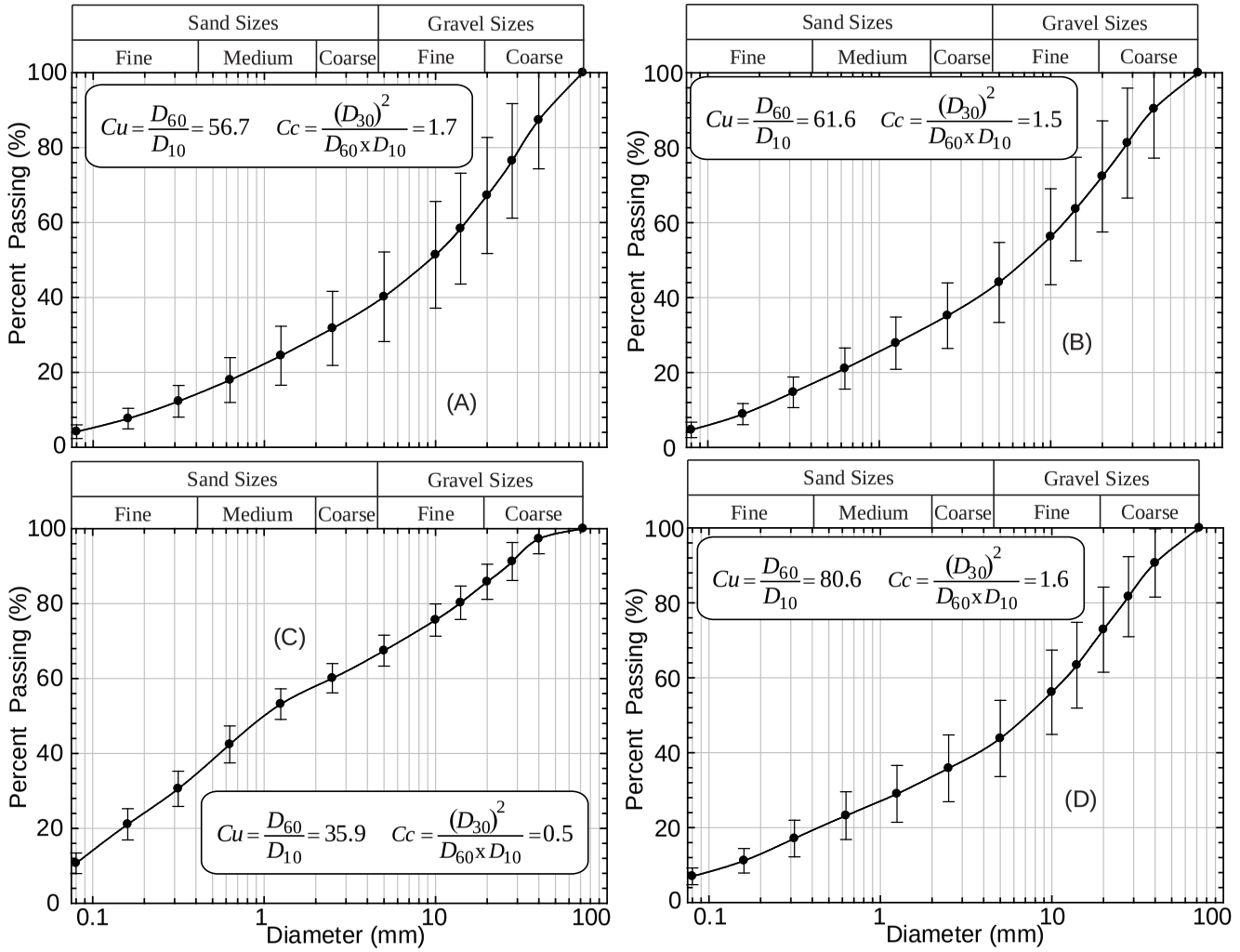

Figure 3.3: Grain size distribution curves of Type I rock (A), Type III rock (B), till layer (C) and Type III rock (D) of covered pile

Table 3.1: Average particle size and one standard deviation for the Type I, Type III, till layer and the Type III of the Covered test piles.

D	Type I pile (σ)	Type III pile (σ)	Covered pile: till (σ)	Covered pile: Type III (σ)
D_{10} (mm)	0.37 (1.20)	0.29 (1.09)	0.08 (0.02)	0.19 (0.18)
D_{30} (mm)	3.08 (4.65)	2.33 (3.14)	0.33 (0.10)	2.22 (2.78)
D_{50} (mm)	10.24 (7.36)	8.48 (6.60)	1.11 (0.33)	8.41 (5.77)
D_{60} (mm)	15.48 (7.89)	13.06 (8.20)	2.79 (0.97)	13.16 (7.53)
C_u	56.70 (18.13)	61.65 (21.50)	35.91 (12.97)	80.57 (21.83)
C_c	1.71 (1.05)	1.53 (1.38)	0.52 (0.17)	1.60 (1.44)
USCS	GW	GW	SP-SM	GW-GM

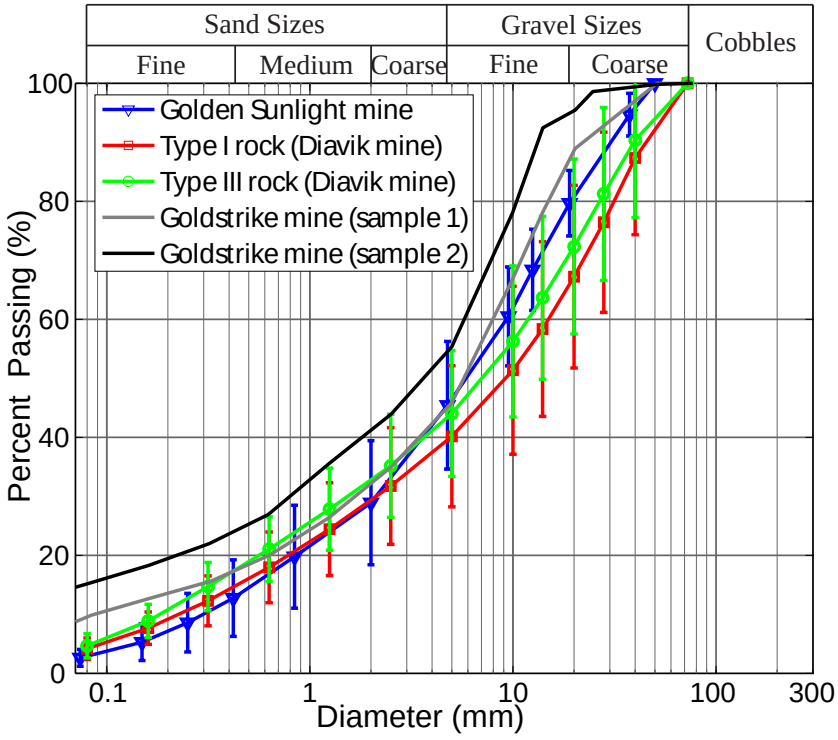

Figure 3.4: Grain size distribution curves of Type I and III rocks compared with waste rock materials of other mines (other data from Martin et al., 2004)

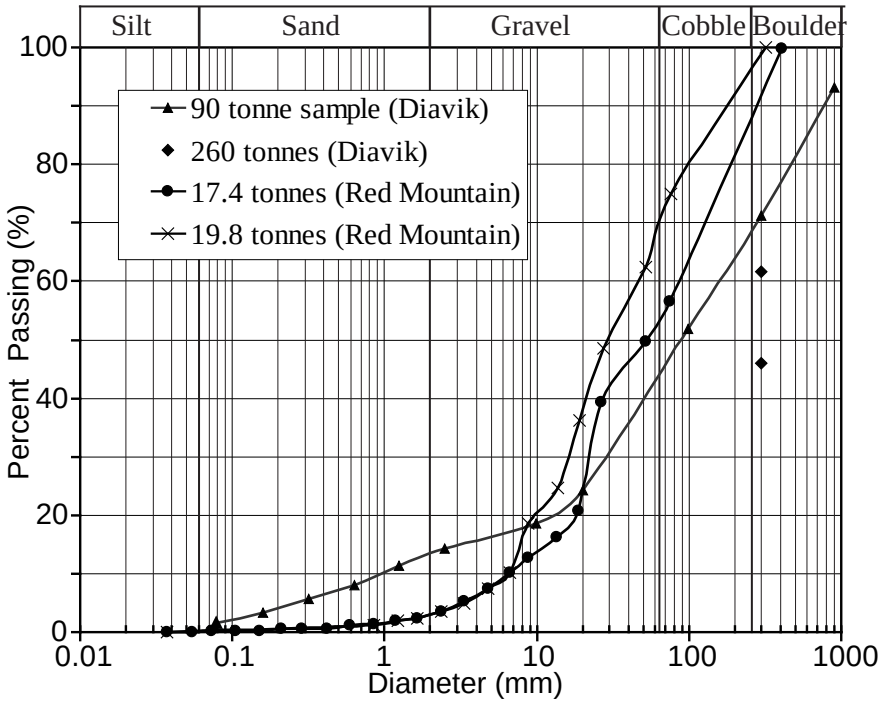

Figure 3.5: Grain size distribution of large scale samples at Diavik and Red mountain mines (data from Frostad et al., 2005; Neuner et al., 2012)

mines and in general, the waste rock materials at Diavik are coarser than those of other mines. The gravel fractions of Type I and III rock (from 48 to 72 %) are much higher than the above mean fractions of gravel reported by McLemore et al. (2009) (between 5 and 70%). The grain size distribution of large-scale samples shows that there were about 56 % by weight of cobbles and boulders in a 90 tonne sample and two 200 tonne samples and these values are greater than that of large-scale waste rock at Red mountain mine (a gold – silver deposit) (Fig. 3.5). Moreover, there were only about 14 % of the 90 – tonne sample passing the 2 mm sieve (i.e. sand size) and this value indicates that the waste rock test piles at Diavik would behave in a rock-like manner (Dawson and Morgenstern, 1995). The most important characteristic of rock-like piles is that they have a larger contribution of flow via macro-pore/preferential flow of water and support air convection/advection.

3.3.2 Thermal conductivity measurements

Fig. 3.6A shows typical temperature curves measured by three thermistors in the conductivity probe in which the temperatures rise rapidly for the first two hours of the heating phase due to the low thermal conductivity of the liner (PVC) followed by a much slower temperature increase due to the thermal properties of waste rock materials (Fig. 3.6A). This section of the heating period can be modeled using Eqn. 3.5 and the slope in the semi-log plot was used to determine thermal conductivity during the heating period (Fig. 3.6B).

Likewise, after the heating period, the heat source was turned off, the instantaneous-sharp drop in the temperatures over about two hours was due to the liner effects (Fig. 3.6A). The slower decrease after was again used to determine thermal conductivity using Eqn. 3.6 during the cooling period (Fig. 3.6C). Temperatures at the end of the cooling phase returned to the surrounding waste rock temperatures. The effective thermal conductivity is an average of thermal conductivities measured during the heating and cooling periods. As shown in the Fig. 3.6, temperature curves during the heating and cooling plotted in semi-log plots are straight and parallel. Fig. 3.6 indicates that the calculated thermal conductivities are consistent between the thermistors and between the cooling and heating phases of each test.

There were more than 189 measurements of thermal conductivity within the test piles and some of them were duplicated at a given location. However, they were measured on different dates, as a result they may have different initial temperatures, moisture contents and dry density which may affect thermal conductivity values. Fig. 3.7 shows a linear trend of measured thermal conductivities versus temperatures in which thermal conductivities were higher at negative temperatures. The measured data has considerably scattered, and this is because of the heterogeneous characteristics of the test piles. Further, the change in thermal conductivity over a temperature range between -12.5 and $12.5\,^{\circ}\mathrm{C}$ was relatively small about $0.1\,\mathrm{W/(m\cdot K)}$ (according to the fitting curve in Fig. 3.7).

The averaged values of thermal conductivity at Type I and III pile have increased steadily since 2006 but had a smaller increase during the years 2008, 2009 and 2010 (Fig. 3.8). Whereas, the averaged values of thermal conductivity at the covered test pile decreased (measured within the Type III rock). This is primarily because of the decrease in moisture content below the till cover of the covered test pile where most measurements are located (Fretz et al., 2011). Over the five years, the mean values of thermal conductivity were 1.7 ± 0.4, 1.8 ± 0.4 and $1.7\pm0.5\,\mathrm{W/(m\cdot K)}$ in the Type I, III and Covered test piles respectively (Table 3.2). The till was frozen and had an average thermal conductivity of $3.0\,\mathrm{W/(m\cdot K)}$ (Table 3.2). Based on measured water content of till samples collected during the construction, till has a porosity of 0.2 and a degree of saturation about 90 %. The Type III test pile has the highest value as it has higher volumetric moisture content (VMC) due to artificial rainfall events. Neuner et al. (2012) conducted six rainfall events at the Type III test pile during summer 2006 and 2007 with a total rainfall of 118.2 mm.

However, the difference between the average values of thermal conductivity of Type I and III test pile is not large (1.7 and $1.8\,\mathrm{W/(m\cdot K)}$) as water is mainly held in matrix fractions not the clasts. The matrix fractions are small, which is about 8 % of the total waste rock volume. An other reason could be the Type III rock has higher fine fractions than Type I rock and therefore the Type III rock has more grain to grain connections (higher thermal conductivity). In comparisons to other waste-rock piles, these results are similar to in-situ measurement of waste-rock piles at the Kelian mine (Indonesia) having an average value of $1.89\pm0.21\,\mathrm{W/(m\cdot K)}$ (Tan and Ritchie, 1997) and Côté and Konrad (2005a) reported a

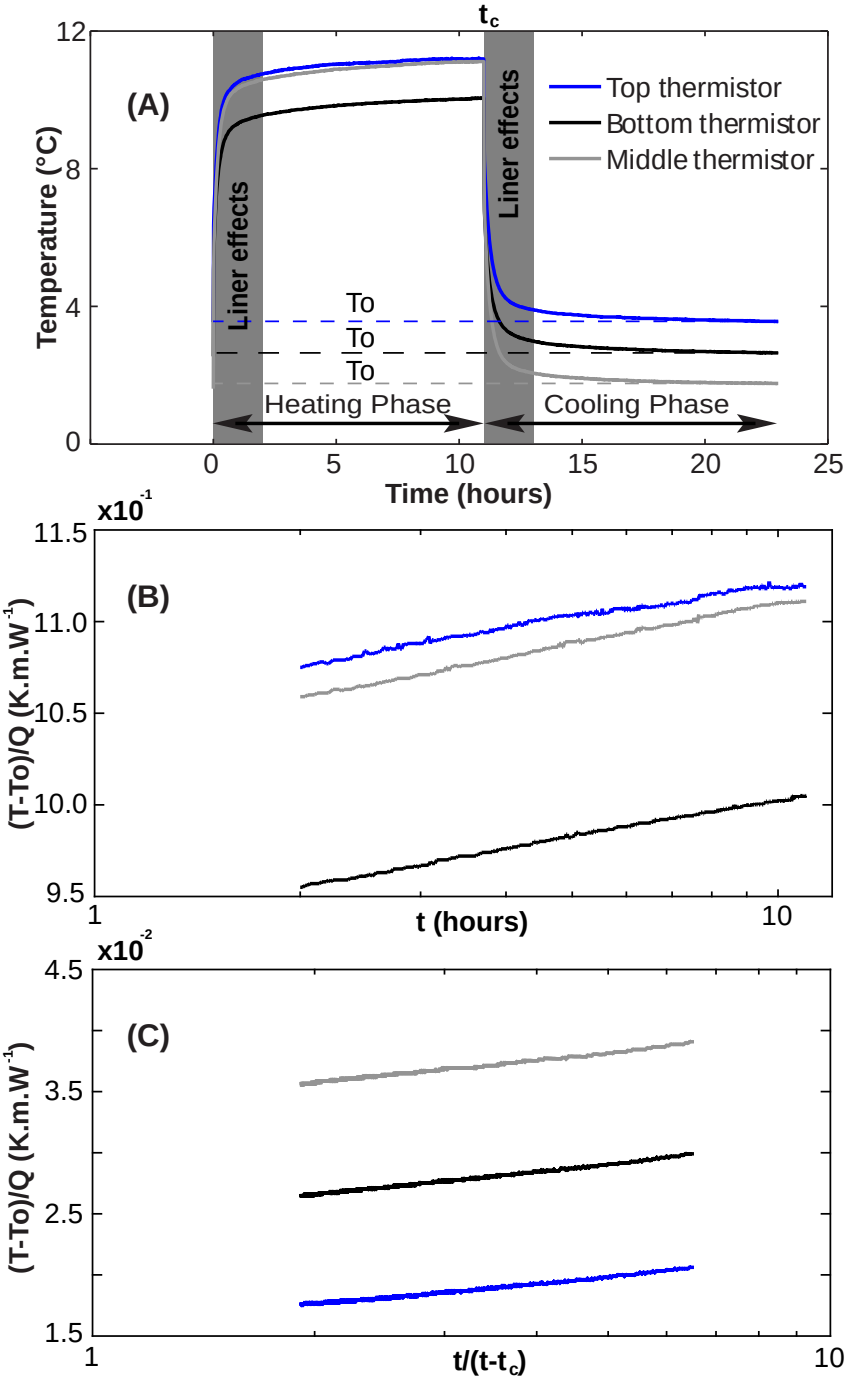

Figure 3.6: A typical result of temperature response with time (A); heating (B) and cooling (C) curves were plotted in the form of Eqn. 3.5 and Eqn. 3.6. Data during the first 2 hours of the heating and cooling phase was eliminated. These curves give an average thermal conductivity of $2.1\,\mathrm{W/(m\cdot K)}$ at $7.5\,\mathrm{W/m}$ line heat source.

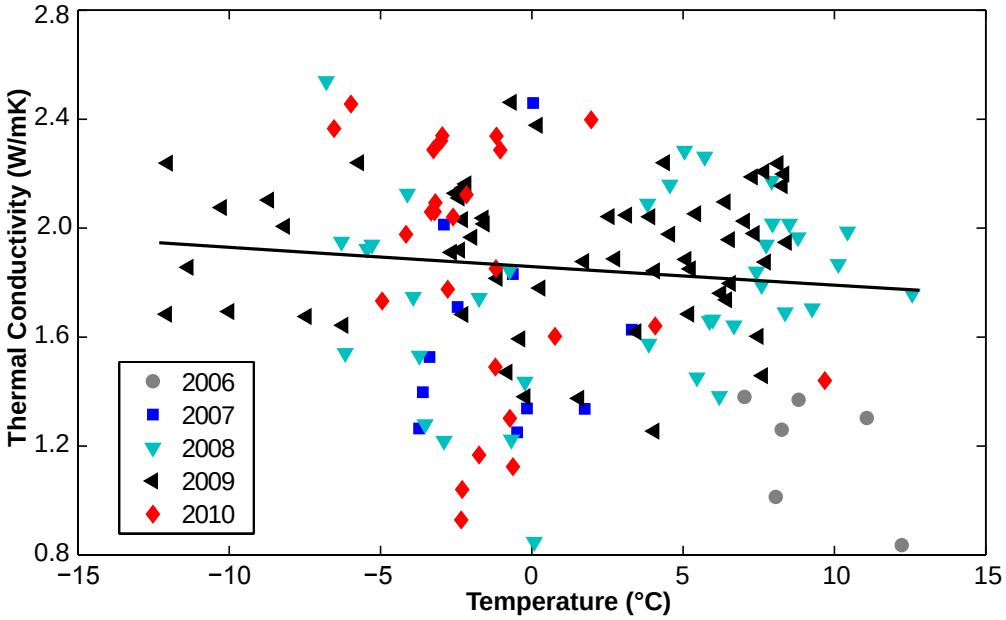

Figure 3.7: Measured thermal conductivity versus initial temperature of the three test piles.

value of 1.85 $\mathrm{W/(m \cdot K)}$ (based on the calculation procedure described by the authors) at a gravimetric moisture content of 5 % of granite coarse rock and a dry density of 2060 $\mathrm{kg/m^3}$ (Smith, 2012).

Fig. 3.9B shows the linear trend lines between thermal conductivity with depth and at a particular depth, the values of thermal conductivity are all measurements from 2006 and 2010. The trend lines indicate the thermal conductivity of the Type I test pile decreases with depth meanwhile the reverse is true for the Type III test pile. However, the values are quite disperse and the variation with depth based on the trend line is small. The heterogeneous nature of the test piles and insignificant moisture content variations (relatively dry waste rock) may contribute to these trends.

Table 3.2: Measured thermal conductivity of the test piles $\mathrm{(W/(m \cdot K))}$

	Type I test pile		Type III test pile		Covered test pile Type III rock		Covered test pile Till	
	Average	Std.	Average	Std.	Average	Std.	Average	Std.
2006			1.2	0.4				
2007	1.4	0.3	1.6	0.5	1.8	0.6		
2008	1.7	0.4	1.9	0.4	1.7	0.5		
2009	2.0	0.3	1.9	0.4	1.7	0.5	3.0	0.5
2010	2.0	0.5	2.2	0.4	1.6	0.5		
Average	1.7	0.4	1.8	0.4	1.7	0.5		

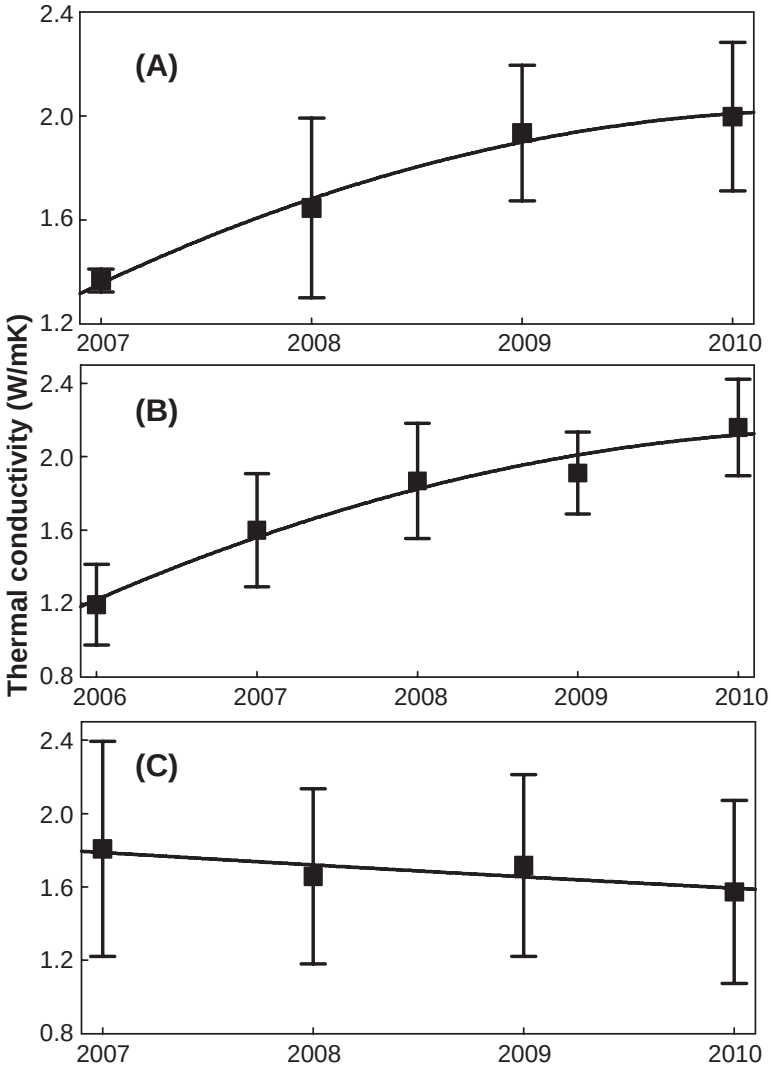

Figure 3.8: Averaged thermal conductivity over the years: Type I test pile (A), Type III test pile (B), and Covered test pile (C).

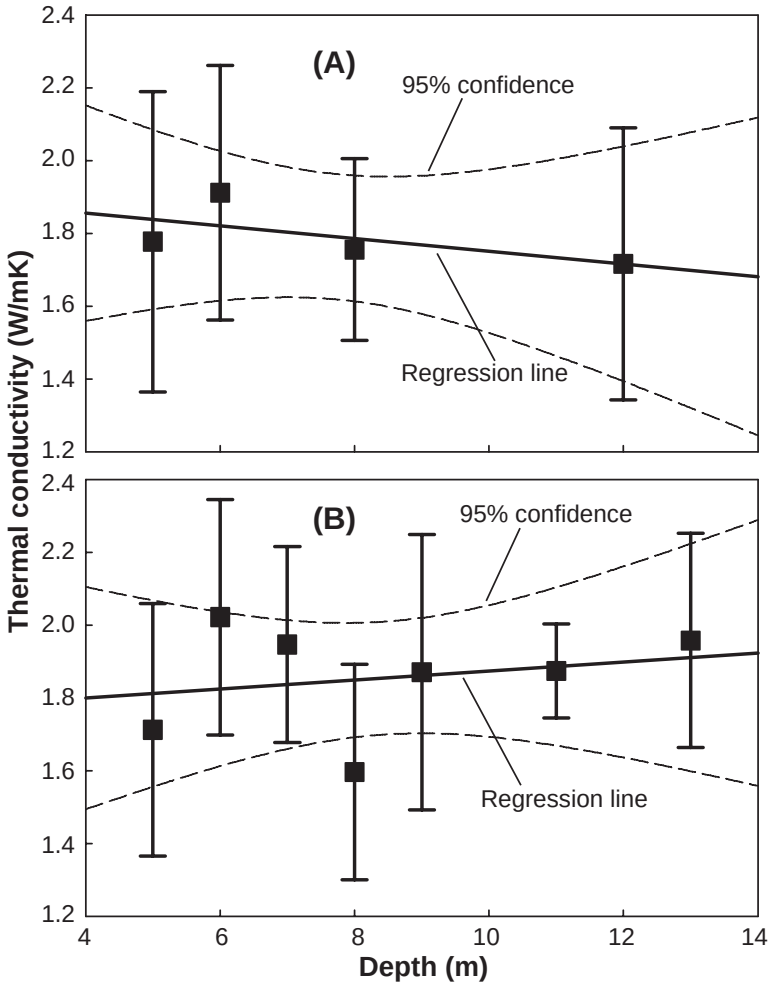

Figure 3.9: Relation between thermal conductivity with depth: (A) Type III test pile and (B) Type I test pile .

3.3.3 Relation between the effective thermal conductivity and degree of saturation.

As shown in the Fig. 3.9A, thermal conductivity increases with time likewise measurements of moisture content from Time Domain Reflectrometry (TDR) probes reported by Fretz et al. (2011) and Neuner et al. (2012). Therefore, thermal conductivity correlates to moisture content. There are four TDR probes located at the same depths (between 7 and 9 m depth) but are located about 2 m horizontally from thermal conductivity access lines in the Type III test pile. All thermal conductivities at these locations were obtained at temperatures above 0 °C and thus they are unfrozen thermal conductivities. A method described by Johansen (1975) and Côté and Konrad (2005a) was used to obtain the relation between thermal conductivity and degree of saturation for fine- and coarse-grained materials. A normalized thermal conductivity for unfrozen waste rock is defined as:

$$\lambda_r = \frac{\lambda - \lambda_{dry}}{\lambda_{sat} - \lambda_{dry}} \tag{3.9}$$

Where λ_{sat} and λ_{dry} are thermal conductivity at saturated and dry states. $\lambda_{sat} = 2.4\,\mathrm{W/(m\cdot K)}$ (Fig. 3.9A) was the highest measured thermal conductivity at a 5 m depth where TDR indicating saturation during summers within the matrix fractions Neuner et al. (2012). Meanwhile λ_{dry} is calculated through a modified geometric mean method as (Côté and Konrad, 2005a):

$$\lambda_{dry} = \lambda_s^{(1-\phi)^{\alpha}} \lambda_a^{\phi^{\beta}} \tag{3.10}$$

Where $\phi = 0.25$ is the porosity of Type III waste rock (Neuner et al., 2012), $\lambda_s = 3.0\,\mathrm{W/(m\cdot K)}$ is the thermal conductivity of granite rock at Diavik, which is an assumed value, and this value is common for granite rocks (Farouki, 1981b). $\lambda_a = 0.024\,\mathrm{W/(m\cdot K)}$ is the thermal conductivity of air, $\alpha = 0.59$ and $\beta = 0.73$ are provided by Côté and Konrad (2005a) due to errors associated with air saturated coarse materials. Substituting with these parameters into Eqn. 3.10, one has $\lambda_{dry} = 0.7\,\mathrm{W/(m\cdot K)}$.

$$\text{This study} \qquad \lambda_r = \frac{12S_r}{1+11S_r} \tag{3.11}$$

$$\text{Johansen (1975)} \qquad \lambda_r = 0.7\log(S_r) + 1 \tag{3.12}$$

$$\text{Cote and Konrad (2005)} \qquad \lambda_r = \frac{4.7S_r}{1+3.7S_r} \tag{3.13}$$

$$\lambda = 0.7 + 1.7\frac{12S_r}{1+11S_r} \tag{3.14}$$

A relation between λ_r and degree of saturation S_r were obtained through the fitting curve of the field data (Eqn. 3.11) and plotted in Fig. 3.10A. The relationships suggested by

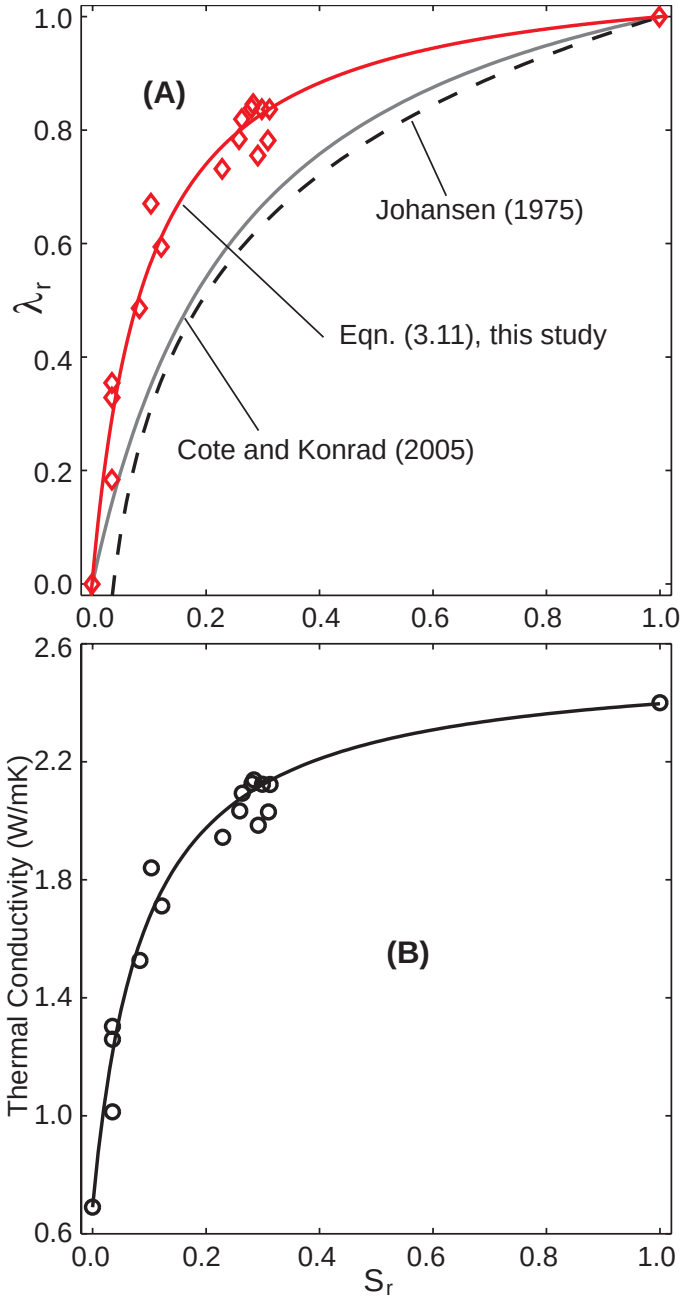

Figure 3.10: Relation between normalized thermal conductivity (A) and effective thermal conductivity (B) and degree of saturation.

Johansen (1975) and Côté and Konrad (2005a) give lower values for λ_r at a given S_r. This is because the materials in their study are finer than waste rock materials. In fact, the D_{50} of materials in the study conducted by Côté and Konrad (2005a) was between 3.5 and 7.0 mm whereas the mean D_{50} of waste rock (< 100 mm in diameter) varied between 10.24 mm of the Type I test pile and 8.48 mm of the Type III test pile (Table 3.1). The materials in the study of Johansen (1975) were mainly fine to medium sands. Therefore the relation between λ_r and S_r is mainly controlled by the gain size of materials or "fabric effect" as mentioned by Côté and Konrad (2005a). At a specific value of S_r, coarser materials have higher values of λ_r. Finally, the relation between the effective thermal conductivity λ and degree of saturation S_r was fitted by Eqn. 3.14 and plotted in Fig. 3.10B.

3.4 Conclusions

This chapter presented a study on grain size characterization and thermal conductivity of three waste rock test piles constructed at Diavik. The analyses of samples ($\leq$ 100 mm) indicated that the waste rock materials (Type I and III waste rock) were classified as well-graded gravel with sand, cobbles and boulders (GW) and slightly coarser than waste rock of other mines. The test piles have rock-like characteristics which may promote air convection/advection and preferential water flow in macro-pores flow rather than matrix flow. The insitu-measured values of the effective thermal conductivity have increased over five years since 2006 but at much lower rate in the later years. The mean values of effective thermal conductivities were 1.7 ± 0.4, 1.8 ± 0.4 and $1.7 \pm 0.5\,\mathrm{W/(m \cdot K)}$ at Type I, III and Covered test piles respectively. The effective thermal conductivities were temperature dependent values but in a relatively small range and the results were quite scattered due to the heterogeneity of the test piles. There were also spatial variations of the effective thermal conductivities, in which at the Type III test pile thermal conductivity increased with depth while the opposite was at the Type I test pile. Finally, the effective thermal conductivities mainly depended on the degree of saturation through normalized thermal conductivities and the normalized thermal conductivities increased with the increase in grain size at a specific value of degree of saturation.

References

Amos, R. T., Blowes, D. W., Smith, L., and Sego, D. C. (2009a). Measurement of wind-induced pressure gradients in a waste rock pile. *Vadose Zone J*, 8(4):953–962.

Arenson, L. and Sego, D. (2007). Protection of mine waste tailing ponds using cold air convection. Assessment and Remediation of Contaminated Sites in Arctic and Cold Climates.

ASTM-D2487 (2000). Standard practice for classification of soils for engineering purposes (Unified Soil Classification System).

ASTM-D422-63 (2007). Standard Test Method for Particle-Size Analysis of Soils.

Azam, S., Wilson, G., Herasymuik, G., Nichol, C., and Barbour, L. (2007). Hydrogeological behaviour of an unsaturated waste rock pile: A case study at the Golden Sunlight Mine, Montana, USA. *Bulletin of Engineering Geology and the Environment*, 66(3):259–268.

Blackford, M. and Harries, J. (1985). A heat source probe for measuring thermal conductivity in waste rock dumps. Technical report, Australian Atomic Energy Commission, Research Establishment, Lucas Heights Research Laboratories.

Blackwell, J. H. (1956). The axial-flow error in the thermal-conductivity probe. *Can. J. Phys.*, 34(4):412–417.

Carslaw, H. S. and Jaeger, J. C. (1959). *Conduction of heat in solids*. Oxford University Press.

Côté, J. and Konrad, J.-M. (2005a). Thermal conductivity of base-course materials. *Canadian Geotechnical Journal*, 42:61–78(18).

Dawson, R. and Morgenstern, N. (1995). Liquifaction flowslides in Rocky Mountain coal waste dumps. Technical report, Natural Resources Canada, Ottawa, Ontario. Contract Report 23440-3-9135/01.

Farouki, O. T. (1981b). *Thermal properties of soils*. United States Army Corps of Engineers, Cold Regions Research and Engineering Laboratory, Hanover, New Hampshire, USA.

Fretz, N., Momeyer, S., Neuner, M., Smith, L., Blowes, D., Sego, D., and Amos, R. (2011). Diavik waste rock project: Unsaturated water flow. In *Tailings and Mine Waste 2011: Vancouver, Canada*.

Frostad, S., Klein, B., and Lawrence, R. (2005). Determining the weathering characteristics of a waste dump with field tests. *International Journal of Mining, Reclamation and Environment*, 19(2):132–143.

Johansen, O. (1975). *Thermal conductivity of soils*. PhD thesis, Institute for Cold Technology, Norwegian Institute of Technology (NTH).

Lefebvre, R., Hockley, D., Smolensky, J., and Gelinas, P. (2001a). Multiphase transfer processes in waste rock piles producing acid mine drainage. 1: Conceptual model and system characterization. *Journal of contaminant hydrology*, 52(1-4):137–164.

Martin, V., Aubertin, M., Bussiere, B., and Chapuis, R. P. (2004). Evaluation of unsaturated flow in mine waste rock. In *57th Canadian geotechnical conference*.

McLemore, V. T., Fakhimi, A., van Zyl, D., Ayakwah, G. F., Anim, K., Boakye, K., Ennin, F., Felli, P., Fredlund, D., Gutierrez, L. A., Nunoo, S., Tachie-Menson, S., and Viterbo, V. C. (2009). Literature review of other rock piles: Characterization, weathering, and stability. Technical report, New Mexico Bureau of Geology and Mineral Resources.

Neuner, M., Smith, L., Blowes, D. W., Sego, D. C., Smith, L. J., Fretz, N., and Gupton, M. (2012). The Diavik waste rock project: Water flow though mine waste rock in a permafrost terrain. *Applied Geochemistry*, (0):–.

Robertson, A. M. (1987). Alternative acid mine drainage abatement measures. Technical report, Steffen, Robertson and Kirsten (B.C.) Inc., Vancouver, B.C., Canada.

Smith, L. (2012). Personal communication.

Smith, L., Lopez, D., Beckie, R., Morin, K., Dawson, R., and Price, W. (1995). Hydrogeology of waste rock dumps. Technical report, Department of Natural Resources Canada, Ottawa, Ontario, Canada.

Smith, L. J., Moncur, M. C., Neuner, M., Gupton, M., Blowes, D. W., Smith, L., and Sego, D. C. (2012). The Diavik Waste Rock Project: Design, construction, and instrumentation of field-scale experimental waste-rock piles. *Applied Geochemistry*, (0):–.

Tan, Y. and Ritchie, A. I. M. (1997). In situ determination of thermal conductivity of waste rock dump material. *Water, Air, & Soil Pollution*, 98(3):345–359.

CHAPTER 4

The Diavik Waste Rock Project: Measurement of the thermal regime of an uncovered waste-rock test pile in a permafrost environment

4.1 Introduction

The amount of waste rock that must be removed at an open pit or underground mine are large and waste rock is usually placed in large piles that are commonly heterogeneous and unsaturated. Traces of sulfide minerals are usually found in waste rock and the oxidation of sulfide minerals can release acidity and high concentration metals in seepage water. Control of acidic rock drainage (ARD) and metal contaminants in water from waste-rock piles are a common issue for the decommission of mines and the impact that release waters may have on the environment near mines is of significant concern. Mine management is required to meet water quality and other environmental regulations. By understanding the oxidation mechanisms, prediction of the rate and controls on oxidation in a particular waste-rock pile may be possible as well as development of management strategies to limit releases to the environment.

Local temperatures and the rate of oxygen supply control the oxidation rate (Jaynes et al., 1984b; Lefebvre et al., 2001a). Furthermore, sulfide oxidation is an strong exothermic process resulting in temperatures at oxidation sites to increase. The amount of temperature increases above background temperatures can be used to determine the oxidation rate. At Rum Jungle, Northern Territory, Australia, internal temperature measurements reached 56 °C within a waste-rock with a heat production of 5.0 W/m^3 and corresponding O_2 usage rate of 8.0×10^{-8} $kg\,(O_2)/J$ (per joule of heat release) (Harries and Ritchie, 1981). Subsurface temperature at a 10 m depth in a drill hole was around 65 °C at Doyon mine due to oxidation (Lefebvre et al., 2001a). This temperature was significantly higher than observed at other locations, where background temperatures were approximately 40 °C (Sracek et al., 2006). Sracek et al. (2006) also reported that the average pyrite oxidation rate at this lo-

cation of Mine Doyon waste rock was estimated around 2.2×10^{-9} mol$(O_2)/(kg \cdot s)$ (in which kg is per weight of waste rock). Pyrite oxidation within a waste-rock pile constructed on a permafrost foundation showed elevated temperatures up to 5 °C as reported by Hollesen et al. (2009, 2011).

Permeability of waste-rock pile is an important parameter controlling the oxygen supply. The consumption of oxygen and localized temperature increases may create an unstable air density stratification within the waste-rock pile. This unstable air stratification in turn can induce convective air cells which can be a more rapid heat and mass (oxygen) transport processes than conduction/diffusion if the permeability of waste rock is high. Simulations by Pantelis and Ritchie (1992); Lefebvre et al. (2001c) indicated that $K = 10^{-9}\,m^2$ is the threshold value for strong air convection formed within a reactive waste-rock pile. Smaller values of permeability than this threshold value, the air convection is so weak that its oxygen transport is dominated by diffusion. Furthermore, wind induces forced advection/convection within waste-rock piles may have significant impacts on the overall heat and mass transport.

The objective of this chapter is to present temperature measurements obtained from 2006 to 2009 within a field-scale experimental waste-rock pile (test pile) at the Diavik Diamond Mine in the Northwest Territories, Canada. Heat budgets of the test pile were calculated based on internal temperatures for 2007 and 2008. Temperature profiles versus depth throughout and beneath the test pile are presented with the inferred air-flow patterns based on measured temperatures within the test pile. Measured temperature was used to assess the extent that sulfide mineral affects the internal temperatures and to determine the principal thermal transport mechanism active within the test pile.

4.2 Site description

The Diavik Diamond Mine is located in a continuous permafrost region and is located approximately 300 km northeast of Yellowknife, Northwest Territories, Canada (Fig. 4.1). The mean annual air temperature (MAAT) at the study site over the study period was -9.0 °C. The average monthly maximum temperature of 12 °C occurs in July, and the average monthly minimum temperature of -30 °C occurs in January/February (Table 4.1). The site is characterized by an active freeze-thaw zone extending approximately 4 m into the bedrock. Precipitation at the study site is low at an average of 280 mm, 60 % of which occurs as snow and the dominant winds are from the north and east with an average of 17 km/h (Environment-Canada, 2008a).

Waste rock at the site is segregated into three categories according to its sulfur content: Type I (< 0.04 wt % S); Type II (0.04 to 0.08 wt % S); and Type III (> 0.08 wt % S). Type I and II waste rock is comprised predominantly of granite and is considered non- and low-acid generating with an average sulfur content of 0.035 wt% S. Type III waste rock

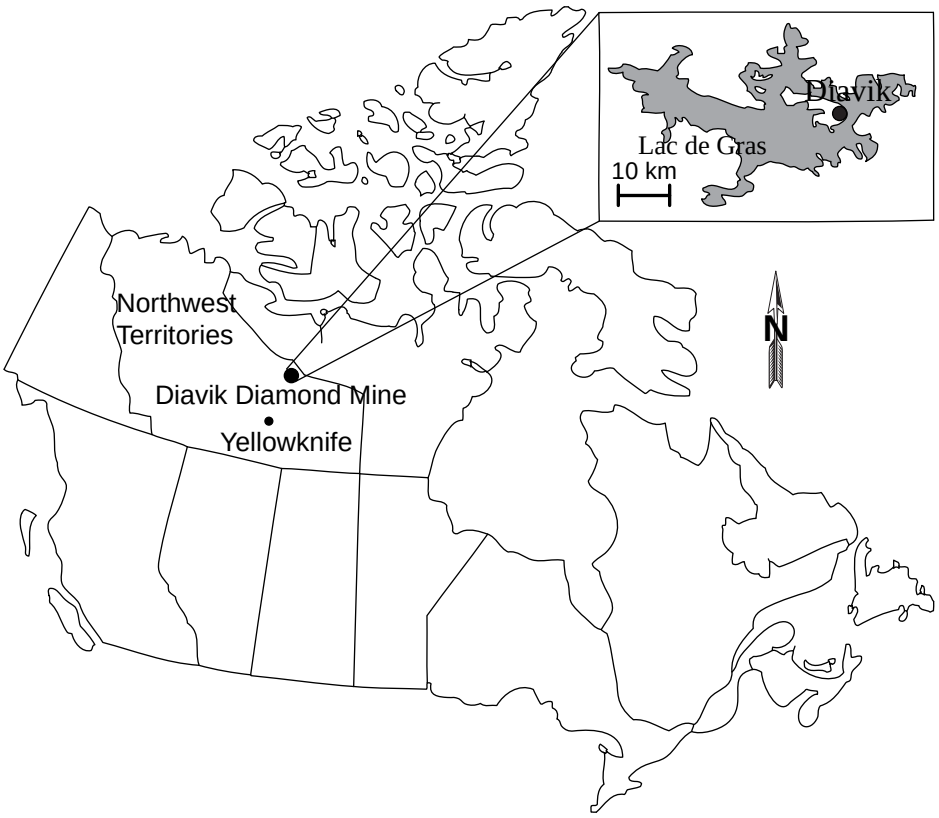

Figure 4.1: Location of the Diavik Diamond Mine.

Table 4.1: Monthly average air temperature and relative humidity at Diavik in 2008

Monthly Summary	Extreme Maximum (°C)	Extreme Minimum (°C)	Average Temperature (°C)	Average relative Humidity (%)
January	-9.5	-42.9	-28.5	71.3
February	-15.4	-44.3	-31.5	67.7
March	-9.4	-40.4	-28.3	69.9
April	1.5	-36.3	-15.4	77.9
May	15.8	-17.9	-2.3	79.5
June	22.0	-4.9	7.4	67.1
July	23.0	4.7	13.0	69.2
August	24.8	1.5	10.8	78.4
September	10.2	-4.0	1.6	81.3
October	9.7	-21.0	-4.2	87.0
November	-1.9	-27.1	-16.5	83.9
December	-14.5	-40.4	-28.5	72.3

contains a small amount of biotite schist that has traces of sulfide minerals, therefore Type III waste rock is considered potentially acid generating with an average sulfur content of 0.053 wt% S. Three field-scale experimental waste-rock piles (test piles) were constructed at the study site between September 2004 and July 2007. Two test piles were constructed and instrumented with final dimensions of 15 m in height and 50 by 60 m in the area at the base: Type I Test Pile contained Type I waste rock, and the Type III Test Pile contained Type III waste rock. A third test pile referred to as the Covered Test Pile was constructed of Type III waste rock with an engineered cover comprised of layers of till and Type I waste rock designed to limit oxygen and water transport into the underlying waste rock.

4.3 Experimental methods

The current study examines the internal thermal regime of the Type III test pile. Smith et al. (2012) provided details of the construction methods for the test piles and instrumentation. In general, instruments were placed on the faces of the test piles during construction, which results in five instrumented faces (Face 0 to Face 4) within the test piles (Fig. 4.2). Numerous thermistor strings were installed for measuring temperatures within the Type III test pile. Strings consisting of 12 thermistor beads were located on Faces 1, 2 and 4, with a 5-m longitudinal spacing between individual instrumentation faces (Fig. 4.2). Thermistors located on Faces 1 and 4 were used to analyze the internal thermal regime of the test pile. Two strings were located along the north and south batter beginning 5 m from the centre line and extending down the face to about 12 m below the surface; two additional strings were placed down the face to a depth of 12 m and located 5 m on both sides from the centre line (Fig. 4.2A). Data from these thermistor strings were recorded at a 4-h interval.

To measure the impacts of test pile construction on the thermal regime of the bedrock

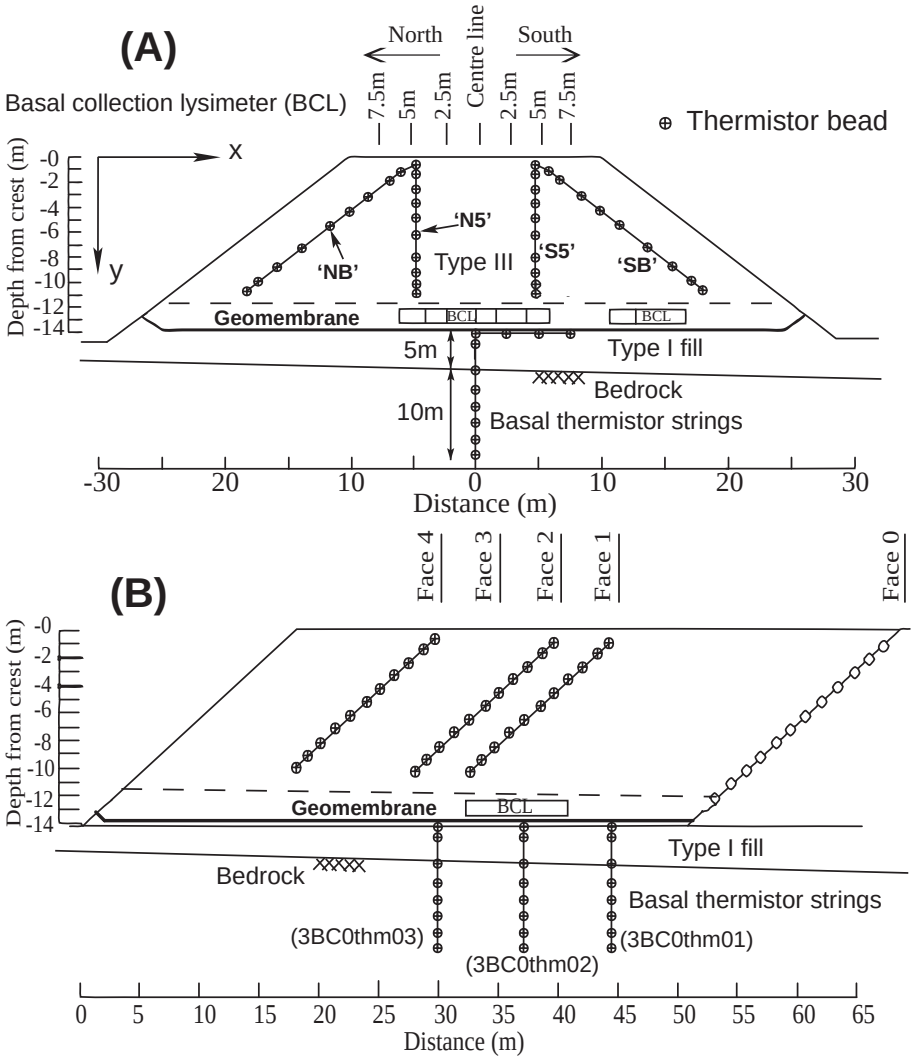

Figure 4.2: Cross-section of a typical face of the Type III test pile having thermistor strings (A); and longitudinal section showing instrumented faces, basal lysimeters, and basal thermistor strings (B).

beneath the test pile, three thermistor strings (basal thermistor strings: 3BC0thm01, 3BC0thm02 and 3BC0thm03) were installed in 2005 below the centre line of the base of each test pile. They pass through a layer of bedding sand below the geomembrane liner underlying the test pile (Fig. 4.2B). These thermistor strings were buried 10 m into the bedrock foundation (six thermistors at 2-m spacing), and four thermistors are located at the base in the bedding material (Fig. 4.2). Data from these basal thermistor strings were recorded at a 4-h interval. To establish baseline temperatures for both preconstruction and ongoing development on the internal thermal regime of the bedrock at the test pile site, a bedrock thermistor string located approximately 100 m northwest of the Type III test pile was installed in July 2005 and recorded at a 4-h interval. This thermistor string was installed 10 m below the ground surface and was used to determine the depth of the active layer and the annual variation of subsurface temperatures in native bedrock. The uppermost thermistor is located near the ground surface and recorded the ground surface temperatures of the bedrock. A data-logger system consists of a Campbell Scientific (Edmonton, AB, Canada) CR23X data-logger and six AM16/32-XT multiplexers. The data-logger system records 384 thermistor beads installed inside and at the base of the Type I and III test piles and bedrock. The thermistor beads are YSI 44007 type, providing a precision of $\pm$0.2 °C and a wide range working temperature from -80 to 120 °C.

4.4 Results and discussion

4.4.1 Air, surface, basal and bedrock temperatures

Construction of the Type I and III test piles was completed in September 2006. Monthly average temperature data from the uppermost thermistors (less than 0.05 m deep from the surface) in the test piles (the average surface temperatures of the Type I and III test pile) were plotted over time (Fig. 4.3A). The data vary sinusoidally (Fig. 4.3A) with an average amplitude of 20 °C, a maximum value of about 15 °C in July, a minimum value of -25 °C in January/February and a mean annual surface temperature (MAST) of -5 °C. The MAST is warmer than the MAAT and this may be due to the variations of the parameters that affect the energy balance between the air above and surface such as solar radiation, wind, humidity and surface conditions of the test piles such as snow cover (during winter). Snow was significant at the site (60% of precipitation) as indicated by measurements of snow thickness around 25 cm during the winter 2006 - 2007 (from end of October to end of April) at the nearby Ekati Diamond Mine which has similar weather conditions to those of Diavik (Neuner et al., 2012). Snow is a good insulator and keeps the surface temperatures of the test piles warmer than air temperatures.

Smith and Burgess (2000a) provided a statistical relationship between MAAT and MAST for northern Canada (Fig. 4.3B). The relationship is linear with a considerable scatter due to site-specific conditions. MAST at 0 °C occurs at a MAAT of about -4.3 °C. However,

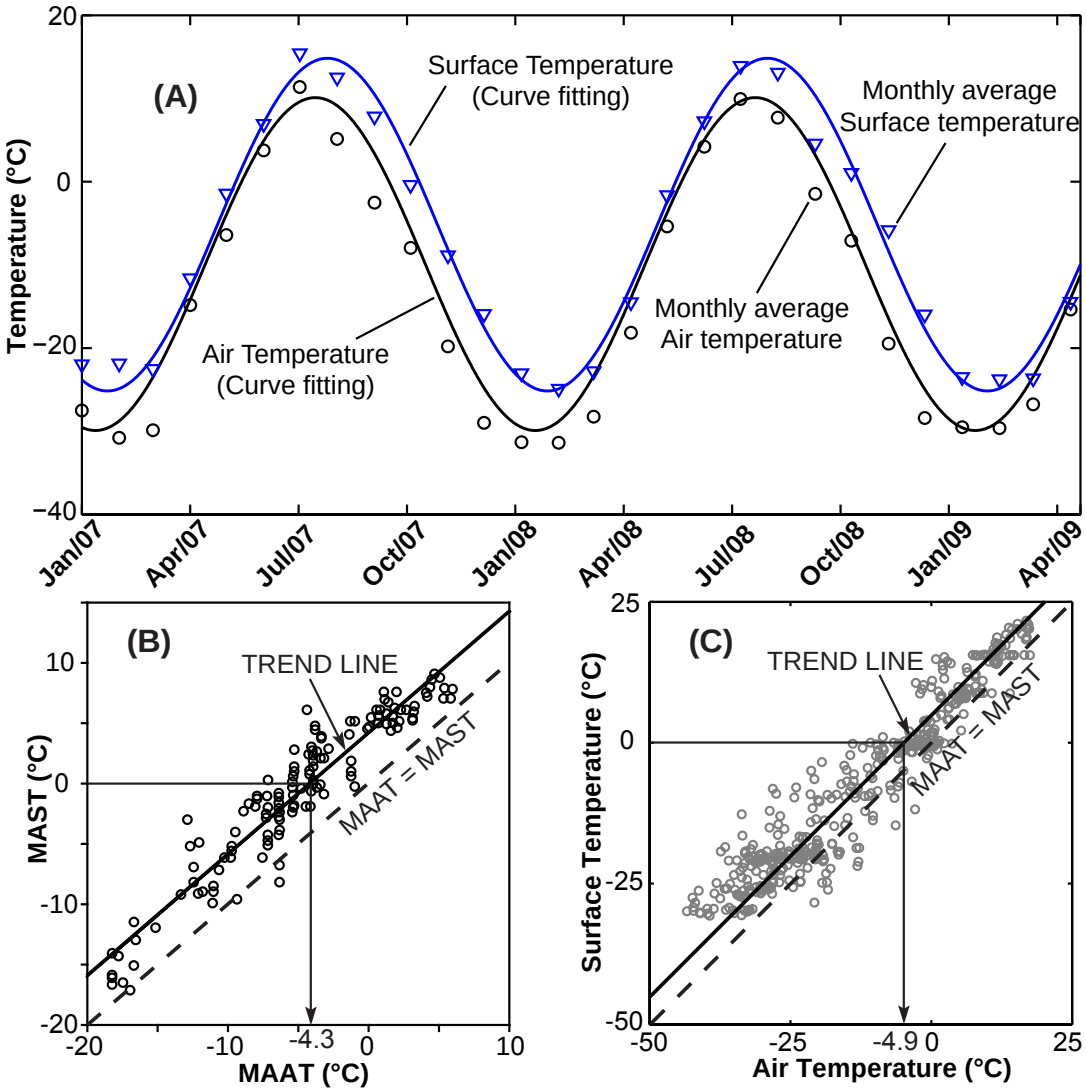

Figure 4.3: (A) Monthly average and curved fits of air temperatures and ground temperatures near the top surface of the Type I and Type III test piles (< 0.05 m deep = surface temperatures); (B) plot of MAST versus MAAT for northern Canada (data from Smith and Burgess, 2000a); and (C) surface versus air temperatures at the Type I and III piles.

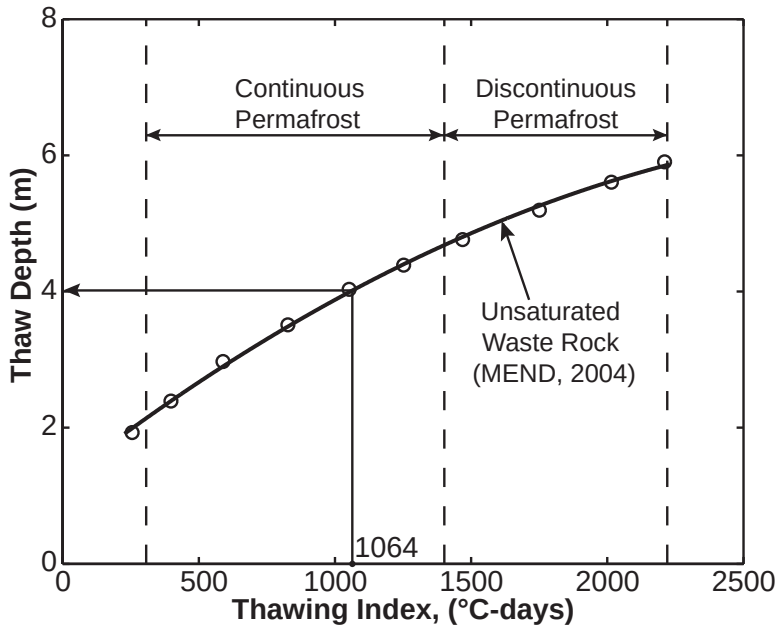

Figure 4.4: Estimation of thaw depth based on the air thawing index for unsaturated waste rock (data from MEND1.61.2, 1996)

because of the scatter, MAST at 0 °C has been observed between a MAAT of -2 and -7.5 °C. At the Diavik site, the relationship between surface and air temperature is also linear, and surface temperatures of 0 °C correspond to air temperatures of -4.9 °C (Fig. 4.3C). When surface temperatures are colder than 0 °C (during winter), the relationship between air temperature and surface temperature varies considerably (Fig. 4.3C).

Fig. 4.4 shows a relationship between the thickness of thaw depth (active layer) and thawing index I_{at} (the summation of the positive degree-days over a year) for unsaturated waste rock, which is based measured values at several mines. It indicates that thaw depth reduces with a decrease in air temperature. However, the relationship is only relevant for low-permeability waste rock dominated by conductive heat transfer. At the Diavik site, the air thawing index is $I_{at} = 1{,}064$ °C-days, giving an expected thaw depth of 4 m in unsaturated waste rock far from boundary effects (near the slopes), negligible oxidation and convective heat transport (Fig. 4.4).

In 2008, the variations in monthly average bedrock temperature versus depth and the maximum-minimum temperature values or trumpet curve (a trumpet curve is the envelope surrounding all of the temperatures occurring throughout a year) are plotted in Fig. 4.5A. These data demonstrate that the active layer in the bedrock is 4-m deep adjacent to the test pile site. The minimum and maximum surface temperatures recorded between September 2004 and April 2009 were -25 °C and 15 °C, respectively, and the MAST was -5 °C. The temperature at a depth of 10 m was still influenced by surface temperature variations, but the variations were generally between -5.5 and -3 °C (Fig. 4.5A). Following construction,

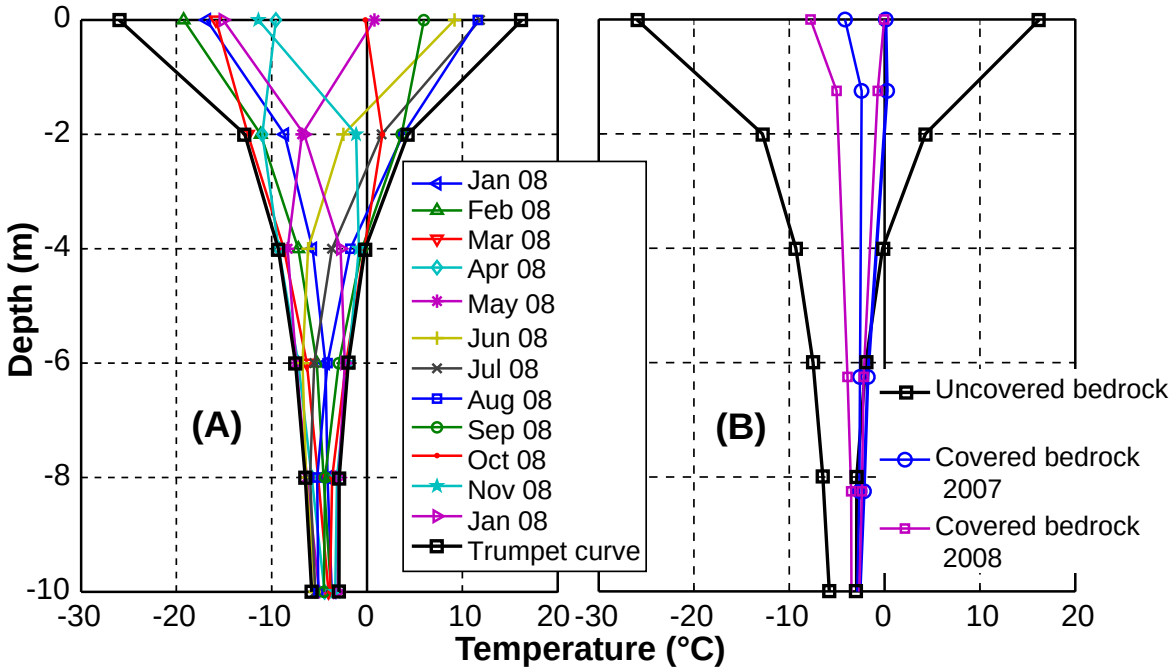

Figure 4.5: Trumpet curve of bedrock temperatures (black solid lines with squares) during the study period (based on temperatures at a 4-h interval) adjacent to the Type III test pile and variations in bedrock temperatures in 2008 (monthly average) (A). Trumpet curves at the thermistor string 3BC0thm01 (Fig. 4.2) beneath the Type III test pile in 2007 and 2008 compared to the trumpet curve of bedrock temperatures without the test piles above (B).

the amplitudes of bedrock temperatures beneath the test pile changed due to the added overlying waste rock (Fig. 4.5B). There is a modest cooling trend in the bedrock beneath the test pile between 2007 and 2008 as it corresponds to a shift of the trumpet curve to negative temperatures following construction of the test pile at the end of the summer in 2006 (Fig. 4.5B). Temperatures at the interface between the base of the test pile and the ground surface vary over a small range between 0 and -3 °C in 2007 and between -1 and -5 °C in 2008 (Fig. 4.5B).

Since construction, temperature data from the thermistor strings at the base of the test pile (3BC0thm01 and 3BC0thm03) (Fig. 4.2) have been generally below 0 °C (Fig. 4.6). However, some data from the base and beneath the geomembrane liner remained near 0 °C from September to December during both 2007 and 2008 due to latent heat effects. Meanwhile, from December to July in both 2007 and 2008, these thermistors cooled well below 0 °C. This cooling can be explained by rapid convective cooling in the coarse rock above the geomembrane. Furthermore, data from thermistors installed into bedrock below the test pile were below 0 °C year round, and the bedrock temperatures gradually decreased during the measurement period. Thermal behavior of the basal thermistors (3BC0thm01 and 3BC0thm03) was quite similar; however, the temperature data from 3BC0thm01 were colder due to lower initial temperatures in September 2006 (Fig. 4.6). Moreover, thermistor strings beneath the test pile located closer to the exterior margin of the test pile reflected colder winter temperatures compared to those beneath the centre of the test pile.

4.4.2 Internal temperatures and temperature-induced pore airflow along instrumented faces

Seasonal measurements from thermistor strings located on Faces 1 and 4 reveal that the internal thermal regime changes within the test pile on a seasonal and annual basis (Fig. 4.7) that mirrors temporal variations in ambient air temperatures. At 2 m below the surface, temperatures have exhibited a steady cooling trend of about 4 °C/a during each winter since 2006. During the summer, temperatures at these locations increased to values above 0 °C. Temperatures were colder on Face 4 compared to Face 1 during both the winter and summer at the same depth. This trend indicates that the entire test pile was cooling during the study period, but Face 4 cooled faster than other faces because it is the most westerly (outer) face and thus releases more heat during winter due to closer to boundary and more affected by climate conditions compared to the interior of the test pile.

4.4.2.1 Contour plots of temperatures (isotherms) and pore airflow

Internal pile temperatures along with waste-rock thermal properties were used to delineate internal temperature distributions and calculate initial heat budgets for Faces 1 and 4. Isotherm plots were prepared from discrete temperature values using a triangular mesh

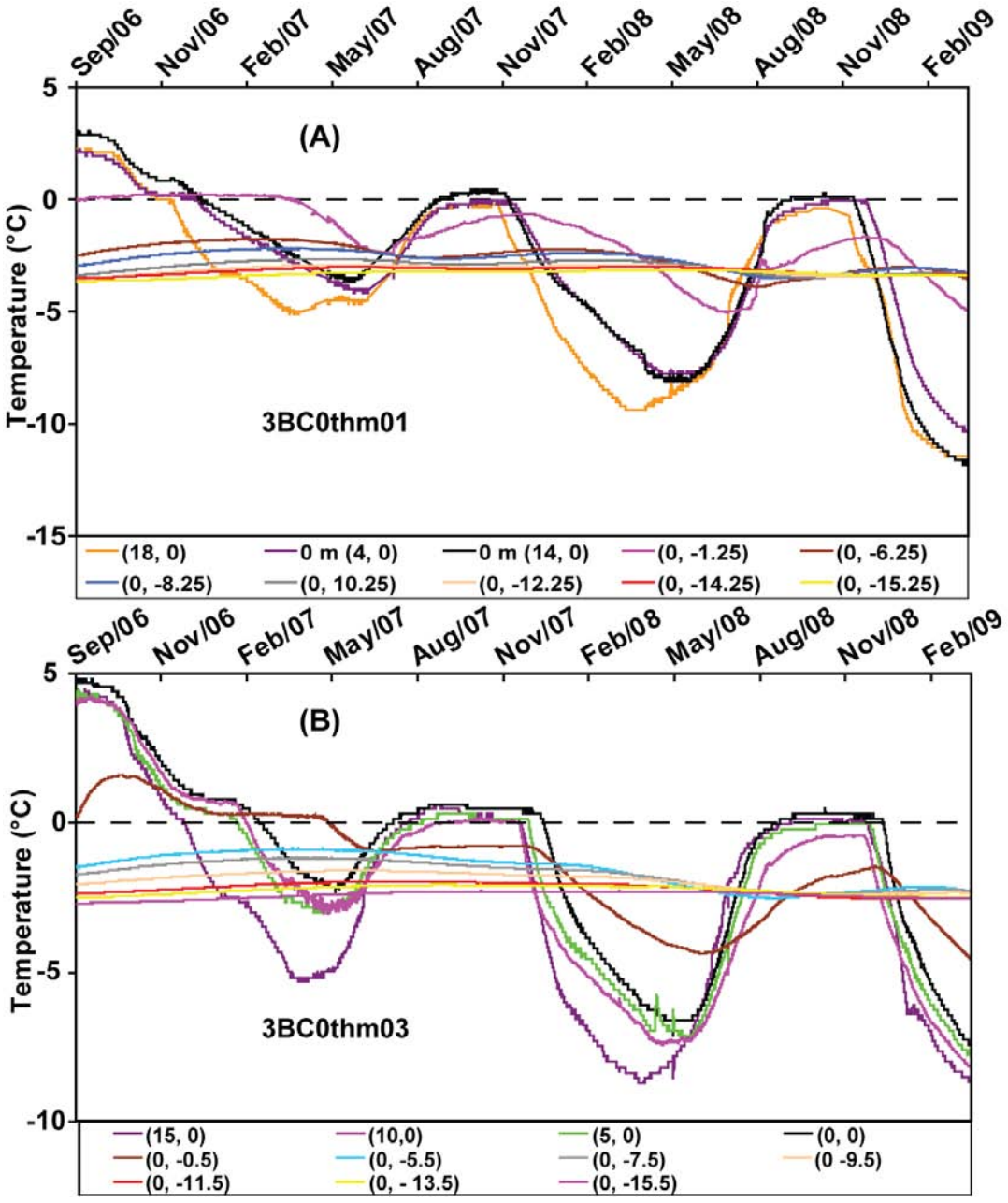

Figure 4.6: Temperatures at thermistor strings (A) 3BC0thm01and (B) 3BC0thm03. The origin of the coordinates in brackets (in meters) is at the centre of the base (4.2A).

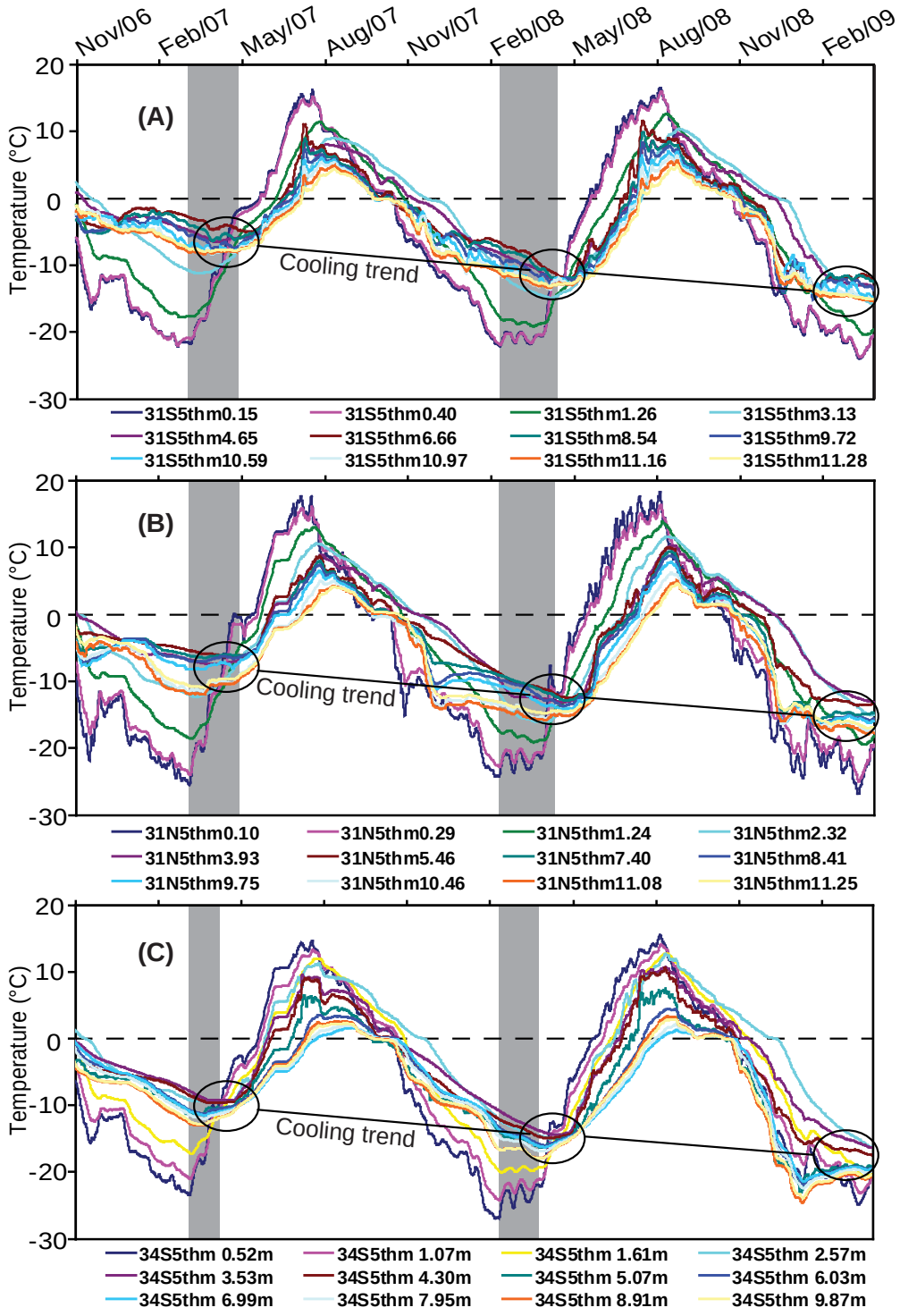

Figure 4.7: Temperatures of thermistor (A) 31S5thm (3 - Type III pile; 1 - Face 1 of the pile; S - South; 5 - 5m offset of centre to the south; thm - thermistor; 0.15 - depth from the surface of the pile with unit in meters); (B) 31N5thm; and (C) 34S5thm show a similar cooling trend since 2007.The shaded area shows the approximate time lag between the surface temperature (thermistor 31N5thm0.10) and the temperature at the greatest depth of each thermistor string.

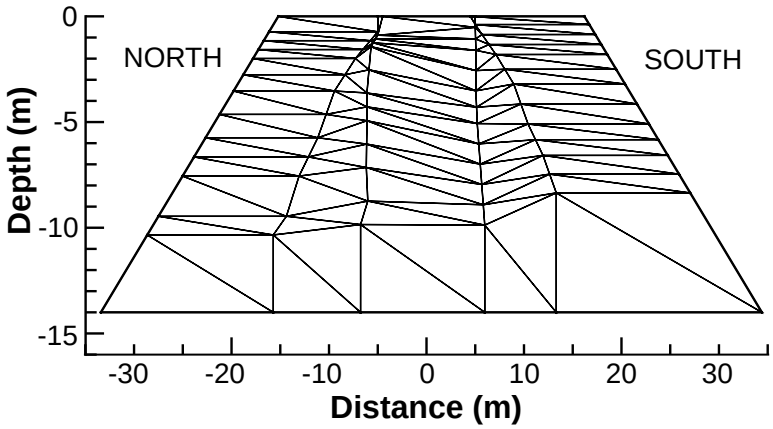

Figure 4.8: Triangular mesh of Face 4 used to construct contour plots. The nodes represent actual thermistor locations. Basal temperatures were from 3BC0thm03, which is the closest thermistor cable to Face 4.

for each instrumentation face (Fig. 4.8). The exterior nodes were assigned surface temperatures. Interior nodes were located to correspond with thermistor locations and were assigned corresponding temperatures. The two-dimensional isotherms at a face were obtained by kriging all available data points on that face. Velocity vectors for air in the pore space were determined using these 2-D isotherms along with Darcy's law, the ideal gas law and an average barometric pressure of $p_{atm} = 101\,kPa$ at the ground surface. According to Darcy's law (Bear, 1972):

$$\mathbf{u} = -\frac{K}{\mu}\left(\nabla p + \rho_a g \mathbf{n}\right) = -\frac{K}{\mu}\left(\nabla p + \rho_a^o g\left(1 - \beta\left(T - T_o\right)\right)\mathbf{n}\right) \tag{4.1}$$

Where K is permeability in m^2; $\mu = 1.72 \times 10^{-5}$ $(\mathrm{Pa \cdot s})$ is the dynamic viscosity of air at a standard temperature and pressure (22 °C and 101 kPa) (Tipler, 1999); $p = p_{atm} - \rho_a g y$ is air pressure as a function of height y; $\mathbf{n}(0,1)$ is unit vector; ρ_a is air density; ρ_a^o is air density at reference temperature T_o; T is temperature; and $\beta = \frac{1}{T}$ $(1/\mathrm{K})$ is the thermal expansion of air as an idea gas (Bear, 1972). With a given 2-D isotherm, one can use Eqn. 4.1 to estimate the air velocity vector. These calculated velocities are based on temperature gradients (natural air convection) and do not include wind effects or barometric pumping.

Permeability of the test pile was assigned a value of 2.0×10^{-9} m^2 (Amos et al., 2009a) (Table 4.2) at the surface, and it increases linearly to the bottom of the pile with an assigned value of 2.0×10^{-8} m^2 (Chi, 2010). The assumed linear permeability increase with depth is based on material segregation during pile construction that results in increased particle size and permeability at the base.

Air buoyancy can potentially result in airflow and depends on the difference between the air density within the test pile and that of atmospheric air. In January 2007 and 2008 at Face

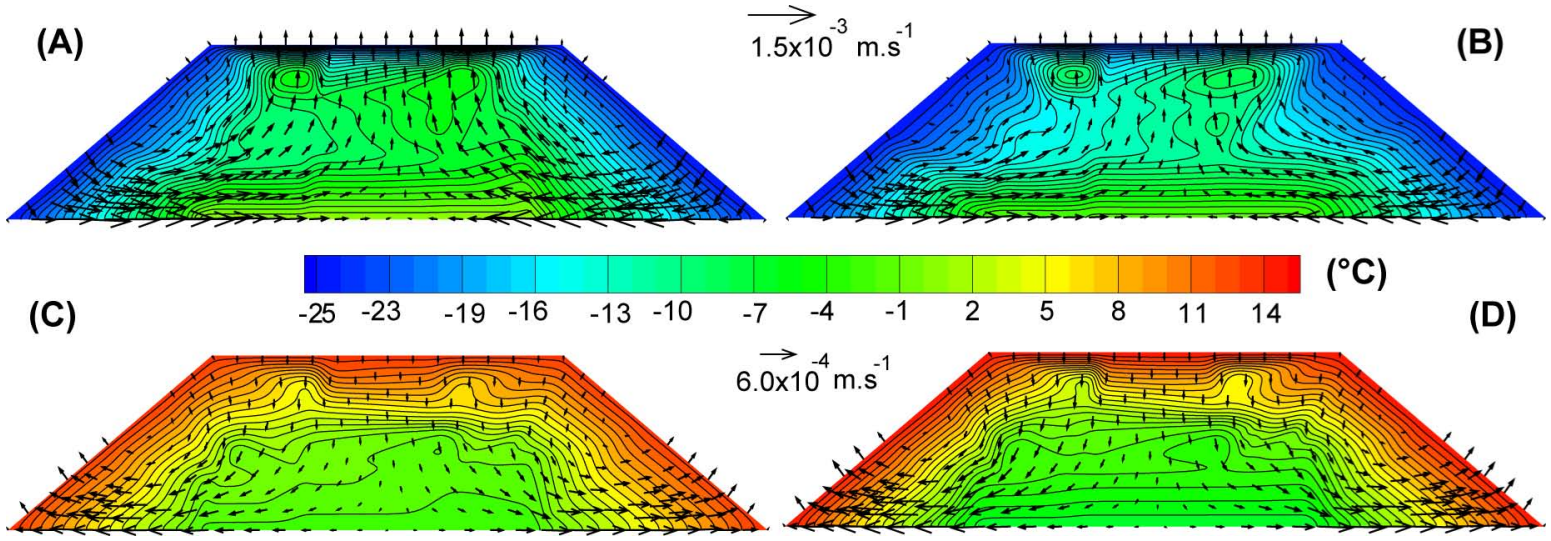

Figure 4.9: Isotherms (temperature in °C) and density-driven airflow vectors along Face 1 in (A) January 2007; (B) January 2008; (C) July 2007; and (D) July 2008. Average air velocity was 1.8×10^{-4} and 9.1×10^{-5} m/s at this face in January (2007 and 2008) and July (2007 and 2008), respectively.

1, surface temperatures of the test pile were -25 °C and interior temperatures were around -3 °C (Fig. 4.9A) and -7 °C (Fig. 4.9B), respectively. Predicted air velocities calculated based on these thermal gradients indicate lighter air from the warmer interior rose to the outer surface, which created horizontally inward gradients drawing air through the sides (inward airflow) (Fig. 4.9A and B). The air velocity was highest near the base and reached a value of 1.5×10^{-3} m/s due to the high temperature gradients and permeability. An average inflow air velocity of 1.8×10^{-4} m/s was estimated in January for both years at Face 1 (Fig. 4.9A and B).

Conversely, when the ambient air temperatures were warmer than the test pile's interior temperatures during summer, the ambient air density was lower than the air density within the test pile and the airflow was therefore in the opposite direction (Fig. 4.9C and D). When surface temperatures were around 15 °C in July, the basal temperature of the test pile was -1 °C (2007) and -3 °C (2008). The calculated density-driven air velocity during the winter is about twice that of the summer, which was estimated at 9.1×10^{-5} m/s (Fig. 4.9C and D) and is of the same magnitude as wind-induced airflow (Amos et al., 2009a).

The thermal and airflow behavior on Face 4 resembles that of Face 1; however, the 0 °C isotherm was higher within the test pile on Face 4 (Fig. 4.10). The location of the 0 °C isotherm is important because it is used to track frozen/unfrozen interfaces and potential oxidation regions in the test pile. In frozen regions, it is known that temperatures below zero can reduce significantly the oxidation rate (Jaynes et al., 1984b).

The 0 °C isotherm progresses deeper into the test pile along the sides than the centre due to two possible reasons (Fig. 4.9 and Fig. 4.10). The first reason may be due to larger thermal conductivity on the sides because of greater water infiltration into the batters (Neuner et al., 2012), which warms the rock that was initially below 0 °C. The water then freezes to form ice, thus increasing the thermal conductivity (ice is about 3.7 times more conductive than water). Furthermore, as the water content increases, the thermal conductivity of waste rock also increases (Farouki, 1981c; Côté and Konrad, 2005a). The second reason may be due to wind-induced and/or natural convection acting on the test pile sides, deepening the 0 °C isotherm. In addition, these isotherms have a near-symmetrical shape, which is an indication of a similar amount of energy entering from each side.

Isotherms and air velocity vectors due to density differences in the sections perpendicular to the faces are shown in Fig. 4.11. Similar to Face 1 and 4, isotherms of the perpendicular sections indicate a decrease in interior temperatures of the test pile between 2007 and 2008 (Fig. 4.11). During winter, air flows inward into the interior of the test pile, and its magnitude is large in the region between the location of Face 4 and the boundary because of the large temperature gradient (Fig. 4.11A and B). In the region between Face 1 and 4, the air velocity is slow as a result of the small thermal gradient (temperatures at Face 1 and Face 4 are close in value) (Fig. 4.11A and B). The average inward air velocity was 1.8×10^{-4} and 1.6×10^{-4} m/s in January 2007 and 2008, respectively, which are in the same magni-

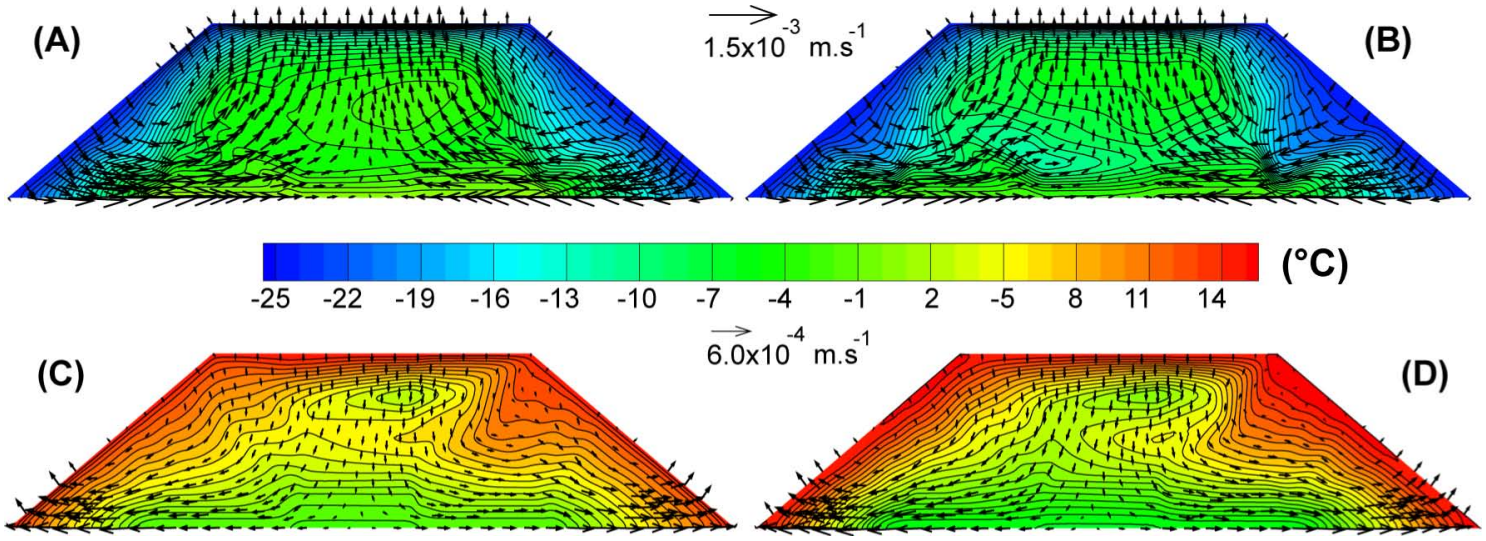

Figure 4.10: Isotherms (temperature in °C) and density-driven airflow vectors along Face 4 in (A) January 2007; (B) January 2008; (C) July 2007; and (D) July 2008. Average air velocity was 1.6×10^{-4} and 8.0×10^{-5} m/s at this face in January (2007 and 2008) and July (2007 and 2008), respectively.

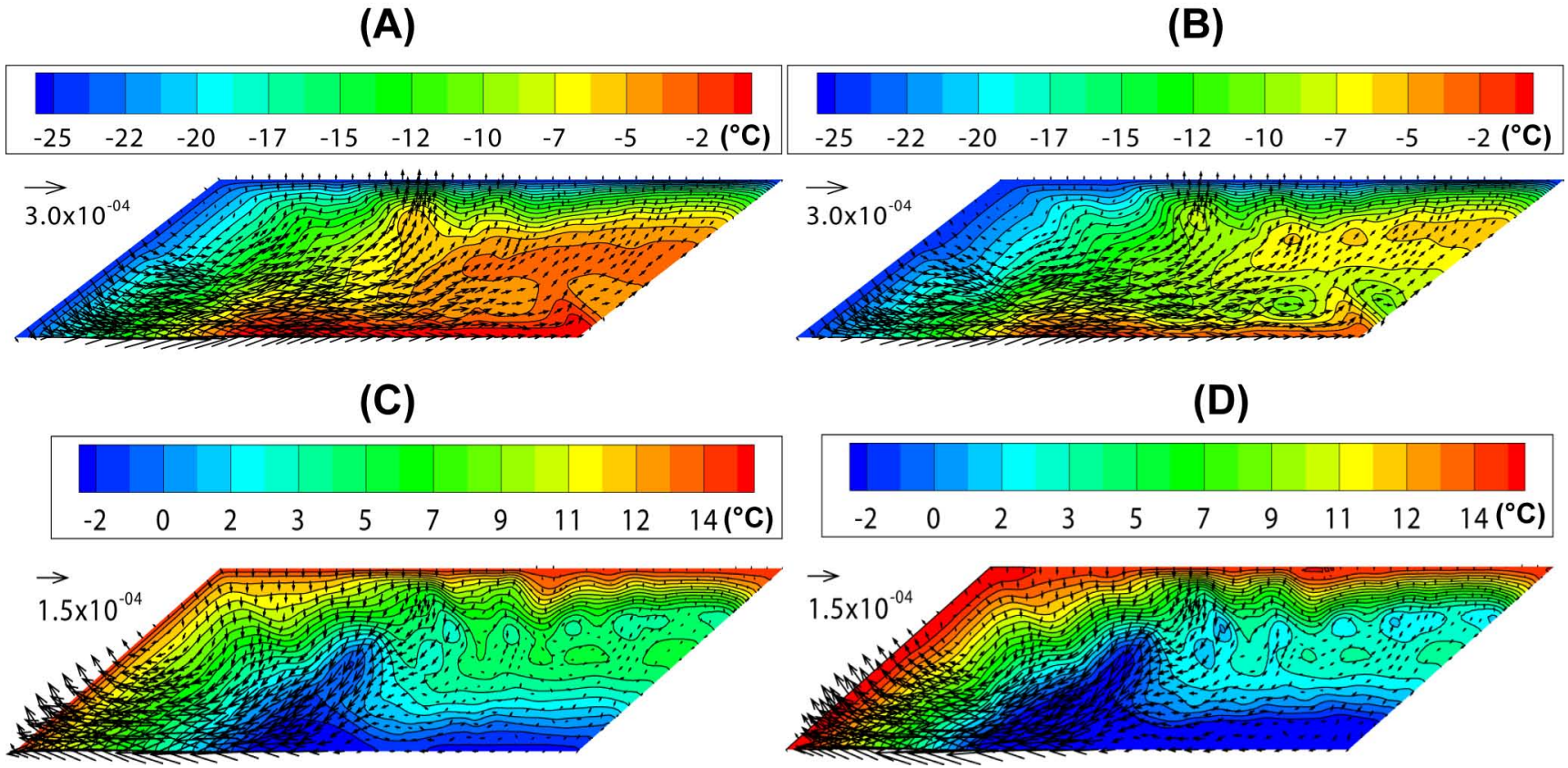

Figure 4.11: Isotherms (temperature in °C) and density-driven airflow vectors of the longitudinal section at the centre of the test pile (Fig. 4.2B) in (A) January 2007; (B) January 2008; (C) July 2007; and (D) July 2008. The isotherms are obtained from three-dimensional kriging of all available data points in the test pile. Average air velocity at this section was about (A) 1.8×10^{-4} m/s and (B) 1.6×10^{-4} m/s in January 2007 and 2008, respectively, and (C) 6.0×10^{-5} m/s and (D) 5.0×10^{-5} m/s in July 2007 and 2008, respectively.

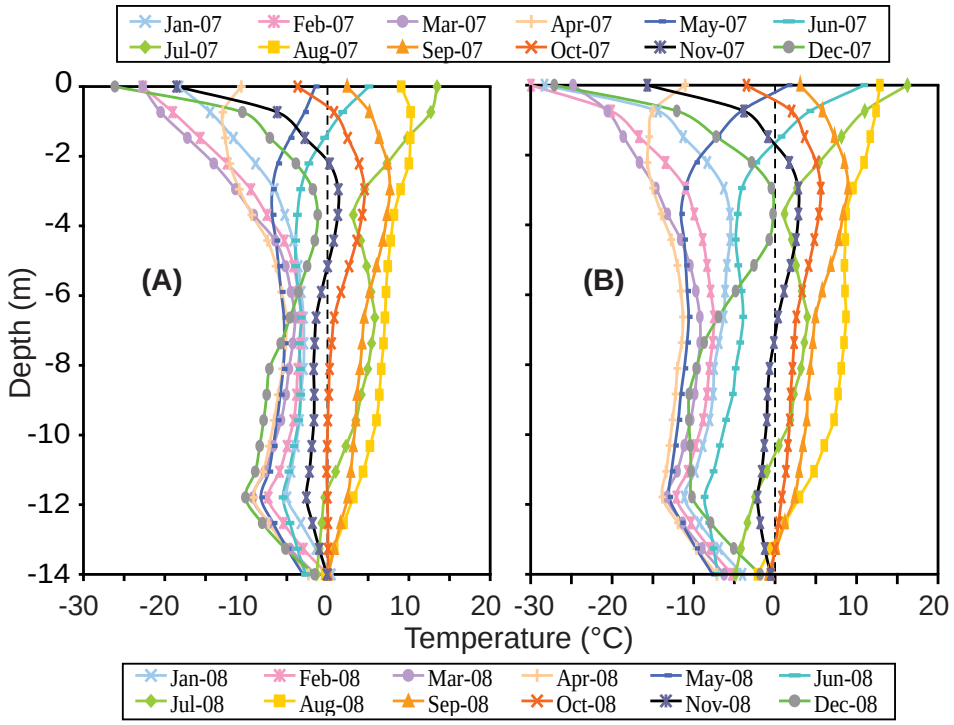

Figure 4.12: Temperature variations along Face 1's centre line in 2007 (A) and 2008 (B), which were interpolated linearly from thermistor strings 31S5thm and 31N5thm.

tude to air velocity at Face 1 and 4 (Fig. 4.9 and Fig. 4.10). During the summer, air flows in the inverse direction, and its average magnitude was 6.0×10^{-5} and $5.0 \times 10^{-5}\,\mathrm{m/s}$ in July 2007 and 2008, respectively (Fig. 4.11C and D). The average air velocity in July 2007 and 2008 was about three times smaller in magnitude than that during January of each year. Therefore, due to higher air velocity during the winter, it is expected that, in the absence of wind-driven advection and barometric pumping, heat transfer is greater during winter.

4.4.2.2 Temperature profiles at Face 1

The evolution of temperatures on the centre line along Face 1 and 4 with time is shown in Fig. 4.12 and Fig. 4.13. Following construction in 2006, initial temperatures within the test pile varied from 3 to 6 °C, and data from the subsequent three years are described. In 2007, all of Face 1 underwent a freeze-thaw cycle (Fig. 4.12A). The shape of the temperature plot differs from the temperature variations observed in the bedrock (Fig. 4.5A), which respond only to heat conduction. Thus, heat conduction is not the only heat transfer mechanism active within the test pile.

From January to May 2007, temperatures within the test pile were $< 0\,°C$, whereas temperatures in most regions of the test pile increased to $> 0\,°C$ from June through November 2007. Temperatures at the centre line of the test pile were $> 0\,°C$ in August and September 2007, and the $0\,°C$ isotherm on Face 1 extended 14 m below the crest of the test pile

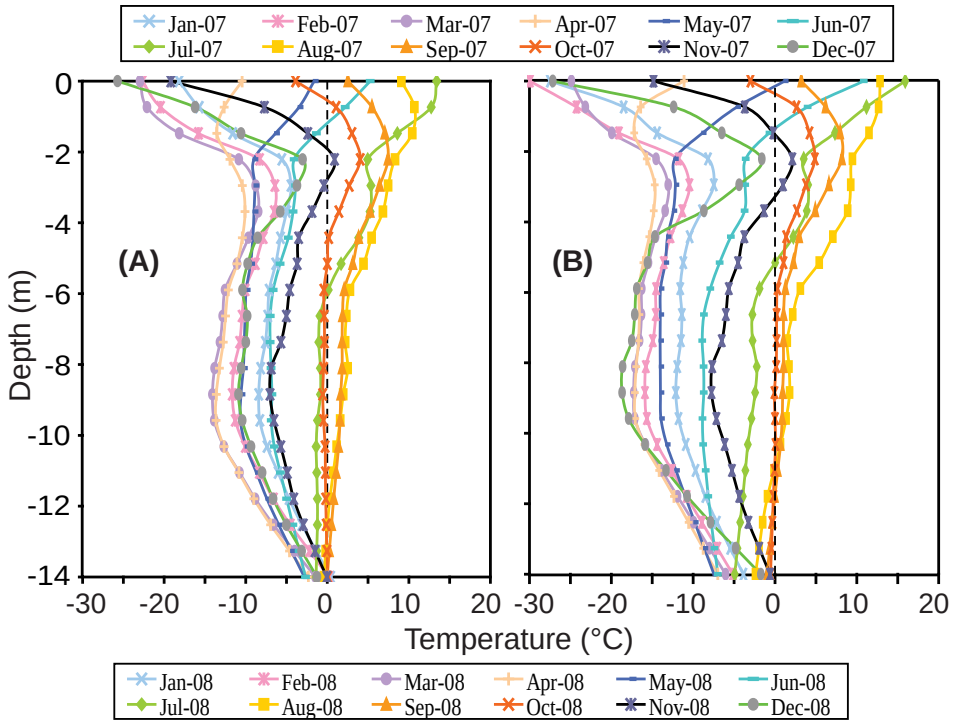

Figure 4.13: Temperature variations along Face 4's centre line in 2007 (A) and 2008 (B), which were interpolated linearly from thermistor strings 34S5thm and 34N5thm.

(Fig. 4.12A). Given the lack of thermistors between depths of 12 m and the base of the test pile, temperatures in between were assumed to have a linear variation. Between July and September 2007, heat flowed from the base of the test pile into the ground, whereas, in the other months of 2007, heat flowed into the test pile from the ground beneath (Fig. 4.12A).

In 2008, the depth of the 0 °C isotherm decreased to 13 m below the crest of the test pile. The shape of the temperature profiles in 2008 is similar to those from 2007 (Fig. 4.12B), but with a greater range of surface temperatures. Similar to the internal thermal regime in 2007, the test pile was below 0 °C from December 2007 to May 2008; during the other months, portions of the test pile rose $> 0\,°C$. In summary, the depth of the 0 °C isotherm on this face decreased by about 1 m in 2008 and steady state thermal conditions were not reached.

4.4.2.3 Temperature profiles at Face 4

The 2007 temperature profiles for Face 4 (Fig. 4.13A) were similar, both in the shape and the thickness of the active layer, to those for Face 1 (Fig. 4.12A). The centre of this face was thawed from August to September 2007, but temperatures in the lower region of Face 4 remained $< 0\,°C$ during the warmest month (July). Temperatures at all locations on Face 4 were $< 0\,°C$ between December 2006 and May 2007, with the upper 1.5 m thawing by June 2007 and the upper 6 m by July 2007.

In 2008, the frozen zone at the base of the test pile grew to 2.1 m, and the 0 °*C* isotherm decreased from 14 to 11.9 m below the test pile surface. In addition, the temperature profiles for Face 4 were similar in 2007 and 2008, but the larger ranges in 2008 reflect the greater range in surface temperatures.

4.4.3 Heat budget of the test pile during 2007 and 2008

A heat budget is important for establishing the internal thermal state (cooling or warming) of the test pile via the amount of heat being gained or released annually. The cross section at any face is assumed to be a control volume in two dimensions. Heat flow of the control volume in a typical summer month includes heat entering from the exposed surfaces and leaving via the test pile base (Fig. 4.14). Conservation of heat is written as (Beck et al., 1992):

$$\text{Net rate of heat flow in} + \text{Rate of heat generation} = \text{Rate of storage of heat} \tag{4.2}$$

The calculated heat energy budget of the control volume assumes: (1) conduction and convection are the main heat transfer mechanisms at the perimeter of the control volume; (2) the waste rock is homogeneous and isotropic with respect to thermal properties; (3) local thermal equilibrium between the fluid and solid phase, and (4) 2-D heat transfer is calculated for one unit width at each face. Amos et al. (2009b) showed that O_2 consumption was low and therefore oxidation rates are low and therefore heat release is expected to be low in the Type III rock. According to Fourier's law of heat conduction along with convection by air (Acrivos et al., 1980; Beck et al., 1992; Nield and Bejan, 1999):

Heat flux in x direction:

$$q_x = -\lambda \frac{\partial T}{\partial x} + u_x \rho_a c_a T \tag{4.3}$$

Heat flux in y direction:

$$q_y = -\lambda \frac{\partial T}{\partial y} + u_y \rho_a c_a T \tag{4.4}$$

Rate of storage of heat E_s:

$$E_s = C \frac{\partial T}{\partial t} \tag{4.5}$$

Where λ is the effective (bulk) thermal conductivity $(\mathrm{W}/(\mathrm{m}\cdot\mathrm{K}))$; C is the volumetric heat capacity $\left(\mathrm{J}/\left(\mathrm{m}^3\cdot\mathrm{K}\right)\right)$; u_x and u_y are Darcy air velocity (m/s) in x and y direction; c_a is the specific heat of air $(\mathrm{J}/(\mathrm{kg}\cdot\mathrm{K}))$; and $\rho_a = 1.22$ kg/m^3 is the air density at the standard temperature and pressure (Tipler, 1999).

Table 4.2: Thermal conductivity and air permeability of waste rock at the Diavik Diamond Mine and other mine sites. Diavik data measured during 2008 was provided by Amos et al. (2009a) and data of other mine sites is cited below.

Location	Thermal conductivity $(W/(m \cdot K))$ Range	Thermal conductivity $(W/(m \cdot K))$ Average	Air permeability (m^2) Range	Air permeability (m^2) Average
Diavik - Type III	1.0 - 2.5	1.9 ± 0.4	$2.0 \times 10^{-10} - 4.0 \times 10^{-9}$	2.0×10^{-9}
Aitik Mine, Sweden (Ritchie, 1994b)	0.7 - 1.6	1.2 ± 0.4	$2.6 \times 10^{-11} - 1.4 \times 10^{-10}$	
Heath Steele, Canada (Bennett et al., 1995)	1.0 - 1.2	1.2 ± 0.1	$1.6 \times 10^{-10} - 4.7 \times 10^{-9}$	
Kelian, Indonesia (Tan and Ritchie, 1997)	1.6 - 3.3	2.1 ± 0.6	$3.9 \times 10^{-13} - 9.3 \times 10^{-10}$	
Rum Jungle, Australia (Kuo and Ritchie, 1999)	1.8 - 3.1	2.2 ± 0.5	$8.9 \times 10^{-13} - 1.5 \times 10^{-9}$	

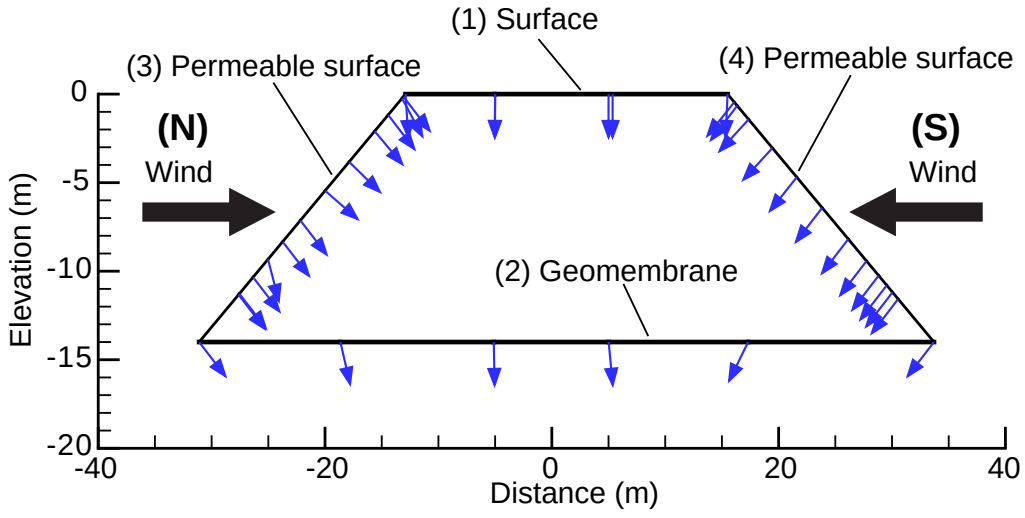

Figure 4.14: Typical vector heat flux (in blue) across a control volume (Face 1 or 4 of the test pile) in July 2007 at Face 4 showing heat gain at the surfaces and heat loss to the foundation rock.

The first term on the right of Eqn. 4.3 and Eqn. 4.4 indicates heat transfer by conduction, and the second term indicates heat transfer by convection. The convection term is only applied at the boundaries (3) and (4) in Fig. 4.14, which are wind-facing slopes. The upper surface of the test pile was compacted by construction equipment (boundary (1) in Fig. 4.14), and its permeability is about three orders of magnitude smaller than in the middle of the test pile (Neuner et al., 2012). At the base there is an impermeable geomembrane liner. Therefore, conduction dominates at the boundaries (1) and (2) in Fig. 4.14. Amos et al. (2009a), based on the internal air pressure measurements, indicated that the preferential airflow in the test pile is in the horizontal direction for an average wind speed of 20 km/h in the north-south direction that contributes about 44 % of all directions. This speed caused an average inward flux of 1×10^{-3} m/s and around 4×10^{-4} m/s at boundaries (3) and (4) in Fig. 4.14, respectively (Amos et al., 2009a). These inward air velocities were used to calculate convective heat transfer into the test pile. The conductive heat transfer was calculated through a monthly average temperature gradient along the perimeter of control volume, which was determined from the isotherms of Face 1 and 4 constructed in Section 4.4.2.1. A total heat transfer per one unit width at Face 1 and 4 was determined by multiplying the above-calculated heat fluxes with the perimeter length of Face 1 and 4, which is 121.2 and 127.2 m, respectively. Monthly average values of the total heat transfer are determined by multiplying the total heat transfer with time to come up with a MJ unit.

4.4.3.1 Thermal properties of the waste rock

To analyze heat transfer in porous media, physical and thermal properties of the waste rock (e.g., permeability, thermal conductivity and heat capacity) must be determined. Thermal conductivity of waste rock was measured using a transient probe installed at various depths in the test pile. The probe consists of four-pair heating wires attached to Teflon discs (36 mm in diameter and 7 mm thick) mounted at a 0.23-m interval on a 6.3-mm diameter steel rod and the length of the probe is 1.15 m. Three thermistors are attached to the probe to measure its temperatures. For measurements, the probe is lowered down an access port to a given depth and left at the measured depth for one hour to obtain thermal equilibrium. A heat source of 7.5 W/m is then supplied to the probe for 11 hours. Temperatures within the probe are recorded through heating phase and cooling phase during a measurement by the three thermistors; thermal conductivity is determined based on the response of measured temperatures (refer Chapter 3 for details of thermal conductivity measurements). In situ gas permeability was measured using permeability balls placed inside the test pile during construction (Amos et al., 2009a).

As shown in Table 4.2, the measured thermal conductivity range of waste rock in the Diavik test piles is higher than other mine sites and could be the result of the freeze-thaw cycle of water within the test pile. The average thermal conductivity of the test pile was determined to be $\lambda = 1.9\,\mathrm{W/(m \cdot K)}$ during this study period. Furthermore, the magnitude

of the measured air permeability of waste rock in the Diavik test piles is also greater than at other sites: Diavik's $K_{average} = 2.0 \times 10^{-9}\,(\mathrm{m}^2)$ is higher than the suggested value for natural air convection of $K_{average} = 1.0 \times 10^{-9}\,(\mathrm{m}^2)$ of reactive waste rock at the Rum Jungle mine, Australia, by Pantelis and Ritchie (1992).

The bulk volumetric heat capacity (C) was calculated based on volume fractions of solid, water and air:

$$C = \rho\left(\phi_s c_s + \phi_w c_w + \phi_a c_a\right) \tag{4.6}$$

Where ϕ_s, ϕ_w and ϕ_a are volume fractions of solid, water and air, respectively; and c_s, c_w and c_a are the specific heats of solid, water and air, respectively. Based on measurements conducted by Neuner et al. (2012), the porosity of the Diavik waste rock is 0.25, and an average in situ volumetric water content (ϕ_w) is 0.06 at field capacity. Thus, the values of volume fractions used in Eqn. 4.6 are 0.75 for solid, 0.06 for water and 0.19 for air. The solid fraction of the test pile is dominated by granite having specific heats $c_s = 790\,\mathrm{J/(kg \cdot K)}$, $c_w = 4,181.3\,\mathrm{J/(kg \cdot K)}$ and $c_a = 1,003.5\,\mathrm{J/(kg \cdot K)}$ (Farouki, 1981b; Andersland and Ladanyi, 2004). An average bulk density of waste rock, ρ, is assumed to be $2060\,\mathrm{kg/m^3}$ (Smith, 2012). The resulting volumetric heat capacity value $C = 2.1 \times 10^6\,\mathrm{J/\left(m^3 \cdot K\right)}$ was used to calculate heat budgets within the Type III test pile.

4.4.3.2 2007 heat budget

The monthly average heat transfer was -4.2×10^3 MJ at Face 4 and -3.9×10^3 MJ at Face 1 from January to March 2007 (Fig. 4.15A), indicating that heat was released from within the test pile during this period. On average, these heat transfers lowered the internal temperature by 2.7 °C at Face 1 and 2.8 °C at Face 4. The total heat released during this period (from January to March 2007) was -1.2×10^4 MJ from Face 1 and -1.3×10^4 MJ from Face 4, corresponding to an average decrease in temperature of 8.3 °C at Face 1 and 8.4 °C at Face 4. This difference is due to the location of Face 4 near the western end of the test pile: at this location, the face also was cooled by longitudinal winds (and/or natural air convection) entering the west end of the test pile (Fig. 4.11).

During the summer months (May to September 2007), a small amount of heat crossed the boundaries because interior temperatures of the test pile were similar to surface temperatures, resulting in a small temperature gradient (Fig. 4.15A). The maximum monthly heat transfers of 2.2×10^3 and 1.7×10^3 MJ occurred in July at Face 1 and 4, respectively, meanwhile in May and September the heat transfer was in significant (Fig. 4.15A). The total heat energy gained during this period was 4.8×10^3 MJ at Face 1 and 3.8×10^3 MJ at Face 4. These values result in an average increase in temperature of 3.4 °C at Face 1 and 2.5 °C at Face 4. A significant amount of heat was released between October and December 2007 compared to other months, with the maximum occurring in December. The total amount

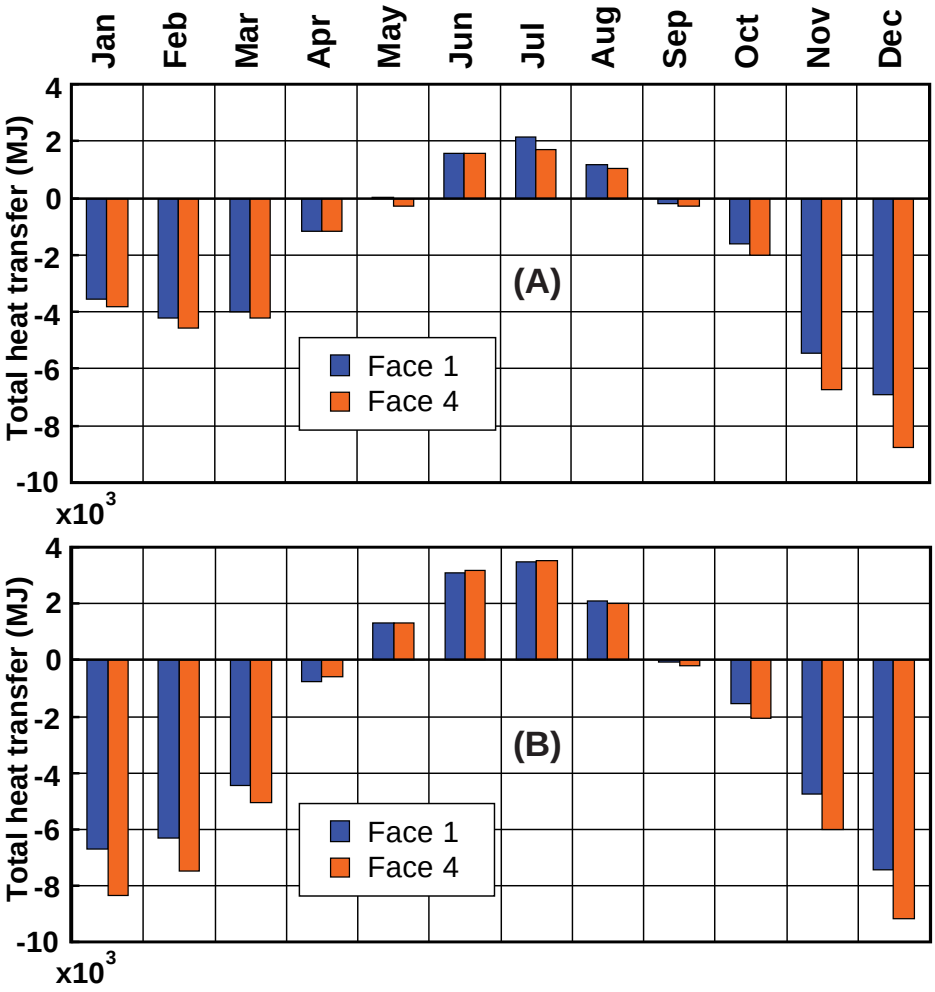

Figure 4.15: Calculated heat transfer at Face 1 and Face 4 of the Type III test pile in (A) 2007 and (B) 2008. Negative values indicate heat release and positive values indicate heat gain.

Table 4.3: Summary of heat budget in 2007 and 2008 for a unit width at Face 1 and Face 4.

	2007			2008		
Location	Face 1	Face 4	Average	Face 1	Face 4	Average
Heat gain (MJ)	5.0×10^3	4.4×10^3	4.7×10^3	1.0×10^4	1.0×10^4	1.0×10^4
Heat release (MJ)	-2.7×10^4	-3.2×10^4	-3.0×10^4	-3.2×10^4	-3.9×10^4	-3.6×10^4
Total (MJ)	-2.2×10^4	-2.8×10^4	-2.5×10^4	-2.2×10^4	-2.9×10^4	-2.6×10^4

of heat transfer at Face 1 and 4 during this period was -1.4×10^4 and -1.8×10^4 MJ, respectively. The total heat transfer in 2007 was -2.2×10^4 and -2.8×10^4 MJ at Face 1 and 4 (Table 4.3), respectively; therefore, the test pile was cooling.

4.4.3.3 2008 heat budget

From January to March 2008, a large amount of heat was released from Face 1 (-1.8×10^4 MJ) and from Face 4 (-2.1×10^4 MJ) compared to 2007 (Fig. 4.15B). However, the wind-induced inflow of warm air to the test pile and heat conduction during the summer brought in a large amount of heat energy from May to August 2008, and the maximum heat transfer was again observed in July. Overall, the summer heat transfer of 9.2×10^3 MJ at Face 1 and 9.3×10^3 MJ at Face 4 in 2008 represented relative increases in heat fluxes compared to the summer of 2007, and heat transfer at Face 4 was again greater than at Face 1 (Fig. 4.15B). On average, in 2008, the total heat gain during the summer of 1.0×10^4 MJ for Face 1 and Face 4 was about twice that of the summer of 2007 (4.7×10^3 MJ) (Table 4.3). However, the total heat transfer was similar in both years (-2.5×10^4 MJ in 2007 and -2.6×10^4 MJ in 2008) (Table 4.3).

4.4.4 Discussion

Based on the temperature measurements inside the test pile, elevated temperatures were not observed, and temperature variations were generally uniform within the test pile with no local warm or hot spots. This is in contrast to the high local temperatures recorded in waste-rock piles with sulfide contents greater than the Type III test pile (Harries and Ritchie, 1981; Lefebvre et al., 2001a; Sracek et al., 2006). Measured depletion of O_2 has not been observed in the Type III test pile (O_2 concentrations stayed at atmosphere values) (Amos et al., 2009a), likely due to the low sulfide content (0.053 wt % S), illustrating less significant oxidation (small heat release) compared to other sites. Amos et al. (2009b) estimated the oxidation rate of the Type III rock to be $2.9 \times 10^{-11}\,\mathrm{kg\,(O_2)/\left(m^3 \cdot s\right)}$ (in which m^3 is per unit volume of waste rock), which is equivalent to $4.9 \times 10^{-13}\,\mathrm{mol\,(O_2)/\,(kg \cdot s)}$. Therefore, the heat production by oxidation was about $4.1 \times 10^{-4}\,\mathrm{W/m^3}$ in the Type III rock at Diavik. The heat production rate at a bulk volumetric heat capacity of $C = 2.1 \times 10^6\,\mathrm{J/\left(m^3 \cdot K\right)}$ increases the waste rock temperature by about 6.1×10^{-3} °C annually, which is negligible. Therefore, the heat release due to oxidation of pyritic materials had no impact

on the internal thermal regime of the test piles.

Amos et al. (2009b), based on the measured internal air pressure gradient of the test pile, determined air velocity of 2.9×10^{-5} m/s that is equivalent to 7.7×10^{-6} kg $(O_2)/\left(m^2 \cdot s\right)$ (in which m^2 is per unit cross-sectional area at the waste rock/atmosphere surface). This rate has the same magnitude as density-driven airflow during summer (Fig. 4.9, Fig. 4.10 and Fig. 4.11). Therefore, the wind-induced and temperature-induced airflow provide sufficient O_2 for sulfide-mineral oxidation and enhance heat transfer between the interior of the test pile and the ambient environment.

The observed time lag between the surface temperature and temperature at a depth of 11 m varies between 1.5 and 2 months, and the amplitude ratio is about 0.4 (Fig. 4.7). In contrast, an analytical solution of heat conduction yields a time lag of 6.7 months and an amplitude ratio of 0.03, with a thermal diffusivity of 9.7×10^{-7} m^2/s used in this study (calculated based on Eqns. 10 and 11, p.66, Carslaw and Jaeger, 1959). The time lag and amplitude ratio indicate that convection/advection of air is an important heat transfer mechanism within the Type III test pile, despite the absence of strong pyrite oxidation. Therefore, convection/advection of air (due to wind (forced) and temperature-induced) appears to cause a rapid temperature response within the test pile to variation in ambient air temperatures. Furthermore, the impact of wind on the interior thermal regime of waste-rock pile depends not only on the characteristics of the wind (speed, direction and frequency), but also the characteristics of the waste-rock pile (permeability, size, shape and obstructions around the waste-rock pile). Overall, a long-term decrease in internal temperatures was recorded, indicating a net loss of heat from the Type III test pile during 2007 and 2008 (Table 4.3).

4.5 Conclusions

Since construction, bedrock temperatures beneath the Type III test pile have decreased and have been dampened from typical large-amplitude sinusoidal variations to nearly constant small amplitudes below 0 °C. Temperatures fluctuated between 0 and -3 °C in 2007 and -1 and -5 °C in 2008 at the contact points between the bedrock and the test pile. Below 2 m of the test pile surface, temperatures exhibited an annual cooling trend of about 4 °C. The change of the 0 °C isotherm in the test pile between 2007 and 2008 indicates permafrost was developing upward from the base into the test pile. The average growth rate was estimated to be about 1.5 m/a in 2008 (1.0 m/a for Face 1 and 2.5 m/a for Face 4).

The test pile cooled with time, and its annual heat energy release was -2.5×10^4 MJ in 2007 and -2.6×10^4 MJ in 2008. Temperature-induced convection influenced heat transfer between the test pile and the ambient atmosphere. Based on internal temperature measurements, upward airflow was expected during the winter, and the reverse occurred during the summer. However, airflow during the winter was higher than that of the summer; therefore,

heat transfer was higher in the winter. Elevated internal temperatures were not observed, and spatial temperature variations were relatively uniform in contrast to waste-rock piles undergoing more rapid oxidation, which generally are located in regions with high temperatures. Furthermore, internal temperatures showed a rapid response to ambient temperatures due to wind and natural air convection.

References

Acrivos, A., Hinch, E. J., and Jeffrey, D. J. (1980). Heat transfer to a slowly moving fluid from a dilute fixed bed of heated spheres. *Journal of Fluid Mechanics*, 101(02):403–421.

Amos, R. T., Blowes, D. W., Smith, L., and Sego, D. C. (2009a). Measurement of wind-induced pressure gradients in a waste rock pile. *Vadose Zone J*, 8(4):953–962.

Amos, R. T., Smith, L., Neuner, M., Gupton, M., Blowes, D. W., Smith, L., and Sego, D. C. (2009b). Diavik waste rock project: Oxygen transport in covered and uncovered piles. In *The 8th ICARD International Conference On Acird Rock Drainage, Skelleftea, Sweden, 2009*.

Andersland, O. B. and Ladanyi, B. (2004). *Frozen Ground Engineering*. John Wiley & Sons.

Bear, J. (1972). *Dynamics of fluids in porous media*. Dover Publications, Inc.

Beck, J. V., Cole, K. D., Haji-Sheikh, A., and Litkouhi, B. (1992). *Heat conduction using Green's functions*. Hemisphere publishing corporation.

Bennett, J. W., Garvie, A., Pantelis, G., Rictchie, A., Bell, A. V., and Noel, M. (1995). Comparison of measured and predicted transport processes controlling oxidation in the waste rock piles at the heath steele mine site. In *Conference on Mining and the Environment, Sudbury, Ontario, May 28th - June 1st, 1995*.

Carslaw, H. S. and Jaeger, J. C. (1959). *Conduction of heat in solids*. Oxford University Press.

Chi, X. (2010). Characterizing low-sulfide instrumented waste-rock piles: image grain-size analysis and wind-induced gas transport. Master's thesis, University of Waterloo.

Côté, J. and Konrad, J.-M. (2005a). Thermal conductivity of base-course materials. *Canadian Geotechnical Journal*, 42:61–78(18).

Environment-Canada (2008a). Climate data online. national climate data and information archive. Technical report, Environment Canada.

Farouki, O. T. (1981b). *Thermal properties of soils*. United States Army Corps of Engineers, Cold Regions Research and Engineering Laboratory, Hanover, New Hampshire, USA.

Farouki, O. T. (1981c). The thermal properties of soils in cold regions. *Cold Regions Science and Technology*, 5(1):67–75.

Harries, J. R. and Ritchie, A. I. M. (1981). The use of temperature profiles to estimate the pyritic oxidation rate in a waste rock dump from an opencut mine. *Water, Air and Soil Pollution*, 15(4):405–423.

Hollesen, J., Elberling, B., and Hansen, B. (2009). Modelling subsurface temperatures

in a heat producing coal waste rock pile, svalbard (78°n). *Cold Regions Science and Technology*, 58(1-2):68–76.

Hollesen, J., Elberling, B., and Jansson, P. (2011). Modelling temperature-dependent heat production over decades in high arctic coal waste rock piles. *Cold Regions Science and Technology*, 65(2):258–268.

Jaynes, D. B., Rogowski, A. S., and Pionke, H. B. (1984b). Acid mine drainage from reclaimed coal strip mines: 1. model description. *Water Resour. Res.*, 20:233–242.

Kuo, E. and Ritchie, A. (1999). The impact of convection on the overall oxidation rate in sulfidic waste rock dumps. In *Conference Proceedings, Sudbury 99 - Mining and the Environment*, volume 1, pages 9–18.

Lefebvre, R., Hockley, D., Smolensky, J., and Gelinas, P. (2001a). Multiphase transfer processes in waste rock piles producing acid mine drainage. 1: Conceptual model and system characterization. *Journal of contaminant hydrology*, 52(1-4):137–164.

Lefebvre, R., Hockley, D., Smolensky, J., and Lamontagne, A. (2001c). Multiphase transfer processes in waste rock piles producing acid mine drainage. 2. applications of numerical simulation. *Journal of contaminant hydrology*, 52(1-4):165–186.

MEND1.61.2 (1996). Acid mine drainage in permafrost regions: Issues, control strategies and research requirements. Technical report, Department of Indian and Northern Affairs Canada.

Neuner, M., Smith, L., Blowes, D. W., Sego, D. C., Smith, L. J., Fretz, N., and Gupton, M. (2012). The diavik waste rock project: Water flow though mine waste rock in a permafrost terrain. *Applied Geochemistry*, (0):–.

Nield, D. and Bejan, A. (1999). *Convection in porous media*. Springer, New York.

Pantelis, G. and Ritchie, A. I. M. (1992). Rate-limiting factors in dump leaching of pyritic ores. *Applied Mathematical Modelling*, 16(10):553–560.

Ritchie, A. I. M. (1994b). Bio-oxidation heaps and amd from waste rock dumps: The importance of the intrinsic oxidation rate. In *Proceedings of the 1994 Annual Conference the Australasian Institute of Mining and Metallurgy*, page 473, Carlton, Australia. Australasian Inst of Mining & Metallurgy.

Smith, L. (2012). Personal communication.

Smith, L. J., Moncur, M. C., Neuner, M., Gupton, M., Blowes, D. W., Smith, L., and Sego, D. C. (2012). The diavik waste rock project: Design, construction, and instrumentation of field-scale experimental waste-rock piles. *Applied Geochemistry*, (0):–.

Smith, S. and Burgess, M. (2000a). Ground temperature database for northern canada. *Geological Survey of Canada Open File Report 3954*.

Sracek, O., Gelinas, P., Lefebvre, R., and Nicholson, R. V. (2006). Comparison of methods

for the estimation of pyrite oxidation rate in a waste rock pile at mine doyon site, quebec, canada. *Journal of Geochemical Exploration*, 91(1-3):99 – 109.

Tan, Y. and Ritchie, A. I. M. (1997). In situ determination of thermal conductivity of waste rock dump material. *Water, Air, & Soil Pollution*, 98(3):345–359.

Tipler, P. A. (1999). *Physics for Scientists and Engineers*. W.H. Freeman.

CHAPTER 5

Wind, barometric and pore-air pressures in correlation to internal temperatures of an uncovered test pile located in a continuous permafrost region of Northern Canada

5.1 Introduction

Low-concentration-of-valuable-mineral rock is removed to reach ore from open or underground mining and the rock is chiefly stockpiled in large unsaturated piles called waste-rock piles (waste rock dumps or stockpiles). Biochemical oxidation of sulfide minerals in waste rock can result in Acid Rock Drainage (ARD) when in the present of oxygen and water. Acidic drainage (low pH) and high dissolved metal contaminants in water from waste-rock piles are a common problem for the mining industry. Without treatments, ARD can last for years after a mine has ceased its operation. The rate of oxygen supply restricts the oxidation rate and one of the main mechanism of oxygen transport is diffusion through the void in waste rock. However, if permeability of waste rock is sufficiently high, thermally driven convections resulting from heat generated by oxidation or temperature gradients between the surface and the interior have been also considered as sources of oxygen. Other sources of oxygen are usually omitted when analyzing heat and mass transfer in waste-rock piles are wind-induced advection and barometric pumping.

Internal temperatures of waste-rock piles are influenced by the heat fluxes at the surface of waste-rock piles which are ultimately controlled by solar radiation, fluid velocity (both air and water) in the pore space and surface and subsurface conditions (Lunardini, 1981; Wilson, 1990). The fluid velocity especially air, in turn, is governed by temperature gradients (natural air convection) within waste-rock piles, addition to advection by wind and barometric pumping. These processes are highly coupled and one may have a stronger effect on temperatures than the other depending on properties of waste-rock piles specially permeability. To determine the correlations between these variables, cross-correlation analyses are an excellent approach (Nakajima and Hayakawa, 1982; Cardaci et al., 1993; Guan

et al., 2007; Yndestad et al., 2008). Cross-correlation analyses have been successfully used to analyze the correlations of tidal current, water temperature and salinity in the Seto Inland Sea (Nakajima and Hayakawa, 1982), to study "reservoir-triggered earthquakes" at Koyna (India) based on measured data by Telesca (2010) and to examine the dependencies of soil temperatures at various depths to its surface temperature and determine soil thermal diffusivity using these correlations (Demetrescu et al., 2007).

The objectives of this chapter are: (1) to present the measured data including wind speed and direction, barometric pressure, pore air pressures and temperatures of one constructed test pile at Diavik Diamond Mine, Northwest Territories, Canada, (2) to utilize cross-correlation analyses of time-series data of wind, pressure and surface temperatures to determine which have the most significant influence on the interior temperatures of waste-rock pile, (3) the results of cross-correlation analyses along with one dimensional (1-D) conduction/advection transport was used to obtain in situ thermal diffusivity, permeability, air velocity.

5.2 Site Description and measured instruments

The Diavik Diamond Mine is located approximately 300 kilometers Northeast of Yellowknife, Northwest Territories, Canada and the Arctic Circle is located 220 kilometers North of the mine in the Canadian Arctic (64°31' N, 110°20' W, el. 440 m) (Fig. 5.1). The mine is located within a continuous permafrost region with prolonged and cold temperatures during winter: the mean annual air temperature (MAAT) and surface temperature (MAST) was of -9.0 °C and -5.0 °C respectively, an average precipitation of 283 mm with 60% from snow and northerly and easterly dominated winds with an average speed of 4.75 m/s (17.0 km/h) (Environment-Canada, 2008a).

Waste rock at the mine was segregated into three categories according to sulfur content: Type I (< 0.04 wt % S); Type II (0.04 to 0.08 wt % S); and Type III (> 0.08 wt % S). Three experimental waste-rock piles (test piles) were constructed at the study site between September 2004 and July 2007. Two test piles, Type I and Type III test piles containing Type I and III waste rock respectively, were constructed and instrumented with final dimensions of 15 m in height and 50 by 60 m in the area at the base. The covered test pile was constructed of Type III waste rock with a soil cover comprised of layers of till and Type I waste rock designed to limit oxygen and water transport into the underlying waste rock.

According to collected data up to the end of 2010, there are no intuitive differences of recorded internal temperatures between the Type I and III test pile. Moreover, due to the higher potential acid generation of the Type III test pile, intensive instruments were installed on and in the test pile to measure wind speeds and directions, barometric and pore-gas (air) pressure (Amos et al., 2009a). Therefore, the measured interior temperatures of the Type III test pile were used to correlate to wind, surface temperature, barometric and pore air

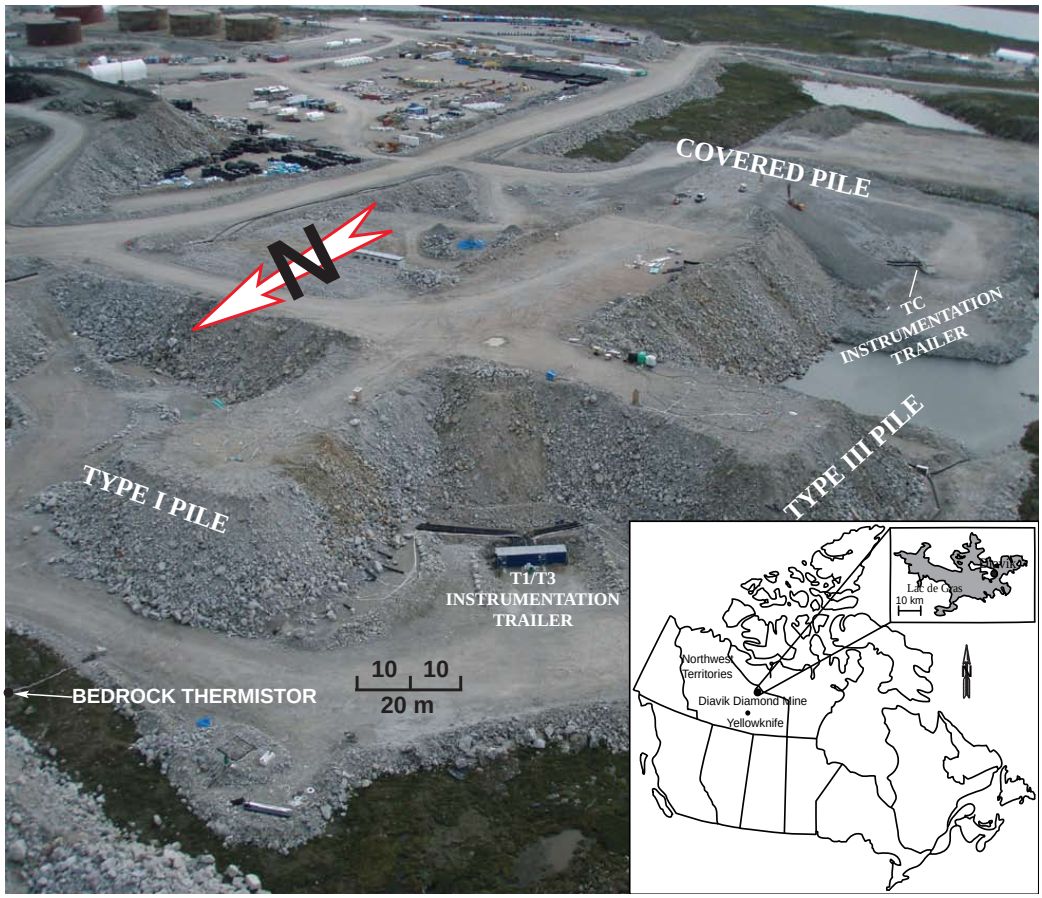

Figure 5.1: Aerial photo of the test piles at Diavik Diamond Mine and the location of the mine in Canada

pressure data. The Fig. 5.2 shows a typical cross-section of the Type III test pile (the test pile for short) with thermistor beads and gas ports (to measure pore-air pressures), other instruments were eliminated from the figure to enhance comparison of location.

There are 10 thermistors string (12 beads/string) installed in the test pile including 4 strings at face 1 and 4; 2 strings at face 2. At face 1 and 4, starting at 5 m off the centre line, two strings were installed vertically on the faces and the other twos are running along the batters. Meanwhile at face 2 there are only two vertical strings at 5 m off the centre line (Fig. 5.2). Temperatures are recorded at 4 hours interval using an automated data-logger system consisting of a Campbell Scientific (Edmonton, AB, Canada) CR23X data-logger and 6 AM16/32-XT multiplexers. The data-logger system is managing 384 thermistors beads installed inside and at the base of the Type I & III piles and bedrock (Fig. 5.1). The thermistor beads are YSI 44007 type providing precision of $\pm 0.2\,^{\circ}C$ and a wide-range working temperature of -80 - +120 °C.

A gas pressure line includes: a 50-mm PVC (casing) houses a cluster of 15 polypropylene tubings of either 3.2 mm or 6.4 mm o.d. to measure pore-air pressure and concentration of O_2 and CO_2 of the interior of the test piles. To achieve a 1-m vertical resolution on the slope face 1.3:1 of the test pile, each tubing was ended at 1.3-m intervals via a drill hole in the PVC casing. The gas pressure line was installed during construction at 2.5 m and 7.5 m on each side off the centre line of each face (Fig. 5.2). Pore air pressures are measured differentially to a reference point of 25 mm below the test pile's surface and they are called differential pressure. Differential pressures are measured at 49 points within the test pile and 14 points around the surface at one-minute intervals. However, due to the rapid changes of wind speed and wind direction, the pressure data were averaged for every 10 minutes. Wind speeds and wind directions are recorded at 10-minute intervals using an RM Young Model 05305, wind monitor mounted approximately 7 m above the surface of the test pile. A more-detailed description of the data-logger system of the differential pressures was provided by Amos et al. (2009a).

The labeling convention for temperature strings and gas sampling bundles is as following; 31N5thm10.5: '3' for Type III test pile ('1' for Type I test pile and 'C' for Covered test pile), face '1', offset 'N' north of center line vertically ('S', 'E', 'W' correspond to south, east and west), '5' = 5 m offset of centre vertically ('2' = 2.5 m offset and '7' = 7.5 m offset), 'thm' = thermistor ('gas' = gas line), '10.5' is deep from the top surface of the test pile (Fig. 5.2).

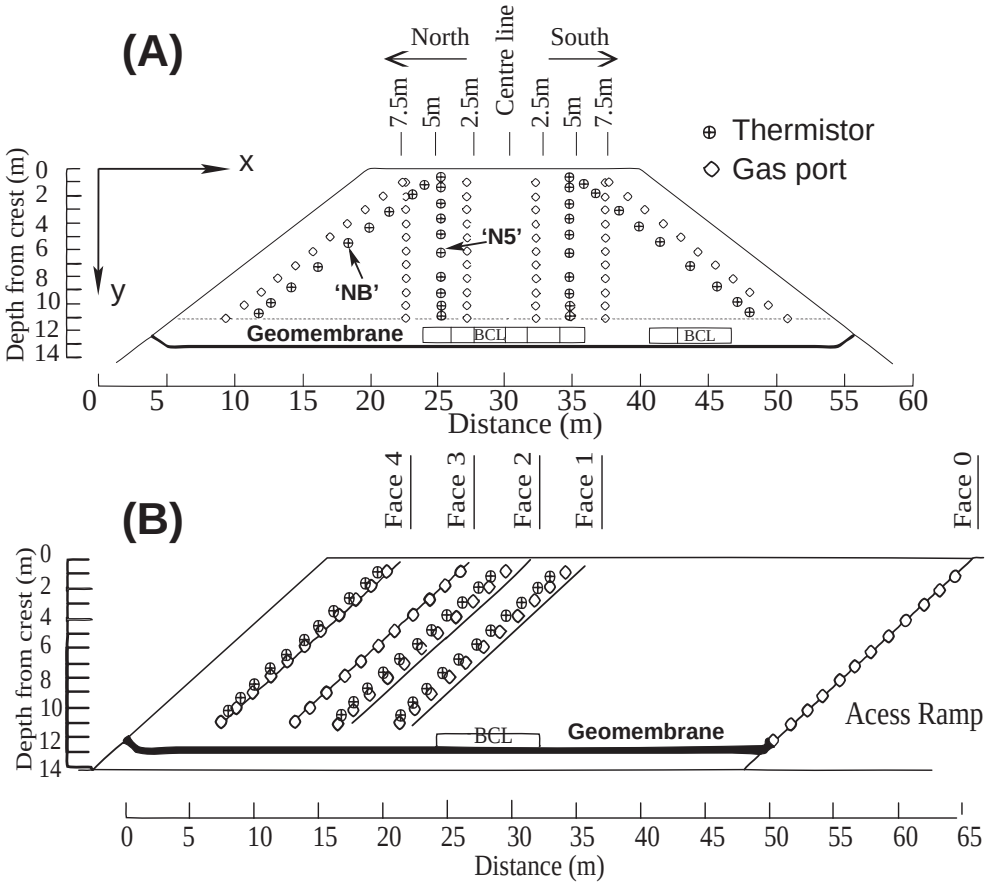

Figure 5.2: Typical cross-section (A) and long section (B) of the Type III pile

5.3 Results and Discussion

5.3.1 Measured data and Discrete Fourier Transform (DFT) of time series

5.3.1.1 Basic measured data

The data-logging systems described above were installed at the Diavik site in September 2005 for temperatures logging and June 2007 for weather and pore air pressures logging; pore-air pressure data were averaged every 10 minutes to eliminate short-term oscillations due to erratic changes of wind speed and direction. Wind speed fluctuated extensively and frequently surpassed 20 km/h and it could reach 60 km/h during gusting conditions. The mean wind speed was 15.4 km/h with a standard deviation (STD) of 8.5 km/h furthermore there were about 44 % and 87 % of the time wind speed exceeding 20 km/h and 10 km/h respectively. North and southward wind were most frequent and the least frequent was westward (Fig. 5.3B). Meanwhile barometric pressures were less fluctuating and the histogram was fitted with a normal-probability-distribution function having a mean of 960 hPa and STD of 19.1 hPa (Fig. 5.3). Pore air pressures at a port "34N2gas6.00" were highly variable and they mainly responded to wind speeds with a mean of 2.5 Pa. Furthermore, the fitting curve of pore-air pressures shows a correlation to nearby ground temperatures at an approximate depth of 6 m (Fig. 5.3C).

Surface temperatures of the test pile were adopted from ground temperatures at a depth within 5 cm below the surface. Fig. 5.3 shows an annual fluctuation and lowest values of temperatures occurred during the winters 2008 and 2009 while winters 2006 and 2007 showed the average temperatures during the measurement period. Conversely, the winter of 2010 was warm and fluctuated less. The summer of 2008 showed a great variation and high values of surface temperatures while the other summers were quite consistent (Fig. 5.3D). The recorded surface temperature can be represented using a harmonic function, $T_s\,(^{\circ}\mathrm{C}) = -5.0 + 20.0 \sin\left(\frac{2\pi t}{365}\right)$, in which t is time in day, having a MAST of -5 °C and an amplitude of 20 °C. Fig. 5.4A shows that the zero MAST corresponds to a MAAT of about -4.3 °C, which is based on temperature data of northern Canada. Moreover, temperature data at Diavik is fitted well by this trend line. Air temperatures were measured at Diavik meteorological station located about 1 km from the test piles and the zero surface temperature corresponds to -4.9 °C air temperature (Fig. 5.4B based on daily average values measured at the Diavik site).

Owning its high permeability, the thermal behavior of the test pile is remarkably different than that of bedrock which usually has a much lower permeability. Fig. 5.5 shows the temperature variations at the surface of both the test pile and bedrock were similar. However, ground temperature amplitudes in the test pile were much larger than in the bedrock at the same depths, conversely the phase lags (time lags) were much smaller in the test pile compared to bedrock (Fig. 5.5). For instance, the time lag, which is the time different

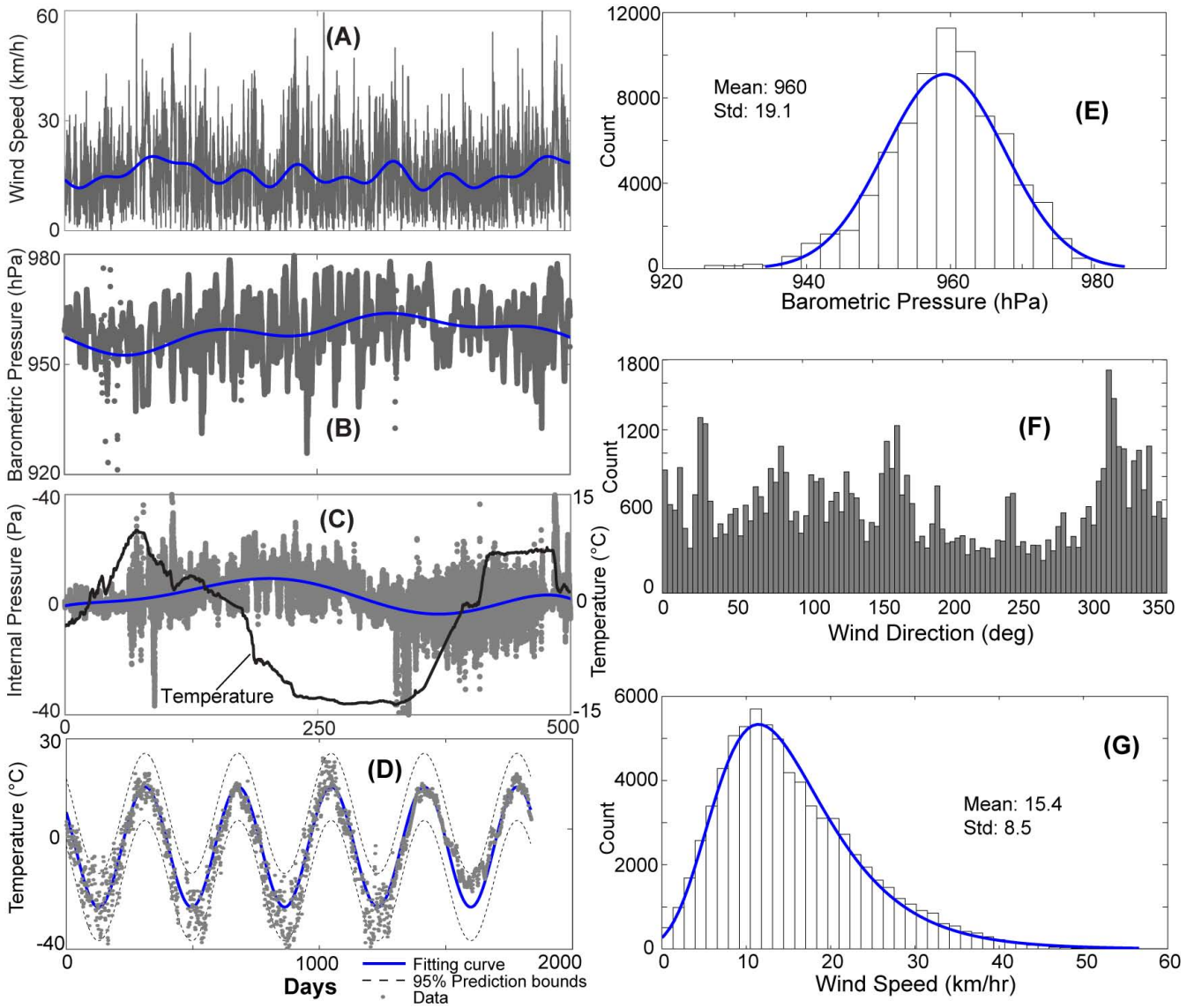

Figure 5.3: Time series of wind speed (A), barometric pressure fluctuation (B), pore air pressures at 34N2gas6.00 and temperatures at 31N5thm5.80 (C), data from June 10, 2008 to Nov. 11, 2009 and surface temperature (D) measured at 5 cm below the test pile's surface, from September 14, 2005 to September 26 2010, histograms of barometric pressure (E), wind direction (F): 360 deg = North, 270 deg = West and wind speed (G) .

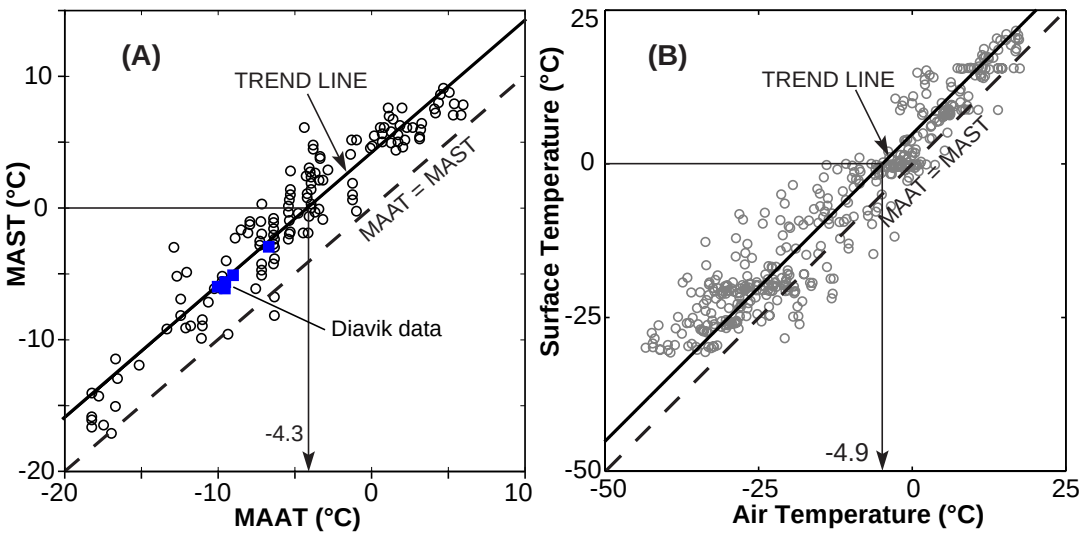

Figure 5.4: Relation between air and surface temperatures, for Northern Canada (A) (data from Smith and Burgess, 2000b) and at Diavik (B)

between peaks of time series data, of temperature between surface and 10 m depth thermistors was about 60 days in the test pile whereas it was about 160 days in bedrock. Detailed analyses of time lags and amplitudes are provided in the later sections.

5.3.1.2 Discrete Fourier transform (DFT) of time-series of measured data

It is helpful to recognize the dominated frequencies of the climatic time-series data and from the known dominated frequencies, one can correlate between these climatic variables. Time series of a continuous-periodic signal can be described by of a sum of sines and cosines, or Fourier representation, as (Morrison, 1994):

$$Y(t) = \frac{1}{2}Y_o + \sum_{n=1}^{\infty} a_n \cos(\omega_n t) + \sum_{n=1}^{\infty} b_n \sin(\omega_n t) \tag{5.1}$$

With

$$a_n = \frac{1}{\pi}\int_{-\infty}^{\infty} Y(t)\cos(\omega_n t)\mathrm{d}t \quad n = 1, 2, \ ,\infty \tag{5.2}$$

$$b_n = \frac{1}{\pi}\int_{-\infty}^{\infty} Y(t)\sin(\omega_n t)\mathrm{d}t \quad n = 1, 2, \ ,\infty \tag{5.3}$$

$$Y_o = \frac{1}{\pi}\int_{-\infty}^{\infty} Y(t)\mathrm{d}t \tag{5.4}$$

Fourier transform

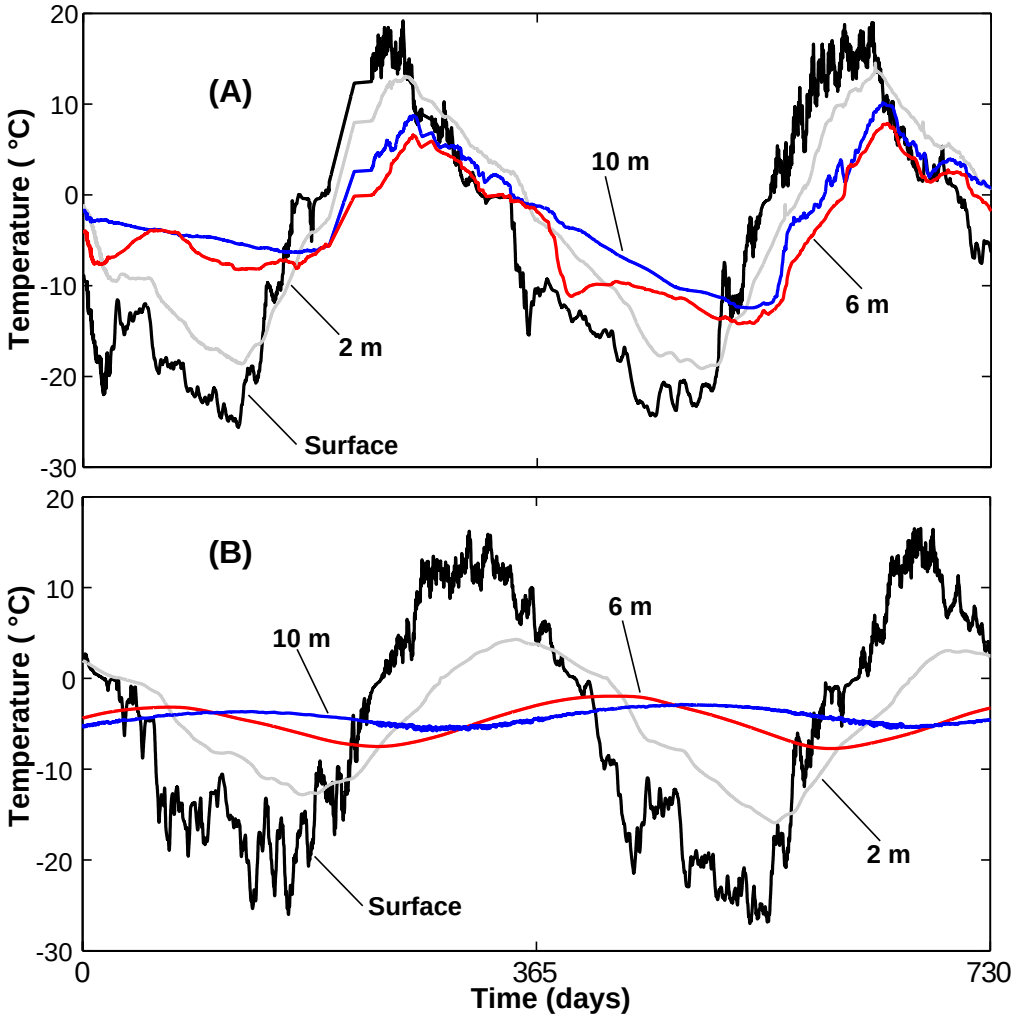

Figure 5.5: Temperatures at thermistor string 31N5thm, from Nov. 20, 2006 (A) and bedrock temperatures (located in the lower left corner of Fig. 5.1) from September 14, 2005 (B)

$$\hat{Y}(\omega_n) = \frac{1}{\sqrt{2\pi}} \int_{-\infty}^{\infty} Y(t) e^{-i\omega_n t} \mathrm{d}t \tag{5.5}$$

Where: $\frac{1}{2}Y_o$ is the mean value of a time series, ω is an angular frequency, the value of $\sqrt{a_n^2 + b_n^2}$ represents the power spectral density at various frequencies. By using DFT of a signal or time series, one can convert a signal from a time to frequency domain, and DFT in this study was performed by using a Matlab function fft (Fast Fourier Transform) (Matlab, 2012).

The Fig. 5.6A shows the dominant periods of wind speed were 1, 4, 5, 14, 50 and 182 days having the largest amplitudes of 2.1 and 2.2 (km/h) at periods of 14 days and 182 days (semi-annual). As shown later the periods of 1, 4, 5 and 14 days of wind speed caused rapid variations in ground temperatures within the test pile with ambient temperatures due to advection associated with high pore air velocity (Fig. 5.6A). Meanwhile the dominated period in barometric pressure time series was 365 days and it was probably correlated to the annual fluctuation of air temperatures. Furthermore, various periods of less than 50 days were likely correlated to wind speed (Fig. 5.6B). The DFT of pore air pressure time series at port "34N2gas6.00" poses an interesting result and it contained two distinct-dominated periods: 1 and 365 days in which the 1-day period was apparently correlated to daily variation of wind speed and the 365-day period was related to the annual fluctuation of temperatures within the test pile through the ideal gas law (Fig. 5.6A, C, B). However, there were also periods between 10 and 50 days in the pore air pressure time series and these periods were correlated to wind speed. The 365-day period was dominated in time series of the surface temperatures and it was related to the annual variation of air temperatures. Meanwhile the other periods with much less power were likely correlated to wind and/or barometric pressure fluctuations (Fig. 5.6D).

5.3.2 Cross-correlation analyses of ground temperatures within the test pile to wind speeds, barometric and pore-air pressures, and surface temperatures.

5.3.2.1 Fundamental theory

The cross-correlation of two time-series signals A and B, $R_{AB}(t_l)$, is a function of time to synchronize the two signals (Deutsch and Journel, 1992; Li et al., 2007; Telesca, 2010). $R_{xy}(t_l) \in [-1, 1]$ is defined as:

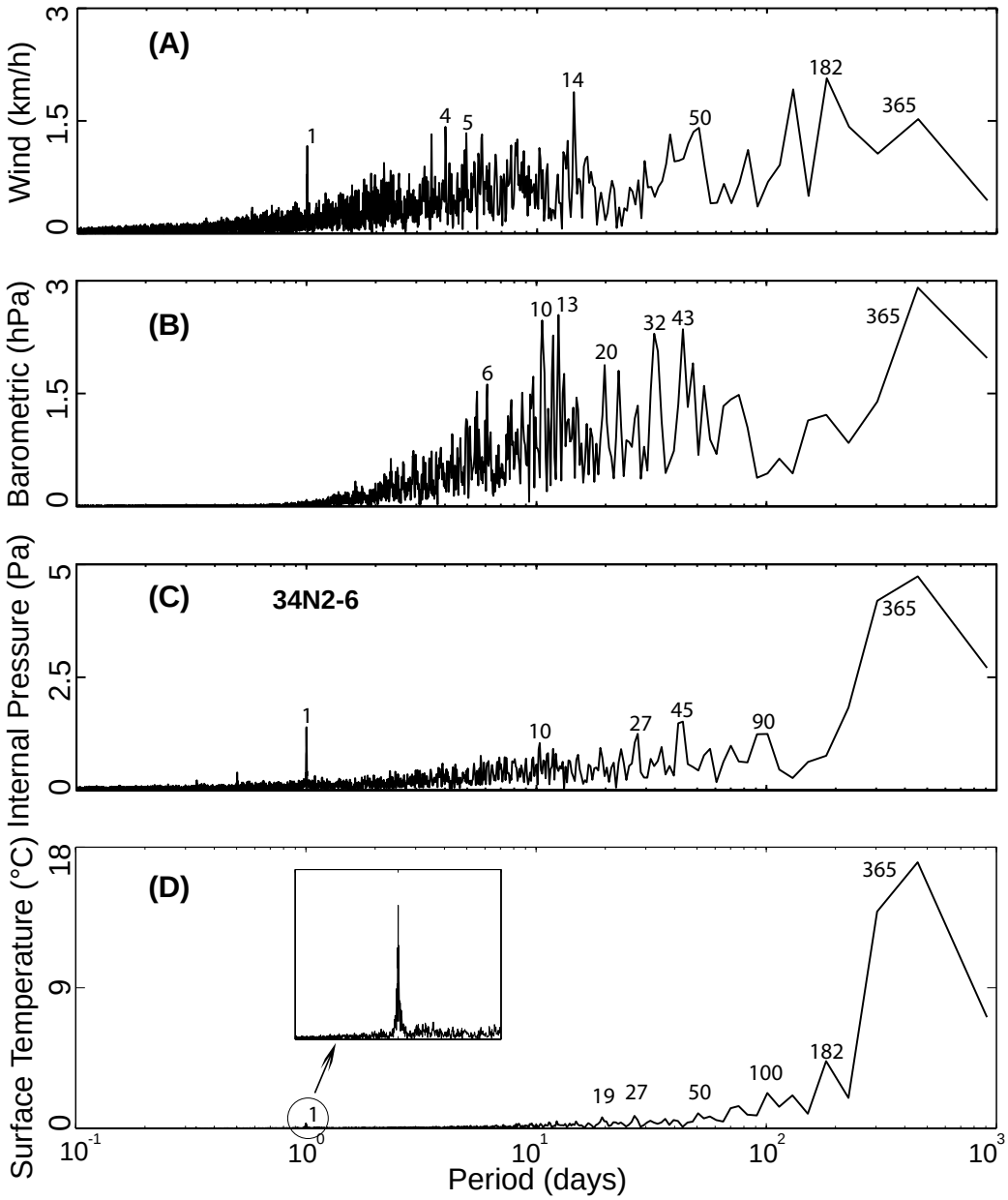

Figure 5.6: DFT of wind speed (A), barometric pressure (B), internal pressure at port 34N2gas6.00 (C) and surface temperature (D) time series after subtracting mean values of the corresponding data

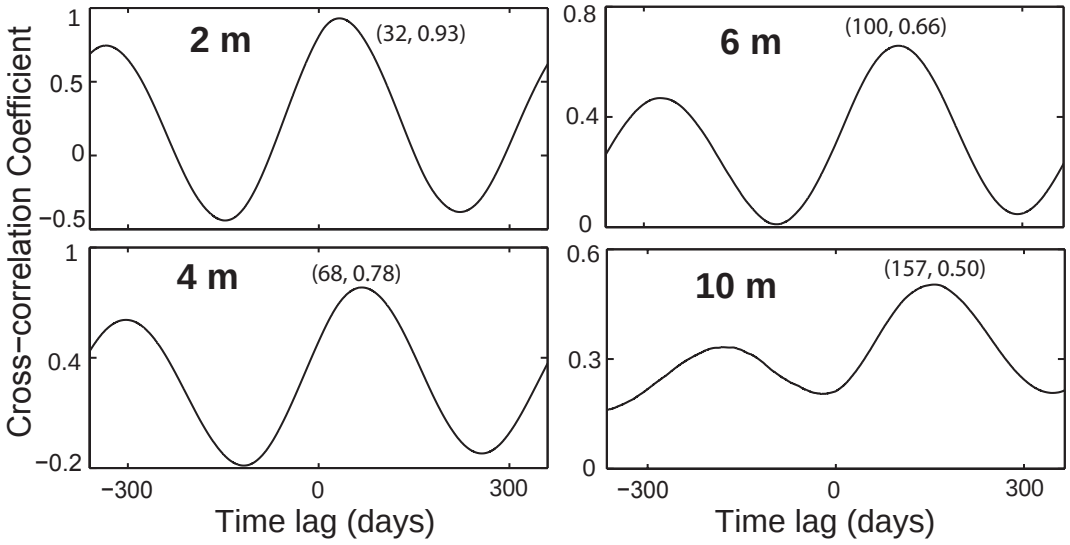

Figure 5.7: Typical relations between the cross-correlation coefficient and time lag of surface thermistors to subsurface thermistors in Bedrock (Fig. 5.5B)

$$R_{AB}(t_l) = \frac{C_{AB}(t_l)}{\sqrt{\sigma_A^2 \sigma_B^2}} \in [-1, 1] \tag{5.6}$$

$$C_{AB}(t_l) = \frac{1}{N}\sum_{n=1}^{N}\left(A_{n+t_l} - \bar{A}\right)\left(B_n - \bar{B}\right) \tag{5.7}$$

$$\sigma_A^2 = \frac{1}{N}\sum_{n=1}^{N}\left(A_n - \bar{A}\right)^2 \tag{5.8}$$

$$\bar{A} = \frac{1}{N}\sum_{n=1}^{N} A_n \tag{5.9}$$

Where: $C_{AB}(t_l)$ is the cross-covariance of A and B, σ_A^2 and σ_B^2 are the variances of A and B with means $\bar{A}$ and $\bar{B}$, N is the signal length, A_{n+t_l} and B_n are A and B at time $n+t_l$ and n respectively, t_l is time lag. The bounds of $R_{AB}(t_l)$ indicate the maximum correlations whereas $R_{AB}(t_l) = 0$ indicates no correlation. Cross-correlation analyses were performed using Matlab (Matlab, 2012).

5.3.2.2 Cross-correlation analyses of bedrock temperatures

Bedrock temperatures were used as the reference case of conduction dominated heat transfer at the site and any significant deviation of ground temperatures within the test pile from it was caused by convection and/or advection. The cross-correlation coefficients $R_{AB}(t_l)$ in Fig. 5.7 are between bedrock's surface temperatures to bedrock's subsurface temperatures at depths of 2, 4, 6, 10 m. The figure indicates a decrease in max $(R_{AB}(t_l))$ (an average of

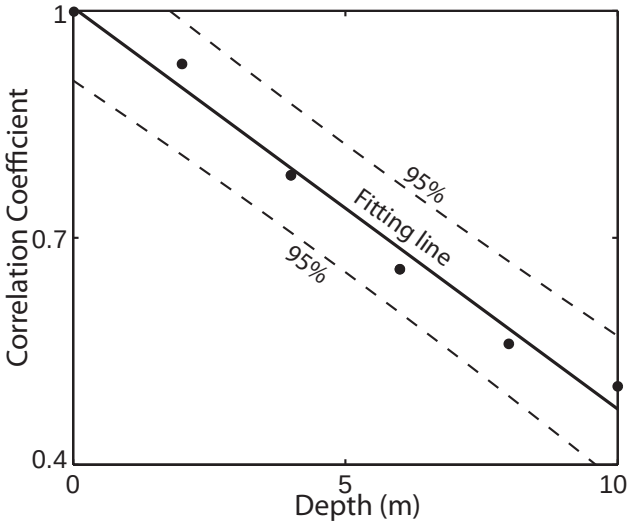

Figure 5.8: Cross-correlation coefficients with depths of bedrock thermistors.

0.72) and an increase in time lag t_l with depths and the relation can be fitted by a linear line (Fig. 5.8). The linear relation in Fig. 5.8 shows an indication of conduction and the bedrock is relatively homogeneous.

5.3.2.3 Cross-correlation analyses of ground temperatures of the test pile to other time series

Temperatures within the test pile (without a heat source due to oxidation of sulfide minerals) are controlled by external actions of surface (air) temperatures, wind, air pressure fluctuations and above all, the source of heat energy supplied to the Earth's surface and the atmosphere comes predominantly from the Sun through solar radiation. All of these weather variables should have some extent of connection to ground temperatures within the test pile and which ones may have the dominant effects depending to the nature of the test pile. Therefore for the purpose of analyzing interior thermal behavior of the test pile, the cross-correlation analyses of the test pile's temperatures to external weather variables give us a conclusive answer.

Fig. 5.9 shows a similar trend but a remarkable difference in the values of the cross-correlation coefficients compared to bedrock at a vertical thermistor, 31N5thm, in the test pile; smaller time lags and larger values of max $(R_{AB}(t_l))$. The larger values of max $(R_{AB}(t_l))$ of the test pile indicate that the temperatures within the test pile have stronger correlations to surface temperatures than those in the bedrock. Indeed, the high permeability of the test pile promoted convection/advection in the test pile which made the test pile's temperatures changed rapidly with surface temperatures. Wind speeds and barometric pressures can also be correlated to the test pile's temperatures. The plots of $R_{AB}(t_l)$ between barometric pressures and wind speeds to the thermistors string, 31NBthm, are represented in Fig. 5.10A and

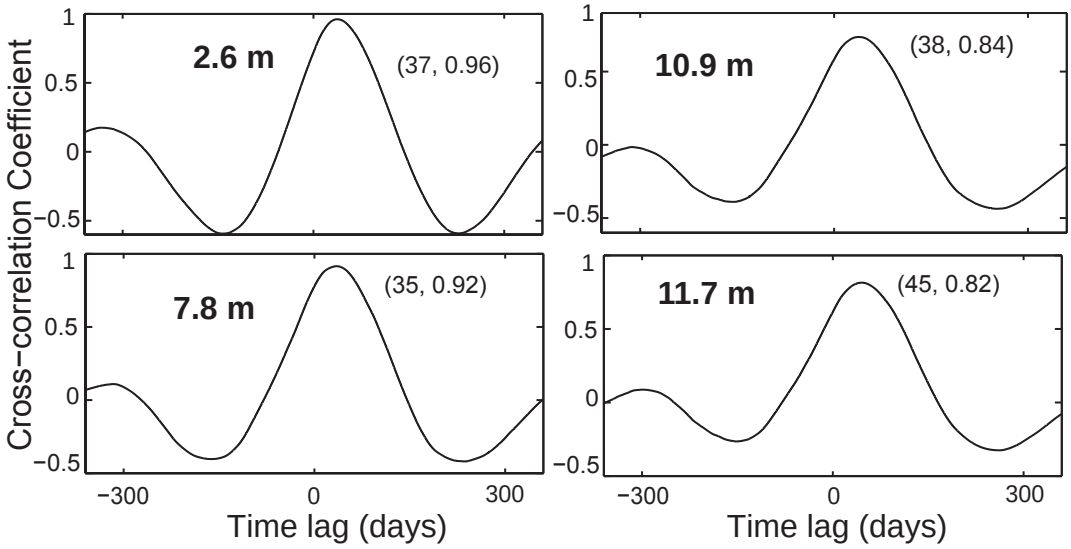

Figure 5.9: Typical relations between the cross-correlation coefficient and time lag of surface thermistors to subsurface thermistors within the test pile at thermistor string 31N5thm (Fig. 5.5A).

B. However the cross-correlation coefficients are much smaller (weaker correlations) and negative in values compared to surface temperatures. The values of max $(R_{AB}(t_l))$ generally increase and conversely time lags decrease with depths due to the tendency of increasing permeability with depths within the test pile.

The cross-correlation coefficients versus depths of the test pile's temperatures to barometric pressures, wind speeds, surface temperatures and nearby pore-air pressures are shown in Fig. 5.11. In general, the cross-correlation coefficients to wind speeds and pressures are negative and increase with depths. However the cross-correlation coefficients to surface temperatures are positive, and decrease with depths. The correlation to surface temperatures is strongest with a mean of 0.91 (Fig. 5.11C) whereas, the correlations to barometric pressures, wind speeds, and internal pressures are much weaker with mean values of -0.46, -0.44 and -0.43 respectively. The negative values of these correlations indicate that an increase in wind speeds or barometric pressures corresponds with a decrease of the test pile's temperatures.

In the top 2 m of the test pile, the cross-correlation coefficients of temperatures within the test pile to wind speeds and barometric pressures are notably small compared to the correlations to surface temperatures as shown in Fig. 5.11A and B. This is because the test pile construction method (end dumping) creates material segregation (from fine to coarse along the depth profile) and the compaction of construction equipments at the surface. The heterogeneity and segregation of materials in waste-rock piles have been recognized in several studies (Smith et al., 1995; Azam et al., 2007). As a result, the segregation has contributed to a much lower permeability within a few meters of the surface. However, below this zone,

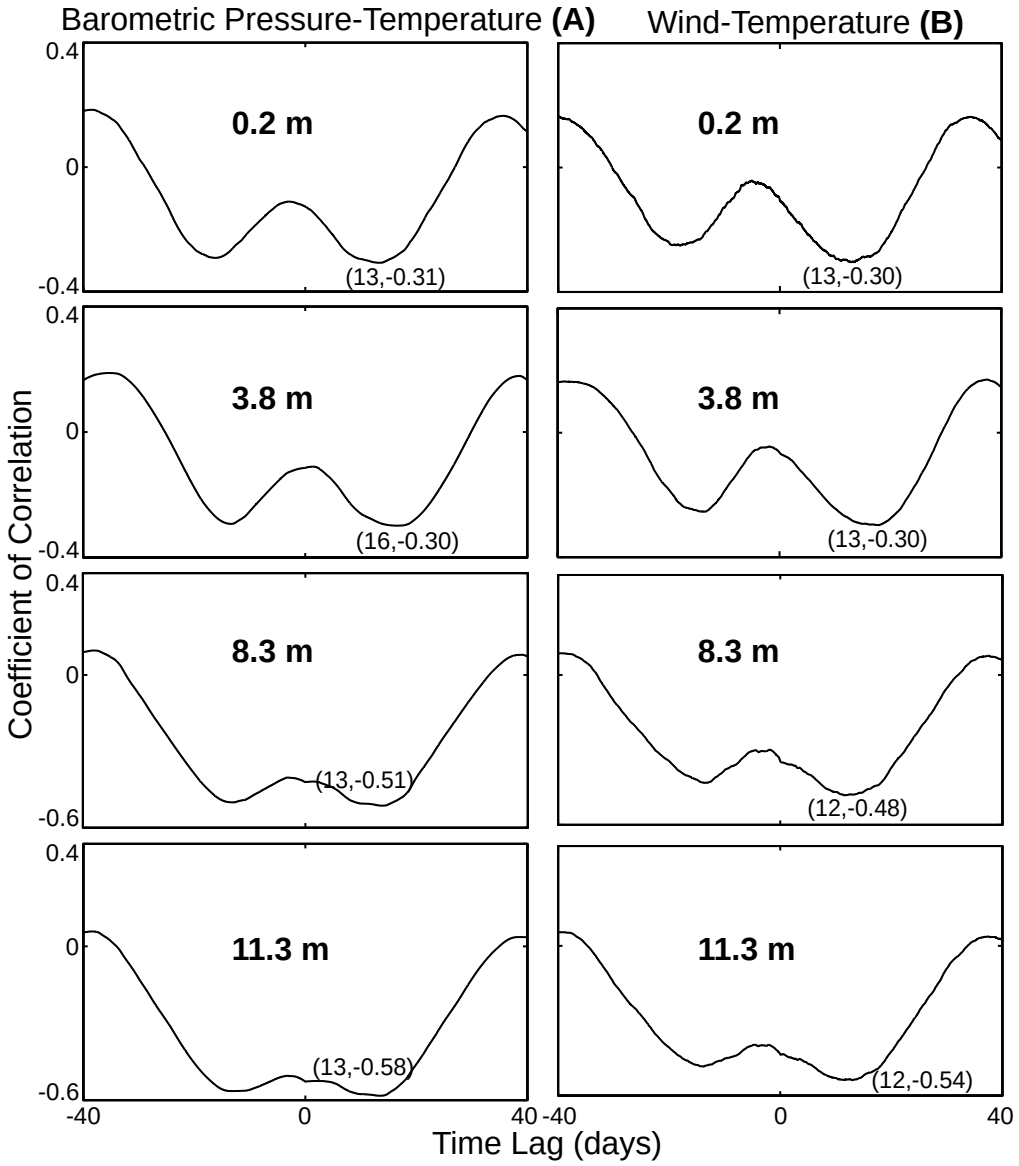

Figure 5.10: Typical relation between cross-correlation coefficient and time lag of barometric pressure (A) and wind speed variation (B) to temperatures of the thermistor string 31NBthm .

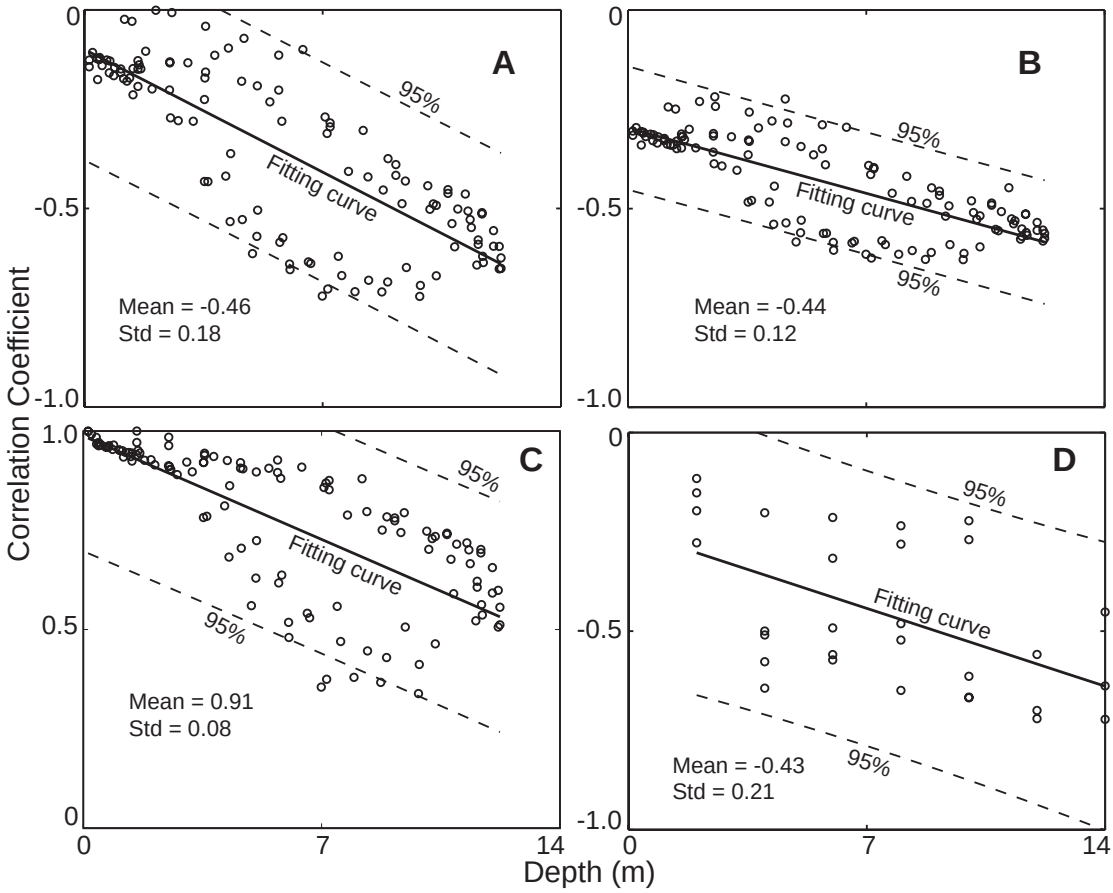

Figure 5.11: Cross-correlation coefficients with depths between the test pile internal temperatures to barometric pressure (A), wind speed (B), the test pile's surface temperature (C) and nearby internal pore-air pressure (D) as a function of distance to the test pile's surface.

permeability is much higher but it is largely heterogeneous with interbedded fine layers. The high permeability but heterogeneity leads to higher but scatter correlations to wind speed and barometric and pore-air pressures. Fig. 5.11D shows the correlations to nearby internal pore-air pressures, the correlations are a result of the ideal gas's law relating between temperature and pore-air pressure.

5.3.3 Evaluation of thermal diffusivity of bedrock and the upper portion of the test pile

5.3.3.1 Bedrock thermal diffusivity

In an ideal conduction heat transfer medium (bedrock in this case), the cross-correlation coefficients of bedrock's temperatures at depths to surface temperatures are 1 at the surface and decrease linearly. Meanwhile the amplitudes reduce logarithm with depths (Fig. 5.12). The decrease of amplitudes and the correlations to surface temperatures with depths can be explained using 1-D thermal conduction analysis as:

$$\frac{\partial^2 T}{\partial y^2} = \frac{1}{\kappa_b}\frac{\partial T}{\partial t} \tag{5.10}$$

Where T is temperature, t is time, y is vertical direction taken as positive downward and κ_b is apparent (effective) thermal diffusivity of bedrock. When the surface temperatures are a simple periodic function of time with a period of $2\pi/\omega$ as a boundary condition.

$$T_s(t) = T_o + |T_o| \sin(\omega t - \varepsilon) \tag{5.11}$$

Where T_o is the mean surface temperatures, ω is the fundamental angular frequency, $|T_o|$ is the amplitude and ε is the phase. The analytical solution of Eqn. 5.10 with the boundary condition Eqn. 5.11 at the surface in a semi-infinite half space is (Carslaw and Jaeger, 1959):

$$T(y,t) = T_o + |T_o| e^{-y\sqrt{\omega/2\kappa_b}} \sin\left\{\omega t - \varepsilon - y\sqrt{\frac{\omega}{2\kappa_b}}\right\} \tag{5.12}$$

The components $e^{-y\sqrt{\omega/2\kappa_b}}$ and $-y\sqrt{\frac{\omega}{2\kappa_b}}$ of Eqn. 5.12 indicate the decrease of the amplitude and phase lag with depths causing the reduction of cross-correlation coefficients (Fig. 5.12 and Fig. 5.8). Moreover, the relations of the logarithm amplitude ratio (in a semi-logarithmic scale) and cross-correlation coefficients with depths are fitted linearly. As a result, the bedrock is relatively homogeneous and its apparent thermal diffusivity is derived explicitly by knowing the time lags or amplitudes of ground temperatures at various depths (Carslaw and Jaeger, 1959).

$$\kappa_b = \frac{1}{2\omega}\left(\frac{y_2 - y_1}{\delta t}\right)^2 \tag{5.13}$$

$$\kappa_b = \frac{\omega}{2}\left(\frac{y_2 - y_1}{ln\left(\frac{|T_2|}{|T_1|}\right)}\right)^2 \tag{5.14}$$

Where δt is phase difference; $|T_1|$ and $|T_2|$ are temperature amplitudes at two depths y_1 and y_2. From Fig. 5.12 and Fig. 5.13B, the apparent thermal diffusivity of bedrock varies between 1.2×10^{-6} and $1.4 \times 10^{-6}\,\mathrm{m^2/s}$ through the Eqn. 5.13 and Eqn. 5.14 respectively. Using $C_b = 2.17 \times 10^6\,\mathrm{J/(m^3 \cdot K)}$ for the granite rock at the site (Farouki, 1981b; Tipler, 1999), the thermal conductivity of bedrock, $\lambda_b = \kappa_b C_b$, is between 2.6 and 3.0 $\mathrm{W/(m \cdot K)}$ and these are the common values found for granite rock (Côté and Konrad, 2009)

5.3.3.2 Thermal diffusivity of the compacted layer near the surface of the test pile

Fig. 5.13A shows a relation of time lags of the test pile's temperatures with depths and it can be represented by a bi-linear equation. In which, from the surface to about 2 m depth,

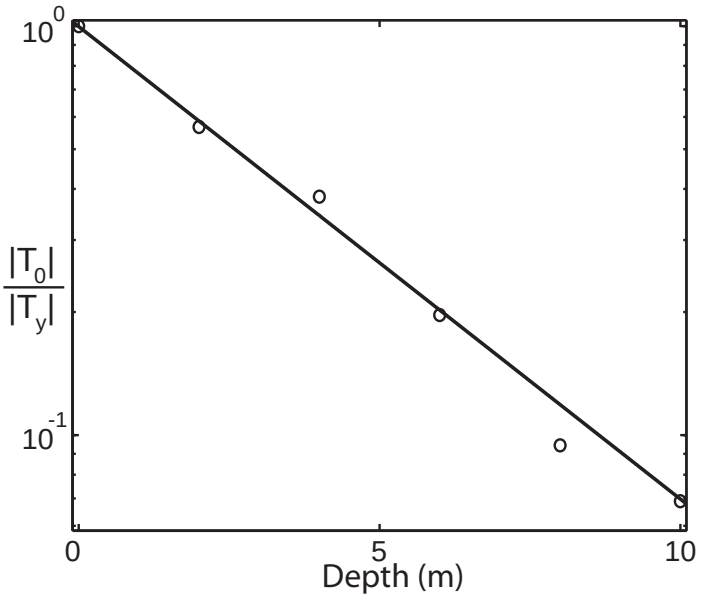

Figure 5.12: The amplitude ratios of surface and subsurface temperatures with depths in bedrock, where $|T|_o$ and $|T|_y$ are the temperature amplitude at the surface and depth y.

the relation between time lags and depths is relatively linear and by following the same procedure as above, the average thermal diffusivity of this zone is $8.3 \times 10^{-7}\,\mathrm{m}^2/\mathrm{s}$; at a measured value thermal conductivity $\lambda = 1.8\,\mathrm{W}/(\mathrm{m}\cdot\mathrm{K})$, therefore $C = 1.8/8.3 \times 10^{-7} = 2.2 \times 10^6\,\mathrm{J}/\left(\mathrm{m}^3\cdot\mathrm{K}\right)$ (bulk volumetric heat capacity of Type III rock)

5.3.4 Time-lag analyses

Below the low surface permeability zone, due to the impacts of higher permeability (material segregation resulting in the rubble zone at the base of the test pile), heterogeneity (the co-existence of fine layers in coarse zones) and wind induced convection/advection, the relation of time lags with depths has considerably scatter (Fig. 5.13A). Moreover, the time lag was about 60 days at a depth of 12 m which is small compared to the pure conduction time lag of 160 days in bedrock (Fig. 5.13B).

The time lags of the test pile's temperatures to barometric pressures and wind speeds were also expected to be influenced by the heterogeneity of the material in the test pile. As shown in Fig. 5.13C and D, the first 2m of the test pile's surface, an increase trend of time lags is observed as permeability of this layer is low. Below this depth, the results are dispersed although a general decrease of time lag is apparent. The response times of the test pile's temperatures to barometric pressures and wind speeds were small in comparison to surface temperatures. The explanation is that when wind and barometric pressure fluctuation act on the test pile's surface, they create a pressure wave that travels at high velocity into the interior of the test pile and causes a fluctuation of temperatures. However, the fluctuation is small as it is indicated by the small cross-correlation coefficients.

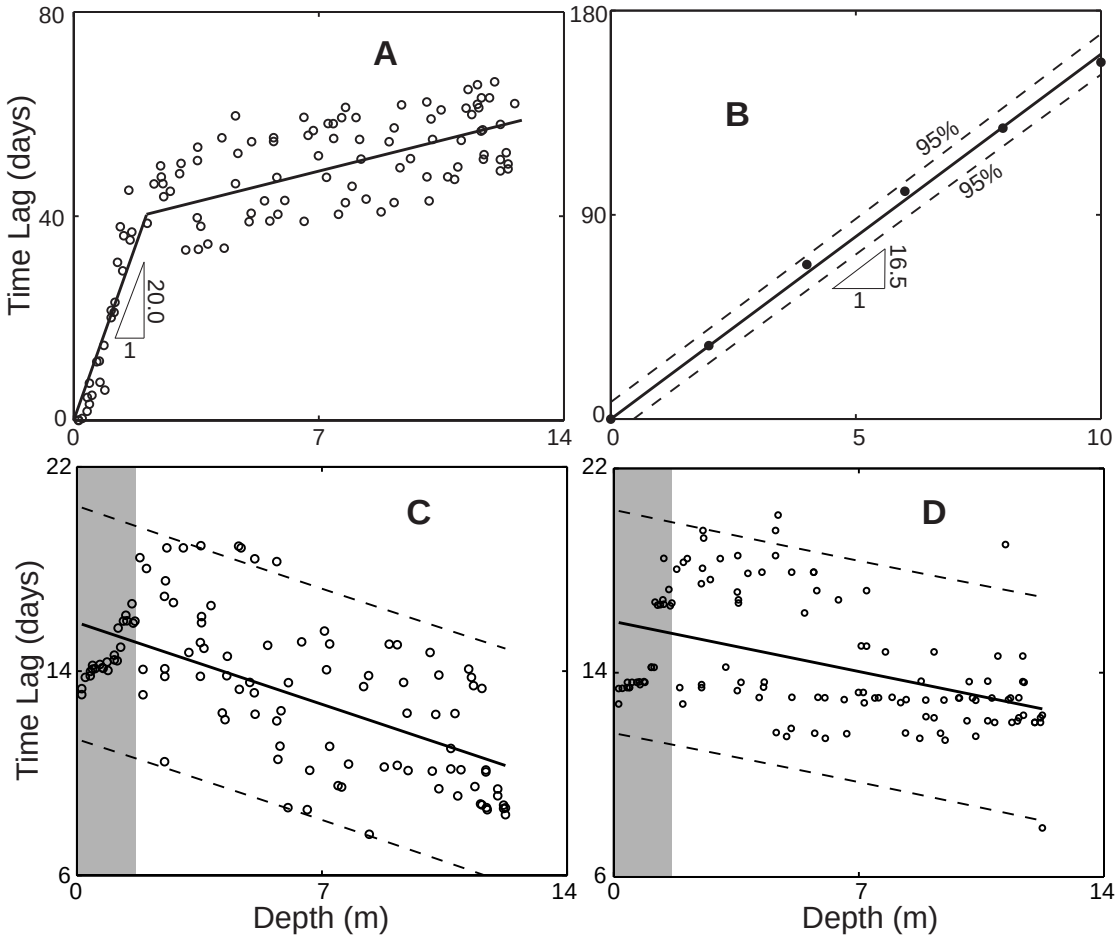

Figure 5.13: The relation of time lags with depths of surface temperature to the test pile's temperatures (A), to bed-rock temperature (B), to barometric pressure (C) and wind speed (D); the shaded area represents a low permeability layer near the surface.

5.3.5 Estimation of pore air velocity

From the above analyses, the heat transfer below 2 m in the test pile is certainly not dominated by conduction. The contribution of forced convection (advection) by wind and barometric pumping along natural convection causes large temperature variations within the test pile. It is important to estimate pore air velocity which then can be used to calibrate permeability of the test pile. As shown earlier, dominated wind speed at the site is from the North and it causes the lateral movement of pore air toward to the south in a horizontal x direction (Fig. 5.2). Thus, assuming the dominated air velocity from the North to South, the pore air velocity will be determined based one-dimensional convection-conduction in a homogeneous and thermal equilibrium porous medium (Stallman, 1965):

$$\lambda \frac{\partial^2 T}{\partial x^2} - uC_a \frac{\partial T}{\partial x} = C \frac{\partial T}{\partial t} \tag{5.15}$$

Where λ and C are the effective (bulk) thermal conductivity and volumetric heat capacity of waste rock, u is the lateral air velocity (Darcy's velocity), $C_a = 1.26 \times 10^3$ J/ $\left(\mathrm{m}^3 \cdot \mathrm{K}\right)$ is the volumetric heat capacity of air (Tipler, 1999). Surface temperature as a boundary condition is the same as Eqn. 5.11 with only a single component of angular frequency ω and period $\tau = 365$ days. The solution of Eqn. 5.15 is (Stallman, 1965):

$$T_x - T_{ox} = |T_o| e^{-ax} \sin\left(\omega t - \varepsilon - bx\right) \tag{5.16}$$

Where T_x is the temperature at a horizontal distance x from the northern boundary of the test pile with a mean T_{ox}. $|T_o|$ is the amplitude of surface temperature, a and b are determined by measuring amplitudes and phase differences at various locations along the x direction. Stallman (1965) provided an analytical solution as:

$$a = \sqrt{\sqrt{R^2 + \frac{V^4}{4}} + \frac{V^2}{2}} - V \tag{5.17}$$

$$b = \sqrt{\sqrt{R^2 + \frac{V^4}{4}} - \frac{V^2}{2}} \tag{5.18}$$

Where $R = \frac{C\pi}{\lambda\tau}$ and $V = \frac{C_a u}{2\lambda}$. The values of a and b can be obtained by plotting the measured data in the forms, $-\ln\left(\frac{|T_2|}{|T_1|}\right) = a\left(x_2 - x_1\right)$ and $b = \dfrac{2\pi\delta t}{\tau\left(x_2 - x_1\right)}$. $|T_1|$ and $|T_2|$ are the temperature amplitudes at x_1 and x_2, τ is the period of the surface temperature and it is 365 days in this study.

The average values of thermal conductivity and volumetric heat capacity of the test pile are $\lambda = 1.8$ W/ $(\mathrm{m} \cdot \mathrm{K})$ and $C = 2.2 \times 10^6$ J/ $\left(\mathrm{m}^3 \cdot \mathrm{K}\right)$ respectively, therefore the value of R is 0.12. The Fig. 5.14 shows the semi-logarithmic plot of the ratio temperature amplitudes of surface temperatures to ground temperatures at distance x to the northern boundary of the

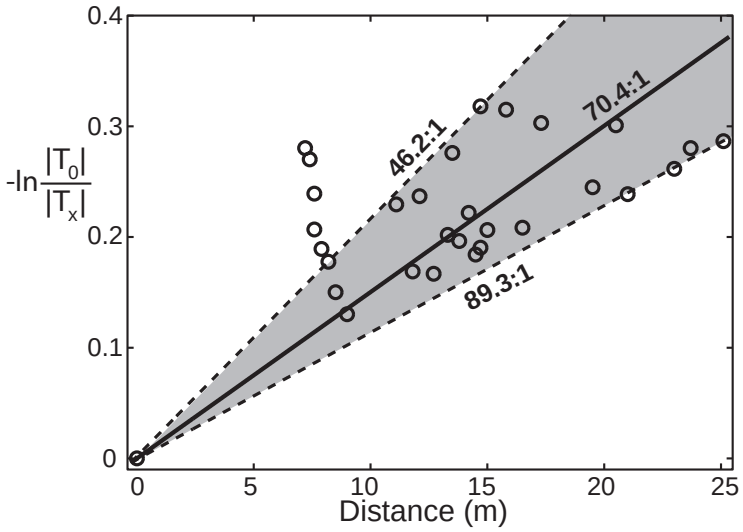

Figure 5.14: Semi-logarithm plot of the ratio temperature amplitude of surface temperature to ground temperatures within the test pile and the shaded area represents the estimated range (90 % confident).

test pile. The results in Fig. 5.14 were based on thermistors at depths greater than 3 m from the surface and these depths were chosen to eliminate data from within the shallow zone which is low in permeability. The range of a determined by Fig. 5.14 vary between 0.011 and 0.022 with a mean of 0.014. Calculating the ranges of V from a and R through Eqn. 5.17 and then calculated pore air velocity, u, ranges between 1.9×10^{-3} and 2.4×10^{-3} m/s with a mean of 2.2×10^{-3} m/s.

Similarly, the work of Amos et al. (2009b) based on measured of in-situ pore air pressures within and on the surface of the test pile suggested that there is a strong correlation of pore air pressures to wind speeds meaning that wind speeds are inducing air pressure gradients around the test pile and airflow within the test pile. In addition, due to the heterogeneity, pore air advection due to wind is highly irregular in both magnitude and direction. The above value of mean pore-air velocity along with measured values of pore air pressures can be used to calibrate in-situ measurements of permeability. The characteristic of wind flow over the test pile is presented by Reynolds number $Re = \frac{u_{wind} L}{\nu} = 7.0 \times 10^6$ which is turbulent at the mean wind velocity $u_{wind} = 17$ km/h, $L = 15$ m is the test pile's height and air viscosity, ν, is in the order of 10^{-5} m^2/s.

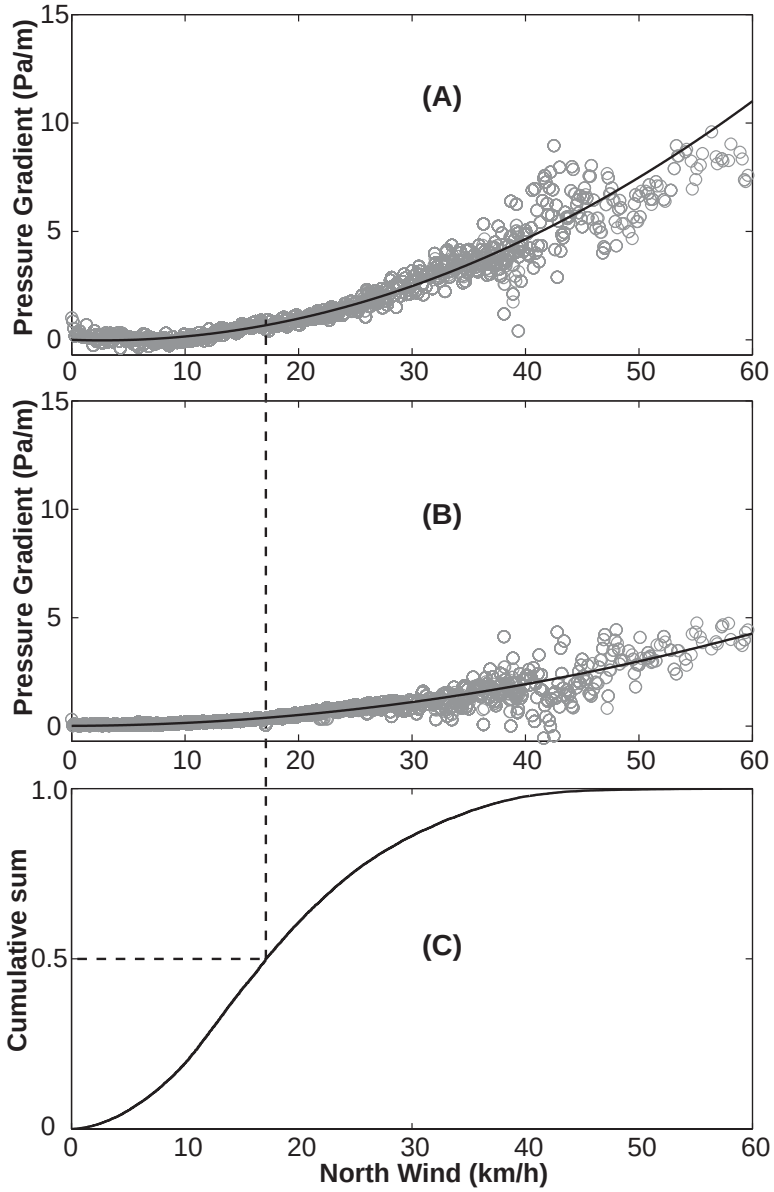

Figure 5.15: Pore air pressure gradients correlated to wind speed at 8 m depths to the North wind at probes: '32N2gas4.00' and '32N7gas4.00' (A); '32N2gas8.00' and '32N7gas8.00' (B); which are 5 m laterally (A) and the cumulative sum of North wind (B).

Fig. 5.15 shows that at the mean wind speed of 17.1 km/h from the North, pressure gradients varied between 0.4 and 0.6 Pa/m for probes at depths 4 and 8 m respectively. At gust of 60 km/h the pore-air pressure gradient could reach 11 Pa/m at 4 m meanwhile at 8 m the pore-air pressure gradient was only about 5 Pa/m. The calculated mean pore air velocity $u = 2.2 \times 10^{-3}$ m/s, the air dynamic viscosity of $10^{-5}\,\mathrm{N \cdot s/m^2}$ along a mean air pressure gradient of 0.5 Pa/m at the mean wind speed from the North, using the Darcy's law the average value of permeability of the test pile at mid height is about $K = 4.4 \times 10^{-8}\,\mathrm{m^2}$. This result is consistent with the results of Chi (2010) which is in the order of $10^{-8}\,\mathrm{m^2}$ using

digital image processing of waste rock images.

The above analysis only gives an average estimation gas velocity and permeability based on 1-D assumptions; in reality, pore air velocity and direction are more complex due to the heterogeneity. These make the calibration of future numerical simulations more challenge. Moreover, the existence of coarse preferential air flows could be the cause of high response times of pore gas pressure to wind speeds in the test pile. Therefore, in order to have a reasonable calibration between numerical results and measured data, the permeability can vary about two orders of magnitude or more which is common (Smith et al., 1995; Lahmira et al., 2009; Neuner et al., 2012).

5.4 Conclusions

Bedrock's thermal diffusivity was found in the range 1.2×10^{-6} to $1.4 \times 10^{-6}\,\mathrm{m^2/s}$, a possible range of thermal conductivity between 2.6 and 3.0 $\mathrm{W/(m \cdot K)}$. Furthermore, the time lags and cross-correlation coefficients were found to increase and decrease with depths respectively with an average cross-correlation coefficient of 0.72 between surface and ground temperatures at depths up to 10 m. However, at the test pile, based on cross-correlation analyses of ground temperatures of the test pile to surface temperatures, wind speeds and barometric pressures, the correlations to surface temperatures were strong and positive (an average cross-correlation coefficient of 0.91) whereas the correlations to wind speeds and barometric pressures were weaker and however negative. Furthermore, the large cross-correlation coefficients between surface and ground temperatures even at great depths ($\geq$ 12 m) were only obtained with the help of convection/advection due to wind.

A zone of 2 m from the surface was found to be dominated by heat conduction having a thermal conductivity of 1.8 $\mathrm{W/(m \cdot K)}$, however below this zone the test pile was greatly heterogeneous, segregated and more permeable. The lower zone of the test pile was characterized by the scatter and larger cross-correlation coefficients and small time lags. By the application of 1-D convection-conduction model, an average air velocity of 2.2×10^{-3} m/s was determined through the relations of temperature amplitudes and time lags with depths. The in-situ measurements of pore air pressures were used to estimate pore-air pressure gradients around the mid height of the test pile and it was found that the pressure gradient was around 0.5 Pa/m with wind from the North at the mean wind speed. As a result, the estimated permeability of $4.4 \times 10^{-8}\,\mathrm{m^2}$ at this zone was determined. Due to this high permeability of the test pile, wind effects must be considered to calibrate numerical simulations to in-situ measurement of thermal behavior.

References

Amos, R. T., Blowes, D. W., Smith, L., and Sego, D. C. (2009a). Measurement of wind-induced pressure gradients in a waste rock pile. *Vadose Zone J*, 8(4):953–962.

Amos, R. T., Smith, L., Neuner, M., Gupton, M., Blowes, D. W., Smith, L., and Sego, D. C. (2009b). Diavik waste rock project: Oxygen transport in covered and uncovered piles. In *The 8th ICARD International Conference On Acird Rock Drainage, Skelleftea, Sweden, 2009*.

Azam, S., Wilson, G., Herasymuik, G., Nichol, C., and Barbour, L. (2007). Hydrogeological behaviour of an unsaturated waste rock pile: A case study at the golden sunlight mine, montana, usa. *Bulletin of Engineering Geology and the Environment*, 66(3):259–268.

Cardaci, C., Falsaperla, S., Gasperini, P., Lombardo, G., Marzocchi, W., and Mulargia, F. (1993). Cross-correlation analysis of seismic and volcanic data at mt etna volcano, italy. *Bulletin of Volcanology*, 55:596–603. 10.1007/BF00301812.

Carslaw, H. S. and Jaeger, J. C. (1959). *Conduction of heat in solids*. Oxford University Press.

Chi, X. (2010). Characterizing low-sulfide instrumented waste-rock piles: image grain-size analysis and wind-induced gas transport. Master's thesis, University of Waterloo.

Côté, J. and Konrad, J.-M. (2009). Assessment of structure effects on the thermal conductivity of two-phase porous geomaterials. *International Journal of Heat and Mass Transfer*, 52(3-4):796–804.

Demetrescu, C., Nitoiu, D., Boroneant, C., Marica, A., and Lucaschi, B. (2007). Thermal signal propagation in soils in romania: conductive and non-conductive processes. *Climate of the Past*, 3(4):637–645.

Deutsch, C. and Journel, A. (1992). *GSLIB: geostatistical software library and user's guide*. Number v. 1. Oxford University Press.

Environment-Canada (2008a). Climate data online. national climate data and information archive. Technical report, Environment Canada.

Farouki, O. T. (1981b). *Thermal properties of soils*. United States Army Corps of Engineers, Cold Regions Research and Engineering Laboratory, Hanover, New Hampshire, USA.

Guan, L., Yang, J., and Bell, J. (2007). Cross-correlations between weather variables in australia. *Building and Environment*, 42(3):1054 – 1070.

Lahmira, B., Lefebvre, R., Hockley, D., and Phillip, M. (2009). Sullivan mine fatalities incident: Numerical modeling of gas transport and reversal in gas flow directions. In *Securing the Future and 8th ICARD, June 23-26, 2009, Skelleftea, Sweden*.

Li, H., Futch, S. H., and Syvertsen, J. P. (2007). Cross-correlation patterns of air and soil

temperatures, rainfall and diaprepes abbreviatus root weevil in citrus. *Pest Management Science*, 63(11):1116–1123.

Lunardini, V. J. (1981). *Heat transfer in cold climates*. Van Nostrand Reinhold Company.

Matlab (2012). *Matlab: Mathematics*. MathWorks.

Morrison, N. (1994). *Introduction to Fourier Analysis*. Wiley-Interscience.

Nakajima, H. and Hayakawa, N. (1982). A cross-correlation analysis of tidal current, water temperature and salinity records. *Journal of Oceanography*, 38:52–56. 10.1007/BF02110290.

Neuner, M., Smith, L., Blowes, D. W., Sego, D. C., Smith, L. J., Fretz, N., and Gupton, M. (2012). The diavik waste rock project: Water flow though mine waste rock in a permafrost terrain. *Applied Geochemistry*, (0):–.

Smith, L., Lopez, D., Beckie, R., Morin, K., Dawson, R., and Price, W. (1995). Hydrogeology of waste rock dumps. Technical report, Department of Natural Resources Canada, Ottawa, Ontario, Canada.

Smith, S. and Burgess, M. (2000b). Ground temperature database for northern canada. Technical report, Geological Survey of Canada, File Report 3954.

Stallman, R. (1965). Steady 1-dimensional fluid flow in a semi-infinite porous medium with sinusoidal surface temperature. *Journal Of Geophysical Research*, 70(12):2821–2827.

Telesca, L. (2010). Analysis of the cross-correlation between seismicity and water level in the koyna area of india. *Bulletin of The Seismological Society of America*, 100(5A):2317–2321.

Tipler, P. A. (1999). *Physics for Scientists and Engineers*. W.H. Freeman.

Wilson, G. W. (1990). *Soil Evaporative Fluxes For Geotechnical Engineering Problems*. PhD thesis, University of Saskatchewan.

Yndestad, H., Turrell, W. R., and Ozhigin, V. (2008). Lunar nodal tide effects on variability of sea level, temperature, and salinity in the faroe-shetland channel and the barents sea. *Deep Sea Research Part I: Oceanographic Research Papers*, 55(10):1201–1217.

CHAPTER 6

Thermal transport in a covered test pile located in a continuous permafrost region

6.1 Introduction

Waste rock is produced by blasting of less-valuable-mineral rock in order to provide access to the high-valued ore. Weathering of waste rock bearing sulfide minerals can cause acid rock drainage (ARD) when the waste rock is exposed to the atmosphere and water. The acid generated is flushed by infiltration water and along the seepage paths hazardous metals in waste rock are dissolved and leached out. Therefore, ARD reduces the quality of surface water and groundwater and poses many environment related issues. Covering reactive waste rock is a common approach for controlling ARD (Newman et al., 1997; Morin and Hutt, 2001; Martin et al., 2004; Wickland and Wilson, 2005a; Molson et al., 2005; Song and Yanful, 2008). The main objective of a soil cover is to inhibit the availability of oxygen and water for oxidation. However, among the covering techniques, insulation covers are mostly used in cold regions where air temperatures are cold and prolonged winter seasons promote permafrost in reactive waste rock (MEND1.61.2, 1996; MEND1.61.4, 2004; Arenson and Sego, 2007).

Insulation cover is used to ensure the frozen waste rock remains frozen and to promote the aggregation of permafrost into unfrozen waste rock. However, adequate cold temperatures is a must to freeze and maintain waste rock in a frozen state and the thickness of the cover has to be sufficient to contain the annual thaw layer (active layer). At a given site there are many factors that influence the determination of the thickness of each layers in the cover, such parameters are air temperatures and duration, wind, solar radiation, the amount of precipitation (rain and snow), soil properties and others (MEND6.1, 1993; MEND1.61.4, 2004). The number of soil layers in the insulation cover is determined by site specific conditions, however it is usually a two-layer system: the bottom layer consists of low permeability and saturated soils and the top layer is made up of coarser materials. The low permeability layer is generally maintained at a high degree of saturation and its high

moisture content slows the influx of oxygen and thaw penetration. The coarse layer is used to promote convective cooling (natural convection) during winter and served as an insulation layer during summer due to its low permeability. Arenson and Sego (2007) reported the use of numerical simulations of natural air convection helps to analyze permafrost degradation beneath mine tailings.

The objectives of this chapter are to present measured temperatures from installed thermistor cables in a covered test pile at Diavik Diamond Mine, Northwest Territories, Canada located in a continuous permafrost region and use these measured temperatures to determine thermal properties and heat fluxes through each layers. Furthermore, based on climate variables at the site, the ratio between net radiation and surface heat flux was determined and compared to other locations. According to the author's knowledge there have not been experimental results of insulation covers for waste-rock piles constructed in continuous permafrost regions.

6.2 Methodology

6.2.1 Determination of thermal diffusivity

6.2.1.1 Based on pure heat conduction

Conduction is driven by temperature gradients which usually high near the surface, therefore cooling and heating rates are maximized near the surface. According to conduction, ground temperature oscillations are rapidly attenuated and lag with depth. Under assumptions of a periodically varying soil surface temperature and one-dimensional conductive heat transfer, the bulk thermal diffusivity of waste rock, κ (m^2/s), can be calculated using the phase or amplitude equations from ground temperature data (Carslaw and Jaeger, 1959):

- Phase equation

$$\kappa = \frac{1}{2\omega}\left(\frac{y_2 - y_1}{\delta t}\right)^2 \tag{6.1}$$

- Amplitude equation

$$\kappa = \frac{\omega}{2}\left(\frac{y_2 - y_1}{ln\left(\frac{|T_2|}{|T_1|}\right)}\right)^2 \tag{6.2}$$

Where δt is the phase difference; $|T_1|$ and $|T_2|$ are temperature amplitudes at two depths y_1 and y_2, ω is the fundamental angular frequency. The phase difference can be obtained by cross-correlation analysis of two temperature time series (Chapter 5) and temperature amplitude can be approximated from the minimum and maximum values over a fundamental period which is 365 days in this case.

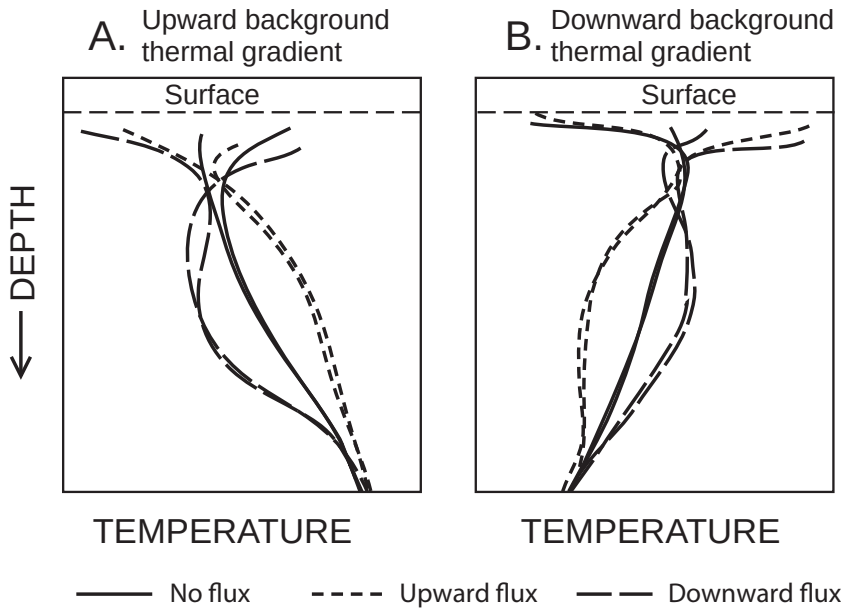

Figure 6.1: The impacts of groundwater flow on temperature: (A) Upward flow, B (Downward flow). (modified from Blasch et al., 2007).

6.2.1.2 Based on 1-D heat conduction and convection

In the previous section the determination of thermal diffusivity considered only conduction heat transport. Conductive/advective heat transport associated with pore air/vapor movement vertically changes the temperature distribution within porous media. Fig. 6.1 demonstrates that temperature profiles at depth are controlled by the vertical flux of ground water and based on the shape of ground temperatures the direction of ground water can be determined. Due to the relative dry waste rock, low precipitation and subzero ground temperatures, convective heat due to air is more significant than water. One-dimensional convection-conduction in homogeneous porous media is expressed as:

$$\lambda \frac{\partial^2 T}{\partial y^2} - u C_a \frac{\partial T}{\partial y} = C \frac{\partial T}{\partial t} \tag{6.3}$$

Where: λ and C are effective (bulk) thermal conductivity and volumetric heat capacity of waste rock; $\kappa = \dfrac{\lambda}{C}$, u is the vertical air velocity, $C_a = 1.26 \times 10^3 \,\mathrm{J}/\left(\mathrm{m}^3 \cdot \mathrm{K}\right)$ is the volumetric heat capacity of air. According in-situ measurements, λ is 1.7, 1.8 and 3.0 $\mathrm{W}/\left(\mathrm{m} \cdot \mathrm{K}\right)$ for Type I, III rocks and till, respectively. Assumption of a periodically varying surface temperature with only single component of angular frequency ω and period τ. The solution of Eqn. 6.3 is (Suzuki, 1960; Stallman, 1965):

$$T_y - T_{oy} = |T_o| \cdot e^{-ay} \sin\left(\omega t - \varepsilon - by\right) \tag{6.4}$$

Where: T_y are the temperature at a distance y beneath the surface of the covered test pile

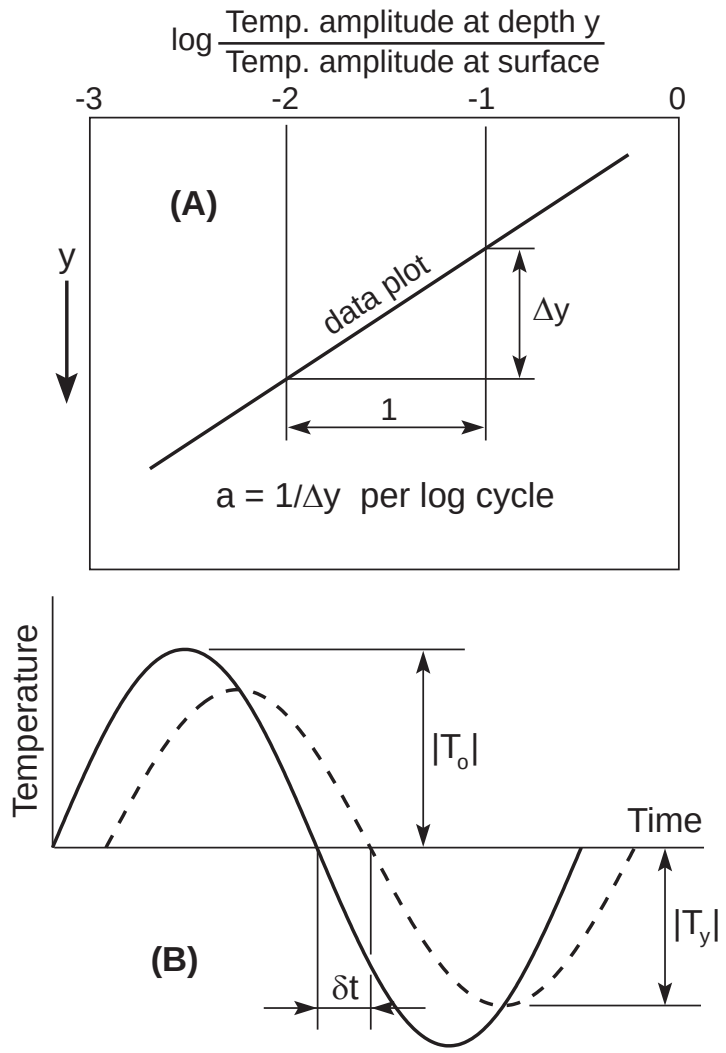

Figure 6.2: A schematic for calculating a and b from temperature time series (modified from Stallman, 1965)

with a mean T_{oy} and ε is the phase. $|T_o|$ is the amplitude of surface temperature; a and b are determined by measuring the amplitude and phase differences at various locations along the y axis as shown in Fig. 6.2. Suzuki (1960); Stallman (1965) provided an analytical solution as:

$$\left.\begin{aligned} a &= \sqrt{\sqrt{R^2+\frac{V^4}{4}}+\frac{V^2}{2}}-V \\ b &= \sqrt{\sqrt{R^2+\frac{V^4}{4}}-\frac{V^2}{2}} \\ R &= \frac{\pi}{\kappa\tau} \\ V &= \frac{C_a u}{2\lambda} \end{aligned}\right\} \tag{6.5}$$

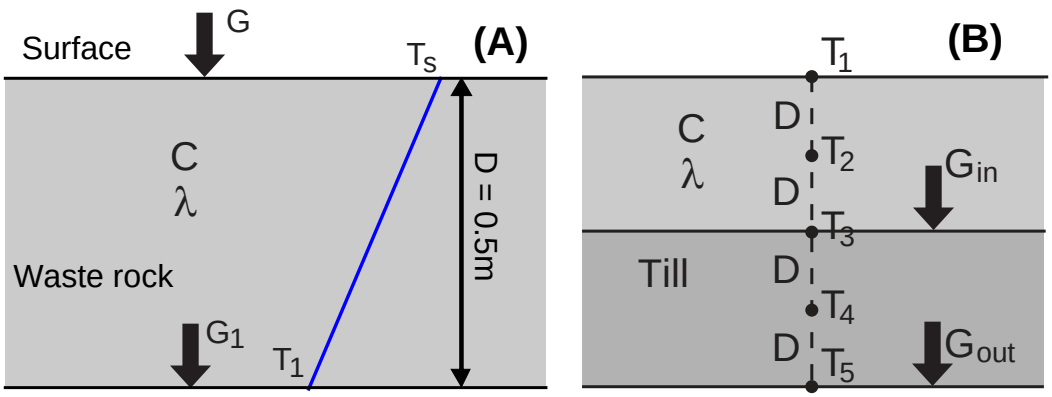

Figure 6.3: A schematic for calculation of heat flux into the ground surface (A) and heat flux out of till layer (B).

Where the values of a and b can be obtained by plotting the measured data in the forms:

$$\left.\begin{aligned} a &= \frac{-\ln\left(\frac{|T_2|}{|T_1|}\right)}{(y_2 - y_1)} \\ b &= \frac{2\pi\delta t}{\tau\,(y_2 - y_1)} \end{aligned}\right\} \tag{6.6}$$

Where $|T_1|$ and $|T_2|$ are the temperature amplitudes at y_1 and y_2, τ is the period of the surface temperature and it is 365 days in this study.

6.2.2 Ground surface heat flux

Ground surface heat flux is an important component to determine the thickness of a soil cover as it contributes in the energy balance between ground surface and the atmosphere. The amount of surface heat flux depends on the surface and subsurface conditions (such as moisture content and vegetation cover) and climatic variables at the site. For a dry and no vegetation cover, surface heat flux is usually large. However in an area where the surface soil is insulated by plant canopy or snow and moist, surface heat flux is insignificant compared to other components (Lunardini, 1981; Sauer et al., 2003; Cobos and Baker, 2003).

Ground surface heat flux is determined by using one of four methods: flux plate, calorimetric, gradient or combination of the gradient and calorimetric methods (Sauer and Horton, 2003; Sauer et al., 2003; Cobos and Baker, 2003; Ochsner et al., 2007; Venegas et al., 2012). In this study, the combined method is used to determine surface heat flux at the waste rock surface. Because of the low permeability of waste rock near the surface, the surface heat flux of the covered test pile is based on the conductive heat transfer applied to the first waste rock layer near the surface, where the upper-most two thermistors located (0.5 m thick in our study):

$$G = DC\frac{\partial T}{\partial t} + G_1 \tag{6.7}$$

$$T \simeq \frac{T_s + T_1}{2} \tag{6.8}$$

$$G_1 \simeq -\lambda \frac{T_s^+ - T_1^+}{D} \tag{6.9}$$

Using Eqn. 6.8, Eqn. 6.7 and Eqn. 6.9, the surface heat flux G can be defined as (Fig. 6.3A)

$$G \simeq -\lambda \frac{T_s^+ - T_1^+}{D} + \frac{DC}{2\Delta t}\left(T_s^+ - T_s^- + T_1^+ - T_1^-\right) \tag{6.10}$$

Where: D (m) and C $\left(\mathrm{J}/\left(\mathrm{m}^3 \cdot \mathrm{K}\right)\right)$ are the thickness and volumetric heat capacity of the layer, Δt is the time interval of measured temperatures. The superscripts "$+$" and "$-$" represent the current and previous times. In Eqn. 6.10 , the first term is heat flux at depth D and the second term is the heat stored by the layer of thickness D near the surface.

6.2.3 Heat flux at the base of till layer

Heat flux at the bottom of till layer is calculated by using five thermistors installed within the till layer and the calculated heat flux is used to predict long term cooling or heating of the reactive waste rock beneath this till layer. By using a central difference approximation with a fourth order error to calculate G_{in} and G_{out}, the equations are written as (Fig. 6.3B):

$$\left.\begin{aligned} G_{in} &\simeq \lambda \frac{T_5 - 8T_4 + 8T_2 - T_1}{12D} \\ G_{out} &\simeq G_{in} - \frac{2DC}{3\Delta t}\left(T_5^+ - T_5^- + T_4^+ - T_4^- + T_3^+ - T_3^-\right) \end{aligned}\right\} \tag{6.11}$$

6.2.4 Net radiation

Net radiation is the most important term in the energy balance at the surface because it controls other transport processes such as evaporation. Net radiation is determined through short-wave and long-wave radiations from the sun and atmosphere; and the reflected short-wave and emitted long-wave radiation from the waste-rock surface. Net radiation can be written as (Lunardini, 1981; Oke, 2002; Weeks and Wilson, 2006).

$$R_n = Q_s + Q_{li} - Q_{lo} \tag{6.12}$$

$$\left.\begin{aligned} Q_s &= (1-\alpha_s)\,R_s \\ Q_{li} &= F\left(\sigma T_a^4\right) 1.08\left[1-\exp\left(-0.01\left(P_v^a\right)\frac{T_a}{2016}\right)\right] \\ \log_{10} P_v^a &= 11.40-\frac{2353}{T_{dp}} \\ Q_{lo} &= \varepsilon\sigma T_s^4 \end{aligned}\right\} \tag{6.13}$$

Where: $R_n\left(\mathrm{W/m^2}\right)$ is the net radiation which is received by the soil surface; $Q_s\left(\mathrm{W/m^2}\right)$ is the net short-wave radiation; $Q_{li}\left(\mathrm{W/m^2}\right)$ is the atmospheric long-wave radiation calculated based on air temperature (T_a) and vapor pressure of ambient air P_v^a; $F \geq 1$ is the cloud factor at the site; $Q_{lo}\left(\mathrm{W/m^2}\right)$ is the emitted long-wave radiation from the waste-rock surface; ε and σ are the emissivity of the waste-rock surface and the Stefan-Boltzmann's constant ($5.67\times10^{-8}\,\mathrm{W/(m^2{\cdot}K^4)}$), respectively; T_a, T_s, and T_{dp} are the absolute ambient, surface, and dew-point temperatures (K), respectively; α_s is the surface albedo of the waste-rock surface which can vary due to the surface conditions of the waste-rock pile such as moisture content or snow cover. $R_s\left(\mathrm{W/m^2}\right)$ is the incoming solar radiation. F can be expressed as (Sugita and Brutsaert, 1993)

$$F = 1+cm^p \tag{6.14}$$

Where: m is the cloud cover fraction ($0\leq m\leq 1$); c and p are coefficients describing the cloud characteristics, but they are typically chosen as 0.22 and 2 respectively (Sugita and Brutsaert, 1993).

6.3 Site Description and Meteorological Data

6.3.1 Site Description

The Diavik Diamond Mine is located approximately 300 kilometers northeast of Yellowknife, Northwest Territories, Canada in the barren lands of the Canadian Arctic. The Arctic Circle is located 220 kilometers north of the mine (Fig. 6.4). The site is located within the continuous permafrost region with an average precipitation of 283 mm with 60 % from snow and the dominant winds are from the north and east with an average of 17 km/h (Environment-Canada, 2008a). The hydrogeological processes in the test piles at the site are confined within the active layer during short summer periods because the permafrost beneath the active layer acts as a barrier to ground water.

From 2004 to 2007, three large-scale experimental waste-rock piles (test piles) were constructed including the Type I test pile with average sulfur content of < 0.04 wt% S; the

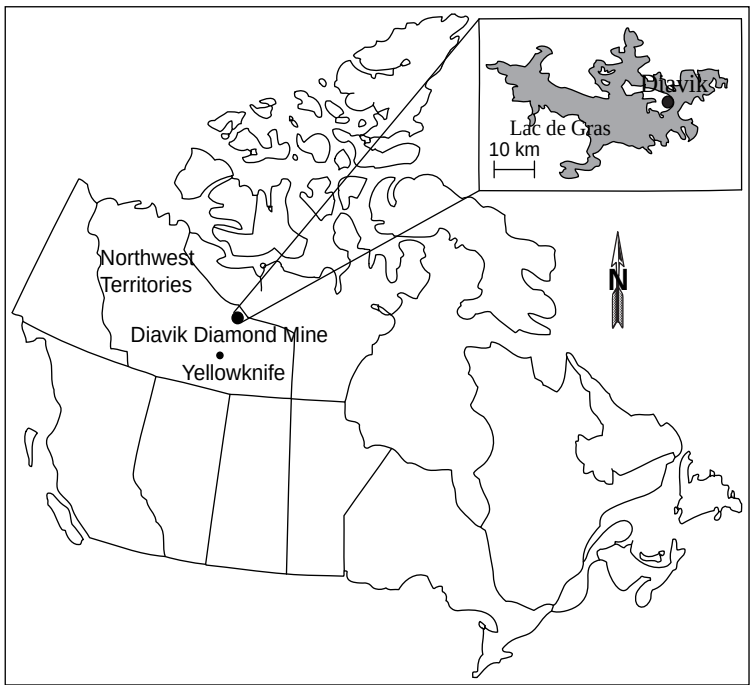

Figure 6.4: Aerial photo of the test piles at Diavik Diamond Mine and the inset shows location of the mine in Canada

Type III test pile with average sulfur content of > 0.08 wt% S and the covered test pile with a Type III core, and a 1.5 m till cover overlain by 3 m of the Type I rock (Fig. 6.5). Temperatures were recorded at 4 hours interval using an automated data-logger system consisting of two sets of a Campbell Scientific (Edmonton, AB, Canada) CR10X data-loggers and 2 AM16/32-XT multiplexers at the east and west side of the test pile. The thermistor beads are YSI 44007 type providing a precision of $\pm 0.2\,^{\circ}\mathrm{C}$ and a wide-range working temperature of $-80 \rightarrow +120\,^{\circ}\mathrm{C}$.

The design concept of the covered test pile is to evaluate the potential of reducing ARD. The low permeability till layer is intended to maintain a high degree of saturation and therefore reduces oxygen infiltration. The Type I rock layer is deliberated to contain the active layer and promotes natural convection during winter. At the base of the covered test pile, there are three basal collection lysimeter (BCL) clusters constructed including two 4×4 m and two 2×2 m collection boxes (Fig. 6.5). Inside each box, there is a Raychem heating cable located at the base which is used to maintain temperature in the BCLs just above the freezing point (e.g. 0 °C).

6.3.2 Meteorological Data

The meteorological station consists of a RM Young wind monitor, a Campbell Scientific HMP35CF (relative humidity), air temperature sensors (at 2 and 10 m above ground) and a Campbell Scientific LI200s pyranometer for solar radiation. Based on the hourly meteo-

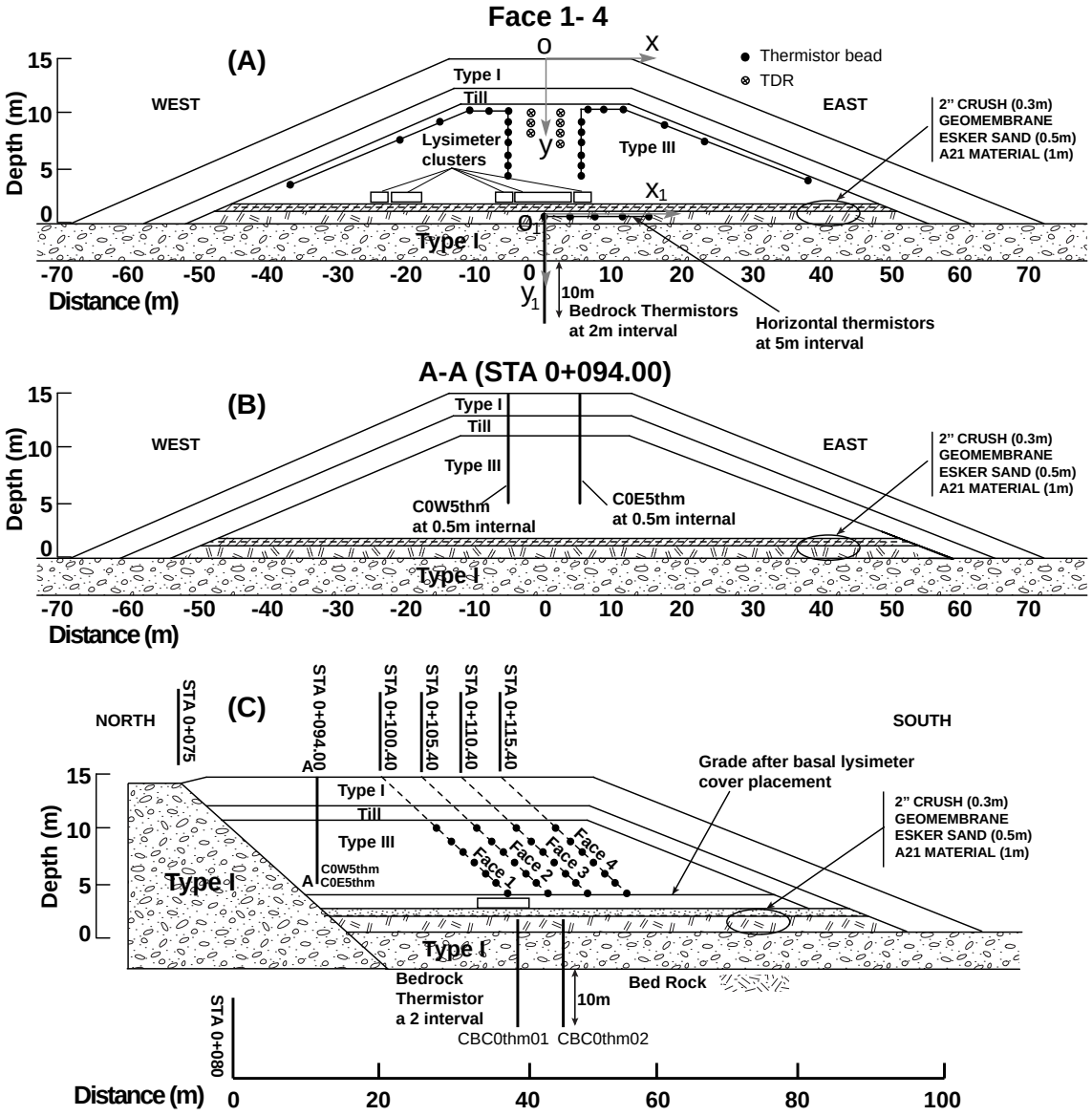

Figure 6.5: Typical cross-section (A) and long section (B) of the covered test pile.

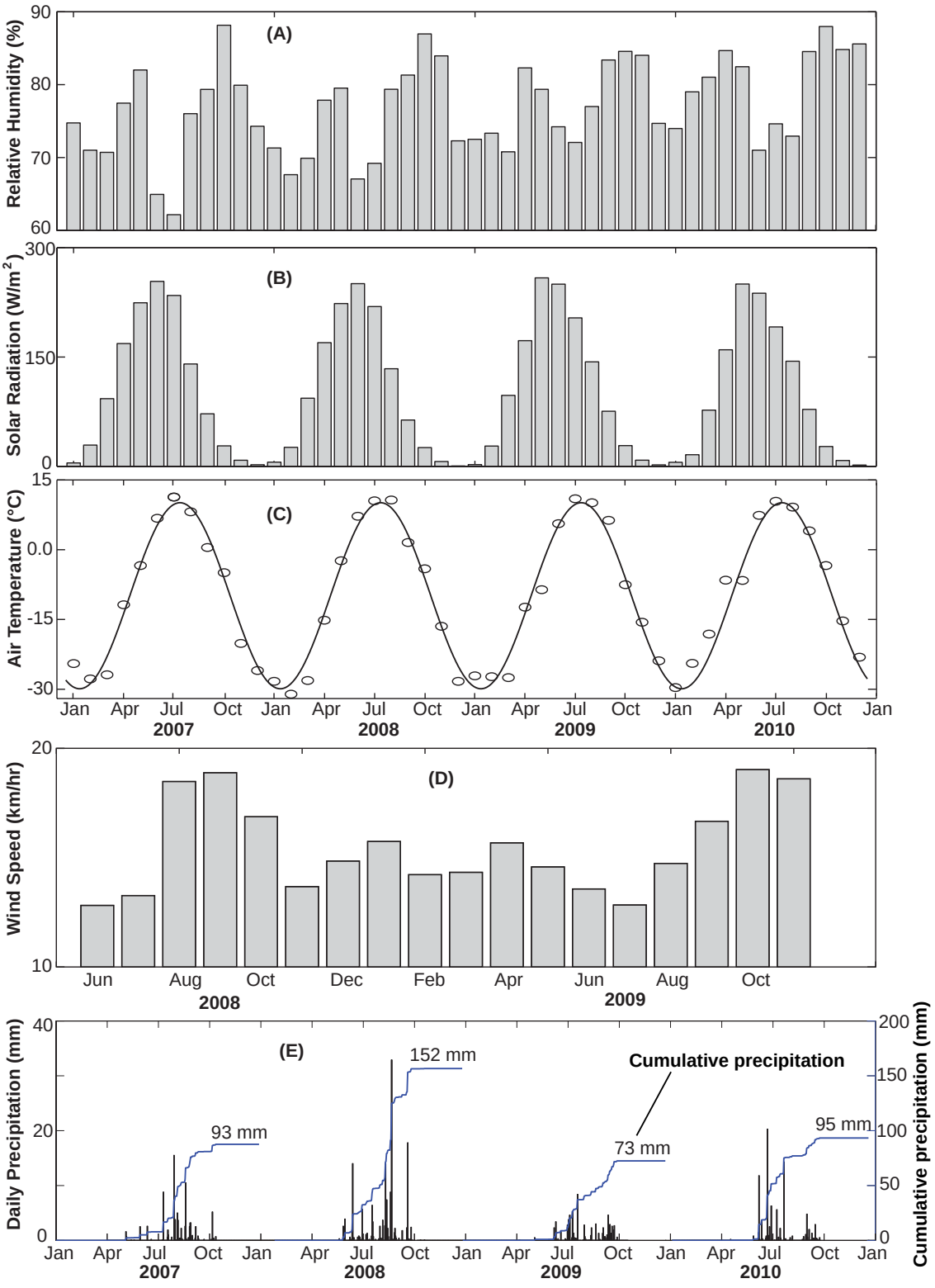

Figure 6.6: Meteorological data at the test piles research site: Relative Humidity (A), Solar Radiation (B), Air Temperature at 10 m from ground surface (C), Wind speed at 10 m (D), and Rainfall (E).

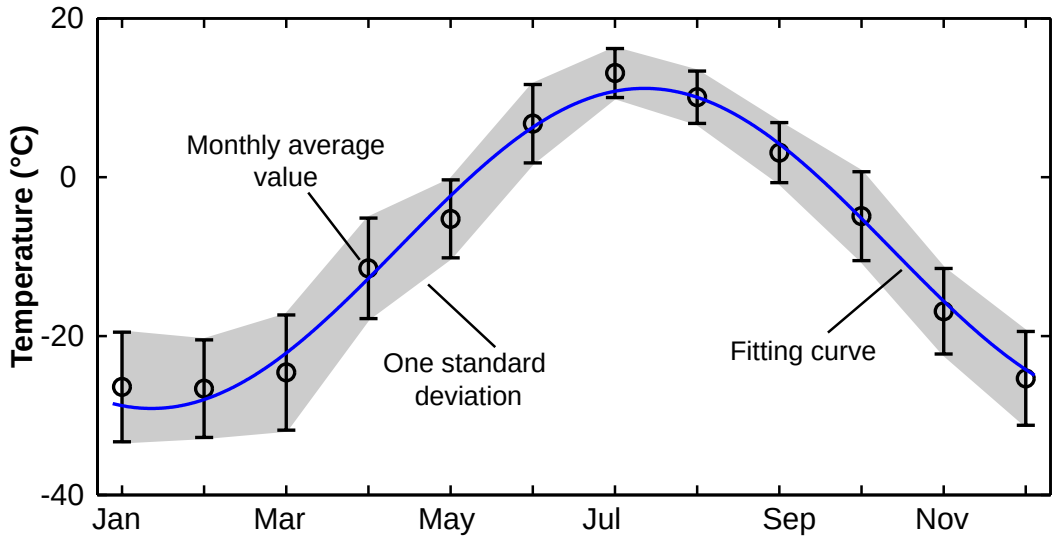

Figure 6.7: Monthly average air temperature for the period 2007-2010.

rological data at the station from 2007 to 2010, the monthly average of relative humidity, solar radiation, air temperature, wind speed is calculated. The mean relative humidity was 77 % during the measurement period and monthly average humidity reaches their highest and lowest values in October and June or July each year, respectively (Fig. 6.6A). Meanwhile, the monthly average of solar radiation reached a peak of 250 $\left(\mathrm{W/m^2}\right)$ in mid June and decreased to a minimum of 1.5 $\left(\mathrm{W/m^2}\right)$ in December annually during the study period (Fig. 6.6B).

Monthly average air temperature varied sinusoidally with the coldest temperature in mid January having a monthly average of -29.1 °C and warmest in mid July with an average in July of 11.1 °C (Fig. 6.6C and Fig. 6.7). Fig. 6.7 also demonstrates that air temperature fluctuated greater in winter than in summer. Furthermore, by averaging over the measuring period, the mean annual air temperature (MAAT) was -9.0 °C and the air temperature can be simulated by a sinusoidal function of time t in days (Eqn. 6.15).

$$T_a\ (^{\circ}\mathrm{C}) = -9.0 + 20.1 \sin\left(\frac{2\pi t}{365}\right) \tag{6.15}$$

Wind speed varies significantly and has major frequencies of 1 day and 14 days (Chapter 5). Further, from August to November, wind speed is high with a monthly average of 18.5 km/h and the common winds are northerly to easterly with an average speed of 17 km/h (Fig. 6.6D). Rainfall occurs from May to October annually. During the study period, the rainfall reached 153 mm in 2008 that is 93 % of the mean annual rainfall at Diavik, 164 mm, reported by Environment Canada (2008a) in the Lac de Gras area. Meanwhile, the rainfalls in 2007, 2009 and 2010 were 93 mm, 73 mm and 95 mm, respectively, which is significant lower than the mean 164 mm (Fig. 6.6E).

Table 6.1: MAAT, thawing and freezing indices of air temperature

Year	MAAT (°C)	Thawing Index (°C-days)	Freezing Index (°C-days)
2007	-9.6	978.4	4457.4
2008	-10.0	1069.0	4739.8
2009	-9.6	1019.8	4508.7
2010	-6.7	1188.8	3632.9
Average	-9.0	1064.0	4335.0

6.4 Results and Discussion

6.4.1 Air, surface temperatures and n-factors

The MAAT averaged over the period of measurements (2007 - 2010) was -9.0 °C. It was quite consistent from 2007 to 2009 however 2010 was an unusually warm winter with MAAT of -6.7 °C (Table 6.1). This warm year increased ground temperatures within the covered test pile. Air freezing index, I_{af}, the number of negative degree days, is 4335 °C-days and air thawing index, I_{at}, the number of positive degree days, is 1064 °C-days during the measured period. However in 2010, the values of I_{at} and I_{af} increased to 1188.8 °C-days and 3632.9 °C-days (Table 6.1).

The surface temperature of the covered test pile, which is measured within 5 cm of the test pile surface, followed the variation of air temperature (and solar radiation) but was warmer (Fig. 6.9). The average value of mean annual surface temperature (MAST) for the period of measurements was -4.6 °C at C0E5thm and -5.0 °C at C0W5thm. The average of MAST for the two thermistor string was -4.8 °C and the amplitude of the mean monthly ground surface temperature was 20.1 °C (Fig. 6.9). The difference between the values of MAST and MAAT is controlled by the energy transport processes occurring at the surface and waste-rock properties specially moisture content. The surface temperature of the covered pile can be represented by a sinusoidal function:

$$T_s\ (^{\circ}\mathrm{C}) = -4.8 + 20.1 \sin\left(\frac{2\pi t}{365}\right) \tag{6.16}$$

The n-factors, a ratio of ground surface freezing or thawing indices to air freezing or thawing indices, are used to represent the surface offset in permafrost conditions. The average ground surface freezing and thawing indices of thermistor cable C0E5thm and C0W5thm, I_{sf} and I_{st}, are -3342 °C-days and 1551 °C-days (Fig. 6.8). The n-factors $n_f = 0.77$ and $n_t = 1.46$ were calculated (Eqn. 6.17 and Eqn. 6.18) corresponding to gravel and concrete pavement type surfaces; n_t = 1.3-2.1 and n_f = 0.7 - 0.95 (Andersland and Ladanyi, 2004).

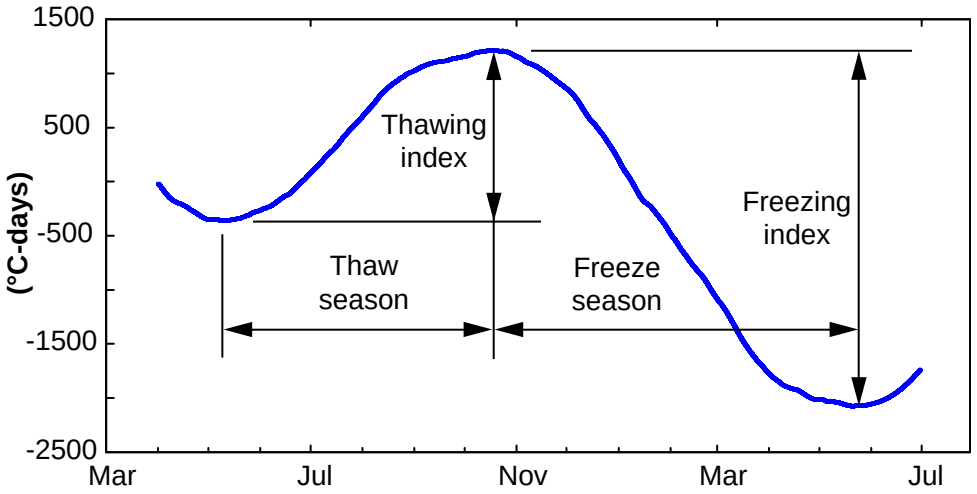

Figure 6.8: Freezing and thawing indices of surface temperature of the test pile (°C-days) based on daily average values

$$n_f = \frac{I_{sf}}{I_{af}} = \frac{-3342}{-4335} = 0.77 \tag{6.17}$$

$$n_t = \frac{I_{st}}{I_{at}} = \frac{1551}{1064} = 1.46 \tag{6.18}$$

6.4.2 Ground temperatures at STA 0+094.00

The fluctuation of soil surface temperatures of the covered test pile causes changes in ground temperatures within the covered test pile but with smaller means and amplitudes depending on their distance from the surface. At the depth of 0.5 m, mean monthly ground temperatures (averaged of C0E5thm and C0W5thm over the period of measurements) reached a maximum value of 10.2 °C in August and decreased to a minimum value of -18.2 °C in mid February annually. Mean annual ground temperature and amplitude at this depth were -4.0 and 14.2 °C. At the depths of 3.0 and 4.5 m (above and below the till layer), ground temperatures varied at much smaller amplitudes; 8.3 °C (between 0 and -8.3 °C) at the 3 m depth and 5.7 °C (between 0 °C and -5.7 °C) at 4.5 m depth in winters 2008 and 2009 (Fig. 6.9 and Fig. 6.10). However during winter 2010 due to significant warm weather, the amplitudes dropped to 6.7 and 4.5 °C at 3 and 4 m depths respectively (Fig. 6.9 and Fig. 6.10). At 10 m depth, ground temperatures varied at a small amplitude 1.6 °C (between 0.2 and -1.4 °C) during the period of measurements and showed an insignificant change in temperature during the warming associated with 2010. This is due to the effects of till cover and the distance that damped the temperature variations.

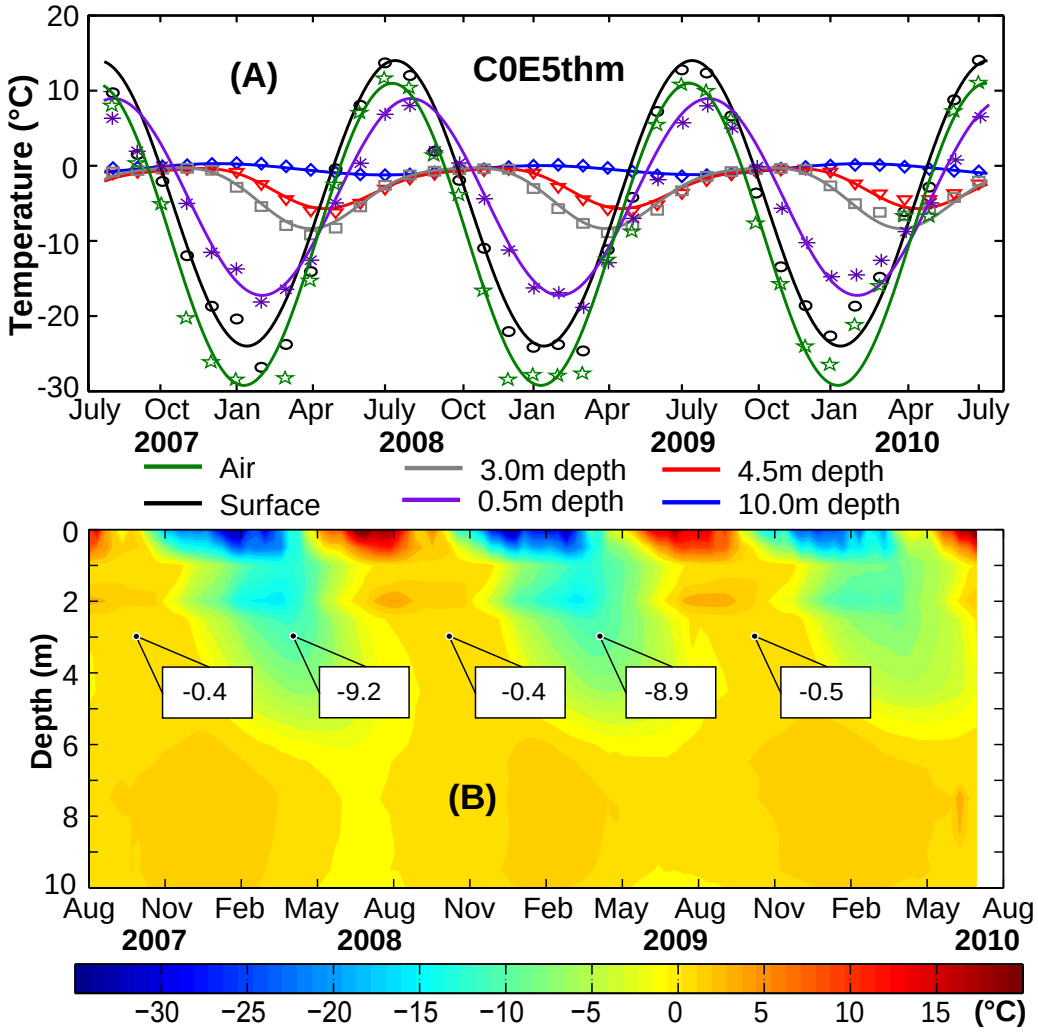

Figure 6.9: Monthly average air and ground temperatures at selected depths (A) and 2-D plot of ground temperatures (B) of thermistor cable C0E5thm.

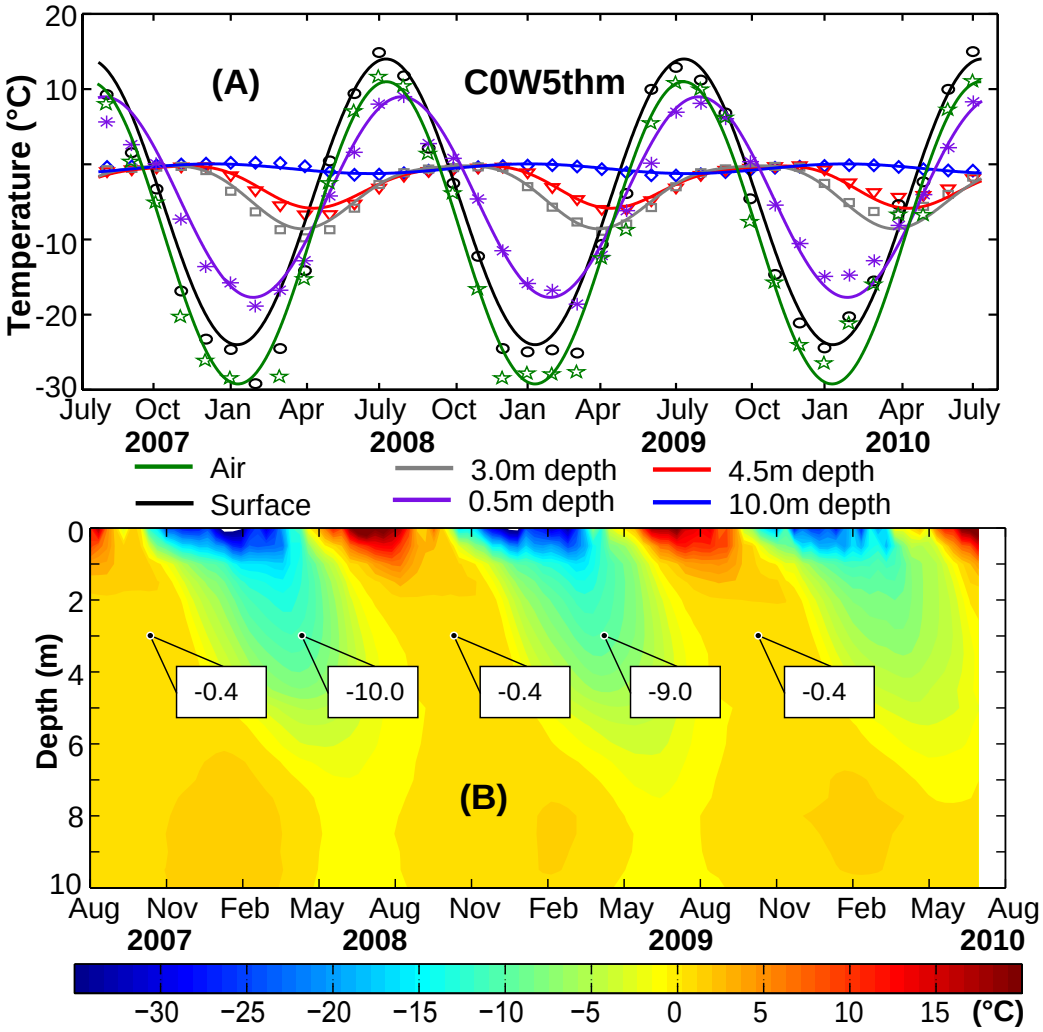

Figure 6.10: Monthly average air and ground temperatures at selected depths (A) and 2-D plot of ground temperatures (B) of thermistor cable C0W5thm.

6.4.3 Temperatures below till layer at Face 1 and Face 4

Besides, the two vertical thermistor strings C0E5thm and C0W5thm, there are also thermistor strings below the till along face 1 and face 4 (Fig. 6.5). Thermistor strings on Face 1 are above the lysimeter clusters that has heating cables at the base (Fig. 6.5) and thus any excessive heat releases from the heating cables will be monitored up by these thermistors. The idea of having heating cables inside the lysimeters is to maintain the temperature inside the lysimeters just above freezing (3 to 5 °C), so that any water entering the lysimeters will be collected for hydrogeology and geochemistry analysis. However, the temperatures of the heating cables were set too high (around 28 °C) and they have altered the thermal behavior at this measuring face and the heat has spread to nearby measuring faces (Fig. 6.11). In fact, temperatures at this face did not respond to the ambient temperature fluctuations but responded to the heat from the heating cables (Fig. 6.11). When the heating cables were turned off at the end of July 2008, temperatures near the lysimeters decrease gradually to around 1° C from 6.5 °C (Fig. 6.11B, C). The heating cables were turned on with a recorded temperature near 28 °C since the end of August 2008. Immediately, the nearby thermistors increased to a temperature around 6.5 °C and have remained at this temperature. Only thermistors at (-35.0, 12.2) and (34.4, 11.8) which are near the batters and far from the lysimeters show a response to the outside ambient temperatures and they are below 0 °C year around (Fig. 6.11B, C).

At Face 4 which is 15 m south of the lysimeters (Fig. 6.5C), temperatures are less influenced by the heating cables. The initially average temperature below the till was around 3 °C and gradually decreases. Temperatures measured by thermistors away from the till layer show a small fluctuation with an average of 1.5 °C about a mean of 0 °C, thermistor cable C4W5 (Fig. 6.12). Near the till temperatures fluctuates with larger amplitudes and show colder temperatures (below 0 °C year round). However thermistors at locations (-20.3, 8.1) C4W5 and (19.4, 7.9) C4E5 recorded temperatures of 2.5 °C in Oct 2009 and 2010. This may be due to heat from heating cables has spread to these locations. In summary, thermistors on Face 4 indicate that regions closed to the till were cold. However temperatures adjacent to the till and close to the batters are colder than at the top due to convective cooling of air that moves downward and outward to the toe. Temperatures at the center near the base were warmer and fluctuated less as it is less influenced by the cold base of the till.

6.4.4 Active layer

Active layer is the layer near the surface that subjected to freeze and thaw each year and its thickness is controlled by the energy balance at the surface. Based on the monthly averaged temperatures of the two thermistor strings, C0E5thm and C0W5thm, temperature profiles were plotted in 2008 and 2009 (Fig. 6.13). The temperatures within and below the till stay

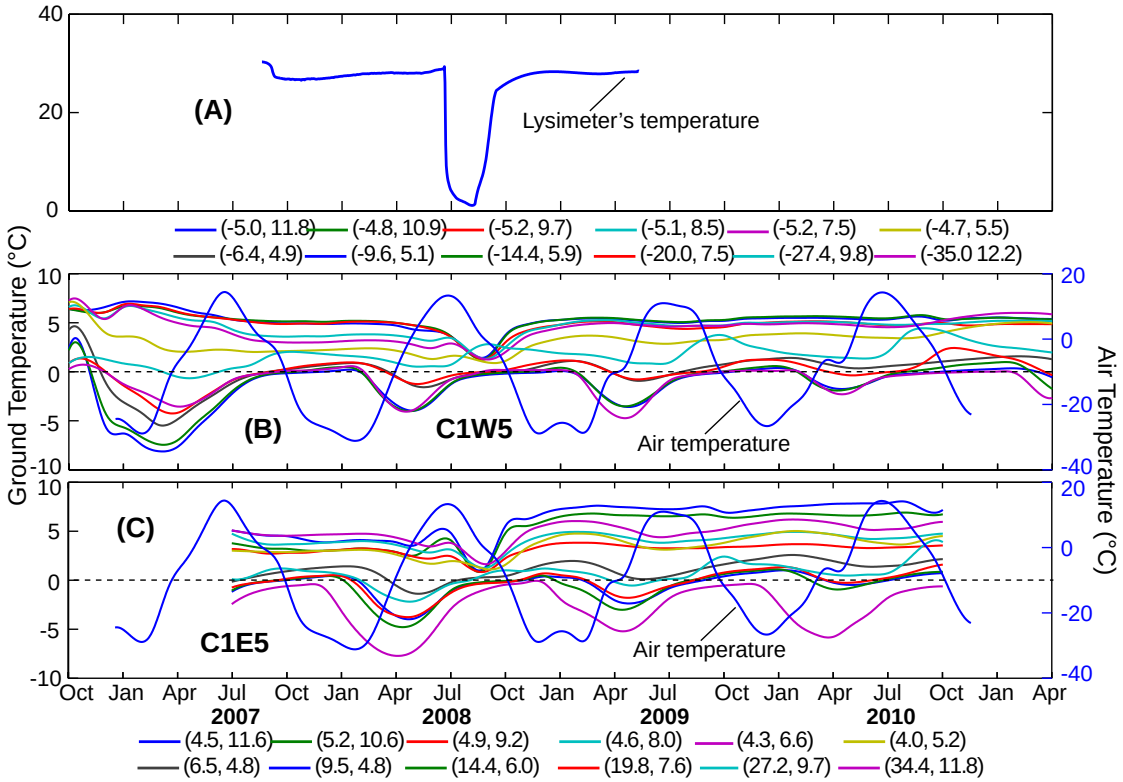

Figure 6.11: Lysimeter temperature (A) which is measured at the base, temperatures at thermistor string C1W5thm (B), temperatures at thermistor string C1W5thm (C). The numbers in bracket are (x, y) coordinates with the origin (*xOy*) shown in Fig. 6.5A.

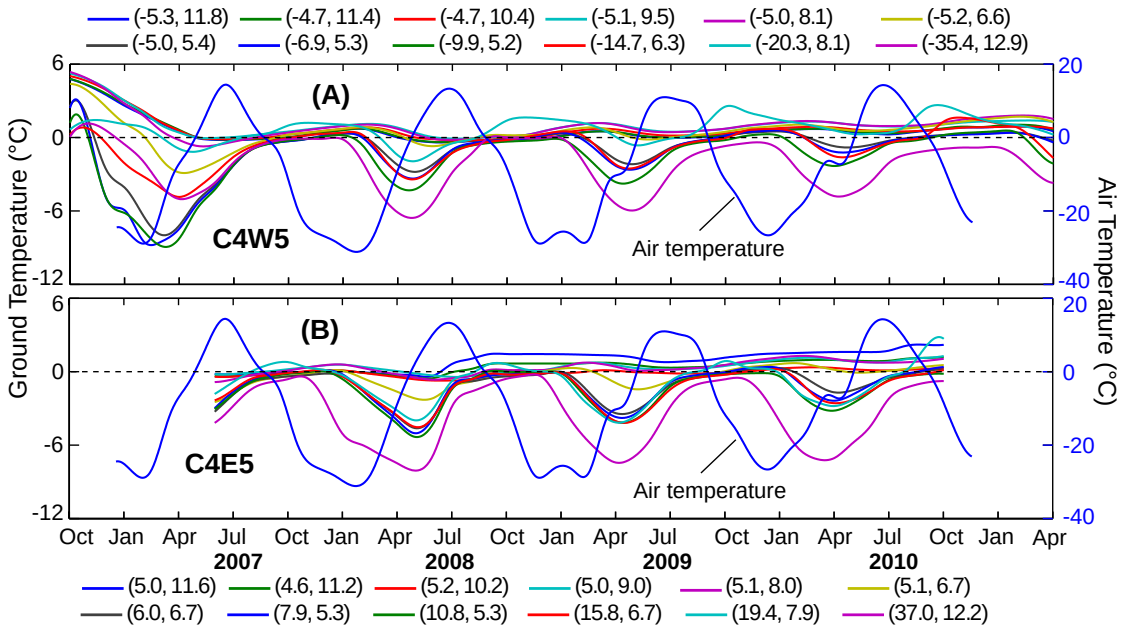

Figure 6.12: Lysimeter temperature (A) which is measured at the base, temperatures at thermistor string C1W5thm (B), temperatures at thermistor string C1W5thm (C). The numbers in bracket are (x, y) coordinates with the origin (*xOy*) shown in Fig. 6.5A.

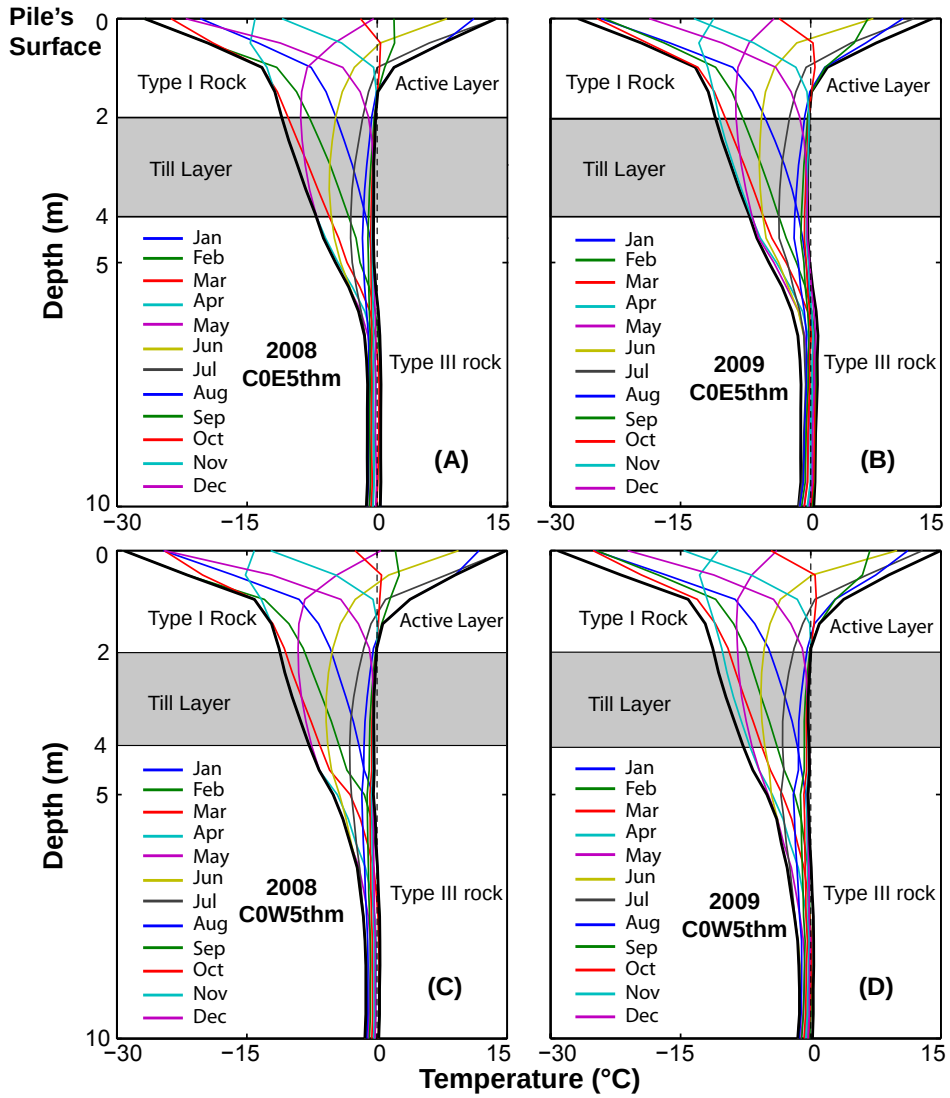

Figure 6.13: Temperature profiles (monthly averaged) of thermistor string C0E5thm in 2008 (A) and 2009 (B), and thermistor string C0E5thm in 2008 (C) and 2009 (D).

at and below 0 °C year round, whereas the temperatures above the till varies with season. From June to October each year there were certain depths above 0 °C and the rest of the year the entire profiles were below 0 °C (Fig. 6.13). Therefore, the active layer is contained within the Type I rock.

6.4.5 Bedrock Temperature

Initial temperatures at the base of the covered test pile (basal temperatures) below the geomembrane (Fig. 6.5), were around 7 °C and temperatures at the bottom of the Type I fill or on the bedrock surface were at 0 °C. Temperatures between 2 m and 12 m into bedrock (bedrock temperatures) or between 7 and 17 m from the base varied between -2 and -3 °C

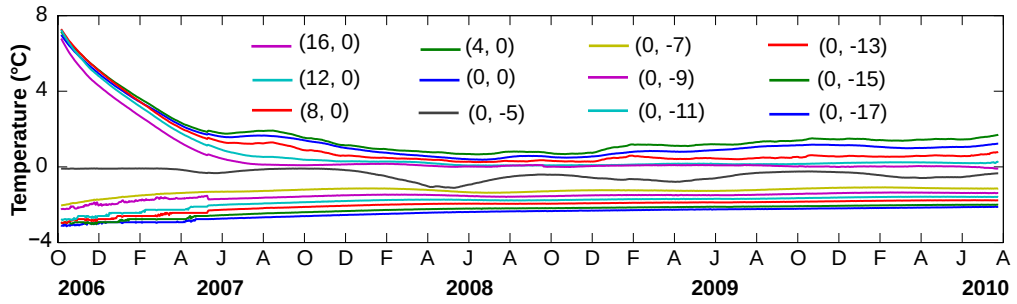

Figure 6.14: Daily averaged temperatures of CBC0thm02 Fig. 6.5A, C, at locations with coordinates showed in the brackets and the origin (x_1Oy_1) showed in Fig. 6.5A.

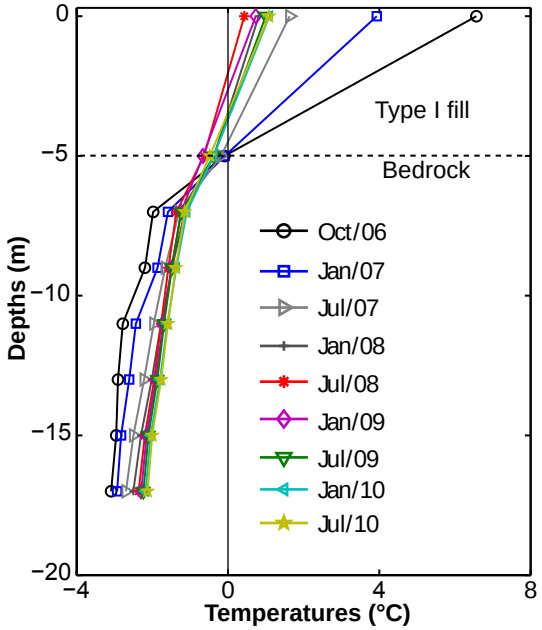

Figure 6.15: Temperature profile of CBC0thm02 at the centre of the covered test pile plotted at selected months.

initially (Fig. 6.14 and Fig. 6.15). The basal temperatures decrease significantly from 7 °C to between 1 and 2 °C in June 2007. This is due to initial high temperatures (high thermal gradients) at the base cooling during the first winter. At the base, temperatures at the centre (0, 0) which is 8 m South of the heating lysimeters were around 1.5 °C whereas at 16 m (16, 0) which is 18 m Southeast of the heating lysimeters (Fig. 6.5A) temperatures are maintained at and below 0 °C year round. The temperatures at the surface of the bedrock stayed constant at 0 °C until Dec 2007 and fluctuated afterward with small amplitudes (mean $<$ 0 °C).

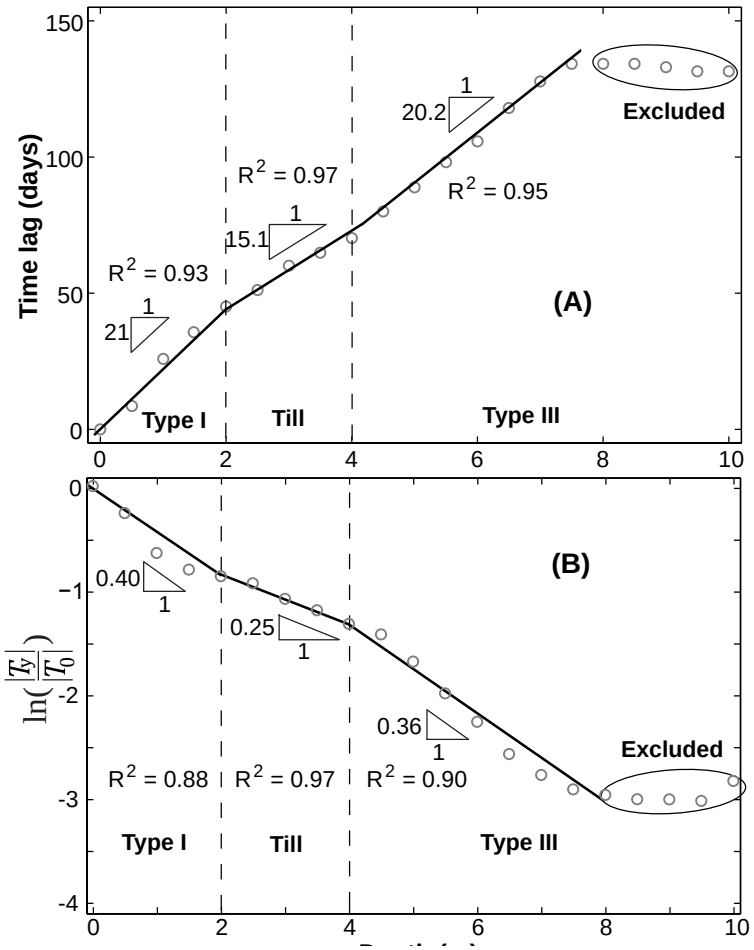

Figure 6.16: Estimation of thaw depth based on the air thawing index.

6.4.6 Determination of thermal diffusivity

6.4.6.1 Based on conduction

The average temperature was used to determine the bulk thermal diffusivity of the Type I, Till and Type III waste rocks. Time lag and amplitude damping between the surface temperature and the ground temperature time series of the covered test pile clearly show three distinct regions corresponding to Type I rock, till and Type III rock and ground temperatures below 8 m depth were excluded because of their weak correlation to surface temperatures (Fig. 6.16).

The calculated thermal diffusivities of Type I rock, till and Type III rock are 6.9×10^{-7}, 1.5×10^{-6} and 8.0×10^{-7} m^2/s respectively and the calculated values of thermal diffusivity using Eqn. 6.1 or Eqn. 6.2 give slightly different results (Table 6.2). Below 2 m, temperatures remained below 0 °C, therefore the calculated thermal diffusivity of the till and Type III rock are for frozen materials. However the thermal diffusivity of the till is

Table 6.2: Calculation of thermal diffusivity based on conduction

	Thermal Diffusivity (m^2/s)				
	Phase lag (Eqn. 6.1)	Amplitude (Eqn. 6.2)	Average	λ_e	C_e
Type I rock	7.6×10^{-7}	6.2×10^{-7}	7.0×10^{-7}	1.7	2.4×10^6
Till	1.5×10^{-6}	1.6×10^{-6}	1.5×10^{-6}	3.0	2.0×10^6
Type III rock	8.2×10^{-7}	7.7×10^{-7}	8.1×10^{-7}	1.8	2.2×10^6

higher due to its high moisture content, low void ratio of 0.2, which is based on measured water content of samples taken during construction, and being frozen. Meanwhile, the calculated thermal diffusivity of the Type I rock is in a range of the frozen and thawed values. The thermal diffusivities of the Type I and Type III rock are quite comparable with a value of $6.71 \pm 0.21 \times 10^{-7}\,m^2/s$ measured at Aitik mine (Tan and Ritchie, 1997) and $6.8 \pm 0.3 \times 10^{-7}\,m^2/s$ of waste rock at Rum Jungle mine (Harries and Ritchie, 1981).

6.4.6.2 1-D convection/conduction heat transport

The calculation starts with the determination of a and b in the Eqn. 6.6 using data in Fig. 6.16 for each layer. Then Eqn. 6.5 were solved for V and R which then were used along with the in-situ measured thermal conductivities to determine thermal diffusivities and vertical pore air velocity. With the known values of pore air velocity, a Peclet number (Pe) can be determined for each layer which is used to assess the relative magnitude of convection/advection and conduction heat transport and is defined as (Bear, 1972):

$$Pe = \frac{D_{50} C_a}{\lambda_e} u \tag{6.19}$$

Where $D_{50} = 90\,mm$ is the characteristic length of the medium (mean grain diameter) of Type I and III waste rock at large scale. If Pe is larger than 2, this indicates that the convective effects dominate over the conduction effects (Zienkiewicz et al., 2005).

The final result is shown in Table 6.3. The results of thermal diffusivities are very similar to the calculated thermal diffusivities based on pure conduction through time lag (Table 6.2) and the calculated Pe is much less than 2. Therefore, conduction is the dominated heat transfer process in the covered test pile.

6.4.7 Net Radiation and heat fluxes

Net radiation was calculated based on the Eqn. 6.12 with the surface albedo $\alpha_s = 0.46$ during summer (bare surface) and $\alpha_s = 0.70$ for snow surface during winter (Oke, 2002;

Table 6.3: Calculation of thermal diffusivity based on convection and conduction

	a	b	λ_e	V	R	κ (m^2/s)	u (m/s)	Pe
Type I rock	0.40	0.36	1.7	0.037	0.129	7.7×10^{-7}	1.0×10^{-4}	6.8×10^{-3}
Till	0.25	0.26	3.0	0.011	0.071	1.4×10^{-6}	5.3×10^{-5}	2.0×10^{-3}
Type III rock	0.36	0.35	1.8	0.010	0.120	8.3×10^{-7}	2.8×10^{-5}	1.8×10^{-3}

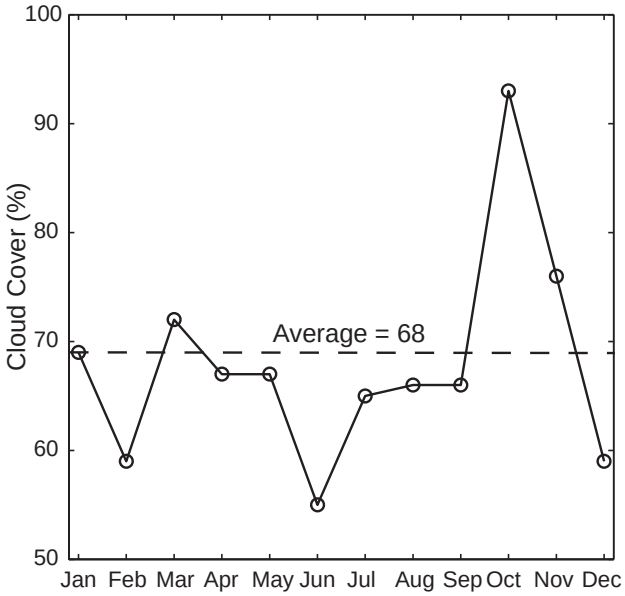

Figure 6.17: Monthly averaged of measured cloud cover at Diavik in 2006 (DDMI, 2007).

Carey et al., 2005; Montero S. et al., 2005). The surface emissivity, ε, are 0.94 and 0.82 for summer and winter respectively and these values are similar to those of bare dry soils and snow. Due to the lack of measured cloud cover data during the period of calculations, the cloud cover factor F was calculated based on the measured data in 2006 with the mean cloud cover of 68 % (Fig. 6.17). Surface heat flux at the horizontal surface of the covered test pile was calculated based on the temperatures of the surface and 0.5 m depth by using Eqn. 6.10. Heat flux at the bottom of the till was determined by utilizing five thermistors installed within the till and Eqn. 6.11.

Monthly average net radiation varied harmonically and reached a maximum value of 96.5 W/m^2 in July and a minimum value of -69.7 W/m^2 in mid December annually (Fig. 6.18A). In fact, it can be fitted by a sinusoidal function

$$R_n = 13.4 + 83.1 \sin\left(\frac{2\pi}{365}t - 1.30\right) \tag{6.20}$$

It has a mean annual net radiation of 13.4 W/m^2. Similarly, the monthly averaged-calculated surface heat flux varies sinusoidally between 20.4 W/m^2 in July and -28.6 W/m^2

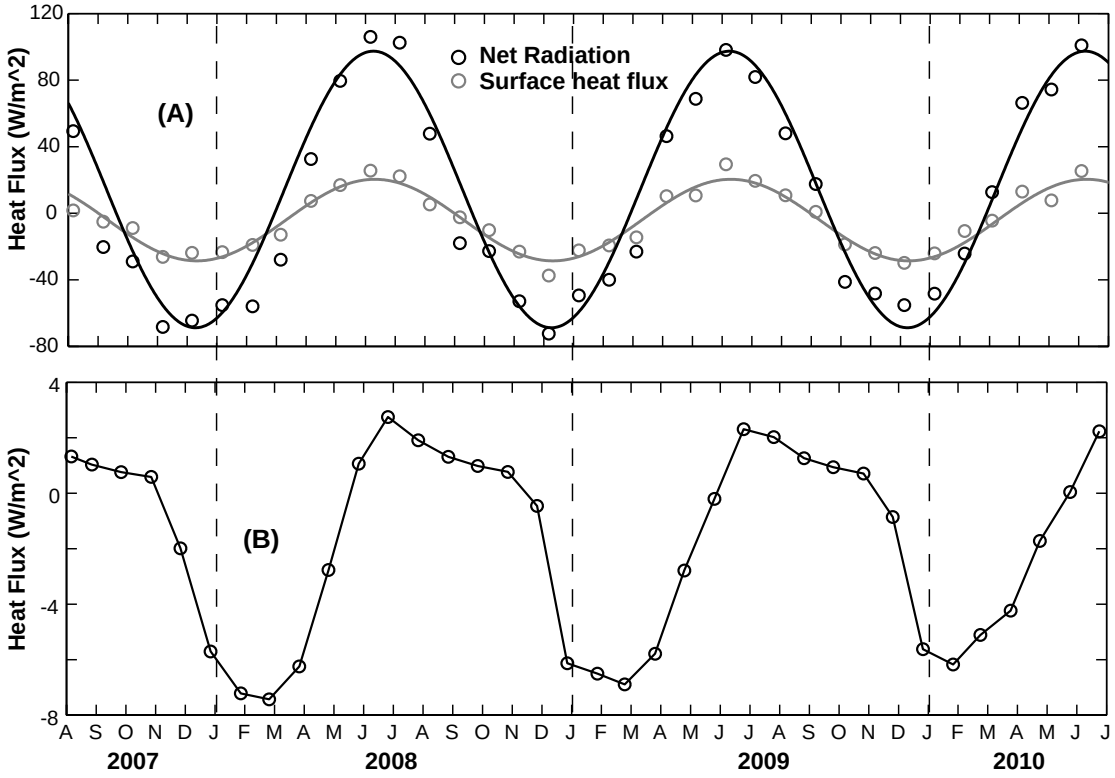

Figure 6.18: Monthly averaged of net radiation and surface heat flux (A) and heat flux across the bottom of the till layer (B).

in mid December annually (Fig. 6.18A) and the fitting curve of the surface heat flux is:

$$G = -4.1 + 24.5 \sin\left(\frac{2\pi}{365}t - 1.35\right) \tag{6.21}$$

With a mean annual surface heat flux of -4.1 $\mathrm{W/m^2}$, net radiation and surface heat flux are only positive from April to August annually which means during this period heat is available for water evaporation and to increase the interior temperatures of the covered test pile.

The magnitude of G varies with the covered test pile's surface characteristics (e.g. snow cover, moisture content, vegetation cover et al.) and solar radiation. In fact, due to the lack of vegetation on the surface of the test piles, low precipitation, and high evaporation during summer at the site, the ratio of mean ground heat flux to mean net radiation, $G/R_n = 0.33$, is considerably high (Fig. 6.19A). However, this value is common for bare soil surfaces ranging from 0.22 to 0.51 (Idso et al., 1975; Kustas and Daughtry, 1990; Jacobsen, 1999; Gavilan et al., 2007). This value is also comparable to 0.28 ± 0.03 obtained by Carey et al. (2005) from a study of evaporation from a waste-rock's surface (a similar surface condition) located in the northern Saskatchewan, Canada.

Owing to the high moisture content, low permeability of the till, and distance from the

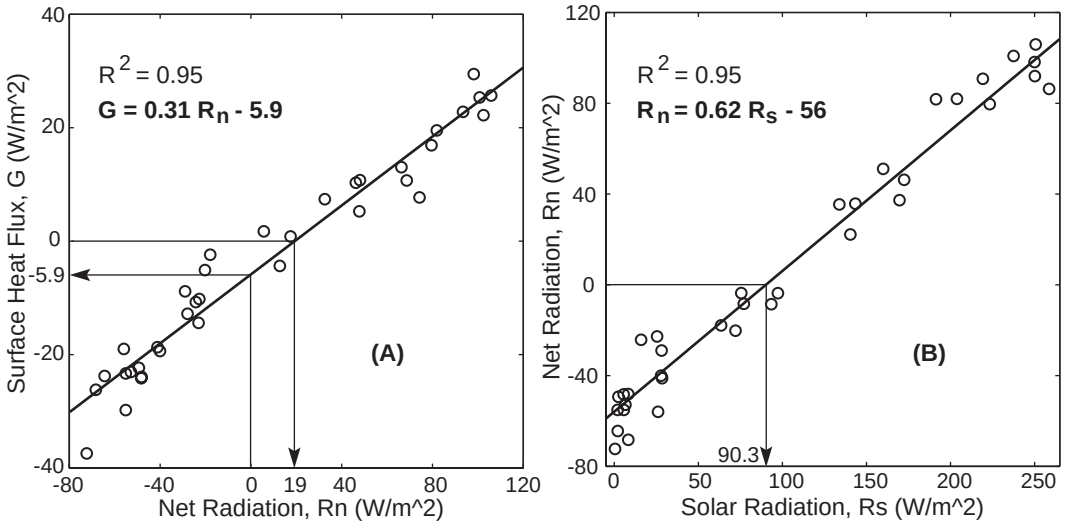

Figure 6.19: Monthly average net radiation, R_n, versus surface heat flux G (A) and incoming solar radiation, R_s, versus net radiation, R_n (B).

surface, the heat flux at the boundary between the till and the Type III rock is low. In fact, the monthly average of heat flux from June to December was around 1.2 $\mathrm{W/m^2}$ which is about 5.9 % of the monthly average surface heat flux in summer (Fig. 6.18B). For the period December to June of the consecutive year, the heat flux was negative and reached a peak of -5.8 $\mathrm{W/m^2}$ (averaged over three winters) around mid February (Fig. 6.18B), which is 4.8 times larger than heat flux during the summer. This is 20.2 % of surface heat flux during the winter. Moreover, the mean annual heat flux across the bottom of the till was -1.78 $\mathrm{W/m^2}$ and the negative value of mean annual heat flux indicates that heat is being removed from the underlying Type III rock.

Due to the high surface reflectivity of the covered test pile during both winter and summer, the ratio between the total incoming short-wave radiation, R_s, and the net radiation is low and it can be expressed by $R_n = 0.62R_s - 56$. For example, in July the monthly average of $R_s = 250$ $\mathrm{W/m^2}$ and the value of R_n is 99 $\mathrm{W/m^2}$. Therefore, the ratio between R_n and R_s in July is 0.4 which is similar to the finding of Carey et al. (2005) of 0.35 in midsummer (July). However, in areas covered by vegetation and high moisture, the ratio ranges between 0.55 and 0.84 (Cole and Green, 1963; Lafleur et al., 1997; Sharratt, 1998; Baldocchi et al., 2000). Further, in permafrost regions, the ratio has a considerable variation throughout a given year due to the substantial variations of solar radiation between summer and winter. In fact, when solar radiation is less than 90.3 $\mathrm{W/m^2}$ typically from October to March, the net radiation is less than 0 and thus the ratio is negative (Fig. 6.19B). Whereas, during summer the net radiation is positive, the mean ratio was 0.31 corresponding to $R_s = 170$ $\mathrm{W/m^2}$ and $R_n = 52.7$ $\mathrm{W/m^2}$.

6.5 Conclusions

The results of temperature and gas pressure measurements of a covered test pile constructed in a continuous permafrost region are presented. The MAAT and MAST between 2007 and 2010 were -9.0 °C and -4.8 °C and using daily averages with a linear regression between air temperature and the pile's surface temperature is $T_a = T_s - 4.2$ (°C). In addition, the surface condition's of the covered test pile was represented using n-factors of $n_f = 0.77$ and $n_t = 1.46$. Ground temperatures in the Type I rock above the till fluctuated with air temperatures with large amplitudes and the Type III rock below the till varied with much smaller amplitudes. Further, the active layer was contained in the Type I rock; the till and Type III rock stayed frozen year round except where internal heat sources kept the Type III rock thawed. At cross sections close to lysimeters where heat was released from heating cables, temperatures of Type III rock beneath the till warm and fluctuated accordingly with this heat source. Further away from the lysimeters, temperatures were colder.

Based on temperature measurements, the thermal diffusivities of the Type I, till and Type III rock were 6.9×10^{-7}, 1.5×10^{-6} and 8.0×10^{-7} m^2/s, respectively. Heat transfer in the covered test pile was dominated by conduction. Net radiation varied significantly with a large amplitude through the year whereas surface heat flux had a smaller amplitude. Further, based on a daily average, the linear regression between net radiation and surface heat flux was $G = 0.31R_n - 5.9$ $\left(\mathrm{W}/\mathrm{m}^2\right)$, meanwhile the relation between total solar radiation and net radiation was $R_n = 0.62R_s - 56$ $\left(\mathrm{W}/\mathrm{m}^2\right)$. The mean annual heat flux through the bottom of the till was 43 % of mean annual surface heat flux.

References

Andersland, O. B. and Ladanyi, B. (2004). *Frozen Ground Engineering*. John Wiley & Sons.

Arenson, L. and Sego, D. (2007). Protection of mine waste tailing ponds using cold air convection. Assessment and Remediation of Contaminated Sites in Arctic and Cold Climates.

Baldocchi, D., Kelliher, F. M., Black, T. A., and Jarvis, P. (2000). Climate and vegetation controls on boreal zone energy exchange. *Global Change Biology*, 6(S1):69–83.

Bear, J. (1972). *Dynamics of fluids in porous media*. Dover Publications, Inc.

Blasch, K. W., Constantz, J., and Stonestrom, D. A. (2007). Thermal methods for investigating ground-water recharge. *Ground-water recharge in the arid and semiarid southwestern United States, U.S. Geological Survey Professional Paper 1703*, pages 351–373.

Carey, S. K., Barbour, S., and Hendry, M. (2005). Evaporation from a waste-rock surface, key lake, saskatchewan. *Canadian Geotechnical Journal*, 42(4):1189 – 1199. Acid rock drainage;Eddy covariance method;Surface energy balance;Waste-rock;Water balance;.

Carslaw, H. S. and Jaeger, J. C. (1959). *Conduction of heat in solids*. Oxford University Press.

Cobos, D. R. and Baker, J. M. (2003). In situ measurement of soil heat flux with the gradient method. *Vadose Zone J.*, 2(4):589–594.

Cole, J. A. and Green, M. H. (1963). Measurements of net-radiation over vegetation and other climatic factors affecting transpiration losses in water catchments. *Intern. Assoc. Hydrol. Sci.*, 62:190–202.

DDMI (2007). Meteorological report 2006. Technical report, Diavik Diamond Mines Inc.

Environment-Canada (2008a). Climate data online. national climate data and information archive. Technical report, Environment Canada.

Gavilan, P., Berengena, J., and Allen, R. G. (2007). Measuring versus estimating net radiation and soil heat flux: Impact on penman - monteith reference et estimates in semiarid regions. *Agricultural Water Management*, 89(3):275–286.

Harries, J. R. and Ritchie, A. I. M. (1981). The use of temperature profiles to estimate the pyritic oxidation rate in a waste rock dump from an opencut mine. *Water, Air and Soil Pollution*, 15(4):405–423.

Idso, S. B., Aase, J. K., and Jackson, R. D. (1975). Net radiation - soil heat flux relations as influenced by soil water content variations. *Boundary-Layer Meteorology*, 9:113–122. 10.1007/BF00232257.

Jacobsen, A. (1999). Estimation of the soil heat flux/net radiation ratio based on spectral

vegetation indexes in high-latitude arctic areas. *International Journal of Remote Sensing*, 20(2):445–461.

Kustas, W. P. and Daughtry, C. S. (1990). Estimation of the soil heat flux/net radiation ratio from spectral data. *Agricultural and Forest Meteorology*, 49(3):205 – 223.

Lafleur, P. M., McCaughey, J. H., Joiner, D. W., Bartlett, P. A., and Jelinski, D. E. (1997). Seasonal trends in energy, water, and carbon dioxide fluxes at a northern boreal wetland. *J. Geophys. Res.*, 102(D24):29009–29020.

Lunardini, V. J. (1981). *Heat transfer in cold climates*. Van Nostrand Reinhold Company.

Martin, V., Aubertin, M., Bussiere, B., and Chapuis, R. P. (2004). Evaluation of unsaturated flow in mine waste rock. In *57th Canadian geotechnical conference*.

MEND1.61.2 (1996). Acid mine drainage in permafrost regions: Issues, control strategies and research requirements. Technical report, Department of Indian and Northern Affairs Canada.

MEND1.61.4 (2004). Covers for reactive tailings in permafrost regions. Technical report, The Mining Association of Canada-Mine Environment Neutral Drainage (MEND) Program.

MEND6.1 (1993). Preventing amd by disposing of reactive tailings in permafrost. Technical report, Mine Environment Neutral Drainage (MEND).

Molson, J., Fala, O., Aubertin, M., and Bussière, B. (2005). Numerical simulations of pyrite oxidation and acid mine drainage in unsaturated waste rock piles. *Journal of Contaminant Hydrology*, 78(4):343–371.

Montero S., I. C., Brimhall, G. H., Alpers, C. N., and Swayze, G. A. (2005). Characterization of waste rock associated with acid drainage at the penn mine, california, by ground-based visible to short-wave infrared reflectance spectroscopy assisted by digital mapping. *Chemical Geology*, 215(1-4):453–472.

Morin, K. A. and Hutt, N. M. (2001). Relocation of net-acid-generating waste to improve post-mining water chemistry. *Waste Management*, 21(2):185–190.

Newman, L. L., Barbour, S. L., and Fredlund, D. G. (1997). Mechanisms for preferential flow in vertically layered unsaturated waste rock. In *50th Canadian Geotechnical Conference of Canadian Geotechnical Society*.

Ochsner, T. E., Sauer, T. J., and Horton, R. (2007). Soil heat storage measurements in energy balance studies. *Agron. J.*, 99(1):311–319.

Oke, T. (2002). *Boundary Layer Climates*. Taylor & Francis.

Sauer, T. and Horton, R. (2003). Soil heat flux. In *Micrometeorologicalmeasurements in agricultural systems*. ASA Monograph. American Society of Agronomy, Madison, WI.

Sauer, T. J., Meek, D. W., Ochsner, T. E., Harris, A. R., and Horton, R. (2003). Errors in heat flux measurement by flux plates of contrasting design and thermal conductivity. *Vadose Zone Journal*, 2(4):580–588.

Sharratt, B. (1998). Radiative exchange, near-surface temperature and soil water of forest and cropland in interior alaska. *Agricultural and Forest Meteorology*, 89(3–4):269–280.

Song, Q. and Yanful, E. K. (2008). Monitoring and modeling of sand-bentonite cover for ard mitigation. *Water, air, and soil pollution*, 190(1-4):65–85. Compilation and indexing terms, Copyright 2008 Elsevier Inc.

Stallman, R. (1965). Steady 1-dimensional fluid flow in a semi-infinite porous medium with sinusoidal surface temperature. *Journal Of Geophysical Research*, 70(12):2821–2827.

Sugita, M. and Brutsaert, W. (1993). Cloud effect in the estimation of instantaneous downward longwave radiation. *Water Resour. Res.*, 29(3):599–605.

Suzuki, S. (1960). Percolation measurements based on heat flow through soil with special reference to paddy fields. *J. Geophys. Res.*, 65(9):2883–2885.

Tan, Y. and Ritchie, A. I. M. (1997). In situ determination of thermal conductivity of waste rock dump material. *Water, Air, & Soil Pollution*, 98(3):345–359.

Venegas, P., Grandón, A., Jara, J., and Paredes, J. (2012). Hourly estimation of soil heat flux density at the soil surface with three models and two field methods. pages 1–15.

Weeks, B. and Wilson, G. W. (2006). Prediction of evaporation from soil slopes. *Canadian Geotechnical Journal*, 43(8):815–829.

Wickland, B. and Wilson, G. W. (2005a). Research of co-disposal of tailings and waste rock. *Geotechnical News*, 23(3):35–38.

Zienkiewicz, O., Taylor, R., and Nithiarasu, P. (2005). *The Finite Element Method for Fluid Dynamics*. Elsevier, 6th edition.

CHAPTER 7

Heat transport and the effects of climate change in a waste-rock pile located in a continuous permafrost region of Northern Canada

7.1 Introduction

Mining involves the removal of significant quantities of waste rock to reach ore bodies and the waste rock is usually placed in engineered stockpiles. The stockpiles are often far above water table therefore they are generally unsaturated. Waste rock often contains some amount of sulfide minerals and the oxidation of sulfide minerals has the potential to produce acid rock drainage (ARD). Acidic drainage (low pH), high dissolved metal contaminants and other harmful components in leaching water from waste rock are a major concern for the environments at and nearby the mine (Olson et al., 1979; Nordstrom and Alpers, 1999; Lefebvre et al., 2001a; Moncur et al., 2005). Based on the closure objectives of waste rock piles at a mine, engineered soil covers can be created for different types of waste rock and they can be grouped into (MEND1.61.5b, 2010): "isolation covers", "barriers covers", "store and release covers", "water covers", "insulation covers". However, in cold regions, cold temperatures are known to slow chemical and biological processes that are responsible for oxidation of sulfide minerals and thus limit the generation of ARD (Lowson, 1982; Jaynes et al., 1984b; Meldrum et al., 2001; MEND1.61.4, 2004; Amos et al., 2009b). Therefore, to promote permafrost aggradation into reactive waste rock places in a continuous permafrost region, insulation covers are a candidate as they transport significant amounts of heat during long winter and they serve an insulation layer during short summer (MEND1.61.2, 1996; MEND1.61.4, 2004; Arenson and Sego, 2007).

However, if climate change and global warming occur, increasing air temperatures, changes of snow cover thickness and distribution, precipitation and others will significantly alter the subsurface thermal regime. The equilibrium between air temperatures and ground temperatures will change and causes a gradual increase in ground temperatures. The ef-

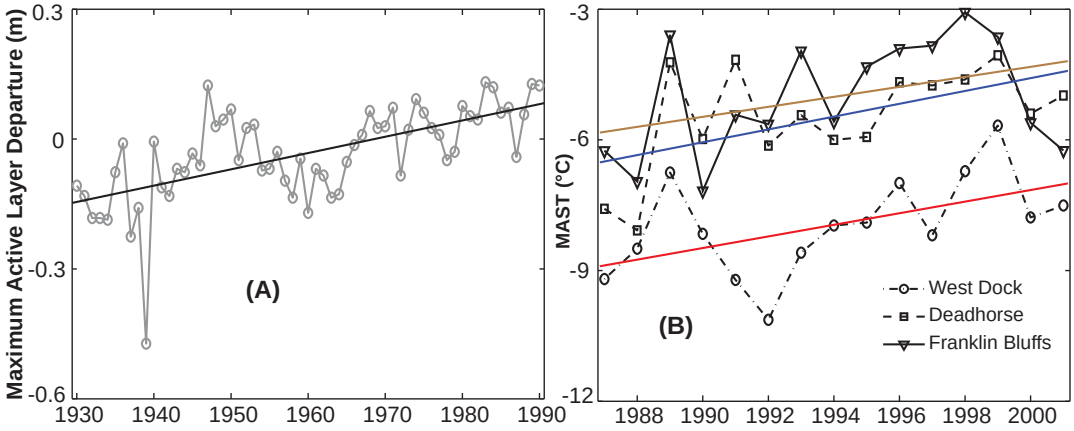

Figure 7.1: Variations of active layer in the Russian permafrost regions (A) (data from Frauenfeld et al., 2004), mean annual surface temperatures (MAST) of sites in Northern Alaska (B). The solid lines are linear least squares regression (data from Romanovsky et al., 2003).

fects of warming in continuous permafrost regions would be a thickening of the active layer (the freeze and thaw soil layer near the surface) (Fig. 7.1A) as a result of increases in ground temperatures (Fig. 7.1B) however the ground temperatures may remain below 0 °C. However, the impacts of warming would be more severe in discontinuous permafrost regions: such as thawing permafrost causing slope instability and loosing bearing capacity of infrastructure in these regions (Esch and Osterkamp, 1990; Environment Canada, 1998). If a waste-rock pile is placed in a discontinuous permafrost area, the increase in ground temperatures due to warming can trigger the oxidation of sulfide minerals causing ARD. Various methods have been used to protect the underlying permafrost and to overcome potential global warming in buildings and infrastructure, which can be used in waste-rock piles. Such methods are: ventilation pipes or ducts, thermosyphons and thermal piles, natural air convection embankments, foam insulation and other artificial ground freezing techniques (Goering and Kumar, 1996; Andersland and Ladanyi, 2004; Arenson and Sego, 2007; Zhang et al., 2008a; Xu and Goering, 2008b).

This chapter presents ground temperatures between July 2010 and July 2011 from three-installed thermistor cables in a full-scale waste rock dump (pile) at Diavik Diamond Mine, Northwest Territories, Canada, which is located in a continuous permafrost region. Numerical simulations of natural air convection were carried out for various mitigative strategy scenarios which are based on a closure concept at the site and the impact of a proposed long-term climate change on ground thermal regime within the waste rock dump.

7.2 Site Description

The Diavik Diamond Mine is located on East Island, a 17 km^2 island in Lac de Gras, approximately 300 kilometers northeast of Yellowknife, Northwest Territories, Canada in the Canadian Arctic (64°31' N, 110°20' W, el. 440 m). The site is located within the continuous permafrost region with an average precipitation of 283 mm with 60 % from snow (Environment-Canada, 2008a). Based on ground temperature measurements, the permafrost may extend to a depth of around 400 m and the active layer varies from 1.0 m in high moisture content areas to around 5.0 m in bedrock (Hu et al., 2003; Mareschal et al., 2004; DDMI, 2006). Due to the cold and lengthened winter season and relatively high evaporation at the site (Neuner et al., 2012), water transport is limited into the active layer (it is thin) during summer, which is relatively short. Therefore, for the purpose of thermal modeling the convective part associate with water is usually small and neglected however the convective transport due to air is sometimes significant because of high permeability of waste rock.

Depending on the sulfur content, waste rock is sorted into: Type I rock ($<$ 0.04 wt % S), Type II rock (0.04 to 0.08 wt % S) or Type III rock ($>$ 0.08 wt % S). Furthermore, the amount of biotite schist in waste rock was used to classify between acid and non acid-generating waste rock. As a result, Type I rock is non-acid generating, Type II rock is low acid generating and Type III rock is potentially acid generating. At the end of the mine life in 2020, about 184 Million tonnes (Mt) of waste rock will be stockpiled in 60 to 80 m high piles covering about 3.5 km^2. Insulation cover are a closure concept for the Type II and Type III waste rock, including re-sloping the Type II and III areas to 18.4° (3H:1V) and covering with a 1.5-m low permeability layer of till, and a 3-m layer Type I waste rock to act as an active freeze-thaw layer (DDMI, 2006).

To monitor the evolution of thermal, geochemical and hydrogeological processes within a Type III waste-rock dump, three 8-inch holes spaced at 5 m, FD1 (32.2 m depth), FD2 (30.7 m depth) and FD3 (40.2 m depth), were drilled in May 2010 to install instruments. The instruments include thermistor cables, gas lines, soil water suction samplings (SWSS), ECH_2O moisture content sensors and permeability balls (Fig. 7.2). The drill holes were back filled with 3/4 inch crush and silica filter sand. Thermistors were installed at 5 m vertical spacing and ground temperatures are recorded at a 12-h interval. Hourly air temperature is measured at Diavik meteorological station, which is about 1 km from the waste rock dump.

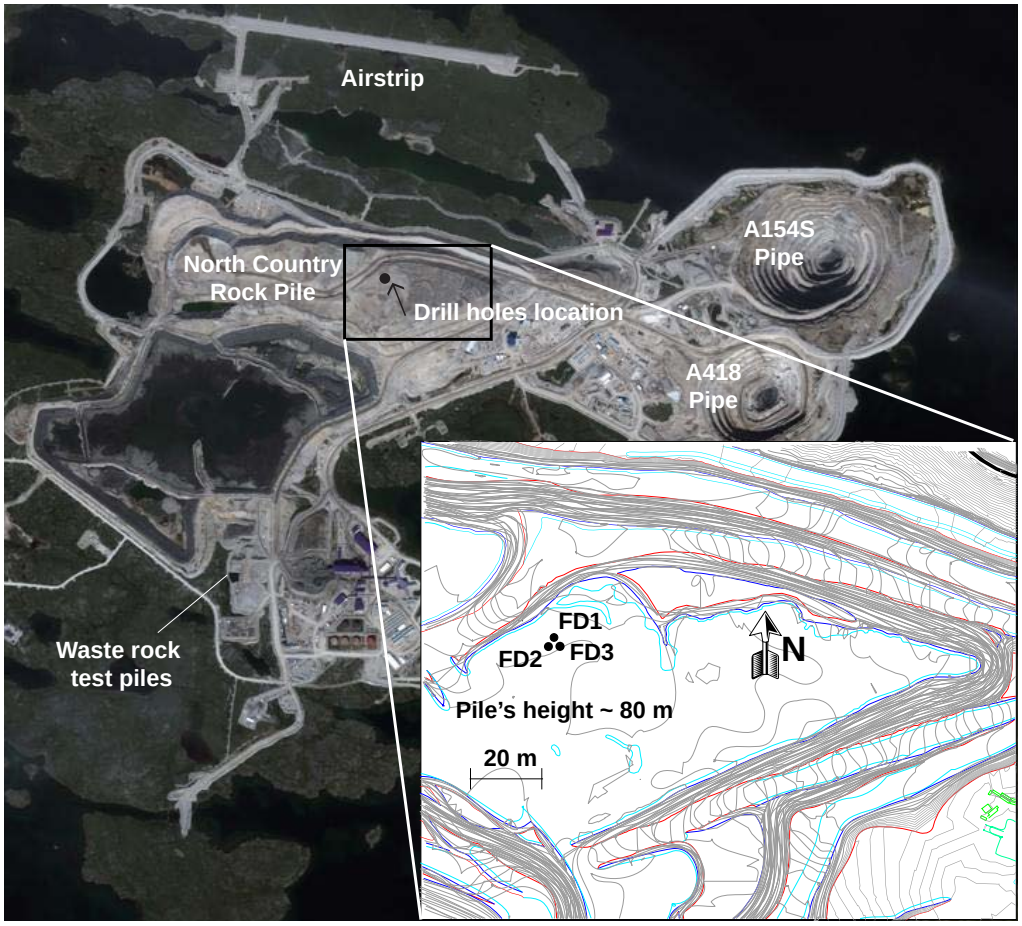

Figure 7.2: The location of drill holes

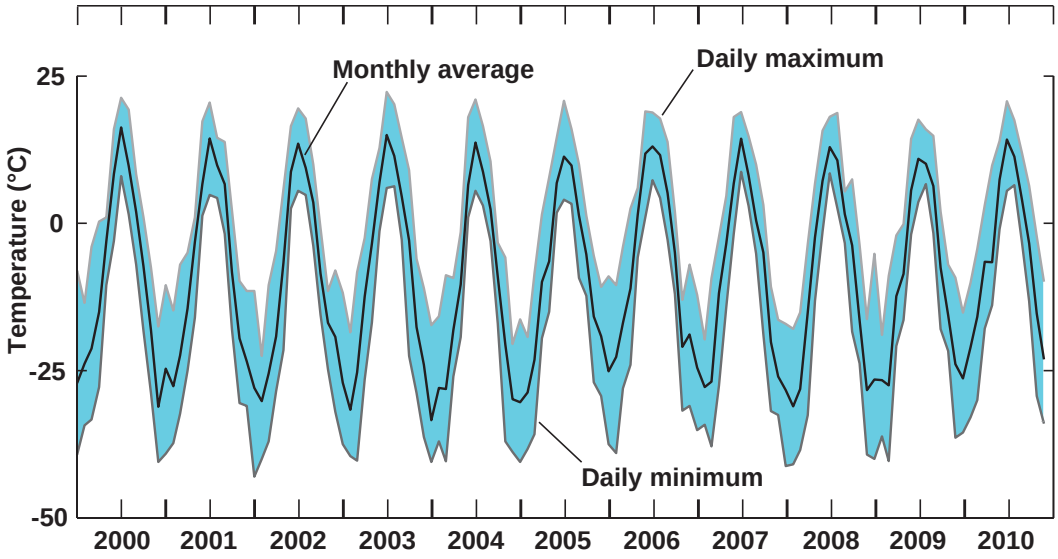

Figure 7.3: Monthly averaged air temperatures plotted with daily maximum and minimum air temperatures.

7.3 Experimental results and climate change

7.3.1 Air temperatures

Monthly average air temperatures varied significantly throughout the year, with the warmest temperatures in July and the coldest in January. Over a ten-year period (from 2000 to 2010), the monthly average air temperature in January and July was -29.3 °C and 11.5 °C, respectively (Fig. 7.4A). Daily average air temperatures also fluctuated considerably, however they showed more fluctuation in winter (peak in January) than in summer (peak in July). For example, the daily average air temperatures were -43 °C on January 21, 2002 and -5.2°C on January 19, 2009 and varied between 22.3 °C on July 27, 2003 and 4.8 °C on July 2, 2003 (Fig. 7.3).

Air freezing and thawing indices, I_{af} (°C-days) and I_{at} (°C-days) which are used in describing the intensity of air-temperature variations were calculated using Eqn. 7.1 and Eqn. 7.2 in which t is time and T is air temperature in °C. Over the measured period, the averaged value of I_{af} was 4426.3 (°C-days) and the averaged value of I_{at} was 1082.7 (°C-days). A linear trend line shows that I_{at} has increased whereas I_{af} has reduced over this 10-year period (Fig. 7.4A). However, the increase of I_{at} was smaller than the reduce of I_{af}. The thawing-index trend line indicates that I_{at} has increased 36 °C-days/decade (between 2000 and 2010) compared to 44.4 °C-days/decade reported by Frauenfeld et al. (2007). Whereas the freezing-index trend line shows that I_{af} has reduced about 120 °C-days/decade (Fig. 7.4A) compared to 85.6 °C-days/decade found by Frauenfeld et al. (2007). The results of Frauenfeld et al. (2007) are average values of whole regions north of 50 °N between

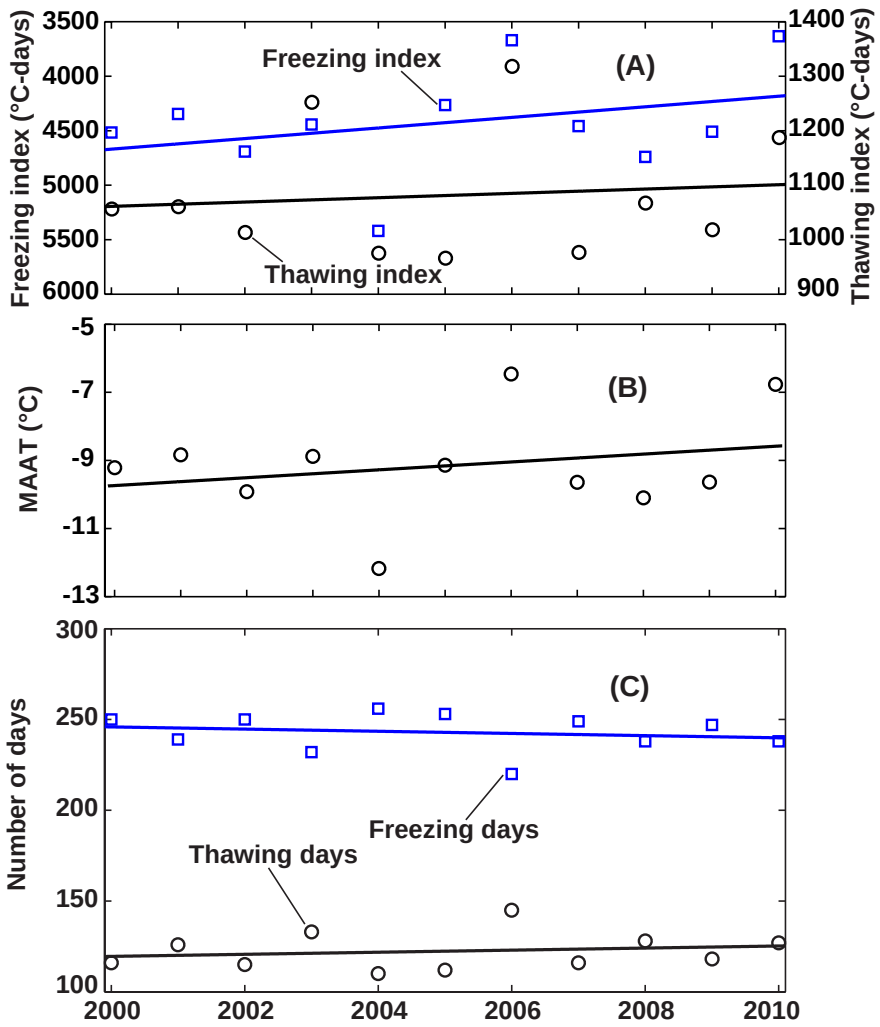

Figure 7.4: Calculated air thawing and freezing indices based on daily averages (A), calculated mean annual air temperate (MAAT) (B), and thawing and freezing days of air temperatures (C)

1966 and 2001. Therefore, the differences in the rates (both I_{af} and I_{at}) between this study and Frauenfeld et al. (2007) could reflect the shorter length that data has been available to determine the rates (a decade versus three decades) and/or local variations.

$$I_{af} = \int_{t_0}^{t_1} |T| \, \mathrm{dt}, \; T < 0\,^{\circ}\mathrm{C} \tag{7.1}$$

$$I_{at} = \int_{t_0}^{t_1} T \, \mathrm{dt}, \; T > 0\,^{\circ}\mathrm{C} \tag{7.2}$$

An average mean annual air temperature (MAAT) was -9.1 °C over the last decade and the trend line indicates an increasing rate of 0.73 °C/decade (Fig. 7.4B) which is higher than a result of climate models shown in a later section. Whereas, Chylek et al. (2009) reported

a warming of 0.38 °C/decade during the period between 1970 and 2008 at the latitudes between 64 °N and 70 °N. The difference again may be due to the length of the analysis and local fluctuations. Fig. 7.4B also shows that in 2004 air temperature was significantly colder than MAAT at -12.1 °C, whereas in the years between 2006 and 2010 MAATs were much warmer at -6.4 °C and -6.7 °C, respectively. The warming of air temperatures can also be associated with an increase in thawing days and a decrease in freezing days. Average thawing and freezing days were 122.4 and 242.9 days. The number of thawing days has increased 5.7 days/decade and the number of freezing days has decreased 6.0 days/decade over the measurement period (Fig. 7.4C). The above results indicate that warming has significant impacts on air temperatures during winter than summer.

7.3.2 Ground Temperatures

Ground temperatures below the surface of the waste rock dump can be represented using periodic functions, or Fourier series. The following is such an expression, which describes temperature as a function of time:

$$T(t) = T_o + \sum_{i=1}^{n} \left(a_i \cos(i\omega t) + b_i \sin(i\omega t)\right) \tag{7.3}$$

Where T_o represents the mean annual ground temperature (MAGT) at a specific depth y, ω is the fundamental angular frequency, $A_i = \sqrt{a_i^2 + b_i^2}$ and $\phi_i = \arctan\left(\frac{a_i}{b_i}\right)$ are the amplitude and phase of ground temperatures corresponding to angular frequency $i\omega$.

Under assumptions of a periodically varying ground surface temperature $(n = 1)$ and one-dimensional conductive heat transfer, the apparent (effective or bulk) thermal diffusivity of waste rock can be calculated using phase or amplitude equations (Carslaw and Jaeger, 1959):

- Phase equation

$$\kappa = \frac{1}{2\omega}\left(\frac{y_2 - y_1}{\delta t}\right)^2 \tag{7.4}$$

- Amplitude equation

$$\kappa = \frac{\omega}{2}\left(\frac{y_2 - y_1}{ln\left(\frac{|T_2|}{|T_1|}\right)}\right)^2 \tag{7.5}$$

Where δt is phase difference; $|T_1|$ and $|T_2|$ are temperature amplitude at two depths y_1 and y_2. $\kappa = \lambda/c$, λ and C are the effective (bulk or apparent) thermal conductivity and volumetric heat capacity of waste rock.

Table 7.1: Calculated Fourier's coefficients with $\omega = \frac{2\pi}{365}$ and $n = 2$. The results indicate that the amplitude A_1 is much larger than A_i $(i \geq 2)$ at depths within one wavelength. Therefore, the values of A_i $(i \geq 2)$ are usually omitted.

Depths (m)	T_o	a_1	b_1	a_2	b_2	A_1
			FD1			
Surface	-6.3	-18.9	-7.6	1.0	-0.1	20.4
1.86	-2.2	-4.6	-9.0	0.4	1.0	10.1
6.86	-1.0	0.8	-2.9	-0.1	0.6	3.0
11.86	-0.6	0.7	-0.2	-0.3	0.2	0.8
16.86	-0.1	0.0	0.0	0.0	0.0	0.0
			FD2			
Surface	-6.4	-18.9	-8.20	1.8	-0.5	20.5
0.66	-4.8	-11.2	-10.2	1.5	-0.2	15.1
5.66	-1.1	0.7	-4.2	-0.2	0.6	4.2
10.66	-1.0	0.9	-0.5	-0.2	0.4	1.1
			FD3			
4.50	-0.2	0.2	-3.3	-0.6	1.1	3.3
9.50	-0.7	0.7	-1.0	-0.3	0.7	1.2
14.50	-0.1	0.1	0.0	-0.1	0.0	0.1
19.50	-0.3	0.0	-0.1	0.0	0.0	0.1

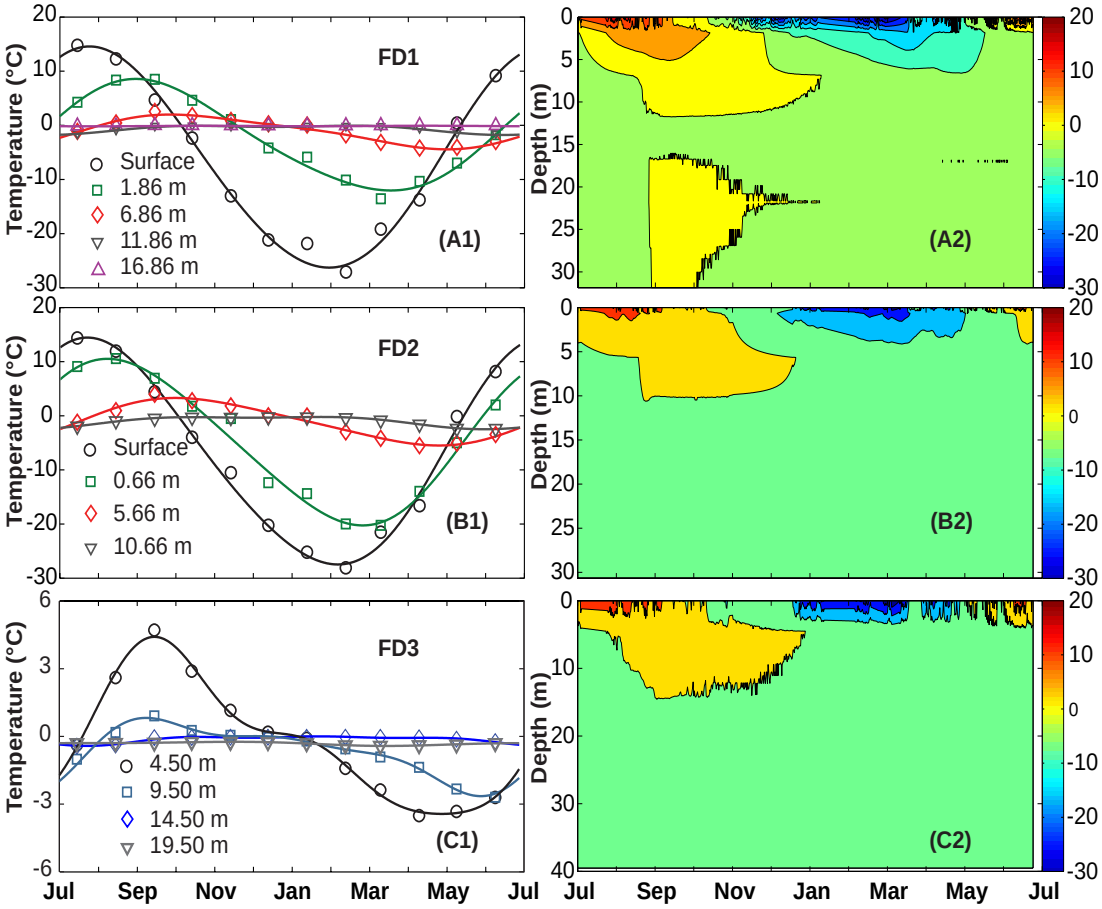

Figure 7.5: Monthly average ground temperatures from July 2010 to July 2011 at selected depths of FD1 (A1), FD2 (B1) and FD3 (C1); time-temperature-depth plot of FD1 (A2), FD2 (B2) and FD3 (C2).

7.3.2.1 Field data

The values of Fourier's coefficients are shown in the Table 7.1 at selected depths and the periodic function of ground temperatures described by Fig. 7.4 are plotted in Fig. 7.5. The Fourier-series curves fit the monthly average ground temperatures very well. Furthermore, the ground surface temperatures measured within 5 cm of the waste rock dump's surface had a mean annual surface temperature (MAST) of -6.3 °C and an amplitude of 20.4 °C. Amplitudes of ground temperatures reduced rapidly with depths from 20.4 °C at the surface to 0.1 °C at 14.50 m depth (Table 7.1).

Based on monthly averages, temperature profiles at FD1, FD2 and FD3 show the 0 °C isotherm at 11.5, 10 and 12.5 m depths, respectively as indicated in Fig. 7.6. However, the depth of 0 °C isotherm is expected to change over time as it evolves toward an equilibrium profile following the dump construction and the superimposed effects of global climate change. The measurements of thermal evolution of a waste-rock pile at Ekati mine which is about 30 km north and similar climate conditions as Diavik mine conducted by EBA

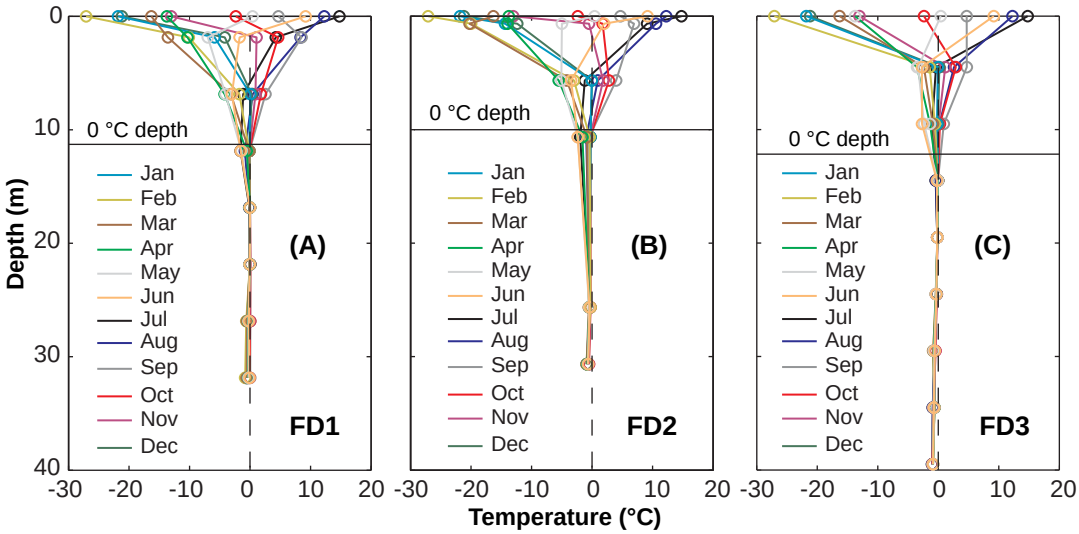

Figure 7.6: Temperature profiles of FD1 (A), FD2 (B) and FD3 (C) from July 2010 to July 2011

Engineering (2011) showed that the initial depth of 0 °C (in 2000) was about 12 m and after 5 years (in 2005) the 0 °C isotherm reduced to about 4.5 m. The period between 2000 and 2005 is considered to regain its thermal equilibrium. Therefore, it would take about 5 years for the ground temperatures at the drill holes at Diavik to retrieve undisturbed temperatures. However, the rate at which ground temperatures regains undisturbed thermal regimes mostly depends on the amount of water has been induced into waste rock during drilling.

From December to April from the surface to the depth of 40 m, ground temperatures were below 0 °C whereas the other months the upper zone of the waste dump was above 0 °C. Furthermore, the ground temperatures did not show any significant increase in temperatures associated with oxidation of sulfide minerals at any depth when the overall temperature trends are examined. In fact, Amos et al. (2009b) measured the oxidation of the Type III rock at this site and they concluded that oxidation rate of the Type III rock was small. The heat release was insignificant.

7.3.2.2 Thermal diffusivity calculation

The relation of amplitude ratios between surface temperature and ground temperatures at depths were fitted well using an exponential curve with $R^2 = 0.96$ (Fig. 7.7A). A linear regression was used to fit the relation between the phase delay with depths up to 14.50 m (Fig. 7.7B) with $R^2 = 0.97$. Below 14.5 m ground temperature variations were very strongly attenuated, as indicated by points that did not follow the linear regression line. An exponential curve was used to fit the relation between amplitude ratios and phase delays with $R^2 = 0.95$ (Fig. 7.7C) for those ground temperatures up to 14.5 m depth. The curves plotted

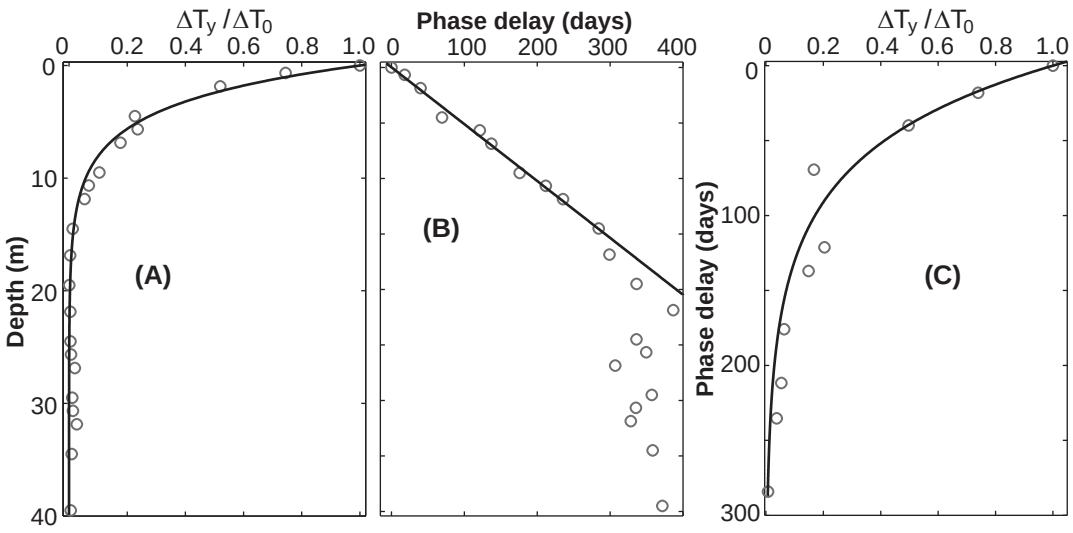

Figure 7.7: Relation between depth and amplitude ratio (A); depth and phase delay (B); phase delay and amplitude ratio (C).

in Fig. 7.7 indicate that heat transfer by conduction dominates in the waste dump. Effective thermal diffusivities were determined to be 5.4×10^{-7} m^2/s (Eqn. 7.5) and 8.5×10^{-7} m^2/s (Eqn. 7.4) with an average of 7.0×10^{-7} m^2/s. The effective thermal diffusivity is comparable to a value of 8.0×10^{-7} m^2/s determined in a 15-m high experimental waste-rock pile at the site (Chapter 4).

7.3.3 Annual heat flow

MAGTs are below 0 °C in the entire profile of FD1, FD2 and FD3 drill holes and strongly attenuated (Fig. 7.8A). The annual variations of ground temperatures at a depth around one wavelength ($\Gamma = 16.6$ m (Eqn. 7.6) with $\kappa = 7.0 \times 10^{-7}$ m^2/s $= 0.0605$ m^2/d) are so small compared to that of the surface. Therefore the one-wavelength thickness layer is considered to be affected by the annual variation of surface temperature.

$$\Gamma = \left(\frac{4\pi\kappa}{\frac{1}{365}} \right)^{0.5} \tag{7.6}$$

$$F = -\lambda \frac{\partial T}{\partial y} \tag{7.7}$$

The annual heat flux at depth was determined based on the MAGTs and an average thermal conductivity, λ, of 1.8 W/(m·K) through Eqn. 7.7. The shaded area in the Fig. 7.8B represents the total annual heat flux within one wavelength depth. Dividing this total heat flux by one wavelength, the average annual heat flux of one wavelength was 0.8 W/m^2 in an upward direction and the heat flux at the surface was 5.7 W/m^2 which was removed from the waste dump (the waste dump is cooling) between July 2010 and July 2011 (Fig. 7.8B).

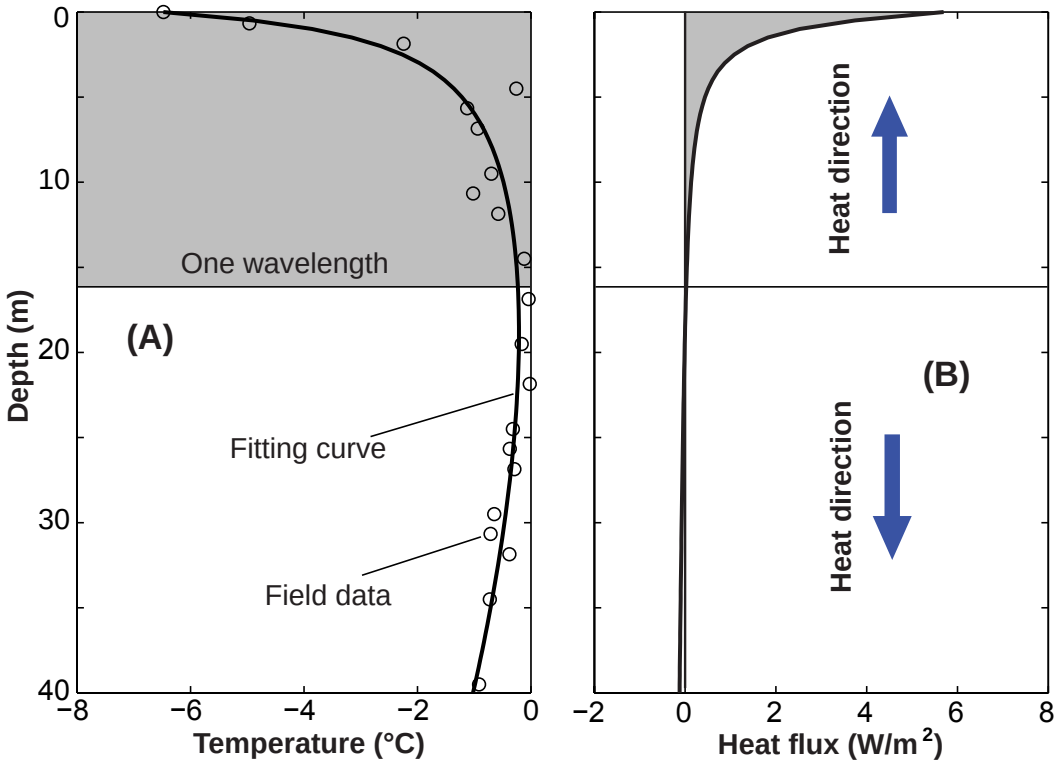

Figure 7.8: MAGTs with depths (A) and calculated heat flux (B) at FD1, FD2 and FD3.

Heat flux of the layer between one wavelength and the end of drill holes (40.2 m) was small and in a downward direction (Fig. 7.8B).

7.3.4 Climate change

Future climate modeling analyses for the site were conducted by Environmental Modeling and Prediction P/L Australia (2008) for the period between 1970 and 2060. Measured climatic variables at Diavik and the surrounding regions were used to check the results of climate models. The predictions of annual air temperature rise (warmest, mean and coldest temperatures) between 1970 and 2060 are shown in detail in the Fig. 7.9 and a summary follows:

- Warmest temperatures: +0.061 °C/year, from -8.3 °C to -2.8 °C.
- Mean temperatures: +0.056 °C/year, from -11.0 °C to -6.0 °C.
- Coldest temperatures: +0.060 °C/year, from -14.7 °C to -9.3 °C.

The predicted annual temperatures show a relatively constant rate of temperature increase over the predicted period. The predicted-mean annual temperatures matches closely

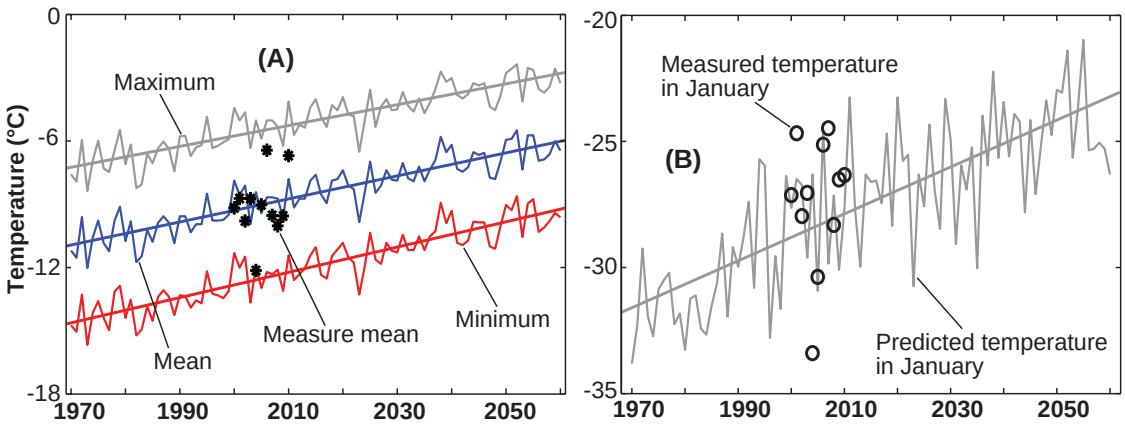

Figure 7.9: Predicted minimum, mean and maximum annual temperatures (A) and predicted mean January temperatures (B) for Diavik (data from Environmental Modeling and Prediction P/L Australia, 2008).

Table 7.2: Predicted future air temperatures for selected months at Diavik (data extracted from Environmental Modeling and Prediction P/L Australia, 2008).

	Maxima		Mean		Minima	
	1970:2060 (°C)	Rate (°C/year)	1970:2060 (°C)	Rate (°C/year)	1970:2060 (°C)	Rate (°C/year)
January	-27.4:-19.8	+0.084	-30.3:-22.6	+0.086	-33.6:-25.4	+0.091
April	-11.5:-7.9	+0.040	-15.7:-11.0	+0.052	-19.3:-13.7	+0.062
July	15.7:17.5	+0.020	11.6:13.7	+0.023	7.5:9.4	+0.021
October	-4.8:-0.6	+0.047	-7.4:-2.5	+0.054	-9.9:-4.4	+0.061

to the measured MAATs although there were some years the measured MAATs was closer to the predicted minimum or maximum (Fig. 7.9A). In Fig. 7.9A, the predicted minimum and maximum annual temperatures are the predictions of the coldest and warmest climate models while the predicted mean annual temperatures are the mean of coldest and warmest climate models. Warming rates for months in the transition between four seasons are shown in Table 7.2. In January, the warming trends are quite significant for both the minima and maxima which are the largest warming rates however the warming rate of minima temperatures are slightly higher (Table 7.2 and Fig. 7.9B). The warming rates in April and October are similar and quite comparable to the mean-annual warming rate of 0.056 (°C/year) whereas, the warming rates in July are the smallest (Table 7.2).

7.4 Numerical simulation of heat transfer of the waste rock dump with climate change and using mitigative strategies

For the purpose of long-term prediction of the impacts of global warming on the thermal behaviour of the waste-rock pile, numerical simulations were performed. The above ground temperatures and the prediction of global warming on temperature were used as initial and boundary conditions. Furthermore, several mitigation techniques to compensate for the global warming were proposed and checked during these simulations.

7.4.1 Mathematical description

Waste rock is considered as a porous media and further assuming that the validity of ideal gas law for air and the Darcy's law. Due to the low oxidation rate of the Type III waste rock, the heat release by oxidation is neglected (Amos et al., 2009b). In this study, only convective component of air is considered. The convective component due to water is omitted because of low moisture content of waste rock (Neuner et al., 2012) and frozen conditions of the ground. The following governing equations are considered (Nield and Bejan, 1999).

- Conservation of Mass (continuity) of air

$$\phi\left(\frac{\partial \rho_a}{\partial t}\right) + \nabla \cdot (\rho_a \mathbf{u}) = 0 \tag{7.8}$$

- Conservation of Momentum (Darcy's law)

$$\mathbf{u} = -\frac{K}{\mu}(\nabla p + \rho_a \mathbf{g}) \tag{7.9}$$

- Conservation of Heat

$$C\frac{\partial T}{\partial t} + \nabla \cdot (-\lambda \nabla T + \rho_a c_a \mathbf{u} T) = 0 \tag{7.10}$$

- Ideal gas of air

$$pM = \rho_a RT \tag{7.11}$$

Where $\phi = 0.25$ is the porosity of waste rock (Neuner et al., 2012), ρ_a is the air density defined using Eqn. 7.11, $\mathbf{u}$ is air velocity vector, p is air pressure, T is temperature, μ is dynamic viscosity of air, K is permeability, C is the volumetric heat capacity of the waste rock including the latent heat of fusion of water around the freezing temperature (i.e. 0 °C), c_a is the specific heat capacity of air, M and R are the molar mass and gas constant of air. The above balance equations were solved using COMSOL Multiphysics software package which is a finite element analysis for various physics and engineering applications especially for coupled phenomena (Comsol, 2009).

7.4.2 Material properties

Thermal properties of the Type I, Type III rock and till were determined through in-situ measurements and calculated from measurements of ground temperatures of experimental waste rock test piles at the site (Table 7.3). Permeabilities of waste rocks were obtained through in-situ measurement of air permeability (Amos, 2009) and in-situ hydraulic conductivity tests (Neuner et al., 2012). Volumetric moisture contents of the Type I and Type III are assumed to be at field capacity about 6.0 % which was observed in the field (Neuner et al., 2012). Type I coarse rock is an engineered material and it is based on Type I rock with no particles less than 3 cm sizes. The elimination of fine fractions (≤ 3 cm) would make the Type I coarse rock have a low thermal conductivity, high porosity ≥ 0.3, and high permeability ($\geq 3 \times 10^{-7}\,\mathrm{m}^2$), which is calculated by using either Hazen or Kozeny-Carman equations (Bear, 1972). Assuming that the Type I coarse rock is dry and therefore there will be only one value of thermal properties for both thawed and frozen states and no latent heat. Bulk thermal conductivity and volumetric heat capacity of the Type I coarse rock were determined by using the geometric and volumetric mean, respectively as follows (Farouki, 1981b) (Table 7.3).

- Bulk thermal conductivity

$$\lambda = \lambda_a^{\phi} \lambda_s^{(1-\phi)} \tag{7.12}$$

- Volumetric heat capacity

$$C = \rho \left(c_a \phi + c_s (1-\phi) \right) \tag{7.13}$$

Where: $\lambda_a = 0.024$ and $\lambda_s = 3.0$ W/(m·K) are thermal conductivity of air and solid rock (granite) (Farouki, 1981b; Tipler, 1999; Côté and Konrad, 2005a), $\phi = 0.3$ is the porosity of the Type I coarse rock, $\rho = 1840\,\mathrm{kg/m^3}$ bulk density of the Type I coarse rock (Neuner et al., 2012), $c_a = 1005$ and $c_s = 790$ J/(kg·K) are specific heat capacity of air and solid rock (Farouki, 1981b).

7.4.3 Simulation cases

There are four simulation cases that correspond to a baseline case and three cases with different mitigation methods. Case 1 is the baseline case in which no cover layer is placed on the top of the Type III rock having a thickness of 80 m. It is used to investigate the change of 0 °C isotherm and ground temperatures under the climate change presented in Section 7.3.4). Case 2 is a mitigation strategy in which the Type III rock is capped using a 1.5 m till overlaid with 3 m Type I rock which is a closure concept for waste rocks at Diavik. Both cases 1 and 2, heat transfer is via conduction. Meanwhile, cases 3 and 4 utilize natural air convection during winter in the Type I coarse rock which is assumed to have significantly higher permeabilities (Table 7.3). Natural air convection in the Type I

Table 7.3: Thermal and hydraulic properties for materials used in simulation

Property	Value	Comments
Type I Rock		
Porosity	0.25	In-situ measurements (Neuner et al., 2012)
Thermal conductivity	1.7 $W/(m \cdot K)$	In-situ measurements using line heat source probe
Frozen bulk heat capacity	2.3×10^6 $J/(m^3 \cdot K)$	Using thawed heat capacity plus heat capacity differences between thawed and frozen water
Thawed bulk heat capacity	2.4×10^6 $J/(m^3 \cdot K)$	Ratio between in-situ thermal conductivity and thermal diffusivity determined by temperature measurements.
Volumetric water content	0.06	Average in-situ measurement values using TDR (Neuner et al., 2012). This volumetric water content contains a latent heat of $2.0 \times 10^4 kJ/m^3$
Permeability	$2 \times 10^{-9} m^2$	In-situ measurements using air permeability balls which were conducted at depths up to 6 m (Amos et al., 2009a)
Type III Rock		
Porosity	0.25	Same as Type I rock
Thermal conductivity	1.8 $W/(m \cdot K)$	—-
Frozen bulk heat capacity	2.1×10^6 $J/(m^3 \cdot K)$	—-
Thawed bulk heat capacity	2.2×10^6 $J/(m^3 \cdot K)$	—-
Volumetric water content	0.06	—-
Permeability	$2 \times 10^{-9} m^2$	—-
Till		
Porosity	0.2	Obtained from Terzaghi et al. (1996)
Frozen thermal conductivity	3.2 $W/(m \cdot K)$	Multiply thermal diffusivity determined by temperature measurements and calculated bulk heat capacity.
Thawed thermal conductivity	2.9 $W/(m \cdot K)$	From frozen value minus thermal conductivity difference between thawed and frozen of water.
Frozen bulk heat capacity	2.1×10^6 $J/(m^3 \cdot K)$	Calculated based on weight fraction of mixture with specific heat capacity of solid of $790 J/(kg \cdot K)$ (Farouki, 1981b)
Thawed bulk heat capacity	2.5×10^6 $J/(m^3 \cdot K)$	Calculated as frozen bulk heat capacity
Volumetric water content	0.18	In-situ measurements of samples taken during construction of the test pile. This volumetric water content contains a latent heat of $6.0 \times 10^4 kJ/m^3$
Permeability	$5 \times 10^{-16} m^2$	Converted from hydraulic conductivity of glacial till of $5.0 \times 10^{-9} m/s$ (Hendry, 1982)
Type I coarse rock		
Porosity	≥ 0.3	Assumed (Bear, 1972)
Thermal conductivity	0.7 $W/(m \cdot K)$	Calculated through Eqn. 7.12
Bulk heat capacity	1.6×10^6 $J/(m^3 \cdot K)$	Calculated through Eqn. 7.13
Permeability	from 9×10^{-8} to $6 \times 10^{-7} m^2$	Varied for sensitivity analyses

Table 7.4: Description of simulation cases

Case 1	1-D Conduction: 80 m thick of Type III rock
Case 2	1-D Conduction: 80 m thick Type III rock with a 1.5 m till and 3 m Type I
Case 3	2-D Conduction/Convection: 80 m thick Type III rock with a 1.5 m till and 3 m Type I coarse rock (change in permeability)
Case 4	2-D Conduction/Convection: 80 m thick Type III rock with a 4 m Type I coarse rock (change in permeability)

coarse rock cover rapidly cools the underlying Type III rock and the till below (Table 7.4 and Fig. 7.10). The width of the domain of cases 3 and 4 was chosen to be large (ten times) compared to the thickness of the Type I coarse rock layer to consider the domain as an infinite horizontal layer. A boundary condition at the bottom of Type III rock (bottom of waste rock dump) is no heat flux. This boundary condition can be justified as at depths (≥ 30 m) ground temperatures are relatively constant (small heat flux as shown in Fig. 7.8) besides there is a low thermal conductivity geomembrane liner placed at the base of the pile prior construction. An assigned surface temperature at the top surface of the simulations which is an average of measured values (Section 7.3.2) is:

$$T_s\,(^{\circ}\mathrm{C}) = -6.3 + 20.4\sin\left(\frac{2\pi t}{365}\right) + \frac{0.056t}{365} \tag{7.14}$$

Where: 0.056 °C/year is the annual temperature increase due to warming climate assigned to the surface. Initial temperatures resemble measured ground temperatures in July 2010 for all cases. Cases 3 and 4 have boundary conditions of temperature and air pressure as shown in the Fig. 7.10 with $p_s = p_{atm} - \rho_a g y$, $y = 84.5$ and 84.0 m for case 3 and 4 respectively, $p_{atm} = 101.3$ kPa is assigned as the atmospheric pressure at the ground surface. The initial conditions of air pressure are hydrostatic with air density calculated from initial temperatures using Eqn. 7.11.

7.4.4 Results and Discussion

The simulation cases were run for 100 years from July 2010, with the assigned surface temperature T_s. According to Eqn. 7.14, after 100 years the MAST of the 80 m waste rock dump will increase to -0.7 °C. This is similar to the current MAST at Yellowknife, Northwest Territories, Canada which is in the zone of discontinuous permafrost (Heginbottom et al., 1995).

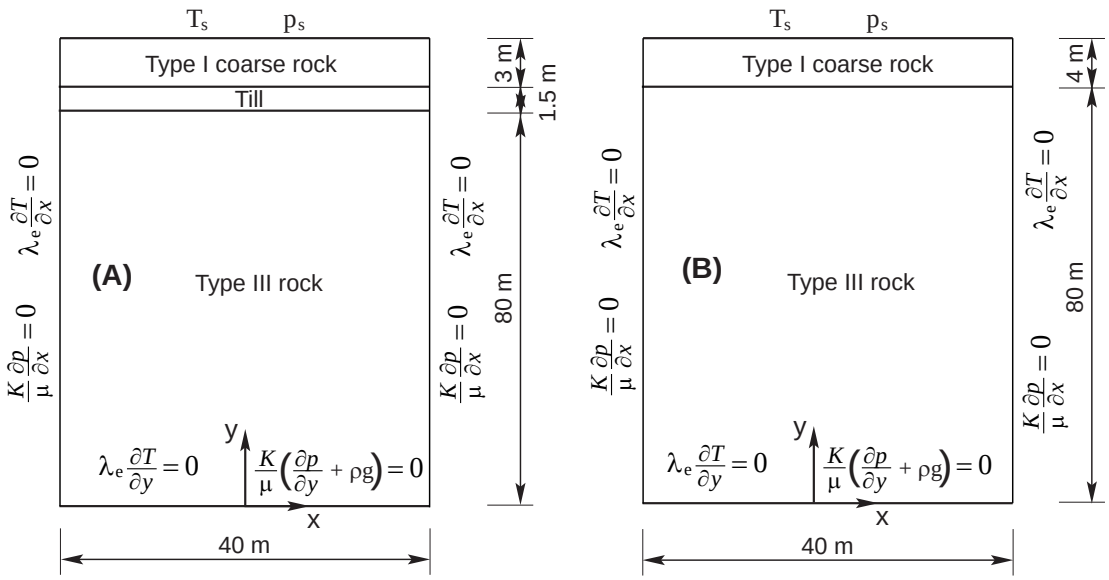

Figure 7.10: Geometry domains and boundary conditions of case 3 (A) and case 4 (B).

7.4.4.1 Case 1

Numerical results are quite comparable to field results however discrepancy still exists due to the heterogeneous nature of waste rock dumps and added water during drilling (Fig. 7.11). Fig. 7.12A shows 0 °C isotherm was initially about 11 m depth and this initial depth may not be the actual depth of 0 °C isotherm. Because the 0 °C isotherm could be deepened by the thermal disturbance of the drilling process which had introduced additional water into the ground at the bore holes. This additional water could maintain the ground temperatures at or near the freezing point (i.e. 0 °C) at some depths. Therefore, undisturbed ground temperatures are expected to be colder and the 0 °C isotherm shallower. The Root Mean Square Error (RMSE) between measured and simulated values was calculated through Eqn. 7.15 and showed in Fig. 7.11.

$$RMSE = \sqrt{\frac{1}{n}\sum_{i=1}^{n}(T_{sim} - T_{obs})^2} \tag{7.15}$$

Due to cold temperatures at the site, the 0 °C isotherm is rapidly reduced to 3.9 m from an initial depth of 11 m (Fig. 7.12A). From 2014 to 2020, the 0 °C isotherm slowly decreases further to a depth of 3.7 m which is its minimum depth. After 2020, the 0 °C isotherm gradually increases with an averaged rate of 3.6×10^{-2} m/year (or 3.6 cm/year) to 7.0 m in 2110 (Fig. 7.12A) and this increase is due to the warming of surface temperature. At 4 m depth, ground temperature varies with an amplitude of around 10 °C. Its maximum value reaches 0 °C and 3.5 °C between 2040 and 2110, respectively. Meanwhile its minimum value is -10 °C in 2020 and increases to -6 °C in 2110. Whereas the temperature amplitude at 7 m is smaller about 3 °C and its maximum temperature does not reach 0 °C until 2110

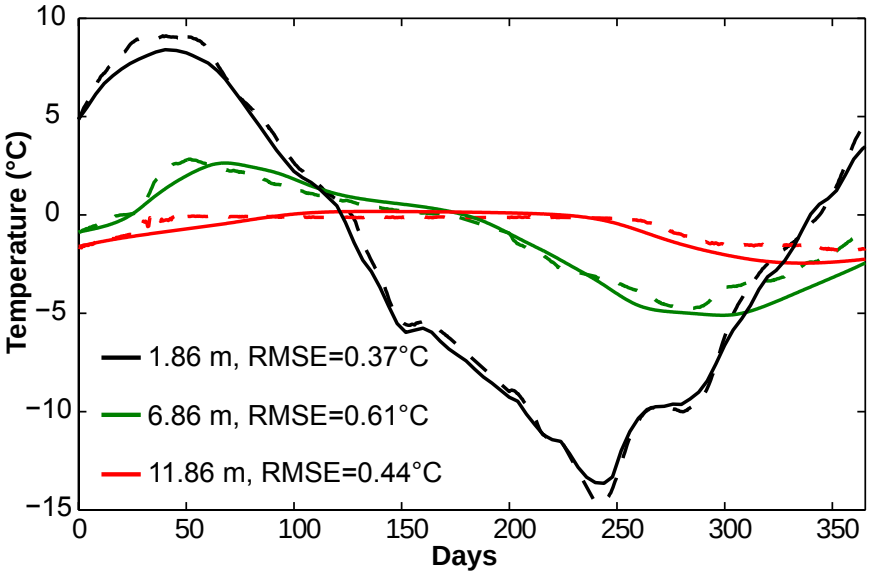

Figure 7.11: Numerical modeling and field measurements of ground temperatures at selected depths of one year between July 2010 and July 2011. The solid lines represent modeling results whereas the dashed lines show field results. The numbers in the legend indicate depths below the waste-rock surface.

(Fig. 7.12B).

Below 20 m, the annual ground temperature amplitudes are small and can be negligible. At 20 m, the ground temperature reaches a minimum value of -3.4 °C in 2040 and then it gradually increases to a value of -1.6 °C in 2110. The initial decrease is due to the initial temperature at 20 m being lower than that of the MAST and the later increase is due to the warming of MAST associated with climate change. Deeper beneath the surface, the larger delay in the ground temperatures reaches their minimum before increasing (Fig. 7.12C) due to the warming and conduction behavior of the pile. In other words, the material acts as a low-pass filter to temperature signal by removing short-term fluctuations (annually or shorter) and leaving long-term trends (long-term climate change). Fig. 7.12D shows that by 2110, the surface temperature fluctuates between -21.0 and 19.6 °C and the active layer is at 7 m depth. Therefore, to protect the Type III rock from thawing, the cover assumed to have similar thermal properties as Type III rock will need to be at least 7 m in thickness under the proposed warming scenario.

7.4.4.2 Case 2

In the case 2 scenario, the 0 °C isotherm decreases to 3.0 m above the till within the first 5 years and remains stationary until 2040 due to latent heat affects of water in the till. Then, it gradually increases to 3.9 m (or 0.9 m into the till) by 2110 (Fig. 7.13A). Similarly, the maximum temperature at the top of the till rapidly reduces to a temperature just below 0 °C and stays constant until 2040. Then it increases slowly to 1.9 °C by 2110 (Fig. 7.13B).

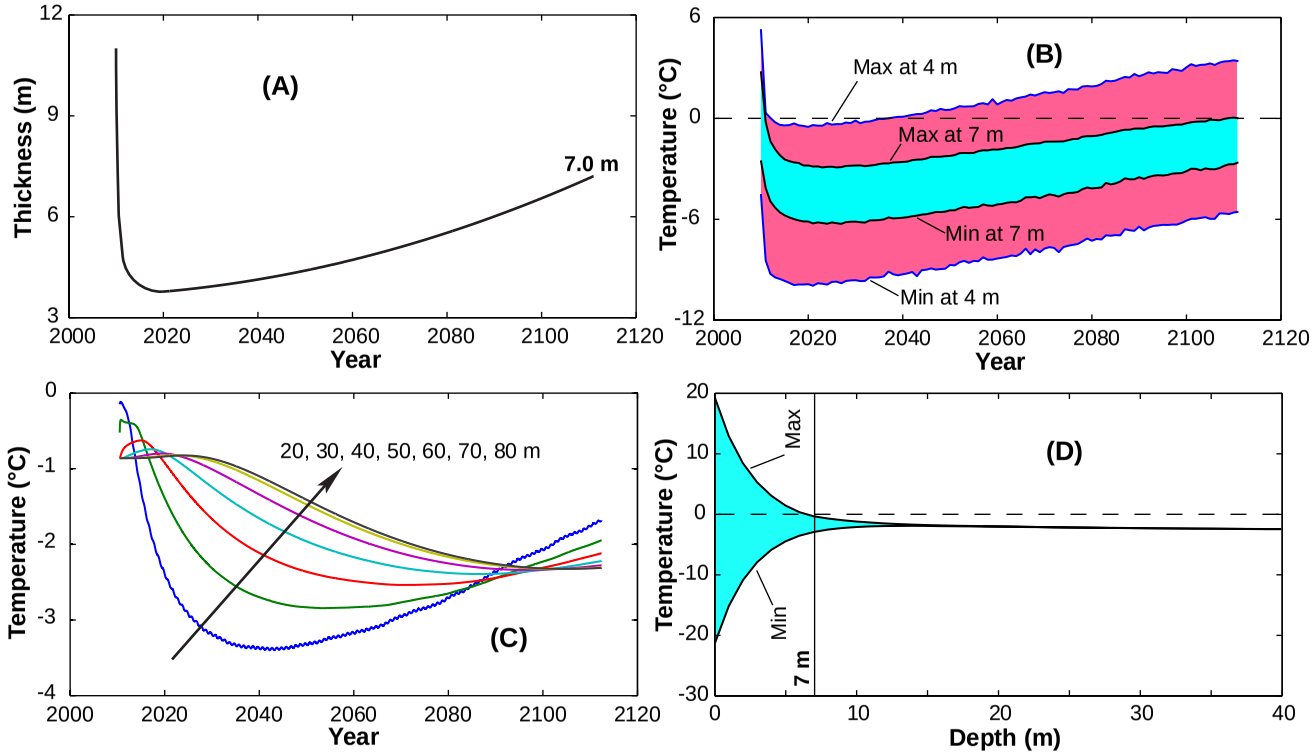

Figure 7.12: Case 1 scenario simulation results: 0 °C isotherm variation (A), temperature amplitudes at 4 and 7 m (B), temperature variations between 20 and 80 depths (C), minimum and maximum temperatures in the year 2110 (D).

While, the minimum temperature reaches -10.1 °C in 2020 and increases to -5.1 °C in 2110 (Fig. 7.13B). At the base of the till, the temperatures remain below 0 °C. However, the maximum temperature ranges from -1.1 to -0.3 °C between 2020 and 2110 respectively. The minimum temperature ranges from -9.2 to -3.6 °C between 2020 and 2110 (Fig. 7.13B). Temperatures below 20 m depth show similar results as discussed for case 1 with a insignificantly small derivation (Fig. 7.12C and Fig. 7.13C). Fig. 7.13D shows the 0 °C isotherm penetrates 0.9 m (or 3.9 m from the surface) into the till by 2110 and the figure also indicates the depth of zero annual amplitude is at 20 m.

7.4.4.3 Case 3

The case 3 scenarios were run with the permeability of Type I coarse rock ranging between 9×10^{-8} and 6×10^{-7} m^2. In the case $K = 4 \times 10^{-7}$ m^2, due to the low thermal conductivity and high permeability, the thickness of the 0 °C isotherm reduces significantly to a depth of 2.5 m by 2110 (Fig. 7.14A), besides the maximum and minimum temperatures at the top and bottom of the till are about 4 °C cooler than the case 2 (Fig. 7.14B). At depths greater than 20 m, ground temperatures are about 3 °C cooler than for case 2 and the 0 °C isotherm in 2110 is at 2.5 m (Fig. 7.14C and D).

The significant reduction in temperatures for case 3 is possible due to natural air convection during winter in the Type I coarse rock. Natural air convection in the Type I coarse rock does not initiate unless a critical temperature difference ΔT_c between the top and bottom of the Type I coarse rock is established. The hydrostatically unstable condition of density increasing upwards is stabilized by viscosity and thermal diffusivity until the density gradient is sufficient to allow the cooler upper layer to sink and the warmer lower layer to rise. Instead of ΔT_c the natural convection is usually characterized by a dimensionless number called the Rayleigh number, defined as (Nield and Bejan, 1999):

$$Ra = \frac{\rho_a g \beta K H \Delta T}{\mu \alpha} \tag{7.16}$$

Where: $\beta = \frac{1}{T}\,(\mathrm{K}^{-1})$ for an ideal gas of air is the coefficient of thermal expansion for air, $\alpha = \frac{\lambda}{C_a}$ and other parameters are described earlier.

To characterize the strength of natural convection relative to conduction, the Nusselt number, Nu, which is the ratio of total heat transport to conductive transport is defined as (McKibbin and O'Sullivan, 1981):

$$Nu = 1 + 1.44\left(\frac{Ra}{Ra_c} - 1\right) \tag{7.17}$$

Where $Ra_c = 27.1$ (Nield and Bejan, 1999) is the critical Rayleigh number for the case of permeable surface similar to the Type I coarse rock surface (or cases 3 and 4 in this study).

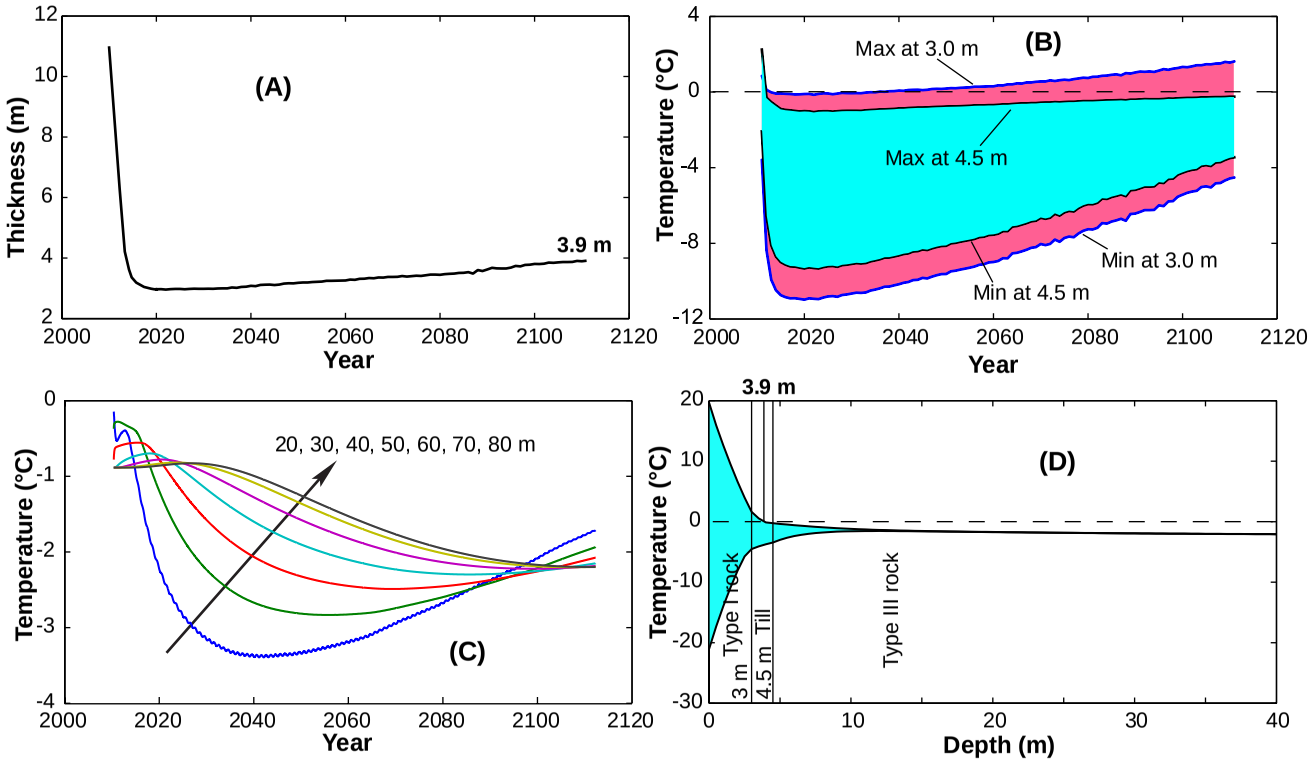

Figure 7.13: Case 2 scenario simulation results: 0 °C isotherm variation (A), temperature amplitudes at 3.0 m (top of the till) and 4.5 m (bottom of the till) (B), temperature variations between 20 and 80 depths (C), minimum and maximum temperatures in 2110 (D).

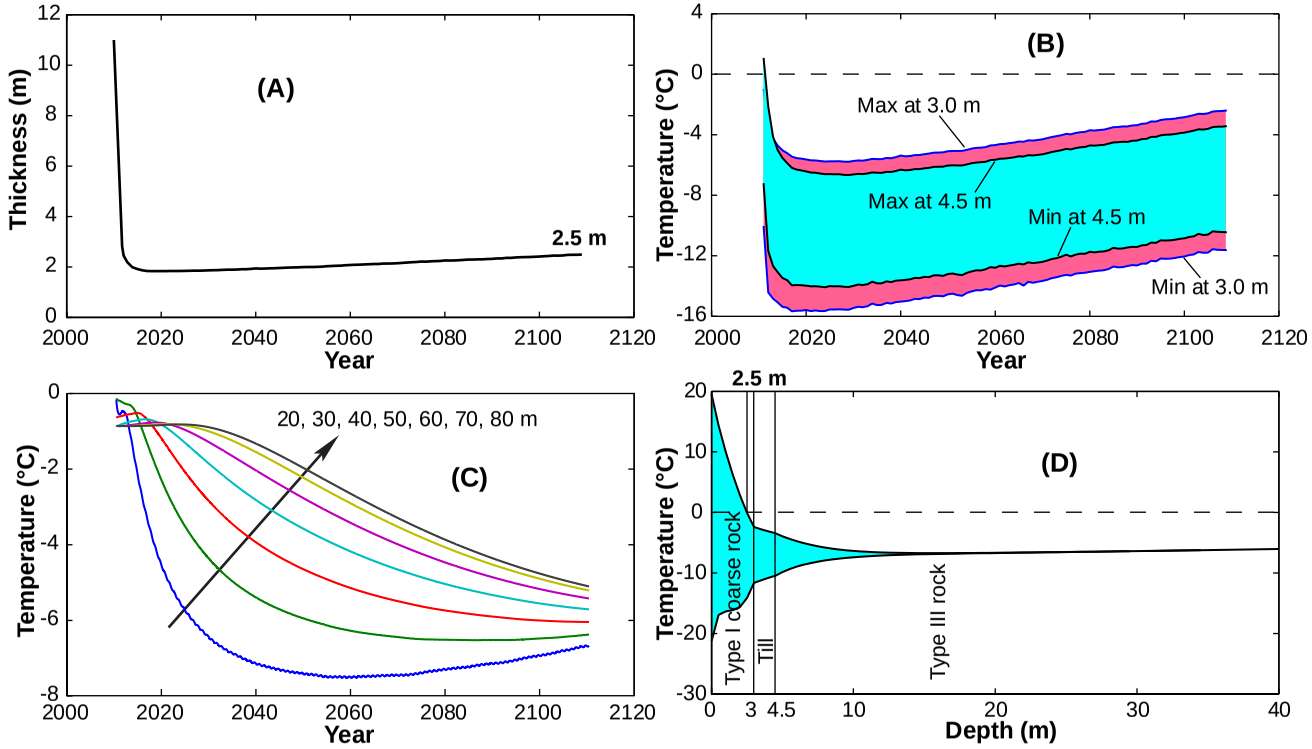

Figure 7.14: Case 3: 0 °C isotherm variation over years (A), amplitudes of temperatures at 3.0 m (top of the till) and 4.5 m (bottom of the till) (B), temperature variations between 20 and 80 depths, minimum and maximum temperatures in year 2110 (D) with $K = 4 \times 10^{-7}\,\mathrm{m}^2$.

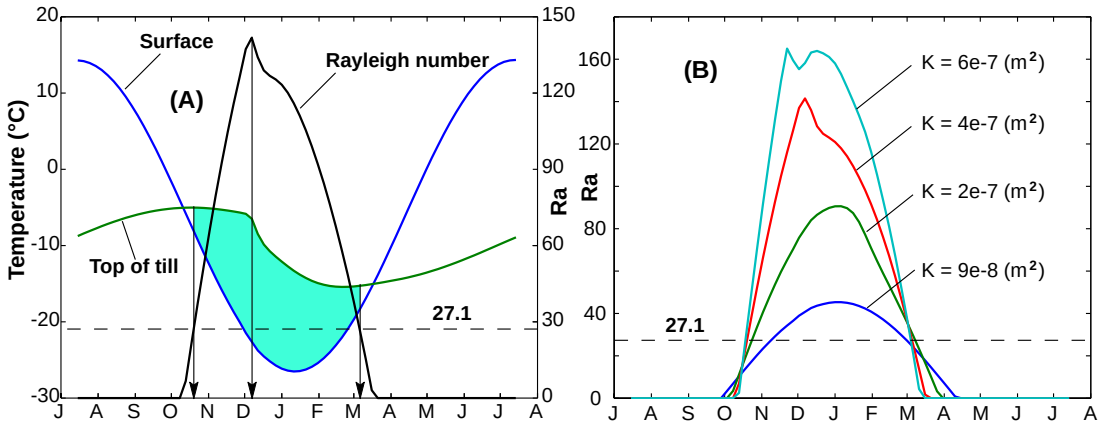

Figure 7.15: Case 3: Schematic for calculation *Ra* through surface temperature and temperatures of the top of the till with $K = 4 \times 10^{-7}\,\mathrm{m}^2$ (A) and calculated values of *Ra* with *K* ranging between 9×10^{-8} and $6 \times 10^{-7}\,\mathrm{m}^2$ in between 2015 and 2016 (B) .

During winter, the value of *Ra* starts to rise drastically in early October (when surface temperatures are colder than temperatures at the top of the till) and it reaches Ra_c in mid October. However it only obtains a maximum value of 141 in early December and then decreases to Ra_c in early March for $K = 4 \times 10^{-7}\,\mathrm{m}^2$ (Fig. 7.15A). Therefore, the air natural convection occurs for about 4.5 months (mid October to early March) during winter.

Peak values of *Ra* increase as the values of *K* increase. In fact, it can reach 160 which is about 5.9 times larger than Ra_c at $K = 6 \times 10^{-7}\,\mathrm{m}^2$ (Fig. 7.15B). Based on the area having *Ra* larger than Ra_c, averaged values of *Ra* were calculated as 38.9, 66.5, 96.0 and 122.3 corresponding to *Nu* of 1.6, 3.1, 4.7 and 6.1 (through Eqn. 7.17) with $K = 9 \times 10^{-8}$, 2×10^{-7}, 4×10^{-7} and $6 \times 10^{-7}\,\mathrm{m}^2$ respectively. Therefore, when *K* is larger than $2 \times 10^{-7}\,\mathrm{m}^2$ the values of *Nu* are larger than 3. It means that heat transfer during the natural air convection periods is three times larger than via conduction alone or convection dominates the heat transfer.

With the increasing permeability of the Type I coarse rock, maximum temperatures at the surface of the till reduced correspondingly. As shown in Section 7.3.2A, initial temperatures reduce to minimum temperatures of between -1.6 and -6.7 °C in 2025 and then gradually increase (due to the warming) to temperatures between 0 and -3.2 °C in 2110 at *K* between 9×10^{-8} and $6 \times 10^{-7}\,\mathrm{m}^2$. In other words, the till layer stays frozen until 2110 for any $K > 9 \times 10^{-8}\,\mathrm{m}^2$. At 30 m depth, ground temperatures vary between -1.9 and -7.2 °C in 2110 at $K = 9 \times 10^{-8}$ and $6 \times 10^{-7}\,\mathrm{m}^2$ respectively (Fig. 7.16B). However, for $K = 9 \times 10^{-8}$ and $2 \times 10^{-7}\,\mathrm{m}^2$ ground temperatures at 30 m depth start to detect the impacts of the warming around 2065 meanwhile at $K = 4 \times 10^{-7}$ and $6 \times 10^{-7}\,\mathrm{m}^2$ the warming does not show until 2110 (Fig. 7.16B).

Natural convection during winter is characterized by multiple "convective rolls" pattern as shown in Fig. 7.17 with air velocity reaching $6.5 \times 10^{-3}\,\mathrm{m/s}$ in mid January 2016. These

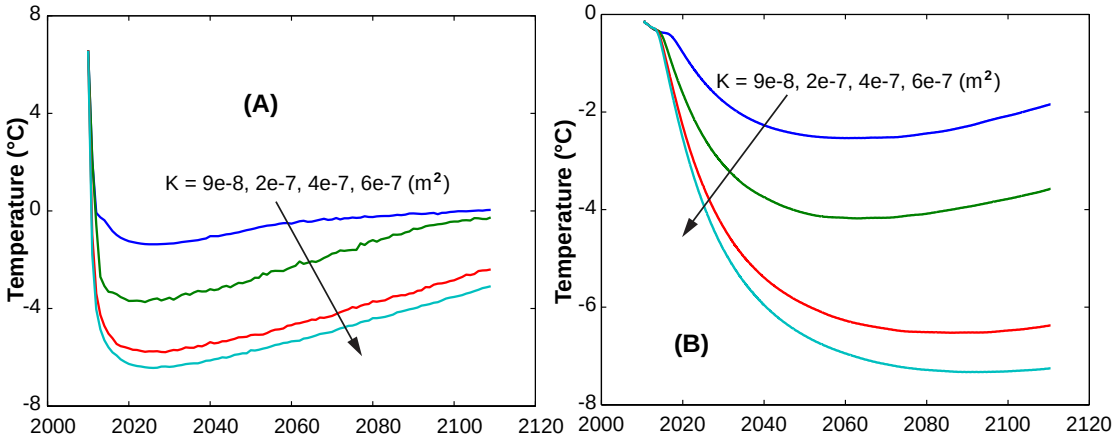

Figure 7.16: Case 3: Maximum temperatures at the top of the till (3 m from the surface) (A), ground temperatures at 30 m depth (B) with $K = 9 \times 10^{-8}, 2 \times 10^{-7}, 4 \times 10^{-7}$ and $6 \times 10^{-7}\,\mathrm{m}^2$.

convective rolls are only formed in the Type I coarse rock due to its high permeability and the distance between two warm rising plumes are about 6 m. Therefore, the dimension of a convective cell is 3 m height and 3 m width (Fig. 7.17).

7.4.4.4 Case 4

Case 4 scenario simulates the case without till available to cover the entire Type III rock and the objective is to keep the Type III rock frozen. Therefore, the Type I coarse rock thickness was increased to replace the till layer. The maximum temperature at the top of the Type III rock (or 4 m from the surface) reduces from its initial temperatures to temperature values between -2 and -9 °C depending on permeability in 2025 and then they increase steadily to values between 0.7 and -6.2 °C in 2110 (Fig. 7.18A). Besides, at $K = 9 \times 10^{-8}\,\mathrm{m}^2$ the maximum temperature reaches 0 °C by 2090. Ground temperatures at 30 m depth show similar trends as case 3 (Fig. 7.16B), however the ground temperatures in case 4 is slightly colder especially for $K \geq 2 \times 10^{-7}\,\mathrm{m}^2$ because of their large Rayleigh numbers (Fig. 7.18B).

Rayleigh numbers depend linearly on the thickness of the convective layer (Eqn. 7.16) and therefore it is expected that the Rayleigh numbers in case 4 is higher than case 3. For instance, Rayleigh numbers in case 4 are about 20 % larger than case 3 and average values over convection periods ($Ra \geq Ra_c$) are 50.0, 82.8, 117.9 and 149.3 at $K = 9 \times 10^{-8}, 2 \times 10^{-7}, 4 \times 10^{-7}$ and $6 \times 10^{-7}\,\mathrm{m}^2$ respectively (Fig. 7.18C). By the year 2110, at $K = 9 \times 10^{-8}\,\mathrm{m}^2$ the simulation predicts the 0 °C isotherm would penetrate 1.1 m into the Type III rock (or 5.1 m below the surface) unlike case 3 despite having a thinner convective layer, the 0 °C isotherm still remains at 3 m depth. This is because the latent heat of water in the till retains the 0 °C isotherm at a shallow depth. However, at $K \geq 2 \times 10^{-7}\,\mathrm{m}^2$, the 0 °C isotherm remains in the Type I coarse rock (Fig. 7.18D).

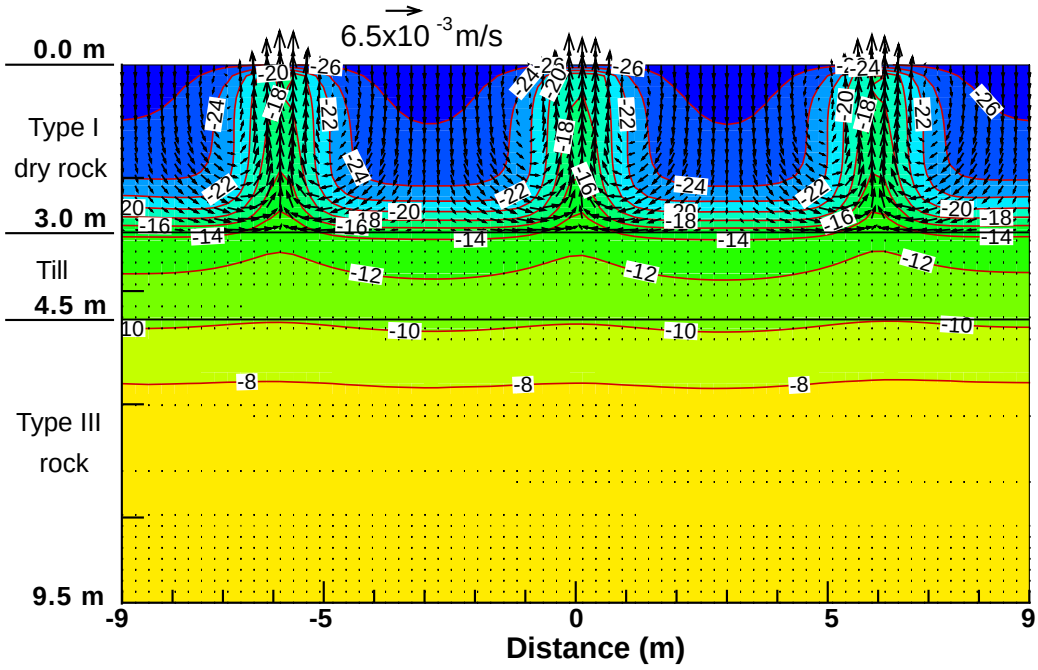

Figure 7.17: Case 3: Isotherms and air velocity vector field in mid January 2016 with $K = 4 \times 10^{-7}\,\mathrm{m}^2$

7.5 Recommendations

Even though the effectiveness of the mitigation techniques has to be proven in the field, recommendations can be made based on the numerical simulations carried out.

The simulations showed that case 3 is the favored mitigation technique to keep the Type III rock frozen even with the warming climate. However, if there is not sufficient till available to cover the potentially-acid-generating Type III rock, fine fractions ($\leq 3\,$cm sizes) of the non-acid-generating Type I rock can be used as a substitute for the role of the till. The fine factions ($\leq 3\,$cm sizes) contribute about 32 % of the total volume of Type I rock (Neuner et al., 2012). In other words, by separating the Type I rock, the result is 32 % fine fractions could replace till and 68 % of the remaining coarser fractions can be used as Type I coarse rock. The ratio of the separation is close to the thickness ratio between the till and the coarse cover (1.5 : 3). As a result, there will be sufficient materials for the low permeability cover (replacement for the till). A high permeability layer should overlay the finer material with properties similar to the Type I coarse rock (case 3 scenario). However, the downsides are the need for equipment to segregate the size faction and cost associated with segregating the material prior/during placement.

The porosity of the fine fractions ($\leq 3\,$cm sizes) would be about 0.25 based on an estimation of Neuner et al. (2012). Field measurements of moisture contents in the fine fractions conducted by Neuner et al. (2012) indicated that capillary water maintained about 90 % saturation. This amount of water would store a sufficient latent heat to prevent thawing of the

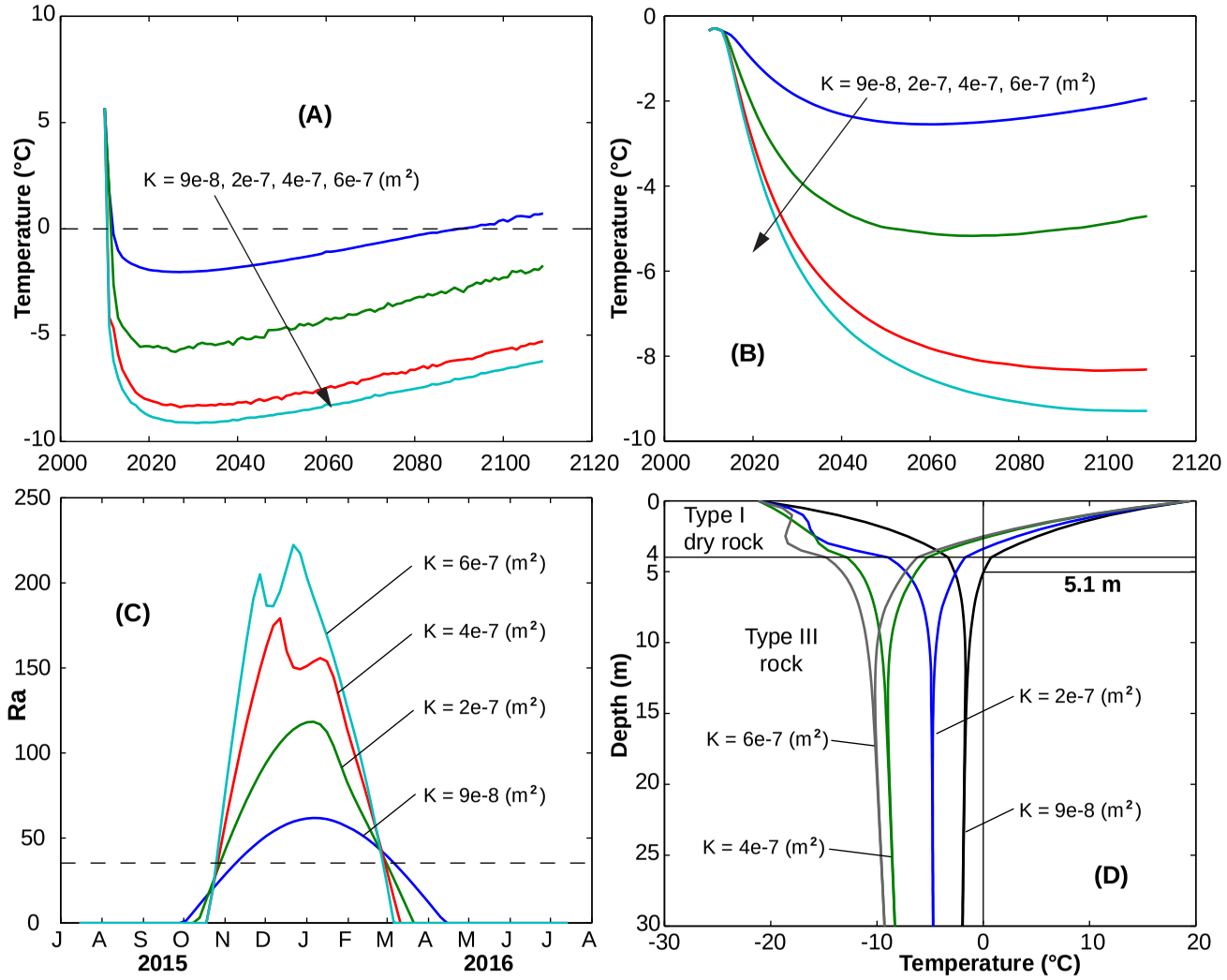

Figure 7.18: Case 4: Maximum temperatures at the top of the Type III rock (4 m from the surface) (A), ground temperatures at 30 m depth (B), calculated values of *Ra* (C) and maximum and minimum temperatures at depth in 2110.

Type III rock beneath.

The placement of the till layer would decelerate the freeze back of the Type III waste rock beneath it because the till cover will act as a thermal insulating blanket. A recommendation is to expose the Type III waste rock until the active layer (the 0 °C isotherm depth) reaches its minimum which is about 4 m. This would be achieved by 2020 based on the case 1 simulation. Placement of the till cover should occur starting in November and continue until end of April when the entire temperature profile of the waste rock dump is below 0 °C. Likewise, the construction of the high permeability coarse layer should occur immediately to keep as much of the cold in the pile until convection begins the following winter. However, before placement, volumetric water content of the till should be checked and its saturation should be above 90 %. This can be carried out in late summer when a certain thickness near the surface of the till is above 0 °C. If the required volumetric water content is not achieved, water should be added. In summary, construction of the layers of the cover should occur during winter to take advantages of cold weather placement.

7.6 Conclusions

Measured air temperature over a 10-year period (2000 - 2010) at the Diavik site in a continuous permafrost region had a MAAT of -9.1 °C and the trend lines indicated the warming of air temperature is expressed through the changes of freezing, thawing indices and numbers of freezing and thawing days. Based on the measured air temperature at the site and other long-term air temperatures at nearby sites, climate modeling predicted the highest and lowest rates of temperature change occur in January and July respectively, while in October and April temperature changes were predicted to be similar to the rate of increase of the mean annual temperature.

Ground temperature measurements indicated the 0 °C isotherm was at 11 m below the surface and heat transfer in the waste-rock pile was controlled by conduction. At depth, no elevated temperatures due to oxidation of sulfide minerals have been observed and the calculated thermal diffusivity from ground temperature measurements was comparable to measured values found in the test piles. Conduction model (case 1) predicted 0 °C isotherm will be at 7 m with climate change by 2110. However, with the aid of the till layer, the case 2 simulation predicted a reduction of the 0 °C isotherm to 3.9 m and ground temperatures below 20 m for case 1 and case 2 will be similar by 2110. In case 3 although the thickness of Type I coarse rock is thinner compared to case 4, the 0 °C isotherm remains shallow (on top of the till) due to latent heat of water stored in the till layer. Ground temperatures for case 3 are colder than cases 1 and 2 because of convective-enhanced heat transfer during winter. Besides, due to the lack of the till layer in case 4, the 0 °C isotherm will penetrate into the Type III rock at $K \leq 9 \times 10^{-8}\,\mathrm{m}^2$ by 2110. However, for $K \geq 2 \times 10^{-7}\,\mathrm{m}^2$ the 0 °C isotherm is retained in the Type I coarse rock and ground temperatures are colder compared

to those of case 3.

References

Amos, R. T. (2009). Personal communication.

Amos, R. T., Blowes, D. W., Smith, L., and Sego, D. C. (2009a). Measurement of wind-induced pressure gradients in a waste rock pile. *Vadose Zone J*, 8(4):953–962.

Amos, R. T., Smith, L., Neuner, M., Gupton, M., Blowes, D. W., Smith, L., and Sego, D. C. (2009b). Diavik Waste Rock Project: Oxygen Transport in Covered and Uncovered Piles. In *The 8th ICARD International Conference On Acird Rock Drainage, Skelleftea, Sweden, 2009*.

Andersland, O. B. and Ladanyi, B. (2004). *Frozen Ground Engineering*. John Wiley & Sons.

Arenson, L. and Sego, D. (2007). Protection of mine waste tailing ponds using cold air convection. Assessment and Remediation of Contaminated Sites in Arctic and Cold Climates.

Bear, J. (1972). *Dynamics of fluids in porous media*. Dover Publications, Inc.

Carslaw, H. S. and Jaeger, J. C. (1959). *Conduction of heat in solids*. Oxford University Press.

Chylek, P., Folland, C. K., Lesins, G., Dubey, M. K., and Wang, M. (2009). Arctic air temperature change amplification and the Atlantic Multidecadal Oscillation. *Geophys. Res. Lett.*, 36(14):L14801–.

Comsol (2009). *Comsol multiphysics' manual*. Comsol, Inc., 744 Cowper Street, Palo Alto, CA 94301, USA.

Côté, J. and Konrad, J.-M. (2005a). Thermal conductivity of base-course materials. *Canadian Geotechnical Journal*, 42:61–78(18).

DDMI (2006). Interim Closure and Reclamation Plan. Version 2, September 2006.

Engineering, E. (2011). Waste Rock Stoarge Area Thermal Monitoring. Technical report, Waste Rock Stoarge Area Thermal Monitoring.

Environment-Canada (2008a). Climate Data Online. National Climate Data and Information Archive. Technical report, Environment Canada.

EnvironmentCanada (1998). Climate change impacts on permafrost engineering design. Technical report, Panel on Energy Research and Development (PERD), Environment Canada.

Esch, D. and Osterkamp, T. (1990). Cold Regions Engineering: Climatic Warming Concerns for Alaska. *Journal of Cold Regions Engineering*, 4(1):6–14.

Farouki, O. T. (1981b). *Thermal properties of soils*. United States Army Corps of Engi-

neers, Cold Regions Research and Engineering Laboratory, Hanover, New Hampshire, USA.

Frauenfeld, O. W., Zhang, T., Barry, R. G., and Gilichinsky, D. (2004). Interdecadal changes in seasonal freeze and thaw depths in Russia. *J. Geophys. Res.*, 109(D5):D05101–.

Frauenfeld, O. W., Zhang, T., and Mccreight, J. L. (2007). Northern Hemisphere freezing/thawing index variations over the twentieth century. *Int. J. Climatol.*, 27(1):47–63.

Goering, D. J. and Kumar, P. (1996). Winter-time convection in open-graded embankments. *Cold Regions Science and Technology*, 24(1):57–74.

Heginbottom, J., Dubreuil, M., and Harker, P. (1995). Canada Permafrost. In *National Atlas of Canada*. National Atlas Information Service, Natural Resources Canada, Ottawa.

Hendry, M. J. (1982). Hydraulic Conductivity of a Glacial Till in Alberta. *Ground Water*, 20(2):162–169.

Hu, X., Holubec, I., Wonnacott, J., Lock, R., and Olive, R. (2003). Geomorphological, geotechnical and geothermal conditions at Diavik Mines. In *8th International Conference on Permafrost. Zurich, Switzerland.*

Jaynes, D. B., Rogowski, A. S., and Pionke, H. B. (1984b). Acid mine drainage from reclaimed coal strip mines: 1. Model description. *Water Resour. Res.*, 20:233–242.

Lefebvre, R., Hockley, D., Smolensky, J., and Gelinas, P. (2001a). Multiphase transfer processes in waste rock piles producing acid mine drainage. 1: Conceptual model and system characterization. *Journal of contaminant hydrology*, 52(1-4):137–164.

Lowson, R. T. (1982). Aqueous oxidation of pyrite by molecular oxygen. *Chemical Reviews*, 82(5):461–497.

Mareschal, J. C., Nyblade, A., Perry, H. K. C., Jaupart, C., and Bienfait, G. (2004). Heat flow and deep lithospheric thermal structure at Lac de Gras, Slave Province, Canada. *Geophys. Res. Lett.*, 31(12):L12611–.

McKibbin, R. and O'Sullivan, M. J. (1981). Heat transfer in a layered porous medium heated from below. *Journal of Fluid Mechanics*, 111:141–173.

Meldrum, J. L., Jamieson, H. E., and Dyke, L. D. (2001). Oxidation of mine tailings from Rankin Inlet, Nunavut, at subzero temperatures. *Canadian Geotechnical Journal*, 38(5):957–966.

MEND1.61.2 (1996). Acid mine drainage in permafrost regions: Issues, control strategies and research requirements. Technical report, Department of Indian and Northern Affairs Canada.

MEND1.61.4 (2004). Covers for reactive tailings in permafrost regions. Technical report, The Mining Association of Canada-Mine Environment Neutral Drainage (MEND) Program.

MEND1.61.5b (2010). Cold Regions Cover Research - Phase 2. Technical report, Indian and Northern Affairs Canada and Mine Environment Neutral Drainage (MEND).

Modelling, E. and Australia, P. P. (2008). Climate Change Adaptation Project Rio Tinto: Climate Change Impacts in the Diavik Region of Northern Canada.

Moncur, M., Ptacek, C., Blowes, D., and Jambor, J. (2005). Release, transport and attenuation of metals from an old tailings impoundment. *Applied Geochemistry*, 20(3):639–659.

Neuner, M., Smith, L., Blowes, D. W., Sego, D. C., Smith, L. J., Fretz, N., and Gupton, M. (2012). The Diavik waste rock project: Water flow though mine waste rock in a permafrost terrain. *Applied Geochemistry*, (0):–.

Nield, D. and Bejan, A. (1999). *Convection in porous media*. Springer, New York.

Nordstrom, D. K. and Alpers, C. N. (1999). Negative pH, efflorescent mineralogy, and consequences for environmental restoration at the Iron Mountain Superfund site, California. *Proceedings of the National Academy of Sciences of the United States of America*, 96(7):3455–3462.

Olson, G. J., Turbak, S. C., and McFeters, G. A. (1979). Impact of western coal mining–II. Microbiological studies. *Water Research*, 13(11):1033 – 1041.

Romanovsky, V., Sergueev, D., and Osterkamp, T. (2003). Temporal variations in the active layer and near-surface permafrost temperatures at the long-term observatories in northern Alaska. In Phillips, M., S. S. and Arenson, L. U., editors, *Permafrost*, pages 989–994. Swets & Zeitlinger, Lisse.

Terzaghi, K., Peck, R. B., and Mesri, G. (1996). *Soil Mechanics in Engineering Practice*. John Wiley & Sons, third edition.

Tipler, P. A. (1999). *Physics for Scientists and Engineers*. W.H. Freeman.

Xu, J. and Goering, D. J. (2008b). Experimental validation of passive permafrost cooling systems. *Cold Regions Science and Technology*, 53(3):283–297.

Zhang, M., Lai, Y., Dong, Y., and Li, S. (2008a). Laboratory investigation on cooling effect of duct-ventilated embankment with a chimney in permafrost regions. *Cold Regions Science and Technology*, 54(2):115–119.

CHAPTER 8

Conceptual model for heat and mass transfer in waste-rock piles under permafrost conditions

8.1 Introduction

Acidic drainage (or Acid rock drainage, ARD) and metal contaminants in water that seeps through waste-rock piles containing sulfide minerals are harmful to the environment and their treatment costs are expensive and time-consuming. Therefore, understanding sulfide minerals oxidation mechanisms and other processes of controlling ARD are crucial. The understanding of the mechanisms aids in predicting the rate and how oxidation proceeds in waste-rock piles.

Temperature, acidity and oxygen availability at the oxidation locations control the oxidation rates through constraint of the bacterial catalysis in sulfide oxidation reactions (Jaynes et al., 1984b). Moreover, spatial temperature distributions and elevated temperatures within waste-rock piles are good indicators of the locations and oxidation rates, because oxidation of sulfide minerals is a strong exothermic process (Lowson, 1982; Jaynes et al., 1984b). Heat transport within waste-rock piles is mainly governed by conduction, heat source due to oxidation and latent heat of water during freezing and evaporation. In an area where precipitation is high, the convective part of water can be significant and it can alter spatial ground temperature distributions (Stallman, 1965; Smith et al., 1989; Blasch et al., 2007). Furthermore, if waste-rock piles are constructed in a continuous permafrost region, water transport is confined within the active layer during summer, which is thin. Therefore, convection associated with seepage water is often neglected. However, the convective part due to moving air can be significant in regions of high permeability of the waste-rock piles (Pham et al., 2008a, 2009). In addition, Anne and Pantelis (1997); Moghtaderi et al. (2000); Wessling (2007); Amos et al. (2009a); Hollesen et al. (2011) demonstrated the importance of wind-induced advection to heat/mass transfer in waste-rock piles and underground coal fires. The variations of ambient air pressure can cause soil respiration known as barometric pumping, which is another potential source of oxygen supply (Mass-

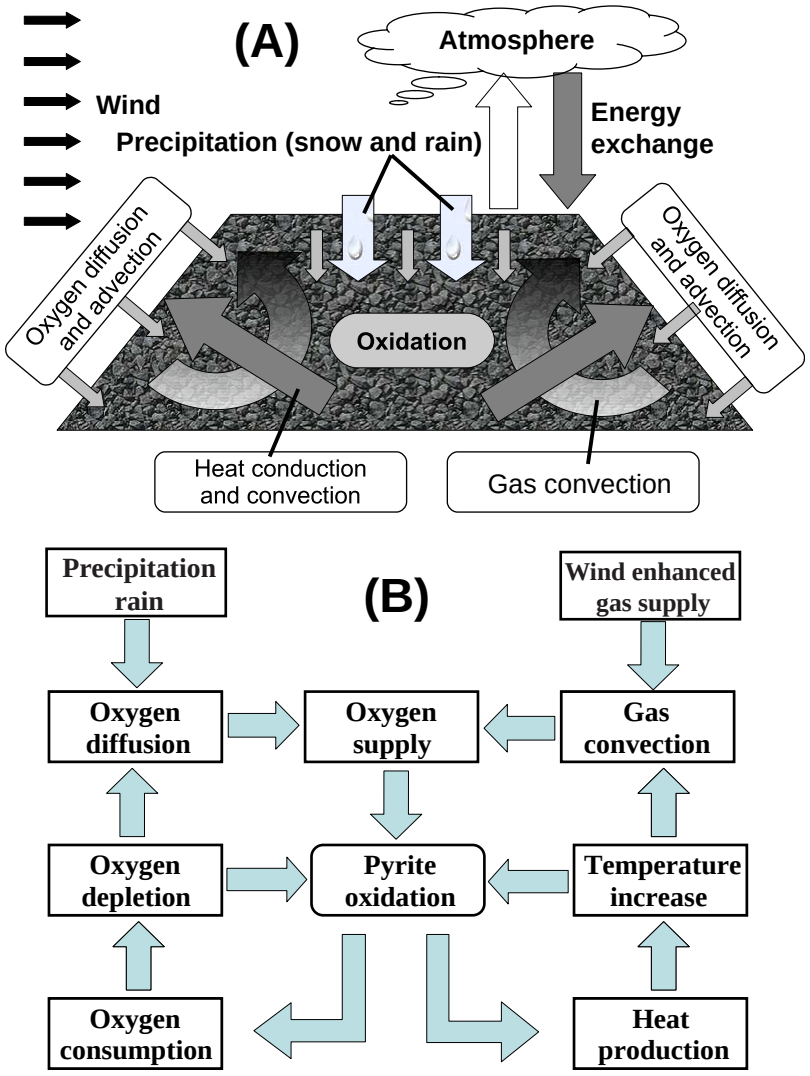

Figure 8.1: Processes occur within a waste-rock pile and its interaction with the atmosphere (A) and the relation between these processes (B) (modified from Lefebvre et al., 2001a).

mann and Farrier, 1992a; Neeper, 2003; Neeper and Stauffer, 2005). The effectiveness of the above mechanisms for heat and mass transport into and within waste-rock piles depends on physical properties of the waste-rock piles of which permeability is the most important.

The objectives of this chapter are to present a set of equations and constitutive relations that describe air, water and heat transport in a pile of waste rock where oxidation of sulfide sulfur is the major component of oxygen consumption and heat production as shown in Fig. 8.1, a conceptual model of the main processes related to heat transfer occurring within waste-rock piles including phase change of water and the interaction with the atmosphere. The waste-rock pile is modeled as a three-phase system consisting of a rigid solid porous phase through which air flow under gravitational, buoyancy and wind forces and water flows under a gravitational force.

8.2 Governing equations for heat and mass transfer in isotropic porous media

Based on the concept of representative elementary volume (REV) and balance equations written in macroscopic level (Bear, 1972), governing equations for both the solid and fluid regions of undeformable porous media can be written. In REV, a system of three phases including air (gas), liquid and solid, is considered and in each phase, there may be N_α components; in which α represents the phases (air, liquid and solid). The air phase (moist air) includes oxygen in dry air and water vapor, liquid water is the only component in the liquid phase and the solid phase includes sulfur, ice and the remaining solid rock. It is assumed that there is unfrozen water (in liquid state) in frozen waste rock expressed by the soil freezing characteristic curve (SFCC).

A general equation for conservation of mass (continuity) of each component $j = 1 \div N_\alpha$ in α phase is stated by (Bear, 1972)

$$\frac{\partial\left(\phi_\alpha \omega_\alpha^j \rho_\alpha\right)}{\partial t} + \operatorname{div}\left(\phi_\alpha \omega_\alpha^j \rho_\alpha \mathbf{q}_\alpha^j\right) = Sr_\alpha^j \tag{8.1}$$

Where the subscript $\alpha = a$, w, and s denote air, water and solid phases respectively. $\rho_\alpha = \sum_{j=1}^{N_\alpha} \rho_\alpha^j$ is the intrinsic density of α phase and $\rho_\alpha^j = \frac{m_\alpha^j}{V_\alpha}$ is the bulk density of component j in α phase; m_α^j is the mass of component j in α phase. Mass fraction of component j in α phase is $\omega_\alpha^j = \frac{\rho_\alpha^j}{\rho_\alpha}$, thus $\sum_{j=1}^{N_\alpha} \omega_\alpha^j = 1$. Volume fraction of α phase in REV is $\phi_\alpha = \frac{V_\alpha}{V}$ in which V_α is the volume of α phase and V is the volume of REV, furthermore ϕ_α must satisfy the relation $\sum_{\alpha=a,\ w,\ s} \phi_\alpha = 1$. The components $\left(\phi_\alpha \omega_\alpha^j \rho_\alpha \mathbf{q}_\alpha^j\right)$ and Sr_α^j are the mass flux and source/sink of component j in α phase in REV respectively.

8.2.1 Mass conservation of each component in phases

Assuming that the density of the air phase (dry air and water vapour) can be determined through an equation of state for ideal gases as follow, Dalton's law:

$$\rho_a = \frac{M_a^d\, p_a^d}{RT} + \frac{M_a^v\, p_a^v}{RT} \tag{8.2}$$

Where: the first term on the right is the density of dry air and the second is the density of water vapour in air ($\rho_a^v = \omega_a^v \rho_a$). It will be defined in a later section (Eqn. 8.25); ρ_a is the intrinsic humid air density $\left(\mathrm{kg/m^3}\right)$; p_a^d and p_a^v are the partial pressure of dry air and water vapour in (Pa). The pressure of humid air is $p_a = p_a^d + p_a^v$. R = 8.314 $\left(\mathrm{kg \cdot m^2 / \left(s^2 \cdot K \cdot mol\right)}\right)$ is gas constant. $M_a^d = 2.897 \times 10^{-2}$ and $M_a^v = 1.800 \times 10^{-2}$ (kg/mol) are the molar mass of dry air and water vapour respectively. T is temperature in Kelvin (K).

Eqn. 8.2 shows humid air density changes as the pressure (both dry air and water vapour) and temperature change however the density change due to a change in percentage of each component in dry air is not considered (M_a^d is a constant). However density change due to temperature change is more significant than pressure change. As temperatures can vary over a large range especially in cold regions whereas air pressure change is small around its mean values at a given site. Heat release via oxidation increases temperature and the temperature increase leads to a decrease in air density. As a result, buoyant forces increase and therefore convection cells may form.

In air phase, two components oxygen and water vapor have the main impact on heat and mass transfer in this study are considered. Mass conservation of vapor and oxygen can be written as:

$$\frac{\partial\left(\phi_a\omega_a^j\rho_a\right)}{\partial t}+\operatorname{div}\left(-\phi_a\mathbf{D}_a^j\nabla\left(\omega_a^j\rho_a\right)+\mathbf{u}_a\left(\omega_a^j\rho_a\right)\right)=Sr_a^j \tag{8.3}$$

Where $j=$ is either oxygen o or vapor v; $\mathbf{u}_a$ is the macroscopic air velocity vector calculated using Darcy's law; $\mathbf{u}_a=\phi_a\mathbf{U}_a$ is called Dupuit-Forchheimer relation and $\mathbf{U}_a$ is the pore air velocity (Bear, 1972; Nield and Bejan, 1999). Sr_a^j is the rate of production or consumption of component j in the air phase. $\mathbf{D}_a^j$ is a tensor, which is called the *hydrodynamic dispersion coefficient*. It is composed of two terms describing diffusion and dispersion (Bear, 1972).

$$\phi_a\mathbf{D}_a^j=\underbrace{\phi_a\tau D_m^j\mathbf{I}}_{\text{Diffusion}}+\underbrace{\alpha_T\|\mathbf{u}_a\|\mathbf{I}+\frac{\alpha_L-\alpha_T}{\|\mathbf{u}_a\|}\mathbf{u}_a\mathbf{u}_a^T}_{\text{Dispersion}} \tag{8.4}$$

Where: D_m^j denotes the diffusion coefficient of vapor or oxygen in air and it is a function the temperature and pressure as (Vargaftik, 1975):

$$D_m^j=\overline{D}_m^j\left(1+\frac{T}{\overline{T}}\right)^{7/4}\frac{p_{atm}}{p_a} \tag{8.5}$$

Where $\overline{D}_m^j$ is the coefficient of diffusion in air at $\overline{T}=273.15$ (K) and $p_{atm}=1$ (atm): $\overline{D}_m^o=1.78\times10^{-5}\left(\mathrm{m}^2/\mathrm{s}\right)$ for oxygen and $\overline{D}_m^v=2.19\times10^{-5}\left(\mathrm{m}^2/\mathrm{s}\right)$ for vapor (Batchelor, 1970; Tasa et al., 2006). $\mathbf{I}$ is the identify matrix and tortuosity factor $\tau<1$ is the ratio of measured distance to actual travel distance of fluid in the pore between two points. A theoretical analysis by Millington and Quirk (1961) suggests τ to be of the form $\tau=\phi_a^{1/3}S_a^{7/3}$ in which S_a is the degree of air saturation.Carman (1956); Bear (1972) indicated that τ ranges between 0.56 and 0.8. Thus, an average value of $\tau=0.7$ can be used for future modelings; α_L and α_T are longitudinal and transverse dispersivities respectively. Estimations of α_L and α_T are (Bear and Cheng, 2010):

$$\alpha_L = \frac{1}{10} L_s \tag{8.6}$$

$$\alpha_T = \frac{1}{10} \alpha_L \tag{8.7}$$

Where: L_s is the travel distance of fluid.

Considering the air phase as a whole, therefore the conservation of mass of air phase can be described as:

$$\frac{\partial (\phi_a \rho_a)}{\partial t} + \operatorname{div} (\rho_a \mathbf{u}_a) = 0 \tag{8.8}$$

Assuming that $\mathbf{u}_s = \mathbf{0}$ and no diffusion of sulfur (denoted by s) or ice (denoted by i during freezing) in the solid phase, the mass conservations of sulfur and ice are expressed as:

$$\frac{\partial (\phi_s \omega_s^s \rho_s)}{\partial t} = -Sr_s \tag{8.9}$$

$$\frac{\partial (\phi_s \omega_s^i \rho_s)}{\partial t} = \rho_i \frac{\partial \phi_s^i}{\partial t} = Sr_i \tag{8.10}$$

Where: $-Sr_s \left(\mathrm{kg}/\left(\mathrm{m}^3 \cdot \mathrm{s}\right)\right)$ and $Sr_i \left(\mathrm{kg}/\left(\mathrm{m}^3 \cdot \mathrm{s}\right)\right)$, which will be determined later, are the rates of consumption of sulfur due to oxidation and freezing/thawing of ice; ϕ_s^i is the volumetric ice content in REV $\left(m^3/\mathrm{m}^3\right)$ and $\rho_i = 920\,\mathrm{kg/m}^3$ is the density of ice (Batchelor, 1970).

By using Eqn. 8.10, the mass conservation of water is written as:

$$\frac{\partial (\phi_w \rho_w)}{\partial t} + \operatorname{div} (\rho_w \mathbf{u}_w) = Sr_w - Sr_i = Sr_w - \rho_i \frac{\partial \phi_s^i}{\partial t} \tag{8.11}$$

Where: the term, Sr_w, describes the source/sink of water condensation or vaporisation and is determined in a later section. Velocity vector $\mathbf{u}_w$ is determined using Richard's equation for the flow of water in unsaturated porous media.

The intrinsic water density, ρ_w, is assumed to be a constant (or temperature independent). Therefore Eqn. 8.11 can be simplified to an expression for volumetric water content, ϕ_w:

$$\frac{\partial (\phi_w)}{\partial t} + \operatorname{div} (\mathbf{u}_w) = \frac{Sr_w}{\rho_w} - \frac{\rho_i}{\rho_w} \frac{\partial \phi_s^i}{\partial t} \tag{8.12}$$

8.2.1.1 Two-phase flow model in unsaturated porous media

Air and liquid phases both occupy the void of porous media and assuming that in REV, the volume of the void is a constant. Therefore, any changes of the volume of one phase

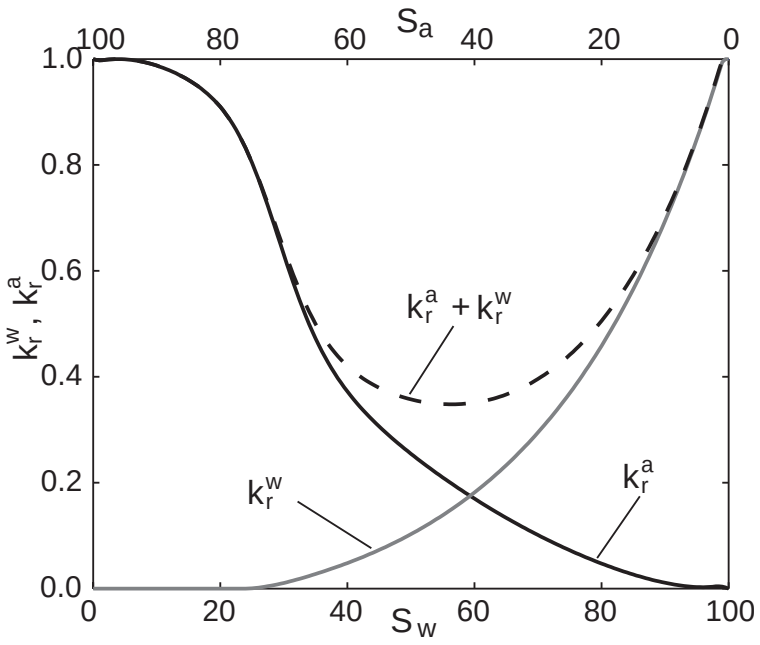

Figure 8.2: Typical relative permeability curves for sands (data from Wyckoff and Botset, 1936).

will influence the flow of the other phase due to the changes of permeability relative to that phase. The motion of α phase (a air, w water) in porous media can be described using Darcy's law for unsaturated porous media or Richard's equation (Bear, 1972) as:

$$\mathbf{u}_\alpha = -\frac{k_r^\alpha K_{in}}{\mu_\alpha}\left(\nabla p_\alpha - \rho_\alpha \mathbf{g}\right) \tag{8.13}$$

Where $K_{in}\,(\mathrm{m}^2)$ is the intrinsic permeability of porous media. It depends only on the structure of the medium and does not depend on the type of the flowing fluid; μ_α $(\mathrm{kg}/(\mathrm{m}\cdot\mathrm{s}))$ is the dynamic viscosity of air or water and it is a function of temperature; $\mathbf{g} = (0,0,-9.81)$ $\left(\mathrm{m}/\mathrm{s}^2\right)$ is the gravitational acceleration vector, z - axis is in upward-vertical direction, p_α is the pressure of α phase in (Pa). The relative permeability of α phase, $k_r^\alpha \varepsilon\,[0,\,1]$, depends on the degree of water saturation and can be approximated by Van Genuchten's equations (van Genuchten, 1980). Typical curves of relative permeability for unsaturated sands are shown in Fig. 8.2.

$$k_r^\alpha = \bar{S}_\alpha^{\varepsilon}\left(1-\left(1-\bar{S}_\alpha^{\frac{n}{n-1}}\right)^{\frac{n-1}{n}}\right)^2 \tag{8.14}$$

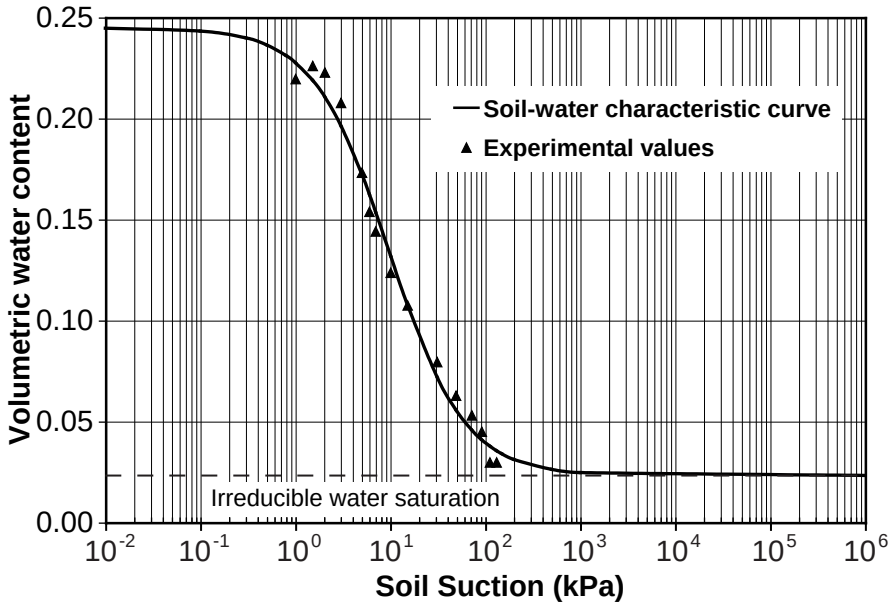

Figure 8.3: Soil Water Characteristic Curve (SWCC) of waste rock matrix material (i.e. grain size ≤ 5 mm) at Diavik Diamond Mine (data from Neuner et al. (2012)).

$$p_c(S_w) = p_a - p_w = -p_w = \frac{1}{\alpha_o}\left(\bar{S}_w^{-\frac{1}{m}} - 1\right)^{\frac{1}{n}} \geq 0 \tag{8.15}$$

Where: $\alpha_o(1/\text{kPa})$ is the fitting parameter and the form parameter, ε, is typically chosen as $\varepsilon = \frac{1}{2}$ (Fredlund and Rahardjo, 1993). The parameter $m = 1 - \frac{1}{n}$ is used to correlate capillary pressure to the degree of saturation and it is determined through fitting experimental data. The plot of capillary pressure versus degree of saturation is called the Soil Water Characteristic Curve (SWCC), in which $p_c(S_w)$ is the capillary pressure defined as a function of water saturation, S_w. The effective saturation coefficients of water and air, $\bar{S}_w, \bar{S}_a$ are defined as:

$$\bar{S}_\alpha = \frac{S_\alpha - S_r^\alpha}{1 - S_r^\alpha} \tag{8.16}$$

Where S_r^α is the residual saturation of α phase (w water, a air). Liquid water usually ceases to flow at a saturation below the residual value, S_r^w (Fredlund and Rahardjo, 1993). As the residual saturation is approached a large increase in capillary pressure produces a little decrease in water saturation as shown in Fig. 8.3 ($\psi = \frac{-p_w}{\gamma_w}$ is capillary head or soil matric suction). Air phase is discontinuous (no airflow) at the residual air saturation or water saturation around 90 % (Fredlund and Rahardjo, 1993; Bear and Cheng, 2010).

During winter, liquid water changes its phase into ice that may block the flow paths

of unfrozen water or air. Therefore, Jame and Norum (1980); Lundin (1990a); Zhao et al. (2002); Hansson et al. (2004) suggested an impedance factor to account for the existence of ice:

$$K_{in} = K_{in}^{u} 10^{-E\phi_s^i} \tag{8.17}$$

Where, K_{in} and K_{in}^{u} are the actual and unfrozen coefficient of permeability; E is an empirical constant ranging from 1.4 to 8 for fine-grained soils but up to 20 for coarse-grained soils (Lundin, 1990a).

8.2.1.2 Water source/sink during freezing and thawing cycles

Liquid water can exist in soil under frozen conditions and the amount of unfrozen water is primarily a function of soil texture, soil temperature, chemical and mineralogical properties of soil (Miller, 1963; Williams, 1963; Miller, 1973; Hohmann, 1997). The source/sink term Sr_i in the mass conservation of water or ice is defined as Eqn. 8.10:

$$Sr_i = \rho_i \frac{\partial \phi_s^i}{\partial t} = \rho_i \frac{\partial \phi_s^i}{\partial T} \frac{\partial T}{\partial t} \tag{8.18}$$

The total volumetric water content expressed as the equivalent liquid water content during freezing is defined as:

$$\Xi = \phi_w + \frac{\rho_i}{\rho_w} \phi_s^i \tag{8.19}$$

Where: Ξ is independent on temperature and neglecting thermal expansion. By taking the partial derivative of Eqn. 8.19 w.r.t. temperature T, Eqn. 8.19 becomes:

$$\frac{\partial \Xi}{\partial T} = \frac{\rho_i}{\rho_w} \frac{\partial \phi_s^i}{\partial T} + \frac{\partial \phi_w}{\partial T} = 0 \tag{8.20}$$

Therefore

$$-\frac{\rho_i}{\rho_w} \frac{\partial \phi_s^i}{\partial T} = \frac{\partial \phi_w}{\partial T} \tag{8.21}$$

Where $\frac{\partial \phi_w}{\partial T}$ is the slope of SFCC. Fig. 8.4 shows a typical experimental data of SFCC of fine-sandy soils and $\phi_w(\psi, T)$ during thawing/freezing is a function of soil (matric) suction and temperature which can be determined by experiments or by theory through the use of SWCC (Miller, 1963; Koopmans and Miller, 1966; Miller, 1973; Amico, 2010).

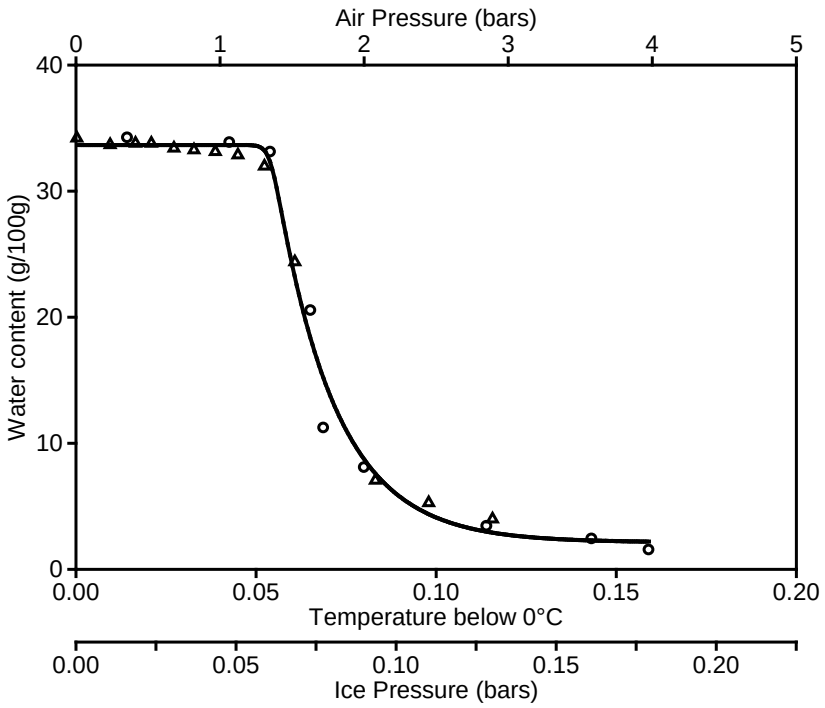

Figure 8.4: Typical SFCC for fine-sandy soils (data from Koopmans and Miller, 1966).

Using the van Genuchten (1980) model of SWCC, the assumption of freezing=drying processes and the validity of Clausius-Clapeyron relation, SFCC can be expressed as (Amico, 2010):

$$\phi_w = \phi_r^w + (\phi_s - \phi_r^w)\left\{1 + \left(\alpha_o \psi_o + \alpha_o \frac{L_{fw}}{g T_o}|T - T_1|\right)^n\right\}^{-m} \tag{8.22}$$

Where $\alpha_o(\mathrm{m}^{-1})$ is the fitting parameter, $\psi_o\,(\mathrm{m})$ is soil suction at $T_o = 273.15\,\mathrm{K}$; $L_{fw}\ (\mathrm{J/kg})$ is the latent heat of fusion. T_1 is the initial temperature of phase change under unsaturated conditions (water in soil is under tension) (Miller, 1963):

$$T_1 = T_o - \frac{g T_o}{L_{fw}} \psi_o \tag{8.23}$$

The Eqn. 8.22 is used to determine unfrozen water content ϕ_w in frozen conditions, therefore it couples water and thermal transports during freezing. The illustration of Eqn. 8.22 is shown in Fig. 8.5.

8.2.1.3 Water evaporation and condensation in porous media

It is assumed that $Sr_a^v = -Sr_w$. Relative humidity in the void of waste rock or soils, RH, which is the ratio between actual vapor density, $\rho_a^v = \omega_a^v \rho_a$, and saturated vapor density ,ρ_{sat}^v, is a function of soil suction and temperature. Gibb's function of soil water expresses an equilibrium condition between liquid water and water vapor in soil via an equation as

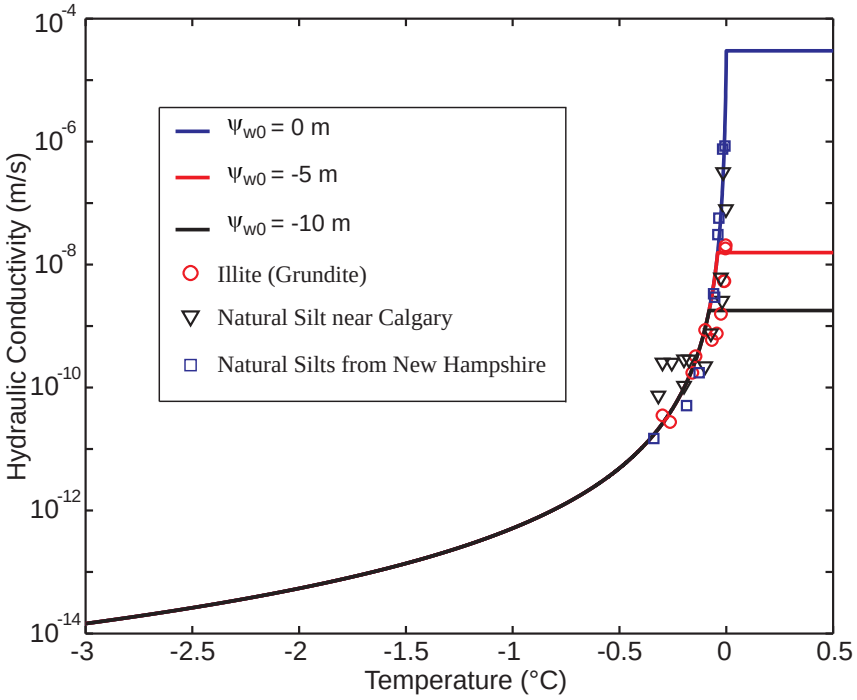

Figure 8.5: The relation between hydraulic conductivity and temperature with saturated hydraulic conductivity $k_s = 3 \times 10^{-5}\,(\mathrm{m/s})$, $n = 1.5$, $\alpha_o = 1.0\,(1/\mathrm{m})$ (experimental data from Horiguchi and Miller, 1983).

(Bear, 1972; Wilson, 1990).

$$RH = \frac{\rho_a^v}{\rho_{sat}^v} = \exp\left(\frac{g\psi M_a^v}{R.T}\right) \tag{8.24}$$

The vapor density is also called absolute humidity or vapor concentration in pore air within porous media which describes the amount of water vapor per unit volume of air. Applying the ideal gas law to saturated vapor density, the Eqn. 8.24 becomes

$$\omega_a^v \rho_a = \frac{p_v^s(T) M_a^v}{RT} \exp\left(\frac{p_w M_a^v}{\rho_w RT}\right) \tag{8.25}$$

Where $p_v^s(T)$ is the saturated vapor pressure. $p_v^s(T)$ in (hPa) depends on temperature T (°C) and is defined by Buck (1981) as:

$$p_v^s(T) = 6.11\, e^{\frac{17.50T}{240.97+T}} \tag{8.26}$$

The dependence of absolute humidity and saturated vapor pressure on temperature is shown in Fig. 8.6 at a soil matric suction of 98.1 kPa (or a head of -10 m). Eqn. 8.25 and Eqn. 8.26 allow us to calculate the absolute humidity $\left(\mathrm{g/m^3}\right)$ in the pore space of a porous medium which depends on other parameters such as temperature, capillary pressure and volumetric air content. From the know values of vapor distribution, $\phi_a \omega_a^v \rho_a$, the source

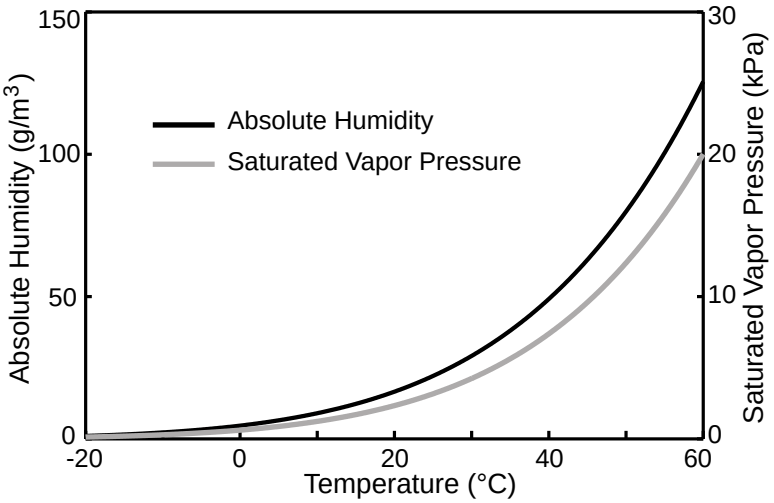

Figure 8.6: Absolute humidity, $\omega_a^v \rho_a \left(\mathrm{g/m^3}\right)$ in the pore calculated from Eqn. 8.25 and Eqn. 8.26 at $p_w = -98.1\,\mathrm{kPa}$.

function of water vapor can be calculated through Eqn. 8.11 as:

$$Sr_a^v = -Sr_w = \frac{\partial\left(\phi_a \omega_a^v \rho_a\right)}{\partial t} + \mathrm{div}\left(-\phi_a \mathbf{D}_a^v \nabla\left(\omega_a^v \rho_a\right) + \mathbf{u}_g\left(\omega_a^v \rho_a\right)\right) \tag{8.27}$$

8.2.1.4 Oxygen, sulfur depletion and heat generation

In waste rock, the main component of sulfide minerals is pyrite (FeS_2) therefore ARD is usually expressed via the reaction of pyrite. Furthermore, due to the complexity of chemical processes associated with producing ARD from pyrite, a relatively simple but widely used version of chemical reaction of pyrite can be expressed as (Lowson, 1982; Evangelou, 1995):

$$\mathrm{FeS_2} + 3.5\,\mathrm{O_2} + \mathrm{H_2O} \rightarrow \mathrm{Fe^{2+}} + 2\,\mathrm{SO_4^{2-}} + 2\,\mathrm{H^+} \tag{8.28}$$

Eqn. 8.28 shows that FeS_2 is oxidized by O_2 to produce not only Fe^{2+}, SO_4^{2-} and H^+ but also a strongly exothermic process. The relation between the rate of consumption of oxygen and sulfur in the oxidation reaction is:

$$Sr_s = \frac{Sr_a^o}{\varepsilon} \tag{8.29}$$

Where Sr_a^o is the rate of consumption of oxygen and $\varepsilon = 1.746$, which is based on the Eqn. 8.28, is the ratio between oxygen consumed and sulfur used.

Fig. 8.7 shows the basic concept of the shrinking core model, which is used to describe the oxidation of pyrite. The sulfur conservation can be rewritten as (Pantelis and Ritchie, 1991):

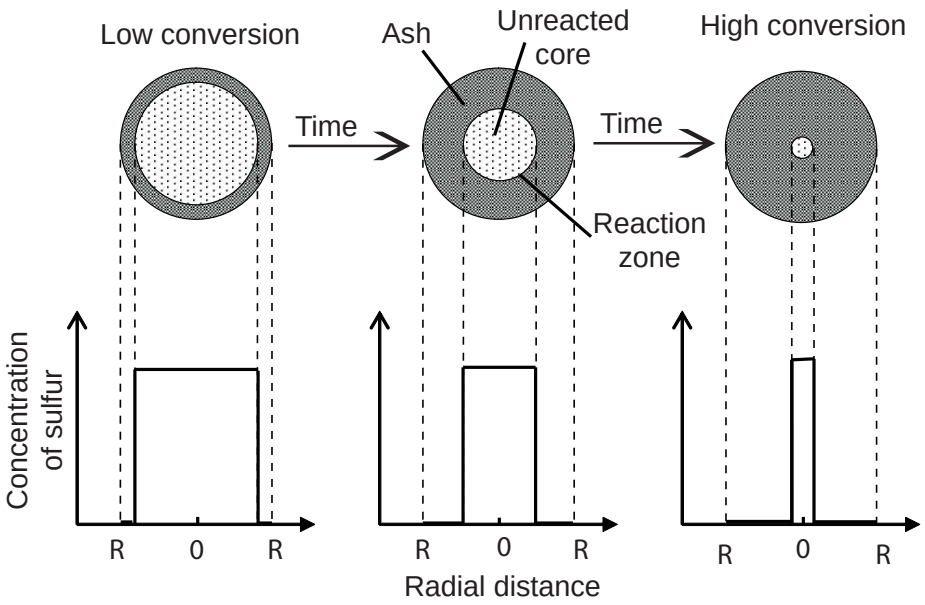

Figure 8.7: The processes of oxidation (modified from Levenspiel, 1972).

$$\frac{\partial \rho_s^s}{\partial t} = -X_T X_O \frac{3\gamma D_e^s}{\varepsilon R^2} \frac{\left((\rho_s^s)^{1/3}\right)\rho_a^o}{(\rho_s^s)_{ini}^{1/3} - (\rho_s^s)^{1/3}} \tag{8.30}$$

Therefore Sr_s can be expressed as:

$$Sr_s = -X_T X_O \frac{3\gamma D_e^s \phi_s}{\varepsilon R^2} \frac{\left((\rho_s^s)^{1/3}\right)\rho_a^o}{(\rho_s^s)_{ini}^{1/3} - (\rho_s^s)^{1/3}} \tag{8.31}$$

Where: $R\,(\mathrm{m})$ is the average radius of the solid phase, $(\rho_s^s)_{ini}$ is the initial mass concentration of sulfur in the solid phase $(\mathrm{kg/m^3})$, $\gamma = 3.18 \times 10^{-2}$ is the Henry's law constants of O_2, $D_e^s = 2.6 \times 10^{-9}\,(\mathrm{m^2/s})$ is the effective diffusion coefficient of oxygen in the solid phase (rock) (Pantelis and Ritchie, 1991). X_T and X_O are two inhibition factors in which X_T and X_O depend on temperature and O_2 concentration respectively. As shown in Fig. 8.8A, the oxidation rate varies with temperature and a quadratic equation was fit through the measured points such that

$$X_T = -1.5\,10^{-3}T^2 + 9.1\,10^{-2}T - 0.34 \tag{8.32}$$

$$4\,^{\circ}\mathrm{C} \leq T \leq 55\,^{\circ}\mathrm{C} \tag{8.33}$$

The oxygen dependence of oxidation rate is represented by X_O. $X_O = 1.0$ at a mole fraction $\geq 1\,\%$ and X_O declines linearly as shown in Fig. 8.8B.

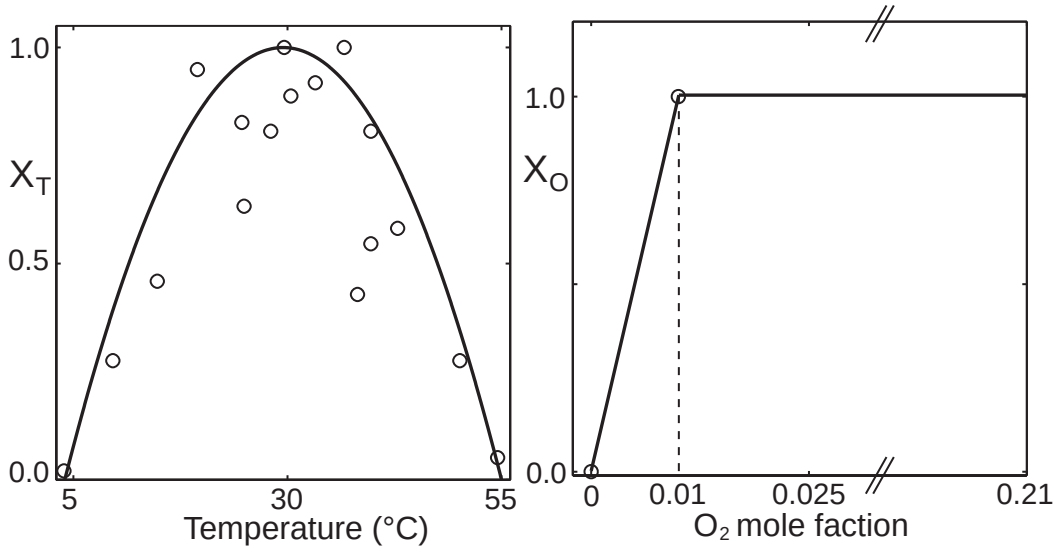

Figure 8.8: The dependence of oxidation on temperature (°C) (A) and oxygen concentration (B) (point data from Jaynes et al., 1984b).

8.2.2 Conservation of Energy

The assumptions are: thermal equilibrium of all phases in REV, no viscous dissipation nor radiative effects. One can obtain the following equation of conservation of energy in porous media (Nield and Bejan, 1999).

$$C\frac{\partial T}{\partial t}+\nabla\cdot\left(-\lambda\nabla T+\sum_{\alpha=a,w}C_\alpha\mathbf{u}_\alpha T\right)=\delta_h Sr_s-L_{vw}Sr_w \tag{8.34}$$

Where: T is temperature (in K), which is a dependent variable; C $\left(\mathrm{J}/\left(\mathrm{m}^3\cdot\mathrm{K}\right)\right)$ and λ $\left(\mathrm{W}/\left(\mathrm{m}\cdot\mathrm{K}\right)\right)$ denote the bulk volumetric heat capacity and thermal conductivity of waste rock/porous materials; $C_\alpha=\rho_\alpha c_\alpha$ is the volumetric heat capacity $\left(\mathrm{J}/\left(\mathrm{m}^3\cdot\mathrm{K}\right)\right)$ of the fluid phases α (water or air); c_α is the specific heat capacity of α phase $\left(\mathrm{J}/\left(\mathrm{kg}\cdot\mathrm{K}\right)\right)$; $\delta_h=2.19\times10^7$ $\left(\mathrm{J/kg(S)}\right)$ is heat released per mass of sulfur consumed (Lowson, 1982); Sr_s and Sr_w are as described previously. L_{vw} is latent heat of vaporisation per unit mass of water $\left(\mathrm{J/kg}\right)$ which depends on temperature as the following equation (Eqn. 8.35) in which T is in K (Henderson-Sellers, 1984).

$$L_{vw}\left(T\right)=1.92\,10^6\left(\frac{T}{T-33.91}\right)^2 \tag{8.35}$$

Here, C counts for phase change of water and λ is defined using either arithmetic or geometric means (Lunardini, 1981; Andersland and Ladanyi, 2004).

$$C=\sum_{\alpha=s,a,w}\phi_\alpha\rho_\alpha c_\alpha-L_{fw}\rho_i\frac{\partial\phi_s^i}{\partial T}=\sum_{\alpha=s,a,w}\phi_\alpha\rho_\alpha c_\alpha+L_{fw}\rho_w\frac{\partial\phi_w}{\partial T} \tag{8.36}$$

- Arithmetic mean

$$\lambda = \sum_{\alpha=s,a,w} \phi_\alpha \lambda_\alpha \tag{8.37}$$

- Geometric mean

$$\lambda = \lambda_s^{(1-\Sigma\phi_\alpha)} \prod_{\alpha=a,w} \lambda_\alpha^{\phi_\alpha} \tag{8.38}$$

Where: λ_α is the thermal conductivity of α phase $(\mathrm{W}/(\mathrm{m}\cdot\mathrm{K}))$ and latent heat of fusion of water, $L_{fw} = 3.34 \times 10^5$ $(\mathrm{J/kg})$ (Batchelor, 1970).

8.2.3 Ground surface heat flux as a boundary condition for thermal transport

Ground surface heat flux of a waste-rock pile is dictated by several energy processes including long-wave and short-wave radiations, latent and sensible heat transports. Ground surface heat flux has been described by many researchers as (Price and Dunne, 1976; Lunardini, 1981; Wilson, 1990; Qin et al., 2002; Herb et al., 2008; Cammalleri et al., 2010):

$$G = R_n - Q_{evap} - Q_{conv} \tag{8.39}$$

$$\left.\begin{aligned} R_n &= Q_s + Q_{li} - Q_{lo} \\ Q_s &= (1-\alpha_s)\, R_s \\ Q_{li} &= F\left(\sigma T_a^4\right) 1.08 \left[1 - \exp\left(-0.01\,(P_v^a)^{\frac{T_a}{2016}}\right)\right] \\ \log_{10} P_v^a &= 11.40 - \frac{2353}{T_{dp}} \\ Q_{lo} &= \varepsilon\sigma T_s^4 \end{aligned}\right\} \tag{8.40}$$

$$\left.\begin{aligned} Q_{evap} &= \rho_a L_{vw} \chi_{ev} \zeta \left(0.622 \frac{p_v^o - p_v^a}{p_a}\right) \\ Q_{conv} &= \rho_a c_a \chi_{cv} \zeta \left(T_s - T_a\right) \end{aligned}\right\} \tag{8.41}$$

Where $G\left(\mathrm{W/m^2}\right)$ is the ground surface heat flux; R_n is the net radiation, which is the available energy to heat the ground or evaporate water, and it is calculated by Eqn. 8.40; Q_s is the net short-wave solar radiation; Q_{li} is the long-wave radiation of the atmospheric calculated based on air temperature (T_a) and cloud conditions; Q_{lo} is the long-wave radiation of the waste-rock's surface emission. Q_{evap} and Q_{conv} are the energy transports of latent and sensible heat respectively; $F \geq 1$ is the cloud factor to account for cloudy conditions; χ_{ev} and χ_{cv} are the heat transport coefficients for latent and sensible heat respectively depending on surface roughness of the waste-rock pile; ζ is a stability function and it is a function of Richardson's number, R_i; ε and σ are the emissivity of the waste-rock's surface and Stefan–Boltzmann's constant. T_a, T_s, and T_{dp} are the ambient, surface, and dew-point temperatures

in K, respectively; $p_v^a$and p_v^o are the vapor pressure of the ambient and at the surface in Pa; α_s is the surface albedo and R_s is the total solar radiation (direct and diffuse).

The coefficients, χ_{ev}, χ_{cv}, the stability function ζ and the Richardson number, R_i are determined as followings:

$$\chi_{ev} = \chi_{cv} = \frac{\kappa^2 U_z}{\left(\ln \frac{z}{z_o}\right)^2} \tag{8.42}$$

$$\zeta = \frac{1}{1+10R_i} \tag{8.43}$$

$$R_i = \frac{g\,z\,(T_s - T_z)}{T_a U_z^2} \tag{8.44}$$

Where $\kappa = 0.4$ is the Von Karman's constant (Garratt et al., 1996), U_z and T_z are the wind speed $(\mathrm{m/s})$ and air temperature (K) at a measured height $z\,(\mathrm{m})$, and $z_o = 0.01\ (\mathrm{m})$ is a surface roughness for bare soils (Garratt, 1993). The parameters required for the calculation of ground surface heat flux are tremendous involving many measurements and some parameters can rapidly vary in the course of seconds such as wind speed. Therefore, in permafrost engineering applications ground surface temperatures are often used as temperature boundary conditions and ground surface temperatures are measured within 1 cm of the surface (Andersland and Ladanyi, 2004). The surface temperature approach will be used in this thesis.

8.3 The influences of wind and barometric pressure

Wind induced advection and barometric pressure fluctuations can be incorporated into the above conceptual model by adding pressure perturbations around waste-rock piles created by wind and barometric pressure fluctuations as boundary conditions of the partial differential equation (PDE) of air conservation (Eqn. 8.1). The pressure perturbations due to wind can be achieved using field measurements (Amos et al., 2009a) or computational fluid dynamics (CFD) approach (Anne and Pantelis, 1997; Moghtaderi et al., 2000). Therefore, air pressure at the surface of the waste-rock pile can be defined for a 2-D problem as:

$$p_a\,(z,t) = p_a\,(z_o,t) + g\frac{p_a\,(z_o,t)}{T_{air}\,(t)}\frac{M_{air}}{R}\Delta z + p_a^{wind}\,(z,t) \tag{8.45}$$

Where $p_a\,(z,t)$ and $p_a\,(z_o,t)$ are the air pressure at a height z (along the waste-rock pile's surface) and a reference height z_o (measuring height), respectively. $p_a^{wind}\,(z,t)$ is the wind induced pressure perturbation and it mainly changes with wind speed and direction. By using CFD simulations, the values of $p_a^{wind}\,(z,t)$ are usually obtained by assuming a fixed wind speed and direction and thus $p_a^{wind}\,(z)$ does not change with time. Eqn. 8.45 is

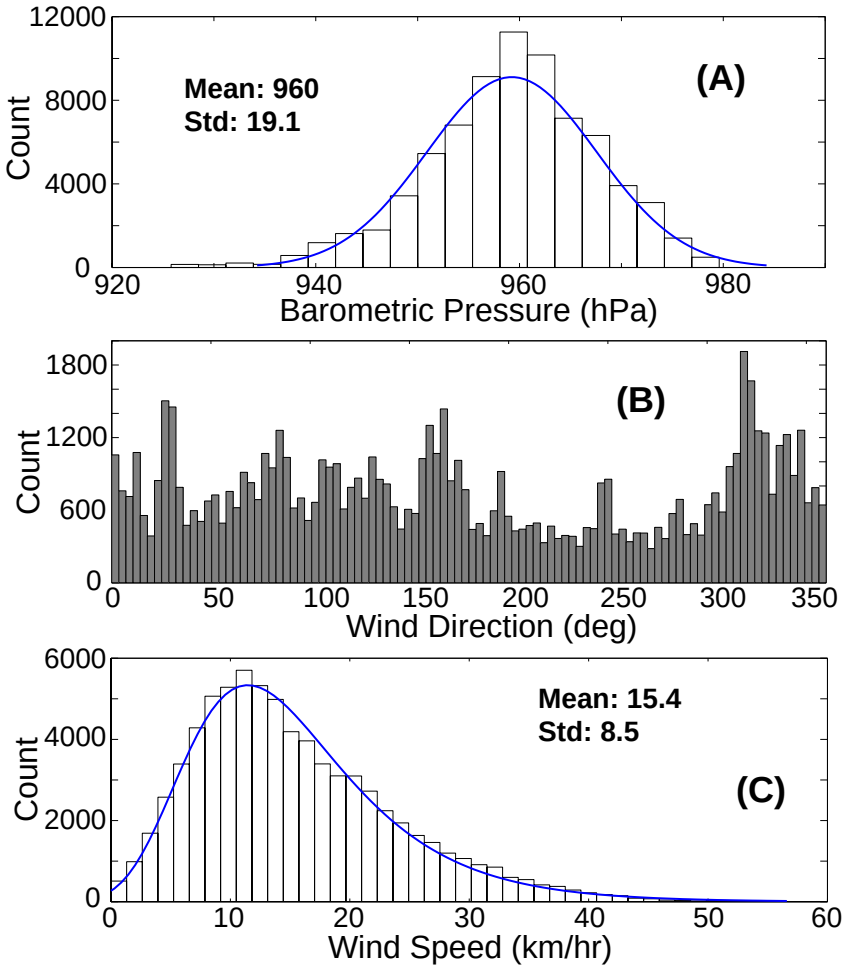

Figure 8.9: Histograms of barometric pressure (A), wind direction (B) and wind speed (C) of field measurements at a rock pile at Diavik Diamond Mine.

used to assign temporal and spatial variations of air pressure along the waste-rock pile's surface. The first two terms on the right side correspond to air pressure variations at the site and the last term is wind induced pressure along the pile's surface. Because atmospheric pressure can vary erratically with time and its time series can contain several frequencies and noises. Discrete Fourier Transform (DFT) can be used to analyze the time series for dominated frequencies and then the atmospheric pressure can be represented by these frequencies through Fourier series.

At the Diavik Test Pile Research site, a small weather station has been installed on top of the waste-rock piles and some of the measured data is wind and barometric pressure available. Fig. 8.9A shows a histogram of barometric pressure fluctuation which can be fitted with a normal probability distribution function (PDF) having a mean of 960 hPa and a standard deviation of 19.1 hPa. The histogram of wind direction can not be fitted into any PDF and it scatters about in all directions. Although it shows the predominant wind direction was from the east ($\sim 60 - 145$ deg) and the north ($\sim 335 - 10$ deg) (Fig. 8.9B).

The measured-mean wind speed and standard deviation are 15.4 km/h and 8.5 km/h, respectively and the PDF curve can be fitted.

8.4 Boundary and initial conditions

The boundaries between the waste-rock pile and atmosphere are denoted by Γ_a; Γ_b defines the boundaries between the waste-rock pile and its foundation; $(\Gamma = \Gamma_a \cup \Gamma_b)$. Let $\mathbf{n}$ be the unit outward normal vector.

8.4.1 Boundary conditions

- At the boundary Γ_a

$$\omega_a^o \rho_a = \Theta_o, \quad \mathbf{n} \cdot \frac{k_r^w K_{in}}{\mu_w} (\nabla p_w + \rho_w g) = F_w(t) \text{ or } p_w = p_w^o \tag{8.46}$$

$$p_a = p_a(z,t) \text{ (calculated using Eqn. 8.45)}, \; T = T_s \text{ or } \mathbf{n} \cdot (-\lambda \nabla T) = G \tag{8.47}$$

- At the boundary Γ_b

$$\mathbf{n} \cdot \left(\phi_a \mathbf{D}_a^i \nabla \left(\omega_a^i \rho_a\right) - \mathbf{u}_a \left(\omega_a^i \rho_a\right)\right) = 0, \quad \mathbf{n} \cdot \frac{k_r^w K_{in}}{\mu_w} (\nabla p_w - \rho_w \mathbf{g}) = 0 \text{ or } p_w = p_w^o, \; p_a = p_{atm}^o \tag{8.48}$$

The boundary condition of the energy conservation is continuity at the boundary Γ_b. Otherwise, the boundary condition is zero heat flux or an assigned temperature.

Where Θ_o is the oxygen concentration in air, $F_w(t)$ is the assigned water flux at the surface which may include evaporation at the surface, p_w^o is the described water pressure at the surface, p_{atm}^o is the atmosphere air pressure at the base.

8.4.2 Initial conditions

Initial conditions $(t = 0)$ are:

$\omega_a^o \rho_a = \Theta_o, \; \omega_s^s \rho_s = \Theta_s, \; T = T_o, \; p_w = p_w^o(z), \; p_a$ is the hydrostatic pressure condition

Where Θ_s is the initial mass concentration of sulfur, $p_w^o(z)$ is the initial water pressure distribution which can be a function of vertical direction z.

8.5 Discussion and Conclusions

Gas, water and heat transports are described using the above governing equations together with appropriate constitutive relations for a waste-rock pile containing sulfide minerals placed in permafrost regions. The equations were presented in an intuitive way so that additional components of any phases in REV can be added. As shown in Fig. 8.1, gas

transport drives other processes such as thermal transport and oxidation reaction. Oxygen in the gas phase can be transported via diffusion, which is slow, or via advection and convection, which are much faster. However, air advection/convection is controlled not only by physical properties of waste-rock piles such as permeability through grain sizes, heterogeneity and the shape of the pile (height-width ratio and slope angle) but also heat release, changes in atmosphere temperatures, air pressures and wind speeds (Anne and Pantelis, 1997; Moghtaderi et al., 2000; Pham et al., 2008a). In permafrost regions where the seasonal temperatures fluctuate considerably, the temperature dependence of air density may create an unstable stratification in which cold-heavy air stays above warm-light air. Under a sufficient temperature gradient, this stratification of air density may allow air-convection cells to form. The transport of oxygen via these air-convection cells is about two-order of magnitude greater than via diffusion (Pham et al., 2008a). Furthermore, changes in concentrations of vapor and oxygen in the air phase can result in air convection due to changes in the molar mass of moist air (Eqn. 8.2). However, in porous media air convection due to changes in molar mass is insignificant compared to air convection due to changes in temperature (Nield and Bejan, 1999).

Moreover, heat produced by the exothermic reaction of sulfide minerals can produce air-convection cells and during winter these air-convection cells carry cold air from the outside to cool the interior of waste-rock piles. However, the chemical and biological oxidation of sulfide minerals are a temperature-dependent process (Fig. 8.8) therefore cold temperatures within the waste-rock piles created by air convection can limit or reduce the oxidation rate. Furthermore, air convection/advection during winter results in the escape of interior warm air (water vapor venting) and this process was observed clearly during winter from waste-rock piles at Diavik mine. Natural air convection induces inward airflow during winter near the base of waste-rock piles because interior temperatures are warmer than outside air. During summer airflow is in a reverse direction, however the magnitude of the inward airflow is about three times greater than the outward airflow (Chapter 4). Depth understanding of ventilation mechanisms within waste-rock piles throughout a year would have helped preventing a deadly accident (four workers died) at Sullivan Mine in May 2006 (Lahmira et al., 2009).

In a relatively dry and low precipitation environment such as at Diavik Diamond Mine located approximately 300 kilometers Northeast of Yellowknife, Northwest Territories, the moisture content in waste-rock piles is considerably low (Neuner et al., 2012). As a result, if under-going oxidation process, the source component associated with oxidation of sulfide minerals in the energy balance (Eqn. 8.34) may be much greater than other components. However, if the oxidation rate is low, such as at the regions of cold temperatures or low sulfur concentrations in waste rock, the heat source/sink term associated with changes in the water vapor concentration can be important during summer. Furthermore, the convective part associated with moving water in Eqn. 8.34 is also small compared to other components

as a result of low precipitation and frozen ground. Even through water can carry more heat than air due to much larger heat capacity.

Most of the physical properties of waste rocks determining the rates of air, vapor, water and heat transport (diffusion coefficients, thermal conductivity, heat of water vaporisation, coefficient of water viscosity, etc.) is temperature or moisture content dependent and these dependencies make the governing equations highly non-linear and coupled. In addition, the steep slopes of the SWCC and SFCC of waste rock also pose significant challenges. As a result, the convergence of numerical solutions is difficult and time-step taken during transient analyses is small. The vapor transport described by Eqn. 8.27 is brief and a more rigorous description of water vapor transport was introduced by Wilson (1990); Miyazaki (2006).

References

Amico, M. D. (2010). *Coupled Water and Heat Transfer inPermaforst Modeling*. PhD thesis, University of Trento.

Amos, R. T., Blowes, D. W., Smith, L., and Sego, D. C. (2009a). Measurement of wind-induced pressure gradients in a waste rock pile. *Vadose Zone J*, 8(4):953–962.

Andersland, O. B. and Ladanyi, B. (2004). *Frozen Ground Engineering*. John Wiley & Sons.

Anne, R. and Pantelis, G. (1997). Coupled natural covection and atmosphere wind forced advection in above ground reacting heaps. In *Inter Conf on CFD in Mineral Processing and Power Generation, CSIRO*.

Batchelor, G. (1970). *An Introduction to Fluid Dynamics*. Cambridge University Press.

Bear, J. (1972). *Dynamics of fluids in porous media*. Dover Publications, Inc.

Bear, J. and Cheng, A. (2010). *Modeling Groundwater Flow and Contaminant Transport*. Springer.

Blasch, K. W., Constantz, J., and Stonestrom, D. A. (2007). Thermal methods for investigating ground-water recharge. *Ground-water recharge in the arid and semiarid southwestern United States, U.S. Geological Survey Professional Paper 1703*, pages 351–373.

Buck, A. L. (1981). New equations for computing vapor pressure and enhancement factor. *Journal of Applied Meteorology*, 20(12):1527–1532.

Cammalleri, C., Anderson, M., Ciraolo, G., Durso, G., Kustas, W., La Loggia, G., and Minacapilli, M. (2010). The impact of in-canopy wind profile formulations on heat flux estimation in an open orchard using the remote sensing-based two-source model. *Hydrology and Earth System Sciences*, 14(12):2643–2659.

Carman, P. (1956). *Flow of gases through porous media*. Butterworths, London.

Evangelou, V. P. (1995). *Pyrite oxidation and its control (p. 293)*. Boca Raton: CRC Press Inc.

Fredlund, D. and Rahardjo, H. (1993). *Soil mechanics for unsaturated soils*. John Wiley and Sons, Inc. New York.

Garratt, J. R. (1993). Sensitivity of climate simulations to land-surface and atmospheric boundary-layer treatments - a review. *Journal Of Climate*, 6(3):419–449.

Garratt, J. R., Hess, G. D., Physick, W. L., and Bougeault, P. (1996). The atmospheric boundary layer - advances in knowledge and application. *Boundary-Layer Meteorology*, 78(1-2):9–37.

Hansson, K., Simunek, J., Mizoguchi, M., Lundin, L.-C., and van Genuchten, M. T. (2004).

Water flow and heat transport in frozen soil: Numerical solution and freeze-thaw applications. *Vadose Zone Journal*, 3(2):693–704.

Henderson-Sellers, B. (1984). A new formula for latent heat of vaporization of water as a function of temperature. *Quarterly Journal of the Royal Meteorological Society*, 110(466):1186–1190.

Herb, W. R., Janke, B., Mohseni, O., and Stefan, H. G. (2008). Ground surface temperature simulation for different land covers. *Journal of Hydrology*, 356(3-4):327 – 343.

Hohmann, M. (1997). Soil freezing — the concept of soil water potential. state of the art. *Cold Regions Science and Technology*, 25(2):101–110.

Hollesen, J., Elberling, B., and Jansson, P. (2011). Modelling temperature-dependent heat production over decades in high arctic coal waste rock piles. *Cold Regions Science and Technology*, 65(2):258–268.

Horiguchi, K. and Miller, R. D. (1983). Hydraulic conductivity funcstions of frozen materials. In *The Fourth International Conference on Permafrost*.

Jame, Y.-W. and Norum, D. I. (1980). Heat and mass transfer in a freezing unsaturated porous medium. *Water Resour. Res.*, 16(4):811–819.

Jaynes, D. B., Rogowski, A. S., and Pionke, H. B. (1984b). Acid mine drainage from reclaimed coal strip mines: 1. model description. *Water Resour. Res.*, 20:233–242.

Koopmans, R. W. R. and Miller, R. D. (1966). Soil freezing and soil water characteristic curves. *Soil Sci. Soc. Am. J.*, 30(6):680–685.

Lahmira, B., Lefebvre, R., Hockley, D., and Phillip, M. (2009). Sullivan mine fatalities incident: Numerical modeling of gas transport and reversal in gas flow directions. In *Securing the Future and 8th ICARD, June 23-26, 2009, Skelleftea, Sweden*.

Lefebvre, R., Hockley, D., Smolensky, J., and Gelinas, P. (2001a). Multiphase transfer processes in waste rock piles producing acid mine drainage. 1: Conceptual model and system characterization. *Journal of contaminant hydrology*, 52(1-4):137–164.

Levenspiel, O. (1972). *Chemical Reaction Engineering*. John Wiley & Sons Ltd.

Lowson, R. T. (1982). Aqueous oxidation of pyrite by molecular oxygen. *Chemical Reviews*, 82(5):461–497.

Lunardini, V. J. (1981). *Heat transfer in cold climates*. Van Nostrand Reinhold Company.

Lundin, L.-C. (1990a). Hydraulic properties in an operational model of frozen soil. *Journal of Hydrology*, 118(1-4):289–310.

Massmann, J. and Farrier, D. F. (1992a). Effects of atmospheric pressures on gas transport in the vadose zone. *Water Resour. Res.*, 28(3):777–791.

Miller, R. D. (1963). Phase equilibria and soil freezing. In *Permafrost international con-*

ference.

Miller, R. D. (1973). Soil freezing in relation to pore water pressure and temperature. In *North American contribution to the Second International Conference on Permafrost*, Yakutsk, U.S.S.R.

Millington, R. J. and Quirk, J. P. (1961). Permeability of porous solids. *Trans. Faraday Soc.*, 57:1200–1207.

Miyazaki, T. (2006). *Water Flow In Soils*. CRC Press.

Moghtaderi, B., Dlugogorski, B., and Kennedy, E. (2000). Effects of wind flow on self-heating characteristics of coal stockpiles. *Process Safety and Environmental Protection*, 78(6):445 – 453.

Neeper, D. A. (2003). Harmonic analysis of flow in open boreholes due to barometric pressure cycles. *Journal of Contaminant Hydrology*, 60(3-4):135–162.

Neeper, D. A. and Stauffer, P. (2005). Unidirectional gas flow in soil porosity resulting from barometric pressure cycles. *Journal of Contaminant Hydrology*, 78(4):281–289.

Neuner, M., Smith, L., Blowes, D. W., Sego, D. C., Smith, L. J., Fretz, N., and Gupton, M. (2012). The diavik waste rock project: Water flow though mine waste rock in a permafrost terrain. *Applied Geochemistry*, (0):–.

Nield, D. and Bejan, A. (1999). *Convection in porous media*. Springer, New York.

Pantelis, G. and Ritchie, A. I. M. (1991). Macroscopic transport mechanisms as a rate-limiting factor in dump leaching of pyritic ores. *Applied Mathematical Modelling*, 15(3):136–143.

Pham, N., Arenson, L. U., and Sego, D. C. (2008a). Numerical analysis of forced and natural convection in waste-rock piles in permafrost environments. In *Ninth International Conference on Permafrost (NICOP), University of Alaska Fairbanks, June 29 - July 3, 2008*.

Pham, N., Sego, D. C., Arenson, L. U., Blowes, D., Smith, L., Smith, L., Neuner, M. G. M., and Amos, R. (2009). Diavik waste rock project: Heat transfer in experimental waste rock piles at diavik under permafrost environment. In *The 8th ICARD International Conference on Acird Rock Drainage, SKELLEFTEA, SWEDEN, June 23-26, 2009.*

Price, A. G. and Dunne, T. (1976). Energy balance computations of snowmelt in a subarctic area. *Water Resour. Res.*, 12:686–694.

Qin, Z., Berliner, P., and Karnieli, A. (2002). Numerical solution of a complete surface energy balance model for simulation of heat fluxes and surface temperature under bare soil environment. *Applied Mathematics and Computation*, 130(1):171–200.

Smith, L., Forster, C., and Woodbury, A. (1989). Numerical simulation techniques for modeling advectively-disturbed thermal regimes. In *Geophys. Monogr. Ser.*, volume 47,

pages 1–5. AGU, Washington, DC.

Stallman, R. (1965). Steady 1-dimensional fluid flow in a semi-infinite porous medium with sinusoidal surface temperature. *Journal Of Geophysical Research*, 70(12):2821–2827.

Tasa, D., Tarbuck, E. J., and Lutgens, F. K. (2006). *The Atmosphere*. Prentice Hall.

van Genuchten, M. (1980). Closed-form equation for predicting the hydraulic conductivity of unsaturated soils. *Soil Science Society of America Journal*, 44(5):892 – 898.

Vargaftik, N. (1975). *Tables on the thermophysical properties of liquids and gases: in normal and dissociated states*. Hemisphere Pub. Corp.

Wessling, S. (2007). *The investigation of underground coal fires - towards a numerical approach for thermally, hydraulically, and chemically coupled processes*. PhD thesis, University of Munster.

Williams, P. J. (1963). Suction and its effects in unfrozen water of frozen soils. In *Permafrost international conference*.

Wilson, G. W. (1990). *Soil Evaporative Fluxes For Geotechnical Engineering Problems*. PhD thesis, University of Saskatchewan.

Wyckoff, R. D. and Botset, H. G. (1936). The flow of gas-liquid mixtures through unconsolidated sands. *Physics*, 7(9):325–345.

Zhao, L., Gray, D., and Toth, B. (2002). Influence of soil texture on snowmelt infiltration into frozen soils. *Canadian Journal of Soil Science*, 82(1):75–83.

CHAPTER 9

Numerical heat transfer simulation of waste-rock test piles located in a continuous permafrost region of Northern Canada

9.1 Introduction

Acid **R**ock **D**rainage (ARD), which is one of the most common environmental-related issues in mining, comes from the oxidation of sulfide minerals within waste rock exposed to waster and air (oxygen) and stimulated by *Acidithiobacillus ferrooxidans* bacteria. ARD results in low pH, high concentrations of toxic metals and sulfate in seepage water through this waste rock. Waste rock is often stockpiled in large, heterogeneous and often unsaturated **waste-rock piles (waste dumps or stockpiles)** in an area called the waste-rock storage area.

Multilayer soil covers have been suggested as a reliable solution for ARD of reactive waste rock in temperate regions of Canada and around the world (Newman et al., 1997; Morin and Hutt, 2001; Martin et al., 2004; Wickland and Wilson, 2005a; Molson et al., 2005; Song and Yanful, 2008), where the phenomena related in cold regions do not exist such as freeze-thaw cycles, frost heave, ice wedges, pingos, thermokart, solifluction, and patterned ground (Andersland and Ladanyi, 2004). In cold regions, without proper methods to accommodate these phenomena into cover system design, the consequences can be cracking and loosing bearing capacity in the cover system, which can influence the cover functions. The main function of an engineered soil cover for reactive waste rock is to forbid oxygen and water to come into contact with the sulfide minerals in waste rock, therefore reducing or eliminating ARD. However, there are also some other factors that could reduce the oxidation rate of sulfide minerals through controlling the activity of bacteria as shown in Fig. 9.1. The bacteria activity level is maximum under a certain range of temperature (Fig. 9.1A), whereas temperatures ≤ 4 °C or ≥ 55 °C (Jaynes et al., 1984b), where oxidation rates approaching 0, are called threshold temperatures for inhibiting the oxida-

tion of sulfide minerals. The oxidation also depends on pH and the availability of oxygen (Fig. 9.1B and C).

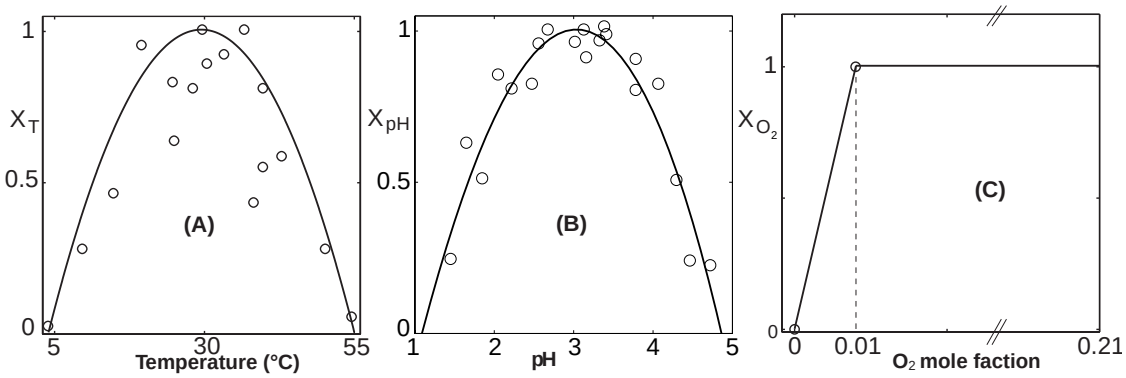

Figure 9.1: Normalized oxidation rate versus temperature (°C) (A), pH (B) and oxygen concentration (C) (modified from Jaynes et al. (1984b))

Oxidation of pyrite is an exothermic process producing $1.41 \times 10^4\,\mathrm{kJ/mole\,(FeS_2)}$ oxidized (or $2.19 \times 10^4\,\mathrm{kJ/kg\,(S)}$) (Lowson, 1982) and this released heat raises temperatures within a waste-rock pile. The rising temperature further accelerates oxidation as it creates natural air convection to further increase oxygen supply. Therefore, more ARD will be released. At Rum Jungle, Northern Territory, Australia, Harries and Ritchie (1981) predicted a heat production of $5.0\,\mathrm{W/m^3}$ that caused an increase in temperatures of around 20 °C compared to annual background temperatures. At mine Doyon, Quebec, Canada, a waste-rock pile had internal temperatures around 65 °C with an average pyrite oxidation rate of 2.2×10^{-9} $\mathrm{mol(O_2)/(kg\,s)}$ (in which kg is per unit weight of waste rock) or a heat production of $1.8\,\mathrm{W/m^3}$ (Lefebvre et al., 2001b; Sracek et al., 2006). Hollesen et al. (2011) reported a heat production of $175 \pm 63\,\mathrm{kJ/(m^3\,day)}$ (or $2.0\,\mathrm{W/m^3}$) in a waste-rock pile located in an arctic region that had a **M**ean **A**nnual **A**ir **T**emperature (MAAT) of -5.8 ± 1.3 °C. This heat release caused temperatures in the bedrock foundation beneath the waste-rock pile (between 5 and 10 m depth) to rise above 2 °C (Hollesen et al., 2011).

At temperatures below 0 °C, the oxidation of sulfide minerals is diminished or is very low (Fig. 9.1A). For this reason it is crucial to rapidly lower waste rock temperatures after placement below the threshold temperatures to keep the oxidation rate extremely low. In continuous permafrost regions, which have a minimum MAAT of -8 °C (Smith and Riseborough, 2002) and a long winter period, these cold temperatures provide a potential solution for ARD, which is **A**ir **C**onvection **C**over (ACC). ACC provides rapid cooling of waste rock and can maintain it under the freezing condition (i.e. 0 °C). ACC usually comprises of a low permeability soil layer with high moisture content such as till or fine-grained soils (called latent heat layer) and an overlaying coarse rock layer having high permeability and relatively dry (called air convection layer) (Fig. 9.2). The latent heat layer is used to constraint the active layer via latent heat (the freezing-thawing layer each year) to re-

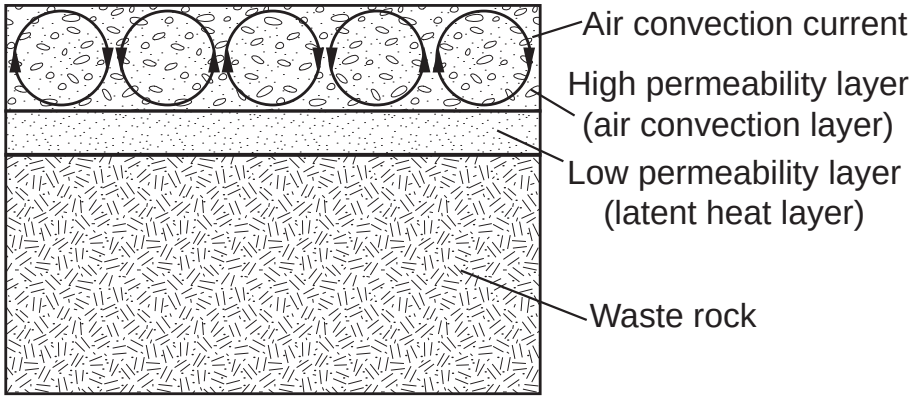

Figure 9.2: Configuration of ACC

main within the air convection layer. The air convection layer utilizes natural air convection to promote rapid cooling and cold penetration into and below the latent heat layer during winter. However during summer the convective layer insulates the latent heat layer due to its low thermal conductivity (high-porosity-coarse-dry rocks). The ACC is a concept that utilizes the design of air convection embankment (ACE). ACE has been used recently by Goering and Kumar (1996); Goering (1998); Arenson (2007); Ma et al. (2008); Xu and Goering (2008b); Cheng (2009) for permafrost aggradation beneath road and railway embankments in Fairbanks, Alaska and Qinghai-Tibet highway in China.

This present study presents field temperature data of a covered and an uncovered waste-rock test pile constructed in a continuous permafrost region. Application of the ACC concept is also examined through numerical simulations with different thicknesses and permeabilities of the air convection layer. These numerical results provide a tool to select the optimum thickness and permeability for the waste-rock test piles at the site. Furthermore, by assuming, waste-rock materials below the ACC are undergoing oxidation, numerical simulations were also performed to assess the effectiveness of the ACC in managing a waste-rock pile with internal heat generation.

9.2 Site Description

Diavik Diamond Mine is located on the East Island, a 17 km^2 island in Lac de Gras, approximately 300 kilometers northeast of Yellowknife, Northwest Territories in the Canadian Arctic (64°31' N, 110°20' W, el. 440 m) (Fig. 9.3). This location is in the continuous permafrost region with an average precipitation of 283 mm with 60 % from snow (Environment-Canada, 2008a). During the 10-year period between 2000 and 2010, MAAT at the site is -9°C and the mean annual surface temperature (MAST) of around -5 °C measured within 5 cm of the surface of the test piles constructed at the site. The waste rock during placement is relatively dry and the amount actual evaporation is almost equal to the

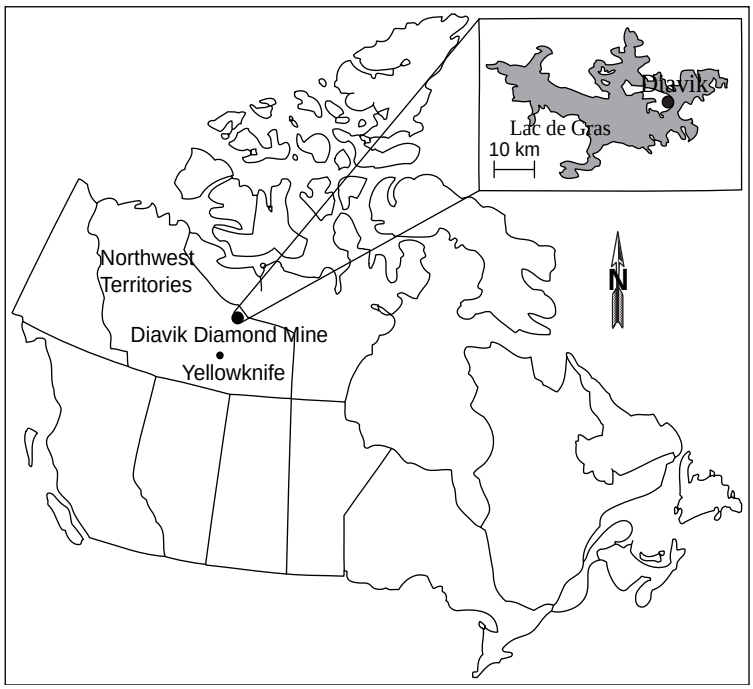

Figure 9.3: Location of Diavik Diamond Mine

precipitation (Neuner et al., 2012). The active layer is thin, which varies between 0.5 to 5 m depending the type of ground, and the active layer only exists in short summer (three to four months). Therefore, the convective transport due to water is not considered in thermal simulations.

Excavated waste rock during mining operations is analyzed for sulfur content and classified into Type I waste rock (or Type I rock) (< 0.04 wt % S), Type II waste rock (or Type II rock) (0.04 to 0.08 wt % S) or Type III waste rock (or Type III rock) (> 0.08 wt % S). Type I waste rock mainly consists of non-acid generating granite and has been used primarily for construction material. Type II waste rock comprises generally of granites and is considered to have low acid generating potential. Type III waste rock is considered potentially acid generating. Dry engineered covers are a mine closure concept for the Type II and Type III waste rock dumps, including re-sloping the Type II and III rock areas to 18.4° (3H:1V) for slope stability and covering with a 1.5-m lower permeability layer of till, and a 3-m layer Type I waste rock to act as an active freeze-thaw layer (DDMI, 2006).

Fig. 9.4 shows the covered test pile with a Type III core, and a 1.5-m till cover overlain by a 3-m Type I rock. This test pile resembles the closure concept of waste-rock piles at the site. Type III test pile (uncovered test pile) contained Type III waste rock were constructed and instrumented with final dimensions of 15 m in height and 50 by 60 m in the area at the base (Fig. 9.5). Temperatures within the test piles were recorded at a 4-hour interval and the thermistor beads are YSI 44007 type providing a precision of $\pm 0.2\,°C$ and a wide-range working temperature of $-80 \rightarrow +120$ °C. There are three basal collection lysimeter

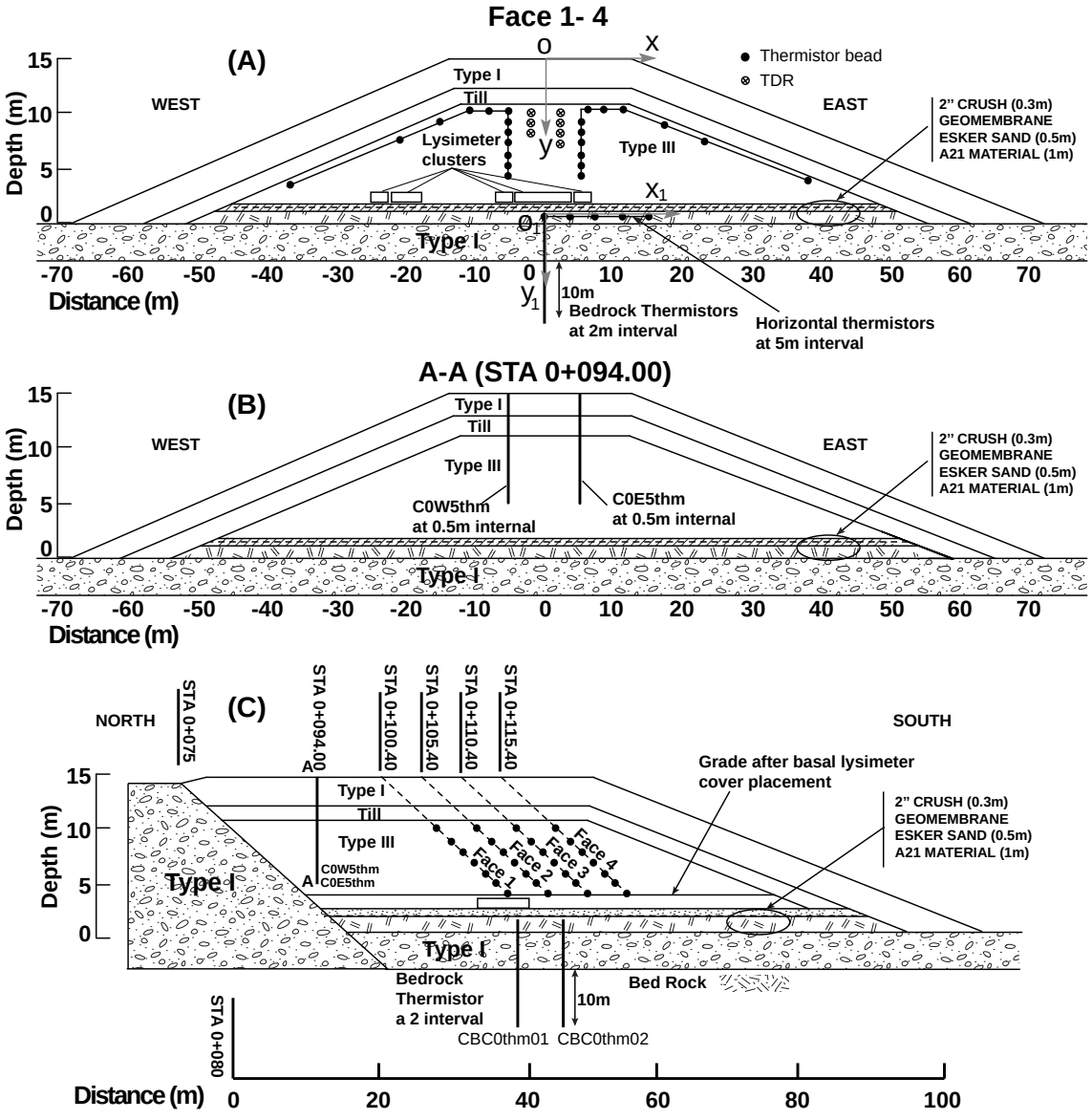

Figure 9.4: Typical cross-section (A and B) and long section (C) of the covered test pile.

(BCL) clusters constructed at the base of each test pile including two 4x4 m and two 2x2 m collection boxes. Inside each box, there is a self-regulating heating cable installed at the base intending to regulate temperatures within the BCLs just above the freezing point (i.e. 0 °C) so that water in the BCLs can flow into for geochemistry properties.

9.3 Governing equations and material properties

9.3.1 Governing equations

Considering waste rock as a porous medium containing a single-mobile fluid (air) and further assume the validity of ideal gas law and the Darcy's law. It is also assumed that the pore air is in thermal equilibrium with the solid matrix and the sinking core model was used to describe oxidation of sulfide materials. Governing equations of the problem are expressed in the Chapter 8. However, due to the relatively dry waste rock of the piles at the site as well as reducing the complexity of the model and computational time, water and vapor components in waste rock were neglected. The governing equations were solved using COMSOL Multiphysics software package which is a finite element method for various physics and engineering applications especially for coupled phenomena (Comsol, 2009).

9.3.2 Material properties

Thermal properties of the Type I, Type III waste rock and till were determined through in-situ measurements and also calculated through measurements of temperatures within the experimental waste-rock piles at the site (Table 9.1). The permeabilities of waste rock were measured using air permeability balls placed at locations within 6 m of the surface (Amos, 2009) and using in-situ hydraulic conductivity tests (Neuner et al., 2012). However, due to the high uncertainty in the measured values of permeability of waste rock as a result of material segregation during construction, the values of permeability will be varied by several orders of magnitude to examine the influence of permeability on thermal transport and to calibrate field data. Volumetric moisture contents of the Type I and Type III are assumed to be at a field capacity of 6.0 %, which was measured in the field resulting from the low precipitation and high evaporation at the site (Neuner et al., 2012). The volumetric water content of till is based on measurements of samples obtained during the construction of the covered test pile and assuming a bulk density of 2120 kg/m^3 (Terzaghi et al., 1996). Thermal properties of bedrock were determined based on temperature measurements using a thermistor cable installed 10 m deep into bedrock next to the test piles. Moreover, due to a relatively low porosity and moisture content, thermal properties of bedrock are assumed to be constant under either thawed or frozen condition.

Type I coarse rock is an engineered material based on Type I waste rock with no passing 3 cm size. The Type I coarse rock would have a low thermal conductivity, high permeability

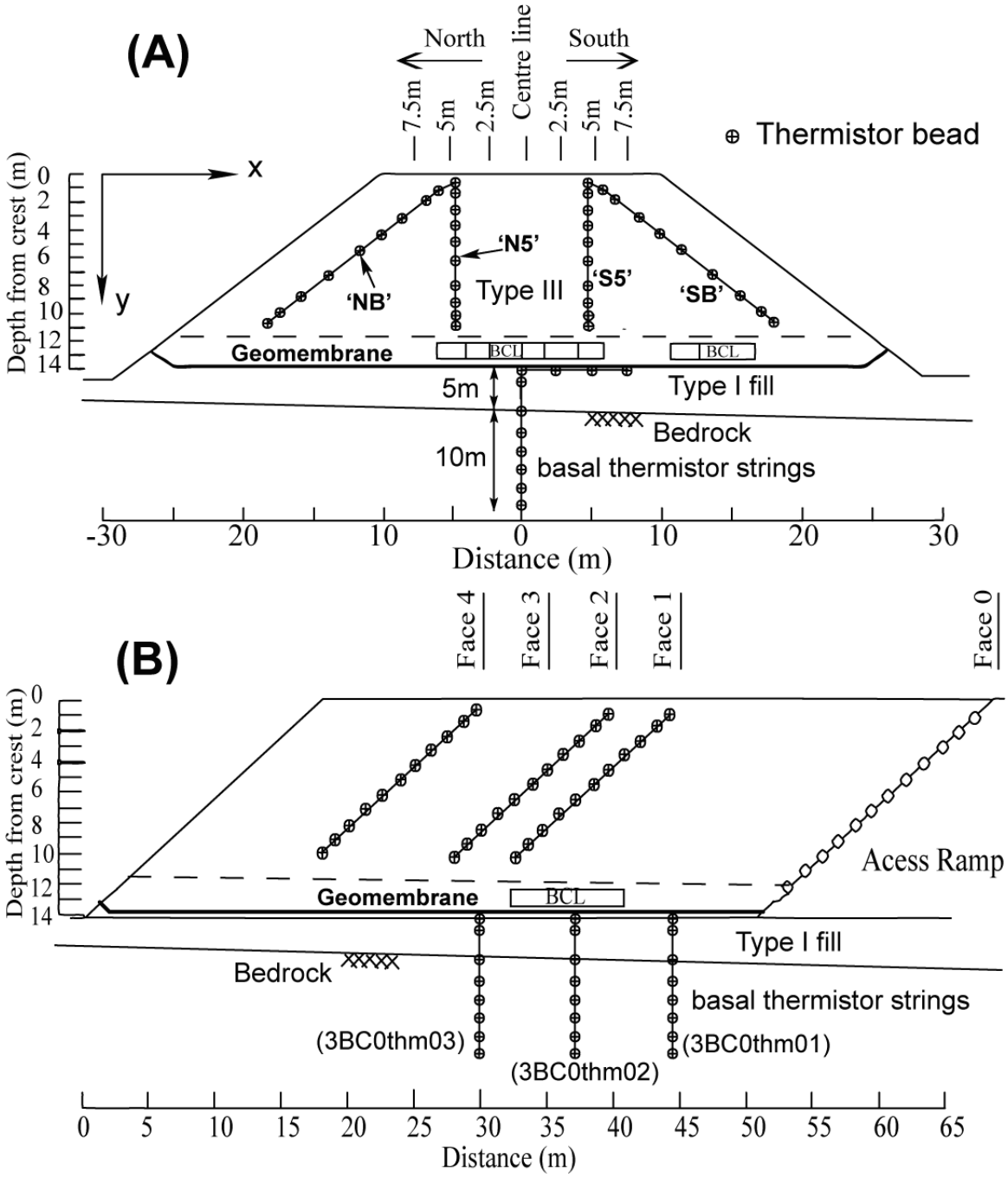

Figure 9.5: Cross-section of a typical face of the Type III test pile showing thermistor strings (A); and longitudinal section showing instrumented faces, basal lysimeters, and basal thermistor strings (B).

($\geq 3\times10^{-7}\,\mathrm{m}^2$) and porosity about 0.3. According to the ACC configuration, Type I coarse rock serves as the air convection cover layer. Bulk thermal conductivity and volumetric heat capacity of Type I coarse rock were determined by using both geometric and volumetric approaches, respectively as followings (Farouki, 1981b) (Table 9.1).

$$\lambda = \lambda_a^{\phi}\lambda_s^{(1-\phi)} \tag{9.1}$$

$$C = \rho\left(c_a\phi + c_s(1-\phi)\right) \tag{9.2}$$

Where $\lambda_a = 0.024$ and $\lambda_s = 3.0\ \mathrm{W/(m\cdot K)}$ are the thermal conductivity of air and solid rock (granite) (Farouki, 1981b), $\phi = 0.3$ is the porosity of Type I coarse rock, $\rho = 1840\,\mathrm{kg/m^3}$ is the bulk density of Type I coarse rock, $c_a = 1005$ and $c_s = 790\ \mathrm{J/(kg\cdot K)}$ are the specific heat capacity of air and solid rock (Farouki, 1981b; Andersland and Ladanyi, 2004).

Table 9.1: Properties of materials used in simulations

Property	Value	Comments
	Type I Waste Rock	
Porosity	0.25	In-situ measurements (Neuner et al., 2012)
Thermal conductivity	$1.7\ \mathrm{W/(m\cdot K)}$	In-situ measurements using a line heat source probe (**Chapter 3**)
Frozen bulk heat capacity	$2.3\times10^6\ \mathrm{J/(m^3\cdot K)}$	Using thawed heat capacity plus heat capacity differences between thawed and frozen water
Thawed bulk heat capacity	$2.4\times10^6\ \mathrm{J/(m^3\cdot K)}$	Ratio between in-situ thermal conductivity and thermal diffusivity determined by temperature measurements.
Volumetric water content	0.06	Average in-situ measurement values using TDR (Neuner et al., 2012)
Permeability	$2.0\times10^{-9}\,\mathrm{m}^2$	In-situ measurements using air permeability balls which were conducted at depths up to 6 m (Amos et al., 2009a)
	Type III Waste Rock	
Porosity	0.25	Same as Type I rock
Thermal conductivity	$1.8\ \mathrm{W/(m\cdot K)}$	Same as Type I rock

Frozen bulk heat capacity	2.2×10^6 J/(m^3 · K)	Same as Type I rock
Thawed bulk heat capacity	2.3×10^6 J/(m^3 · K)	Same as Type I rock
Volumetric water content	0.06	Same as Type I rock
Permeability	2.0×10^{-9} m^2	Same as Type I rock.
Till		
Porosity	0.2	Obtained from Terzaghi et al. (1996)
Frozen thermal conductivity	3.2 W/(m · K)	Multiply thermal diffusivity determined by temperature measurements and calculated bulk heat capacity.
Thawed thermal conductivity	2.9 W/(m · K)	From frozen value minus thermal conductivity difference between thawed and frozen of water.
Frozen bulk heat capacity	2.1×10^6 J/(m^3 · K)	Calculated based on the weight fraction of the mixture in which specific heat capacity of solid grain is 790 J/(kg · K) (Farouki, 1981b)
Thawed bulk heat capacity	2.5×10^6 J/(m^3 · K)	Calculated as frozen bulk heat capacity
Volumetric water content	0.18	In-situ measurements of samples taken during construction of the test pile. This volumetric water content contains a latent heat of fusion of 1.3×10^8 kJ/m^3
Permeability	5.0×10^{-16} m^2	Converted from hydraulic conductivity of glacial till of 5.0×10^{-9} m/s (Hendry, 1982)
Type I Coarse Rock		
Porosity	0.3	Assuming as Goering and Kumar (1996)
Thermal conductivity	0.7 W/(m · K)	Calculated through Eqn. 9.1
Bulk heat capacity	1.6×10^6 J/(m^3 · K)	Calculated through Eqn. 9.2
Permeability	$9 \times 10^{-8} \rightarrow 3 \times 10^{-6}$ m^2	Varied for sensitivity analyses
Bedrock Foundation		
Porosity	0.003	Determined by Golder Associates Ltd. (1999)

Thermal conductivity	2.6→3.0 $W/(m \cdot K)$	Determined by temperature measurements of bedrock and volumetric heat capacity of granite rock
Bulk heat capacity	2.2×10^6 $J/(m^3 \cdot K)$	Based on the volumetric heat capacity of granite rock of (Farouki, 1981b)
Properties relate to Oxygen diffusion and Oxidation		
Standard coefficient of air diffusion	2.2×10^{-5} m^2/s	Tasa et al. (2006)
Tortuosity factor	0.7	Bear (1972)
Effective diffusion coefficient of oxygen in particle	2.6×10^{-9} m^2/s	Pantelis and Ritchie (1991)
Particle radius	0.0085 m	D_{50} of matrix material (< 50 mm) (Chapter 3)
Initial Sulfur concentration in Type III rock	0.05 % by weight or 13.5 kg/m^3	Assumed value

9.4 Simulation cases

9.4.1 Covered test pile

Numerical simulations were run for several cases:

- **Case 1**: This case replicates the current situation of the covered test pile at the site. Heat transfer in the pile is dominated by conduction and no heat is released due to oxidation of sulfide minerals of Type III waste rock. The simulation was run for 1067 days beginning on July 22, 2007 because this period contains continuous data prior to data gaps being observed.
- **Case 2**: In this case, Type I waste rock (Fig. 9.4) is replaced by Type I coarse waste rock (Table 9.1). Permeability and thickness of Type I waste coarse rock was changed in order to examine its effect on the convective cooling of ACC. The simulation was run for five years.
- **Case 3**: Assuming that Type III waste rock beneath the till undergoes oxidation and releases heat, the effectiveness of ACC (variation in permeability and thickness) were investigated. The goal of ACC is to reduce temperatures of the reactive Type III waste rock below threshold temperatures for sulfide oxidation (Fig. 9.1). The simulation was run for five years.

9.4.2 Type III test pile (an uncovered test pile)

Numerical simulations were performed for the uncovered test pile including:

- **Case 1**: Simulations were run for case with natural air convection for various permeabilities of Type III waste rock and with a focus to simulate temperatures that are comparable to field measurements. No wind-induced advection (forced convection) nor heat release due to oxidation of sulfide minerals were evaluated.
- **Case 2**: Wind-induced advection was considered in this case but without heat release due to oxidation of sulfide minerals. An average wind speed and a dominate wind direction for the site was selected and simulation results for various permeabilities of Type III waste rock were checked again field temperature results.
- **Case 3**: Natural air convection was considered while assuming that Type III waste rock was under-going oxidation. Furthermore, simulations were run at various permeabilities to check the system's temperature responses.
- **Case 4**: Temperature of the test pile was examined with wind-induced advection and Type III waste rock under-going oxidation. Various values of permeability of Type III waste rock were used to determine a threshold permeability showing significant changes of temperature with wind.
- **Case 5**: Simulations were run similar to case 3 but at a fix permeability of the Type III waste rock ($K = 2 \times 10^{-9}\,\mathrm{m}^2$). Moreover, various boundary conditions were assigned to the test pile to simulate potential mitigation methods to reduce internal heat generation.

9.4.3 Initial and boundary conditions

9.4.3.1 Convered test pile.

Initial conditions for temperatures of the covered test pile were field temperatures measured within the covered test pile using the thermistor cables C0W5thm and C0E5thm in July 2007 (Fig. 9.4B). Initial temperatures of bedrock foundation were obtained through bedrock thermal cables, CBC0thm01 and CBC0thm02 (Fig. 9.4C). Surface temperatures of the covered test pile and native rock are shown in Fig. 9.7A and B, and assigned to the boundaries in Fig. 9.6A. A geothermal heat flux applied to the base of the modeling domain was 0.02 $\mathrm{W/m^2}$ (thermal conductivity of bedrock is 3.0 $\mathrm{W/mK}$) (Fig. 9.6A) and it is based on temperature measurements of bedrock at the site (Fig. 9.8). Atmospheric pressure is set at 101.3 kPa at the surface and a hydrostatic pressure distribution along the depth profile was used. For case 1 and 2, temperature and pressure initial and boundary conditions are sufficient input to the model.

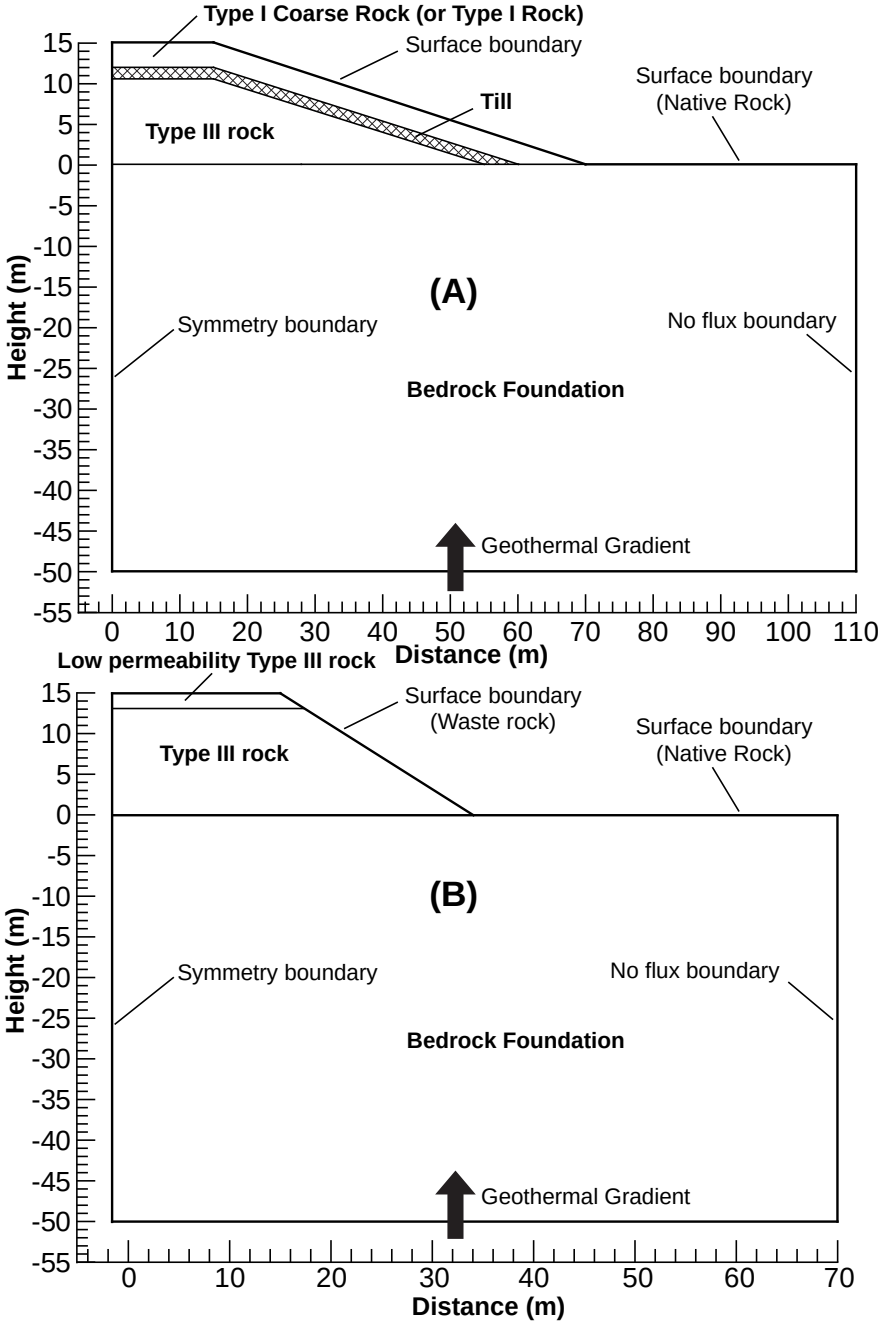

Figure 9.6: Boundary conditions of the covered test pile (A) (Type I coarse rock is substituted by Type I rock in simulation case 1) and uncovered test pile (B)

In the simulation for case 3, initial and boundary conditions for oxygen are needed; an atmospheric oxygen mass fraction of 0.23 was applied as an initial internal and a boundary condition at the surface. Initial sulfur concentration in Type III waste rock was assumed at $13.5\,\mathrm{kg/m^3}$ and it was assumed that there is no sulfur in bedrock, till and Type I coarse rock cover.

9.4.3.2 Type III test pile (uncovered test pile).

The simulation domain of the Type III test and boundary conditions are indicated in Fig. 9.6B. Initial conditions for temperatures of the Type III test pile were obtained from field temperature measurements from October 16, 2006. Surface temperatures of the Type III test pile and native rock were assigned as shown in Fig. 9.7C and B. In addition, for simulation cases accounting for heat release during oxidation, initial and boundary conditions of oxygen and sulfur concentration were similar to initial conditions assigned for the covered test pile simulations.

The modeling domains of the covered and Type III test piles were constructed using a mesh of more than 75,000 quadratic elements and the mesh is finer in the test pile compared to the bedrock. Depending on permeability of the simulated waste rock, higher permeabilities result in a finer mesh being used. Higher permeabilities results in heat transfer in a waste-rock pile dominated by convection and a fine mesh gives improved numerical stability. Furthermore, simulations were run with a decreasing mesh size until mesh-independent results were achieved.

9.4.3.3 Atmospheric wind flow associated with the Type III test pile

Wind flow simulations were run using COMSOL (Comsol, 2009) that solved for steady state, incompressible, turbulent flow around the Type III test pile. The effects of the wind on the transport of heat and oxygen below the till of the covered test pile is insignificant due to its low permeability. The turbulence model of $\mathrm{k}-\varepsilon$ was selected due to its reliability and low computational cost with "the law of the wall" applied to the surfaces of the waste-rock pile and the ground (Launder and Spalding, 1972). The computational domain was 800 x 200 m (width and height). On the left hand side of the domain, an inlet velocity was specified as an inlet boundary condition. On the right hand side of the domain, the outlet boundary condition was a constant pressure of 0 Pa and the outlet is sufficiently far downstream that the imposed boundary condition did not influence the solution. At the top of the domain, the boundary condition was no stress and the top was sufficiently above to minimize the impacts of the boundary condition on the flow. The bottom of the domain where it contains the atmosphere/Type III test pile interface was assigned a no slip boundary condition and logarithmic wall function. The density and viscosity of air used in the simulations were $1.22\,\mathrm{kg/m^3}$ and $1.77\times10^{-5}\,(\mathrm{N\cdot s})\,/\mathrm{m^2}$ which are typical values of air (Tipler, 1999).

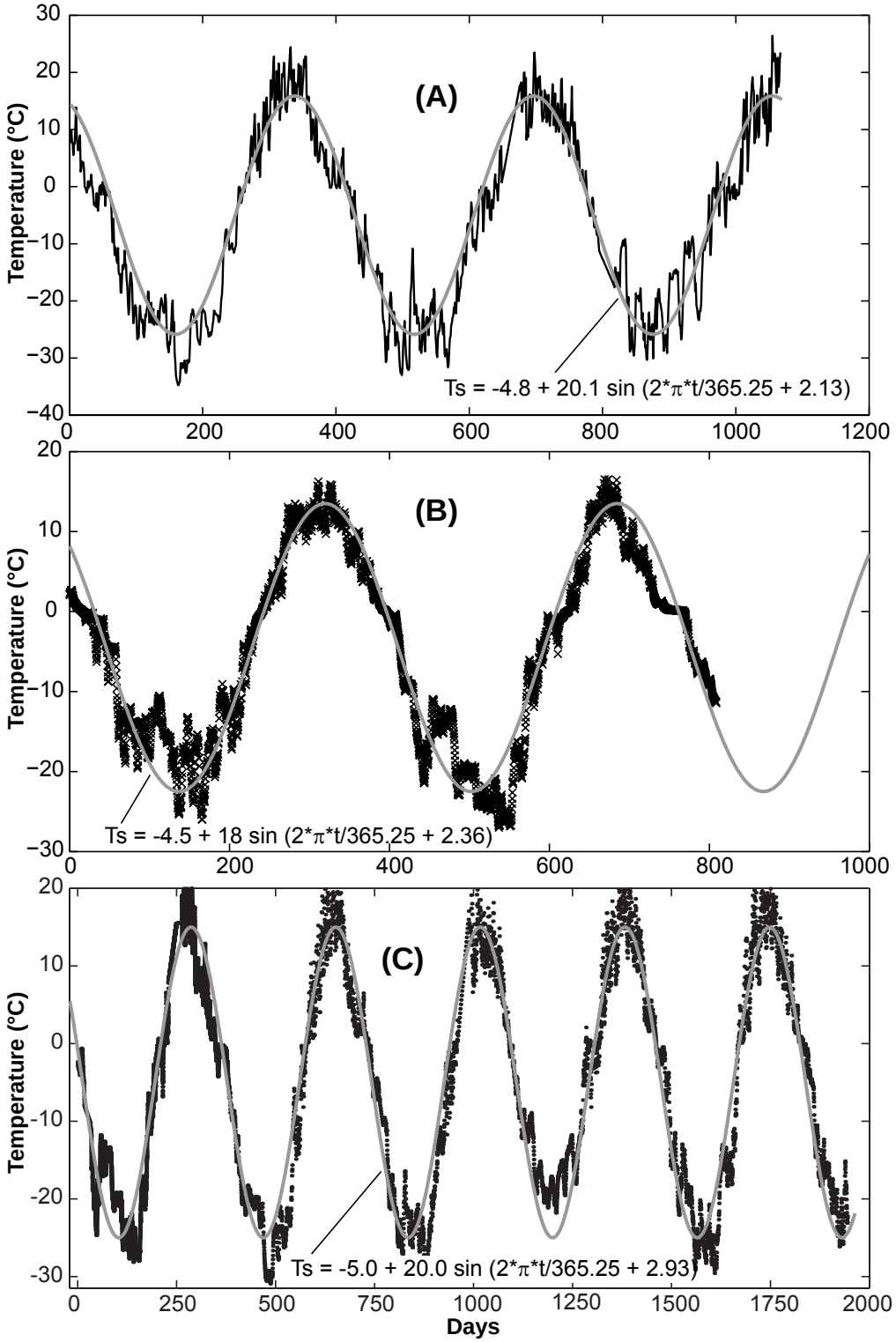

Figure 9.7: Surface temperature measured at about 5 cm below the surface of the covered test pile (A); day 0 is July 22, 2007. The surface temperature of native bedrock which is measured about 100 m from the test piles (B); day 0 is September 14, 2004. The surface temperature of Type III test pile (uncovered test pile) which is measured within 5 cm below the surface (C); day 0 is Oct. 16, 2006.

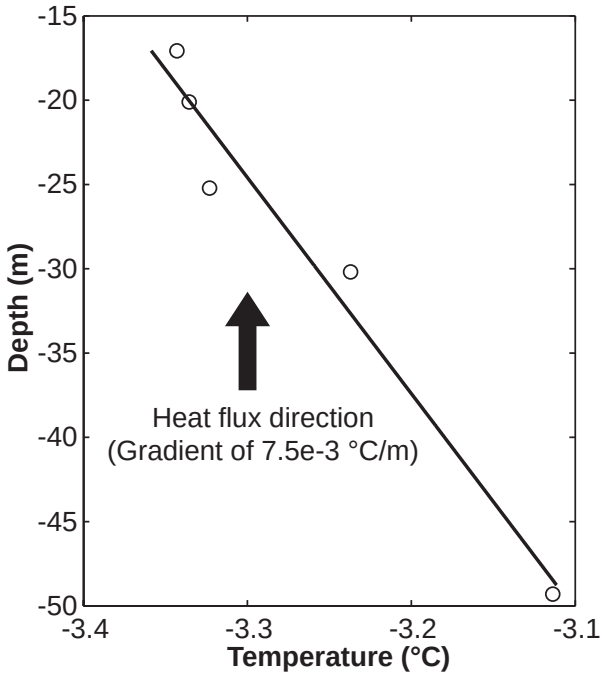

Figure 9.8: Geothermal gradient at Diavik, temperature data obtained from Hu et al. (2003)

Calculations were performed at various wind velocities from 10 to 40 km/h as these velocities are in the range of measured wind speeds at the Diavik test pile site (Amos et al., 2009a). The pressure perturbation around the test pile due to wind of 20 km/h (5.56 m/s) is shown in Fig. 9.9A. It clearly shows the regions of high velocities on the leading face near the top and the recirculation region downwind of the test pile. At a given wind velocity, pressure is higher on the wind-facing slope and the pressure becomes negative on top of the test pile where the flow is directed upward. The negative pressure levels off at a small negative value in the recirculation region downwind of the test pile (Fig. 9.9 and Fig. 9.10). Higher wind speeds induce higher pressure perturbations of both positive and negative values (Fig. 9.10).

9.5 Results and Discussion: Covered test pile

9.5.1 Case 1: Heat transfer of the covered test pile by conduction

Field temperatures measured by thermistors cables within the covered test pile indicate that conduction dominates because the low permeability layer eliminates formation of air convection currents. Numerical simulations predict quite accurately field temperatures as shown in Fig. 9.11 and it indicates the active layer is at 2 m depth which is above the till cover. This is expected since the latent heat of water in the till has stored significant heat to lower the temperatures beneath the till. However, simulation results show colder

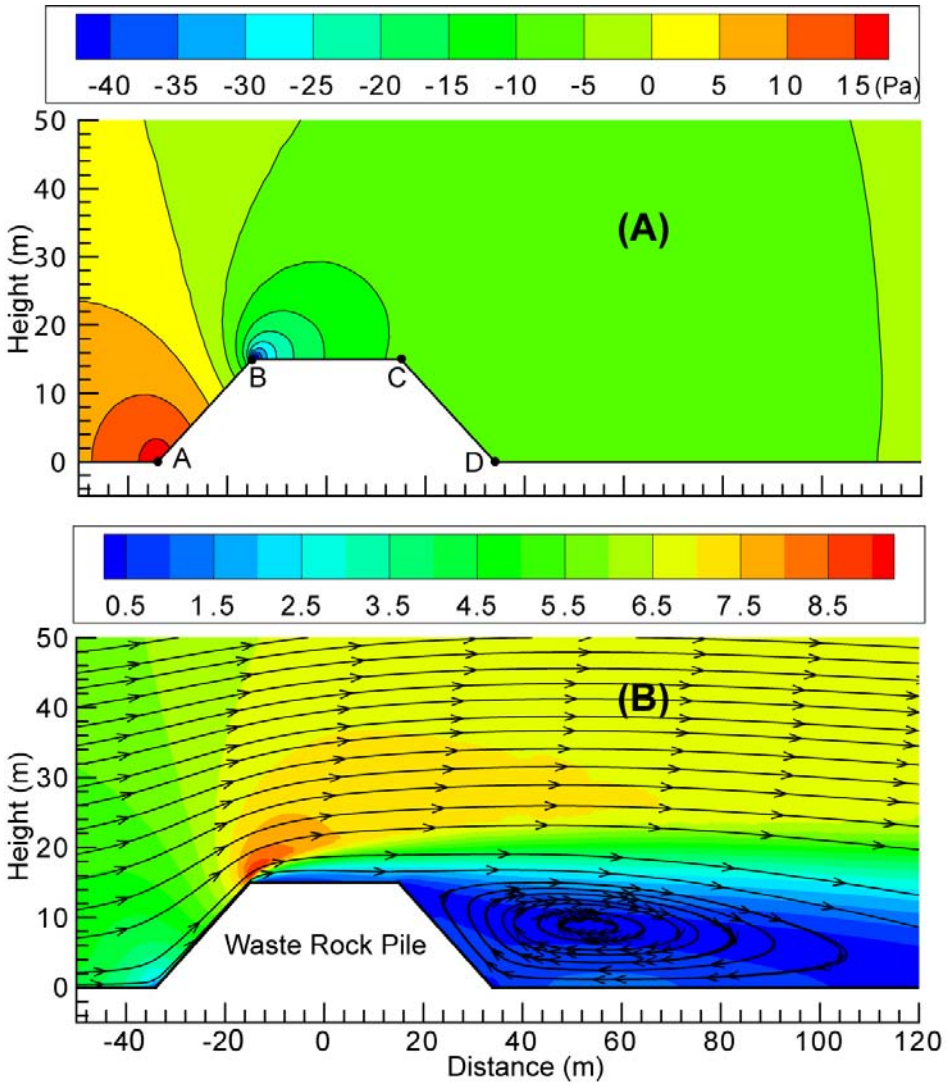

Figure 9.9: Pressure perturbation distribution (Pa) (A); streamlines and velocity distribution (in m/s) (B) around the Type III test pile at a wind speed of 20 km/h (5.56 m/s). The figure only shows the region around the test pile.

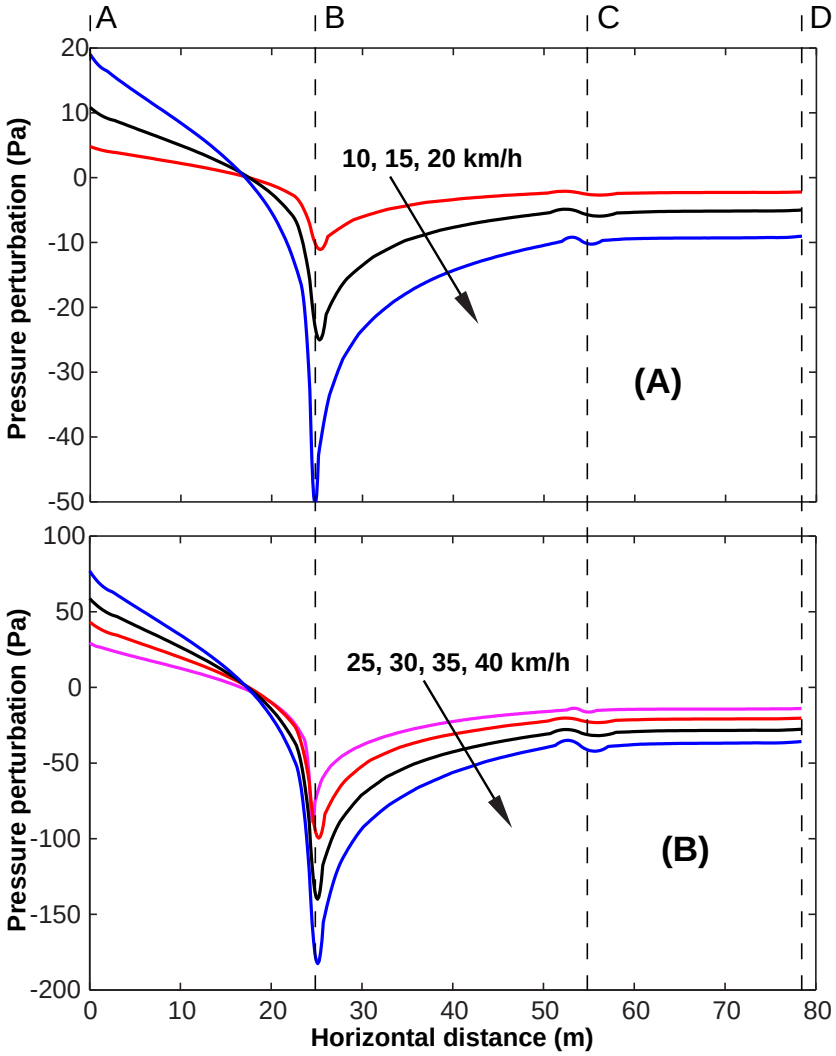

Figure 9.10: The pressure perturbation along the perimeter of Type III test pile (line ABCD in Fig. 9.9A) at velocities from 10 to 20 km/h (A) and from 25 to 40 km/h (B).

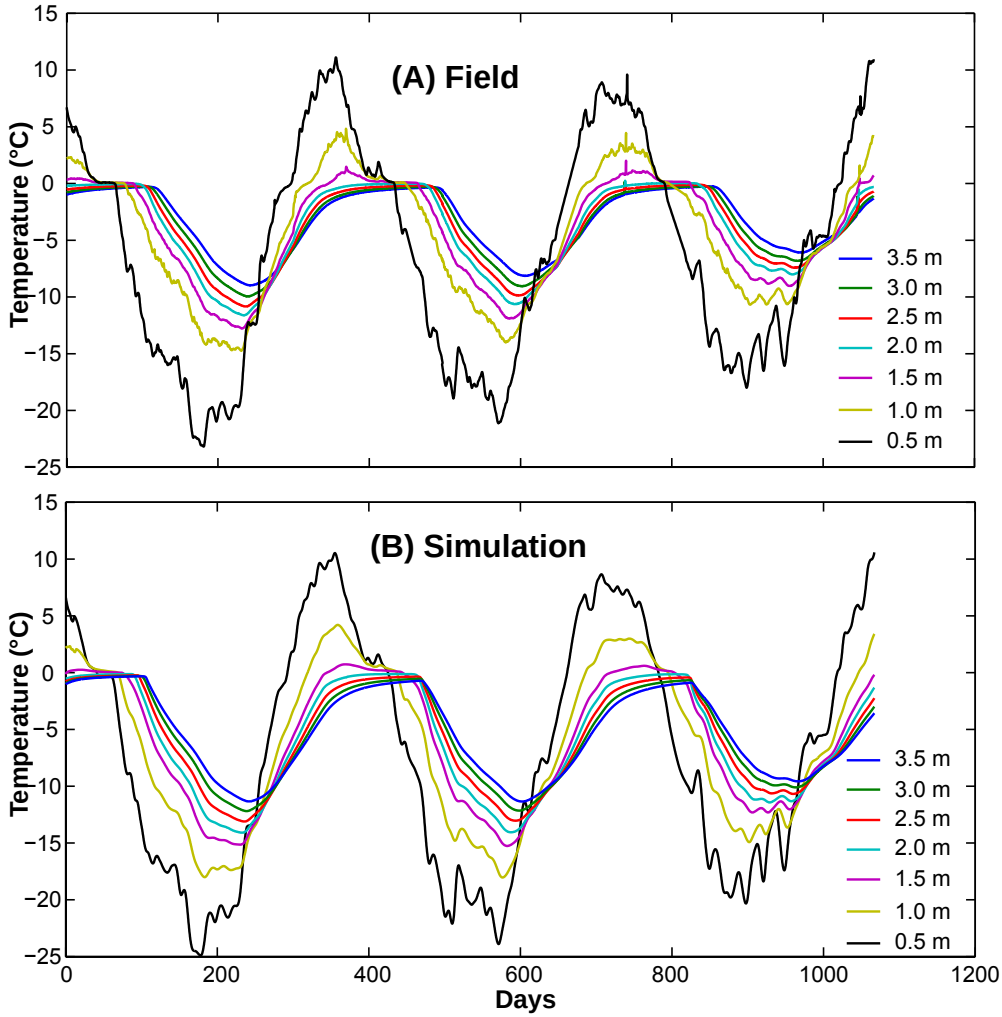

Figure 9.11: Ground temperatures at selected depths and 5 m offset of the centre between field measurements (A) and simulations (B). Day 0 is July 22, 2007.

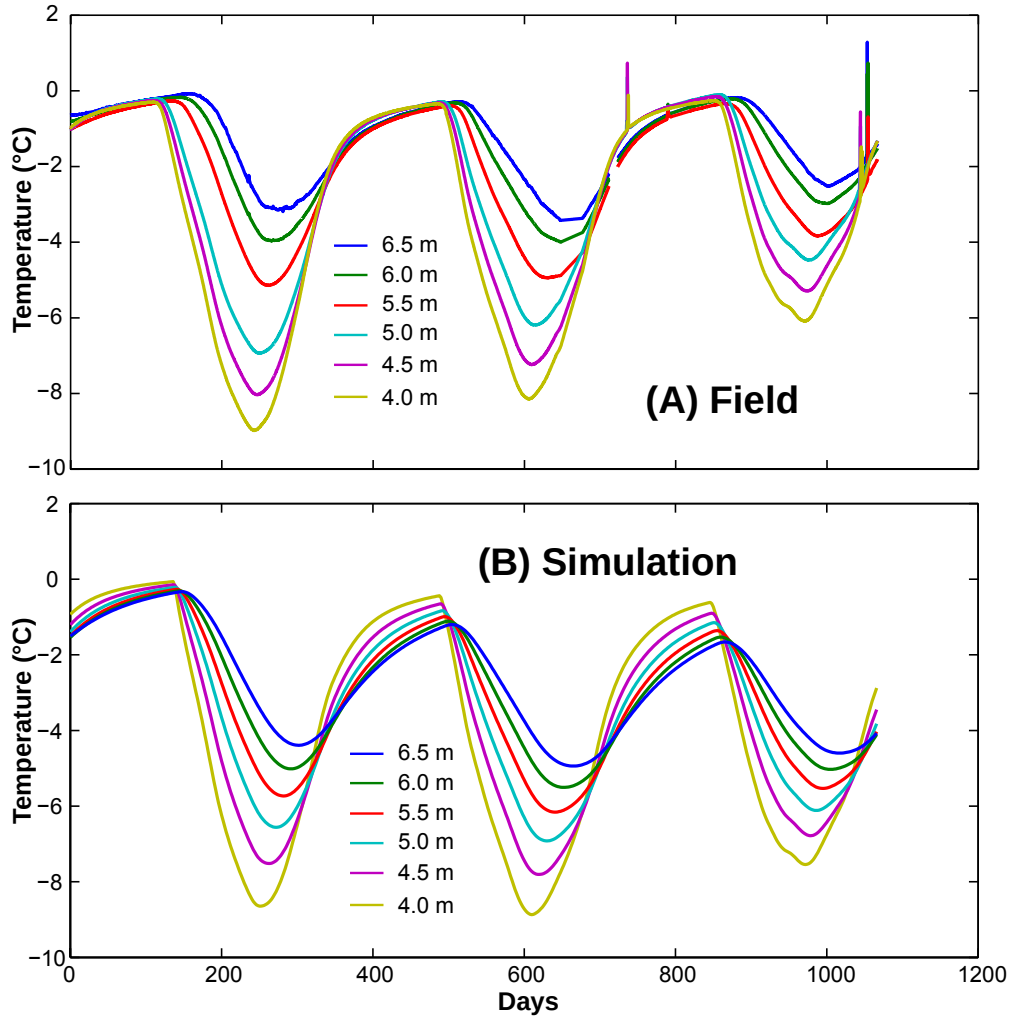

Figure 9.12: Ground temperatures at selected depths and 5 m offset of the centre below the till layer between field measurements (A) and simulations (B).

temperatures within the till compared to field measurements (Fig. 9.11). This is due to the accuracy of estimating moisture content within the till and thermal properties of the waste rock. Moreover, heat release inside the covered test from the lysimeters located at the base may have warmed these locations. Below the till, temperatures stay below 0 °C and again, simulation results were colder than field results. For example, the ground temperature at 6.5 m depth, the simulation indicates a general cooling trend whereas it is not shown in the field results (Fig. 9.12). Furthermore, temperature below the till did not fluctuated considerately compared to that of Type III test pile (the uncovered test pile) which will be presented in later sections .

The existence of the till layer constrains the active layer within the surface layer (Type I rock) even though during the summer peak surface temperatures approached 15 °C as shown in Fig. 9.13A (summer 2010). The figure shows the temperature distributions below

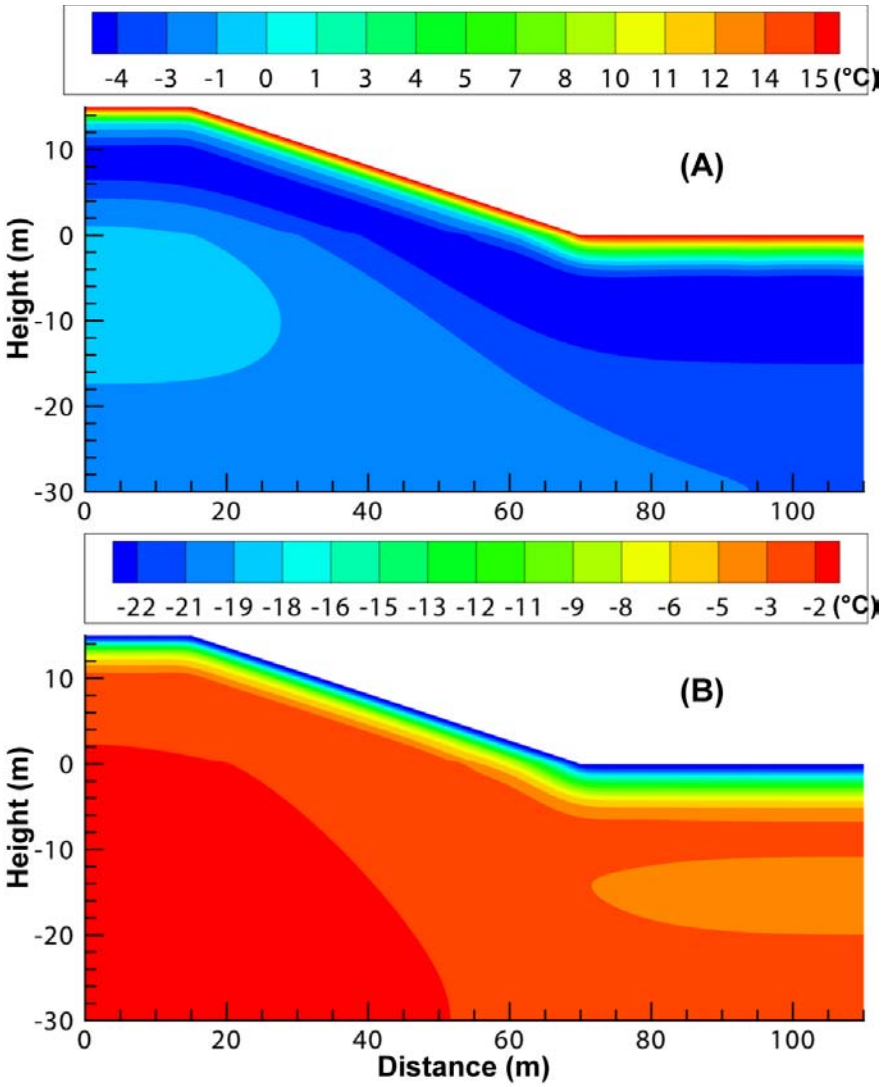

Figure 9.13: Simulation results of isotherms (in °C) of summer July 2010 (A) and winter January 2011 (B)

the till are uniform and colder regions are near the base of the till. This is also observed in 2011 winter isotherms (Fig. 9.13B). The base of the test pile and bedrock temperatures at 7 m depth below the base of the test pile were warming during the first three-year period (between July 2007 and July 2010) (Fig. 9.14). Similarly, the temperature at the base (0 m depth) was about 0 °C and it started to decrease after 1000 days (Fig. 9.14). The initial warming of the bedrock temperatures is because the test pile was constructed during the summer and waste rock was placed at a temperature of around 5 °C. Therefore, the temperature from the waste rock was transferred into the bedrock warming it a small amount. The bedrock temperatures leveled off after 1000 days. Eventually, the bedrock temperatures will cool down as the test pile continues to cool.

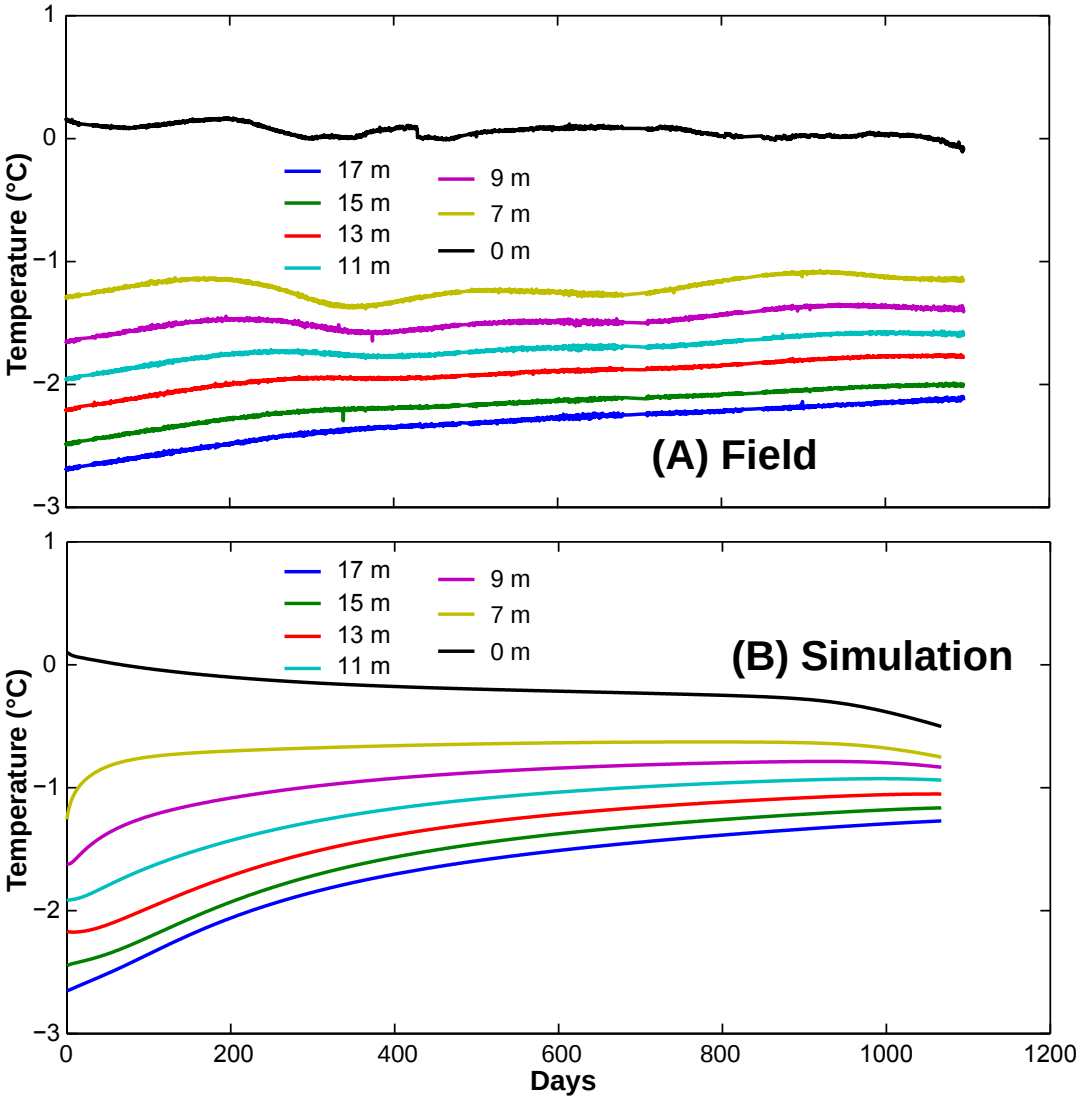

Figure 9.14: Bedrock temperatures below the base of the covered test pile, field CBC0thm02 (A) and simulation (B), numbers in legend indicate depth below the base

9.5.2 Case 2: Air convective cover (ACC) for the covered test pile

9.5.2.1 Results of a 3-m coarse Type I cover

In this section the Type I waste rock was replaced by the Type I coarse rock (the air convection layer) to form an ACC. The ACC is expected to decrease temperatures below the till and maintain them below 0 °C year round (Fig. 9.15, Fig. 9.16 and Fig. 9.17). As the permeability of the air convection layer increases temperatures decrease as shown in Fig. 9.15, Fig. 9.16 and Fig. 9.17. Ground temperatures reduce during both summer and winter when the permeability varies between $K = 2 \times 10^{-7}$ and 8×10^{-7} m^2. However, the differences are indistinguishable between $K = 8 \times 10^{-7}$ and 1×10^{-6} m^2 since above a threshold permeability, increases in permeability provides small additional cooling effects for a given air convection layer thickness. Therefore, for a given thickness there exists a threshold permeability that provides an optimum configuration when used as the ACC.

At $K = 2 \times 10^{-7}$m^2, ground temperatures are between -4 and -6 °C in both summer and winter (Fig. 9.15). Whereas at $K = 8 \times 10^{-7}$ and 1×10^{-6} m^2, they decrease to between -6 and -10 °C (Fig. 9.16 and Fig. 9.17). Similarly, the bedrock temperatures below the base are colder for the case $K = 8 \times 10^{-7}$ and 1×10^{-6} m^2 than for the case $K = 2 \times 10^{-7}$m^2. The insert in Fig. 9.15, Fig. 9.16 and Fig. 9.17 show the rapid cooling of the air convection layer during winter as high permeabilities enhance convective cooling effects. This cold bottom then cools the till and waste rock beneath. However, the blow-up in Fig. 9.15 indicates smaller cooling compared to Fig. 9.16 and Fig. 9.17.

9.5.2.2 Determination of optimum thickness and permeability of Type I coarse rock in ACC (Case 2)

It is important to determine the optimum thickness of ACC layer thickness for a given permeability to assist with its economical selection. This is even more significant when the ACC is constructed in permafrost and remote regions where the cost of material, transportation, and worker is significantly higher than other regions. Even if the needed materials are available at the site, the cost of excavation and transportation can be expensive. As a result, it is important to obtain the optimum thickness and permeability of ACC to achieve the ultimate goal of cooling and maintaining the underlaid waste rock below 0 °C. In this section, the thickness of the till layer was held constant at 1.5 m and the goal is to determine the optimum thickness and permeability of the air convection layer (the Type I coarse rock) (Fig. 9.2). Freezing and thawing indices (I_f and I_t calculated via Eqn. 9.3 and Eqn. 9.4) were used as a criteria to choose the optimum thickness and permeability of the air convection layer because they correlate well with the active layer in the ground and are common in permafrost engineering (Lunardini, 1981; Andersland and Ladanyi, 2004).

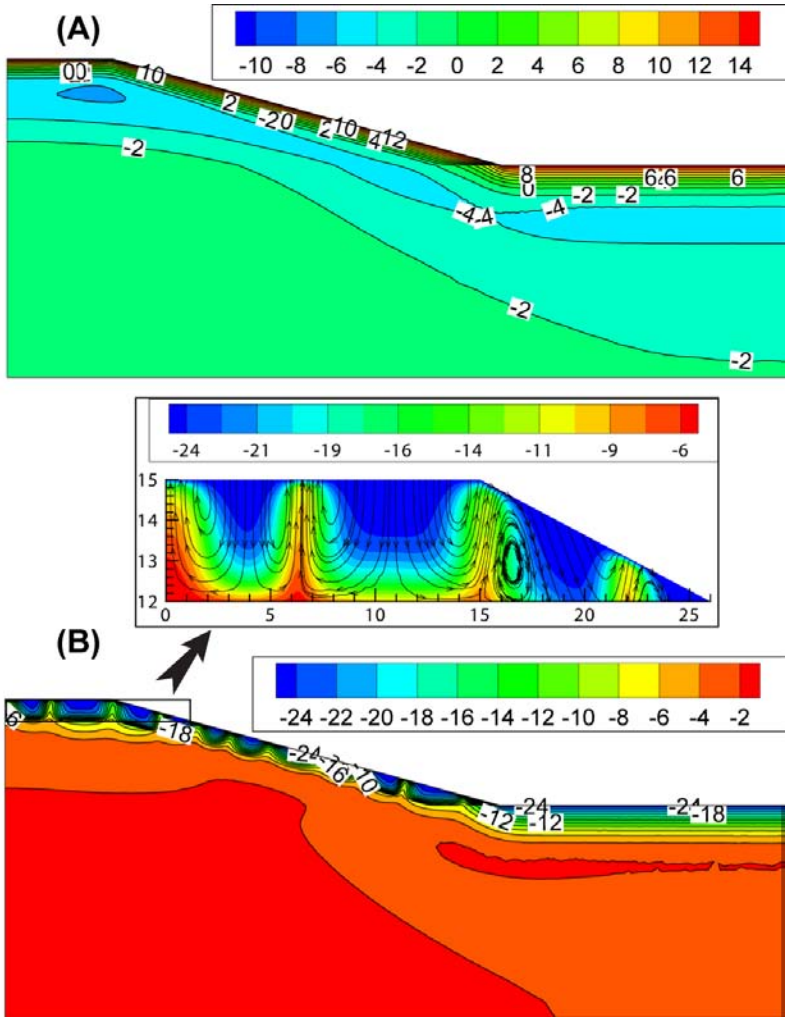

Figure 9.15: Isotherms (in °C) of the covered test pile with ACC thickness of 3 m with permeability $K = 2 \times 10^{-7}$ m^2 of the 4^{th} summer (A) and 4^{th} winter (B). The blow-up shows isotherms and streamlines (convective cells) in the ACC layer.

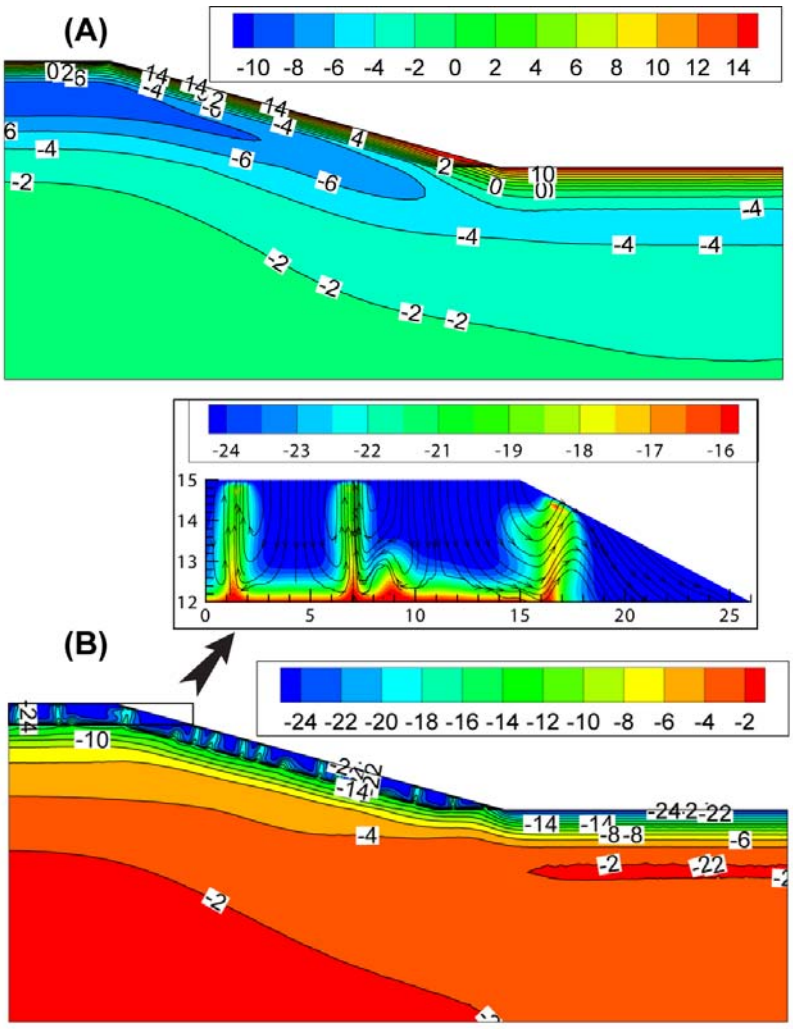

Figure 9.16: Isotherms (in °C) of the covered test pile with ACC with permeability $K = 8 \times 10^{-7}\,\mathrm{m}^2$ of the 4^{th} summer (A) and 4^{th} winter (B). The blow-up shows isotherms and streamlines (convective cells) in the ACC layer.

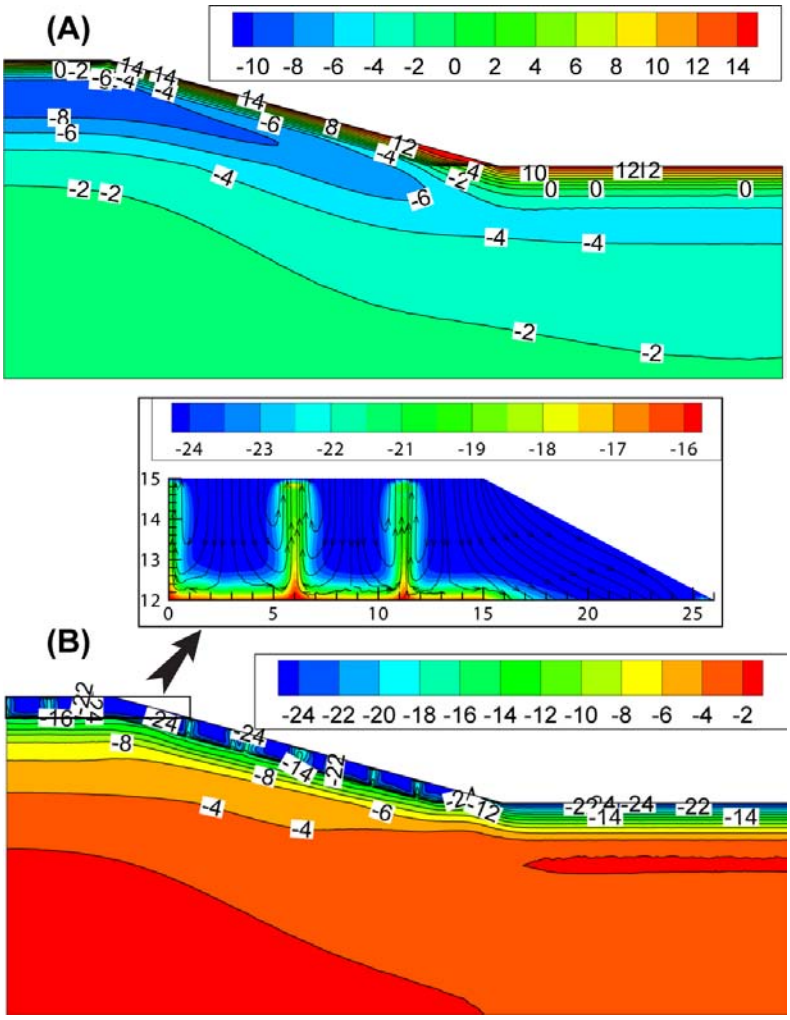

Figure 9.17: Isotherms (in °C) of the covered test pile with ACC with permeability $K = 1 \times 10^{-6}\,\mathrm{m}^2$ of the 4^{th} summer (A) and 4^{th} winter (B). The blow-up shows isotherms and streamlines (convective cells) in the ACC layer.

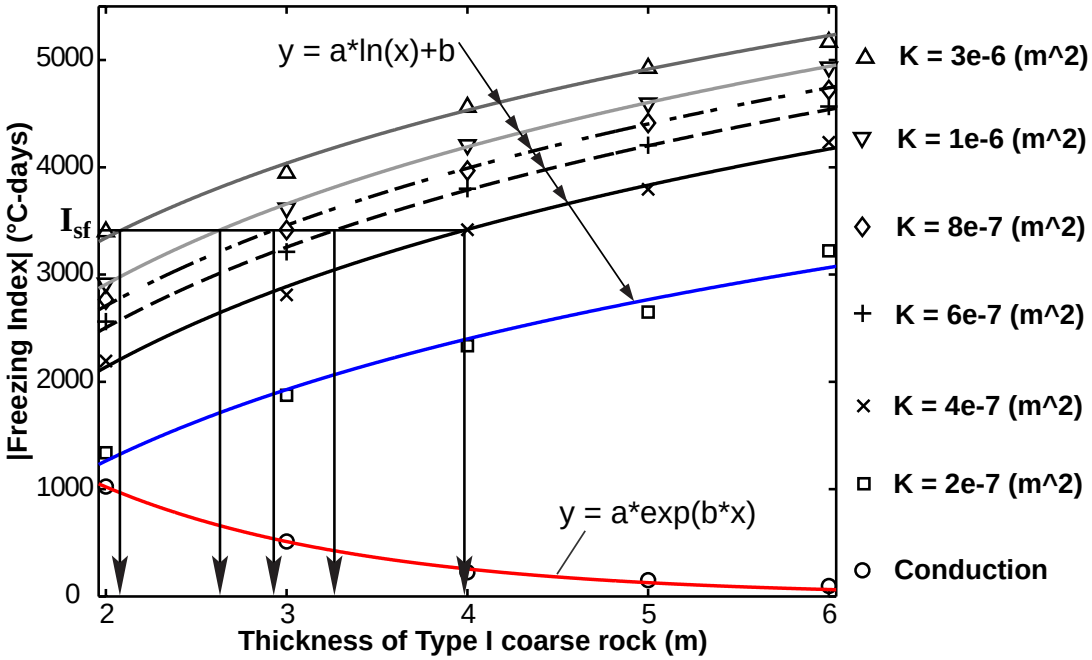

Figure 9.18: Freezing index (°C-days) of ground temperatures at the base of Type I coarse rock versus thickness at different permeabilities between days 1000 and 1365 (the third year of simulation)

$$I_f = \int_{1000}^{1365} |T_{avg}| \mathrm{d}t\,,\ T_{avg} < 0\,^{\circ}\mathrm{C} \tag{9.3}$$

$$I_t = \int_{1000}^{1365} T_{avg} \mathrm{d}t\,,\ T_{avg} \geq 0\,^{\circ}\mathrm{C} \tag{9.4}$$

As the thickness of the Type I coarse rock increases at a given permeability, the freezing index, I_f (°C-days), (calculated using Eqn. 9.3) at the base of the Type I coarse rock with an average temperature, T_{avg}, increases with the layer thickness (Fig. 9.18A); the larger I_f the cooler the base of the Type I coarse rock. However, for the conduction case I_f decreases with increasing thickness as it is expected (Fig. 9.18A). The freezing index of the surface temperature, I_{sf} (°C-days), used in the simulations was $I_{sf} = 3324.7$ (°C-days). For the conduction case, I_f is less than I_{sf} as the thickness increases (Fig. 9.18A). In contrast, in a convection case, at $K = 4 \times 10^{-7}$ m^2 I_f surpasses I_{sf} at a thickness of 4 m. Furthermore for all convection cases, the thawing index of T_{avg} is 0 °C-days except the case $K = 2 \times 10^{-7}$ m^2 and thickness of 2 m that has $I_t = 3.7$ (°C-days) (Eqn. 9.4). Therefore, the ACC is capable of maintaining freezing indices at its base colder than required to maintain permafrost at the site.

If the design criteria is to determine the air-convection-layer thickness and its permeability to have $I_{sf} = I_f$, Fig. 9.19 can be used. It shows that if the permeability increases one

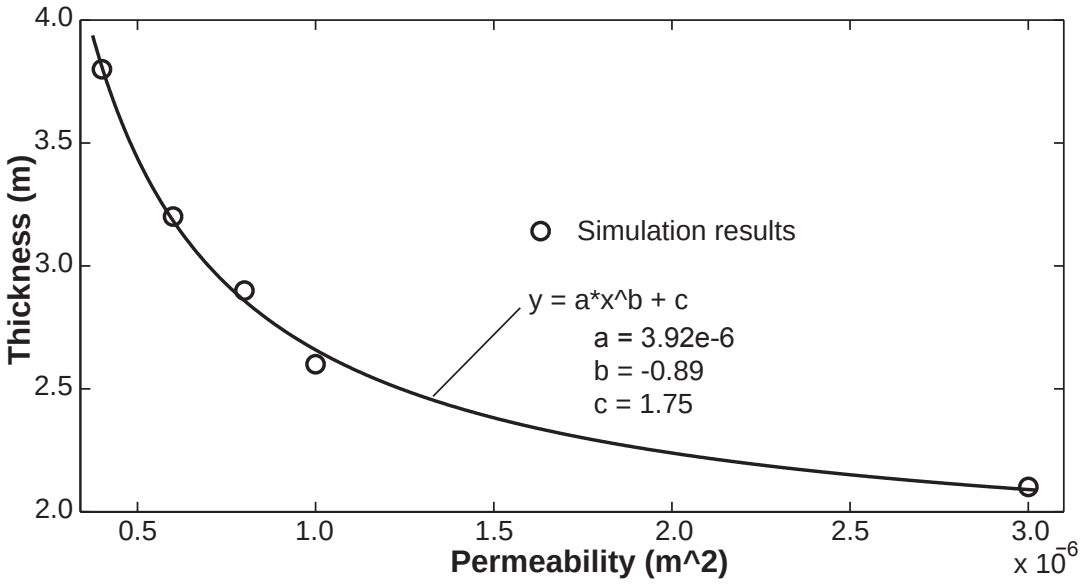

Figure 9.19: The air-convection-layer thickness versus permeability with $I_f = I_{sf} =$ 3324.7 (°C-days). Data of this figure was interpolated using Fig. 9.18.

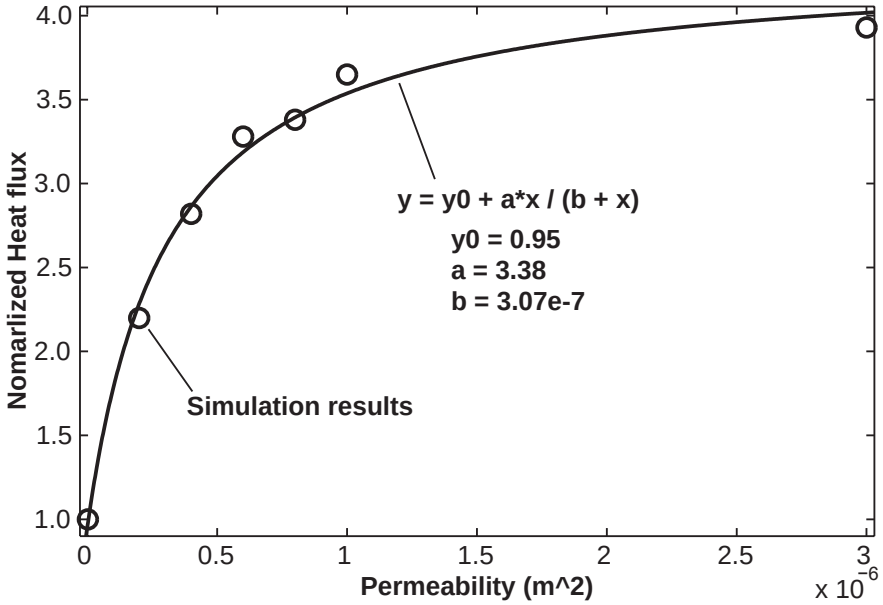

Figure 9.20: Normalized heat flux to conduction of the first year across the till versus permeability of ACC of 3 m

order of magnitude (from 3×10^{-7} to $3 \times 10^{-6}\,m^2$), the air-convection-layer thickness decreases by about half. Furthermore, at a given thickness of air convection layer, the heat flux into the till increases as the permeability of ACC increases (Fig. 9.20). At $K \leq 8 \times 10^{-7}\,m^2$, the change rate of the heat flux is large as the permeability increases; however, at $K > 8 \times 10^{-7}\,m^2$ the increasing rate is not significant. For example, at $K = 8 \times 10^{-7}\,m^2$, the normalized heat flux, which is the ratio between total heat flux and heat flux by conduction, is about 3.5 whereas at $K = 3 \times 10^{-6}\,m^2$ it approaches 4 (Fig. 9.20).

At a given thickness of the air convection layer, the Mean Annual Ground Temperature (MAGT) at 5 m depth below the bottom of the till layer decreases as permeability increases (Fig. 9.21). However, as permeability increases the rate decrease of MAGT is smaller and approaching an optimum MAGT which is 90 % of the MAGT at $K = 3 \times 10^{-6}\,m^2$ (Fig. 9.21). A permeability at which MAGT is at the optimum MAGT is called the optimum permeability. Furthermore, at smaller thicknesses of the air convection layer, larger permeabilities are required to get the optimum MAGT. For example, at $H = 2$ m the optimum permeability is $K = 1.5 \times 10^{-6}\,m^2$ (Fig. 9.21 A1 and A2), however at $H = 6$ m the optimum permeability is $K = 4 \times 10^{-7}\,m^2$ (Fig. 9.21 E1 and E2).

Now let us assume that the air-convection-layer thickness is $H = 3$ m and according to Fig. 9.19 the optimum permeability is about $7 \times 10^{-7}\,m^2$. Fig. 9.21 C1 and C2 suggest that the optimum permeability should be $8 \times 10^{-7}\,m^2$. Fig. 9.22 indicates that for only conduction in the 3-m air convection layer, the ground temperature at 5 m depth below the bottom of the till stays around 0 °C during the third year of the simulation period. Whereas at higher permeabilities, natural air convection within the air convection layer results in colder ground temperatures.

9.5.3 Case 3: ACC for an active heat-generation covered test pile

The above sections, the results of ACC for non-heat-generating waste rock were presented. For oxidation of sulfide minerals, heat is released and causes an increase in ground temperatures at oxidation locations and spreads to surrounding areas. This temperature increase can melt the permafrost foundation and therefore it would increase the stability risk of a rock pile. Melting permafrost lengthens seepage paths that will carry polluted water from the rock pile into ground water, lakes or rivers. At present, ACC was introduced to lower the internal temperatures of the Type III waste rock below the threshold temperatures of enhanced oxidation of sulfide minerals (Fig. 9.1). The simulations were run for two conditions of the till: the first one in which the till is at 0 % saturation (dry till) and this condition simulates a low precipitation and high evaporation scenarios. The second one in which the till could maintain at a high degree of saturation which is about 90 %.

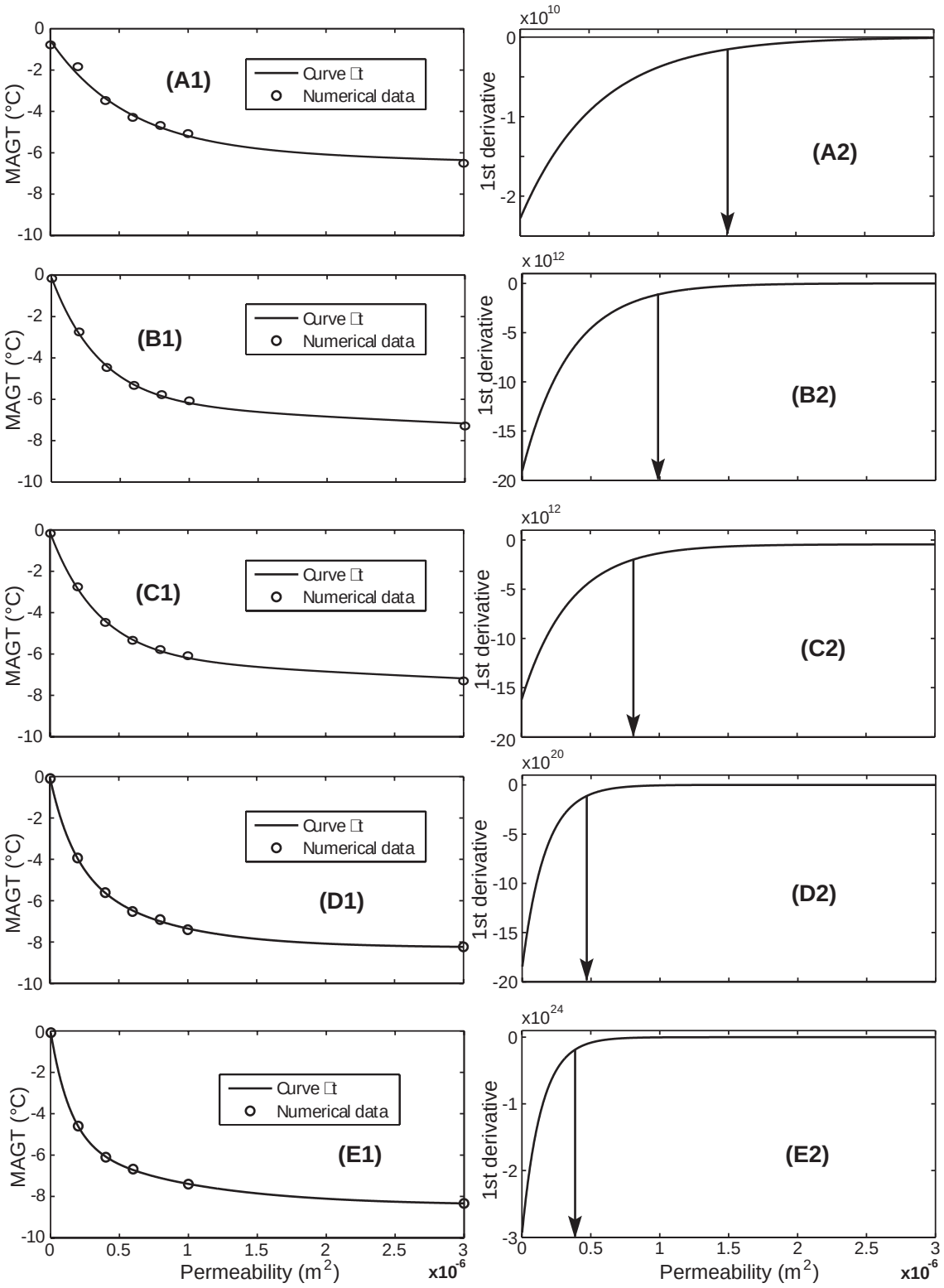

Figure 9.21: MAGT between days 1000 and 1365 at 5 m depth at the centre line below the bottom of the till layer and its 1^{st} derivative versus permeability of different air-convection-layer thickness, $H = 2$ m (A1 and A2), $H = 3$ m (B1 and B2), $H = 4$ m (C1 and C2), $H = 5$ m (D1 and D2), $H = 6$ m (E1 and E2)

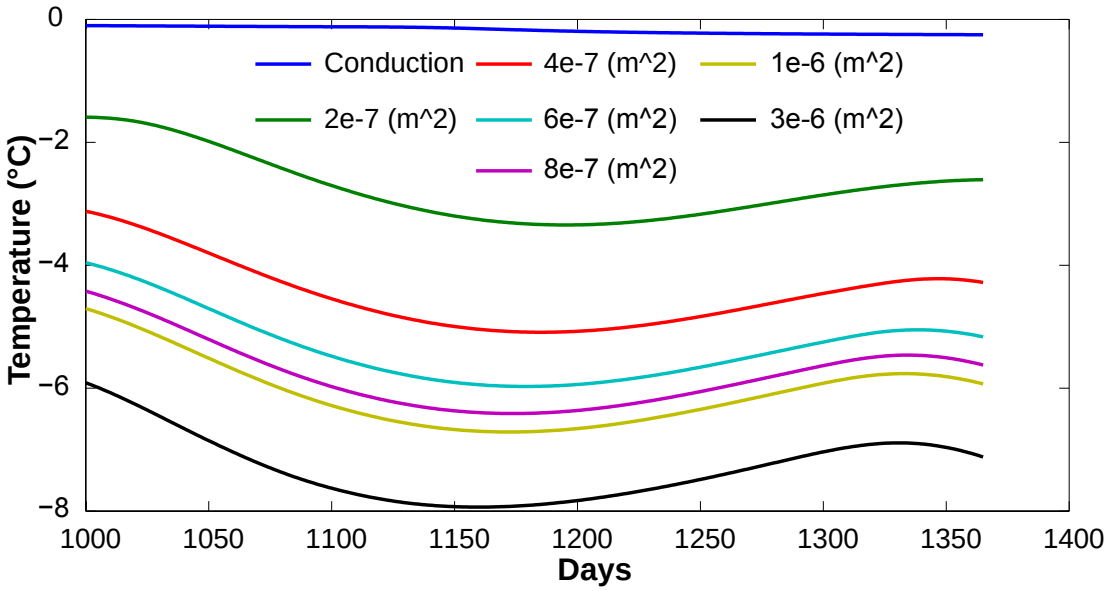

Figure 9.22: Ground temperature at 5 m depth below the bottom of the till at the centre line at various permeabilities for air convection layer thickness of 3 m

9.5.3.1 Thermal evolution

At 0 % saturation (dry till), oxygen diffusion through the till was adequate to retain a high oxidation rate of sulfide minerals and the heat release would increase temperatures (Fig. 9.23A1, B1 and C1). Even though the air convection layer has a high permeability of 4×10^{-7} m^2, the natural air convection could not maintain ground temperatures of the Type III rock below 0 °C (Fig. 9.23C1). Fig. 9.23A1, B1 and C1 also show the circulation of warm air (convective cells) initiated at the oxidation locations and these convective cells spread heat and oxygen to the surrounding-internal regions. These convective currents can be strong as the permeability of the Type III waste rock is high.

The heat release thaws the permafrost foundation beneath the test pile to 12 m (Fig. 9.23A1, B1 and C1). However, the width of the thawed zone at $K = 4 \times 10^{-7}$ m^2 is smaller (Fig. 9.23C1). In cases where the till was set at 90 % of saturation, ground temperatures below the till are always below 0 °C. This occurs even for permeabilities where conduction dominates in the air convection layer (Fig. 9.23A2 and B2). Likewise, at $K = 4 \times 10^{-7}$ m^2 ground temperatures are colder than those of conduction cases (Fig. 9.23C2).

At $K \geq 6 \times 10^{-7}$ m^2, the convective cooling of the air convection layer maintains the temperatures beneath the till below 0 °C despite the 0 % saturation of the till (Fig. 9.24). Nevertheless, in cases where the till is at 90 % saturation, ground temperatures are colder than those of 0 % saturation for given permeability of the air convection layer.

9.5.3.2 Oxygen concentration, sulfur mass fraction and oxidation rate

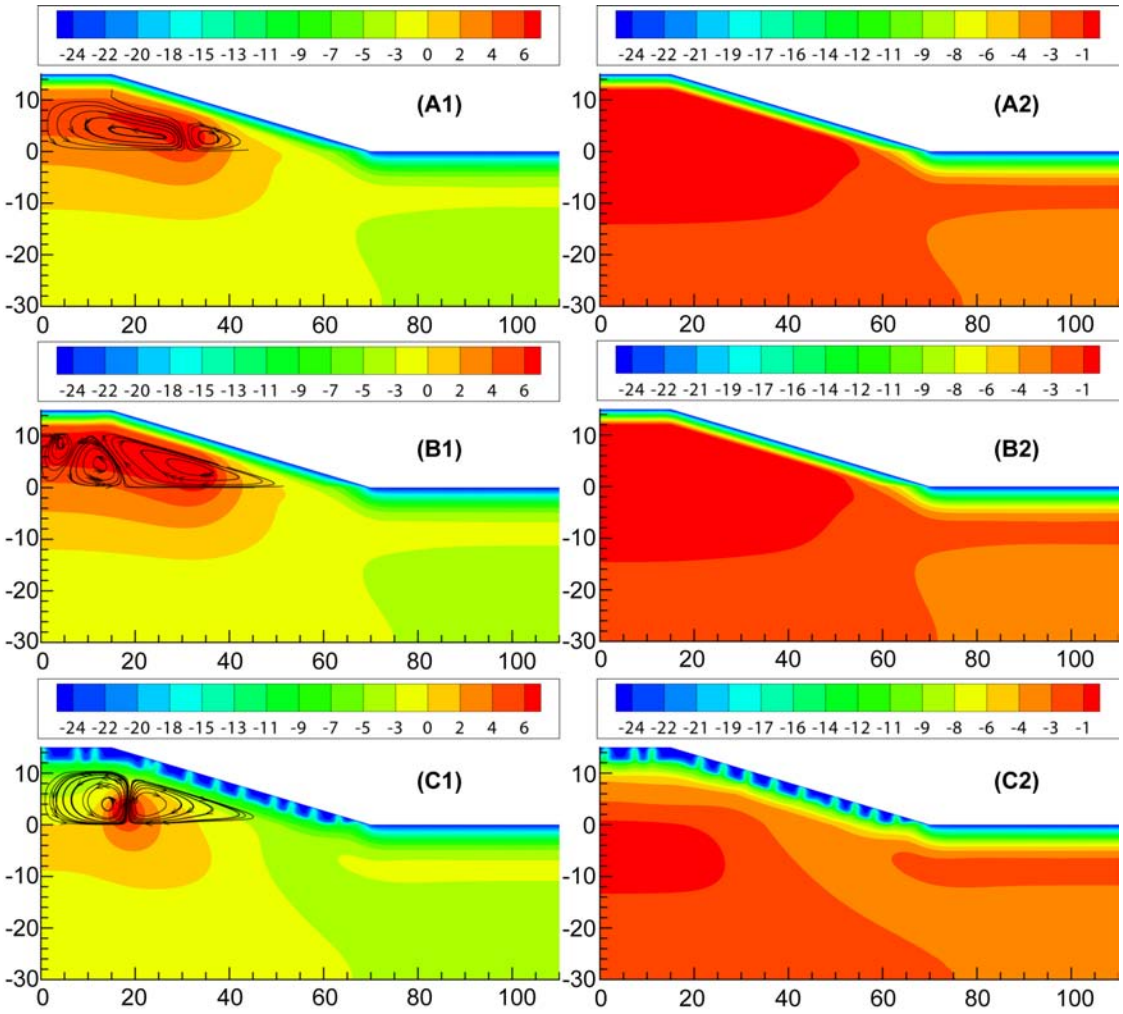

Figure 9.23: Isotherms (in °C) of the covered test pile; the air-convection-layer thickness of 3 m and low permeability of 2×10^{-9} m^2 (A1 and A2) , 5×10^{-8} m^2 (B1 and B2), 4×10^{-7} m^2 (C1 and C2) of the fourth winter (or 1345 days). The left figures are the scenarios of 0 % saturation of till and the right figures for 90 % saturation till.

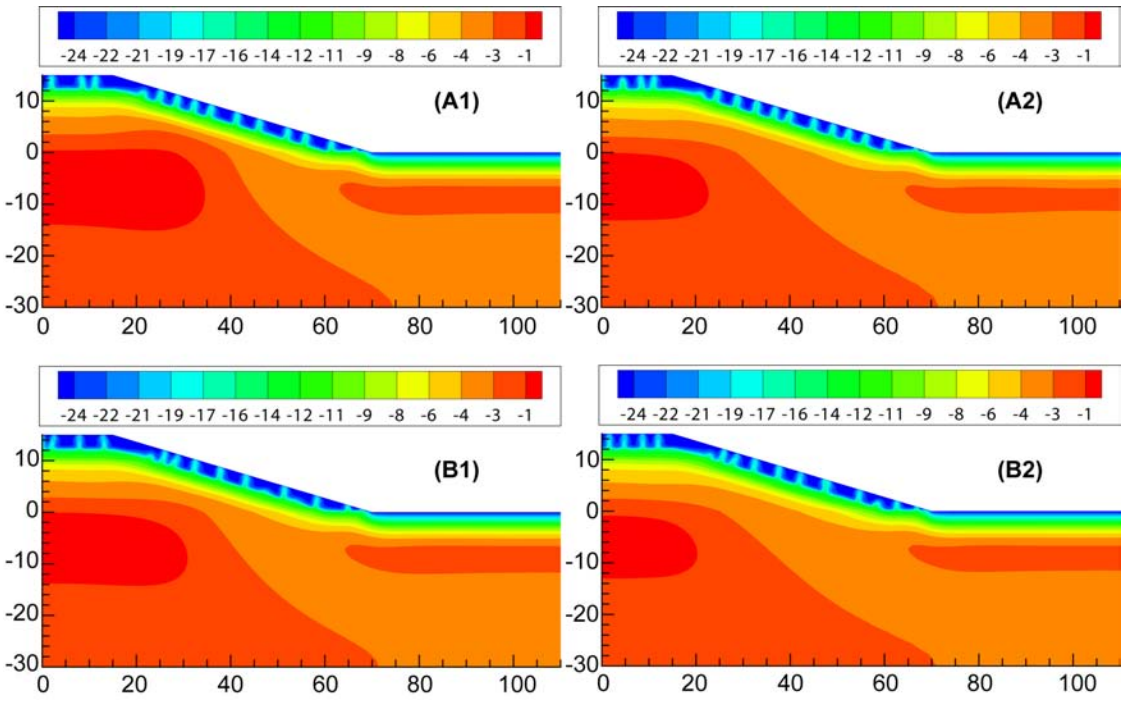

Figure 9.24: Isotherms (in °C) of the covered test pile; the air-convection-layer thickness of 3 m and permeability of 6×10^{-7} m^2 (A1 and A2) and 8×10^{-7} m^2 (B1 and B2) of the fourth winter (or 1345 days). The left figures are the scenarios of 0 % saturation of till and the right figures for 90 % saturation till.

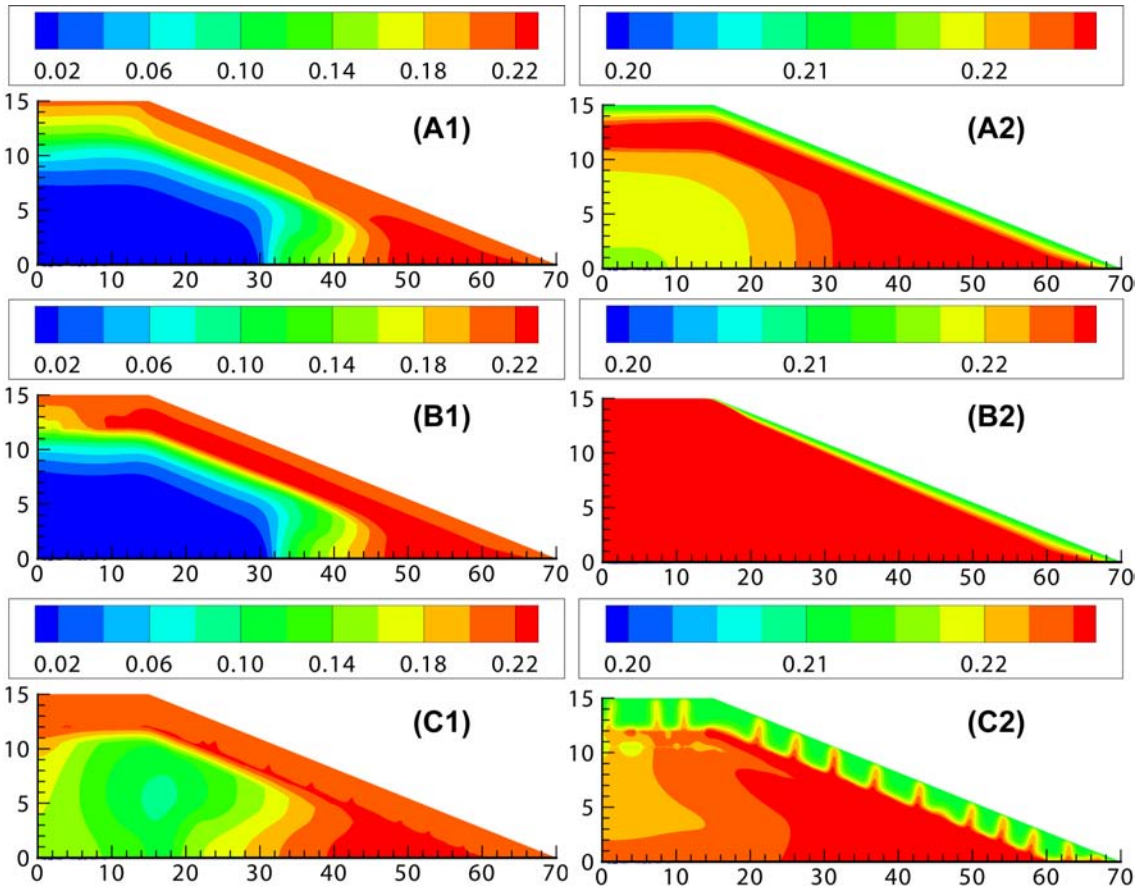

Figure 9.25: Oxygen concentration (mass fraction); the air-convection-layer thickness of 3 m and permeability of the ACC layer of 2×10^{-9} m^2 (A1 and A2) , 5×10^{-8} m^2 (B1 and B2), 4×10^{-7} m^2 (C1 and C2) of the fourth winter (or 1345 days). The left figures are the scenarios of 0 % saturation of till and the right figures for 90 % saturation till.

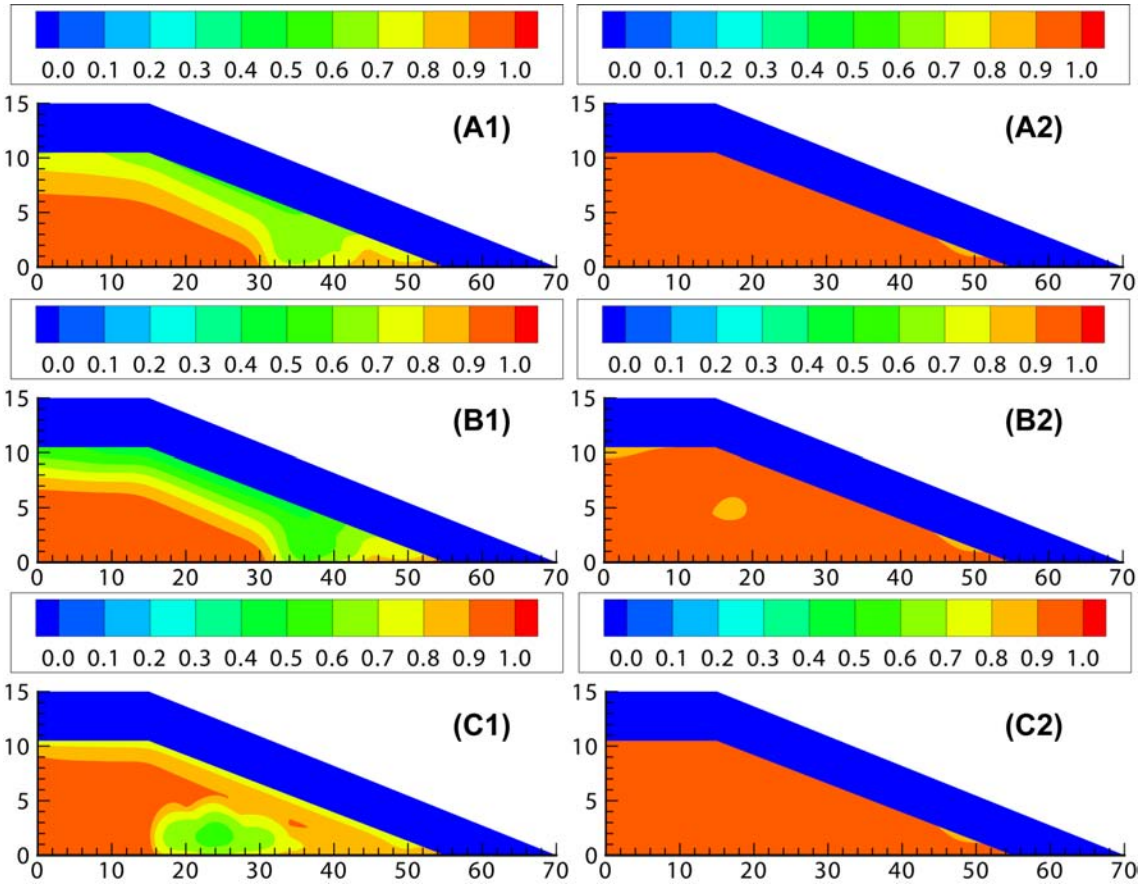

Figure 9.26: Sulfur mass fraction; the air-convection-layer thickness of 3 m and permeability of 2×10^{-9} m^2 (A1 and A2) , 5×10^{-8} m^2 (B1 and B2), 4×10^{-7} m^2(C1 and C2) of the fourth winter (or 1345 days). The left figures are the scenarios of 0 % saturation till and the right figures have 90 % saturation till.

Oxygen concentration

At 0 % saturation, oxygen diffusion through the till was sufficient to maintain a high oxidation rate however oxygen also was consumed at a faster rate. As a result, the oxygen concentrations at the oxidation locations decreases below that of atmospheric air (e.g. mass fraction about 23 %) as shown in Fig. 9.25A1, B1 and C1. Furthermore, the high depletion of O_2 concentration (about 1 %) is widespread for all areas beneath the till for $K = 2 \times 10^{-9}$ and 5×10^{-8} m^2 (Fig. 9.25A1 and B1). However, at $K = 4 \times 10^{-7}$ m^2 (Fig. 9.25C1) the depletion area is narrower and O_2 concentrations are higher than those shown in Fig. 9.25A1 and B1. In contrast at 90 % saturation, the till reduced the oxygen supply for oxidation and therefore the heat release is low. Moreover, the ground temperatures beneath the till are below 0 °C. As a result O_2 concentrations are near or equal to atmospheric air (Fig. 9.25A2, B2 and C2).

Sulfur mass fraction

At 0 % saturation till, oxidation was initiated in regions near the till where the oxygen supply is high. Therefore, the sulfur mass fractions of these regions are low compared to other areas which are around 50 % meaning that about 50 % of the sulfur has been oxidized (Fig. 9.26A1 and B1) at $K = 2 \times 10^{-9}$ and 5×10^{-8} m^2. Whereas in the case $K = 4 \times 10^{-7}$ m^2 the convective cooling reduces temperatures within the regions near the till and therefore oxidation regions move toward the pile base where ground temperatures remain above threshold temperatures for oxidation (Fig. 9.26C1). With the till saturated at 90 %, oxidation is very low and the sulfur mass fraction stays near 1 (Fig. 9.26A2, B2 and C2).

Oxidation rate

Changes in sulfur and oxygen concentration are good indications of heat production within the depleted zones. Fig. 9.27A, B and C show that the average oxidation rate is in the order of 10^{-8} $kg(S)/(m^3 \cdot s)$ and oxygen needs to be supplied by diffusion through the till cover at a rate of 10^{-7} $kg(O_2)/(m^2 \cdot s)$. The corresponding heat production at a consumption rate of 2.3×10^{-8} $kg(S)/(m^3 \cdot s)$ is 1.6×10^7 $J/(m^3 \cdot a)$ (Fig. 9.27B); These values were averaged throughout the Type III rock beneath the till cover. This heat production causes increased waste rock temperature of about 7.4 $°C/(m^3 \cdot a)$ at volumetric heat capacity of 2.1×10^6 $J/(m^3 \cdot K)$and this heat thaws permafrost beneath the test pile. After 1466 days, about 21.6 % of the sulfur has been oxidized and at this rate, it would take about 20 years to completely deplete the sulfur (initial concentration of 13.5 kg/m^3). At $K \geq 6 \times 10^{-7}$ m^2, the convective cooling from the ACC has effectively cooled the waste rock temperatures below the threshold temperatures for oxidation and oxidation is eliminated after 780 and 530 days for $K = 6 \times 10^{-7}$ and 8×10^{-7} m^2, respectively (Fig. 9.27D and E).

For till saturated at 90 %, the mass flux of oxygen and the oxidation rate reduces significantly. In fact, oxygen flow through the till is in the order of 10^{-9} $kg(O_2)/(m^2 \cdot s)$ and oxidation rate is in the order of 10^{-9} $kg(S)/(m^3 \cdot s)$ (Fig. 9.28). At an oxidation rate of 3.1×10^{-9} $kg(S)/(m^3 \cdot s)$(Fig. 9.28B) the heat production is 2.1×10^6 $J/(m^3 \cdot a)$. This heat release causes to increase waste rock temperature about 1.0 $°C/(m^3 \cdot a)$ which is small.

Assuming that due to high evaporation and low precipitation, the till is 50 % saturated and using the ACC with $K = 4 \times 10^{-7}$ m^2 within the air convection layer (Fig. 9.29A), oxidation is reduced to 5.0×10^{-9} $kg(S)/(m^3 \cdot s)$ which is a third of that calculated for a 0 % saturation till. This oxidation rate corresponds to heat production of 3.4×10^6 $J/(m^3 \cdot a)$. However, oxidation occurs only during the first 500 days and then ACC reduces temperatures beneath the till to below 0 °C via convective heat transfer as shown in Fig. 9.29B.

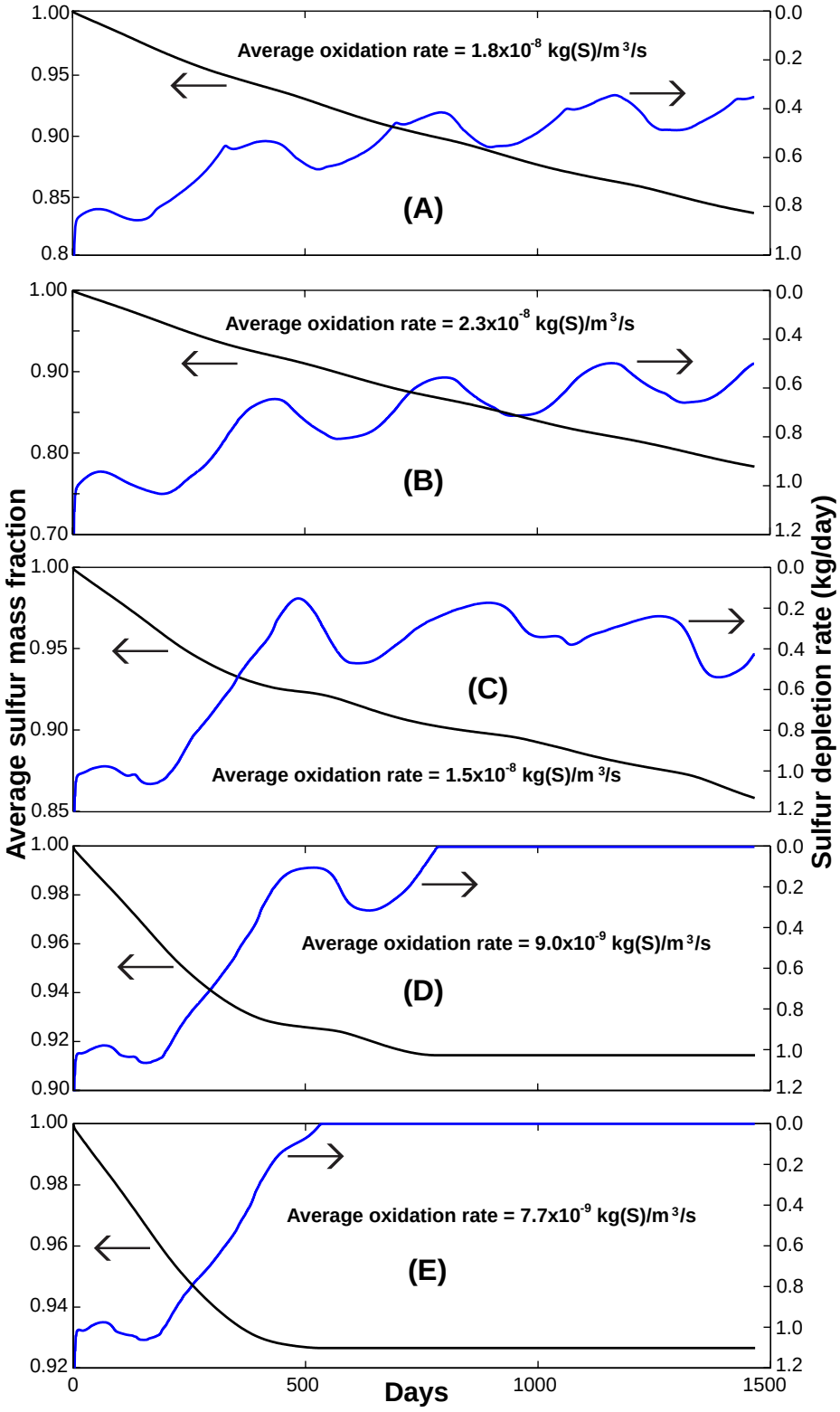

Figure 9.27: Average mass sulfur mass fraction was calculated by dividing the total sulfur concentration of the pile cross section at a given time to the initial total sulfur concentration and oxidation rate. The air-convection-layer thickness of 3 m and permeability of 2×10^{-9} m^2 (A) , 5×10^{-8} m^2 (B), 4×10^{-7} m^2 (C), 6×10^{-7} m^2 (D) and 8×10^{-7} m^2 (E) with the till at 0 % saturation.

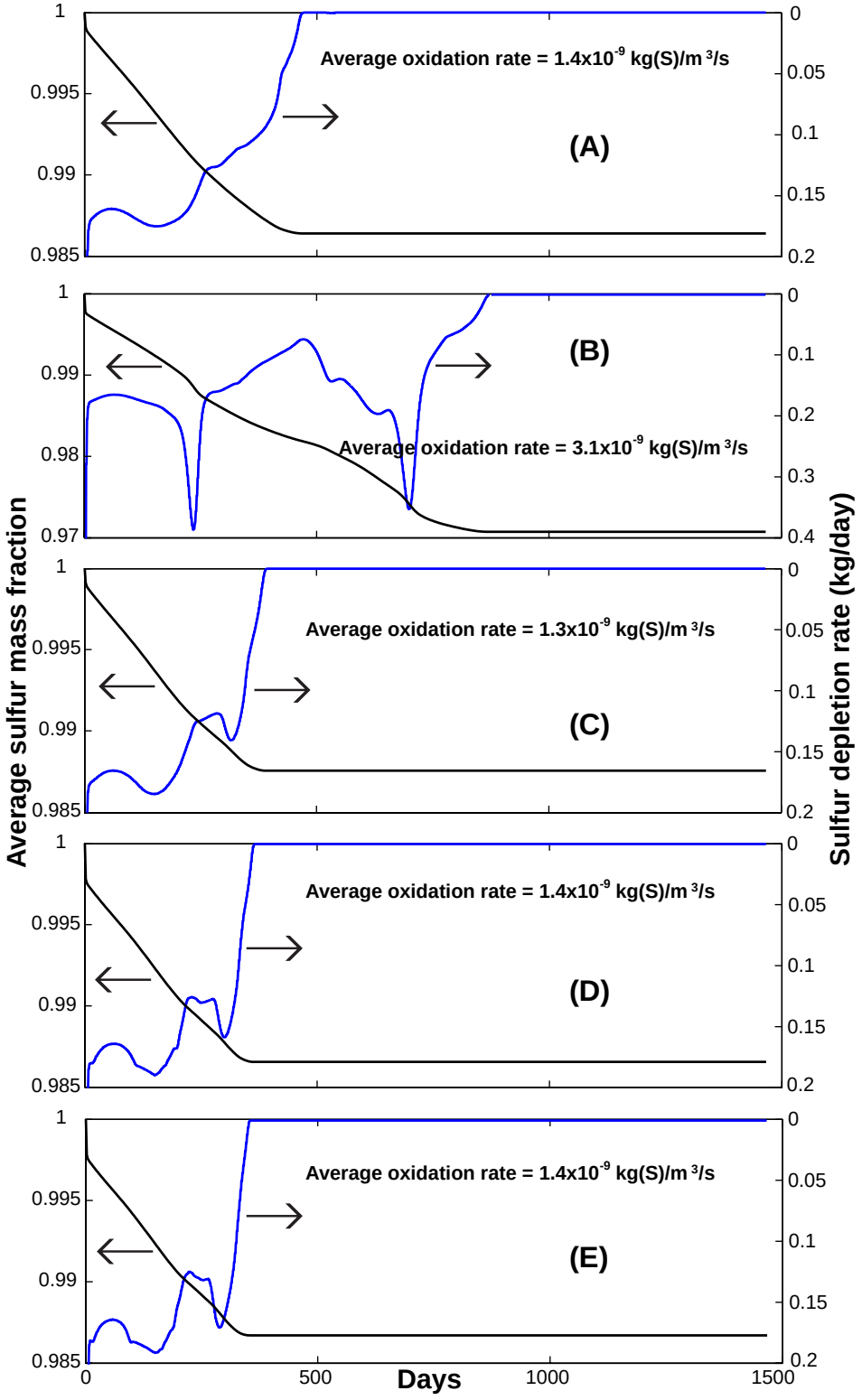

Figure 9.28: Average mass sulfur mass fraction was calculated by dividing the total sulfur concentration of the test pile cross section at a given time to the initial total sulfur concentration and oxidation rate. The air-convection-layer thickness of 3 m and permeability of 2×10^{-9} m^2 (A) , 5×10^{-8} m^2 (B), 4×10^{-7} m^2 (C), 6×10^{-7} m^2 (D) and 8×10^{-7} m^2 (E) with the till at 90 % saturation.

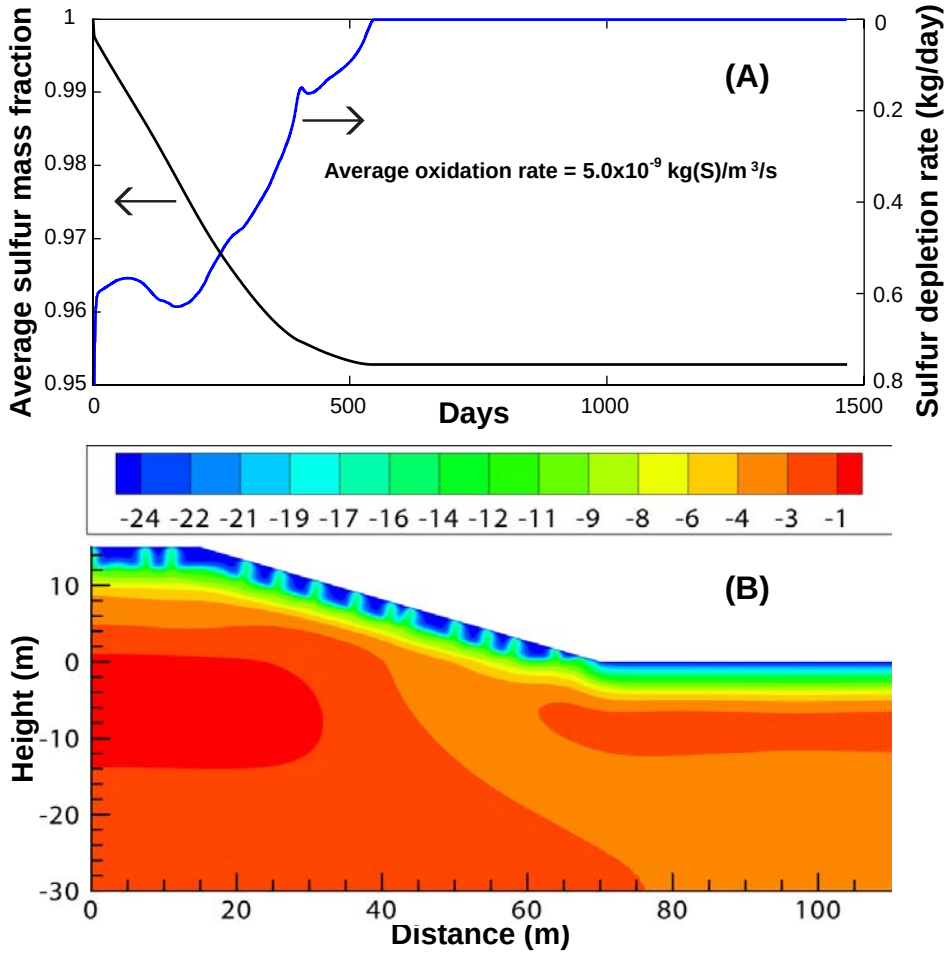

Figure 9.29: Oxidation rate (A) and isotherms (°C) of the fourth winter (or 1345 days) (B). The air-convection-layer thickness of 3 m and permeability of 4×10^{-7} m^2 with the till at 50 % degree saturation.

9.5.4 Summary and discussion of the covered test pile

Measured ground temperatures within the covered test pile at Diavik indicate that heat transfer is conduction dominated. Even though measured permeability of waste rock at the site is quite high typically about $2 \times 10^{-9}\,m^2$ compare to other waste-rock piles in a range between 10^{-10} and $10^{-11}\,m^2$ (Ritchie, 1994b; Bennett et al., 1995; Kuo and Ritchie, 1999). However, the combined effects of low permeability till layer and the heterogeneous natures of waste rock (Smith et al., 1995; Azam et al., 2007) has conduction dominate over convection. The field temperatures show that temperatures at and below the till and bedrock stay at or below 0 °C during the study period as a result of cold site temperatures (freezing index $I_{sf} = 3324.7$ (°C-days)) and the high initial placement volumetric moisture content of the till which maintains it at about 90 % saturation. The closure concept using a 1.5 m till covered with 3 m Type I rock encapsulating the Type III waste rock maintains permafrost within the till. However, accounting for future climate change at Diavik site, the 0 °C isotherm would penetrate about 0.9 m into the till for assumptions that the till is maintained 90 % saturation during a simulation period of 100 years (Chapter 7). Thus, the Type I rock has to be thicker to account for the future climate change if thawing into the till is unacceptable. Due to the cold temperatures and prolonged winter at the site, an alternative cover solution for long-term climate change is the ACC and the ACC would lower the Type III waste rock temperatures much colder than that of the present closure concept. ACC can be achieved by removing small particle size fractions from the Type I waste rock prior to placement as a cover.

With the extremely cold temperatures in each winter at the site, air convective cooling can be used to produce a rapid cooling of waste rock mass. Natural air convection occurs due to the unstable stratification within the air convection layer in the ACC, and the strength of convective cooling depends on permeability and temperatures gradient within the air convection layer. Natural air convection in porous media has been used to protest permafrost foundation beneath embankments in warm permafrost regions of Fairbanks, Alaska (Goering, 1998, 2003) and Qinghai-Tibet Railway in China (Ma et al., 2008). Goering (1998) found that the construction of a 2.5 m height embankment of 5-8 cm rock resulted in a reduction in ground temperatures between 3.2 and 5.6 °C after two winters. Ma et al. (2008) analyzing ground temperatures of embankment sections along Qinghai-Tibet highway with heights between 3.00 m and 6.55 m of coarse rock reported that permafrost aggradation into the foundation of embankments more than 1 m. These experiments demonstrate the effectiveness of convective cooling. Moreover, numerical simulation of this study further confirms the rapid cooling due to convection (Fig. 9.22). As demonstrated in Fig. 9.19, ACC can produce a freezing index of ground temperature at the base of the air convection layer similar to that of surface temperature with a 0 °C-days thawing index. It means that ground temperatures at the base of an air convection layer will never increase above 0 °C.

For the scenarios in which the Type III waste rock below the cover undergoes pyrite

oxidation, the heat production has the potential to thaw permafrost and release ARD to the surrounding areas. Oxygen supplied to fuel pyrite oxidation diffuses through the till provided the till has low saturation. Simulations showed that if the till is 90 % saturation, oxidation rate is low. The ACC can maintain the Type III waste rock below 0 °C (Fig. 9.23 and Fig. 9.24) and these cold temperatures reduce or eliminate oxidation. Heat production was small about 0.1 W/m^3. In comparison, other waste-rock piles such as at Rum Jungle, Northern Territory, Australia produced 5.0 W/m^3 (Harries and Ritchie, 1981) or 2.0 W/m^3 in a waste-rock pile located in an arctic area (Hollesen et al., 2011). However, when the till is completely dry (0 % water saturation), oxygen diffusion was large compared to that of 90 % water saturation till. The oxygen diffusion was then high enough to assure high oxidation rates and heat releases which result in the increase of waste rock temperatures (Fig. 9.23 and Fig. 9.24). For this condition, oxidation rates were in the order of 10^{-8} $kg\,(S)/\left(m^3 \cdot s\right)$, a value observed at other waste-rock piles (Harries and Ritchie, 1981; Lefebvre et al., 2001c; Sracek et al., 2006).

9.6 Results and Discussion: the Type III test pile (uncovered test pile)

9.6.1 Case 1: Heat transfer due to natural air convection

9.6.1.1 Isotherms and pore-air velocity

Fig. 9.30 shows simulations of the evolutions of isotherms, streamlines and velocity with various permeabilities during January 2011. At permeabilities of $\leq 2 \times 10^{-9}\,m^2$ heat transfer in the Type III test pile is via conduction and is shown by the parallel-uniform isotherms around the perimeter of the test pile. Moreover, bedrock temperatures beneath the base of the test pile are quite uniform with an average around -4 °C. Average pore-air velocity is about 2.9×10^{-5} m/s and regions with a large air velocity located at the base and near the batter of the test pile. During winter air flows inward along the slope (Fig. 9.30A1 and A2). As permeability increases, strong natural air convection becomes evident. Natural air convection pushes cold air from the batter into the test pile and warm air escapes near the top. At a permeability of $4 \times 10^{-7}\,m^2$, bedrock temperatures beneath the test pile decrease and are 4 °C colder than those associated with smaller permeability piles ($\leq 5 \times 10^{-8}\,m^2$) (Fig. 9.30); higher permeabilities result in increased air velocities.

At $K \geq 6 \times 10^{-7}\,m^2$, these high permeabilities cause cold air penetration into almost half of the test pile. Specially at $3 \times 10^{-6}\,m^2$ the whole test pile decreases to and is maintained at temperatures colder than -19 °C during January 2011. Several thermal plumes develop at the base due to convective transfer (Fig. 9.31C1). Average pore-air velocity within the test pile with a permeability of $3 \times 10^{-6}\,m^2$ is about twice that for a permeability of $6 \times 10^{-7}\,m^2$. In addition, Peclet number, *Pe*, can be used to examine the heat transport by air convection

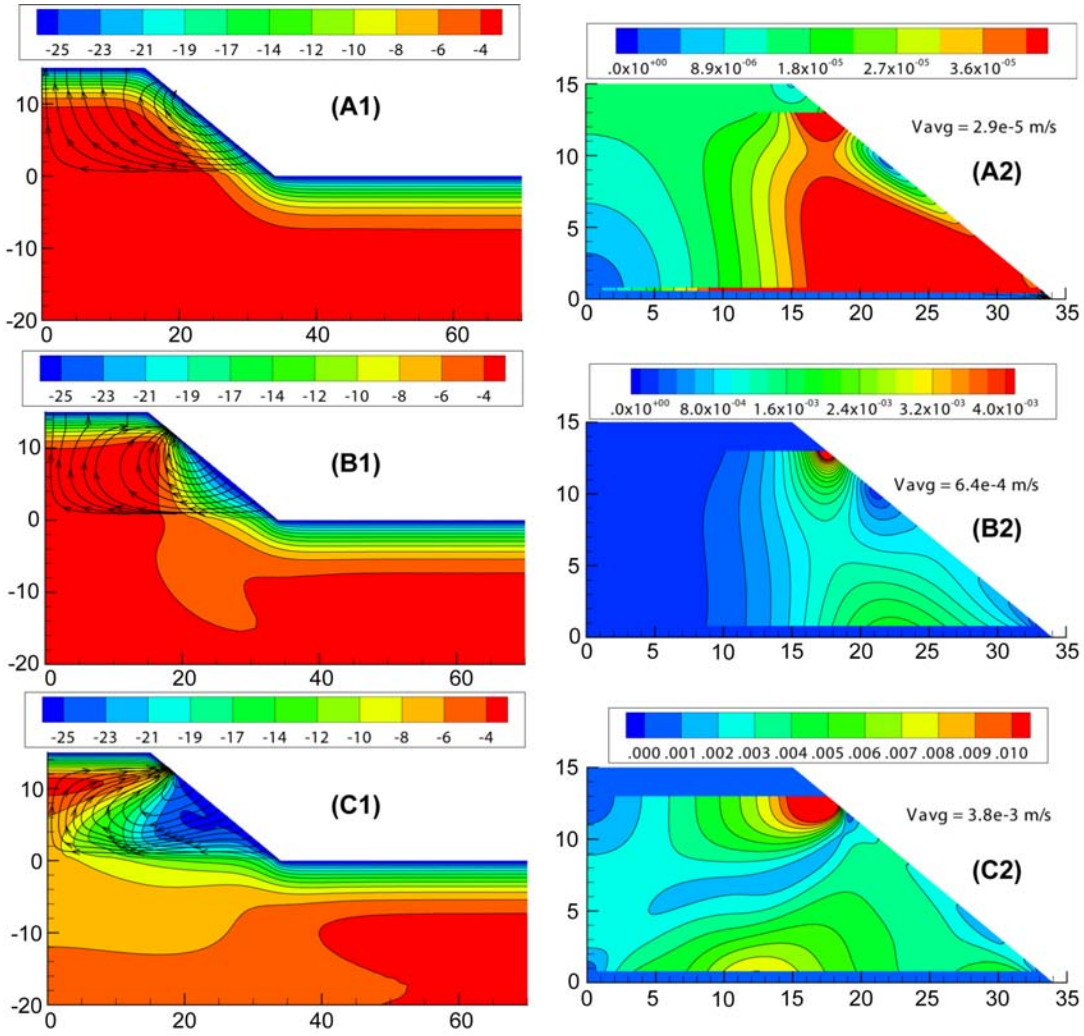

Figure 9.30: Isotherms (in °C), streamlines and velocity of the Type III test pile at various permeabilities in January 2011: $2 \times 10^{-9}\,\mathrm{m}^2$ (A1 and A2), $5 \times 10^{-8}\,\mathrm{m}^2$ (B1 and B2) and $4 \times 10^{-7}\,\mathrm{m}^2$ (C1 and C2).

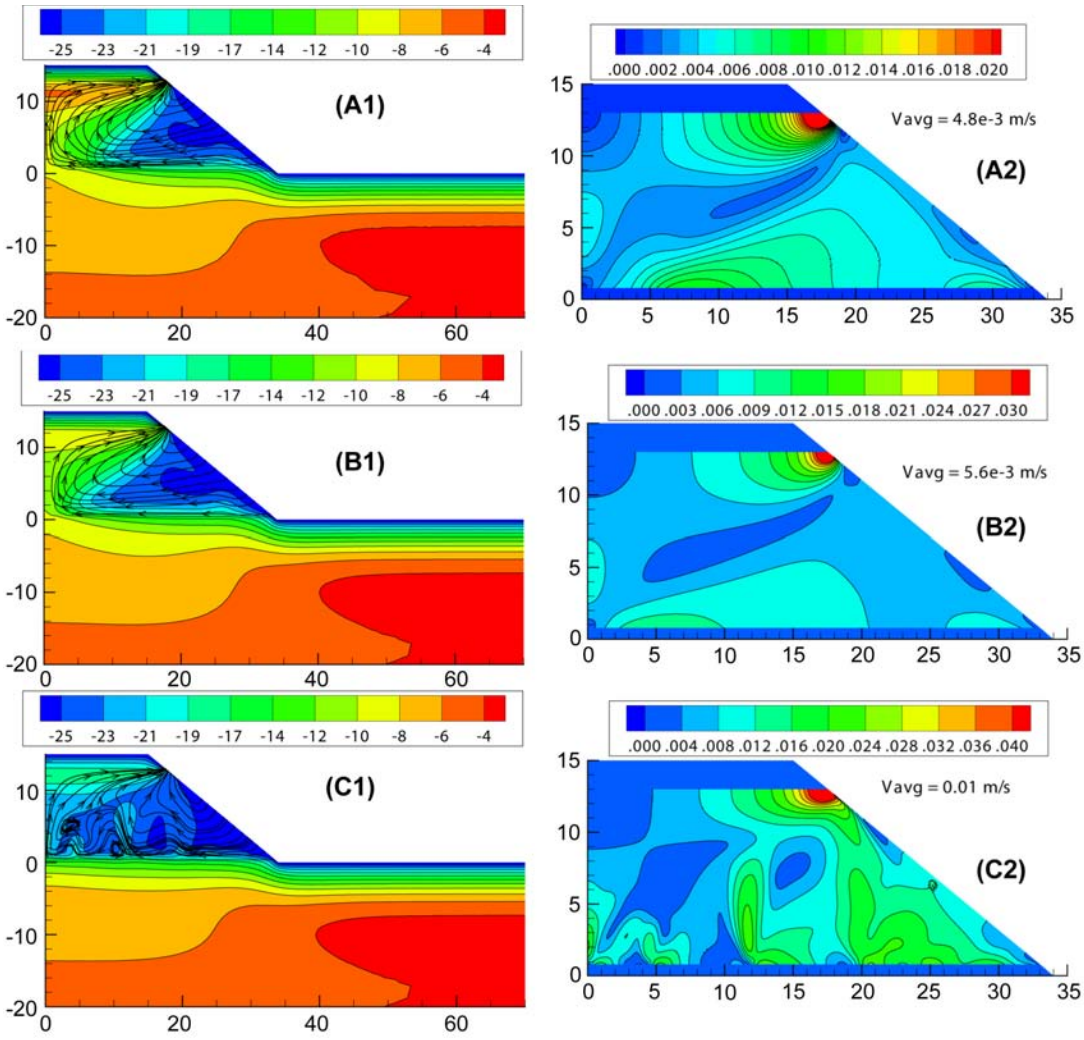

Figure 9.31: Isotherms (in °C), streamlines (on the left) and velocity distribution (on the right) of the Type III test pile at various permeabilities in January 2011: $6 \times 10^{-7}\,\mathrm{m}^2$ (A1 and A2), $8 \times 10^{-7}\,\mathrm{m}^2$ (B1 and B2) and $3 \times 10^{-6}\,\mathrm{m}^2$ (C1 and C2).

relative to conduction (Bear, 1972):

$$Pe = \frac{D_{50} C_a}{\lambda} u \tag{9.5}$$

Where $D_{50} = 90\,\mathrm{mm}$ is the mean grain size of waste rock, u is the average pore-air velocity (Darcy velocity), λ is the effective thermal conductivity of the Type III rock (Table 9.1), C_a is air volumetric heat capacity. Fig. 9.32 shows the relation between Pe and permeability which was calculated using Eqn. 9.5. Nield and Bejan (1999) defined a relation between Pe and Nusselt number (Nu) (Nu is the ratio of total heat transfer to conductive heat transfer) for forced convection over a sphere (Fig. 9.48). Using Eqn. 9.6 for a permeability of $3 \times 10^{-6}\,\mathrm{m}^2$ the value of Nu is 11.8, which is significant (Fig. 9.32). Therefore, in this case, convection is dominated.

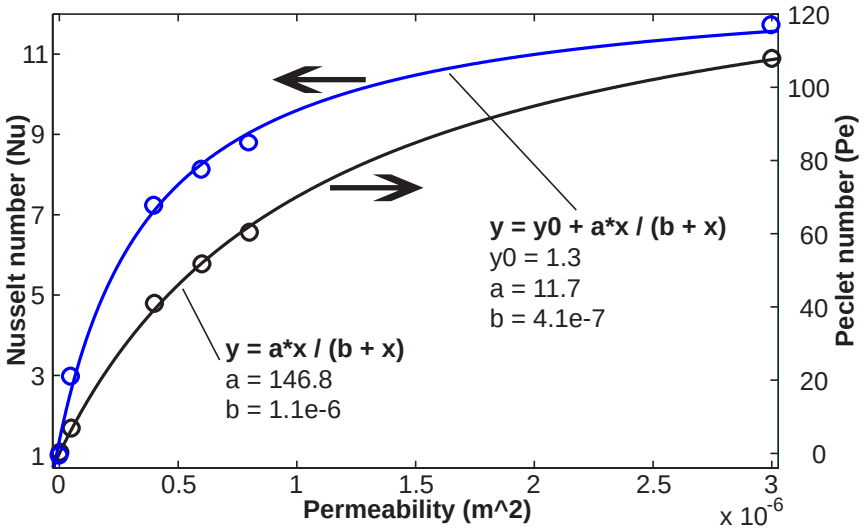

Figure 9.32: The relation between Peclet number and permeability

$$Nu = 1.128\,Pe^{1/2} \tag{9.6}$$

9.6.1.2 Simulation and field temperature results: a comparison

Waste rock dominated with fines near the surface of the test pile was compacted by heavy equipments during the test pile construction. Therefore permeability of this layer is low, in the order of three orders of magnitude lower than deeper into the test pile (Neuner et al., 2012). The low permeability contributes to conduction dominating the heat flow and field temperatures match well to simulation within this layer. At a depth of 2.33 m, simulation with low permeabilities ($\leq 5 \times 10^{-8}\,m^2$) starts to deviate from field measurements which indicates that convective heat transfer increases in importance. In fact, at higher permeabilities ($\geq 4 \times 10^{-7}\,m^2$), simulations are more comparable to field measurements (Fig. 9.33).

At depths between 3.93 and 5.46 m, simulations with permeability using $6 \times 10^{-7}\,m^2$ match field temperatures well. However, near the middle of the test pile (between 7 m and 9 m) modeling results when using $8 \times 10^{-7}\,m^2$ provide a better match (Fig. 9.34). Near the base of the test pile, field results show that temperatures at depths between 9.75 m and 11.25 m are above 0 °C during 90 days of the summer. However, simulation results are below 0 °C at locations deeper than 11 m even with high permeability of $1 \times 10^{-6}\,m^2$. The discrepancy may be due to that fact that the simulations did not account for forced-convective heat transfer (wind-induced advection of warm air during each summer) (Fig. 9.35). It is also noted that lysimeters are located below face 1 at the base of the Type III test pile. These lysimeters release heat from the heat trace and this heat warms the waste rock located on this face.

The comparison of simulation results with field measurements along the 5 m offset

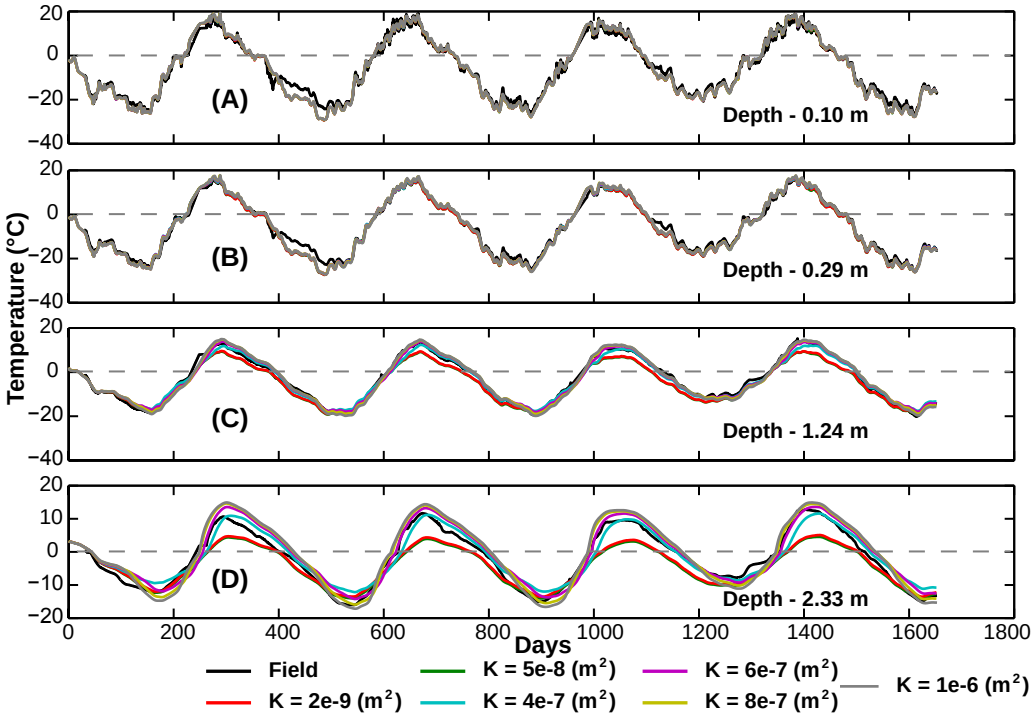

Figure 9.33: Simulation and field temperatures (5 m offset north of centre line at face 1, "31N5thm") at different permeabilities at depths between the surface and about 2.33 m.

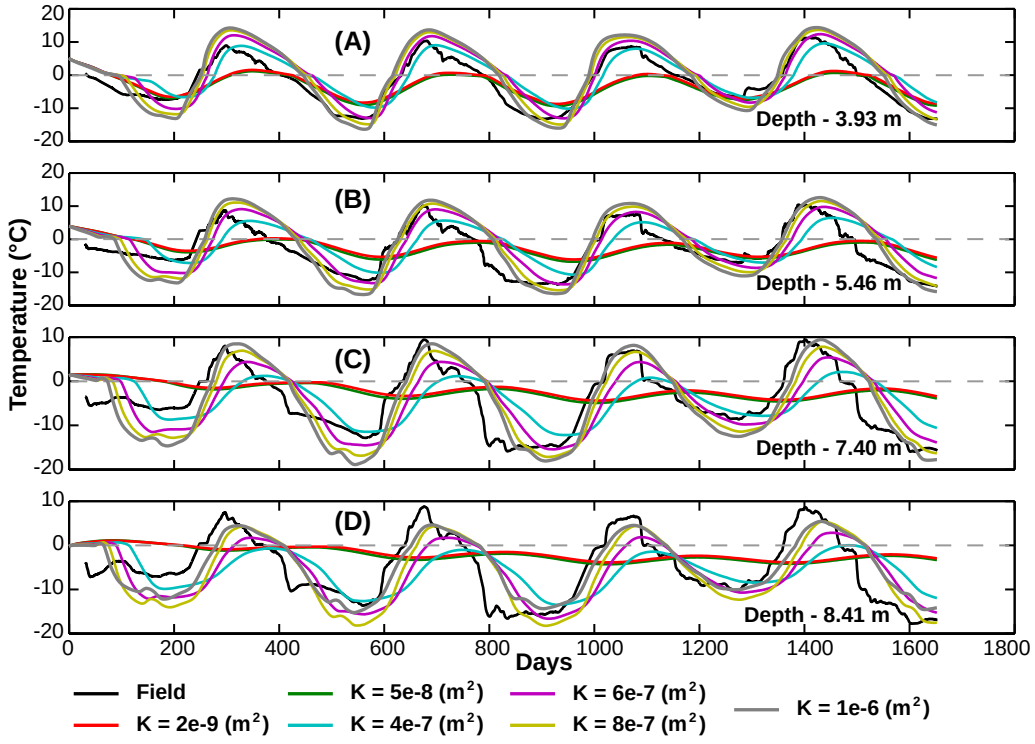

Figure 9.34: Simulation and field temperatures (5 m offset north of centre line at face 1, "31N5thm") at different permeabilities at depths between 3.93 and about 8.41 m.

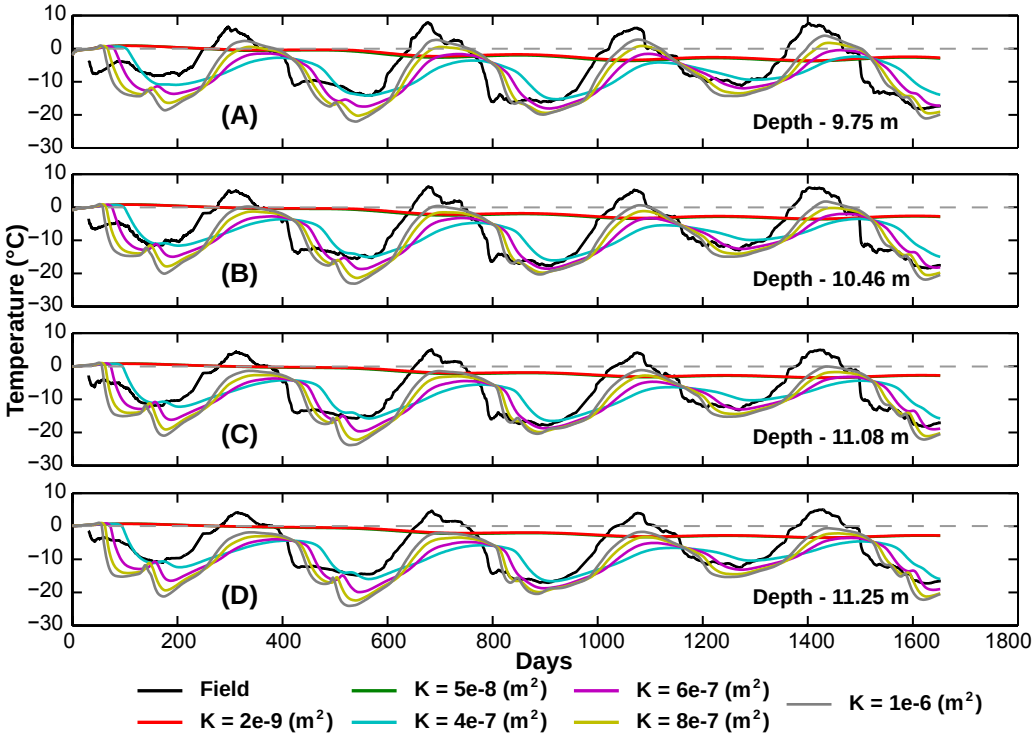

Figure 9.35: Simulation and field temperatures (5 m offset north of the centre line at face 1, "31N5thm") at different permeabilities at depths between 9.75 and about 11.25 m.

south of the centre line at face 4 are shown in Fig. 9.36. They indicate that within 2 m of the surface, simulations are comparable to field values because conduction dominates in this region. Between 2 m and 5 m depth, field values are a close match to simulation using $K = 4 \times 10^{-7}\,\mathrm{m}^2$ (Fig. 9.37). However, between 5 m and 7 m depth simulation results using $K = 6 \times 10^{-7}\,\mathrm{m}^2$ are comparable to field values whereas at depths from 7 m to 9 m field temperatures are close to simulation results when $K = 8 \times 10^{-7}\,\mathrm{m}^2$ is used (Fig. 9.38). These results indicate that permeability within the test pile must increase with depth for the simulation to reproduce field data. However, at high permeabilities $K \geq 10^{-7}\,\mathrm{m}^2$ and relatively high wind speed at the site (Amos et al., 2009a), the wind-induced advection (forced convection) must also be considered when matching field temperature measurements.

9.6.2 Case 2: Heat transfer due to wind-induced advection (Forced convection)

9.6.2.1 Isotherms and pore-air velocity

The spectral analysis of wind speed time series indicates that the dominate frequencies are 1, 4, 5 and 14 days (Chapter 5) and the wind speed and direction changes frequently. To apply such rapid fluctuations as boundary conditions, the time steps in the transient analysis need to be small and numerical convergences can be problematic. Hence, wind is assumed

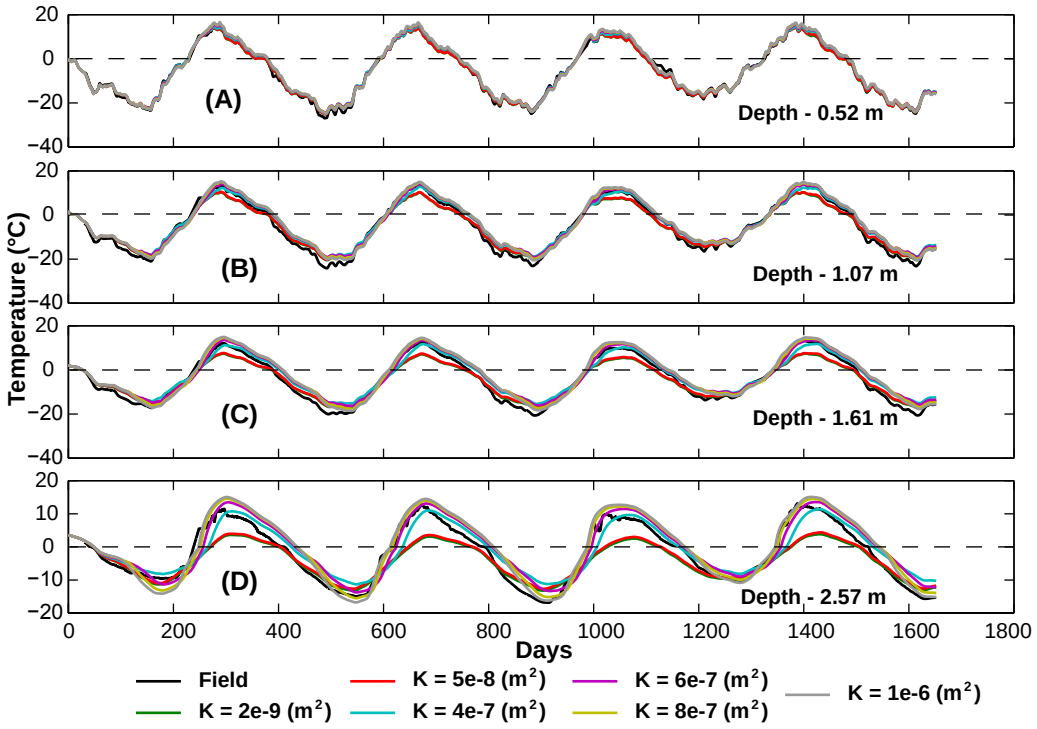

Figure 9.36: Simulation and field temperatures (5 m offset south of the centre line at face 4, "34S5thm") at different permeabilities at depths between the surface and 2.57 m.

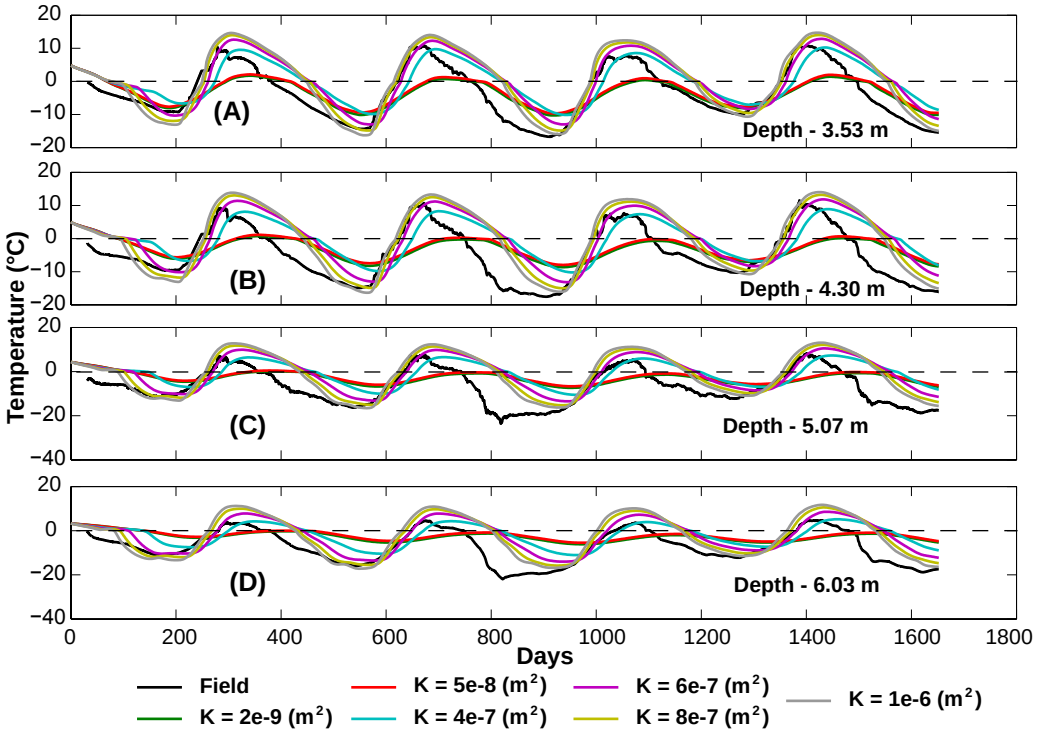

Figure 9.37: Simulation and field temperatures (5 m offset south of the centre line at face 4, "34S5thm") at different permeabilities at depths between the surface and 2.57 m.

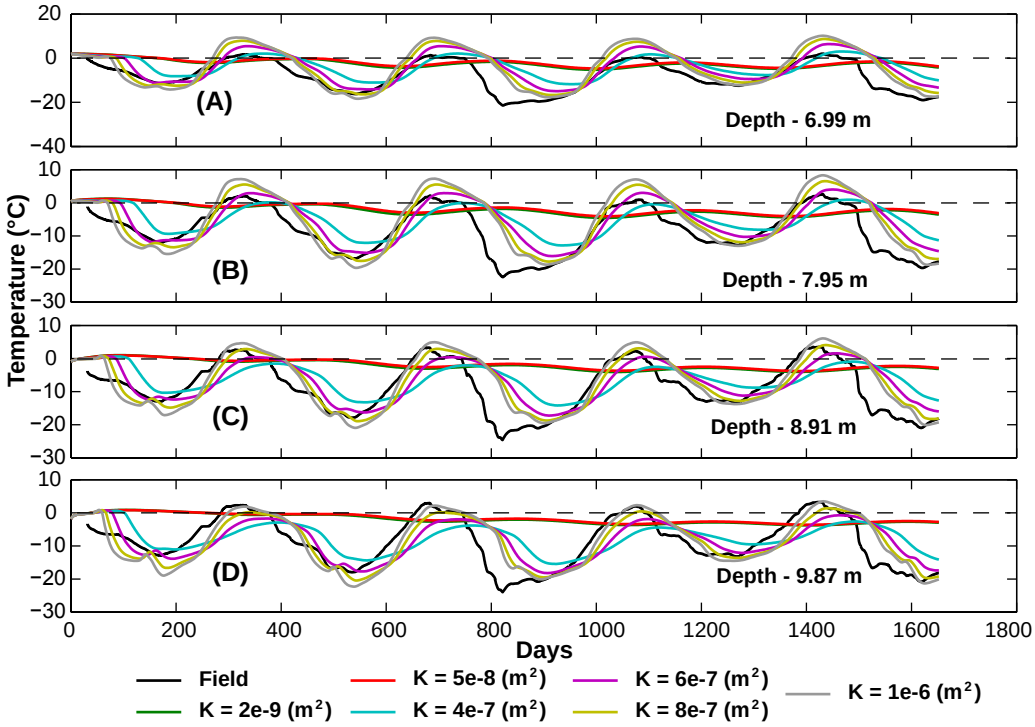

Figure 9.38: Simulation and field temperatures (5 m offset south of the centre line at face 4, "34S5thm") at different permeabilities at depths between the surface and 2.57 m.

to blow from the north and at a magnitude of 20 km/h. The pressure induced around the test pile associated with these conditions are shown in Fig. 9.10.

At permeabilities $K < 1 \times 10^{-7}\,\mathrm{m}^2$, wind-induced advection has little effects on internal temperatures. Therefore, simulations were performed using permeabilities $K \geq 1 \times 10^{-7}\,\mathrm{m}^2$. Fig. 9.39A1 to A4 clearly show the impacts of wind-induced advection on the temperatures. Wind-induced advection/convection from the north causes air to escape from the south upper part of the batter. The isotherms become more and more asymmetrical as the permeability increases (Fig. 9.39). During winter, the wind rapidly pushes cold air deep into the test pile. This causes rapid cooling within the interior of the pile as observed in the field temperature data. Furthermore, the wind causes airflow across the test pile and it is also observed via air pressure measured in the pore space. In fact, Amos et al. (2009a) recognized that wind from this side of the test pile causes pressure fluctuations at probes located on the opposite side. The wind also significantly increases velocity within the test pile. Without wind, the average velocity was 3.8×10^{-3} m/s however, with the wind the average velocity is 9.1×10^{-3} m/s at $K = 4 \times 10^{-7}\,\mathrm{m}^2$. At $K = 6 \times 10^{-7}\,\mathrm{m}^2$ the average velocity associated with the wind increases about three times (Fig. 9.39).

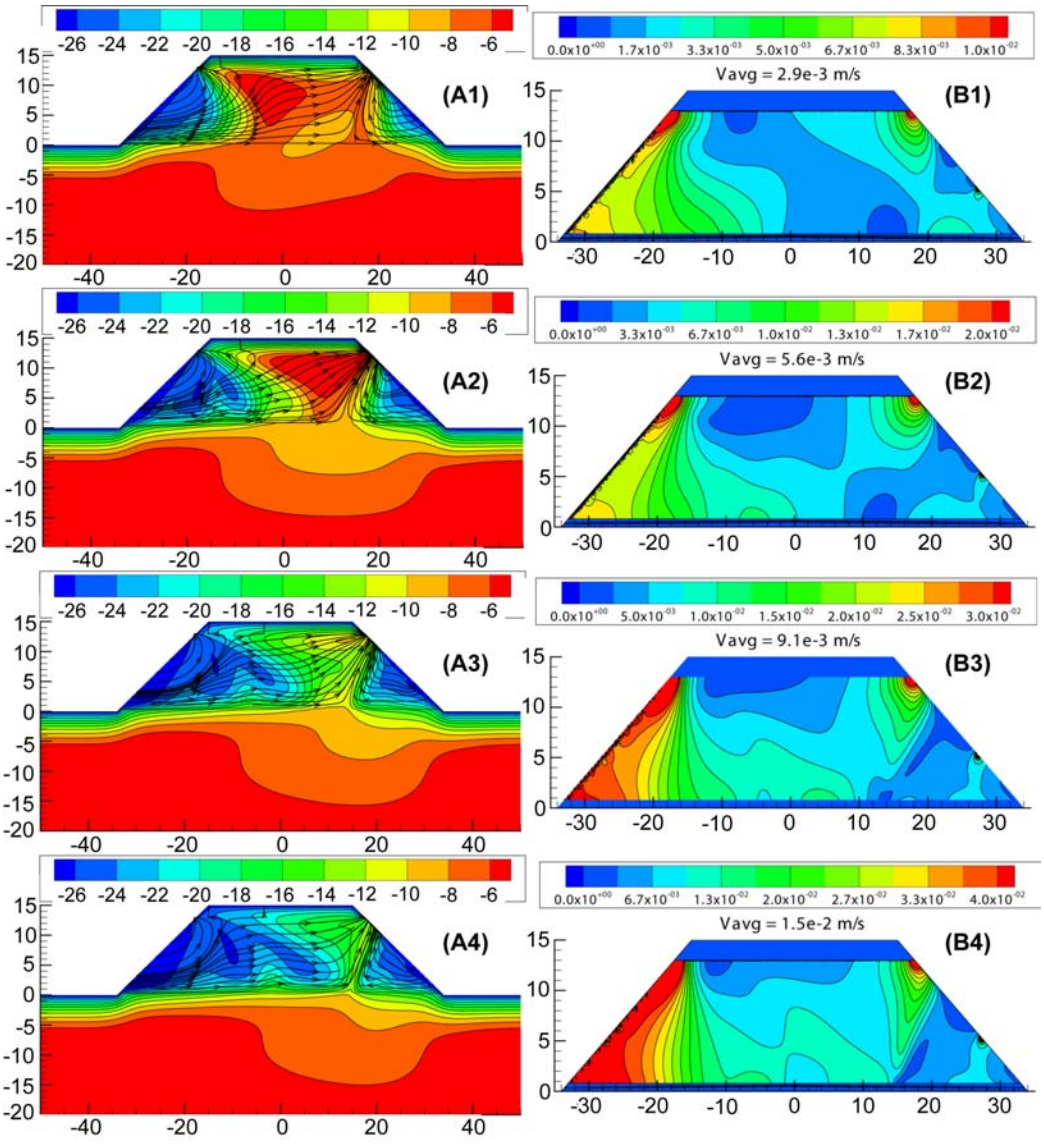

Figure 9.39: Isotherms (in °C), streamlines and pore-air velocity of the Type III test pile at various permeabilities in January 2011: $1 \times 10^{-7}\,\mathrm{m}^2$ (A1 and B1), $2 \times 10^{-7}\,\mathrm{m}^2$ (A2 and B2), $4 \times 10^{-7}\,\mathrm{m}^2$ (A3 and B3) and $6 \times 10^{-7}\,\mathrm{m}^2$ (A4 and B4).

9.6.2.2 Simulation and field temperature results: a comparison

Fig. 9.40 show a comparison between simulation and field measurements. At depths above 7 m, simulation results using $K = 4 \times 10^{-7}\,\mathrm{m}^2$ give the closest match to field values. Furthermore, the simulations provide a very good phase match but with discrepancy in amplitude. Below 7 m depth, simulations using $K = 6 \times 10^{-7}\,\mathrm{m}^2$ are comparable to fields results and again the amplitudes from the simulation results do not match well the field measured amplitudes. The discrepancies may be due to other variables not included in the simulations such as the heterogeneity of waste rock, the erratic changes of wind speed and direction and heat induce into the pile from the heat trace in the lysimeters. However, the simulations match the overall trends from the field data and without inclusion of wind would not be as accurate. The field and simulation comparisons indicate that permeability of the lower portion of the test pile is in the order of $10^{-7}\,\mathrm{m}^2$ and it is one order larger than the values obtained by digital image processing of waste rock reported by Chi (2010).

Field temperatures at the base and within bedrock beneath the test have remained below 0 °C and show a gradual cooling trend (Fig. 9.41). Likewise, simulation results mimic this character however, the simulations show colder temperatures. Below 5 m depth, bedrock temperatures of both field and simulation show initial warm and then cooling. This is because initial heat retained in the test pile which was constructed during the summer was transferred to the underlying bedrock.

9.6.3 Case 3: Heat transfer in active-heat-generating waste rock

9.6.3.1 Temperature evolution

Simulations in the following assume that the Type III waste rock is oxidized and the released heat raises temperatures within the test pile. Depending on the permeability and thermal conductivity of waste rock, heat can be retained or escape to the environment. Furthermore, if the oxidation of sulfide minerals is controlled by threshold temperatures as shown in Fig. 9.1 A, temperatures of the test pile would generally be colder (the right side figures of Fig. 9.42) compared to not accounting for the threshold temperatures (the left side figures of Fig. 9.42). At permeabilities of $2 \times 10^{-10}\,\mathrm{m}^2$ and $2 \times 10^{-9}\,\mathrm{m}^2$, heat is retained within the test pile and creates warm interior temperatures. However, at permeability of $2 \times 10^{-9}\,\mathrm{m}^2$, interior temperatures are warmer and move deeper into the test pile than those with $K = 2 \times 10^{-10}\,\mathrm{m}^2$ (Fig. 9.42 A1, A2, B1 and B2) because this higher permeability creates greater air convection within the pile. Greater air convection results in an increased oxidation and heat release. Besides, the heat released thaws the permafrost in the foundation beneath the test pile. If the foundation is bedrock or non-thaw-susceptible soils, this would not cause instability problems for the test pile. Conversely, if the foundation is composed of thaw-susceptible soils, this thaw would result in potentially large settlement and potential instability in the pile's foundation.

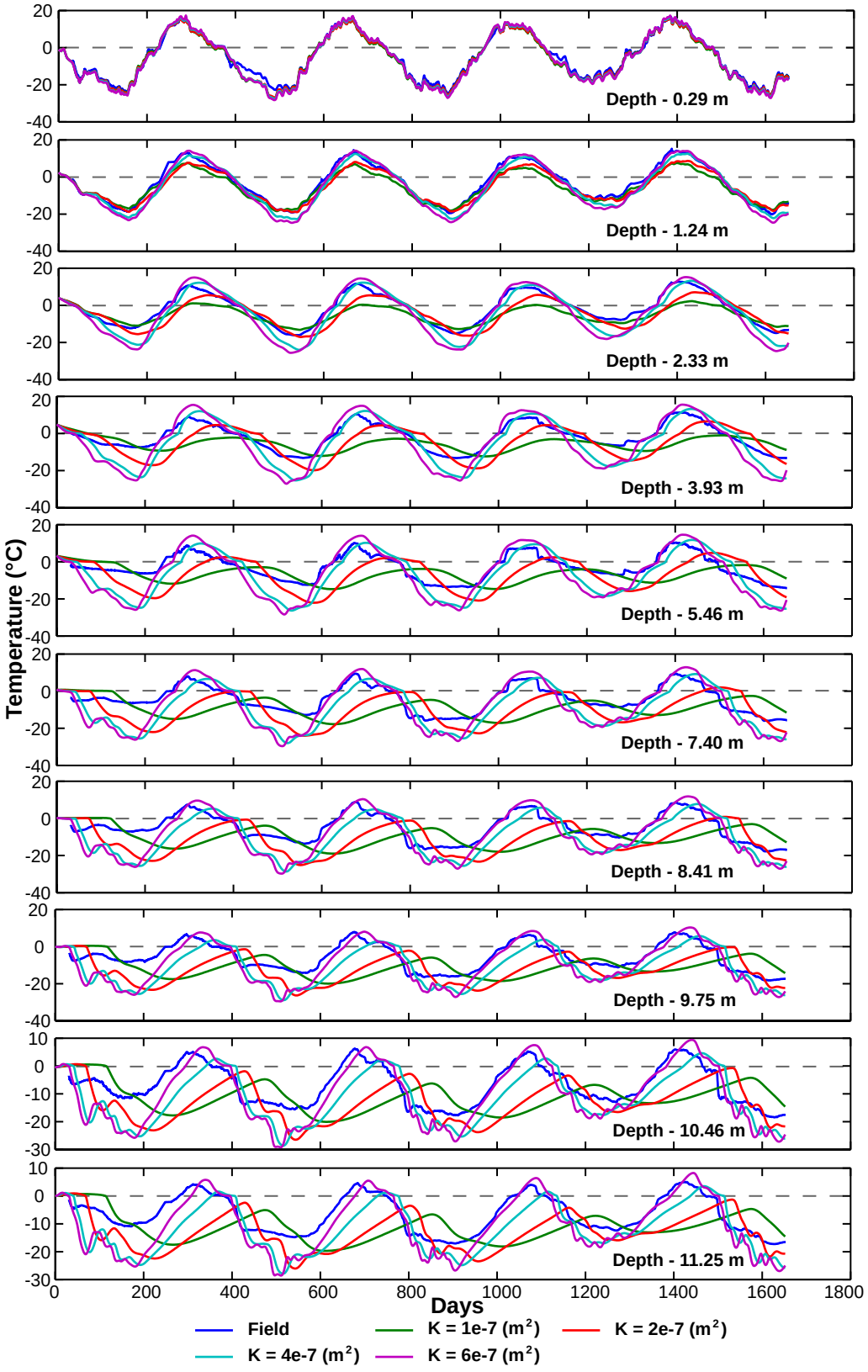

Figure 9.40: Simulation and field temperatures (5 m offset north of centre line at face 1) at different permeabilities and depths.

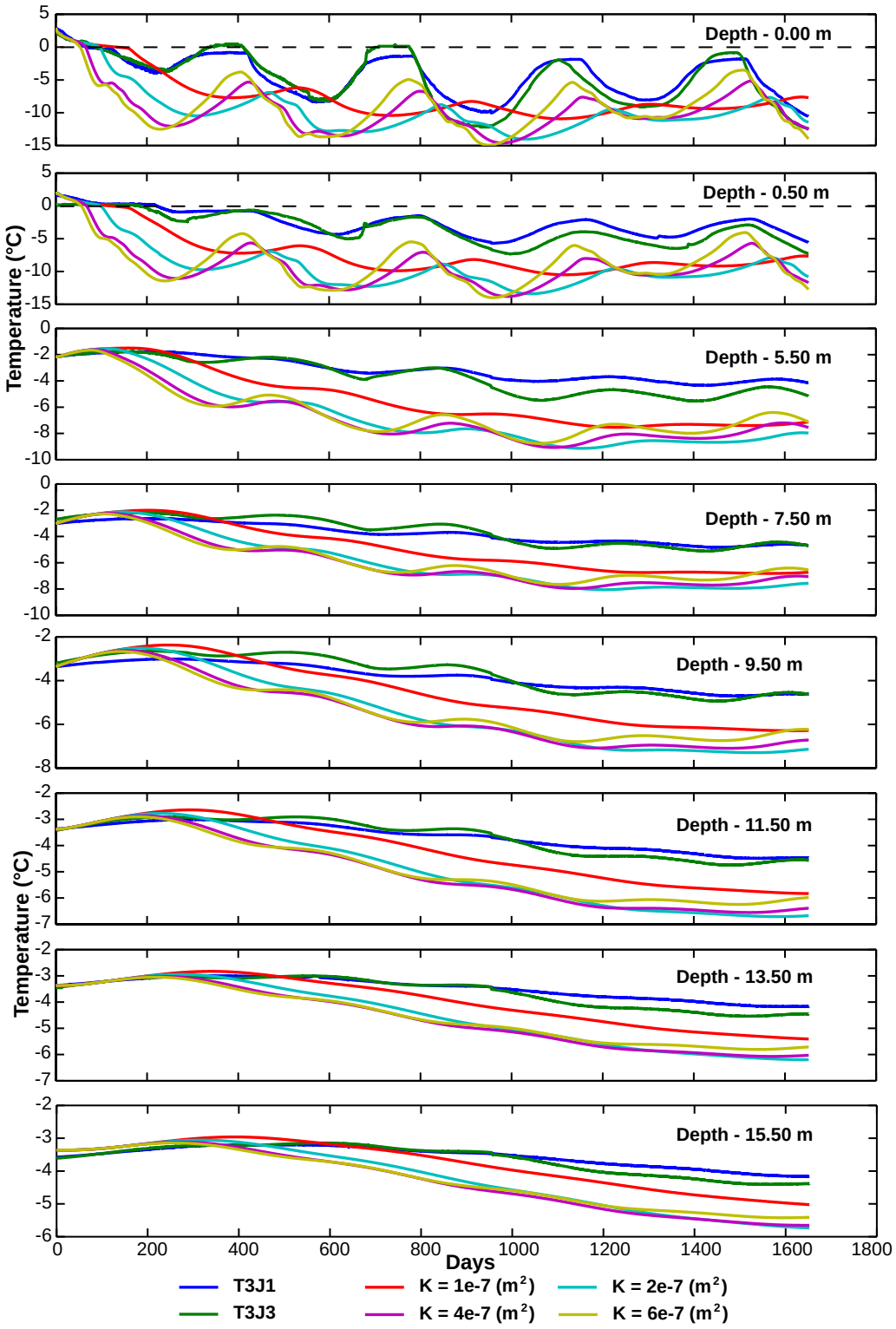

Figure 9.41: Simulation and field temperatures of bedrock beneath the test pile at different permeabilities and depths; Depth - 0.00 m is at the base of the test pile.

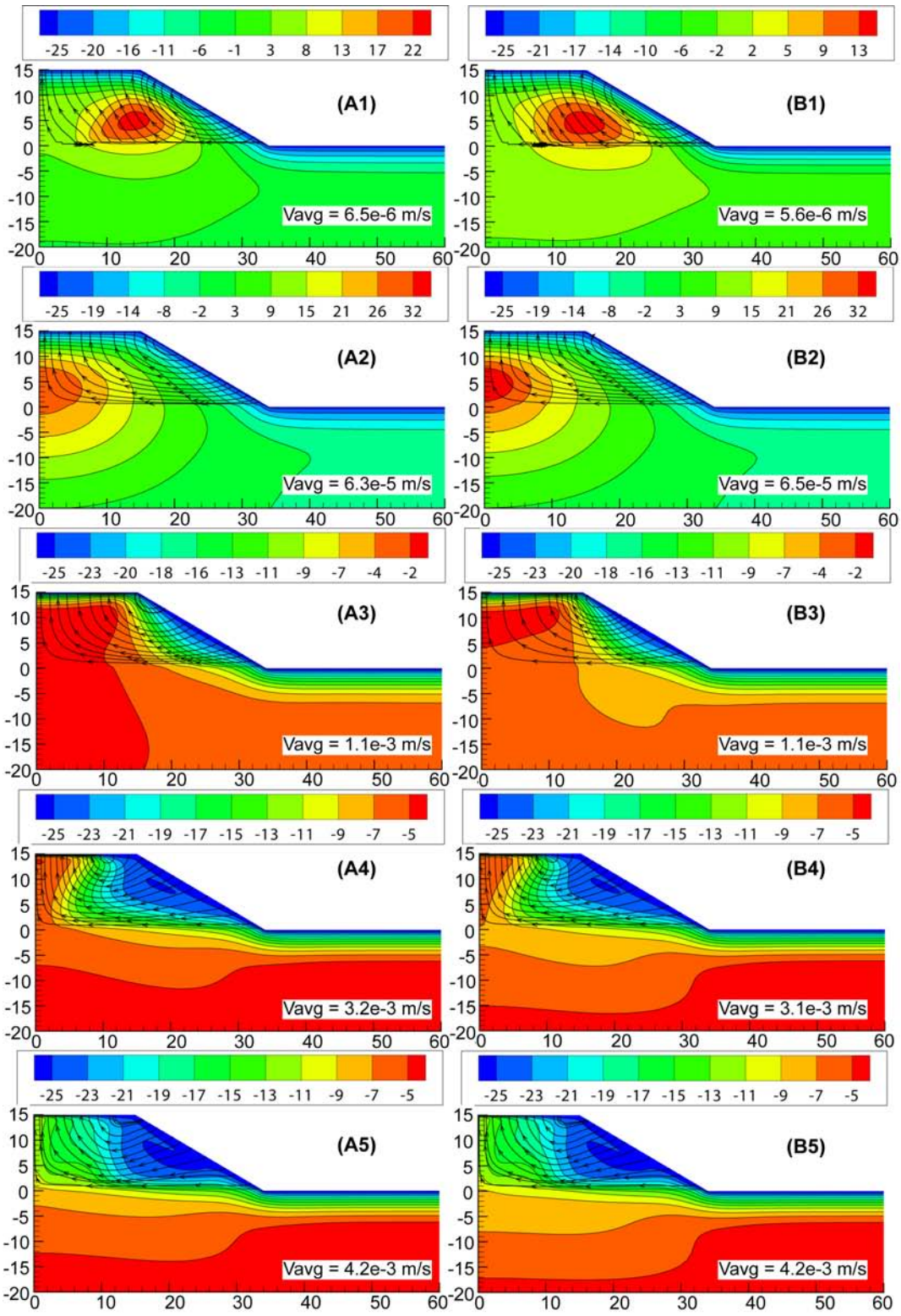

Figure 9.42: Isotherms (in °C) and streamlines of the Type III test pile at various permeabilities in January 2011 without (on the left) and with a temperature-inhibiting factor (Fig. 9.1 A) on oxidation (on the right): $2 \times 10^{-10}\,\mathrm{m}^2$ (A1 and B1), $2 \times 10^{-9}\,\mathrm{m}^2$ (A2 and B2), $5 \times 10^{-8}\,\mathrm{m}^2$ (A3 and B3), $2 \times 10^{-7}\,\mathrm{m}^2$ (A4 and B4) and $4 \times 10^{-7}\,\mathrm{m}^2$ (A5 and B5). The inset in each figure represents an average pore-air velocity of the test pile.

For cases with permeabilities greater than $5 \times 10^{-8}\,\mathrm{m}^2$, the heat release via oxidation within the test pile is effectively removed by natural air convection during winter and the interior temperatures are not significantly higher than those without internal oxidation (Fig. 9.42, Fig. 9.30 and Fig. 9.31). At permeability of $2 \times 10^{-10}\,\mathrm{m}^2$, average air velocity is about 6.5×10^{-6} m/s and the inward flux of oxygen via advection and diffusion at the surface is about $5.2 \times 10^{-7}\,\mathrm{kg(O_2)}/\left(\mathrm{m}^2 \cdot \mathrm{s}\right)$. This flux can only support an oxidation rate of $5.0 \times 10^{-8}\,\mathrm{kg(S)}/\left(\mathrm{m}^3 \cdot \mathrm{s}\right)$. As the permeability increases average air velocity increases as shown Fig. 9.42.

Fig. 9.43 shows the evolution of temperature at 5 m below the surface on the centre line. We see that the temperature at this point is highest for $K = 2 \times 10^{-9}\,\mathrm{m}^2$ which can reach 80 °C if the threshold temperatures were not considered, otherwise it rises to about 54 °C after 1000 days. Meanwhile at $K = 2 \times 10^{-10}\,\mathrm{m}^2$ the temperature at this point is low because of the low oxidation rate. Diffusion is probably the main supply of oxygen at low permeability. At higher permeabilities $K \geq 5 \times 10^{-8}\,\mathrm{m}^2$, the temperature is initially high but it is cooled by natural air convection, and eventually, it remains around or below 0 °C.

9.6.3.2 Oxidation rate

At high permeabilities, natural air convection can supply significant amounts of oxygen that can maintain high oxidation rates within the test pile. In fact, at $K \geq 5 \times 10^{-8}\,\mathrm{m}^2$ and without accounting for the threshold temperatures, the sulfur completely oxidized after 700 days with an average oxidation rate of $2.0 \times 10^{-7}\,\mathrm{kg(S)}/\left(\mathrm{m}^3 \cdot \mathrm{s}\right)$ (or $3.6 \times 10^{-7}\,\mathrm{kg(O_2)}/\left(\mathrm{m}^3 \cdot \mathrm{s}\right)$ and a heat production of 4.5 $\mathrm{J}/\left(\mathrm{m}^3 \cdot \mathrm{s}\right)$). This oxidation rate is considered high but it is well within an expected range in most strongly oxidizing waste rock (between 10^{-6} and $10^{-9}\,\mathrm{kg(S)}/\left(\mathrm{m}^3 \cdot \mathrm{s}\right)$) (Pantelis and Ritchie, 1991, 1992; Anne and Pantelis, 1997; Pantelis et al., 2002). At $K = 2 \times 10^{-9}\,\mathrm{m}^2$ the oxidation rate is $1.0 \times 10^{-7}\,\mathrm{kg(S)}/\left(\mathrm{m}^3 \cdot \mathrm{s}\right)$ and it takes 1562 days to completely oxidized the sulfur. However, when the permeability decreases to $2 \times 10^{-10}\,\mathrm{m}^2$, after 1650 days the sulfur is oxidized by about 50 % at a rate of $5.2 \times 10^{-8}\,\mathrm{kg(S)}/\left(\mathrm{m}^3 \cdot \mathrm{s}\right)$ (Fig. 9.44A).

Now consider the impact of the threshold temperatures on oxidation rate and depending on the in-situ permeability, the oxidation rates decrease to about half of those rates without considering the threshold temperatures (Fig. 9.44B) at $K \geq 5 \times 10^{-8}\,\mathrm{m}^2$. Furthermore, at these permeabilities the sulfur is oxidized to small values after 500 days because cold temperatures significantly reduce the oxidation rate. Oxidation ceases during winter as the whole pile goes below 0 °C as shown in Fig. 9.44B. It is important to observe that at $K \leq 2 \times 10^{-9}\,\mathrm{m}^2$ with or without accounting for the threshold temperatures, the difference in oxidation rate is small 1.0×10^{-7} compared to $8.9 \times 10^{-8}\,\mathrm{kg\,(S)}/\left(\mathrm{m}^3 \cdot \mathrm{s}\right)$.

Fig. 9.45 shows O_2 and sulfur mass fraction at a permeability of $K = 2 \times 10^{-10}\,\mathrm{m}^2$ after 1600 days. At this low permeability, even though air convection occurs, diffusion of oxygen is the dominant mechanism. The combined mechanisms of diffusion and convection could

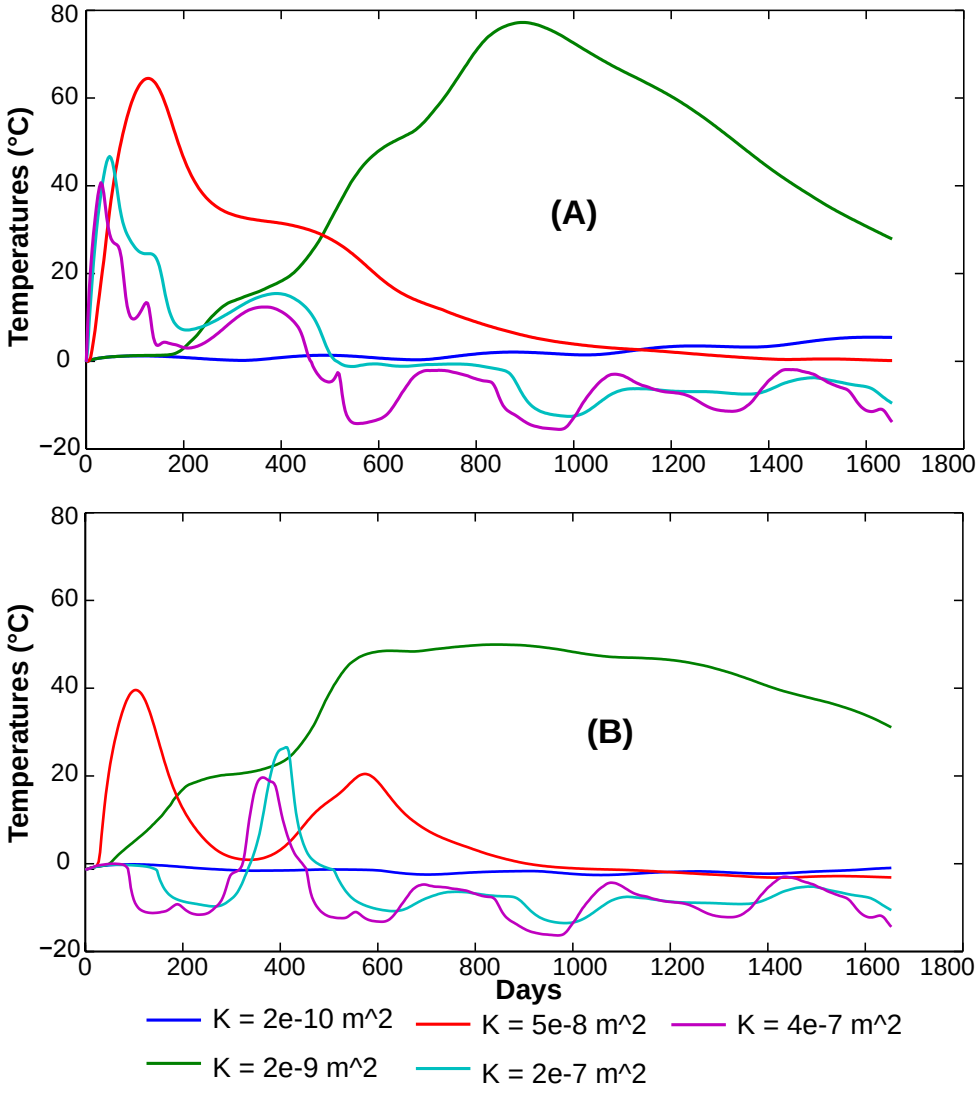

Figure 9.43: Temperature of a point at 5 m below the surface on the centre line of the test pile at various permeabilities with (A) and without (B) temperature-inhibiting factor (Fig. 9.1) on oxidation.

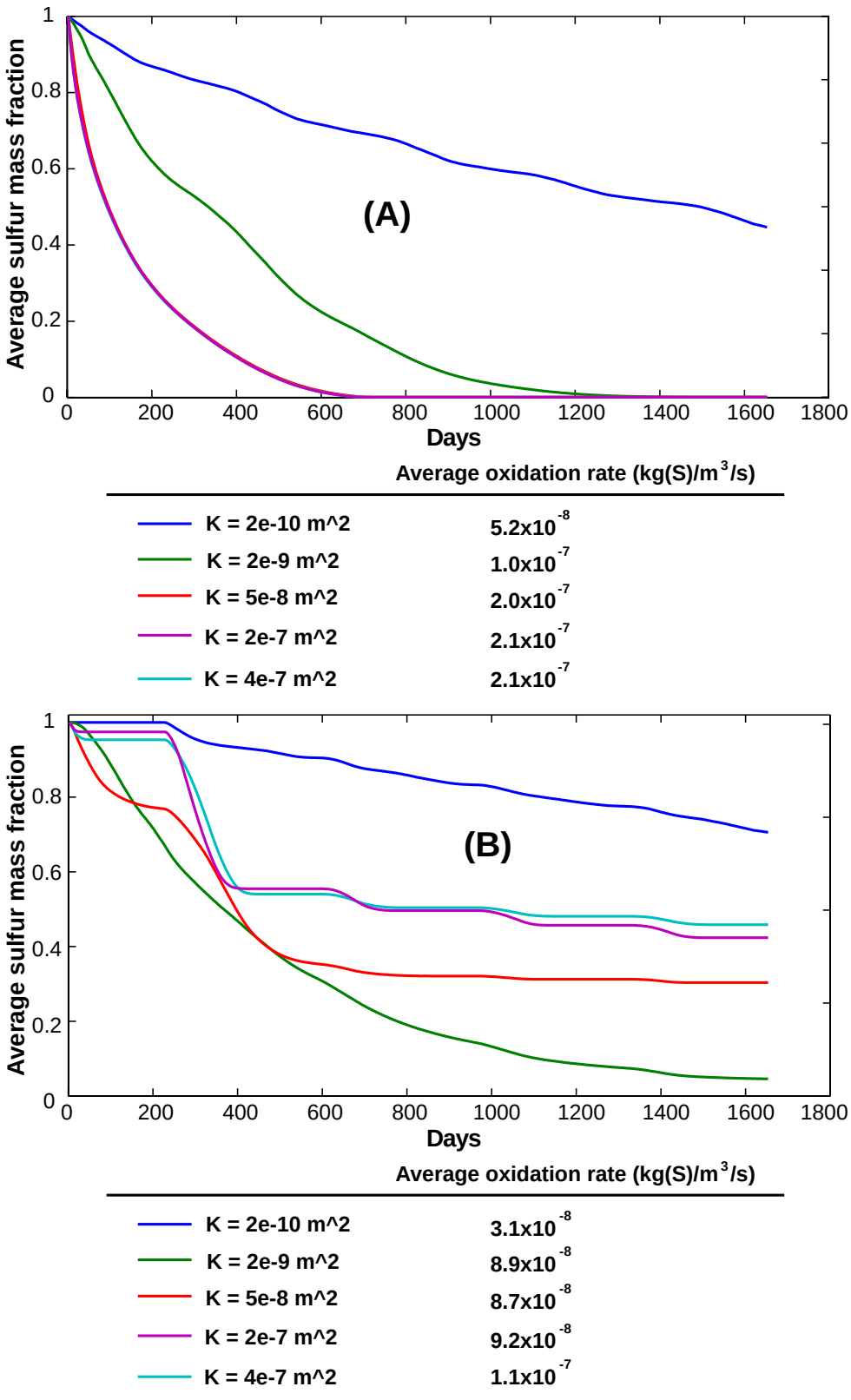

Figure 9.44: Average oxidation rate of the test pile at various permeabilities without (A) and with temperature-inhibiting factor (Fig. 9.1) on oxidation (B).

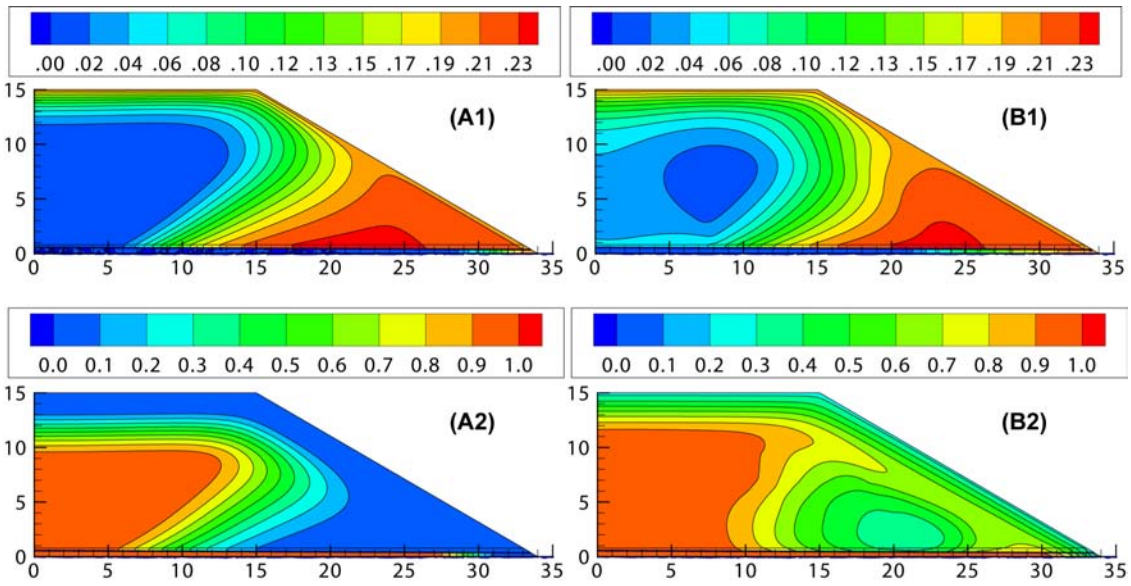

Figure 9.45: O_2 mass fraction (top figures) and sulfur mass fraction (bottom figures) in January 2011 (1600 days) at $K = 2 \times 10^{-10}\,\mathrm{m}^2$ without (A) and with (B) the temperature-inhibiting factor (Fig. 9.1) on oxidation.

not counteract the rate that oxygen is consumed by sulfur oxidation. Oxygen is only high near the surface and at the base whereas around the core oxygen is depleted (Fig. 9.45). Meanwhile, sulfur is totally oxidized near the surface and the batter, when not accounting for the threshold temperatures (Fig. 9.45A2). There is about 50 % sulfur remaining at the same locations due to cold temperatures eliminating oxidation every winter (Fig. 9.45B2).

9.6.4 Case 4: Wind-assisted advection/convection and active-heat-generating waste rock

9.6.4.1 Temperature evolution

A moderate wind flowing over a waste-rock pile can establish pressure gradients around the perimeter of the pile. These pressure gradients cause airflow into the pile from the ambient environment. The strength of this internal airflow depends on the permeability of the waste rock at a given wind speed. This additional airflow can supply significant oxygen and therefore increased oxidation rates. Fig. 9.46A1 and B1 show wind-induced air advection into the test pile and the increased interior temperatures of about twice near the core at $K = 2 \times 10^{-10}\,\mathrm{m}^2$ compared to the case without wind (Fig. 9.42). In contrast, at $K = 2 \times 10^{-9}\,\mathrm{m}^2$ temperatures near the core decrease. In fact, at this permeability natural air convection alone supplies sufficient oxygen for oxidation and therefore stronger airflow removes heat from the test pile decreasing its temperatures. However, if removed heat is not significant, the interior temperatures of the test pile will increase. These warm temperatures thaw the foundation to 20 m depth (Fig. 9.46A2 and B2).

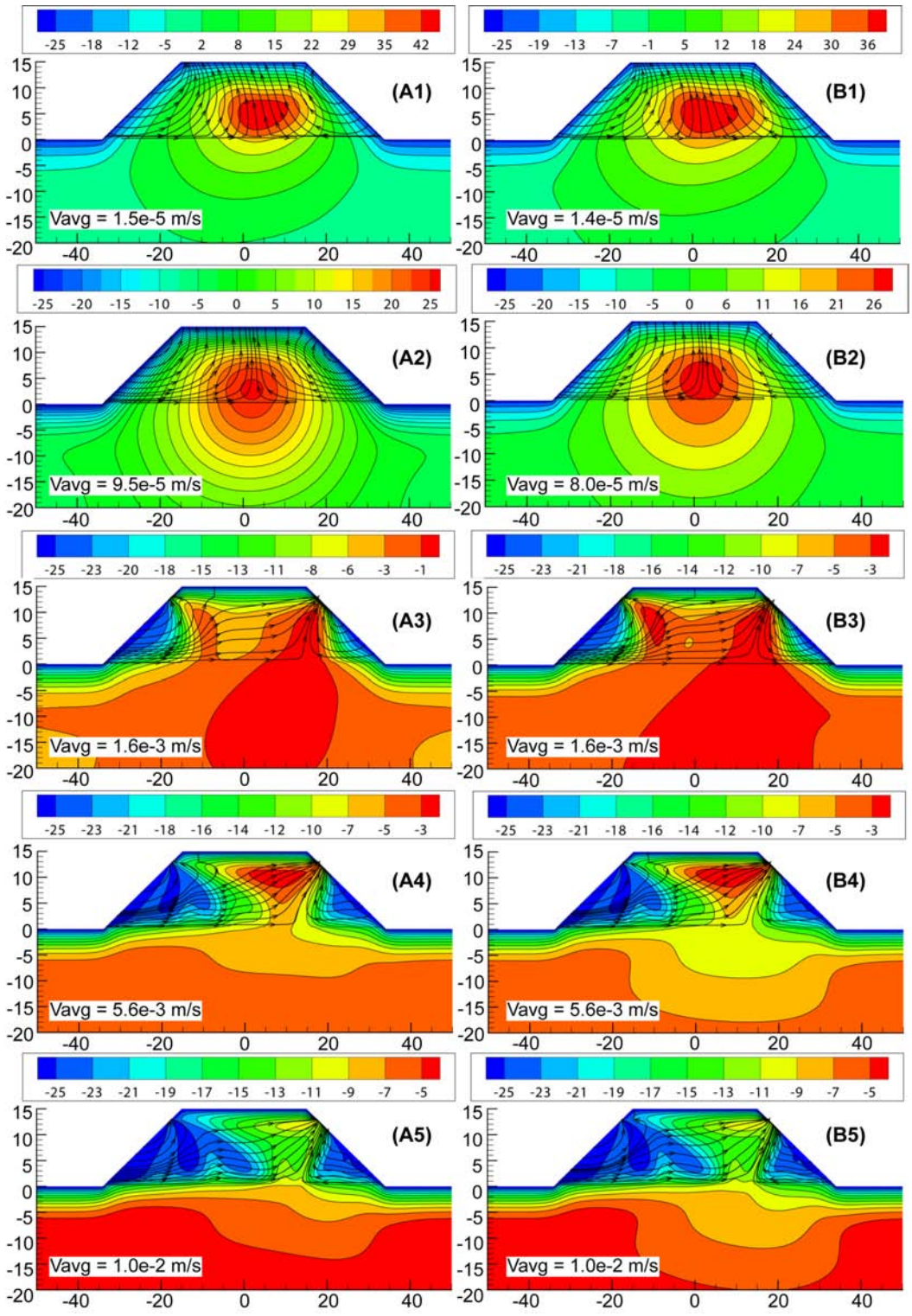

Figure 9.46: Wind-assisted isotherms and streamlines of the Type III test pile at various permeabilities in 1600 days without (figures on the left) and with temperature-inhibiting factor (Fig. 9.1) on oxidation (figures on the right): $2 \times 10^{-10}\,\mathrm{m}^2$ (A1 and B1), $2 \times 10^{-9}\,\mathrm{m}^2$ (A2 and B2), $5 \times 10^{-8}\,\mathrm{m}^2$ (A3 and B3), $2 \times 10^{-7}\,\mathrm{m}^2$ (A4 and B4) and $4 \times 10^{-7}\,\mathrm{m}^2$ (A5 and B5). The inset in each figure represents the average air velocity in the test pile.

At permeabilities $K \geq 2 \times 10^{-9}\,\mathrm{m}^2$, wind-induced advection only enhances thermal transport (rapid cooling or warming during winter or summer) within the test pile and it does not provide a substantial increase in oxidation rate. Furthermore, the average air velocity increases about twice with wind compared to without wind.

Fig. 9.47 shows temperature simulation results of wind-induced advection at 5 m below the surface on the test pile centre line. In a comparison with previous results without wind (Fig. 9.43) at permeabilities between 2×10^{-9} and $4 \times 10^{-7}\,\mathrm{m}^2$ the temperature results of wind-induced advection are comparable to those without wind as the oxidation rates remains constant which will be discussed in a later section. However at a lower permeability such as $K = 2 \times 10^{-10}\,\mathrm{m}^2$, wind-induced advection provides additional oxygen to the test pile and this added oxygen increases oxidation considerably. As a result, temperatures at this point surpasses that when $K = 2 \times 10^{-9}\,\mathrm{m}^2$ after about 1400 days

9.6.4.2 Oxidation rate

When not accounting for threshold temperatures, oxidation rates at permeabilities from 2×10^{-9} to $4 \times 10^{-7}\,\mathrm{m}^2$ are comparable to those without wind. Meanwhile at $K = 2 \times 10^{-10}\,\mathrm{m}^2$ the average oxidation rate has increased about twofold and at the end of the simulation period about 90 % of the sulfur oxidized compared to about 50 % without wind (Fig. 9.48A).

When the threshold temperatures are considered, the oxidation rates with wind-induced advection are lower than those of without wind for permeabilities between $2 \times 10^{-7}\,\mathrm{m}^2$ and $4 \times 10^{-7}\,\mathrm{m}^2$. However, at lower permeabilities, between 2×10^{-10} and $5 \times 10^{-8}\,\mathrm{m}^2$, airflow within the test pile created by wind is not strong enough to cool temperatures but it supplies additional oxygen to increase the oxidation rates compared to the case without wind (Fig. 9.48B).

Fig. 9.49 shows O_2 and sulfur concentration at permeability of $K = 2 \times 10^{-10}\,\mathrm{m}^2$ after 1600 days with wind-induced advection. The contours are asymmetrical and shift to the right as a result of wind blowing from the left side of the test pile. In comparison to the case without wind (Fig. 9.45) the area of complete oxygen depletion is smaller and the area of complete sulfur oxidation is larger. These indicate that the wind enhances the oxidation rate.

Fig. 9.50 shows contours for air pressure and velocity vector field. Air pressure on the batter facing wind has higher gradients than the opposite side of the test pile; the higher pressure gradients produces greater internal air velocity. Air velocity is larger near the batters and deep into the test pile the air velocity is small. Near the core, air pressure is negative and large as a result of warmer temperatures in this region compared to the surrounding regions. These warm temperatures cause airflow in the vertical direction out of the pile.

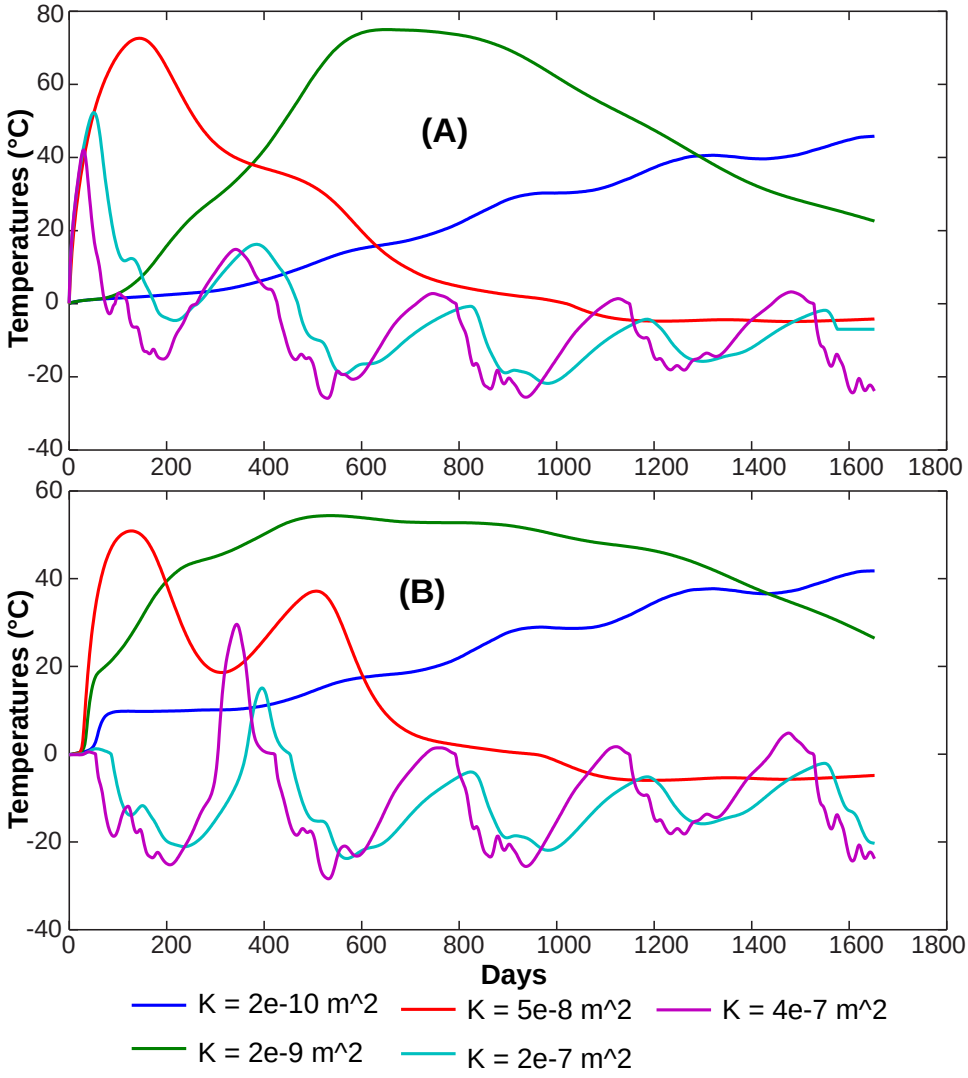

Figure 9.47: Temperature of a point at 5 m below the surface at the centre line of the test pile at various permeabilities with (A) and without (B) temperature-inhibiting factor (Fig. 9.1A) on oxidation.

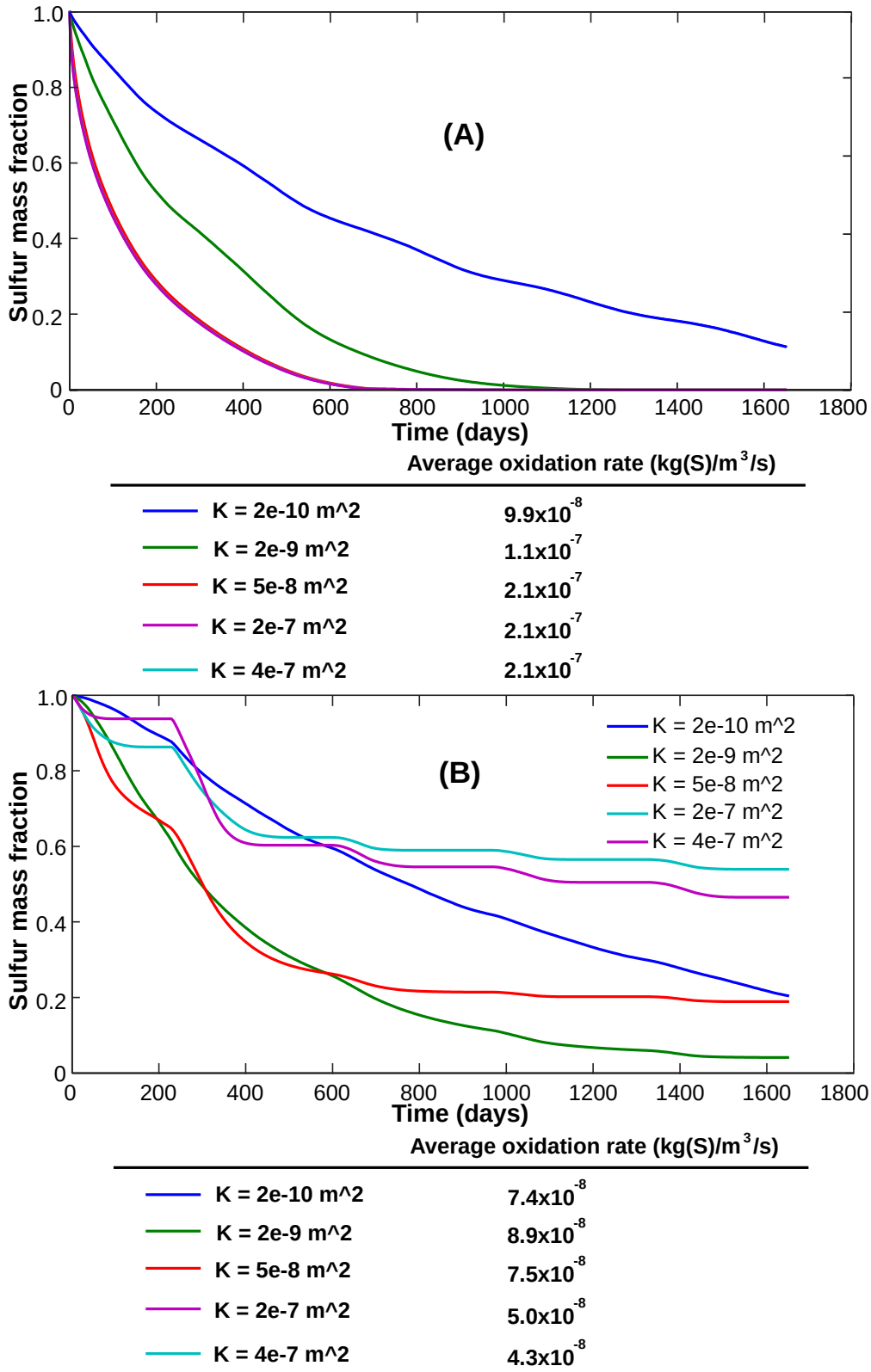

Figure 9.48: Wind-assist average oxidation rate of the test pile at various permeabilities without (A) and with (B) temperature-inhibiting factor (Fig. 9.1A) on oxidation.

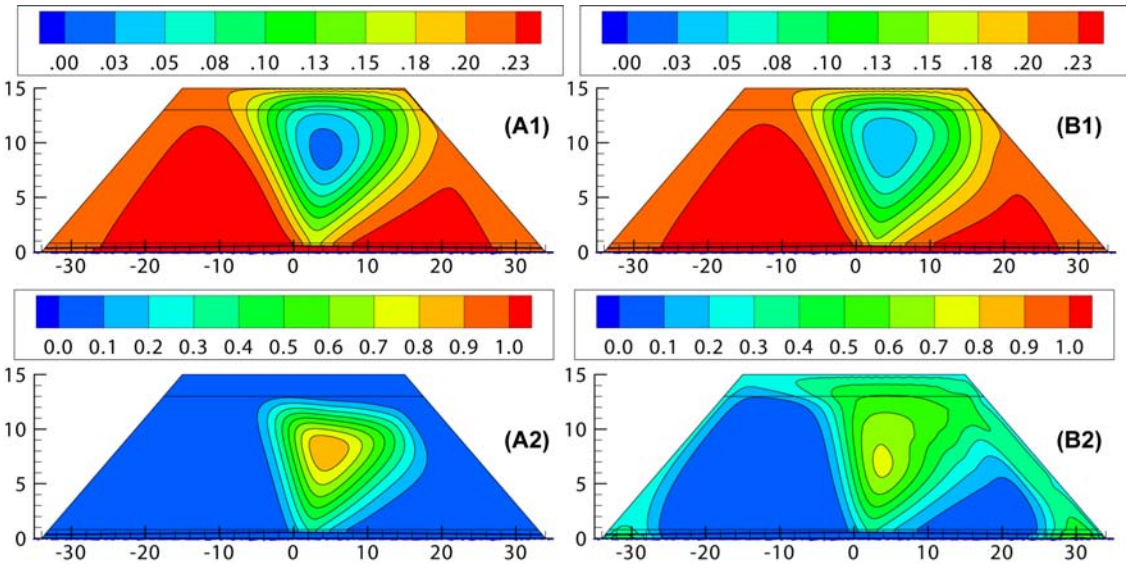

Figure 9.49: O_2 mass fraction (top figures) and sulfur mass fraction (bottom figures) in January 2011 (1600 days) at $K = 2 \times 10^{-10}\,\mathrm{m}^2$ without (A1 and A2) and with temperature-inhibiting factor (Fig. 9.1) on oxidation (B1 and B2).

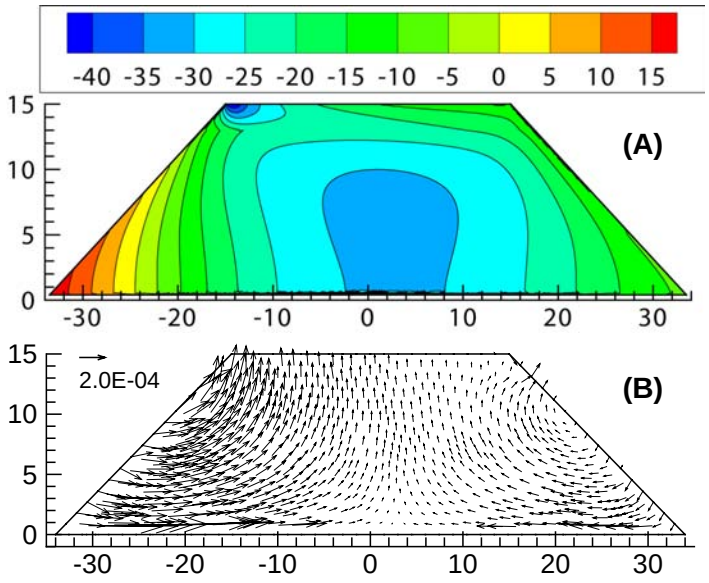

Figure 9.50: Contours for air pressure perturbation (in Pa) and pore-air velocity vector field in the test pile where there is wind-induced advection and no temperature inhibition factor at $K = 2 \times 10^{-9}\,\mathrm{m}^2$.

9.6.5 Case 5: Heat transfer due to active-heat-generation in the waste rock and its mitigation

9.6.5.1 Impeded layers of low permeability within the test pile

Simulations in this section represent studies in which layers of low permeability are placed within the test pile to minimize airflow. These impeded layers can be created during the construction of a pile through dump placement methods. The dumped layers create a low permeable surface within the pile as the surface is compacted by construction equipments and fine materials retained at the surface. The impeded layers have a low permeability that becomes a barrier to both air and water. Therefore placements of these layers would reduce ARD.

Two impeded layers were introduced into the modeling domain; one at the mid-height and the other at the surface of the test pile. The impeded layers can be created in waste-rock piles by end-dumping with immediate benches. Assuming that these layers have properties of the Type III waste rock but its permeability is five orders of magnitude smaller. For this reason, the impeded layers limit natural air convection in the regions near the batter of the test pile. Deep into the test pile, natural air convection is smaller and therefore the oxidation rate is low. The highest temperature within the test pile is lowered by half and the average air velocity is reduced by three times compared to the case without impeded layer (Fig. 9.42B2 and Fig. 9.51A1). Fig. 9.51 A2 and A3 show that oxygen availability and sulfur oxidation is limited to near the batter of the test pile. However, near the core the oxygen is totally depleted and sulfur concentration remains high.

The average oxidation rate within the test pile with the impeded layers is reduced to about half compared to that without these layers from 8.9×10^{-8} to $4.9 \times 10^{-8}\,\mathrm{kg(S)/\left(m^3 \cdot s\right)}$ which is similar to the reduction in temperatures. About 50 % of the sulfur is oxidized compared to more than 90 % without these layers after 1650 days (Fig. 9.44B and Fig. 9.52A).

9.6.5.2 Covering the slopes of the test pile with an impermeable layer to oxygen diffusion

The above simulations show that most air enters the test pile via the batter, therefore covering the batter should reduce ARD production. Covering materials can be glacial till or other low permeability materials and the cover is placed as the test pile is built. The cover materials will have a low permeability in the simulations in this section. It is assumed that the layer is impermeable with very low oxygen diffusion.

The isotherms for this case are similar to those for the impeded layers, however covering the batter lowers the temperatures of the test pile compared to the impeded layers (Fig. 9.51A1 and A2). The average air velocity is similar to those for impeded layers. Airflow patterns change drastically as the air no longer enters the test pile from the batter. To oxidize sulfur deeper in the test pile, oxygen has to be transported downward from the sur-

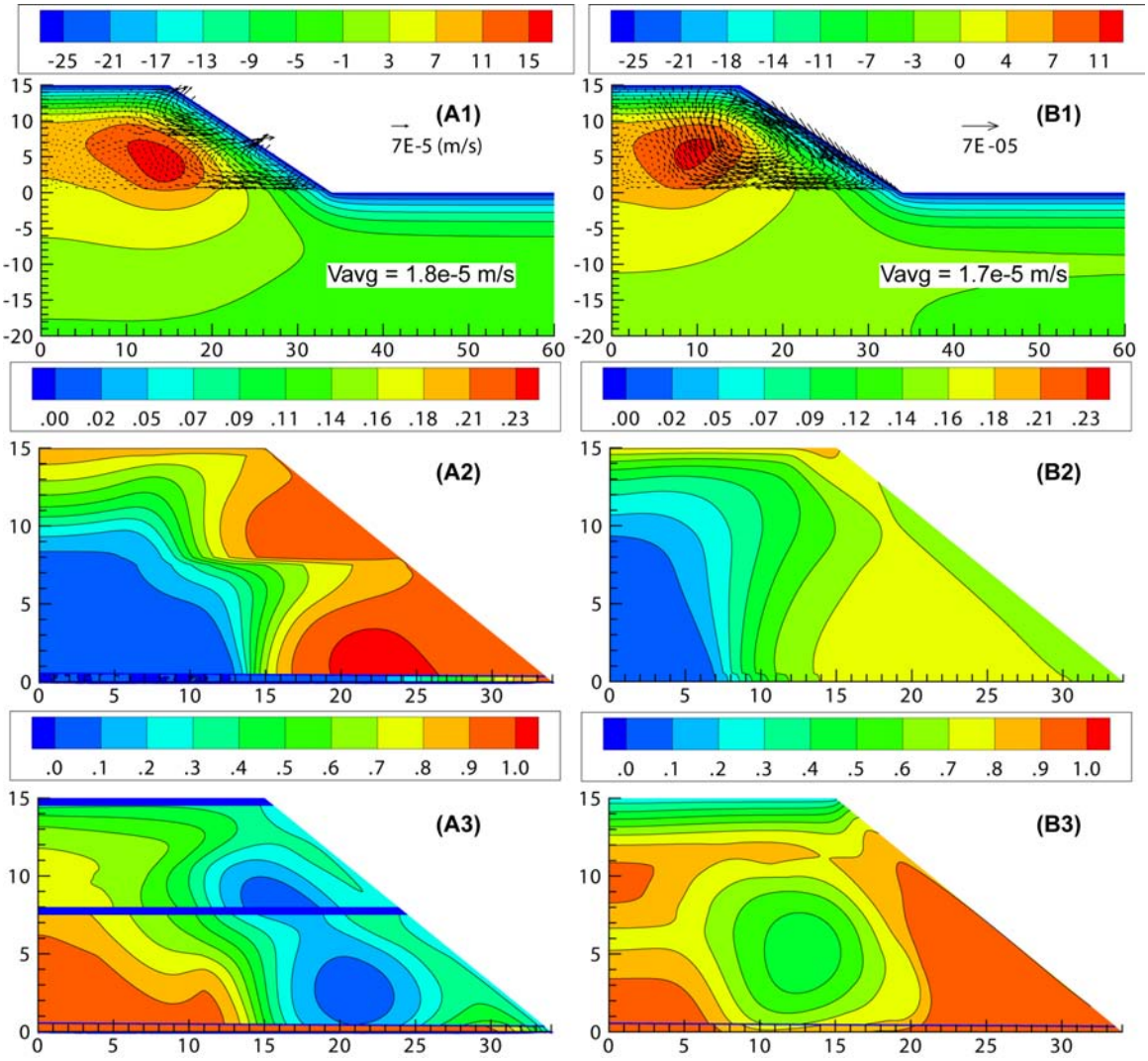

Figure 9.51: Numerical results of impeded layers (A1, A2 and A3) and impermeable slope (B1, B2 and B3) in January 2011 (1600 days): waste rock of $K = 2 \times 10^{-9}\,\mathrm{m}^2$ and the impeded layer of $K = 5 \times 10^{-16}\,\mathrm{m}^2$. A1 and B1: isotherm (in °C); A2 and B2: Oxygen mass fraction; A3 and B3: Sulfur mass fraction.

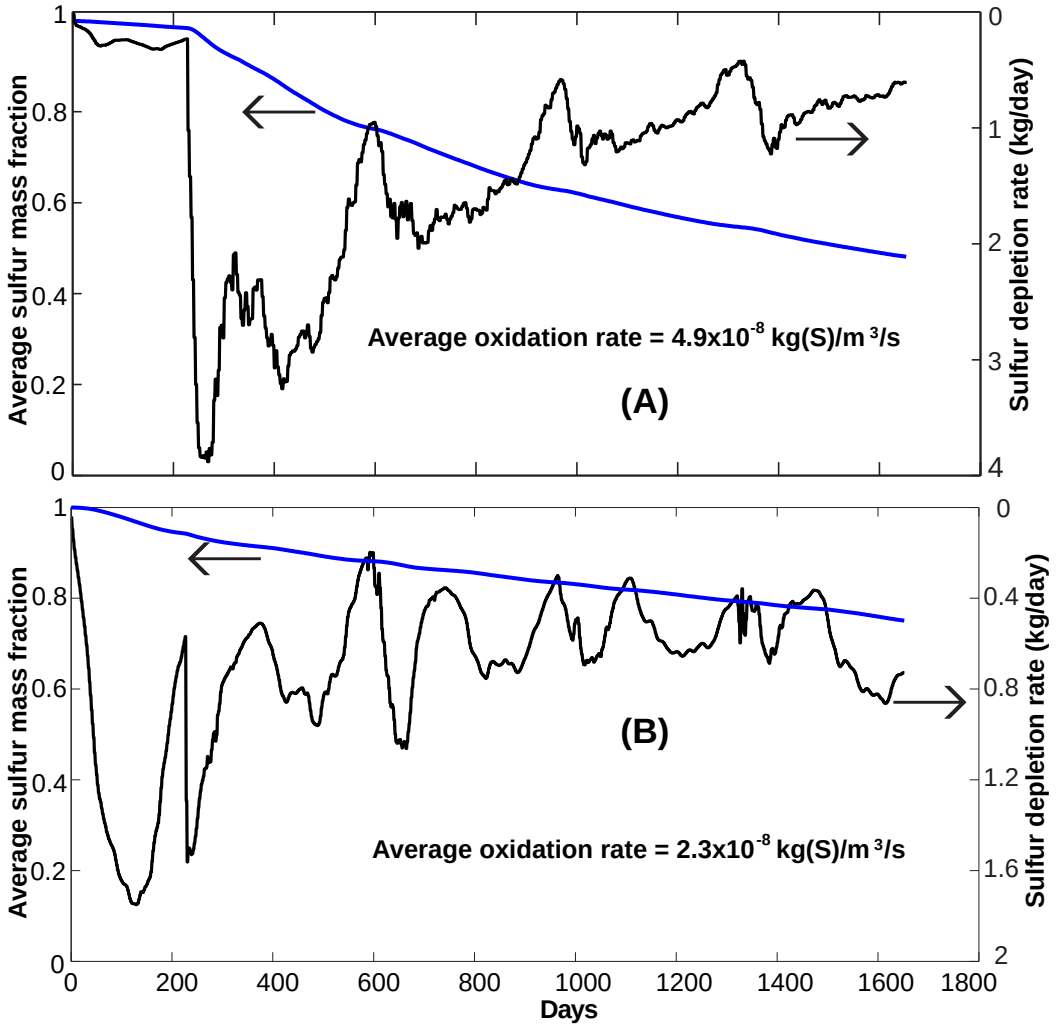

Figure 9.52: Isotherms (in °C) (A), Oxygen mass fraction (B) and Sulfur mass fraction (C) in January 2011 (1600 days): waste rock of $K = 2 \times 10^{-9}\,\mathrm{m}^2$ and the impeded layer of $K = 5 \times 10^{-16}\,\mathrm{m}^2$.

face. However, very little oxygen reaches deep into the pile as it is consumed in the surface regions. Therefore, the oxidation rate is low. At the same time cold temperatures penetrate into the pile and further lowered the oxidation rate. As a result, temperatures are low and therefore temperature gradients within the test pile are small. The small temperature gradients lead to weak natural air convection, as a result low amount of oxygen is transferred into the pile and oxidation rate decreases.

The oxygen concentration is low though out the test pile especially near the core (Fig. 9.51B2). Due to the low oxidation rate, the sulfur concentration after 1650 days is high in the test pile and it is highest near the batter (Fig. 9.51B3). The average oxidation rate is $2.3 \times 10^{-8}\,\mathrm{kg(S)}/\left(\mathrm{m}^3 \cdot \mathrm{s}\right)$ which is about half the value associated with the impeded layers (Fig. 9.52).

9.6.5.3 Covering the slopes of the test pile with a layer permeable to oxygen

In this section, inward fluxes of 1×10^{-7} and $1 \times 10^{-6}\,\mathrm{kg(O_2)}/\left(\mathrm{m}^2 \cdot \mathrm{s}\right)$ were applied to the batter and the cover layer is impermeable to airflow. Therefore, oxygen is supplied through the batter via the applied fluxes. At a low applied flux of $1 \times 10^{-7}\,\mathrm{kg(O_2)}/\left(\mathrm{m}^2 \cdot \mathrm{s}\right)$, the isotherms, oxygen and sulfur concentration are similar to those without an applied flux (Fig. 9.51B1 to B3 and Fig. 9.53A1 to A3). As the applied flux increases to $1 \times 10^{-6}\,\mathrm{kg(O_2)}/\left(\mathrm{m}^2 \cdot \mathrm{s}\right)$, the internal oxidation increases resulting in high temperatures near the core and around the batter. The applied flux through the covering layer of $1 \times 10^{-6}\,\mathrm{kg(O_2)}/\left(\mathrm{m}^2 \cdot \mathrm{s}\right)$ is considered high because in most soils, oxygen diffusion is in the order of $1 \times 10^{-7}\,\mathrm{kg(O_2)}/\left(\mathrm{m}^2 \cdot \mathrm{s}\right)$ (Amos et al., 2009a).

At the applied influx of $1 \times 10^{-7}\,\mathrm{kg(O_2)}/\left(\mathrm{m}^2 \cdot \mathrm{s}\right)$, the oxidation rate is low and at the end of the simulation period (1650 days) only 30 % of the sulfur oxidized with an average oxidation rate of $2.7 \times 10^{-8}\,\mathrm{kg(S)}/\left(\mathrm{m}^3 \cdot \mathrm{s}\right)$ (Fig. 9.54). This is not much larger than the case without an applied flux $2.3 \times 10^{-8}\,\mathrm{kg(S)}/\left(\mathrm{m}^3 \cdot \mathrm{s}\right)$ (Fig. 9.52B). At an inward applied flux of $1 \times 10^{-6}\,\mathrm{kg(O_2)}/\left(\mathrm{m}^2 \cdot \mathrm{s}\right)$ about 70 % sulfur is oxidized with an average oxidation rate of $6.0 \times 10^{-8}\,\mathrm{kg(S)}/\left(\mathrm{m}^3 \cdot \mathrm{s}\right)$.

9.6.6 Summary and discussion of the Type III test pile (the uncovered test pile)

Field temperatures of the Type III test pile showed a rapid response of the interior temperatures to the variation of surface temperatures (Fig. 9.34 and Fig. 9.35). This response can not be achieved if controlled by conduction. According to thermal conduction calculation, the time lag between temperature peaks at the surface and a distance of 11.3 m is 233 days (calculated using Eqn. 9.7 (Carslaw and Jaeger, 1959)) and amplitude of temperature diminishes by 98.2 % over this depth (calculated through Eqn. 9.8 (Carslaw and Jaeger, 1959)). These amplitude and time lag differ significantly from those observed in the field measurements (Fig. 9.34 and Fig. 9.35). Furthermore, field data of the surface temperatures time

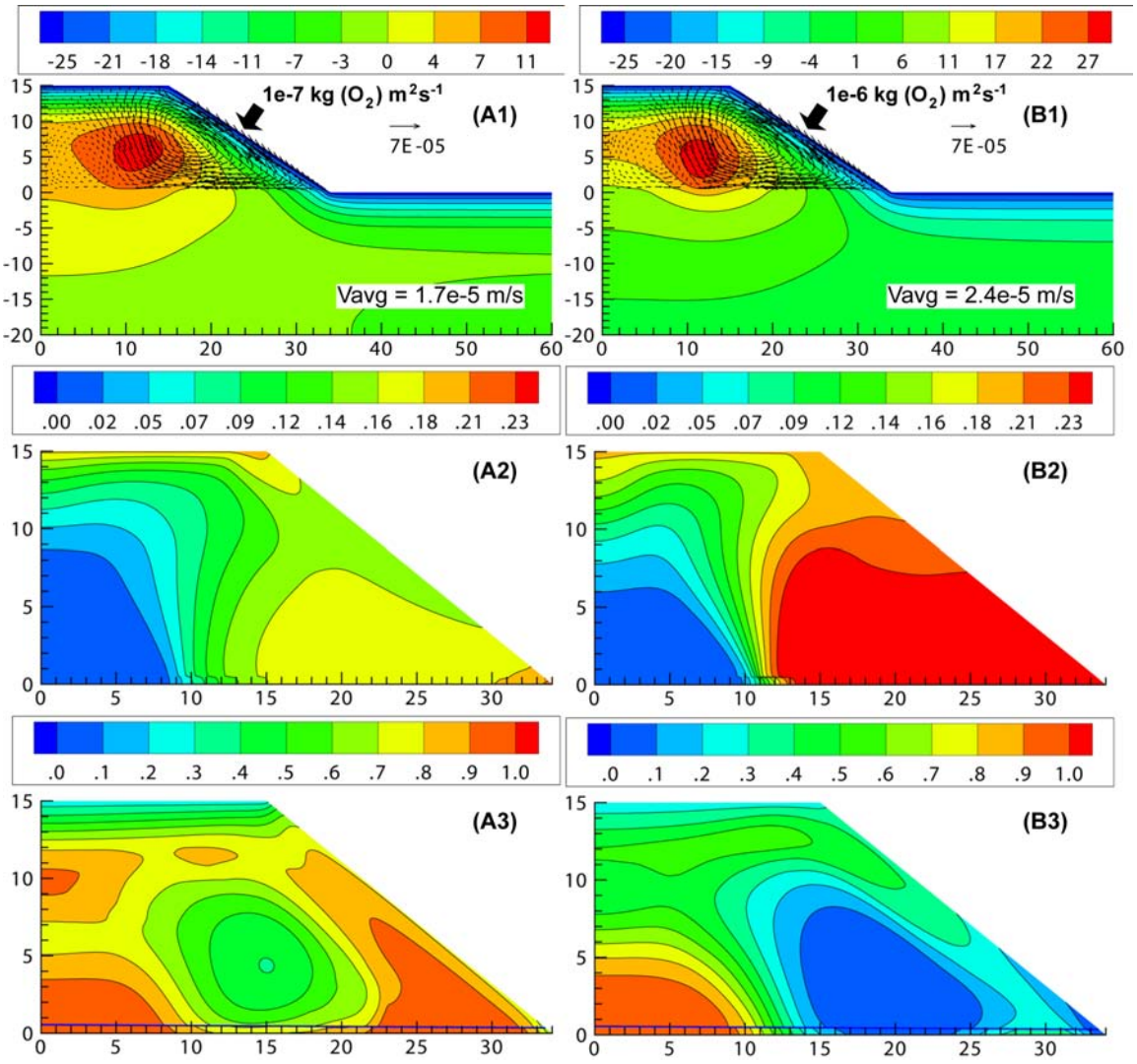

Figure 9.53: Numerical results of an applied flux of $1 \times 10^{-7}\,\mathrm{kg(O_2)/\left(m^2 \cdot s\right)}$ (A1, A2 and A3) and $1 \times 10^{-6}\,\mathrm{kg(O_2)/\left(m^2 \cdot s\right)}$ (B1, B2 and B3) in January 2011 (1600 days), waste rock of $K = 2 \times 10^{-9}\,\mathrm{m^2}$. A1 and B1: isotherm; A2 and B2: Oxygen mass fraction; A3 and B3: Sulfur mass fraction.

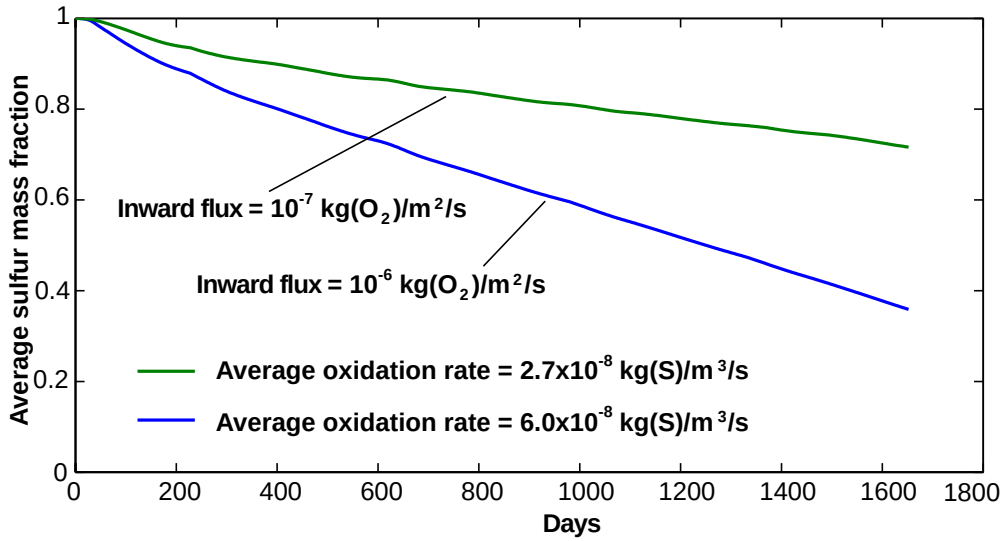

Figure 9.54: Numerical results of an applied flux of $1 \times 10^{-7}\,\mathrm{kg(O_2)/\left(m^2 \cdot s\right)}$ (A1, A2 and A3) and $1 \times 10^{-6}\,\mathrm{kg(O_2)/\left(m^2 \cdot s\right)}$ (B1, B2 and B3) in January 2011 (1600 days), waste rock of $K = 2 \times 10^{-9}\,\mathrm{m^2}$. A1 and B1: isotherm; A2 and B2: Oxygen mass fraction; A3 and B3: Sulfur mass fraction.

series include diurnal variation and this diurnal variation also exits deep within the pile. Conduction is strongly attenuated and this diurnal variation diminishes at a shallow depth. Therefore, the wind-induced advection and natural air convection contribute significantly to the heat transfer within the Type III test pile.

$$\text{Time lag} = x\left(\frac{\omega}{t\kappa}\right)^{1/2} \tag{9.7}$$

$$\text{Amplitude attenuation} = e^{-2\pi x/\lambda} \tag{9.8}$$

Where $x = 11.3\,\mathrm{m}$ is the distance from the surface; $\kappa = 7.9 \times 10^{-7}\,\mathrm{m^2/s}$ is the thermal diffusivity; $\lambda = (4\pi\kappa t)^{1/2} = 17.7\,\mathrm{m}$ is a wavelength for an annual temperature variation; $t = 365$ days is the period of surface temperature.

Conduction modeling can reproduce field values within 1.5 m below the surface because of the low permeability of this layer. Below this surface layer, simulation results with wind-induced advection are only comparable to field data if permeability of the test pile is in the order of $10^{-7}\,\mathrm{m^2}$ which is about two orders of magnitude larger than field measurements of permeability. However, the field-measurements values of permeability were only conducted to 6 m depth (Amos et al., 2009a) and finer materials were placed around the probe to protect it as the waste rock was end-dumped. Therefore, field measured values may not represent the actual permeability of the coarse waste rock in the lower parts of the test piles.

At high permeabilities $\left(K \geq 10^{-7}\,\mathrm{m^2}\right)$, the simulations showed that temperatures within the pile were strongly correlated to surface temperatures (large amplitudes and low time

lag). It is also important to mention that the test piles were built with a small width to height ratio and end-dumping methods which creates layers of high permeability near the base. These properties allow a strong wind to pass through the entire cross section of the test pile (Amos et al., 2009a). However, full-scale-waste-rock piles at the Diavik site are about 80 m in height and about 1 km in diameter. The interior structure of the full-scale piles is highly heterogeneous (Smith et al., 1995). These properties limit wind-induced advection to the batters. Furthermore, conduction would dominate in most regions except regions of high permeability which are usually near the base and the batters.

Even though the oxidation rate of Type III waste rock is low and negligible (Amos et al., 2009b), simulations were run with the assumption that oxidation occurs at much higher rates between 10^{-6} and $10^{-9}\,\mathrm{kg(S)/\left(m^3 \cdot s\right)}$ to evaluate these impacts on internal temperature response. At $K \leq 2 \times 10^{-9}\,\mathrm{m^2}$ temperatures within the test pile were high because heat released via oxidation could not escape effectively from the test pile. However, at permeabilities $\geq 5 \times 10^{-8}\,\mathrm{m^2}$, there were no great differences whether the waste rock was releasing heat or not after 1650 days since at these high permeabilities the wind-induced advection and/or natural air convection during winter sufficiently removed heat release from the test pile while supplying oxygen for oxidation.

Moreover, at $K \geq 2 \times 10^{-9}\,\mathrm{m^2}$ the wind-induced advection did not have a great influence on the oxidation rate as natural air convection supplied adequate oxygen into the test pile. Therefore the oxidation rate was not significantly different. However, at $K \leq 2 \times 10^{-10}\,\mathrm{m^2}$, natural air convection was weak and it did not provide enough oxygen to maintain a strong oxidation rate; a similar result was found by Pantelis and Ritchie (1992). With additional oxygen supplied by wind, the oxidation rate was stronger and the released heat increased internal temperatures within the pile significantly. We can conclude that with the assistance of wind of 20 km/h, permeability of $10^{-10}\,\mathrm{m^2}$ is a threshold value to retain high oxidation rates within the test pile and without wind the threshold value is $10^{-9}\,\mathrm{m^2}$.

Covering the slope or placement of low permeability layers (impeding layers) in the pile lowered oxidation rates and temperatures within the test pile compared to without covering or impeded layers. With the current geometry and waste rock properties, covers provide better solution than low permeability layers as the covers create lower temperatures and oxidation rates within the pile.

9.7 Conclusions

9.7.1 Covered test pile

Numerical simulations were run for a covered waste rock test pile at Diavik and conduction was found to be the dominated heat transfer in the test pile. The cover effectively maintained below 0 °C of the waste rock. However, due to cold temperatures at the site, the use of ACC significantly lowered ground temperatures beneath the cover compared to the conduction

case. The higher permeability of ACC the lower the ground temperatures; it was found that by assuming the permeability of $K = 8 \times 10^{-7}$ m^2, a 3 m thickness of ACC was sufficient to maintain temperature of potential acid generation waste rock beneath the cover around -5 °C. At this cold temperature, it is expected that oxidation of sulfides is eliminated. The ACC effectively lowered temperatures at its base the same as the surface temperature in term of freezing index with a 0 °C-days thawing index.

For cases, where the Type III waste rock beneath the cover was undergoing oxidation, the combined effects of the ACC and high saturation of the till could reduce or eliminate oxidation by keeping the waste rock temperatures below the threshold temperatures for oxidation of sulfide minerals. According to the simulations, the ACC with 1 m till ($\geq 50\,\%$ saturation) and the air-convection-layer thickness of 3 m ($K \geq 4 \times 10^{-7}$ m^2) would keep underlying waste rock below 0 °C.

9.7.2 Type III test pile

Due to the current configuration of the Type III test pile which is narrow compared to the full-scale piles, field values of temperatures were only comparable to simulation results with the combined effects of wind (forced convection) and natural air convection at permeabilities $K \geq 10^{-7}$ m^2. Despite the extremely low oxidation rate of Type III waste rock, by varying the oxidation rate between 10^{-9} and $10^{-7}\,\mathrm{kg(S)}/\left(\mathrm{m}^3 \cdot \mathrm{s}\right)$. At low permeabilities $K \leq 2 \times 10^{-9}$ m^2 and without wind after 1650 days, the heat released due to oxidation created high temperatures within the pile. Whereas at higher permeabilities $K \geq 5 \times 10^{-8}$ m^2 temperatures within the test pile did not differ considerably compared to cases without oxidation. With advection due to wind, a permeability of $10^{-10}\,\mathrm{m}^2$ was the threshold value that was high enough to retain high oxidation rates and temperatures within the test pile. However, without wind the threshold permeability is $10^{-9}\,\mathrm{m}^2$ and by covering the slopes of the test pile oxidation rate were reduced to about one third of that without cover.

References

Amos, R. T. (2009). Personal communication.

Amos, R. T., Blowes, D. W., Smith, L., and Sego, D. C. (2009a). Measurement of wind-induced pressure gradients in a waste rock pile. *Vadose Zone J*, 8(4):953–962.

Amos, R. T., Smith, L., Neuner, M., Gupton, M., Blowes, D. W., Smith, L., and Sego, D. C. (2009b). Diavik waste rock project: Oxygen transport in covered and uncovered piles. In *The 8th ICARD International Conference On Acird Rock Drainage, Skelleftea, Sweden, 2009*.

Andersland, O. B. and Ladanyi, B. (2004). *Frozen Ground Engineering*. John Wiley & Sons.

Anne, R. and Pantelis, G. (1997). Coupled natural covection and atmosphere wind forced advection in above ground reacting heaps. In *Inter Conf on CFD in Mineral Processing and Power Generation, CSIRO*.

Arenson, L.U.a, S. D. N. G. (2007). The use of a convective heat flow model in road designs for northern regions. Ottawa, ON. cited By (since 1996) 0; Conference of 2006 IEEE EIC Climate Change Technology Conference, EICCCC 2006; Conference Date: 10 May 2006 through 12 May 2006; Conference Code: 71708.

Azam, S., Wilson, G., Herasymuik, G., Nichol, C., and Barbour, L. (2007). Hydrogeological behaviour of an unsaturated waste rock pile: A case study at the golden sunlight mine, montana, usa. *Bulletin of Engineering Geology and the Environment*, 66(3):259–268.

Bear, J. (1972). *Dynamics of fluids in porous media*. Dover Publications, Inc.

Bennett, J. W., Garvie, A., Pantelis, G., Rictchie, A., Bell, A. V., and Noel, M. (1995). Comparison of measured and predicted transport processes controlling oxidation in the waste rock piles at the heath steele mine site. In *Conference on Mining and the Environment, Sudbury, Ontario, May 28th - June 1st, 1995*.

Carslaw, H. S. and Jaeger, J. C. (1959). *Conduction of heat in solids*. Oxford University Press.

Cheng, G., W. Q. M. W. (2009). Innovative designs of permafrost roadbed for the qinghai-tibet railway. *Science in China, Series E: Technological Sciences*, 52(2):530–538. cited By (since 1996) 2.

Chi, X. (2010). Characterizing low-sulfide instrumented waste-rock piles: image grain-size analysis and wind-induced gas transport. Master's thesis, University of Waterloo.

Comsol (2009). *Comsol multiphysics' manual*. Comsol, Inc., 744 Cowper Street, Palo Alto, CA 94301, USA.

DDMI (2006). Interim closure and reclamation plan. Version 2, September 2006.

Environment-Canada (2008a). Climate data online. national climate data and information archive. Technical report, Environment Canada.

Farouki, O. T. (1981b). *Thermal properties of soils*. United States Army Corps of Engineers, Cold Regions Research and Engineering Laboratory, Hanover, New Hampshire, USA.

Goering, D. J. (1998). Experimental investigation of air convection embankments for permafrost-resistant roadway design. In *Seven International Conference on Permafrost*.

Goering, D. J. (2003). Passively cooled railway embankments for use in permafrost areas. *Journal of Cold Regions Engineering*, 17(3):119–133.

Goering, D. J. and Kumar, P. (1996). Winter-time convection in open-graded embankments. *Cold Regions Science and Technology*, 24(1):57–74.

Harries, J. R. and Ritchie, A. I. M. (1981). The use of temperature profiles to estimate the pyritic oxidation rate in a waste rock dump from an opencut mine. *Water, Air and Soil Pollution*, 15(4):405–423.

Hendry, M. J. (1982). Hydraulic conductivity of a glacial till in alberta. *Ground Water*, 20(2):162–169.

Hollesen, J., Elberling, B., and Jansson, P. (2011). Modelling temperature-dependent heat production over decades in high arctic coal waste rock piles. *Cold Regions Science and Technology*, 65(2):258–268.

Hu, X., Holubec, I., Wonnacott, J., Lock, R., and Olive, R. (2003). Geomorphological, geotechnical and geothermal conditions at diavik mines. In *8th International Conference on Permafrost. Zurich, Switzerland.*

Jaynes, D. B., Rogowski, A. S., and Pionke, H. B. (1984b). Acid mine drainage from reclaimed coal strip mines: 1. model description. *Water Resour. Res.*, 20:233–242.

Kuo, E. and Ritchie, A. (1999). The impact of convection on the overall oxidation rate in sulfidic waste rock dumps. In *Conference Proceedings, Sudbury 99 - Mining and the Environment*, volume 1, pages 9–18.

Launder, B. and Spalding, D. (1972). *Mathematical Models of Turbulence*. Academic Press.

Lefebvre, R., Hockley, D., Smolensky, J., and Gelinas, P. (2001b). Multiphase transfer processes in waste rock piles producing acid mine drainage: 1: Conceptual model and system characterization. *Journal of Contaminant Hydrology*, 52(1-4):137–164.

Lefebvre, R., Hockley, D., Smolensky, J., and Lamontagne, A. (2001c). Multiphase transfer processes in waste rock piles producing acid mine drainage. 2. applications of numerical simulation. *Journal of contaminant hydrology*, 52(1-4):165–186.

Lowson, R. T. (1982). Aqueous oxidation of pyrite by molecular oxygen. *Chemical Re-*

views, 82(5):461–497.

Ltd., G. A. (1999). Hydrogeological modelling of feasibility mine plan, diavik diamond project, n.w.t. Technical report.

Lunardini, V. J. (1981). *Heat transfer in cold climates*. Van Nostrand Reinhold Company.

Ma, W., Feng, G., Wu, Q., and Wu, J. (2008). Analyses of temperature fields under the embankment with crushed-rock structures along the qinghai-tibet railway. *Cold Regions Science and Technology*, 53(3):259–270.

Martin, V., Aubertin, M., Bussiere, B., and Chapuis, R. P. (2004). Evaluation of unsaturated flow in mine waste rock. In *57th Canadian geotechnical conference*.

Molson, J., Fala, O., Aubertin, M., and Bussière, B. (2005). Numerical simulations of pyrite oxidation and acid mine drainage in unsaturated waste rock piles. *Journal of Contaminant Hydrology*, 78(4):343–371.

Morin, K. A. and Hutt, N. M. (2001). Relocation of net-acid-generating waste to improve post-mining water chemistry. *Waste Management*, 21(2):185–190.

Neuner, M., Smith, L., Blowes, D. W., Sego, D. C., Smith, L. J., Fretz, N., and Gupton, M. (2012). The diavik waste rock project: Water flow though mine waste rock in a permafrost terrain. *Applied Geochemistry*, (0):–.

Newman, L. L., Barbour, S. L., and Fredlund, D. G. (1997). Mechanisms for preferential flow in vertically layered unsaturated waste rock. In *50th Canadian Geotechnical Conference of Canadian Geotechnical Society*.

Nield, D. and Bejan, A. (1999). *Convection in porous media*. Springer, New York.

Pantelis, G. and Ritchie, A. I. M. (1991). Macroscopic transport mechanisms as a rate-limiting factor in dump leaching of pyritic ores. *Applied Mathematical Modelling*, 15(3):136–143.

Pantelis, G. and Ritchie, A. I. M. (1992). Rate-limiting factors in dump leaching of pyritic ores. *Applied Mathematical Modelling*, 16(10):553–560.

Pantelis, G., Ritchie, A. I. M., and Stepanyants, Y. A. (2002). A conceptual model for the description of oxidation and transport processes in sulphidic waste rock dumps. *Applied Mathematical Modelling*, 26(7):751–770.

Ritchie, A. I. M. (1994b). Bio-oxidation heaps and amd from waste rock dumps: The importance of the intrinsic oxidation rate. In *Proceedings of the 1994 Annual Conference the Australasian Institute of Mining and Metallurgy*, page 473, Carlton, Australia. Australasian Inst of Mining & Metallurgy.

Smith, L., Lopez, D., Beckie, R., Morin, K., Dawson, R., and Price, W. (1995). Hydrogeology of waste rock dumps. Technical report, Department of Natural Resources Canada, Ottawa, Ontario, Canada.

Smith, M. W. and Riseborough, D. W. (2002). Climate and the limits of permafrost: a zonal analysis. *Permafrost Periglac. Process.*, 13(1):1–15.

Song, Q. and Yanful, E. K. (2008). Monitoring and modeling of sand-bentonite cover for ard mitigation. *Water, air, and soil pollution*, 190(1-4):65–85. Compilation and indexing terms, Copyright 2008 Elsevier Inc.

Sracek, O., Gelinas, P., Lefebvre, R., and Nicholson, R. V. (2006). Comparison of methods for the estimation of pyrite oxidation rate in a waste rock pile at mine doyon site, quebec, canada. *Journal of Geochemical Exploration*, 91(1-3):99 – 109.

Tasa, D., Tarbuck, E. J., and Lutgens, F. K. (2006). *The Atmosphere*. Prentice Hall.

Terzaghi, K., Peck, R. B., and Mesri, G. (1996). *Soil Mechanics in Engineering Practice*. John Wiley & Sons, third edition.

Tipler, P. A. (1999). *Physics for Scientists and Engineers*. W.H. Freeman.

Wickland, B. and Wilson, G. W. (2005a). Research of co-disposal of tailings and waste rock. *Geotechnical News*, 23(3):35–38.

Xu, J. and Goering, D. J. (2008b). Experimental validation of passive permafrost cooling systems. *Cold Regions Science and Technology*, 53(3):283–297.

CHAPTER 10

Summary, Conclusions and Recommendations

10.1 Summary and Conclusions

The goal of this study was to investigate the thermal transport within waste-rock piles placed on a continuous permafrost region, and find feasible methods to eliminate or reduce Acid Rock Drainage (ARD) in Potential Acid Generating (PAG) waste rock. It is well known that the oxidation rate of sulfide minerals is temperature-dependent and the oxidation rate is significantly lower under cold temperatures. In permafrost regions, one of the methods for producing rapid cooling termed Air Convection Cover (ACC) was used to examine its effectiveness to reduce ARD through numerical simulations. Moreover, thermal data of three experimental waste-rock piles (test piles) and three drill holes to 40 m depth in a 80 m high waste-rock pile were used to achieve the research objectives. In addition, numerical simulations and lab tests of natural air convection were also conducted for calibration and future prediction of thermal transport of waste-rock piles at the site. A conceptual model of heat and mass transports for waste-rock piles in cold region was developed via multi-component and multi-phase transport mechanisms. Based on this conceptual model, numerical simulations were run for various scenarios including the effects of ACC, heat generation due to sulfide oxidation and wind-induced advection. The following conclusions were drawn from this study:

10.1.1 Field results of the test piles

10.1.1.1 Thermal conductivity and grain size distribution of waste rock

- By using grain size analyses, Type I and III waste rock were grouped as well-graded gravel with sand, cobbles and boulders (GW). There were insignificant differences in grain sizes between the test piles based on particle size distributions, waste rock at Diavik was characterized as a rock-like material. Therefore, the test piles are considered as rock-like piles, which should contain preferential flow paths of air or water.

- Based on insitu field measurements, the average thermal conductivities were 1.7 ± 0.4, 1.8 ± 0.4 and $1.7 \pm 0.5\,\mathrm{W/(m \cdot K)}$ for Type I and Type III in the test piles and Type III rock of covered test piles respectively. The effect of temperature on thermal conductivity of waste rock was insignificant whereas the moisture content of the matrix factions of waste rock had a greater impact on thermal conductivity; the higher the moisture the higher the thermal conductivity. The influence of moisture content on thermal conductivity can be expressed through normalized thermal conductivity and the relation between moisture content (or the degree of saturation) and normalized thermal conductivity depends on the particle sizes or "fabric effect".

10.1.1.2 Thermal regimes of the Type III test pile (uncovered test pile)

- Ground temperatures in the bedrock foundation beneath the Type III test pile (an uncovered test pile) has cooled gradually and stayed below 0 °C since construction. Permafrost grades from the base of the test pile at a rate about 1.5 m/a and ground temperatures below 2 m from the surface of the test pile decreased at a trend about 4 °C annually during the two years 2007 and 2008. Wind-induced advection and thermally induced convection have caused the rapid response of internal test pile temperatures to air temperatures. Warm regions above background temperatures were not observed within the test piles due to a very small heat released due to oxidation of the waste rock.

- A calculation based on both conduction and convection indicated that the test pile released -2.5×10^4 MJ in 2007 and -2.6×10^4 MJ in 2008. Air movement within the test pile varied with season such that the average inward airflow $\left(1.8{\times}10^{-4}\,\mathrm{m/s}\right)$ due to temperature gradients during the winters was about three times greater than the outward airflow $\left(6.0{\times}10^{-5}\,\mathrm{m/s}\right)$ during the summers (Chapter 4). Therefore, the convective component of heat transfer in winter was significantly larger than summer, causing the test pile to cool.

- Heat transfer in the bedrock at the site was via conduction and based on measured temperatures at various depths, the thermal diffusivity was calculated, which ranged between 1.2×10^{-6} and 1.4×10^{-6} $\mathrm{m^2/s}$ or the thermal conductivity between 2.6 and 3.0 $\mathrm{W/(m \cdot K)}$ based on a volumetric heat capacity of $2.17 \times 10^6\,\mathrm{J/\left(m^3 \cdot K\right)}$. By using cross-correlation analyses of ground temperatures and surface temperatures, it was found that time lags increased whereas cross-correlation coefficients decreased with depths in the bedrock. An average cross-correlation coefficient of 0.72 was calculated within a 10 m thickness of bedrock meanwhile in the test pile this value was 0.91. The difference in cross-correlation coefficient indicated that heat transfer within the test pile was not only conduction. Whereas the correlations of temperatures in the test pile with wind speeds and barometric pressures were weaker and negative.

- Due to the segregation of waste rock during construction, permeability near the surface of the test pile is much lower than that in the middle and near the toe. It was found as a zone of 2 m near the surface, heat transfer was conduction with a thermal conductivity of 1.8 $\mathrm{W}/(\mathrm{m}\cdot\mathrm{K})$. Convection/advection due to wind and temperature gradients dominated in the lower parts of the test pile resulting in large cross-correlation coefficients and small time lags. 1-D convection-conduction model was constructed to determine an average horizontal air velocity of 2.2×10^{-3} m/s. This air velocity along an average air pressure gradient of 0.5 Pa/m (a measured value) were used to calculate the air permeability of waste rock at $4.4\times10^{-8}\,\mathrm{m}^2$. However, this permeability values is about one order of magnitude smaller than results from calibration of numerical modeling to the internal thermal regime.

10.1.1.3 Thermal regimes of the covered test pile

- Mean annual air temperature (MAAT) and mean annual surface temperature (MAST) measured at the covered test pile were -9.0 °C and -4.8 °C. Based on daily average values, the relation between air and surface temperatures can be expressed as $T_a = T_s - 4.2$ (°C) and the surface condition of the covered test pile can be classified as gravel or concrete pavement types with $n_f = 0.77$ and $n_t = 1.46$. Measured ground temperatures indicated that conduction was the dominated heat transfer within the covered test piles with ground temperatures below the Type I rock layer were below 0 °C year-around. However, at the base of the covered test piles there are lysimeters containing heating cables that released heat therefore ground temperatures around these heating cables were impacted.

- Measured temperatures were used to determine the thermal diffusivity of the Type I, till and Type III rock of the covered test pile which were 6.9×10^{-7}, 1.5×10^{-6} and $8.0\times10^{-7}\ \mathrm{m}^2/\mathrm{s}$, respectively and similar to the other test piles. The relation between net radiation and surface heat flux are $G = 0.31R_n - 5.9\ \left(\mathrm{W}/\mathrm{m}^2\right)$ and between total solar radiation and net radiation are $R_n = 0.62R_s - 56\ \left(\mathrm{W}/\mathrm{m}^2\right)$. Heat flux through the till layer was about 43 % of the surface heat flux based on measured mean annual values of temperature and gradient.

10.1.1.4 Thermal regimes of a full-scale pile and the impacts of warming

- Warming air temperatures were measured at Diavik site during the period between 2000 and 2010. The trendlines indicate the thawing-index increases 36 °C-days/decade while the freezing-index decreases 120 °C-days/decade. MAAT increased 0.73 °C/decade along with smaller number of freezing days (6.0 days/decade) and longer number of thawing days (5.7 days/decade). A proposed climate predicted a warming of 0.56 °C/decade.

- Temperature measurements from three drill holes up to 40 m depth in a 80 m high pile after one year indicated that 0 °C isotherm (active layer) was at 11 m below the surface and heat transfer in the dump was mainly controlled by conduction without heat being released via oxidation. The active layer was affected by the fluid introduced during drilling and it would take 4 to 5 years to regain thermal equilibrium. Without warming and the current climate at site it is expected to maintain an active layer about 4 m below the surface. However, with the predicted warming and based on conduction only, the active layer will increase to 7 m by 2110. If a layer of till is used to cover the Type III waste rock, they active layer will be about 3.9 m in 2110. However, by using an Air convection cover (ACC) with the permeability of the air convection layer $K \geq 2 \times 10^{-7}\,\mathrm{m}^2$ the Type III waste rock will not rise above 0 °C during the next 100 years under the proposed warming.

10.1.1.5 Conceptual model and numerical simulations of heat and mass transports in the test piles

- By using the concept of representative elementary volume (REV) and governing equations written at the macroscopic level, a conceptual model of air, water and heat transports were described through a set of equations together with appropriate constitutive relations for waste-rock piles constructed in permafrost regions. The transports within the waste-rock pile are highly coupled in which gas transport is the most important as it influences all the others. In permafrost regions, air temperatures fluctuate considerably and an unstable-density stratification of air can be created during winter. As a result air convection cells can be developed. Oxygen supply through these convection cells and wind-induced advection are significantly larger than via diffusion.

- The larger oxygen supply can drive other transport phenomena such as heat, vapor and pyrite oxidation. Water transport within the waste-rock piles in continuous permafrost regions is very limited due to frozen grounds and thin active layer that forms during summer. Transport processes within waste-rock piles are highly non-linear and coupled due to the fact that the properties of waste rock related to these processes depend on temperature and moisture content. Generally, some constitutive relations have steep slopes such as SFCC and SWCC, which pose difficulties when used with numerical methods.

- Numerical simulations of heat and mass transfers in the test piles based on the conceptual model were carried out to calibrate physical properties obtained during measurements but also were used for applications of ACC when oxidation of waste rocks were examined.

1. **Uncovered test pile**

- Numerical simulation indicated that permeability of waste rock in the uncovered test piles (Type I and III test piles) must be in the order of 10^{-7} m^2 for the numerical results to be comparable to field results. Furthermore, at this high permeability wind-induced advection must be taken into account and temperatures within the test piles showed a rapid response to the fluctuation of air temperature. Due to the configuration of the uncovered test piles that is quite narrow (small width to height ratio) cross wind easily penetrated throughout the cross section of the piles and this observation was confirmed by pore-air pressure measurements within the test piles. However, in reality, waste-rock piles at Diavik is about 1 km across and about 80 m high, along with the existence of low permeability layers embedded within the piles that were created during construction, therefore wind-induced advection may only affect a small outer edge of the piles. Furthermore, natural air convection can occur during winter within pockets or layers of coarse rock within the piles provided appropriate condition exist.

- Even though the measured oxidation of the Type III waste rock was negligible in the order of $10^{-11}\,\mathrm{kg(S)}/\left(\mathrm{m}^3\cdot\mathrm{s}\right)$. By assuming that the Type III waste rock was under oxidation and releasing heat and the oxidation rate ranged between 10^{-9} and $10^{-7}\,\mathrm{kg(S)}/\left(\mathrm{m}^3\cdot\mathrm{s}\right)$ in the uncovered test pile, which is a common value. Without wind-induced advection, the permeability of waste rock must be in the order of 10^{-9} m^2 to sustain high oxidation rates and smaller than this value oxygen supply was not sufficient. However when accounting for wind effects, permeability could be smaller ($10^{-10}\,\mathrm{m}^2$) to create warm zones due to oxidation within the test pile. By covering the surface of the test pile or inserting low permeability layers, the average oxidation rates were reduced, from 8.9×10^{-8} to $2.3\times10^{-8}\,\mathrm{kg(S)}/\left(\mathrm{m}^3\cdot\mathrm{s}\right)$, and oxidation was limited to the regions near the outside slopes and the surface.

2. **Covered test pile**

- Unlike the uncovered test piles, where thermal transport was greatly influenced by wind-induced advection and natural air convection, the low permeability till layer within the covered test pile eliminated advection or convection. As a result, conduction of heat and diffusion of mass (such as oxygen) dominated the covered test pile.

- The closure concept of waste rock at Diavik proposes a 1.5 m till covered with 3 m Type I rock encapsulating the PAG Type III waste rock. The till cover effectively maintained sub 0 °C temperature in the waste rock beneath as observed in field measurements and during simulations. However, due to the cold temperatures and prolonged winter at the site, an alternative cover solution for long-term climate change termed the Air Convection Cover (ACC) would lower the Type III waste rock temperatures compared to the present closure concept. Materials for the high-permeable

layer in ACC can be achieved by removing small particle size fractions of the Type I waste rock prior to placement. The ACC was so effective and it could maintain reactive waste-rock temperatures below 0 °C even under high oxidation rates.

10.1.1.6 Onset of air convection in a reactive waste-rock pile

- A set of equations was derived for the determination of the onset of air convection in waste-rock piles constructed in cold regions by assuming the waste rock as a porous medium saturated by a compressible fluid (air) and having an internal heat source due to oxidation of pyrite. The equations were solved for the critical Rayleigh number (Ra_c) of the onset of air convection by either analytical or numerical method. The analytical results were approximated and only accurate for the case without internal heat source, however, with internal heat source the numerical results were more precise.

- Without internal heat source and for the physical waste-rock properties at Diavik site, Ra_c is similar to the classical problem, which is $4\pi^2$ if there is an impermeable top surface or 27.10 if the top surface is permeable. These indicate that adiabatic warming or cooling and the pressure work of compressible air are not significant for the full scale waste rock thickness ($\leq$ 80 m) and temperature gradient of around $0.31\,\mathrm{K/m}$. The pressure work and compressibility of air have a stabilizing effect and how much it deviates from the classical values depending the waste-rock pile's properties. However with internal heat source, the values of Ra_c were smaller around 15 and 7 for impermeable and permeable surfaces, respectively. This indicates that internal heat source can create high enough buoyancy forces to promote air convection regardless of external thermal boundary conditions.

10.1.1.7 Numerical modeling and experiment of natural air convection in a cylindrical tank

- Nusselt number Nu and Rayleigh number Ra were calculated based on experimental data and their results were compared with analytical and numerical results. Analytical and numerical results were consistent however they were slightly greater than experimental results. The discrepancy could be a result of errors and limitations of the apparatus. Ra_c for the onset of air convection was somewhat higher than $4\pi^2$ because of the slenderness ratio of the apparatus. Depending on the aspect ratios (diameter to height) of the tank, convective flow pattern can be asymmetric or symmetric. With the aspect ratio of the apparatus $\gamma = 0.39$ resulting in $Ra_c = 46.39$ and the flow structure at the onset is asymmetric and single convection cell.

- The geometry of the laboratory apparatus dictated the convective mode (structure), the convective structure was asymmetric (single convective cell). It was confirmed

using numerical simulation and theoretical analyses. In the periodic state or oscillatory convection, the convective flow was still nonaxisymmetric and temperature within the tank was time dependent. The oscillatory convection was characterized by a dominated fundamental frequency f_1, which is a function of *Ra*. However, due to the slenderness of the cylinder, the fundamental frequency was about one order of magnitude smaller when compared to the results of a 2-D square geometry at a given *Ra*.

10.2 Recommendations for future study

The initial objectives of building two uncovered test pile (Type I test pile and Type III test pile) were to investigate the differences due to the difference of potential acid generating in Type I and III waste rock. However, due to the low sulfur contents in waste rock and low temperatures at the site, from a thermal perspective the two uncovered piles behaved very similar and their narrow configuration made them susceptible to wind-induced advection that was not observed in the full scale pile. Furthermore, the design of the covered pile did not take advantages of the prolonged and cold winter at the site through natural air convection. Therefore, several suggestions are made for future research:

- A newly designed waste-rock pile configuration with large width to height ratios using the same construction methods as real piles be constructed with heat-flux plates at the base to measure heat flux between the pile and bedrock foundation. Furthermore, additional thermistors are needed in bedrock beneath the pile to measure thermal regimes after the piles constructed as well as re-check the results of heat-flux plates. If possible, heat-flux plates are also installed at the surface to measure surface heat flux. Several more thermistor cables place within the pile to investigate thermal evolution.

- Another pile same as above but ACC placed over it. Thickness of the till or low permeability layer in ACC of 1 m is sufficient and degree of saturation should be larger than 50 %. However, the till can be thinner but it needs to be confirmed via numerical simulations and feasibility of its placement. The permeability in the air convection layer of the ACC must be in the order or larger than 10^{-7} m^2 to take advantages of air convection for cooling the pile.

- Laboratory study of ACC can also be constructed including at least three layer systems: the bottom layer represents the PAG waste rock, the middle layer is low in permeability and high in water content; the top layer is dry and high in permeability. The permeability and thickness of the top layer can be varied to examine the changes of air convection and cooling effects. The size and shape of the apparatus would be around 20 cm $\times$ 100 cm $\times$ 100 cm (thickness $\times$ width $\times$ height) because this size is

manageable as one wants to have various porous materials (various permeabilities) to run the experiment. If the apparatus is large, it is time-consuming to change materials or run one test, however if the apparatus is too small, the boundaries may influence the results. Thermal boundary conditions can be insulated or fixed temperatures at the bottom and variation or fixed temperatures at the top. However, the mean value of temperatures must be colder than 0 °C to represent cold temperatures in permafrost regions. Insulation, seal and heating systems for the apparatus are very crucial and one can refer to the work of Lillico (1992); Chen (2010)

- Numerical simulations are needed to examine the influences of water transport on the thermal behavior. The influences may arise from the evaporation, freezing processes and advection of water that have consequences for the energy balance. The equations describing the water transport were presented in the conceptual model chapter (Chapter 8). However, waste rock should be modeled using dual porosity and permeability (or heterogeneity) due to fact that the matrix fraction transports water while air flows in macro-pores. The interaction of transports in these two layers must be described. Furthermore, water frozen during winter and the heat released also must be accounted for during the simulations.

References

Chen, J. F. (2010). Laboratory investigation of natural convection in a porous medium in a cylindrical tank. Master's thesis, University of Alberta.

Lillico, D. A. (1992). *Natural convection in a cylindrical porous medium: one and two fluid phases*. PhD thesis, University of Alberta.

APPENDICES

APPENDIX A

Numerical modeling and experiment of natural air convection in a cylindrical tank of low aspect ratio filled with a porous medium

A.1 Introduction

Natural convection in fluid saturated porous media of an infinite horizontal layer heated from below with the boundaries set to be perfect heat conductors (constant temperatures) and impermeable was first reported by Horton and Rogers Jr. (1945); Lapwood (1948) and natural convection is triggered at a critical Rayleigh number (Ra_c) of $4\pi^2$. Natural convection only occurs under a certain critical temperature gradient that produces sufficient buoyancy forces within the porous body to overcome viscous and diffusive forces. At the onset of natural convection, the saturated fluid is in motion and the natural convection is characterized by stationary two- or three-dimensional convection patterns depending on the geometry of the domain.

The value of Ra_c is not $4\pi^2$ if the geometry and boundary conditions of a problem are different than that of Horton and Rogers Jr. (1945); Lapwood (1948). Beck (1972) utilized both linear theory and energy method to examine natural convection in a box with various aspect ratios. He found that the lateral walls have a significant effect on Ra_c and $Ra_c \to 4\pi^2$ if one of the aspect ratios approaches 1. Horne (1979); Schubert and Straus (1979b); Caltagirone et al. (1981); Kimura et al. (1989) conducted numerical studies of three-dimensional convection in rectangular boxes heated from below. They found that the convective flow has no preferred structures due to sensitivity to aspect ratios and initial conditions; furthermore, they recognized that three-dimensional flow transports more heat than two-dimensional flow in a three-dimensional domain. Analytical analyses conducted by Steen (1983) suggested that two-dimensional convection initiates at $Ra = 4\pi^2$ in a cube and three-dimensional convection does not appear until $Ra = 4.84\pi^2$ with a possibility of 21 %. An analysis of convection in a vertical cylinder with impermeable boundaries was

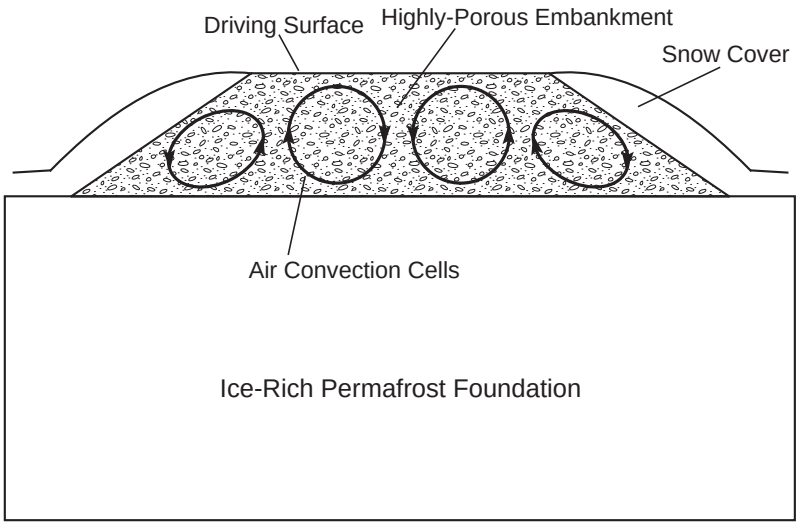

Figure A.1: Air Convection Embankment (ACE) design concept (modified from Goering, 1998)

studied by Zebib (1978) who showed that the flow pattern depends on the geometry (radius to height ratios) however the dominated-convective flow is asymmetric. This finding was confirmed by the experiments of Bau and Torrance (1981a).

As *Ra* increases to a certain value, the initial steady convection begins to oscillate. Oscillatory convection in two-dimensional domains was first studied by Horne and O'sullivan (1974); Straus (1974); Caltagirone (1975); Kimura et al. (1986). Most of the work on oscillatory convection was conducted using numerical methods (mostly spectral and finite difference methods) and therefore, the values of *Ra* at the onset of oscillation varied among the investigators due to truncation errors and/or mesh sizes. Except Horne and O'sullivan (1974) who reported the onset of oscillation at $Ra = 280$, other researchers showed that *Ra* varies between 380 and 400 (Straus, 1974; Caltagirone, 1975; Kimura et al., 1986). However, the onset of oscillatory convection in three-dimensional domains is higher due to the constraint of an extra lateral wall compared to two-dimensional domains. In the case of a cube, the transition occurs at *Ra* of 575 by Kimura et al. (1989), 584 by Graham and Steen (1991) and from 550 to 560 by Stamps et al. (1990a).

In geotechnical engineering, the application of natural air convection in a porous medium is relatively new and has just been known through the experiments and numerical modeling conducted by Goering and Kumar (1996); Goering (1998, 2003). They used a design concept called Air Convection Embankment (ACE) for the protection of ice-rich permafrost foundation under a road embankment (Fig. A.1). Ice-rich permafrost is a high water content soil and it will undergo a large settlement upon thaw. This concept works well in cold regions because of an unique feature associated with large temperature differences between summer and winter. Therefore, an adverse temperature gradient can be created and may trigger air convection in this highly porous embankment during winter.

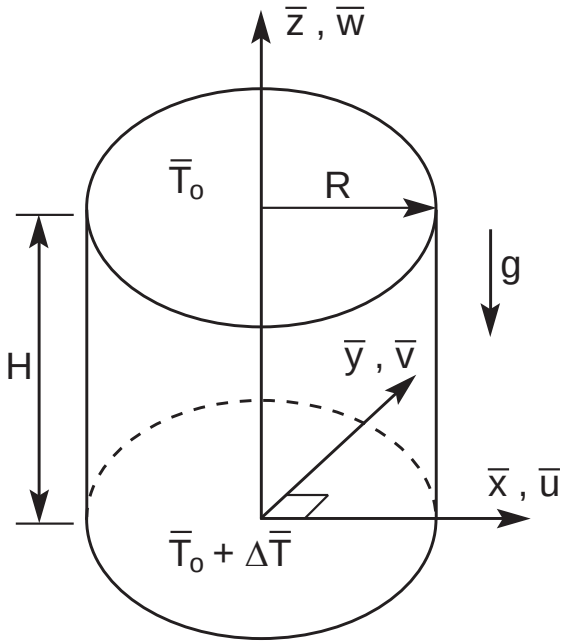

Figure A.2: Air-saturated porous medium bounded in a cylinder of radius R and height H. The top surface is maintained at a constant temperature $\overline{T}_o$ while the bottom surface is heated at a constant temperature $\overline{T}_o + \Delta\overline{T}$. The side walls are insulated.

In this study, the results of experimental study of air convection carried out by Chen (2010) were reexamined to develop further understanding of the air convection mechanisms through detailed calculations and numerical simulations. The numerical simulations are used to check and calibrate the assumed parameters of the experiments. A through understanding of air convection mechanism is beneficial to promote design efficient and economical cooling system for applications in geotechnical engineering especially associated with permafrost regions.

A.2 Governing equations

It is assumed that the air-saturated porous medium is homogeneous and isotropic contained in a vertical cylinder of height H and radius R. The flow is described by Darcy's law and fluid density varies with temperature through the Oberbeck-Boussinesq approximation. Coordinates $\overline{\mathbf{x}} = (\overline{x}, \overline{y}, \overline{z})$ with component velocities $\overline{\mathbf{u}} = (\overline{u}, \overline{v}, \overline{w})$ are employed, as shown in Fig. A.2. The governing equations are (Nield and Bejan, 1999).

- Conservation of mass (continuity equation)

$$\overline{\nabla} \cdot \overline{\mathbf{u}} = 0 \tag{A.1}$$

- Conservation of momentum (Darcy's law)

$$\overline{\mathbf{u}} = -\frac{K}{\mu}\left(\overline{\nabla}\overline{p} + \rho_a^o g\left[1-\beta\left(\overline{T}-\overline{T}_o\right)\right]\mathbf{n}\right) \tag{A.2}$$

- Conservation of energy

$$C\frac{\partial \overline{T}}{\partial t} + C_a\overline{\mathbf{u}}\cdot\overline{\nabla}\overline{T} - \lambda\overline{\nabla}^2\overline{T} = 0 \tag{A.3}$$

By using the Oberbeck-Boussinesq approximation

$$\rho_a = \rho_a^o\left[1-\beta\left(\overline{T}-\overline{T}_o\right)\right] \tag{A.4}$$

Where: ρ_a is the air density, K is the intrinsic permeability of the porous media, μ is the air dynamic viscosity, $\overline{p}$ is the air pressure, gravity g points downward opposite to unit vector $\mathbf{n}\,(0,0,1)$, ρ_a^o is the air density at the top surface at reference temperature $\overline{T}_o$, β is the coefficient of thermal expansion of air, C and λ are the effective (bulk) volumetric heat capacity and thermal conductivity of the porous medium, $\overline{T}$ is temperature which is a dependent variable, $C_a = c_a\rho_a$ is the volumetric heat capacity of air; c_a is the heat capacity of air.

By introducing dimensionless quantities.

$$\mathbf{x}\,(x,y,z) = \frac{\overline{\mathbf{x}}\,(\bar{x},\bar{y},\bar{z})}{H},\quad ,T = \frac{\overline{T}-\overline{T}_o}{\Delta\overline{T}},\quad \mathbf{u} = \frac{C_a H\overline{\mathbf{u}}}{\lambda},\quad \tau = \frac{\lambda}{CH^2}t,\quad p = \overline{p}\frac{C_a K}{\mu\lambda} \tag{A.5}$$

The governing equations can be expressed in dimensionless forms:

$$\nabla\cdot\mathbf{u} = 0 \tag{A.6}$$

$$\mathbf{u} + \nabla p - RaT\mathbf{n} = 0 \tag{A.7}$$

$$\frac{\partial T}{\partial \tau} + \mathbf{u}\cdot\nabla T = \nabla^2 T \tag{A.8}$$

$$Ra = \frac{\rho_a^o g\beta KHC_a\Delta\overline{T}}{\mu\lambda} \tag{A.9}$$

Where: Ra is the Rayleigh number that is the ratio of buoyancy forces created by temperature gradients and the product of thermal and momentum diffusivity. The Rayleigh number along with Nusselt number, Nu, the ratio of actual heat transferred to the heat transfer by conduction only, are the two vital dimensionless numbers for the characterization of natural convection in porous media (Nield and Bejan, 1999). Nu is defined as:

$$Nu = -\frac{1}{A}\int \left.\frac{\partial T}{\partial z}\right|_{z=0} \mathrm{dxdy} \tag{A.10}$$

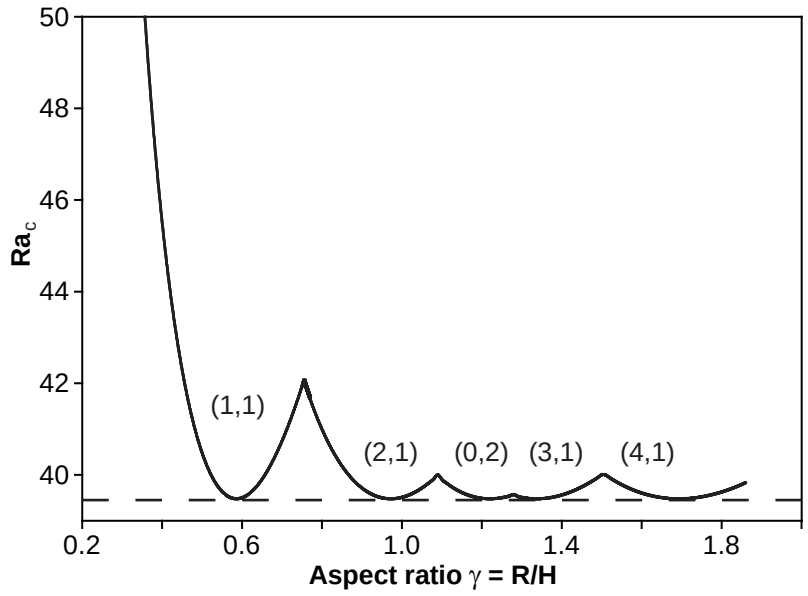

Figure A.3: Critical Rayleigh number (Ra_c) versus aspect ratio γ for different convective modes; the dashed line has $Ra_c = 4\pi^2$.

It is an average Nusselt number at the base, in which A is the cross-sectional area of the cylinder.

When oscillatory natural convection occurs, $Nu(\tau)$ is a function of dimensionless time τ, which is sufficiently long to capture oscillatory frequencies. The mean Nusselt number $\overline{Nu}$ is used:

$$\overline{Nu} = \frac{1}{N}\sum_{i=1}^{N} Nu_i(\tau) \tag{A.11}$$

Where: $Nu_i(\tau)$ is the value of $Nu(\tau)$ at a discrete time i, N is the length of the time series Nu. The above dimensionless equations Eqn. A.6 to Eqn. A.8 were solved using COMSOL Multiphysics 3.5a (Comsol, 2009) which is a finite element analysis and solver package for various physics and engineering applications, especially for coupled phenomena, or multiphysics problems. Numerical computations were carried out by starting at a value of Ra equal to $4\pi^2$ and determined Nu for each Ra using Eqn. A.10 for stable convection or Eqn. A.11 for oscillatory convection. The computations were stopped at a specific value Ra when steady convection was reached or the dimensionless time τ is sufficient to identify accurately the characteristic frequencies of the time series $Nu(\tau)$. Successively larger values of Ra were run with the previous stage as initial conditions. Mesh-independent results for each Ra were also checked for steady convection and more important to make sure that any fluctuation occurring during the oscillatory natural convection stage at large Ra is a real physical oscillation not a mathematical instability.

Table A.1: The values of $Z_{m,p}$ for different values of (m, p) (Abramowitz and Stegun, 1970)

(m, p)	$(1, 1)$	$(2, 1)$	$(0, 2)$	$(3, 1)$	$(4, 1)$	$(1, 2)$	$(5, 1)$
$Z_{m,p}$	1.841	3.054	3.832	4.201	5.318	5.331	6.416

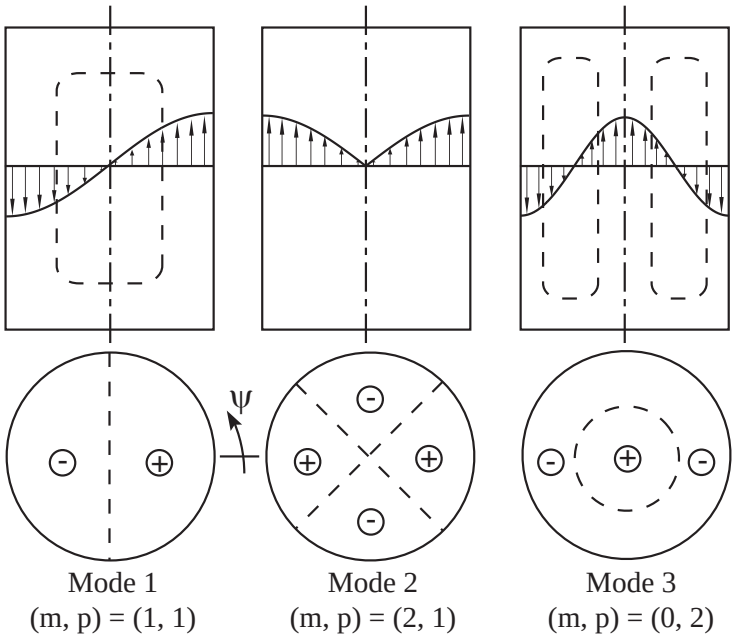

Figure A.4: Different modes of natural convection in a cylindrical tank (modified from Bau and Torrance, 1981a).

Linear stability analysis

Zebib (1978) used linear stability analysis (LSA) and Ra_c was determined using Eqn. A.12 in the case of impermeable boundaries. The result is plotted in Fig. A.3 for various values of γ and at large values of γ, Ra_c asymptotically approaches a value for an infinite horizontal layer which is $4\pi^2$.

$$Ra_c = \left(\frac{\kappa_{m,p}^2 + \pi^2}{\kappa_{m,p}} \right)^2 \tag{A.12}$$

In which, $\kappa_{m,p} = \dfrac{Z_{m,p}}{\gamma}$, the several values of $Z_{m,p}$ are shown in Table A.1.

The flow structures of the typical three modes are shown in Fig. A.4. Modes 1 and 2 are asymmetric in which the mode 1 has one convective cell whereas the mode 2 has four convective cells. Mode 3 is symmetric, which has two convective cells in any radial cross section.

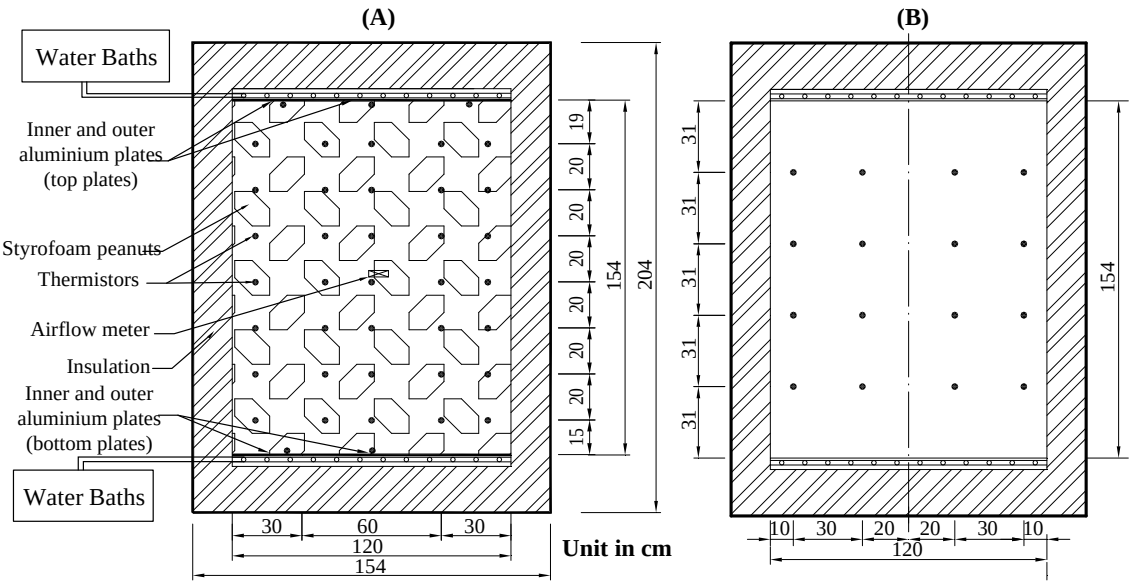

Figure A.5: Two orthogonal cross sections of the apparatus: CS1 (A) and CS2 (B) (modified from Chen, 2010)

A.3 Laboratory apparatus and procedures

Fig. A.5 shows the dimensions of the cylindrical convection tank with two orthogonal cross sections where a total of 56 thermistors located. The aspect ratio of the tank is $\gamma = 0.39$ resulting in $Ra_c = 46.39$ via Eqn. A.12. The lateral walls of the tank were insulated by 17 cm polyurethane foam and the boundaries were covered by 20 cm foam plates. Temperatures at the top and bottom boundaries were controlled by two water baths and the tank was filled with dry "S-shaped Styrofoam" as solid phase. For details of the laboratory apparatus, one can refer to the work of Chen (2010). The two last layers of thermistors near the bottom plate of the two cross sections were used to determine the average temperature gradient at the bottom of the tank during each convection test. This average temperature gradient was then used to calculate the average value of Nu using Eqn. A.10. This temperature gradient gave an estimation of actual heat flux due to convection at the bottom and the corresponding conductive heat flux was derived using the temperature gradient across the tank during each convection test.

Table A.3 shows the values of the properties used in this study. The most uncertain property is the intrinsic permeability, which is extremely high for conventional laboratory tests to determine permeability precisely (Chen, 2010). Therefore, theoretical and empirical methods were used.

The Kozeny-Carman equation that gives a reliable result for laminar flow (Bear, 1972)

$$K = \frac{D_{10}^2}{180}\frac{\phi^3}{(1-\phi)^2} = 1.88 \times 10^{-6}\,(\mathrm{m}^2) \tag{A.13}$$

Material properties used in numerical simulations (data from Chen (2010))

Property	Value	Unit
c_a	1005	$\mathrm{J}/(\mathrm{kg}\cdot\mathrm{K})$
β	3.42×10^{-3}	K^{-1}
μ	1.72×10^{-5}	$(\mathrm{Pa}\cdot\mathrm{s})$
ρ_a^o (at 20°C)	1.21	kg/m^3
λ_a	0.026	$\mathrm{W}/(\mathrm{m}\cdot\mathrm{K})$
K	by Eqn. A.13, Eqn. A.14 or Eqn. A.15	m^2
λ_s	0.035	$\mathrm{W}/(\mathrm{m}\cdot\mathrm{K})$
c_s	1250	$\mathrm{J}/(\mathrm{kg}\cdot\mathrm{K})$
ρ_s	6.5	kg/m^3
ϕ	0.5	

Where $D_{10}(\mathrm{m})$ is the diameter of particle that is 10 % finer than. In this study, $D_{10} = 2.6\,\mathrm{cm}$ is also the effective diameter of the Styrofoam peanuts, which was determined based on an equivalent spherical volume (Chen, 2010).

An empirical equation of Chapuis (2004) that was derived for sand and gravel particles, which was converted to an intrinsic formula by Côté et al. (2011).

$$K = 1.25\times10^{-4}\left(\frac{D_{10}^2\phi^3}{(1-\phi)^2}\right)^{0.7825} = 2.40\times10^{-7}\,(\mathrm{m}^2) \tag{A.14}$$

The Hazen's equation that is suitable for sands and gravels (Bear, 1972).

$$K = 6.54\times10^{-4}D_{10}^2 = 4.42\times10^{-7}\,(\mathrm{m}^2) \tag{A.15}$$

The permeability determined by Eqn. A.13 is about one order of magnitude larger than Eqn. A.14 or Eqn. A.15. Therefore, the system Rayleigh's number defined by Eqn. A.9 can vary significantly depending on what values of permeability we use. The permeability can also be determined through a numerically derived relation between *Ra* and *Nu* for the tank which will be presented in later sections (Côté et al., 2011). The procedure is for each convection test set-up, a value of *Nu* can be determined using Eqn. A.10. Then a value of *Ra* is obtained through the relation between *Ra* and *Nu*. Finally, the permeability is back calculated via Eqn. A.9. Therefore, with a large set of convection tests the mean value and standard deviation of permeability can be back calculated.

The effective (bulk) thermal conductivity and volumetric heat capacity are determined using the geometric and volumetric means value of air (a) and solid (s) phases respectively as:

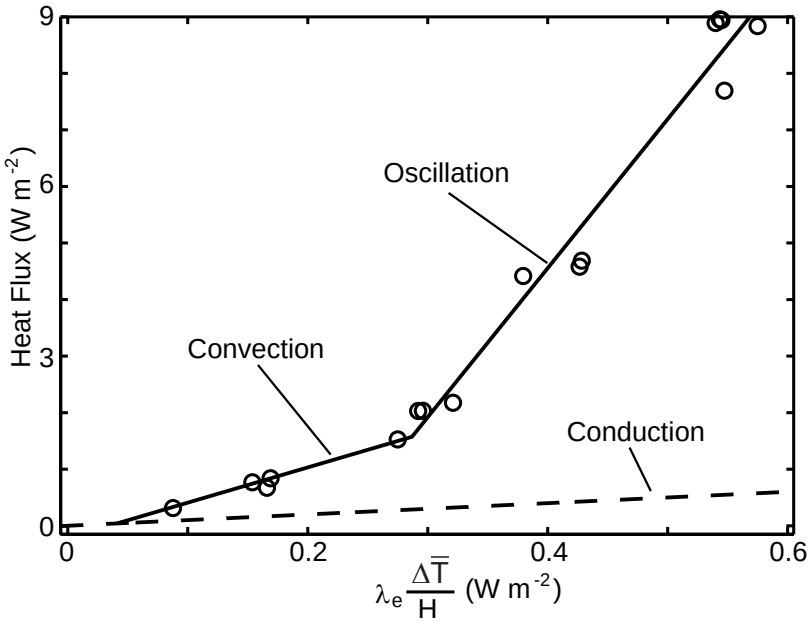

Figure A.6: Calculated heat flux at the bottom plate based on temperature gradients versus heat heat via conduction.

$$\lambda = \lambda_a^{\phi} \lambda_s^{(1-\phi)} = 0.03 \text{ W}/(\text{m} \cdot \text{K}) \tag{A.16}$$

$$C = \rho_a c_a \phi + \rho_s c_s (1-\phi) = 4.67 \times 10^3 \text{ J}/\left(\text{m}^3 \cdot \text{K}\right) \tag{A.17}$$

A.4 Results and Discussion

A.4.1 Laboratory

A.4.1.1 Heat flux and Nusselt numbers

The plot of actual heat flux versus conductive heat flux is shown in Fig. A.6 and the first change of slope occurring at $0.06\,\text{W}/\text{m}^2$ indicates the onset of convective airflow. This value of heat flux is equivalent to $Ra_c = 69$ based on the calculated permeability using Eqn. A.14. However permeability calculated via Eqn. A.15 or Eqn. A.13 would give larger values of Ra_c. $Ra_c = 69$ is about 30 % larger than the value obtained by the above linear stability analysis (Fig. A.3) and numerical simulations presented later. There are many factors that contribute to the discrepancy such as errors associated with the apparatus and test procedure, the accuracy of calculated thermal properties through Eqn. A.16 and Eqn. A.17.

The second change of slope is the onset of oscillation at a heat flux around $0.28\,\text{W}/\text{m}^2$ corresponding to $Ra = 516$. This value is about 12 % larger than that from the numerical simulation (shown in later section). Therefore, the onset of oscillation occurs at the

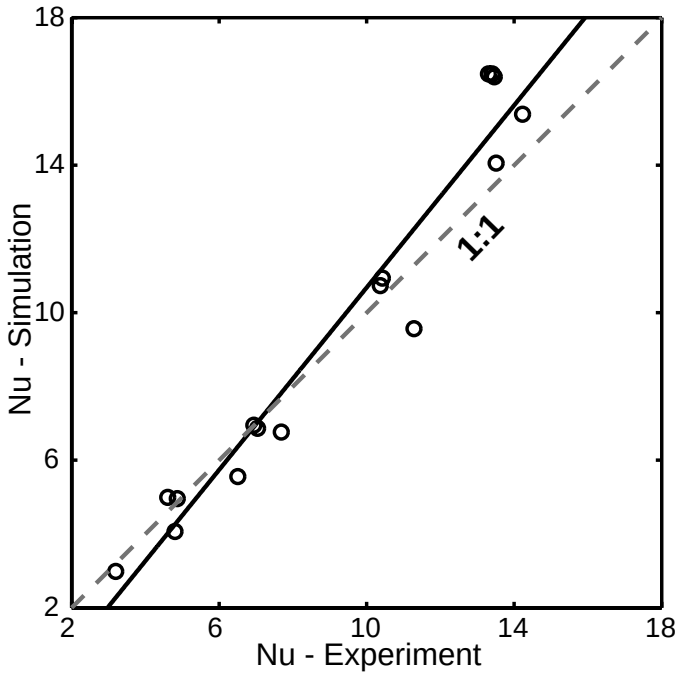

Figure A.7: Nusselt number: Experiment versus Simulation.

ratio $Ra/Ra_c = 7.5$ which is slightly larger than the results between 5.61 and 7.10 by Combarnous and Bories (1975); Bau and Torrance (1981a) with γ between 0.2 and 0.3. However, the numerical results of Ra/Ra_c of three-dimensional convections in a cube are higher around 14 (Kimura et al., 1989; Stamps et al., 1990a; Graham and Steen, 1991), which was calculated by dividing their values of the onset of oscillatory convection to $4\pi^2$.

Based on the permeability obtained using Eqn. A.14, the values of Nu via experiments and numerical results are comparable. However, when Nu is below 7.5, the numerical results are slightly lower than the experiment results (Fig. A.7). The reverse occurs when Nu is above 7.5 (Fig. A.7). This is because of the accuracy in calculation Nu using data from thermistors located on two cross-sections and the associated experimental errors in their measurements.

A.4.1.2 Temperature profiles

Nondimensional centreline temperature profiles are influenced by convection as shown in Fig. A.8. As the values of Ra/Ra_c increase above one, natural air convection becomes more significant. Therefore, the temperature profiles are more S-shaped as shown in Fig. A.8. Temperature profiles below the $z = 0.5$ plane are colder than conduction state (the dash line) and the reverse above the $z = 0.5$ plane. This is because the up-flow warm air elevates temperatures near the top above the conduction state whereas the down-flow cold air reverses temperatures near the bottom. The experimental and numerical temperature profile results along the axis are comparable. However, the temperatures in the lower half of the

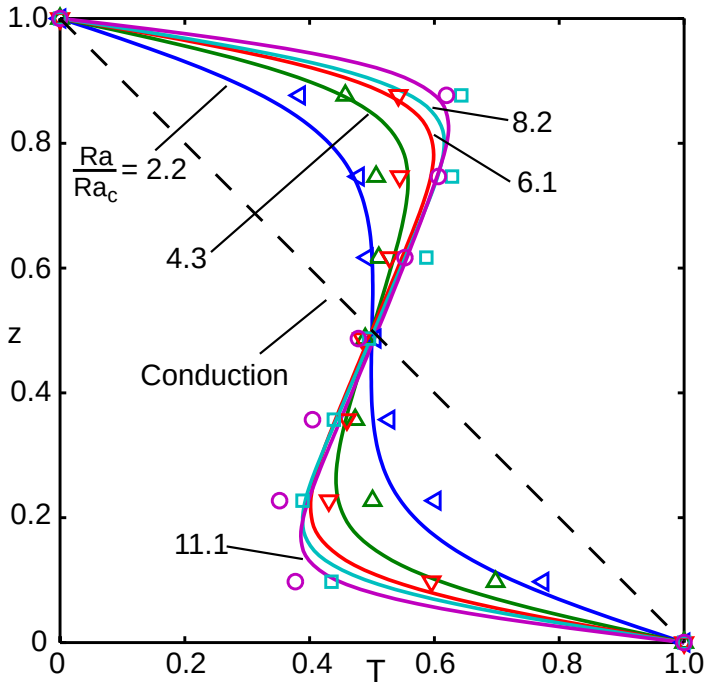

Figure A.8: Nondimensional axial temperature profile: comparison between numerical simulations (solid lines) and experimental results.

tank deviate more from the numerical results. This can result from the thinner insulation of the tank's walls causing additional heat loss near the bottom. Furthermore, the temperature profiles of numerical results are symmetric about the $z = 0.5$ plane due to the symmetry of boundary conditions. Fig. A.8 also shows that with the increase in the ratios Ra/Ra_c, temperature gradients near the top and bottom increase accordingly. Therefore, at a given ratio Ra/Ra_c, the adverse temperature gradient is largest at the boundaries and smaller toward the centre.

The temperature profiles (Fig. A.8) and isotherms of two orthogonal cross sections (Fig. A.9) suggests that the convective movement of air forms a single convective cell. In fact, Fig. A.9A confirms this asymmetric structure by showing that warm air rises from the right and cool air descends to the left. Moreover, the horizontal isotherms in Fig. A.9B reconfirm the unicellular convective pattern (single cell) in the tank.

Chen (2010) found that heating from below results in a convective flow structure similar to the mode 3 (Fig. A.4) rather than the preferred mode 1. Chen (2010) further observation was that at large temperature gradients, isotherms had a tendency to shift to one side of the tank. One of his arguments was that the convections were in transient states as convection tests were terminated after about 48 hours. In fact, the calculated dimensionless time, τ, (Eqn. A.5) is 0.47 for 48 hours. According to numerical simulations, τ is at least 0.6 at $Ra < 200$ and τ decreases slightly with increasing Ra. Furthermore, it has to be mentioned that this number is a numerical result and it does not include any error associated with the

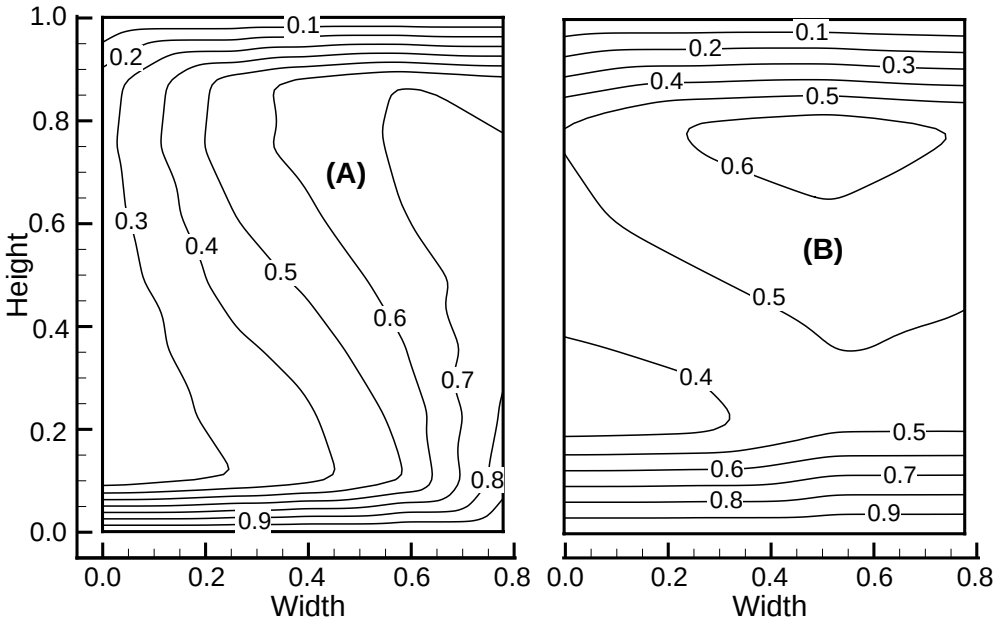

Figure A.9: Nondimensional isotherms, T, shown in two perpendicular-radial cross sections CS1 (A) and CS2 (B) shown in nondimensional coordinates for $Ra/Ra_c = 11.1$ cooling from above.

test apparatus. When convection tests induced by cooling from above were carried out, the convective flow structures were the preferred mode 1 at a similar τ (Chen, 2010). One reason is that when heating from below, the perturbation of temperature initiates at the bottom and rises against gravity. Meanwhile when cooling from above the perturbation of temperature descends with gravity. Therefore, it takes a longer time for heating from below to stabilize and approach a steady state.

A.4.2 Numerical simulations

A.4.2.1 Time-independent convection at low Ra

For the aspect ratio $\gamma = \dfrac{R}{H} = 0.39$ of the tank, Fig. A.3 suggests that the convective mode $(1, 1)$ is a preferred mode at the onset of convection. This mode corresponds to ascending flow in a half of cross-sectional area at the midplane $z = 0.5$ and descending flow in the other half. Fig. A.10 shows isotherms T on the horizontal planes $z = 0.16, 0.50, 0.84$ at different values of Ra. Referring to the plane $z = 0.16$, we see that the area having $T > 0.7$ is smaller and the isotherms are more curved as Ra increases. For the case $Ra \geq 220$ (Fig. A.10C and D), one can imagine the narrow hot plume at the bottom of ascending fluid widens toward the top as it rises. The reverse is for the narrow cold plume at the top. In the midplane, $z = 0.5$, the isotherms is symmetric about $T = 0.5$. The isotherms on the plane $z = 0.84$ are like those on the plane $z = 0.16$ but the area having $T < 0.3$ is getting narrower as Ra increases. This means that the hot plume broadens as it ascends.

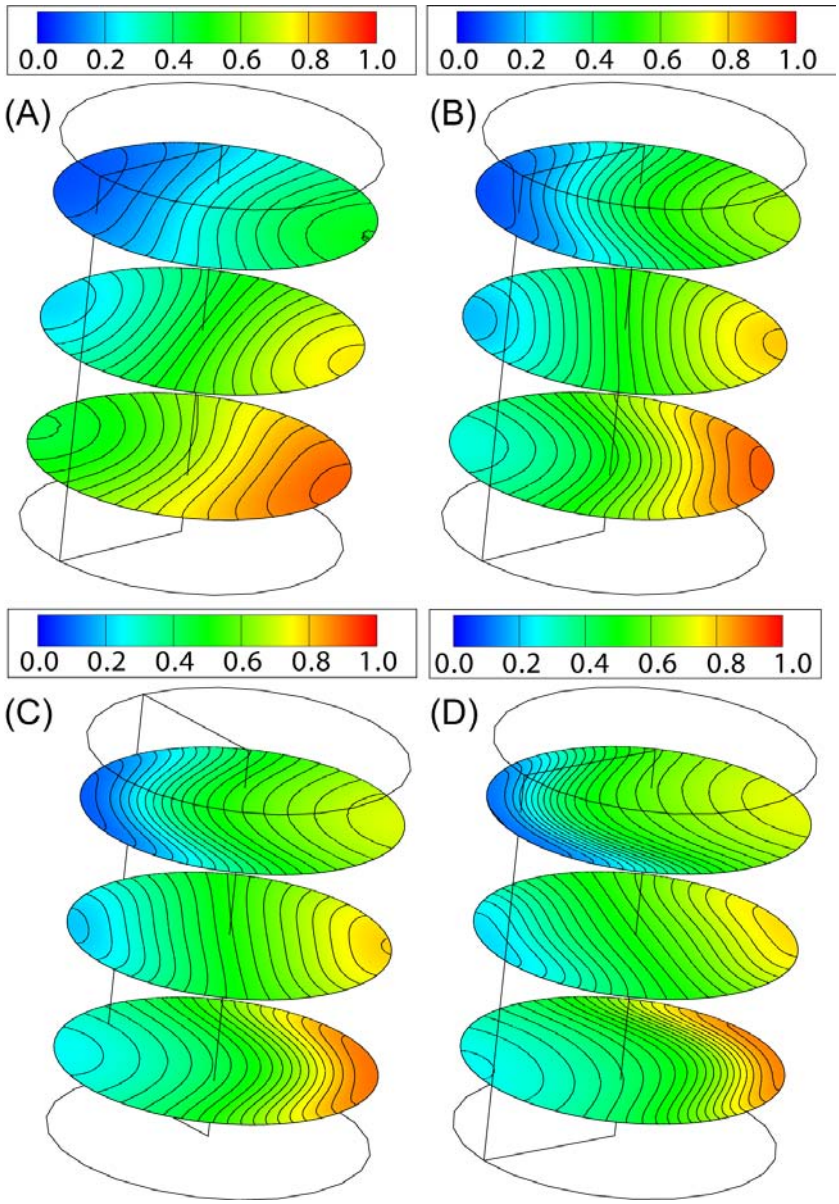

Figure A.10: Contours of dimensionless temperature, T, of the cross sections at $z =$ 0.16, 0.50, 0.84 for Ra = 75 (A), 150 (B), 220 (C), 300 (D).

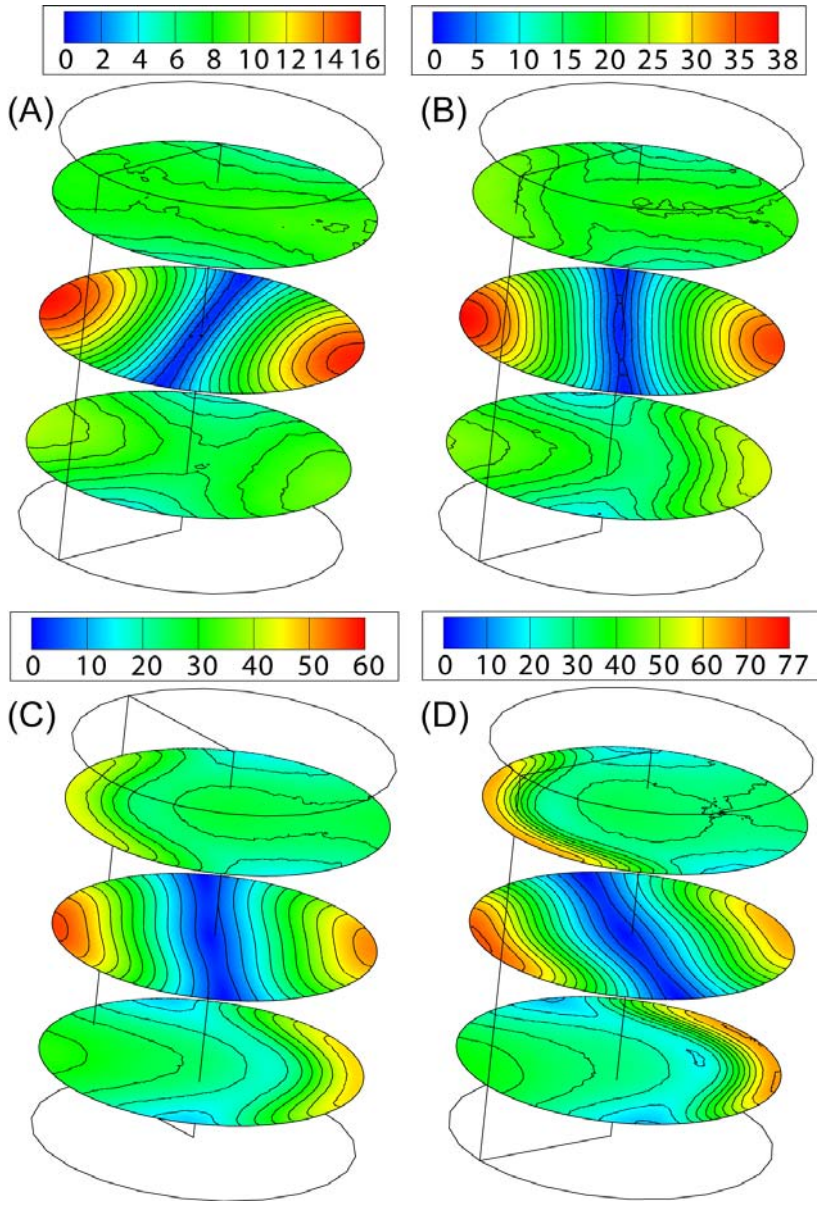

Figure A.11: Contours of dimensionless magnitude of velocity vector , $|\mathbf{u}|$, of the cross sections at $z = 0.16, 0.50, 0.84$ for Ra = 75 (A), 150 (B), 220 (C), 300 (D).

As Ra increases, the magnitude of the dimensionless velocity vector $|\mathbf{u}|$ also increase accordingly (Fig. A.11). At small values of Ra (less than 150), the distributions of $|\mathbf{u}|$ are quite uniform on planes $z = 0.16$ and 0.84 (Fig. A.11A and B). Once Ra is larger than 220, it is easy to recognize the separation of high and low velocity regions (Fig. A.11C and D). This can be interpreted as a narrow hot and high velocity plume has widened and decreased in velocity during its ascent. Meanwhile narrow cold and high velocity plumes have broadened and decreased in velocity but increased the temperature during their descent. At the midplane $z = 0.5$ during the descending air velocity reaches it maximums of 16, 38, 60 and 77 for $Ra = 75$, 150, 220 and 300 respectively. In addition, the contours of $|\mathbf{u}|$ are symmetric about a radial vertical plane like the isotherms. In fact, they are symmetric about the radial vertical plane through the point of maximum temperature and velocity at the midplane $z = 0.5$. However due to the circular cross section of the cylinder, this plane is arbitrary and can only be determined using simulation.

The relations between Nu and Ra from numerical simulations with the added-experimental results of this study are plotted in Fig. A.12A. It shows that between the onset $(Ra_c \simeq 46)$ and $Ra_2 \simeq 450$, Nu increases as Ra increases exponentially through $Nu = -4.44 + 1.72\,Ra^{0.30}$. In comparison to other results, this study falls within the range of studies reported by others. However, this study has slightly smaller values of Nu compared to three-dimensional convection results conducted by Schubert and Straus (1979b); Kimura et al. (1989); Stamps et al. (1990a) for a cube because of larger aspect ratios and most other studies were carried out only using two-dimensional domains (Fig. A.12B).

A.4.2.2 Time-dependent convection

The single convection cell established at the onset remained stable until $Ra_2 = 450 \rightarrow 490$. Ra_2 is the onset of non-stationary convection (oscillatory convection) or the second transition Rayleigh number (Kimura et al., 1986). At $Ra > Ra_2$ the single cell convective flow established at the onset is time dependent. However, it is difficult to determine exactly the value of Ra_2 due to the small variations of temperatures at the boundaries which require sufficient simulation time to detect characteristic frequencies. This problem also occurred in the study of Caltagirone et al. (1981); Schubert and Straus (1982); Kimura et al. (1986); Caltagirone and Fabrie (1989). Therefore, the value of Ra_2 usually varies in a small range.

Beyond $Ra = 490$, the curve $Nu - Ra$ increases slightly through $Nu = 0.01\,Ra^{1.06}$ (Fig. A.12A) that is comparable to a result obtained by Kimura et al. (1986) of $Nu \sim Ra^{11/10}$. The system is in a dynamic state that may cause an increase in heat transport through the increase in $Nu - Ra$ curve. At a value of Ra near Ra_2 the disturbances are small resulting in small fluctuations of temperatures in the boundary layers (Fig. A.13B and C). As Ra increases, the disturbances become larger and grow vertically into the convective flow (Fig. A.13D, E an F). Furthermore, the disturbances usually travel horizontally across a boundary and they may disappear and reappear. These properties cause temperatures to fluctuate at some

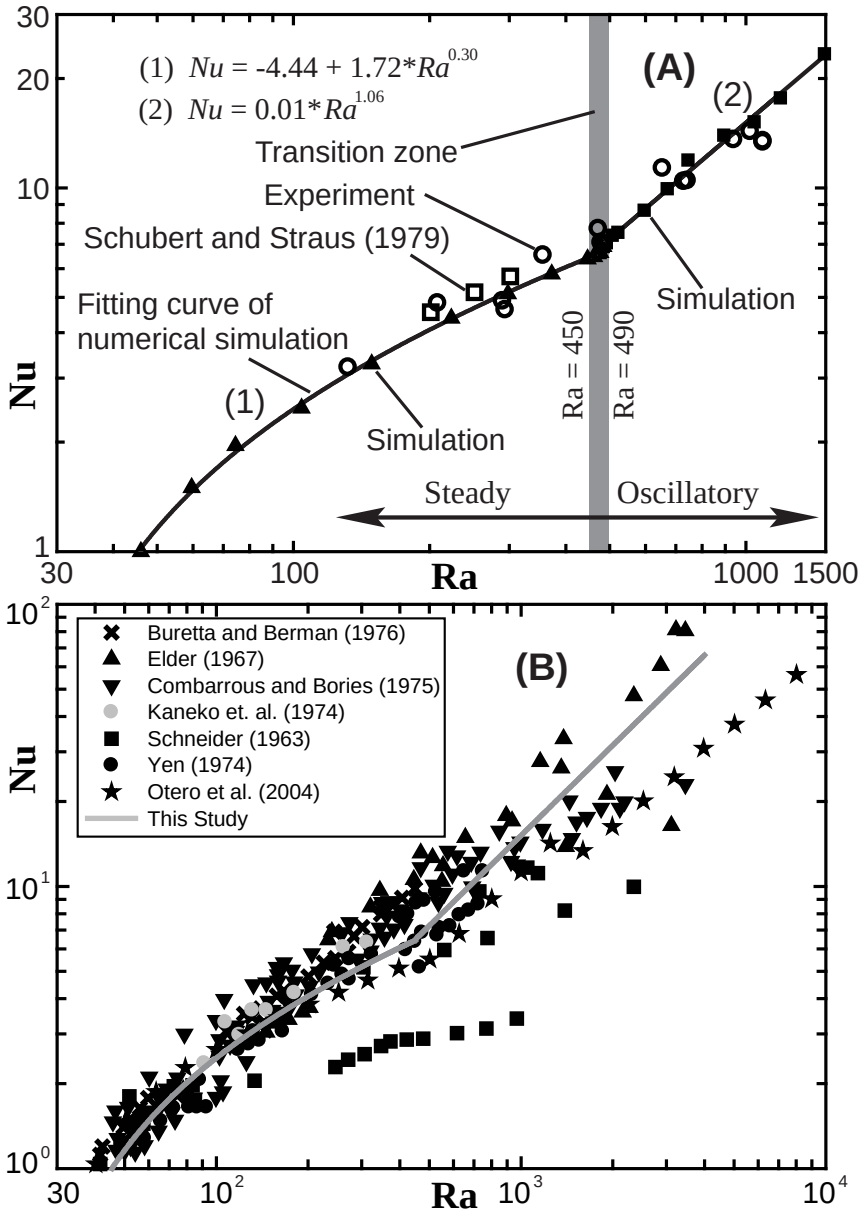

Figure A.12: Plot of *Nu* vs. *Ra*: comparison of experimental and numerical results (A) and comparison of this study to other studies (B) in which data was obtained from Nield and Bejan (1999); Otero et al. (2004).

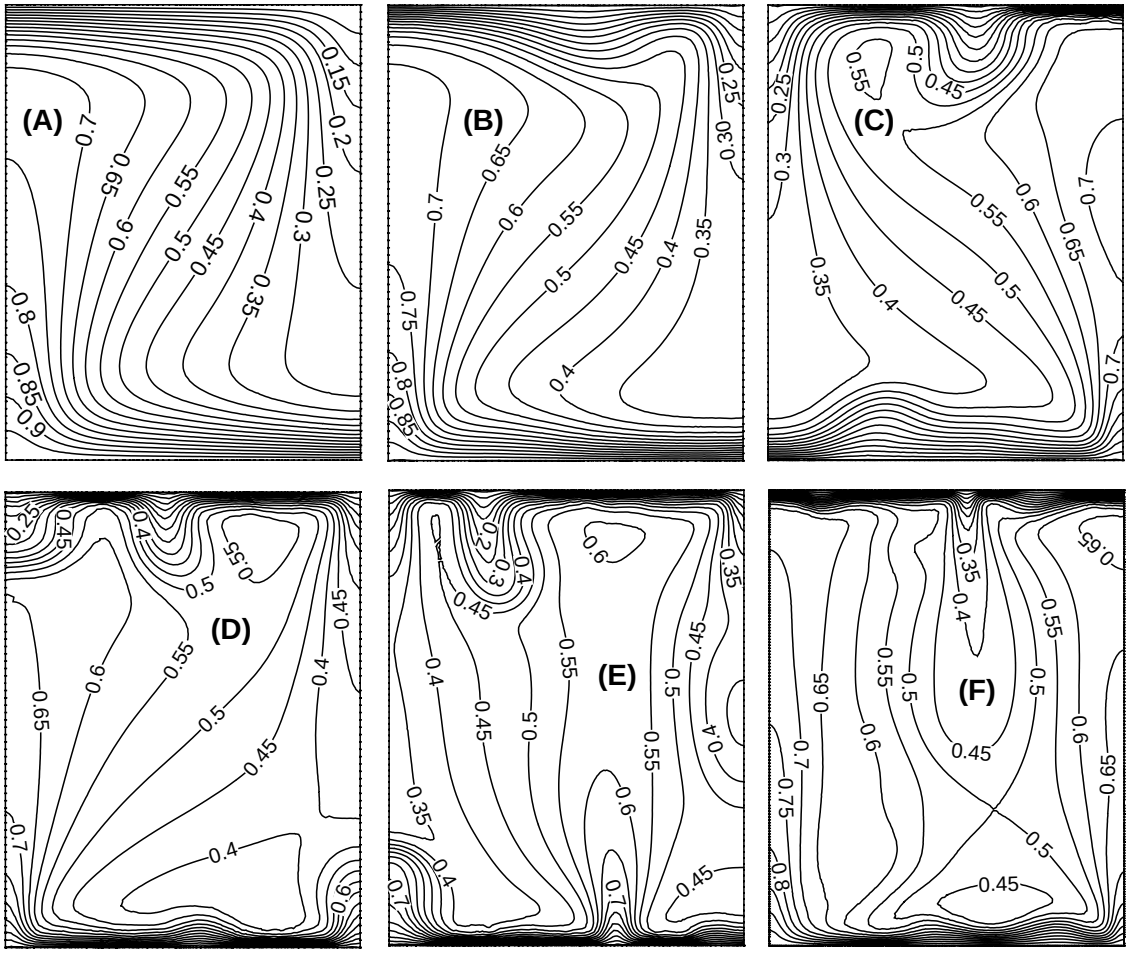

Figure A.13: Nondimensional temperature, T, at $Ra = 300$ (A), 500 (B), 750 (C), 1050 (D), 1200 (E), 1500 (F) at a radial cross section and $\tau = 1$ (corresponding to $t = 96$ hours).

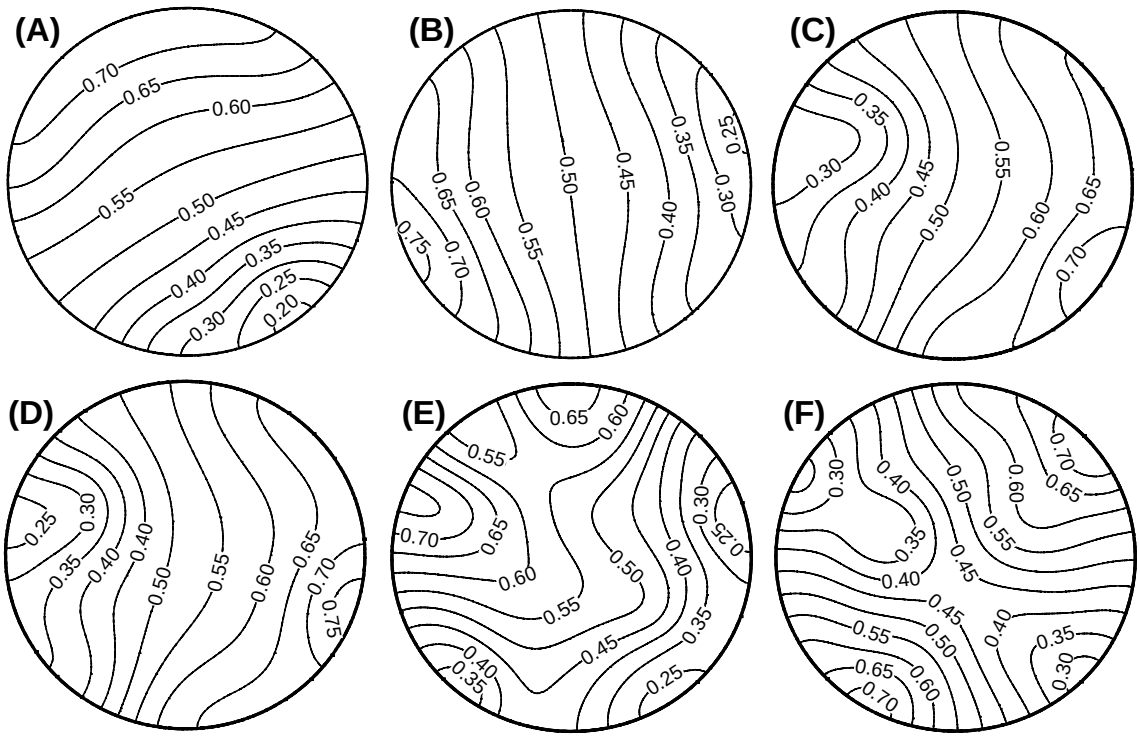

Figure A.14: Nondimensional temperature, T, at the cross section $z = 0.5$ with $Ra = 600$ (A), 750 (B), 900 (C), 1050 (D), 1200 (E), 1500 (F) at $\tau = 1$.

frequencies. However, Ra between 500 and 1200, the spatial-convective structure of the flow is still dominated by the single cell structure created at the onset. Heat is transported mainly by this single cell from the bottom to the top. At $Ra > 1200$, the single convective cell is lost as the disturbances of one boundary connect to those of the other boundary (Fig. A.13F). Therefore at this stage, heat is no longer transported by the initial convective cell but through these connected disturbances.

Representative contours for T in the mid plane $z = 0.5$ at $Ra = 600$, 750, 900, 1050, 1200 and 1500 are shown in Fig. A.14. Above the onset of the oscillatory convection, the symmetry about a radial cross section of T is lost and the asymmetry increases as Ra increases. This is after the disturbances (thermal plumes) in the boundary layer at the top and bottom has penetrated vertically into the core flow (Fig. A.13 and Fig. A.14). However, the single cell flow structure is still maintained at $Ra \leq 1200$ and this is confirmed in Fig. A.13. To prove this, one takes the isotherm of 0.5 as a boundary value. Every value of T on one side of the boundary value is smaller than it and the converse for the other side. As Ra continuously increases ($Ra > 1200$), the thermal plumes of one boundary penetrate deeper into the core flow and eventually connect to those of the other boundary. The flow is characterized by the alternating between hot rising and cold descending spots at this midplane (Fig. A.14F). At this state, the convective flow structure created at the onset is completely changed and is now expressed by a complex vertical-flow structure. The convection proba-

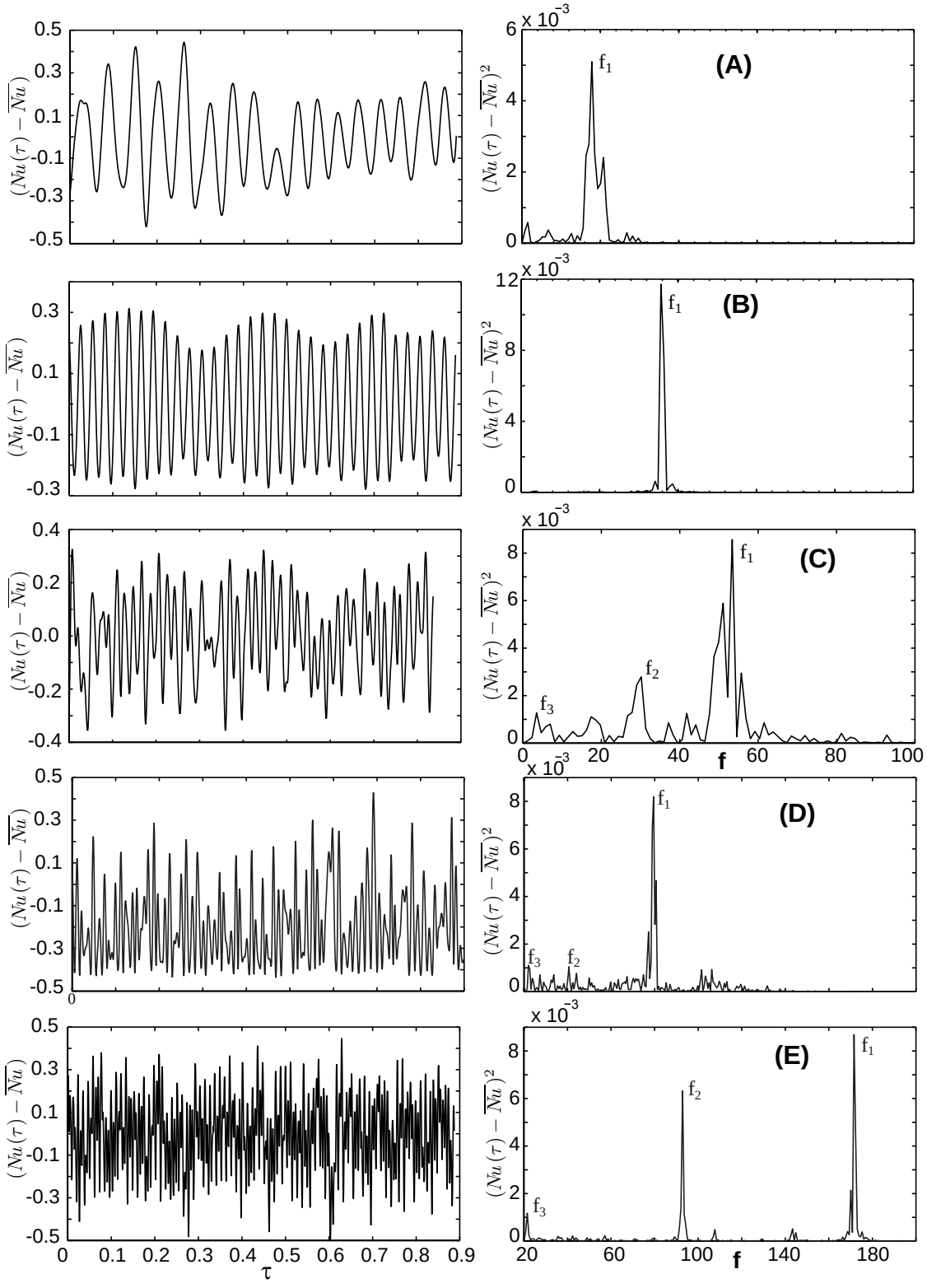

Figure A.15: The time series $Nu(\tau) - \overline{Nu}$ (left) and its power spectrum (right) at $Ra = 600$ (A), 750 (B), 1050 (C), 1200 (D) and 1500 (E).

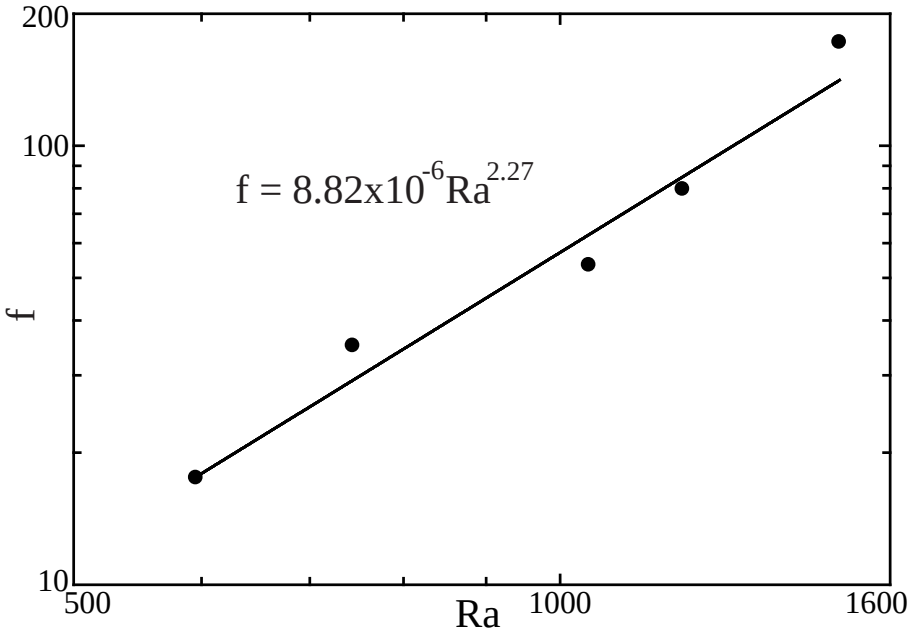

Figure A.16: Fundamental dimensionless frequency, f, versus Rayleigh number, Ra

bly moves to a higher mode similar to the mode 2 (Fig. A.14F).

A.4.2.3 Characteristic frequencies of the time-dependent convection

If Ra is in the range between Ra_2 and Ra_3 (periodic state) in which Ra_3 is the transition between periodic to quasi-periodic flow $Ra_3 < 1500$ in this study, the convection is time dependent. It is characterized by a single fundamental frequency f_1 but other frequencies with much less power may develop. However, at large τ it is expected that the extra frequencies in the periodic state will die out. Time series of $\left(Nu(\tau) - \overline{Nu}\right)$ and its spectral analysis are shown in Fig. A.15A, B, C and D. It shows that the fundamental frequency of the time series $\left(Nu(\tau) - \overline{Nu}\right)$ increases since Ra increases. A functional relation $f_1 = 8.82 \times 10^{-6} Ra^{2.27}$ was used to fit all the frequencies of this periodic state. However, when compare to the studies of Kimura et al. (1989) for three-dimensional convection of a cube, their dimensionless fundamental frequencies are higher. For example at $Ra = 580$ and 740 the values of f_1 of Kimura et al. (1989) were 172.7 and 302.3 respectively compared to 16.6 and 28.9 found in this study. Stamps et al. (1990a) reported a relation $f_1 \propto Ra^{3.6}$, which produces f_1 of 188.7 and 263.2 at $Ra = 580$ and 625, respectively. Therefore, f_1 is about one order of magnitude difference and this may be a consequence of the slenderness of the cylinder. At $Ra = 1500$ the convective flow moves into the quasi-periodic state and during this stage the flow is characterized by two or three fundamental frequencies as shown in Fig. A.15E. The relation between these frequencies f_1, f_2 and f_3 can be expressed by a relation $f_1 = 2f_2 = 4f_3$. The bifurcation of frequency for a cube or square was also observed by Horne and O'sullivan (1974); Kimura et al. (1989); Graham and Steen (1994a) however, only Graham and Steen

(1994a) gave a detailed explanation using bifurcation theory.

A.5 Conclusions

Experiments of Chen (2010) and numerical simulations of air convection in a vertical circular cylinder heated from below were carried out and several conclusions may be presented:

The experimental results showed some agreements to numerical results but discrepancy exists. The cause was due to the difficulty of determining permeability accurately and the limitations of the laboratory apparatus. As a result, Ra_c of the laboratory was about 30 % larger than Ra_cobtained using theoretical and numerical means. The lateral walls of the relatively slender cylinder also had stabilizing effects through increasing the critical Rayleigh number above the corresponding value for an unbounded layer.

The geometry of the laboratory apparatus dictated the convective mode (structure) and in this study, the convective structure was asymmetric (single convective cell). It was confirmed using numerical simulation. The laboratory results showed that the onset of oscillation occurred at the ratio $Ra_2 = 516$ compared to around 490 from numerical simulation.

In the periodic state, $490 < Ra < 1500$, the convective flow was still nonaxisymmetric and was time dependent. It was characterized by a dominated fundamental frequency f_1. This frequency increased as Ra increased. However, due to the slenderness of the cylinder, the fundamental frequency was about one order of magnitude smaller when compared to a 2-D square geometry or a cube at a given Ra. In the quasi-periodic stage, convective flow was denoted by two or more fundamental frequencies.

References

Abramowitz, M. and Stegun, I. A. (1970). *Handbook of Mathematical Functions with Formulas, Graphs, and Mathematical Tables*. National Bureau of Standards.

Bau, H. and Torrance, K. (1981a). Experimental and analytical study of low rayleigh number thermal convection in a vertical cylinder filled with porous material. *American Society of Mechanical Engineers, Heat Transfer Division, (Publication) HTD*, 16:17 – 24.

Bear, J. (1972). *Dynamics of fluids in porous media*. Dover Publications, Inc.

Beck, J. (1972). Convection in a box of porous material saturated with fluid. *Physics of Fluids*, 15(8):1377–1383.

Caltagirone, J. P. (1975). Thermoconvective instabilities in a horizontal porous layer. *Journal Of Fluid Mechanics*, 72(NOV25):269–287.

Caltagirone, J. P. and Fabrie, P. (1989). Natural-convection in a porous-medium at high rayleigh numbers .1. darcy model. *European Journal Of Mechanics B-Fluids*, 8(3):207–227.

Caltagirone, J. P., Meyer, G., and Mojtabi, A. (1981). 3-dimensional thermoconnective structures in a horizontal porous layer. *Journal De Mecanique*, 20(2):219–232.

Chapuis, R. P. (2004). Predicting the saturated hydraulic conductivity of sand and gravel using effective diameter and void ratio. *Canadian Geotechnical Journal*, 41(5):787–795.

Chen, J. F. (2010). Laboratory investigation of natural convection in a porous medium in a cylindrical tank. Master's thesis, University of Alberta.

Combarnous, M. A. and Bories, S. A. (1975). Hydrothermal convection in porous media. *Advances in Hydroscience*, 10:231–307.

Comsol (2009). *Comsol multiphysics' manual*. Comsol, Inc., 744 Cowper Street, Palo Alto, CA 94301, USA.

Côté, J., Fillion, M.-H., and Konrad, J.-M. (2011). Intrinsic permeability of materials ranging from sand to rock-fill using natural air convection tests. *Canadian Geotechnical Journal*, 48(5):679–690.

Goering, D. J. (1998). Experimental investigation of air convection embankments for permafrost-resistant roadway design. In *Seven International Conference on Permafrost*.

Goering, D. J. (2003). Passively cooled railway embankments for use in permafrost areas. *Journal of Cold Regions Engineering*, 17(3):119–133.

Goering, D. J. and Kumar, P. (1996). Winter-time convection in open-graded embankments. *Cold Regions Science and Technology*, 24(1):57–74.

Graham, M. D. and Steen, P. H. (1991). Structure and mechanism of oscillatory convection

in a cube of fluid-saturated porous material heated from below. *J Fluid Mech*, 232:591–609.

Graham, M. D. and Steen, P. H. (1994a). Plume formation and resonant bifurcations in porous-media convection. *Journal of Fluid Mechanics*, 272(-1):67–90.

Horne, R. N. (1979). Three-dimensional natural convection in a confined porous medium heated from below. *Journal of Fluid Mechanics*, 92(04):751–766.

Horne, R. N. and O'sullivan, M. J. (1974). Oscillatory convection in a porous medium heated from below. *Journal of Fluid Mechanics*, 66(02):339–352.

Horton, C. and Rogers Jr., F. (1945). Convection currents in a porous medium. *Journal of Applied Physics*, 16(6):367–370.

Kimura, S., Schubert, G., and Straus, J. M. (1986). Route to chaos in porous-medium thermal convection. *Journal of Fluid Mechanics*, 166:305–324.

Kimura, S., Schubert, G., and Straus, J. M. (1989). Time-dependent convection in a fluid-saturated porous cube heated from below. *Journal of Fluid Mechanics*, 207:153–189.

Lapwood, E. R. (1948). Convection of a fluid in a porous medium. *Mathematical Proceedings of the Cambridge Philosophical Society*, 44(04):508–521.

Nield, D. and Bejan, A. (1999). *Convection in porous media*. Springer, New York.

Otero, J., Dontcheva, L. A., Johnston, H., Worthing, R. A., Kurganov, A., Petrova, G., and Doering, C. R. (2004). High-rayleigh-number convection in a fluid-saturated porous layer. *Journal of Fluid Mechanics*, 500(-1):263–281.

Schubert, G. and Straus, J. M. (1979b). Three-dimensional and multicellular steady and unsteady convection in fluid-saturated porous media at high rayleigh numbers. *Journal of Fluid Mechanics*, 94(01):25–38.

Schubert, G. and Straus, J. M. (1982). Transitions in time-dependent thermal-convection in fluid-saturated porous-media. *Journal Of Fluid Mechanics*, 121(AUG):301–313.

Stamps, D. W., Arpaci, V. S., and Clark, J. A. (1990a). Unsteady three-dimensional natural convection in a fluid-saturated porous medium. *Journal of Fluid Mechanics Digital Archive*, 213(-1):377–396.

Steen, P. H. (1983). Pattern selection for finite-amplitude convection states in boxes of porous media. *J Fluid Mech*, 136:219–241.

Straus, J. M. (1974). Large amplitude convection in porous media. *Journal of Fluid Mechanics*, 64(01):51–63.

Zebib, A. (1978). Onset of natural convection in a cylinder of water saturated porous media. *Physics of Fluids*, 21(4):699–700.

APPENDIX B

Onset of natural air convection in a porous waste-rock pile with internal oxidation process and saturated with an ideal gas (air)

B.1 Introduction

Heavy metal contamination and acidity (low pH) in water (ground and surface runoff) that leaches from waste-rock piles containing sulfide minerals are a major concern at many mines. The reaction between waste rock containing sulfide minerals with oxygen and water can produce acid rock drainage (ARD) in an optimum environment for bacteria (*Acidithiobacillus ferrooxidans*). Besides, oxidation of sulfide minerals is a strong exothermic process and can release a significant amount of heat. The heat release can elevate temperatures within the waste-rock piles significantly above their annual background temperatures (Harries and Ritchie, 1981; Lefebvre et al., 2001a; Sracek et al., 2006; Hollesen et al., 2009, 2011) and this heat release can also create natural air convection. Two primary mechanisms for oxygen transport to oxidation locations are air diffusion and/or air convection/advection. However, air convection/advection is only significant if the permeability of waste rock is sufficiently high. Currently, an engineered soil cover is usually used as a method of reducing ARD through eliminating the ingress of oxygen and/or water from coming in contact with the reactive waste rock. Several versions of engineered soil cover have been proposed and currently used as mine closure methods (Newman et al., 1997; Morin and Hutt, 2001; Martin et al., 2004; Wickland and Wilson, 2005a; Molson et al., 2005; Song and Yanful, 2008).

When a waste-rock pile is constructed in a continuous permafrost region, natural air convection can occur to cool the internal temperatures of the waste-rock pile significantly during winter. The problem of natural fluid convection in porous media saturated with an incompressible fluid is a classical problem that has been studied intensively (Horton and Rogers Jr., 1945; Lapwood, 1948; Nield and Bejan, 1999). A comprehensive survey

of the available literatures related to natural and forced convection in both saturated and unsaturated porous media was reported by Nield and Bejan (1999). The procedure of linear stability analysis for the onset of natural convection in a fluid-saturated porous medium is standardized and used by many researchers (Chandrasekhar, 1961; Nield and Bejan, 1999; Nield and Barletta, 2009; Drazin and Reid, 2004). Onset of natural convection with internal heat source in porous media saturated with a Boussinesq-Oberbeck approximation fluid was conducted by Sparrow et al. (1964); Gasser and Kazimi (1976). They indicated that the internal heat source, which is a constant flux, can create sufficient buoyancy forces to produce natural convection. Saatdjian (1980) worked on the natural convection of an ideal gas without heat source and the result is the critical Rayleigh number (Ra_c) less or greater than $4\pi^2$ depending on temperature boundary conditions. Zhang et al. (1994) conducted an analytical study of moist air convection ($Ra_c < 4\pi^2$ due to latent heat effects) and Ra_c is $4\pi^2$ at zero moisture content. By using finite amplitude analysis for the study of natural convection of air and water without internal heat, Stauffer et al. (1997) concluded that Ra_c for air and water is comparable under a certain range of temperature gradient even though their thermal properties are much different.

In this study, the problem of the onset of natural convection in a reactive waste-rock pile is examined to include the influences of the ideal gas's law, internal heat source, and pressure work. A linear stability analysis is carried out and the analysis indicates the importance of each variable on Ra_c. Furthermore, parameters used in the calculation in this study were based on the ongoing research in the Diavik Waste-Rock test Piles project at the Diavik Diamond Mine on a 20 km^2 island in Lac de Gras, approximately 300 km North-East of Yellowknife, NWT, Canada in a continuous permafrost region.

B.2 Governing equations

Fig. B.1 shows the configuration of the problem (a 2-D problem) and waste rock or porous media are isotropic, homogeneous and in thermal equilibrium between the solid and fluid phase; the ideal gas's law for air and the Darcy's law are valid. Furthermore, viscous dissipation is neglected because of low air velocity of natural air convection (Kundu and Cohen, 2002). The governing equations are defined as (Nield and Bejan, 1999).

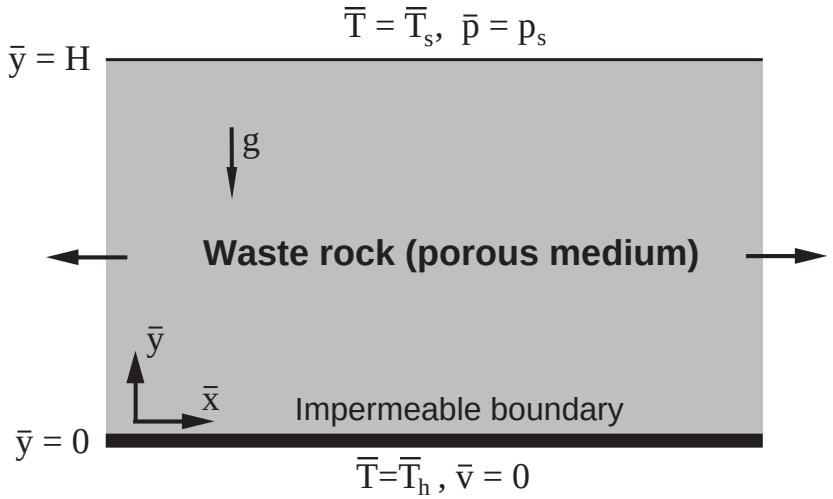

Figure B.1: Schematic illustration of this study.

$$\phi\left(\frac{\partial \bar{\rho}_a}{\partial \bar{t}}\right) + \bar{\nabla}\cdot(\bar{\rho}_a \bar{\mathbf{u}}) = 0 \tag{B.1}$$

$$\frac{\mu}{K}\bar{\mathbf{u}} = -\bar{\nabla}\bar{p} - \bar{\rho}_a g\mathbf{y} \tag{B.2}$$

$$(\bar{\rho}_a c_a)\left(\sigma\frac{\partial \bar{T}}{\partial \bar{t}} + \bar{\mathbf{u}}\cdot\bar{\nabla}\bar{T}\right) = \lambda\bar{\nabla}^2\bar{T} + \beta\bar{T}\left(\frac{\partial \bar{p}}{\partial \bar{t}} + \bar{\mathbf{u}}\cdot\bar{\nabla}\bar{p}\right) + S_h \tag{B.3}$$

$$\bar{p}M = \bar{\rho}_a R\bar{T} \tag{B.4}$$

Where: ϕ is the porosity of waste rock, $\bar{\rho}_a$ is the air density which is defined by Eqn. B.4, μ is the air dynamic viscosity, which is constant, $\bar{t}$ is time, K is the intrinsic permeability of waste rock, $\bar{\mathbf{u}}(\bar{u},\bar{v})$ is the air velocity vector determined via the Darcy's law, $\bar{p}$ and $\bar{T}$ are the air pressure and temperature respectively, β is the expansion of air density due to temperature and for an ideal-compressible gas $\beta = 1/\bar{T}\,(1/\mathrm{K})$. λ is the bulk thermal conductivity of waste rock including solid and fluid phases, g is the gravity of acceleration, $\mathbf{y}$ is the unit vector in a vertical direction, $\sigma = \dfrac{\rho c}{\bar{\rho}_a c_a}$, where $(\rho c) =$ constant is the bulk volumetric heat capacity of waste rock, $(\bar{\rho}_a c_a)$ is the volumetric heat capacity of air. $S_h\ \left(\frac{\mathrm{J}}{\mathrm{m}^3\cdot\mathrm{s}}\right)$ is the internal heat source due to oxidation. M and R are the molar mass and gas constant of air.

The internal heat source due to the oxidation of sulfide minerals, S_h which varies exponentially with depth, is defined as (Lefebvre et al., 1992).

$$S_h = S_o e^{-\dfrac{\zeta(H-\bar{y})}{H}} \tag{B.5}$$

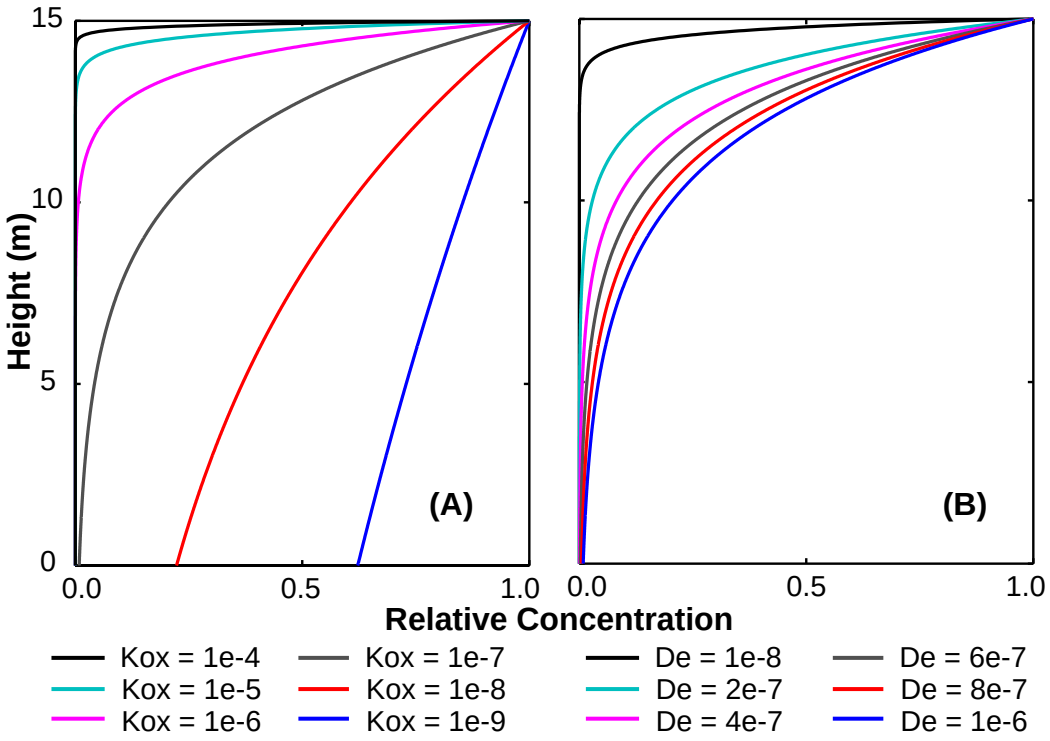

Figure B.2: Oxygen profile versus depth at: different values of K_{ox} with $D_e = 1 \times 10^{-6}\,m^2/s$ (A) and different values of D_e with $K_{ox} = 1 \times 10^{-7} s^{-1}$(B).

Where: $S_o = F \cdot C_o \cdot K_{ox}$ and $\zeta = H\sqrt{\left(\frac{K_{ox}}{D_e}\right)}$, where $F = 1.41 \times 10^7\,J/(kg\,O_2)$ is heat release per unit mass of oxygen depletion (Lowson, 1982; Lefebvre et al., 2001a), $C_o = 0.25\,kg/m^3$ is the ambient oxygen concentration at 0 °C (Tasa et al., 2006), K_{ox} between 1×10^{-7} and $1x10^{-8}\,1/s$ is the kinetic constant of sulfide oxidation, and $D_e = 1 \times 10^{-6}\,m^2/s$ is the oxygen diffusion coefficient in the void of waste rock (Lefebvre et al., 1992, 2001b). With the above parameters, the value of S_o ranges from 0.04 to $0.36\,J/\left(m^3 \cdot s\right)$ and ζ ranges from $0.1\,H$ to $0.32\,H$. The estimation of the oxygen transport through diffusion can be obtained from Eqn. B.5 by dividing both sides by F and is illustrated in Fig. B.2. Fig. B.2A shows that the more reactive the waste rock, the higher the surface oxygen diffusion flux. Because, high reactive waste rock consumes more oxygen resulting in high oxygen gradient therefore producing high oxygen flux at the surface. At the same kinetic oxidation constants the oxygen flux is increased when the diffusion coefficient is increased corresponding to the cases of dry and high porosity waste rock (Fig. B.2B).

B.3 Steady-state solutions

A steady-state solution of Eqn. B.1 to Eqn. B.4 is that the heat transfer is purely via conduction and no airflow. The following boundary conditions are then used to solve for pressure

and temperature distributions under this condition.

- Impermeable at both the upper and lower boundaries

$$\begin{aligned} \bar{y} &= 0: \ \bar{v}=0, \ \bar{T}=\bar{T}_h \\ \bar{y} &= H: \ \bar{v}=0, \ \bar{T}=\bar{T}_s \end{aligned} \tag{B.6}$$

- Permeable at the upper and impermeable at the lower boundaries

$$\begin{aligned} \bar{y} &= 0: \ \bar{v}=0, \ \bar{T}=\bar{T}_h \\ \bar{y} &= H: \ \bar{p}=\bar{p}_s, \ \bar{T}=\bar{T}_s \end{aligned} \tag{B.7}$$

Where $\bar{T}_s$ and $\bar{p}_s$ are the top surface temperature and pressure, $\bar{T}_h$ is temperature at the base.

Solving Eqs. B.1 to B.4 with Eqn. B.6 and/or Eqn. B.7 as boundary conditions yields analytical expressions for the temperature and pressure distributions as:

$$\bar{T}_o = \bar{T}_h(1-y) + y\bar{T}_s + \frac{S_o H^2}{\zeta^2 k}\left(y - e^{\zeta(y-1)} + e^{-\zeta}(1-y)\right) \tag{B.8}$$

$$\bar{p}_o = \bar{p}_s e^{\dfrac{Mg\zeta^2\lambda_e H}{R}\displaystyle\int_1^y \frac{1}{\left(S_o H^2\left(e^{\zeta(y_1-1)} - e^{-\zeta} - y_1(1+e^{-\zeta})\right) - \zeta^2\lambda_e\left(y_1\bar{T}_s + \bar{T}_h(1-y_1)\right)\right)} dy_1} \tag{B.9}$$

$$\bar{\rho}_a^o = \frac{\bar{p}_o M}{R\bar{T}_o} \tag{B.10}$$

Where: the dimensionless quantity $y = \dfrac{\bar{y}}{H}$. $\bar{T}_o$, $\bar{p}_o$, and $\bar{\rho}_a^o$ are the temperature, pressure and air density distributions with depth and air is stationary ($\bar{\mathbf{u}}_o = \mathbf{0}$). The above solutions clearly show that the vertical distributions of temperature, pressure and air density are non-linear because of the heat source. Due to the nonlinearity, air convection can be initiated if an adverse gradient, in which pressure or temperature at the bottom is higher than at the top, of either temperature or pressure is sufficient at any depth.

B.4 Linear stability analysis and dimensionless equations

B.4.1 Linear stability analysis

To examine the stability of the initial conduction state, whether this conduction state is stable or not, assuming that the velocity, temperature, pressure, and density fields of the initial conduction state are perturbed and expressed as:

$$\bar{\mathbf{u}} = \bar{\mathbf{u}}_o + \bar{\mathbf{u}}', \;\; \bar{p} = \bar{p}_o + \bar{p}' \tag{B.11}$$

$$\bar{\rho}_a = \bar{\rho}_a^o + \bar{\rho}_a', \;\; \bar{T} = \bar{T}_o + \bar{T}' \tag{B.12}$$

Where: $\bar{\mathbf{u}}'$, $\bar{p}'$, $\bar{\rho}_a'$ and $\bar{T}'$ are the infinitesimal perturbations of the variables; $\bar{\mathbf{u}}_o = \mathbf{0}$ and $\bar{\mathbf{u}}' = (\bar{u}', \bar{v}')$. The basic principle of "*hydrodynamic stability*" is to determine whether or not the small disturbances to the system will increase or diminish with time. If these disturbances grow with time, the system is unstable otherwise it is stable (Drazin and Reid, 2004). The boundary between the two states (stable and unstable) are *"a marginal state"* (the onset of air convection in our case) (Drazin and Reid, 2004). One inserts these perturbations into Eqs. B.1 to B.4 and only keeps the first power terms of the perturbations. The governing equations become:

$$\phi\left(\frac{\partial \bar{\rho}_a'}{\partial \bar{t}}\right) + \bar{\nabla}\cdot\left(\bar{\rho}_a^o \bar{\mathbf{u}}'\right) = 0 \tag{B.13}$$

$$\frac{\mu}{K}\bar{\mathbf{u}}' = -\bar{\nabla}\bar{p}' + \bar{\rho}_a'\mathbf{g} \tag{B.14}$$

$$\left(\bar{\rho}_a^o c_a\right)\left(\sigma\frac{\partial \bar{T}'}{\partial \bar{t}} + \frac{\mathrm{d}\bar{T}_o}{\mathrm{d}\bar{y}}\bar{v}'\right) = \lambda\bar{\nabla}^2\bar{T}' + \beta\bar{T}_o\left(\frac{\partial \bar{p}'}{\partial \bar{t}} + \frac{\mathrm{d}\bar{p}_o}{\mathrm{d}\bar{y}}\bar{v}'\right) \tag{B.15}$$

$$\bar{\rho}_a = \frac{\bar{p}M}{R\bar{T}} = \bar{\rho}_a^o + \bar{\rho}_a' \tag{B.16}$$

We introduce scaling parameters:

$$(\bar{x}, \bar{y}) = H(x, y), \;\; \sigma = \frac{\rho c}{\bar{\rho}_a c_a}, \;\; t = \frac{\alpha \bar{t}}{\sigma H^2}, \;\; \mathbf{u} = \frac{\bar{\mathbf{u}}' H}{\alpha}, \;\; p = \frac{K\bar{p}'}{\mu\alpha}, \;\; \rho_a = \frac{\bar{\rho}_a'}{\bar{\rho}_a^s}, \;\; T = \frac{\bar{T}'}{(\bar{T}_h - \bar{T}_s)} \tag{B.17}$$

Where $\alpha = \dfrac{\lambda}{(\bar{\rho}_a c_a)}$ and $\bar{\rho}_a^s = constant$ is the air density at the surface, which is calculated though surface temperature and pressure via ideal gas law.

$$\left.\begin{aligned} Ra = \frac{g\beta(\bar{T}_h - \bar{T}_s)H\bar{\rho}_a^s K}{\mu\alpha}, \;\; A_o(y) = \frac{1}{(\bar{T}_h - \bar{T}_s)}\frac{\mathrm{d}\bar{T}_o}{\mathrm{d}y} \\ B_o(y) = \frac{\beta^2 \bar{T}_o g H \bar{\rho}_a^s \alpha}{\sigma\lambda}, \;\; C_o(y) = \frac{g\beta^2 H\bar{\rho}_a^s K\bar{T}_o}{\mu\lambda}\frac{\mathrm{d}\bar{P}_o}{\mathrm{d}y} \\ D_o = \frac{1}{\beta(\bar{T}_h - \bar{T}_s)}, \;\; E_o(y) = \frac{\phi\bar{\rho}_a^s}{\sigma\bar{\rho}_a^o}, \;\; F_o(y) = \frac{M\mu\alpha}{R\bar{T}_o\bar{\rho}_a^s K}, \;\; G_o(y) = \frac{M\bar{p}_a^o(\bar{T}_h - \bar{T}_s)}{R\bar{T}_o^2\bar{\rho}_a^s} \end{aligned}\right\} \tag{B.18}$$

Where, Ra is the Rayleigh number, $A_o(y)$ represents the effects of the heat source which create a nonlinear temperature profile of the conduction state (or temperature gradient with

depth is not constant). Both $B_o(y)$ and $C_o(y)$ are the parameters that take into account the effects of the work done by pressure changes. $E_o(y)$, $F_o(y)$ and $G_o(y)$ are thermodynamic parameters affected by the initial condition of temperature and pressure. D_o is a buoyancy factor.

Using the above scaling parameters, the governing equations are non-dimensionalized and can be written as:

$$E_o\left(\frac{\partial \rho_a}{\partial t}\right)+\nabla\cdot(\mathbf{u})=0 \tag{B.19}$$

$$\mathbf{u}=-\nabla p-RaD_o\rho_a\mathbf{y} \tag{B.20}$$

$$\frac{\partial T}{\partial t}+v\left(A_o-\frac{C_o}{Ra}\right)-\frac{B_o}{Ra}\frac{\partial p}{\partial t}=\nabla^2 T \tag{B.21}$$

$$\rho_a=\frac{M(\bar{p}'\bar{T}_o-\bar{p}_o\bar{T}')}{RT_o^2\bar{\rho}_s}=F_o p-G_o T \tag{B.22}$$

$E_o\to 0$ or more precise 10^{-4} as σ is large due to the volumetric heat capacity of waste rock is much greater than that of air. Therefore, Eqn. B.19 becomes $\nabla\cdot\mathbf{u}=0$.

By introducing a dimensionless streamfunction $\psi(x,y)$ for the 2-D problem being studied in the (x, y)-plane, such that:

$$u=\frac{\partial\psi}{\partial y},\quad v=-\frac{\partial\psi}{\partial x} \tag{B.23}$$

Inserting Eqn. B.23 into the Eqs. B.20 to B.22 results in:

$$\nabla^2\psi+RaD_o\left(F_o\frac{\partial\psi}{\partial y}+G_o\frac{\partial T}{\partial x}\right)=0 \tag{B.24}$$

$$\nabla^2 T+\frac{\partial\psi}{\partial x}\left(A_o-\frac{C_o}{Ra}\right)+\frac{B_o}{Ra}\frac{\partial p}{\partial t}-\frac{\partial T}{\partial t}=0 \tag{B.25}$$

$$\rho=F_o p-G_o T \tag{B.26}$$

The boundary conditions become:

- $T=0$ for the case of constant temperature
- $\dfrac{\partial\psi}{\partial y}=0$ for the case of permeable surface
- $\psi=0$ for the case of impermeable surface

B.4.2 Onset of convection, Numerical solution and Approximate analytical solution

B.4.2.1 Onset of convection

Since Eqs. B.23 to B.26 are linear, by using the separation of variables, the solutions can be expressed as (Farlow, 1993; Nield and Bejan, 1999; Nield and Barletta, 2009):

$$\left.\begin{aligned} \psi = f(y)e^{\eta t}\sin(ax), \quad T = g(y)e^{\eta t}\cos(ax) \\ p = h(y)e^{\eta t}\cos(ax), \quad \rho_a = s(y)e^{\eta t}\cos(ax) \end{aligned}\right\} \tag{B.27}$$

Where: a is a wave number, $\eta = \mathrm{Re}(\eta) + \mathrm{Im}(\eta)i$ is a complex number, assuming the validity of "*the principle of the exchange of stabilities*" and "*marginal stability*" of the system, $\eta = 0$ (Chandrasekhar, 1961; Nield and Bejan, 1999).

Substituting Eqn. B.27 with $\eta = 0$ into Eqs. B.23 to B.26 yields:

$$h(y) = f'(y) \tag{B.28}$$

$$f''(y) - a^2 f(y) + RaD_o\left(F_o f'(y) - aG_o g(y)\right) = 0 \tag{B.29}$$

$$g''(y) - a^2 g(y) + af(y)\left(A_o - \frac{C_o}{Ra}\right) = 0 \tag{B.30}$$

$$s(y) = F_o h(y) - G_o g(y) \tag{B.31}$$

The boundary conditions become

- For the case of impermeability of both the lower and upper surfaces

$$y = 0, 1: \quad f(y) = g(y) = 0 \tag{B.32}$$

- For the case of impermeability of the lower surface while the upper surface is previous

$$\left.\begin{aligned} y = 0: \quad f(0) = g(0) = 0 \\ y = 1: \quad f'(1) = g(0) = 0 \end{aligned}\right\} \tag{B.33}$$

Either the boundary condition Eqn. B.32 or Eqn. B.33 and given values of A_o, C_o, D_o, F_o, and G_o, the problem becomes finding the eigenvalues, Ra, of the boundary-value problem (Eqn. B.28 to Eqn. B.31) for which there exists a non-trivial solution.

B.4.2.2 Approximate analytical solution for the case of impermeable surfaces

Approximation solutions, using Fourier sine series, which satisfy the boundary conditions Eqn. B.32, can be written as (Farlow, 1993; Nield and Barletta, 2009):

$$f(y) = \sum_{n=1}^{N} F_n \sin(\pi n y), \quad g(y) = \sum_{n=1}^{N} G_n \sin(\pi n y) \tag{B.34}$$

The coefficients, F_n and G_n, are unknown and constants. By inserting Eqn. B.34 into Eqn. B.30 and Eqn. B.29 and using the method of weighted residuals with a weight function of $\sin(\pi m y)$, $1 \leq m \leq N$, one obtains a linear system equation:

$$\mathbf{XF} = \mathbf{0} \tag{B.35}$$

With

$$X_{mn} = -\frac{1}{2}\left[(\pi n)^2 + a^2\right]\delta_{mn} + L_{mn}, \quad 1 \leq n, m \leq N \tag{B.36}$$

F is the column vector of F_n, δ_{mn} is the Kronecker tensor and L_{mn} are defined as:

$$L_{mn} = \int_0^1 RaD_o \left(F_o \pi n \frac{\cos(\pi n y)}{\sin(\pi n y)} - a^2 G_o \frac{A_o - \frac{C_o}{Ra}}{(\pi n)^2 + a^2} \right) \sin(\pi n y) \sin(\pi m y)\, \mathrm{d}y \tag{B.37}$$

A nontrivial solution of Eqn. B.35 is defined as:

$$\| \mathbf{X} \| = 0 \tag{B.38}$$

The solution of the Eqn. B.38 gives the results of Ra as a function of a for a given set of waste-rock properties.

B.4.2.3 The lowest order of approximation

The Eqn. B.38 becomes complex as N increases. Therefore, to obtain an analytical solution, the lowest order approximation is examined with $N = 1$.

From Eqs. B.36 and B.37, Eqn. B.38 becomes

$$-\frac{1}{2}\left(\pi^2 + a^2\right) + RaI_1 - \frac{Ra\,a^2}{(\pi^2 + a^2)} I_2 + \frac{a^2}{(\pi^2 + a^2)} I_3 = 0 \tag{B.39}$$

Where:

$$\begin{aligned} I_1 &= \int_0^1 D_o F_o \pi \cos(\pi y) \sin(\pi y)\, \mathrm{d}y \to 0 \\ I_2 &= \int_0^1 D_o G_o A_o \sin^2(\pi y)\, \mathrm{d}y \\ I_3 &= \int_0^1 D_o G_o C_o \sin^2(\pi y)\, \mathrm{d}y \end{aligned} \tag{B.40}$$

Table B.1: Parameters used in the stability analysis*

M	$28.57\ \mathrm{g/mol}$	ζ	1.78 dimensionless	μ	$1.72\times10^{-5}\,\mathrm{kg/(m\cdot s)}$
R	$8.314\ \mathrm{kg\cdot m^2/(s^2\cdot mol\cdot K)}$	β	$3.70\times10^{-3}\,\mathrm{K^{-1}}$	H	$20\,\mathrm{m}$
$\bar{T}_s$	$253.15\ \mathrm{K}$	g	$9.81\ \mathrm{m/s^2}$	λ	$1.8\,\mathrm{W/(m\cdot K)}$
$\bar{P}_s$	$101.325\ \mathrm{kPa}$	$\bar{T}_h$	$273.15\ \mathrm{K}$	c_a	$1005\,\mathrm{J/(kg\cdot K)}$
S_o	$0.00\ \mathrm{J/(m^3\cdot s)}$	K	$2\times10^{-9}\,\mathrm{m^2}$	(ρc)	$2.3\times10^{6}\,\mathrm{J/(m^3\cdot K)}$

* The parameters are used for later calculations and any changes of these parameters will be stated

Eqn. B.39 gives:

$$Ra=-\frac{\left(\pi^2+a^2\right)^2-2a^2I_3}{2a^2I_2} \tag{B.41}$$

For the cases of no heat source $(S_o=0)$ and parameters shown in Table B.1, $I_2\simeq-\frac{1}{2}$, $I_3<0$ (Fig. B.3), Eqn. B.39 becomes

$$Ra=\frac{\left(\pi^2+a^2\right)^2}{a^2}-2I_3 \tag{B.42}$$

Thus, Eqn. B.42 shows that the effects of the pressure work term and the compressibility of air are stabilizing, which increases the value of Ra_c. Eqn. B.41 indicates that Ra is no longer a function of a alone.

By letting $\frac{\mathrm{d}Ra}{\mathrm{d}a}=0$, one has $a_c=\pi$ and:

$$Ra_c=4\pi^2-2I_3 \tag{B.43}$$

Fig. B.3 shows that the dimensionless coefficients $I_1=0$ and $I_2=-\frac{1}{2}$ are independent of H ranging between 15 and 500 m, at $K=2\times10^{-9}\,\mathrm{m^2}$. Moreover, at $H=100\,\mathrm{m}$ and permeability, K, ranges between 2×10^{-9} and $4\times10^{-8}\,\mathrm{m^2}$, $I_1=0$ and $I_2=-\frac{1}{2}$. However, the value of I_3 is close to 0 $\left(Ra_c=4\pi^2\right)$ when H is less than 60 m and gradually increases then starts to accelerate when the height is larger than 200 m (Fig. B.3A). For example, at $H=100\,\mathrm{m}$, I_3 is -0.15 $(Ra_c=40.2)$ at $K=2\times10^{-9}\,\mathrm{m^2}$ and increases at a constant rate to a value of -3.33 $(Ra_c=46.6)$ at $K=4\times10^{-8}\mathrm{m^2}$ (Fig. B.3B).

It is important to mention that the result of Eqn. B.39 $(N=1)$ is approximated and only yields an exact solution if the effects of the pressure work, internal heat source and compressibility are negligible $(A_o(y)\to-1$, $B_o(y)\to0$ and $C_o(y)\to0$, therefore $I_3\to0$ as a result $Ra_c=4\pi^2$ (Eqn. B.43)). In that case, our problem becomes the classical problem of Horton and Rogers Jr. (1945); Lapwood (1948). Nield and Bejan (1999) provided the results of higher modes of the classical problem (Eqn. B.44) for the case of impermeable boundaries heating from below. Therefore, with the effects of internal heat source and com-

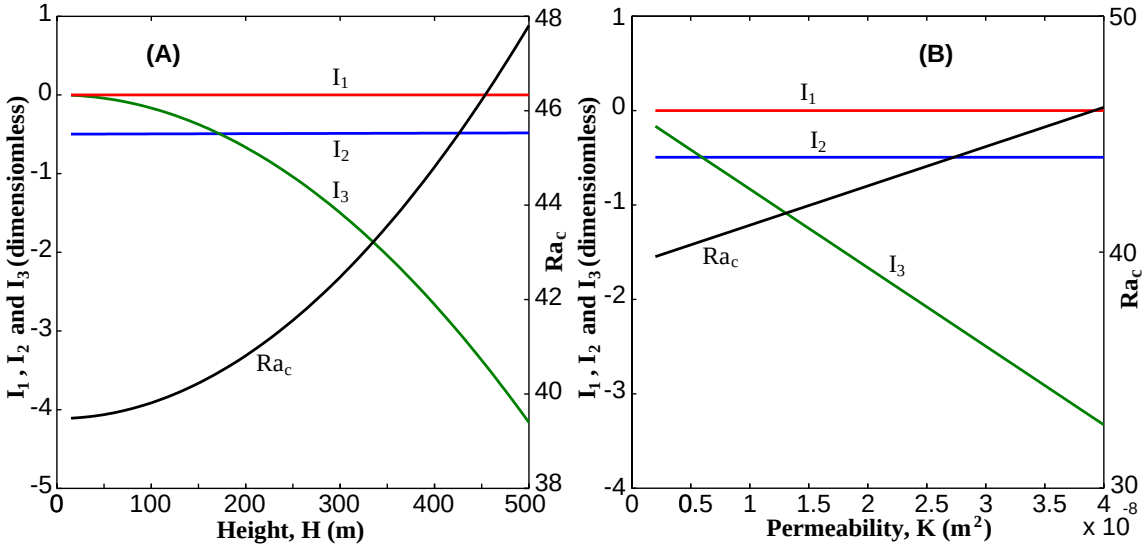

Figure B.3: Illustration of the dimensionless quantities I_1, I_2, I_3 and Ra_c at $S_o = 0$ as a function of thickness H at $K = 2 \times 10^{-9}\,\mathrm{m}^2$ (A) and K at $H = 100\,\mathrm{m}$ (B) by the analytical solution for the case of impermeable top surface.

pressibility of air, a numerical solution of Eqs. B.29 and B.30 is needed and it is presented in the next section.

$$\left.\begin{aligned} Ra_n &= 4\pi^2 n^2 \\ a_{cn} &= n\pi \end{aligned}\right\} \tag{B.44}$$

Fig. B.4 shows a comparison between analytical and numerical solutions in which if there is no internal heat source $(S_o = 0)$ and other properties in Table B.1, the difference is small (Fig. B.4A). However, if there is a heat source $(S_o > 0)$, the discrepancy is quite significant especially at large a (Fig. B.4B). One notable feature of the approximate analytical solution $(N = 1)$ is that the value of the critical wave number , a_c, is always π for the case of impermeability and constant temperatures at the boundaries and this can be proved by letting $\dfrac{\mathrm{d}Ra}{\mathrm{d}a} = 0$.

B.4.2.4 Numerical solution

Eqs. B.29 and B.30 can produce four first-order ordinary differential equations (ODEs) subjected to two-point boundary conditions. They were solved using the boundary value problem solver *bvp4c* in Matlab (Matlab, 2012). In this study, a mesh of 100 equally spaced points in $[0, 1]$ was chosen, which is fine enough to give mesh-independent results, and $f(y) = g(y) = \sum_{n=1}^{N} \sin(\pi n y)$ was used as an initial guess in which N defines the different modes of instability.

Fig. B.5 shows the four modes of instability in which the critical values of (Ra, a) curves of different modes are slightly larger than the results of Eqn. B.44 due to the effects

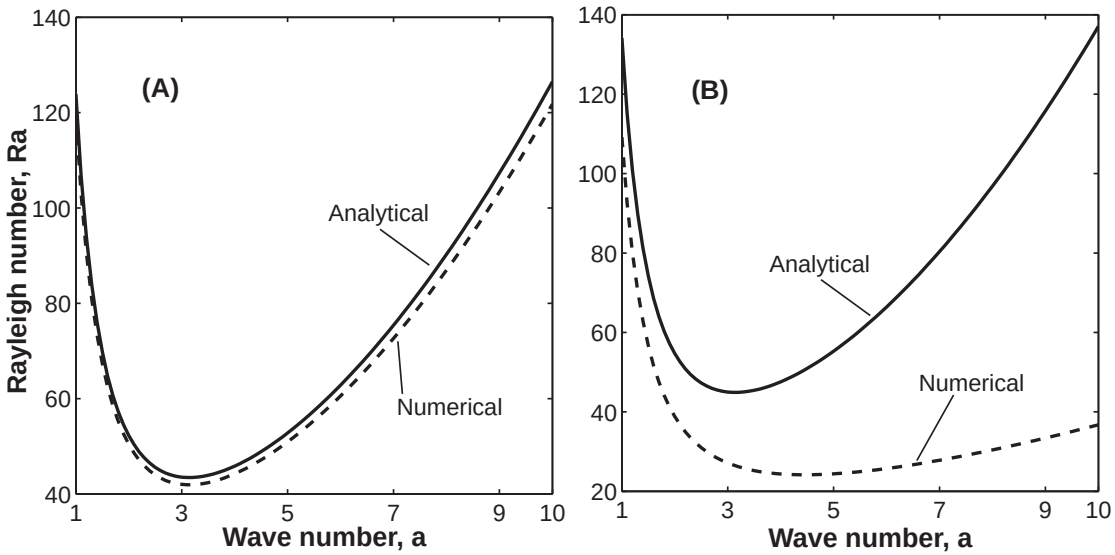

Figure B.4: Comparison between analytical (Eqn. B.41) and numerical solutions (will be described in a later section), the lowest marginal stability curve: (A) $\Delta\bar{T} = 20\,^{\circ}\mathrm{C}$, $S_o = 0$, $H = 300\,\mathrm{m}$, (B) $S_o = 0.1$, $\zeta = 0.5$, $\Delta\bar{T} = 20\,^{\circ}\mathrm{C}$, $H = 100\,\mathrm{m}$ and other parameters are shown in Table B.1. .

Table B.2: Comparison between analytical and numerical solutions of the classical problem and our problem without heat source. The parameters are provided in Table B.1.

	Analytical solution (Eqn. B.44)		Numerical Solution (Eqs. B.29 and B.30)	
Mode	a_c	Ra_c	a_c	Ra_c
1^{st}	3.1416	39.4784	3.1421	39.8958
2^{nd}	6.2832	157.9137	6.2836	159.5919
3^{rd}	9.4248	355.3058	9.4266	359.1589
4^{th}	12.5664	631.6547	12.5716	638.7112

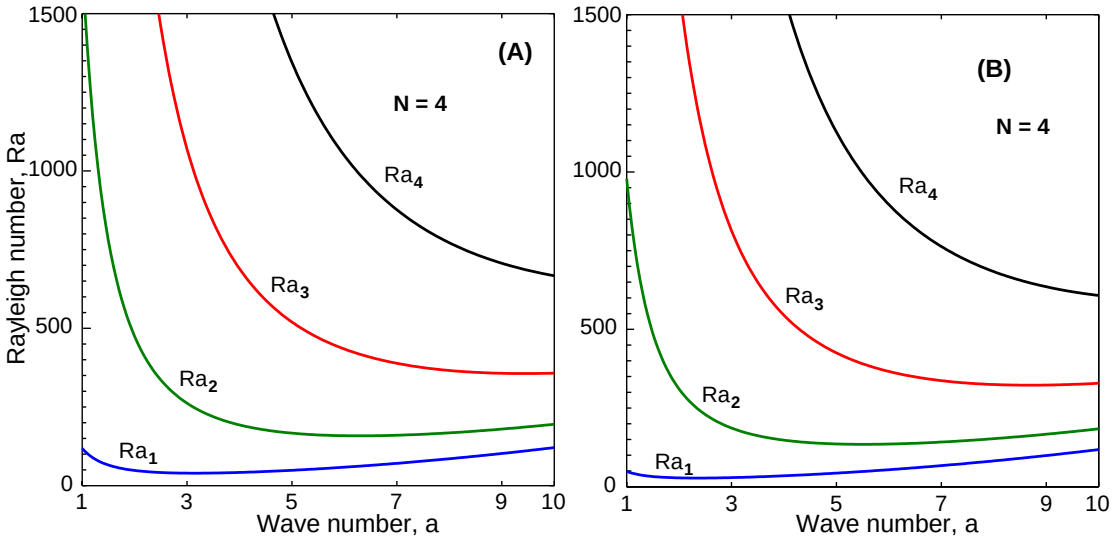

Figure B.5: Marginal stability curves for $\Delta\bar{T} = 20\,^{\circ}\mathrm{C}$, $H = 20\,\mathrm{m}$, $S_o = 0$, and $K = 2 \times 10^{-9}\,\mathrm{m}^2$ in the plane (a, Ra) according to the numerical solution at different modes of instability at $N = 4$ with impermeable surface (A) and permeable surface (B) .

of pressure work and compressibility but without internal heat source (Table B.2). The 1^{st} instability mode is important as it gives a minimum value of Ra (Ra_c) (the onset of convection) among other modes. Therefore, in the following section, the 1^{st} instability mode will be examined and the solution of Eqs. B.29 and B.30 is obtained using this numerical method.

B.5 Results and Discussion

The criterion for the onset of convection is when a waste-rock pile's Rayleigh number (or system's Rayleigh number), Ra, defined by Eqn. B.18 is equal to Ra_c defined using Eqn. B.43 or from the numerical method. Ra and Ra_c are functions of waste rock properties and the local environment (e.g. air temperatures and ambient pressure).

The patterns of dimensionless streamline and temperature distributions at the critical condition can be defined by the corresponding eigenfunctions and are illustrated in Fig. B.6. These convection cells circulate air within a waste-rock pile thus they increase not only heat transfer but also pyrite oxidation process (supply high O_2 concentration air). The increase in pyrite oxidation can create higher temperature gradients within the waste-rock pile. At high temperatures gradients, air convection can transform into higher modes (multi-layer convection cells) with greater air velocities.

For a Boussinesq-Oberbeck flow, in which fluid density depending on temperature in the term associated with gravity otherwise density is a constant, Ra_c is a constant of $4\pi^2$ independent of a waste-rock pile's properties (Horton and Rogers Jr., 1945; Lapwood, 1948). This does not hold in the case of a non-Boussinesq fluid, taking into account the effect

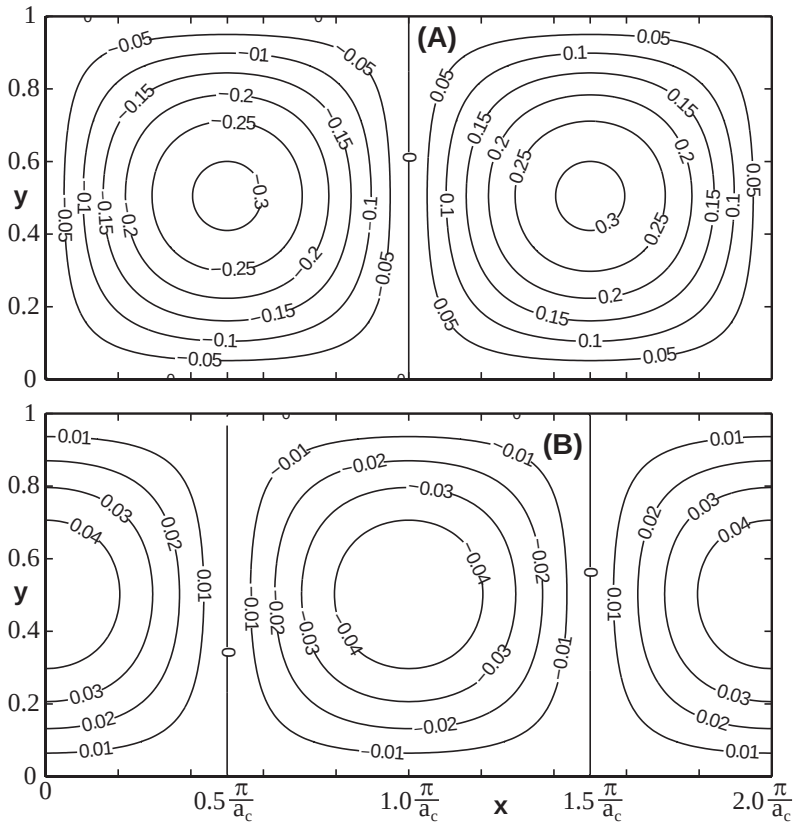

Figure B.6: Dimensionless Streamline ψ (A) and Isotherms T (B) at the onset of convection $\left(Ra_c = 4\pi^2 - 2I_3,\, a_c = \pi\right)$ in the case of impermeable top surface and $S_o = 0$.

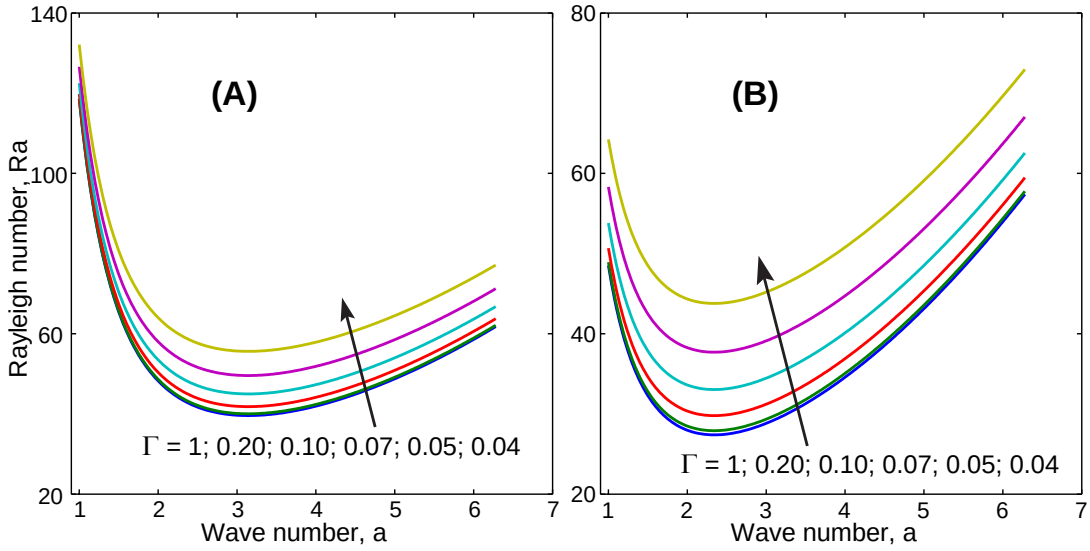

Figure B.7: The relation between critical Rayleigh and horizontal wave number for different values of Γ (K/m), $S_o = 0$, and $K = 2 \times 10^{-9}\,\mathrm{m}^2$ with an impermeable layer at the top surface (A) and when the top surface is open to the atmosphere (B)

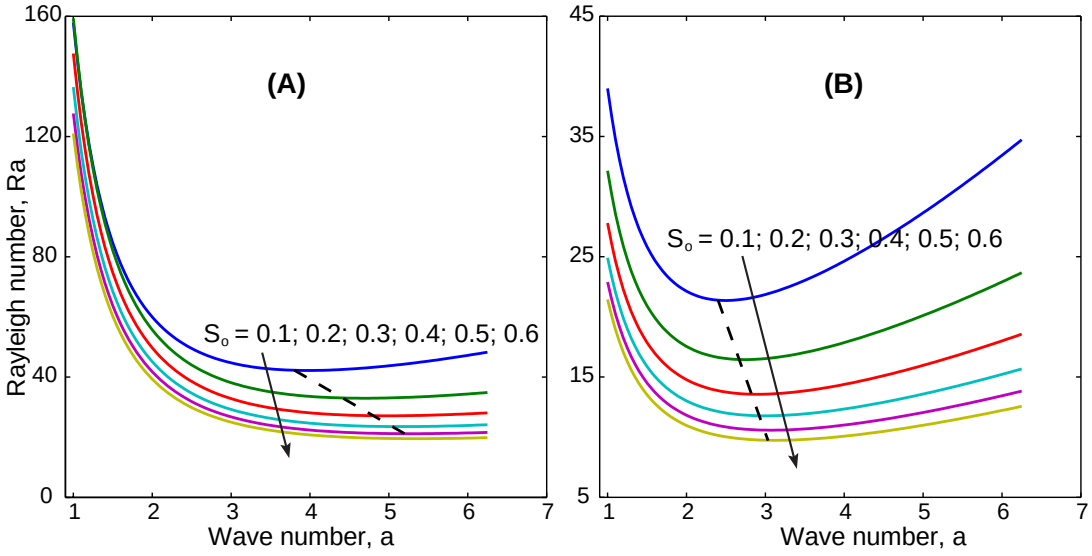

Figure B.8: The relation between critical Rayleigh and horizontal wave number for different values S_o at $\Delta T = 20\,^{\circ}\mathrm{C}$, $K = 2\times10^{-9}\,\mathrm{m}^2$ and $H = 80\,\mathrm{m}$ with an impermeable surface (A) and a permeable surface (B). The dash lines connect the minima of the (Ra, a) curves

of the pressure work, the compressibility of air, and/or internal heat source. This study establishes the variations of Ra_c with the waste rock properties, applied temperature gradients ($\Gamma = \Delta\bar{T}/H$), heat source rates, and boundary conditions (Fig. B.7). When the values of Γ are close to 1, Ra_c approaches the classical values of $4\pi^2$ and 27.1 at wave number $a_c = \pi$ and 2.33 respectively with impermeable and permeable surfaces (Fig. B.7). However, when Γ becomes smaller than 1, Ra_c is larger than $4\pi^2$. The smaller the Γ is, the greater the Ra_c diverges from $4\pi^2$. Therefore, the increase in Ra_c has a stabilizing influence on the marginal stability. The main effect of the compressibility of air is to cool or warm the pore air adiabatically as it ascends or descends respectively. Therefore, when air rises, the effective temperature gradient reduces. Jeffreys (1930) stated that "for a compressible fluid instability cannot arise until the gradient exceeds the adiabatic temperature gradient", $g/c_a \simeq 1\times10^{-2}\,\mathrm{K/m}$ is the adiabatic temperature gradient of air. Below the adiabatic temperature gradient, air convection is not possible for any values of waste rock's properties, because Ra is always less than Ra_c. Permanent waste-rock piles at the Diavik site have a typical height of 80 m and a temperature difference ranging between 20 and 25 °C between the top and bottom layers during winter. Therefore, the temperature gradients of the waste-rock piles ranging between 0.25 and 0.31 K/m result in $Ra_c = 39.9697$ and 40.7140 which are close to $4\pi^2$ for the case of impermeable surfaces.

With the increasing heat generation rate, fluid becomes more susceptible to instability, that is, Ra_c decreases. As shown in the Fig. B.8A for the case of an impermeable surface, at small values of $S_o(< 0.1)$, Ra_c approaches $4\pi^2$ at $a_c = \pi$. When S_o increases to 0.6, Ra_c is about 20 for $a_c = 5.4$. Therefore a_c is no longer a constant of π. It increases as S_o increases.

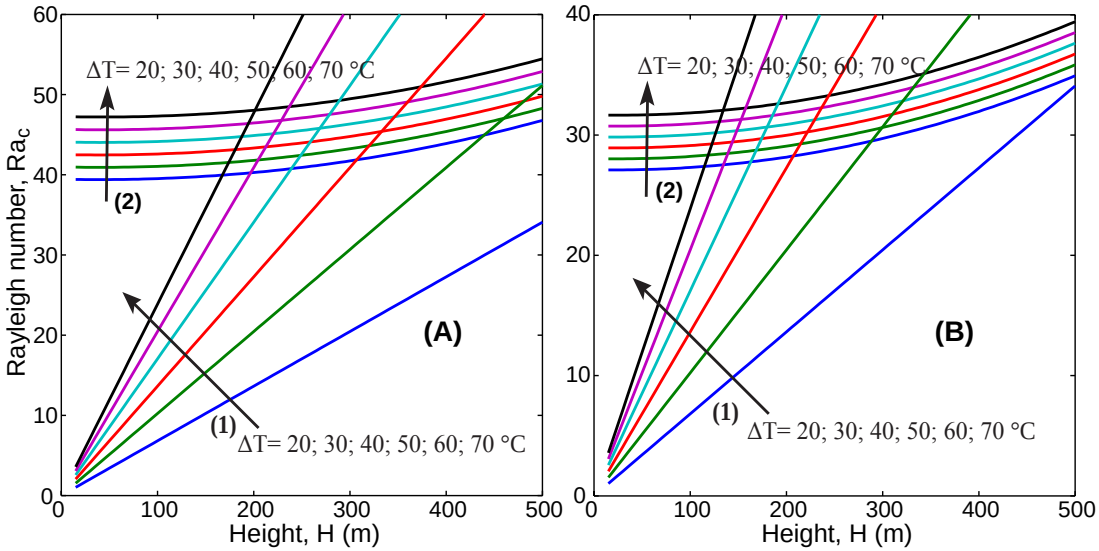

Figure B.9: Plots of Ra_c versus H (curves (2)) and Ra versus H (curves (1)) at different values of $\Delta\bar{T}$, $S_o = 0$ and $K = 2 \times 10^{-9}\,\mathrm{m}^2$ for the case of permeable (A) and impermeable surfaces (B).

Similarly, for the case of the permeable surface, the increasing S_o also shows a decrease in Ra_c (Fig. B.8B). The value of a is not a constant of 2.33. It increases as S_o increases, and at $S_o = 0.6$, Ra_c approaches 9.7 at $a_c = 3.1$ (Fig. B.8B). Hence, at a specific value of $\Delta\bar{T}$, K, H and boundary conditions, the increase in S_o has a destabilizing effect as it decreases Ra_c. Therefore, with the existence of internal heat source, air convection can occurs as soon as there are sufficient buoyancy forces created by the internal heat source regardless of thermal boundary conditions.

As shown in Fig. B.9, Ra_c rises as $\Delta\bar{T}$ increases. As $\beta = 1/T$ for an ideal gas, therefore the buoyancy force reduces. Besides, at a fixed temperature difference, Ra_c also increases with the increase of H (Fig. B.9). Fig. B.9 shows that the value of Ra_c only starts to rise until H is greater than 100 m for both boundary conditions at $K = 2 \times 10^{-9}\,\mathrm{m}^2$, $S_o = 0$. On average, Ra_c increases above 7.5 when H varies between 15 and 500 m (Fig. B.9) meanwhile the system Rayleigh number Ra (curves (1) calculated by Eqn. B.18) increases 33.3 times from its initial values at $H = 15\,\mathrm{m}$. The curves (1) intersect Ra_c curves (2) at various heights depending on $\Delta\bar{T}$ and the surface boundary conditions. At $\Delta\bar{T} = 20°\mathrm{C}$, air convection will not occur as curves (1) does not intersects curves (2) at $H \leq 500\,\mathrm{m}$ (Fig. B.9). However, if $\Delta\bar{T} = 70°\mathrm{C}$ these curves intercept at 200 m and 135 m for the case of permeable and impermeable surfaces (Fig. B.9). Therefore, if the top surface of a waste-rock pile having high temperature differences is permeable to air, the onset of air convection occurs at lower pile heights.

Fig. B.10A and B show that Ra_c is quite insensitive to permeability at a height up to 80 m when $\Delta\bar{T} = 20\,°C$ and $S_o = 0$. Whereas, as H increases greater than 80 m, the

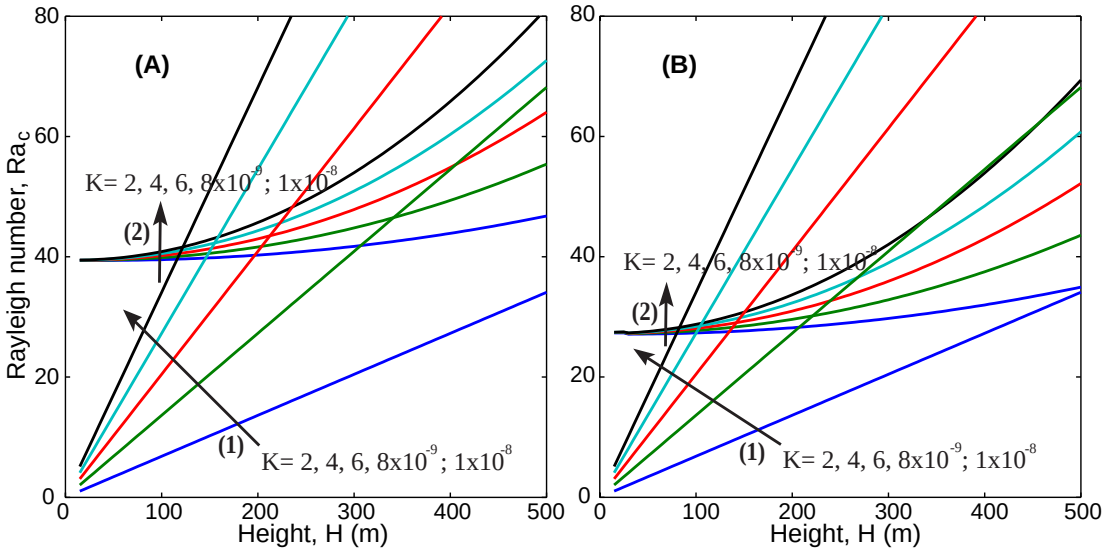

Figure B.10: Plots of Ra_c versus H (curves (2)) and Ra versus H (curves (1)) at different values of $K\,(\mathrm{m}^2)$, $S_o = 0$, and $\Delta\bar{T} = 20\,^{\circ}C$ for the case of the close top surface (A) and open top surface (B).

increments of permeability will increase the values of Ra_c. Consider at $K = 1\times10^{-8}\mathrm{m}^2$, the value of Ra_c at $H = 500\,\mathrm{m}$ is about twice that of 15 m (Fig. B.10A and B). Furthermore, at $K = 1\times10^{-8}\mathrm{m}^2$, the onset of air convection occurs at $H = 110\,\mathrm{m}$ for the impermeable surface (Fig. B.10A) and 80 m for the permeable surface (Fig. B.10B). However, when K is equal to or less than $2\times10^{-9}\,\mathrm{m}^2$, air convection will not initiate for $H \leq 500\,\mathrm{m}$ for both impermeable and permeable surfaces (Fig. B.10).

The existence of heat source in the energy balance equation (Eqn. B.3) makes the curves Ra_c complex as shown in Fig. B.11. At $K = 2\times10^{-9}\,\mathrm{m}^2$, for the case of impermeable surface, the Ra_c curves increase to values larger than $4\pi^2$ at height up to 50 m, then decreases to a minimum value of 15 at heights ranging from 100 to 200 m. It then rises monotonically but they do not exceed Ra_c curve of $S_o = 0$ at H up to 500 m (Fig. B.11A). Whereas, in the case for a permeable surface, the Ra_c curves reduce to its minimum of 7.0 independent of oxidation rate at heights ranging from 100 to 200 m and then increases monotonically (Fig. B.11B). The Ra line (curve (1)) meets the Ra_c curves (curve (2)) at H between 100 and 150 m. Depending on S_o, the Ra_c curves reach a minimum peak at H from 100 to 200 m.

Increasing the value of K to $2\times10^{-8}\,\mathrm{m}^2$, the Ra line meets the Ra_c curves at H between 100 and 150 m (Fig. B.11C). However, if the surface is permeable to air, the value of H reduces further between 30 and 45 m depending on S_o (Fig. B.11D). It also is observed that the higher the value of S_o, the sooner (smaller H) Ra_c reaches the minimum. Despite the increase of K, the optimum values of H for a minimum value of Ra_c are still in the range between 100 and 200 m similar to the case $K = 2\times10^{-9}\,\mathrm{m}^2$ (Fig. B.11). Therefore, the optimum heights of a waste-rock pile having internal heat generations range between 100

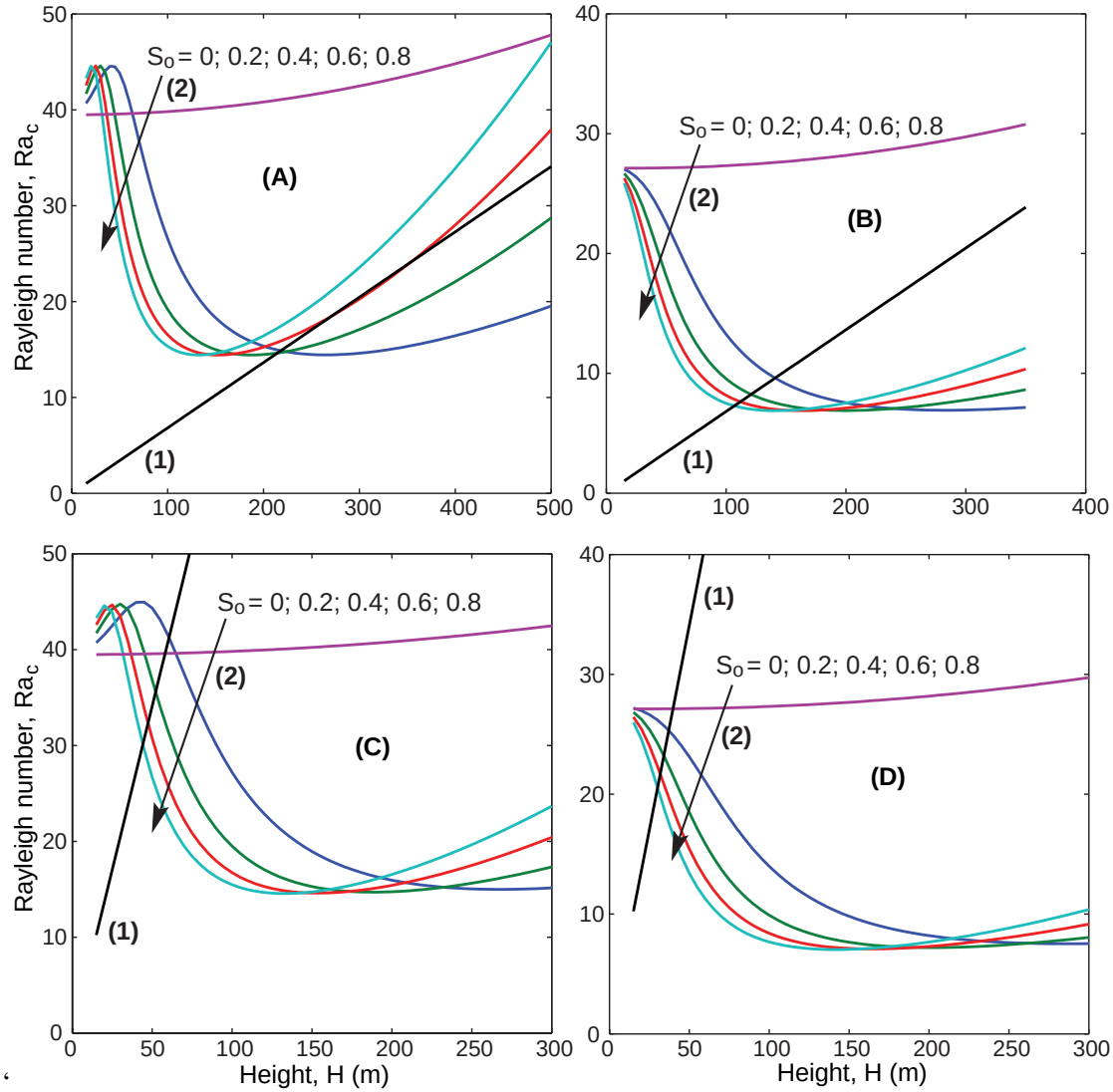

Figure B.11: Plots of Ra_c versus H (curves (2)) and Ra versus H (curves (1)) at different values of S_o, $\Delta\bar{T} = 20\,^{\circ}\mathrm{C}$ and $K = 2 \times 10^{-9}\,\mathrm{m}^2$ for permeable surface (A), impermeable surface (B) and $K = 2 \times 10^{-8}\,\mathrm{m}^2$ for permeable surface (C), impermeable surface (D).

and 200 m while depending on S_o.

B.6 Conclusions

The analysis of the onset of convection in porous media with a compressible air and heat source was carried out for both impermeable and permeable surfaces. It is shown that linearized governing equations can be showed in terms of streamline and temperature fields. A system of ordinary differential equations is obtained using plane wave solutions and a system of ordinary differential equations has been solved both analytically and numerically. It has been shown that the pressure work and compressibility of air have a stabilizing effect by increasing Ra_c. The values of Ra_c are a function of a waste rock's properties, applied temperature gradients and boundary conditions. As the applied temperature gradients approach 1 and the height of the waste-rock pile is less than 80 m, there is no significant divergence of Ra_c from $4\pi^2$. With an internal heat source, air convection can occur if there exists a sufficient buoyancy force created by the heat source within the layer.

It is much easier to achieve air convection when the upper surface is permeable to air. The air convection brings high O_2 concentration air deep into a waste-rock pile. The high O_2 concentration air promotes the oxidation of pyrite which is an exothermic process resulting in large thermal gradients within the waste-rock pile. This causes greater air convection and is a regeneration mechanism. Further, the oxidation process lowers the values of Ra_c significantly and is a destabilizing effect. However, when the waste-rock pile is constructed in permafrost areas, internal temperatures of the waste-rock pile can be lowered to the freezing point via natural air convection and these low-internal temperatures potentially can minimize the oxidation process (Pham et al., 2008a).

References

Chandrasekhar, S. (1961). *Hydrodynamic and Hydromagnetic Stability*. Oxford At The Clarendon Press.

Drazin, P. and Reid, W. (2004). *Hydrodynamic Stability*. Cambridge University Press.

Farlow, S. J. (1993). *Partial differential equations for scientists and engineers*. Dover Publications, Inc.

Gasser, R. D. and Kazimi, M. S. (1976). Onset of convection in a porous medium with internal heat generation. *Journal of Heat Transfer*, 98(1):49–54.

Harries, J. R. and Ritchie, A. I. M. (1981). The use of temperature profiles to estimate the pyritic oxidation rate in a waste rock dump from an opencut mine. *Water, Air and Soil Pollution*, 15(4):405–423.

Hollesen, J., Elberling, B., and Hansen, B. (2009). Modelling subsurface temperatures in a heat producing coal waste rock pile, svalbard (78°n). *Cold Regions Science and Technology*, 58(1-2):68–76.

Hollesen, J., Elberling, B., and Jansson, P. (2011). Modelling temperature-dependent heat production over decades in high arctic coal waste rock piles. *Cold Regions Science and Technology*, 65(2):258–268.

Horton, C. and Rogers Jr., F. (1945). Convection currents in a porous medium. *Journal of Applied Physics*, 16(6):367–370.

Jeffreys, H. (1930). The instability of a compressible fluid heated below. *Mathematical Proceedings of the Cambridge Philosophical Society*, 26(02):170–172.

Kundu, P. K. and Cohen, I. M. (2002). *Fluid Mechanics*. Academic Press.

Lapwood, E. R. (1948). Convection of a fluid in a porous medium. *Mathematical Proceedings of the Cambridge Philosophical Society*, 44(04):508–521.

Lefebvre, R., Gelinas, P., and Isabel, D. (1992). Heat transfer analysis applied to acid mine drainage production in a waste rock dump, la mine doyon (quebec). In *Proceedings of the IAH Canadian Chapter Congress*.

Lefebvre, R., Hockley, D., Smolensky, J., and Gelinas, P. (2001a). Multiphase transfer processes in waste rock piles producing acid mine drainage. 1: Conceptual model and system characterization. *Journal of contaminant hydrology*, 52(1-4):137–164.

Lefebvre, R., Hockley, D., Smolensky, J., and Gelinas, P. (2001b). Multiphase transfer processes in waste rock piles producing acid mine drainage: 1: Conceptual model and system characterization. *Journal of Contaminant Hydrology*, 52(1-4):137–164.

Lowson, R. T. (1982). Aqueous oxidation of pyrite by molecular oxygen. *Chemical Reviews*, 82(5):461–497.

Martin, V., Aubertin, M., Bussiere, B., and Chapuis, R. P. (2004). Evaluation of unsaturated flow in mine waste rock. In *57th Canadian geotechnical conference*.

Matlab (2012). *Matlab: Mathematics*. MathWorks.

Molson, J., Fala, O., Aubertin, M., and Bussière, B. (2005). Numerical simulations of pyrite oxidation and acid mine drainage in unsaturated waste rock piles. *Journal of Contaminant Hydrology*, 78(4):343–371.

Morin, K. A. and Hutt, N. M. (2001). Relocation of net-acid-generating waste to improve post-mining water chemistry. *Waste Management*, 21(2):185–190.

Newman, L. L., Barbour, S. L., and Fredlund, D. G. (1997). Mechanisms for preferential flow in vertically layered unsaturated waste rock. In *50th Canadian Geotechnical Conference of Canadian Geotechnical Society*.

Nield, D. and Barletta, A. (2009). The horton-rogers-lapwood problem revisited: The effect of pressure work. *Transport in Porous Media*, 77(2):143–158.

Nield, D. and Bejan, A. (1999). *Convection in porous media*. Springer, New York.

Pham, N., Arenson, L. U., and Sego, D. C. (2008a). Numerical analysis of forced and natural convection in waste-rock piles in permafrost environments. In *Ninth International Conference on Permafrost (NICOP), University of Alaska Fairbanks, June 29 - July 3, 2008*.

Saatdjian, E. (1980). Natural convection in a porous layer saturated with a compressible ideal gas. *International Journal of Heat and Mass Transfer*, 23(12):1681–1682.

Song, Q. and Yanful, E. K. (2008). Monitoring and modeling of sand-bentonite cover for ard mitigation. *Water, air, and soil pollution*, 190(1-4):65–85. Compilation and indexing terms, Copyright 2008 Elsevier Inc.

Sparrow, E. M., Goldstein, R. J., and Jonsson, V. K. (1964). Thermal instability in a horizontal fluid layer: effect of boundary conditions and non-linear temperature profile. *Journal of Fluid Mechanics*, 18(04):513–528.

Sracek, O., Gelinas, P., Lefebvre, R., and Nicholson, R. V. (2006). Comparison of methods for the estimation of pyrite oxidation rate in a waste rock pile at mine doyon site, quebec, canada. *Journal of Geochemical Exploration*, 91(1-3):99 – 109.

Stauffer, P. H., Auer, L. H., and Rosenberg, N. D. (1997). Compressible gas in porous media: a finite amplitude analysis of natural convection. *International Journal of Heat and Mass Transfer*, 40(7):1585–1589.

Tasa, D., Tarbuck, E. J., and Lutgens, F. K. (2006). *The Atmosphere*. Prentice Hall.

Wickland, B. and Wilson, G. W. (2005a). Research of co-disposal of tailings and waste rock. *Geotechnical News*, 23(3):35–38.

Zhang, Y., Lu, N., and Benjamin, R. (1994). Convective instability of moist gas in a porous medium. *International Journal of Heat and Mass Transfer*, 37(1):129–138.

APPENDIX C

Experimental Results and Construction Photos

C.1 Temperature

This section of the appendix provides additional temperature data that has not included in the chapters

C.1.1 Type I test pile

Typical section, profile, base dimension and thermistor distributions of the Type I test are showed in Fig. C.1 and Fig. C.2. Labeling convection for temperature of the test piles, for example 31S5thm0.15 in which '3' - Type III pile ('1' or 'C' for Type III test pile or Covered test pile); '1' - Face 1 of the test pile; 'S' - South; '5' - 5 m offset of centre to the south; 'thm' - thermistor ('gas' - gas measurement); '0.15' - 0.15 m vertical depth to the surface of the test pile.

Temperatures measured within the Type I test pile are very similar to those of Type III test pile (Chapter 4) which following properties:

- High response to ambient temperatures due to wind-induced advection and convection as a result of narrow configuration of the Type I and III test piles and the construction methods created high permeability regions below the mid height of the test piles
- Regions are the base of the test pile and bedrock foundation is cooling (below °C or permafrost aggradation)
- No significant heat release due to oxidation of sulfide minerals within the test pile.

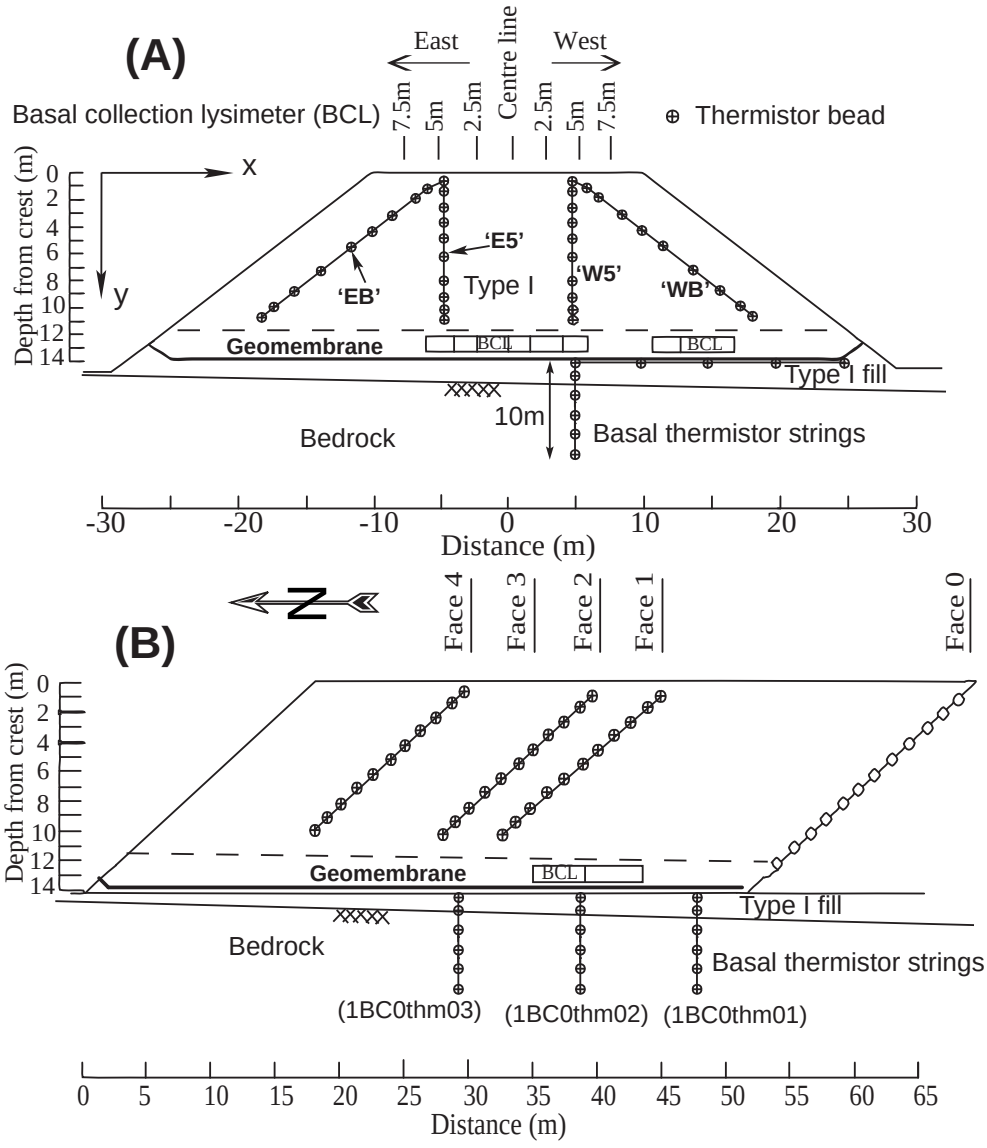

Figure C.1: Typical section of the Type I test pile (A) and profile (B) with thermistors location

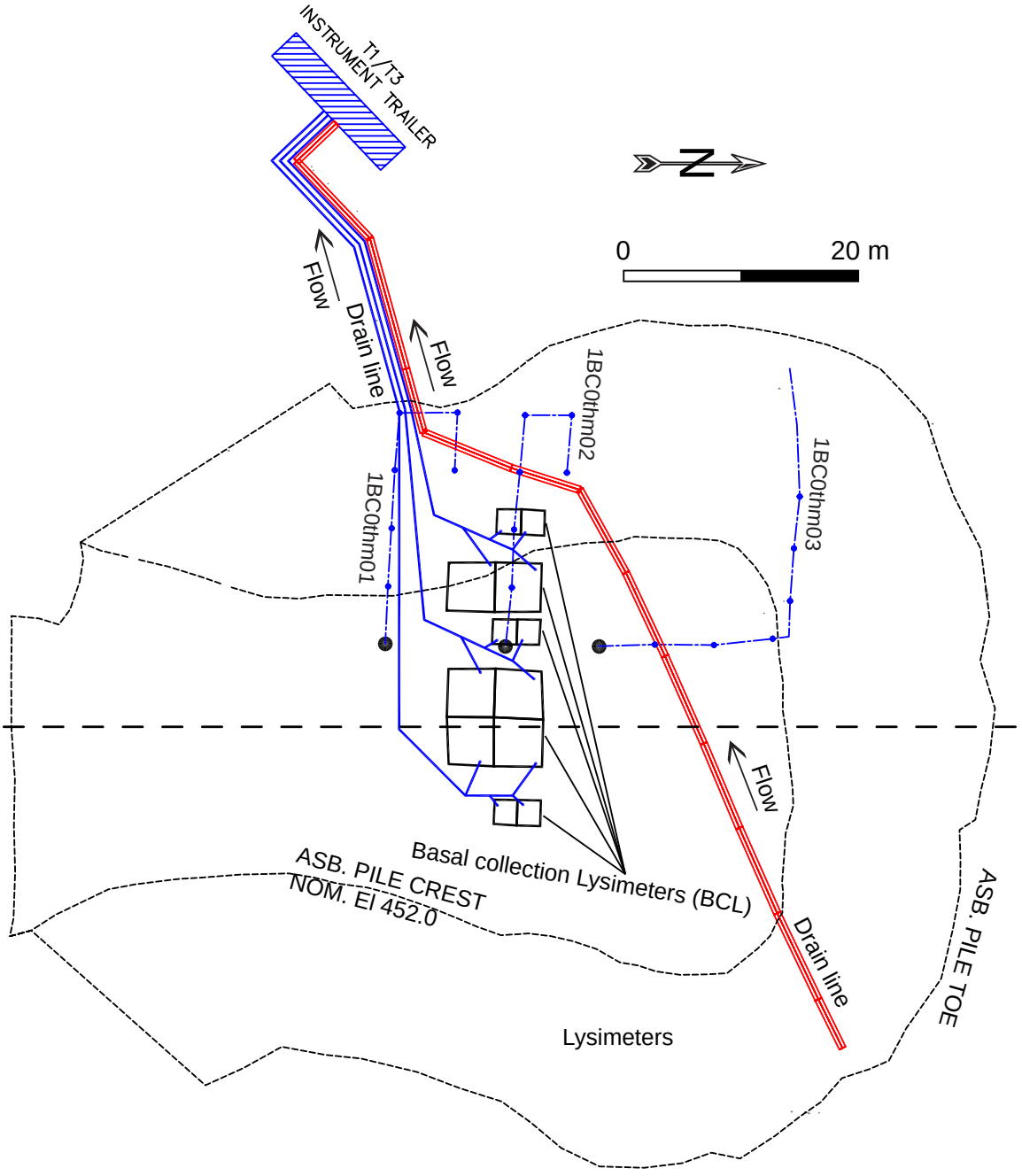

Figure C.2: Type I test pile base dimensions and basal thermistor distributions

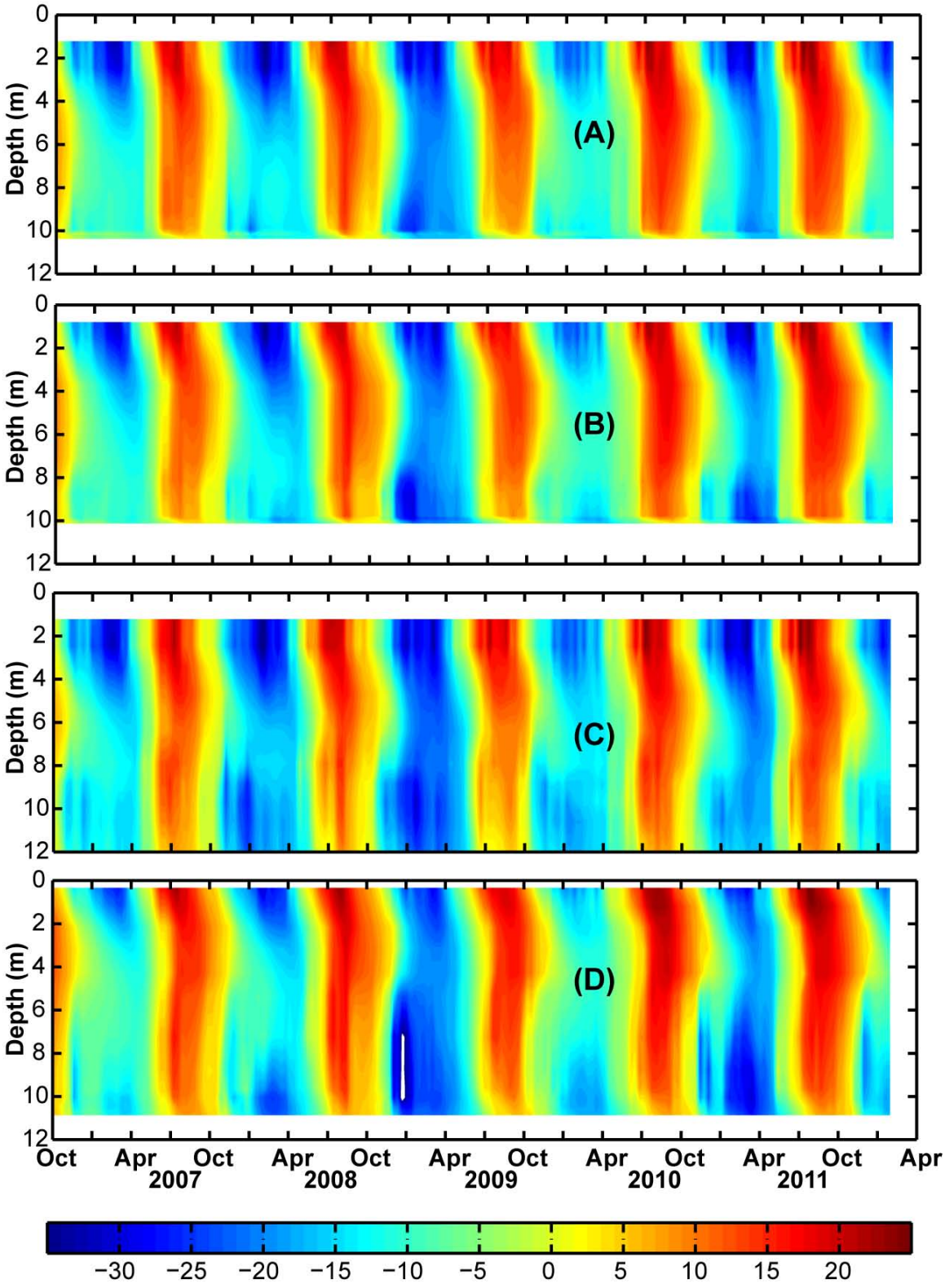

Figure C.3: Temperature (°C) results at Type I Face 1: 11E5thm (A), 11EBthm (B), 11W5thm (C) and 11WBthm (D)

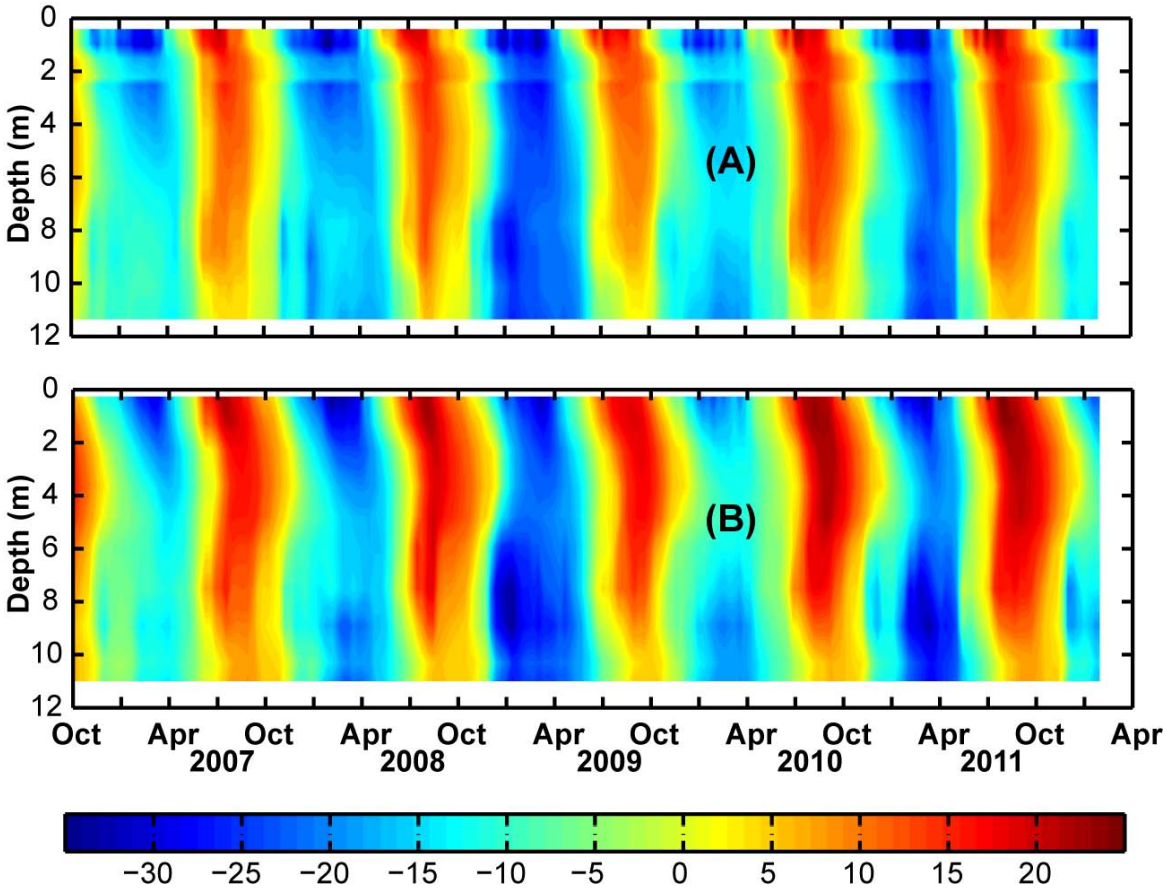

Figure C.4: Temperature (°C) results at Type I Face 2: 12E5thm (A) and 12W5thm (D)

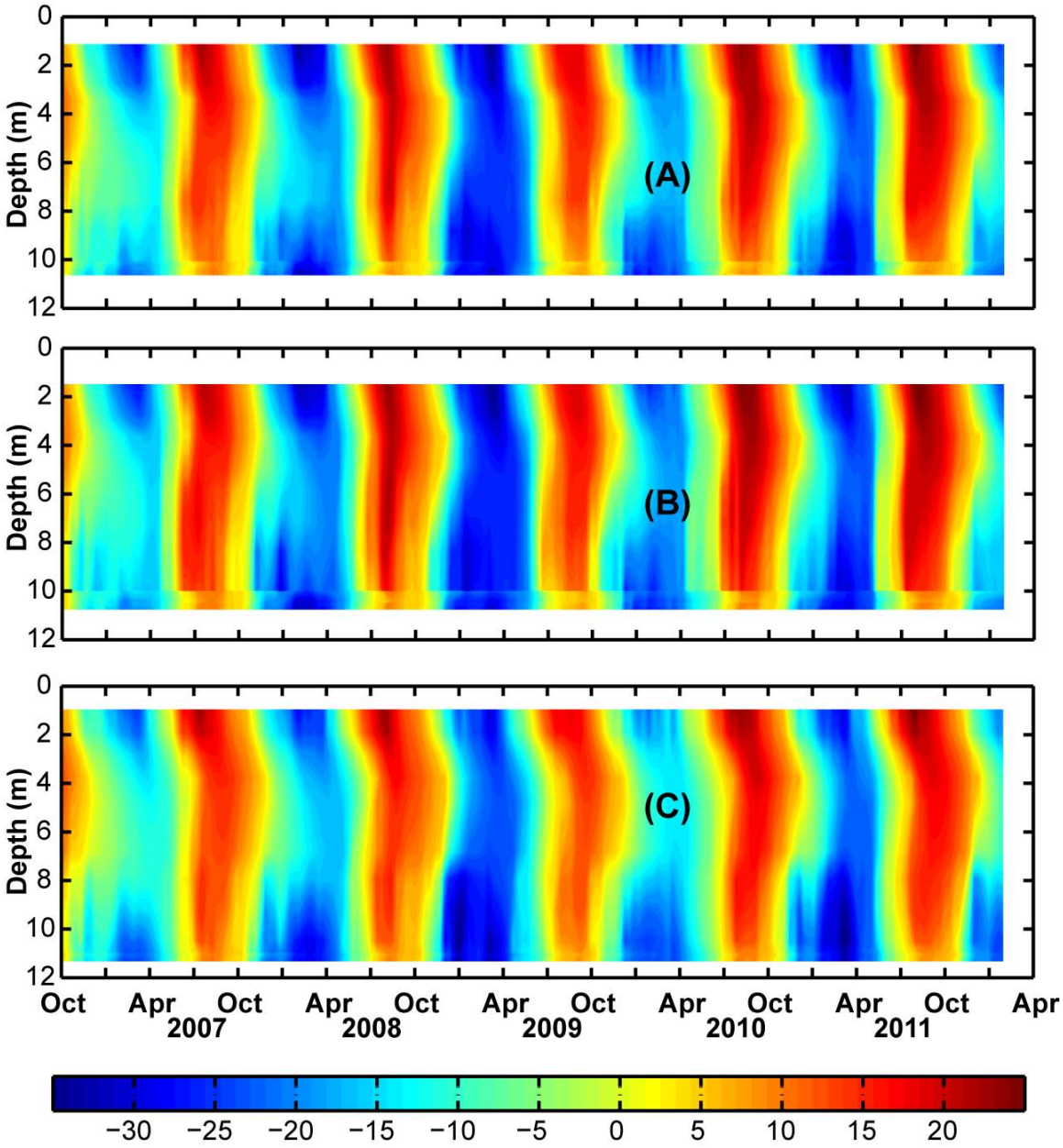

Figure C.5: Temperature (°C) results at Type I Face 4: 14E5thm (A), 14EBthm (B) and 14WBthm (C)

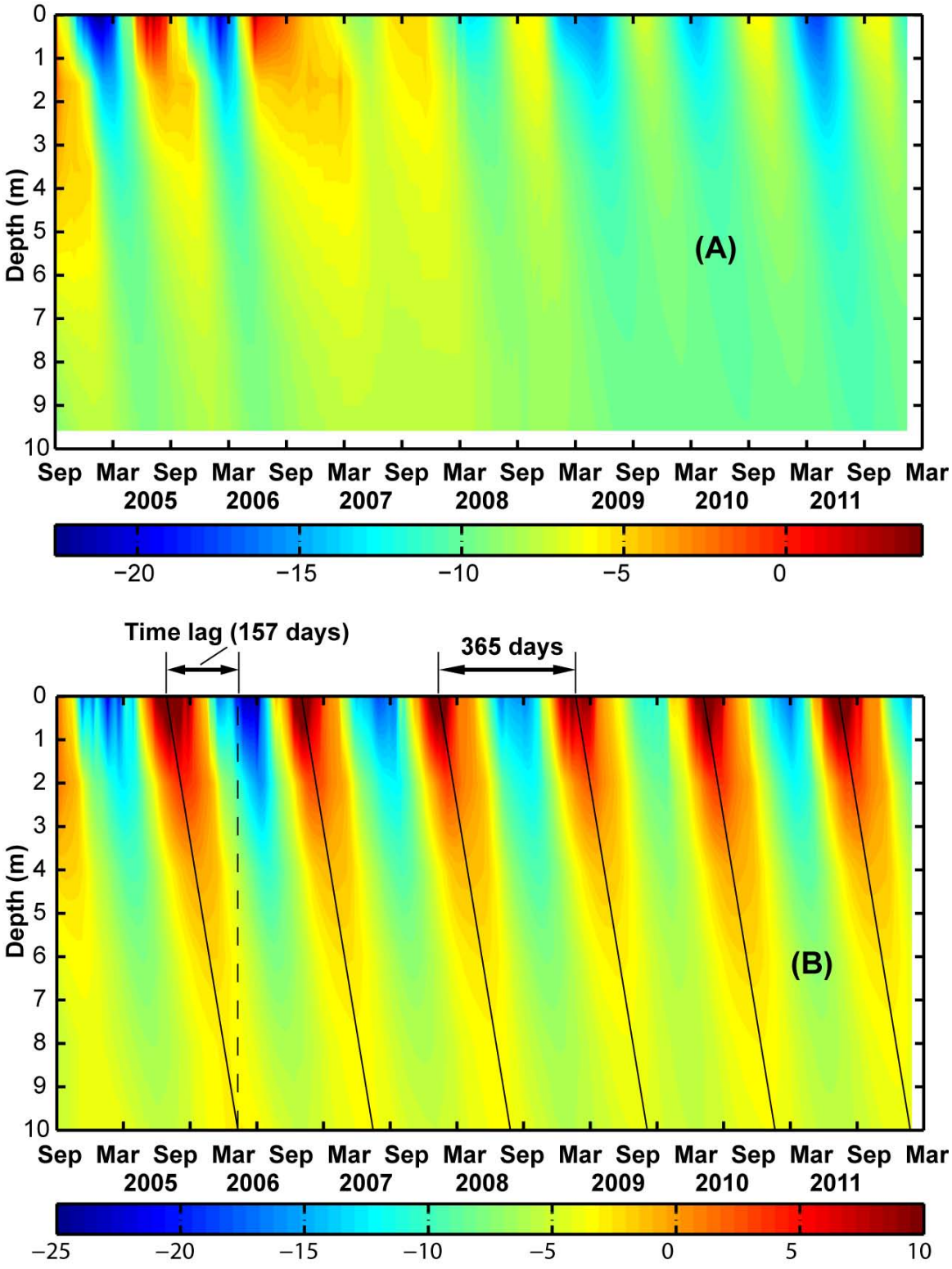

Figure C.6: Temperature (°C) results in Bedrock: Bedrock foundation beneath the Type I test pile, 1BC0thm03 (Fig. C.1), (A), Bedrock foundation without a test pile above and about 100 m away from the test piles (B), prefer Fig. 1.3 for the exact location.

C.1.2 Type III test pile

Temperatures within the test pile indicates a high response (low time lags and large amplitude) to ambient temperatures due to wind-induced advection and convection.

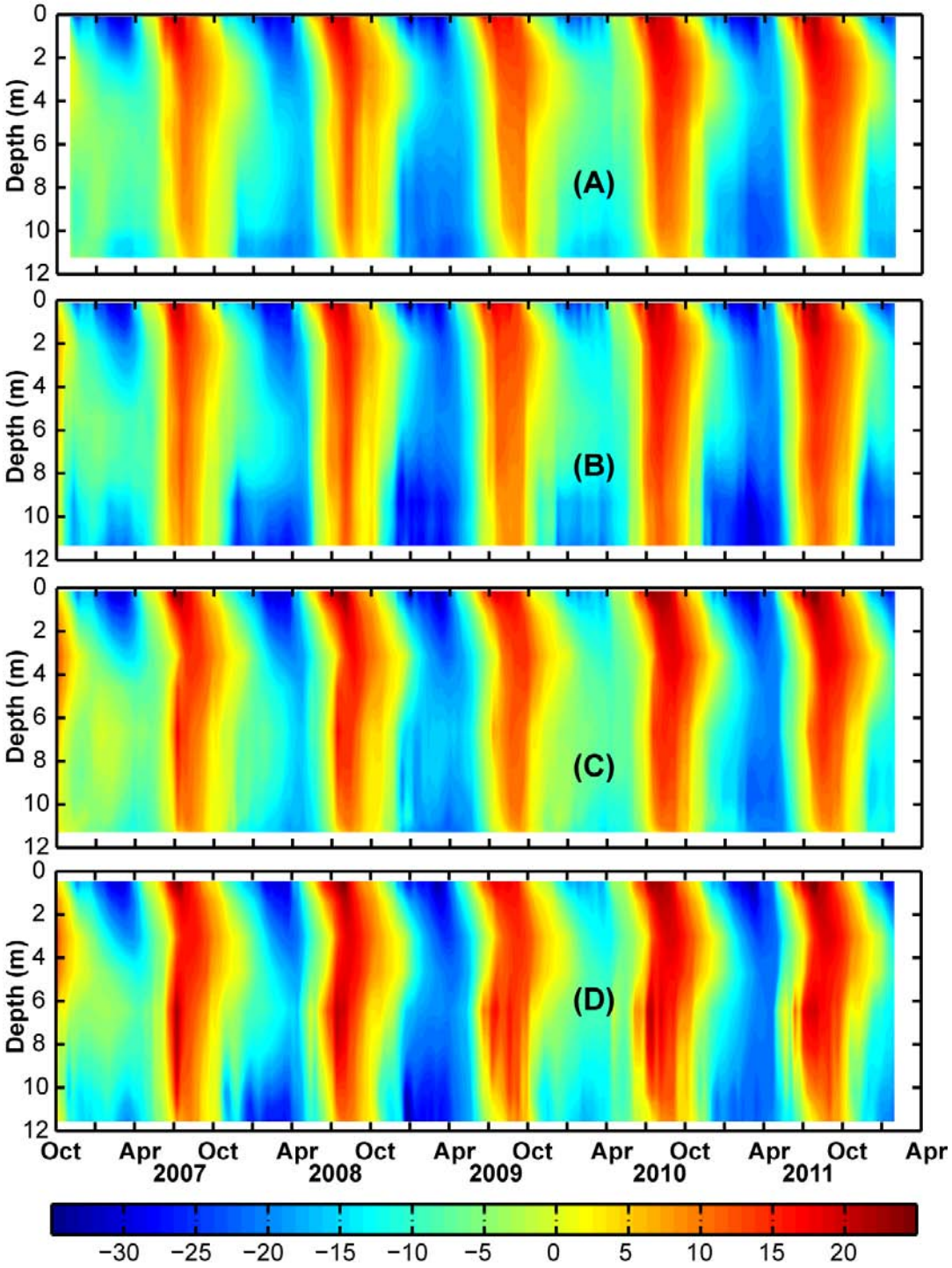

Figure C.7: Temperature (°C) results at Type III Face 1: 31N5thm (A), 31NBthm (B), 31S5thm (C) and 31SBthm (D)

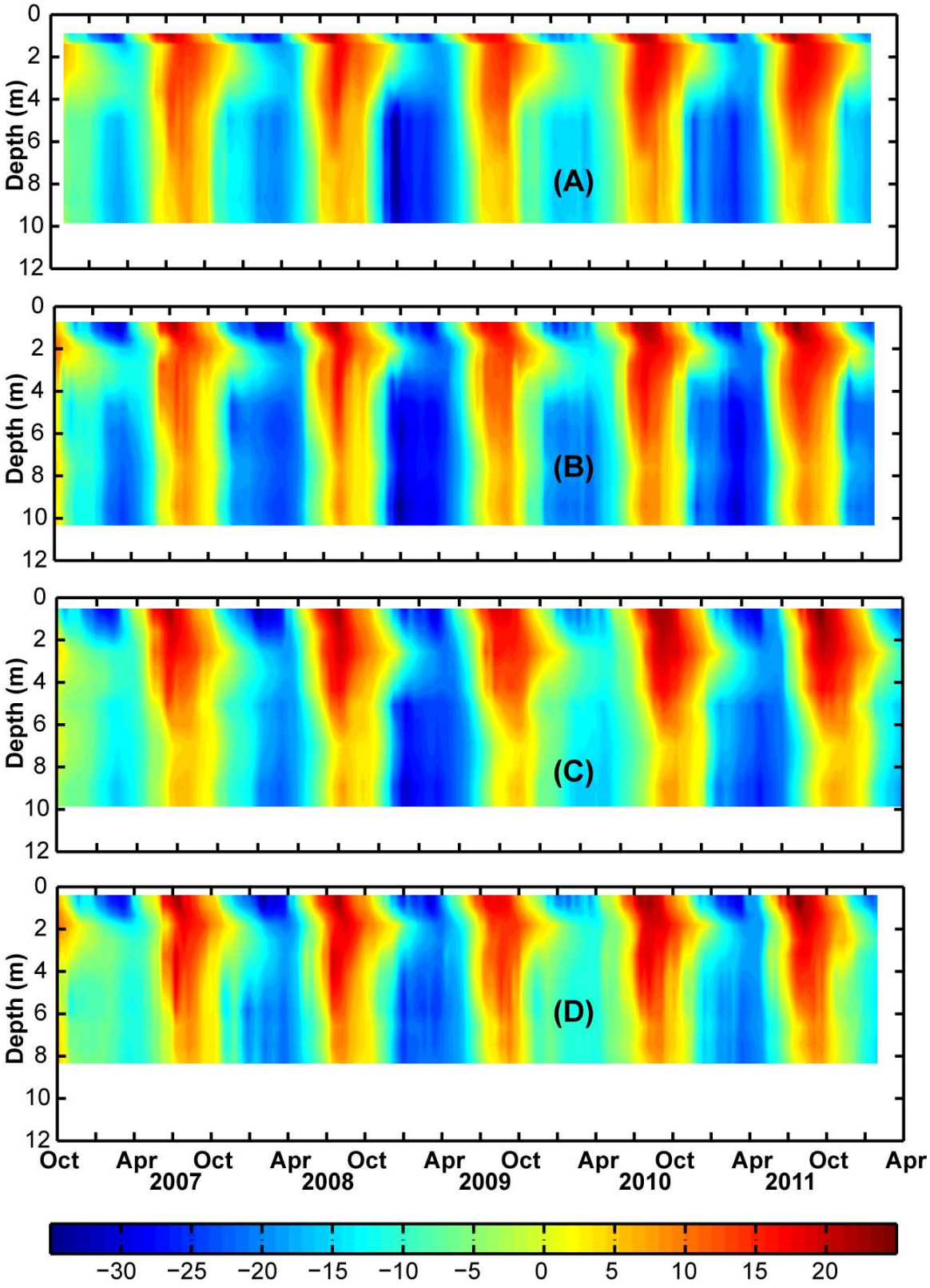

Figure C.8: Temperature (°C) results at Type III Face 4: 34N5thm (A), 34NBthm (B), 34S5thm (C) and 34SBthm (D)

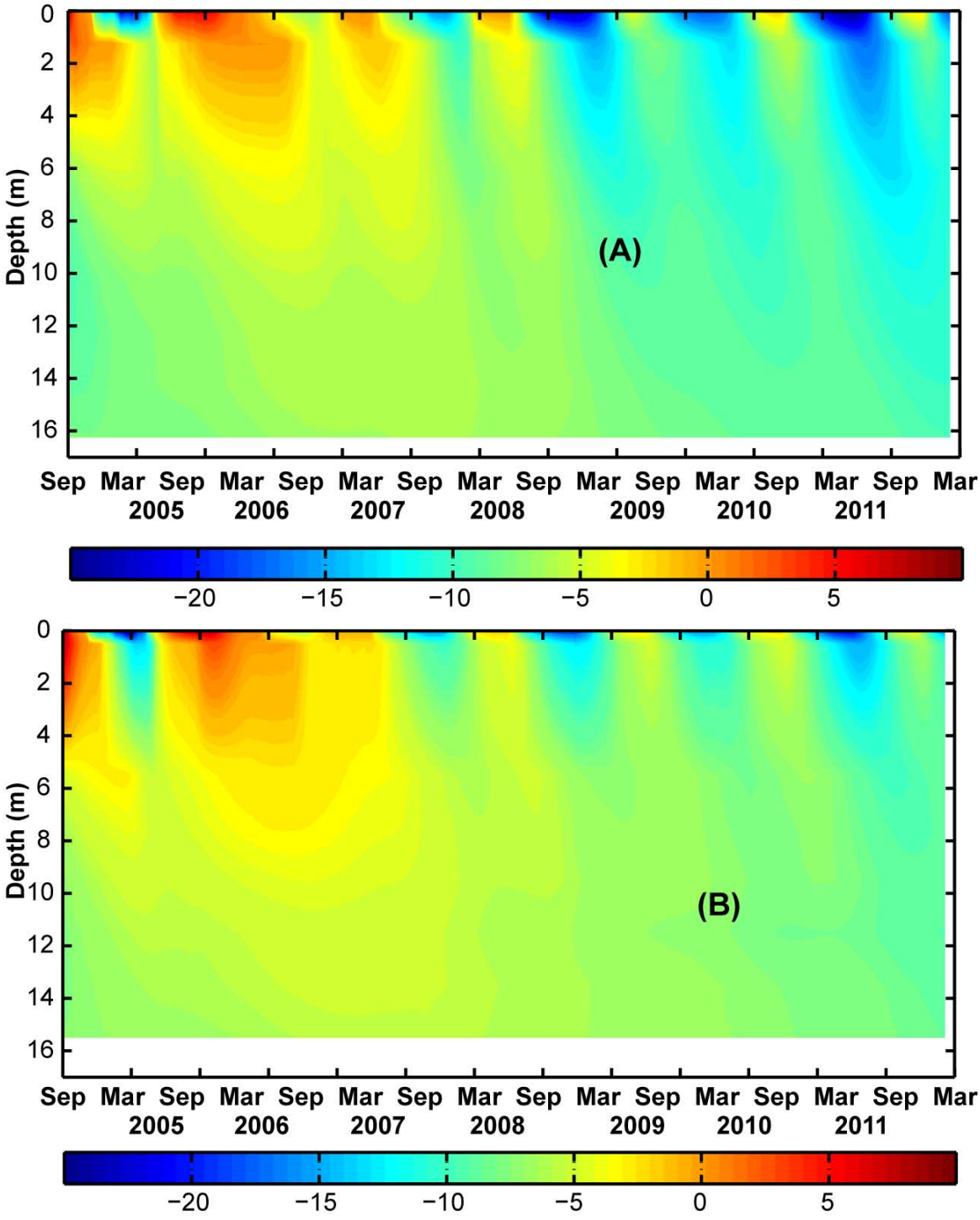

Figure C.9: Temperature (°C) results in Bedrock foundation beneath the Type III test pile: 3BC0thm01 (A) and 3BC0thm03 (B)

C.1.3 Covered test pile

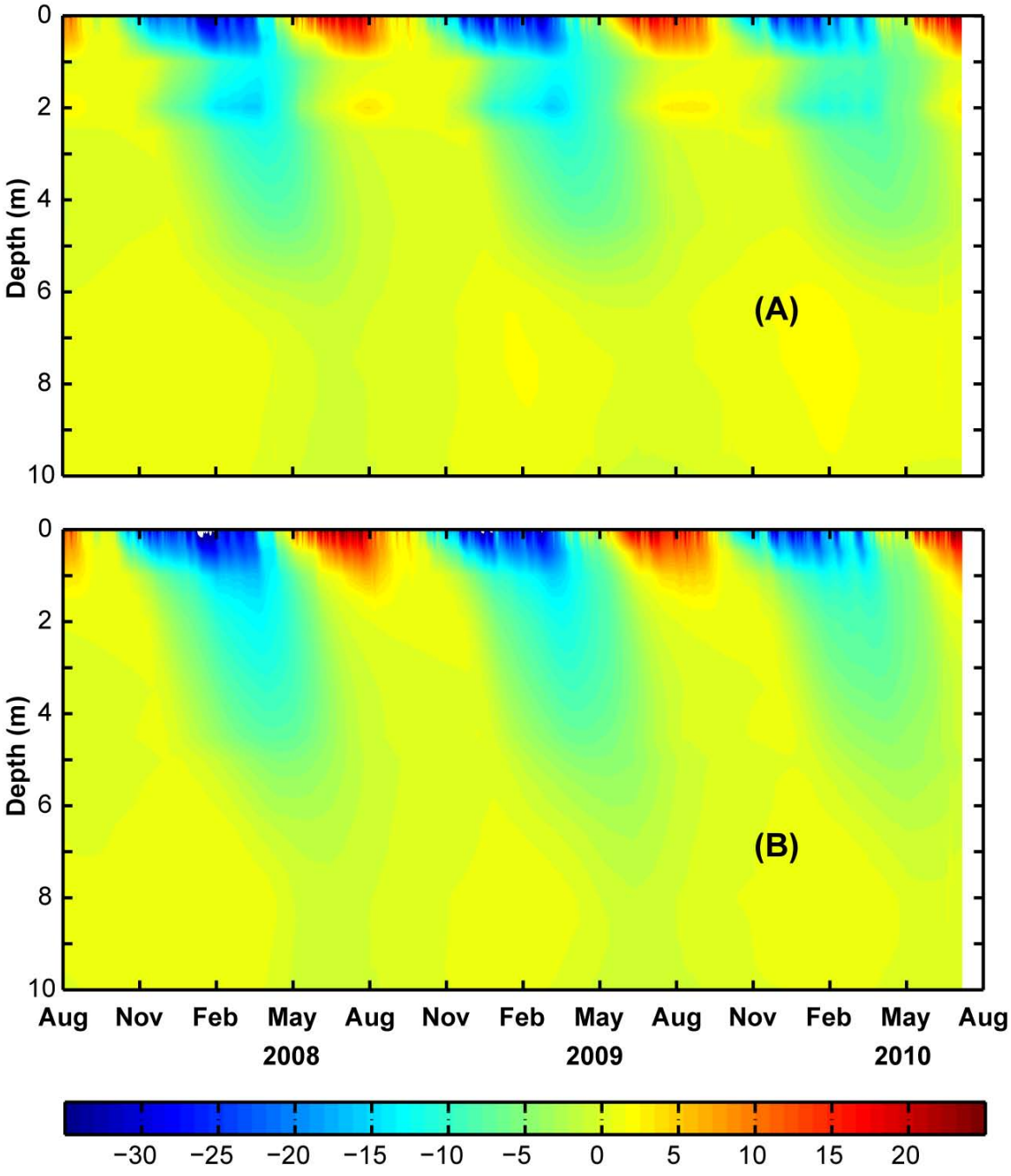

Figure C.10: Temperature (°C) results in Bedrock foundation beneath the Type III test pile: 3BC0thm01 (A) and 3BC0thm03 (B)

C.1.4 Drill holes on a 80 m full-scale pile

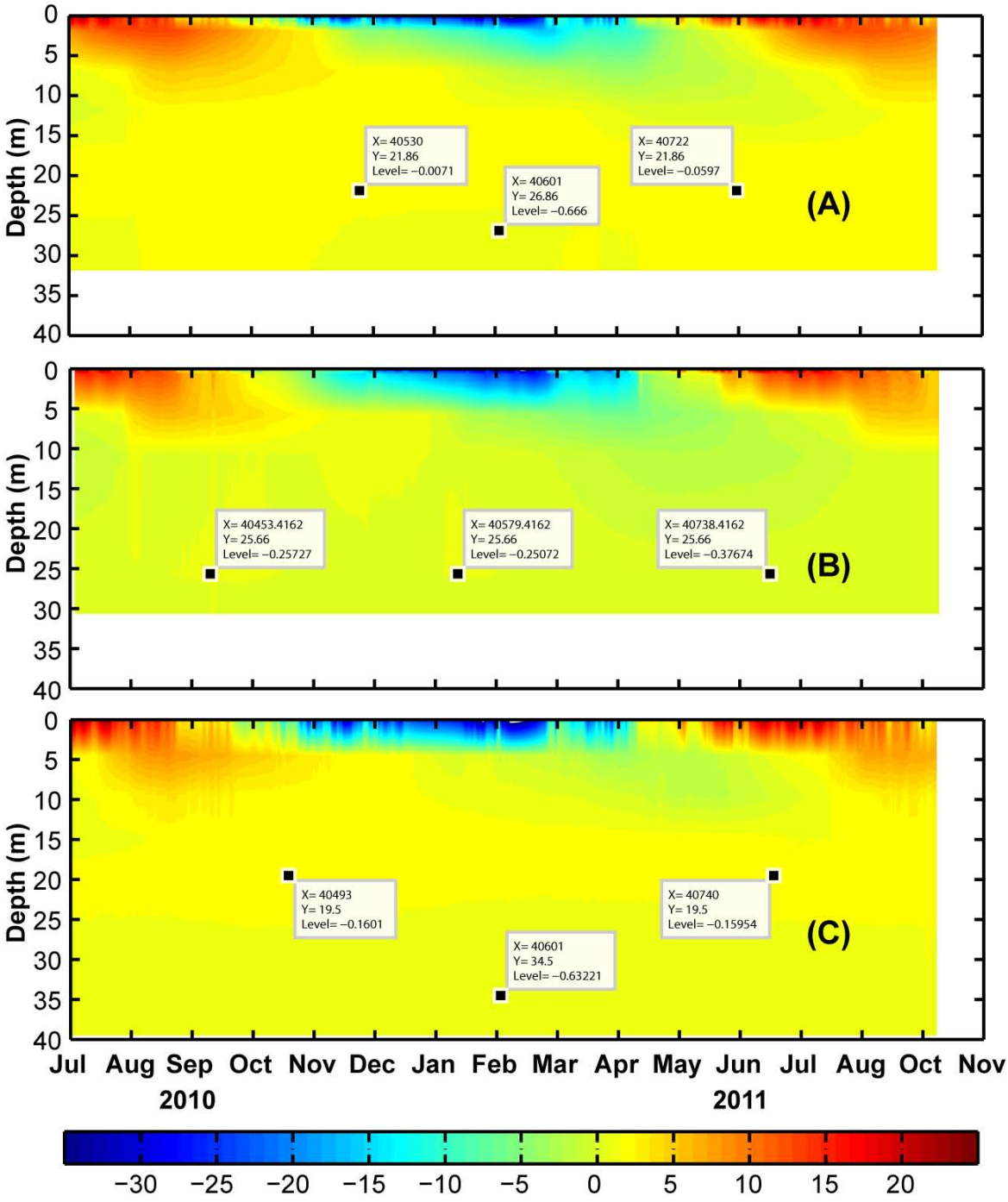

Figure C.11: Temperature (°C) results of drill hole on 80 m full-scale pile: FD1 (A) and FD2 (B) and FD3 (C)

C.2 Pore-air pressure

The data of section provides supplemental results that were not in Chapter 5. Pore-air pressures measured within the Type III test pile are differential pressure which are referenced against surface air pressure and for details of the configuration of the measurement system one can prefer to the work of Amos et al. (2009a). The original data taken every 10 mins was smoothed using a 5001-point moving average method, the smoothed data was then fitted using Fourier series

$$p(t) = a_o + a_1 \cos(t\omega) + b_1 \sin(t\omega) + a_2 \cos(2t\omega) + b_2 \sin(2t\omega) \tag{C.1}$$

Where ω angular frequency and a_o is the mean value of $p(t)$

Pore-air pressure measured within the Type III test pile clearly shows the increase of pressure during winter as temperatures within the test pile decrease (negative correlation between temperature and pore air pressure) (Fig. C.12, Fig. C.13 and Fig. C.14). Labeling convention is as follows. 31N2gas12: Type "3" pile, face "1," offset "N" (north) of centreline, "2"=2.5 m off set (7 = 7.5 m offset), "gas" = gas pressure measurement, "12" = 12 m deep, vertically from top of pile.

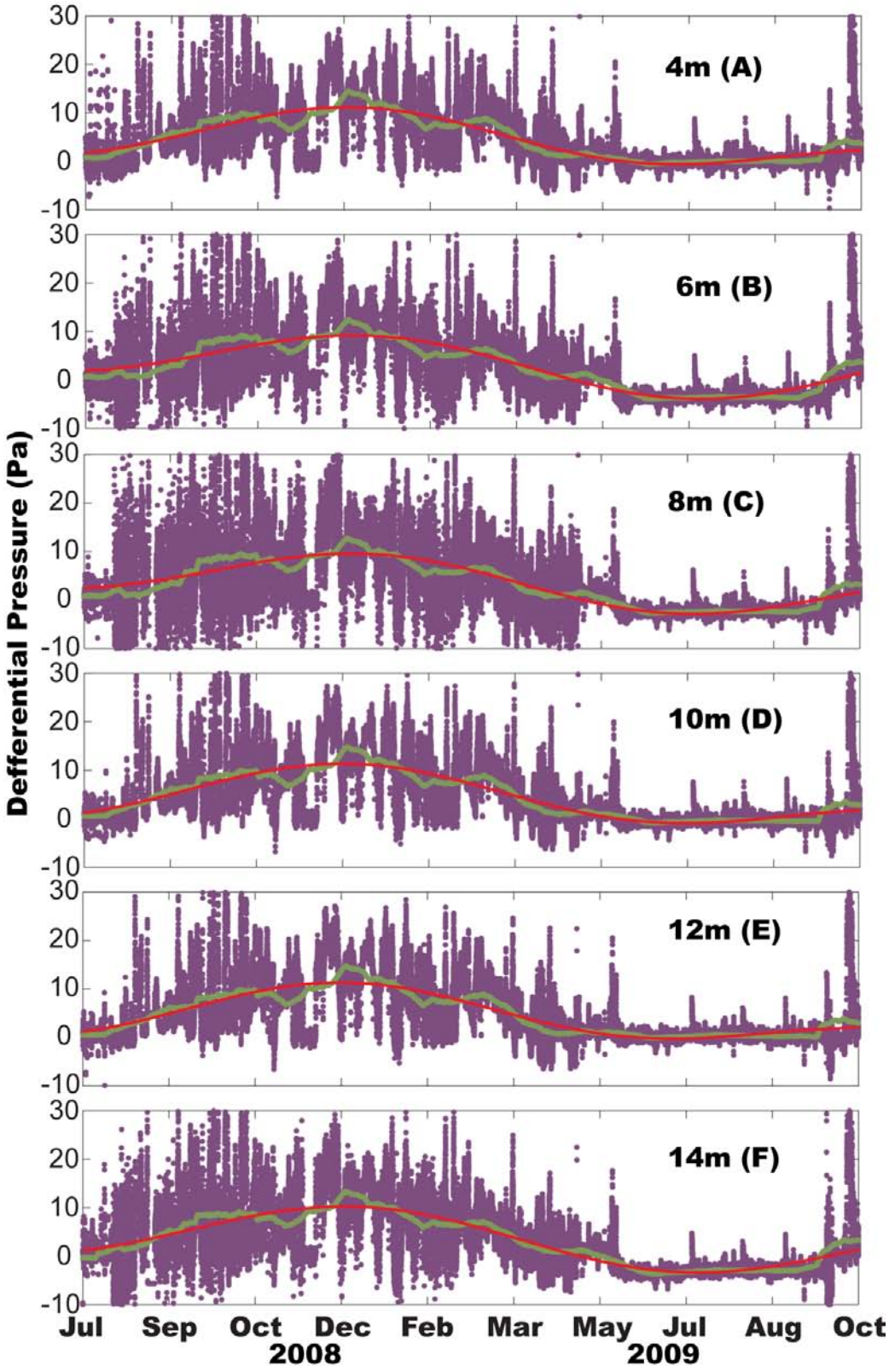

Figure C.12: Deferential pore-air pressures of 32S7gas at various depths

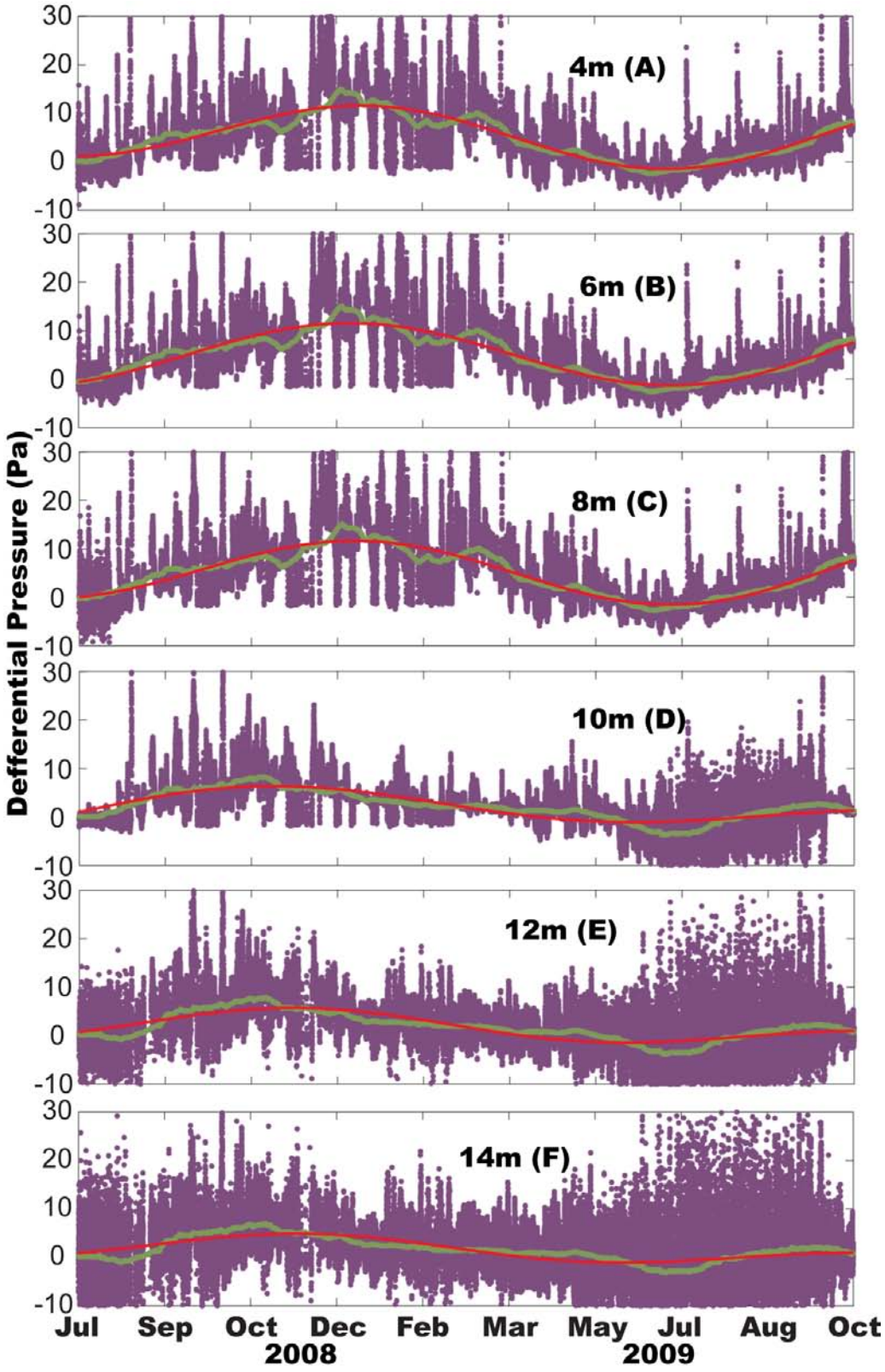

Figure C.13: Deferential pore-air pressures of 33N2gas at various depths

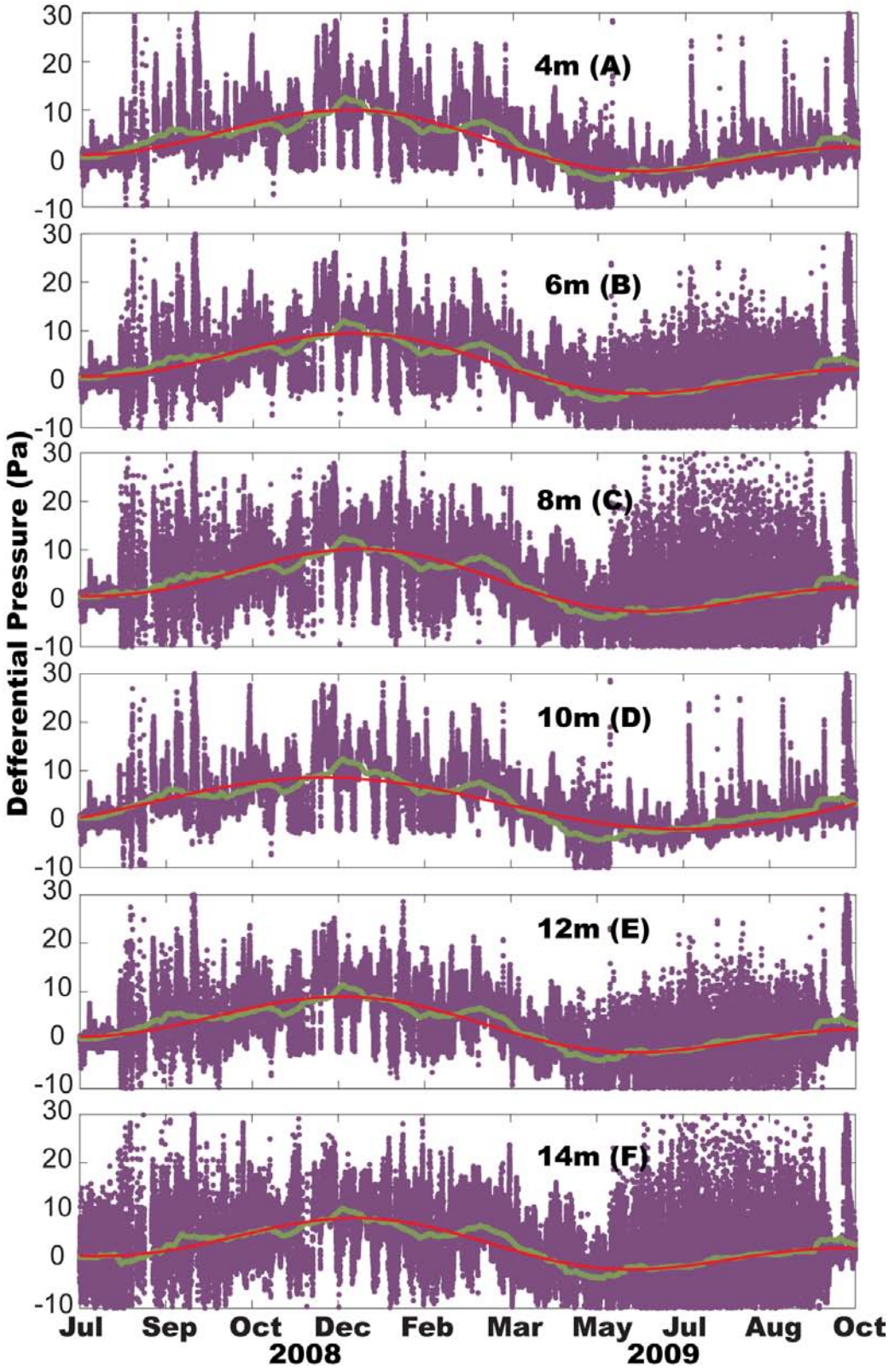

Figure C.14: Deferential pore-air pressures of 34N2gas at various depths

C.3 Construction photos

This section provides some photo taken during the test piles construction and snow cover during winter, for details construction of the test pile, one should prefer to the work of Smith et al. (2012).

Figure C.15: (A) Basal lysimeters, (B) Push-dumping, (C) End-dumping and (D) thermistor cables are housed by flexible PVC tubings for protection during the replacement of waste rock

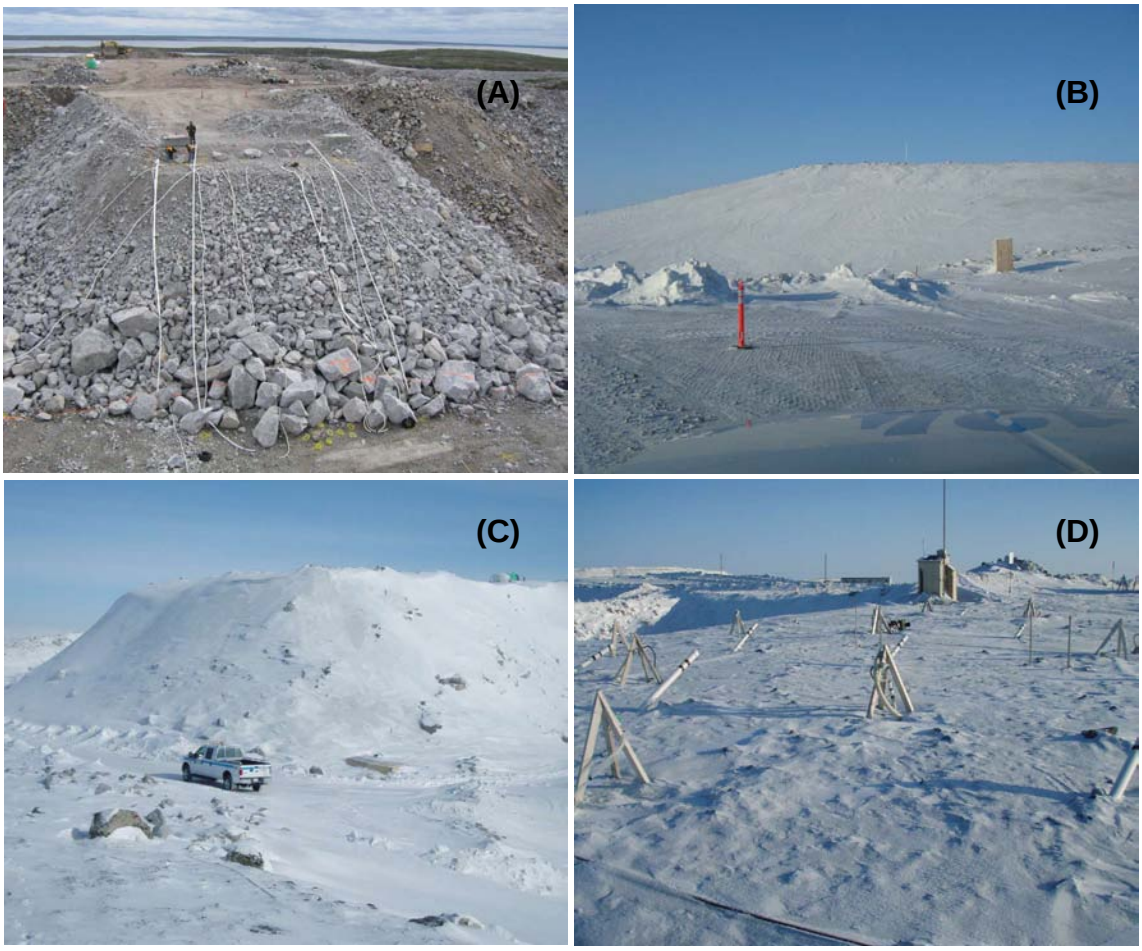

Figure C.16: (A) Typical tip face instrumentation clearly shows the segregation of waste rock, (B) snow covers the east side of the covered pile (photo taken on Feb. 22, 2009 by Richard Amos), (C) on the batter (taken on Mar. 12, 2008 by Matt Neuner) and (D) on the surface (taken on Feb. 22, 2009 by Richard Amos) of the Type III test pile.

References

Amos, R. T., Blowes, D. W., Smith, L., and Sego, D. C. (2009a). Measurement of wind-induced pressure gradients in a waste rock pile. *Vadose Zone J*, 8(4):953–962.

Smith, L. J., Moncur, M. C., Neuner, M., Gupton, M., Blowes, D. W., Smith, L., and Sego, D. C. (2012). The diavik waste rock project: Design, construction, and instrumentation of field-scale experimental waste-rock piles. *Applied Geochemistry*, (0):–.

APPENDIX D

Wiring diagrams and programs of data loggers

D.1 Wiring diagrams

D.1.1 3Bb data logger station

3Bb data logger station is located in the T1/T3 instrumentation trailer (Fig. 1.3) and this data logger station is recording temperature measurements of Type I and III test piles and bedrock temperatures beneath the test piles (384 thermistors under a 4-h interval).

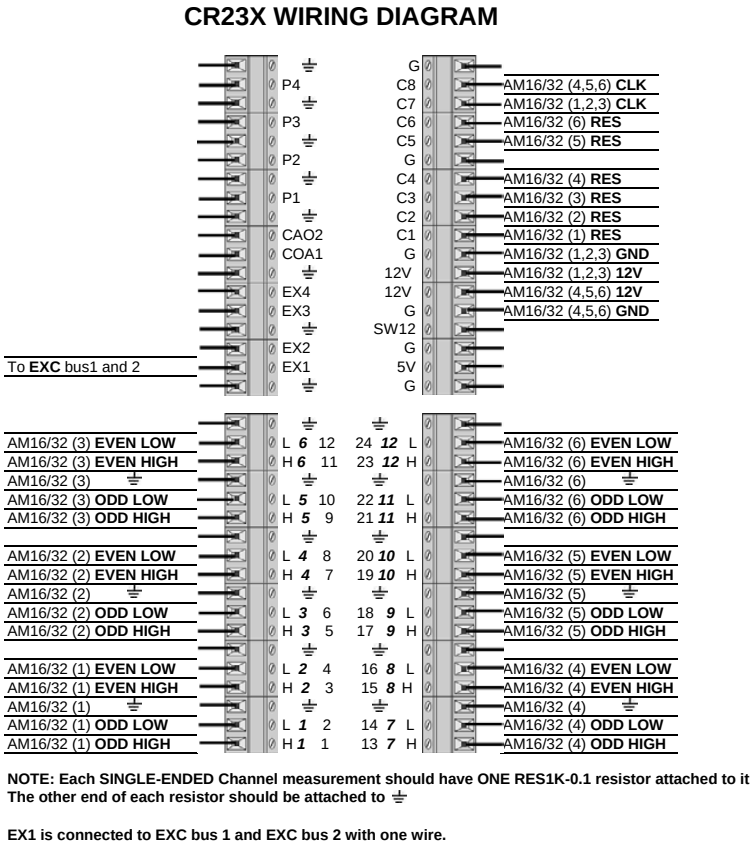

Figure D.1: Wiring diagram of CR23X (Campbell Scientific) of 3Bb data logger station

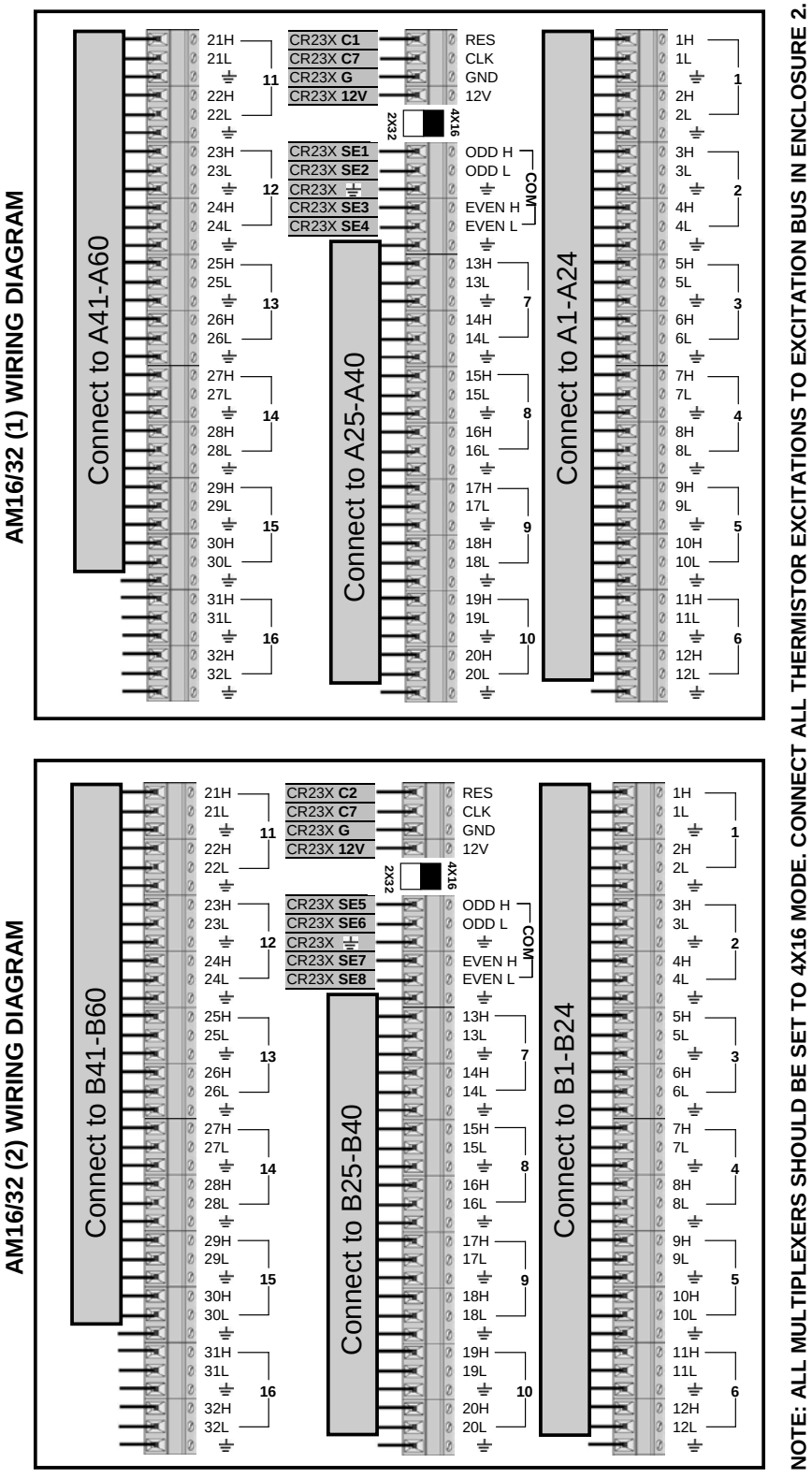

Figure D.2: Wiring diagram of Multiplexer AM16/32 (1) (top figure) and AM16/32 (2) (bottom figure) connected to CR23X. Temperature sensors: A1 to A60 and B1 to B60.

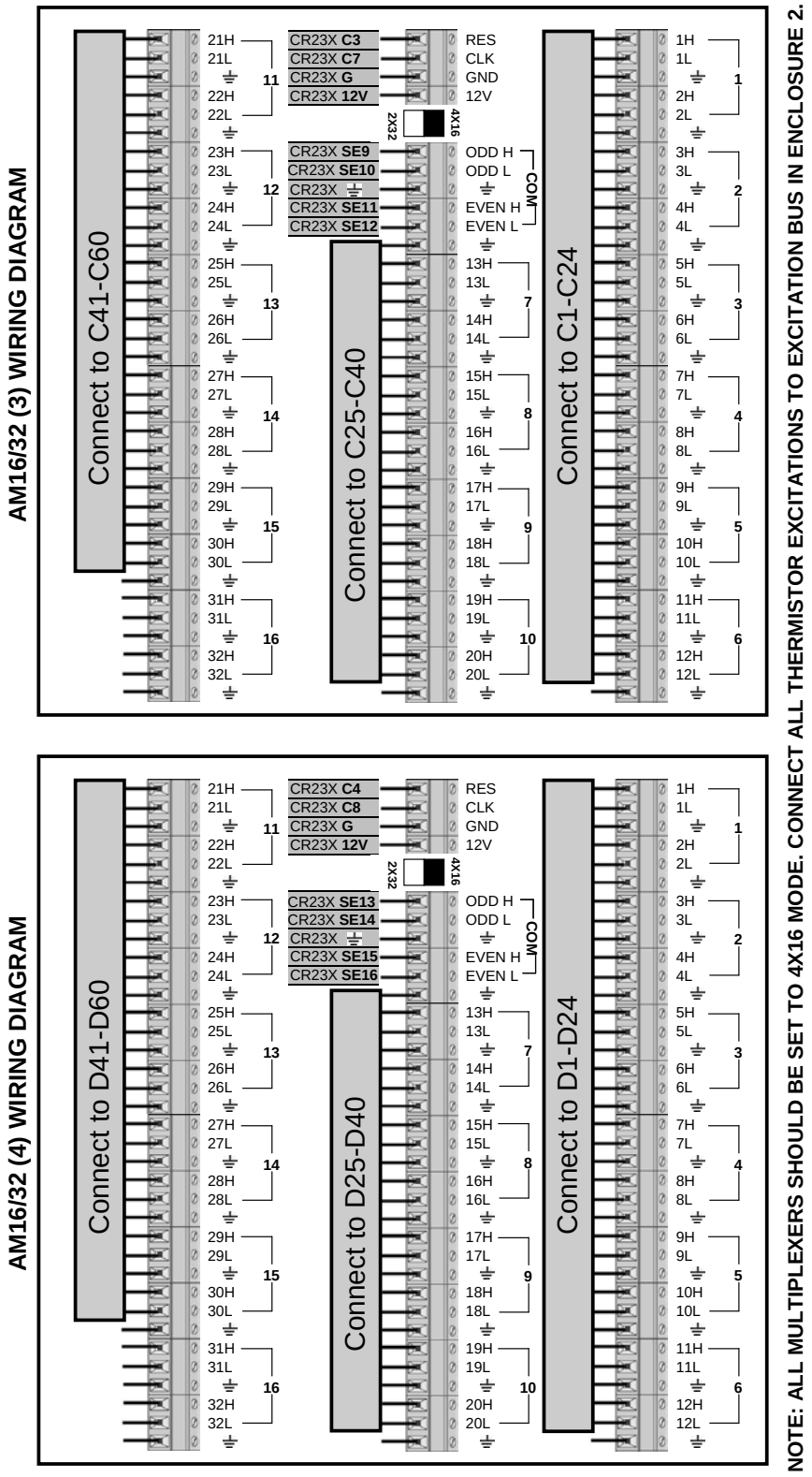

Figure D.3: Wiring diagram of Multiplexer AM16/32 (3) (top figure) and AM16/32 (4) (bottom figure) connected to CR23X. Temperature sensors: C1 to C60 and D1 to D60.

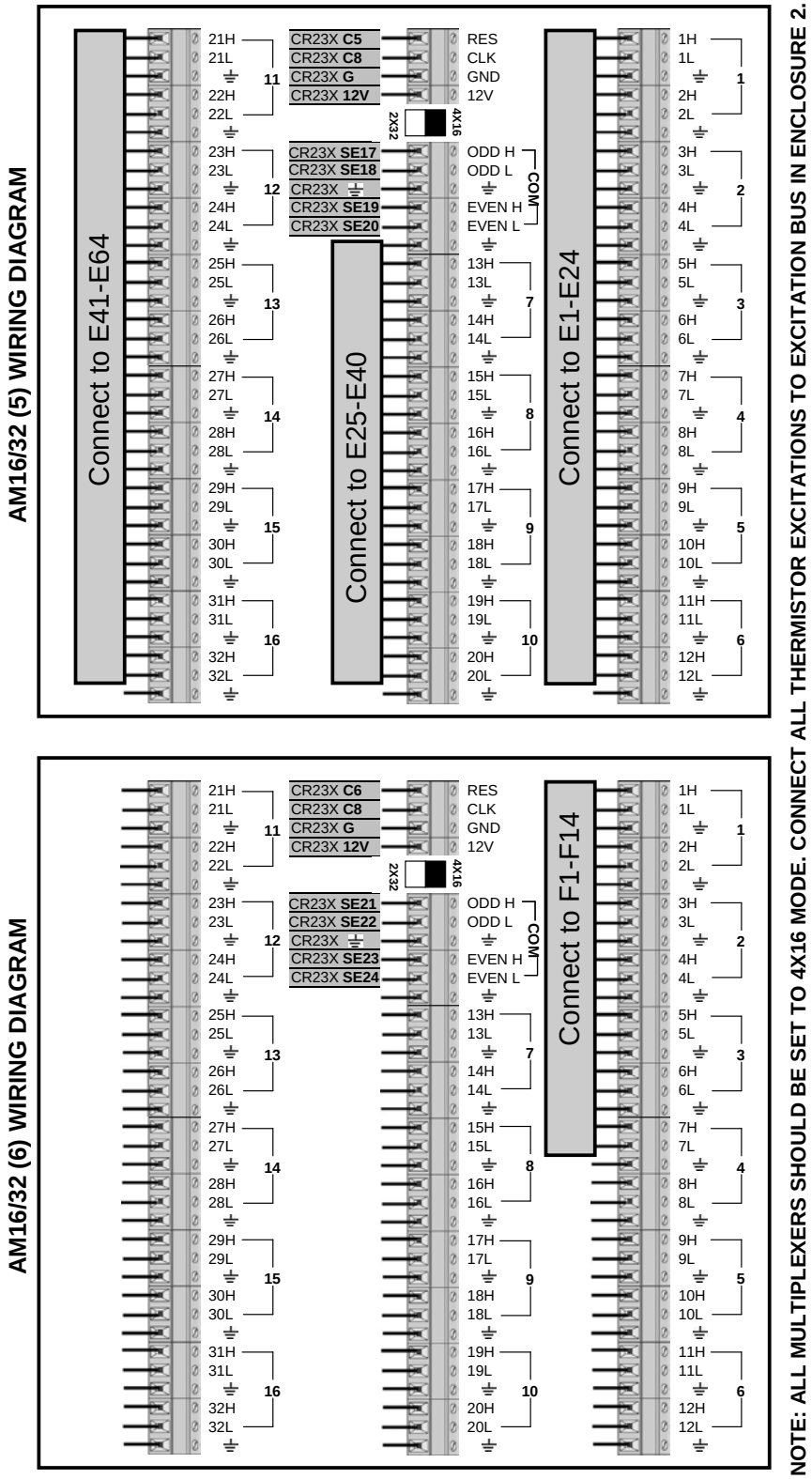

Figure D.4: Wiring diagram of Multiplexer AM16/32 (5) (top figure) and AM16/32 (6) (bottom figure) connected to CR23X. Temperature sensors: E1 to E64 and F1 to F14.

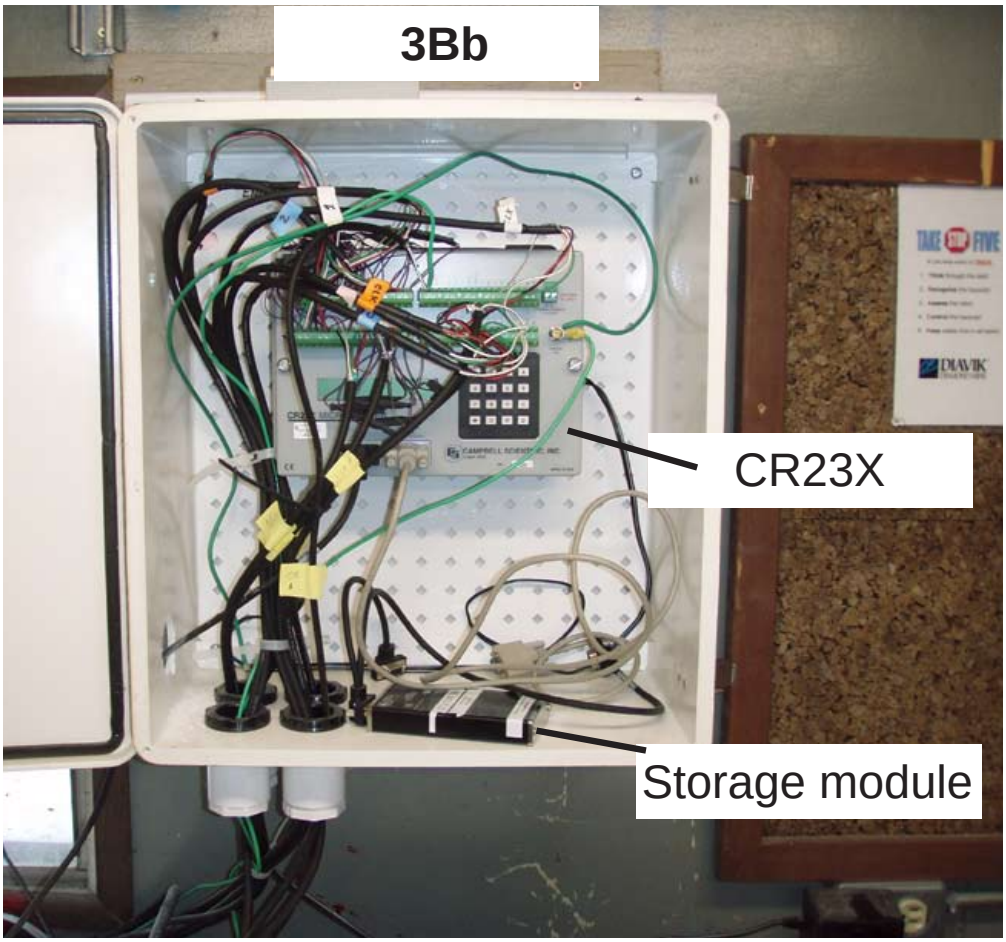

Figure D.5: The 3Bb data logger station (CR23X) is located at the T1/T3 instrumentation trailer (the picture taken on Oct. 21, 2009)

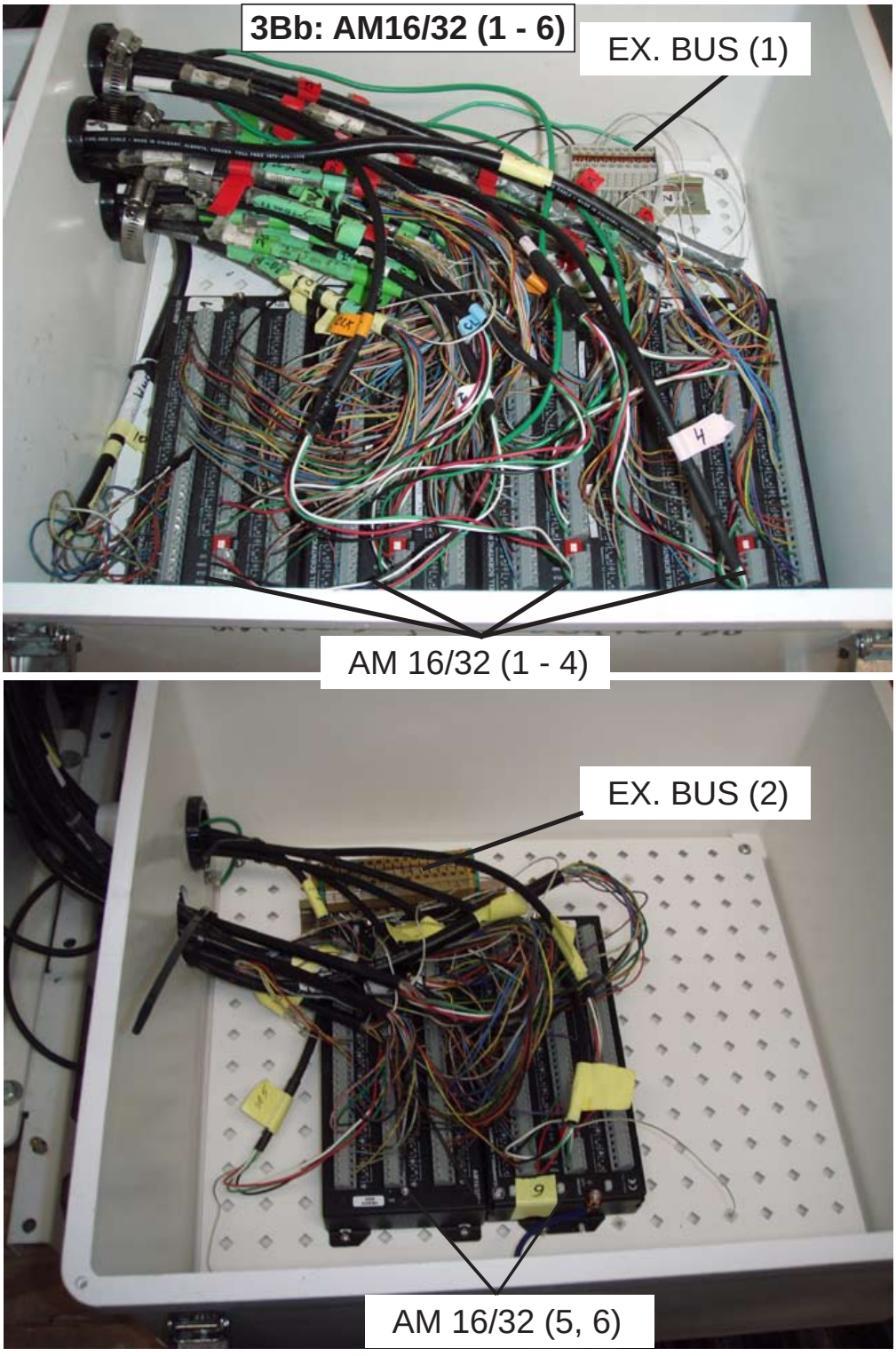

Figure D.6: The 3Bb data logger station (AM 16/32 (1 - 6)) is located at the T1/T3 instrumentation trailer (the pictures taken on Oct. 21, 2009)

D.1.2 CBb and CBc data logger Stations

CBb data logger station is located in the covered pile instrumentation trailer (Fig. 1.3) and it is recording of all thermistors on the west side of the covered test pile and bedrock thermistors beneath the covered test pile (121 thermistors under a 4-h interval). Similarly, CBc data logger station is located in a instrumentation hut on the east side of the test pile and it is recording of all thermistors on the east side (72 thermistors under a 4-h interval)

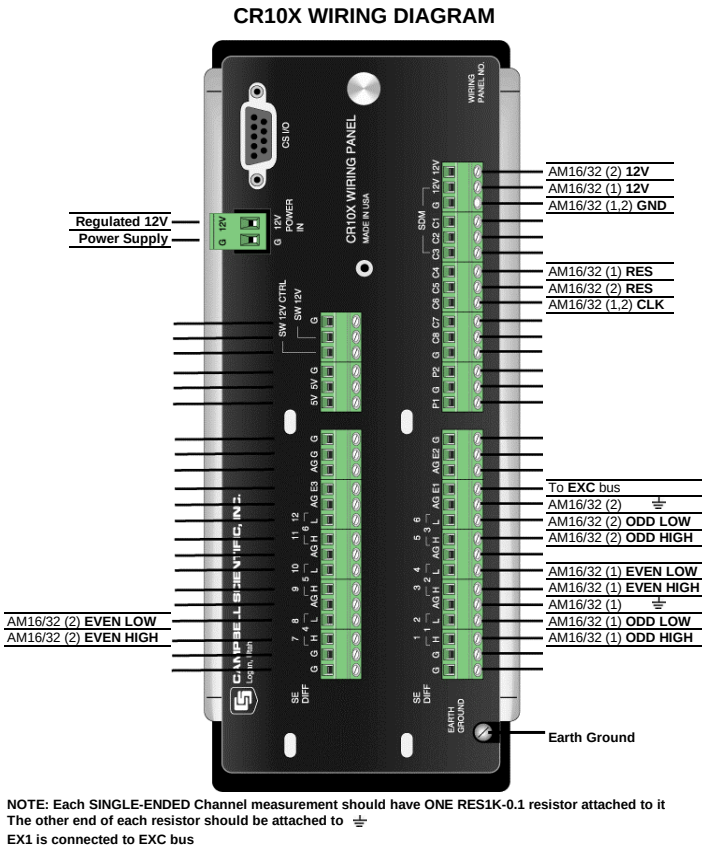

Figure D.7: Wiring diagram of CR10X (Campbell Scientific) of CBb and CBc data logger stations

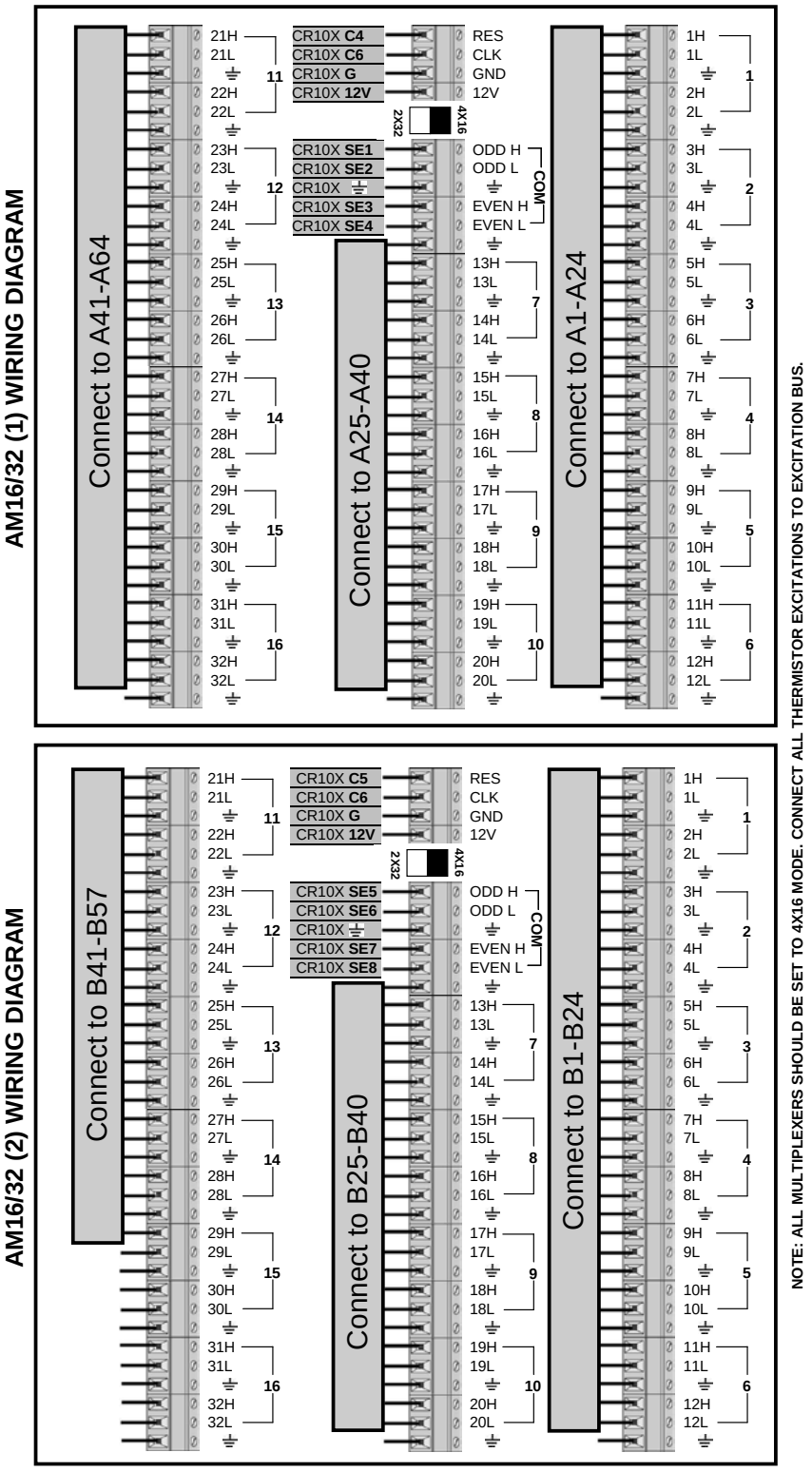

Figure D.8: Wiring diagram of Multiplexer AM16/32 (1) (top figure) and AM16/32 (2) (bottom figure) connected to CR10X of CBb and CBc data logger station. CBc is similar to CBb excepting that AM16/32 (2) of CBc is connected with temperature sensors B1 to B8. Temperature sensors: A1 to A64 and B1 to B57.

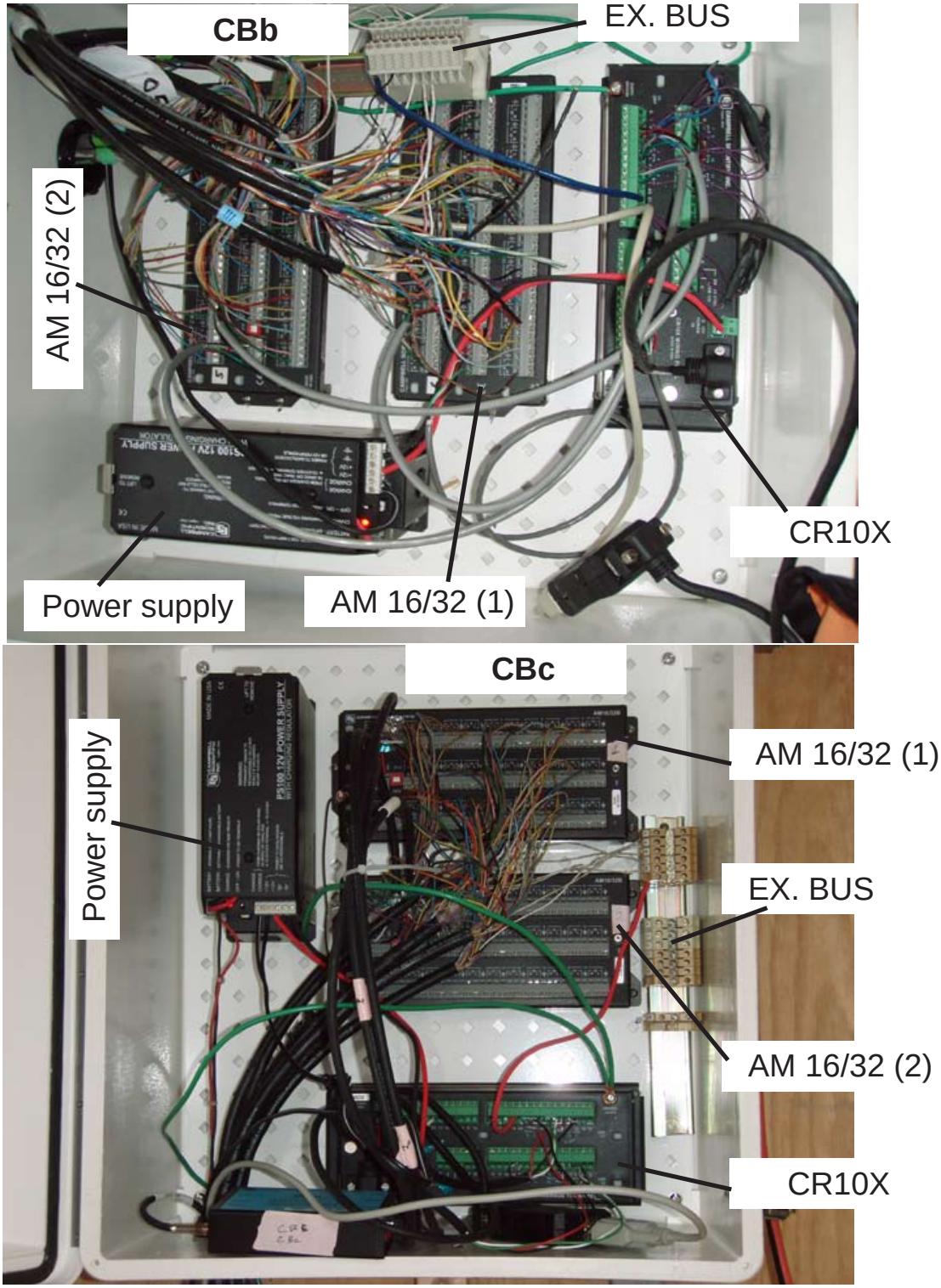

Figure D.9: The CBb and CBc data logger stations are located at the covered test pile instrumentation trailer and in the hut on the east side of the covered test pile (the pictures taken on Oct. 21, 2009).

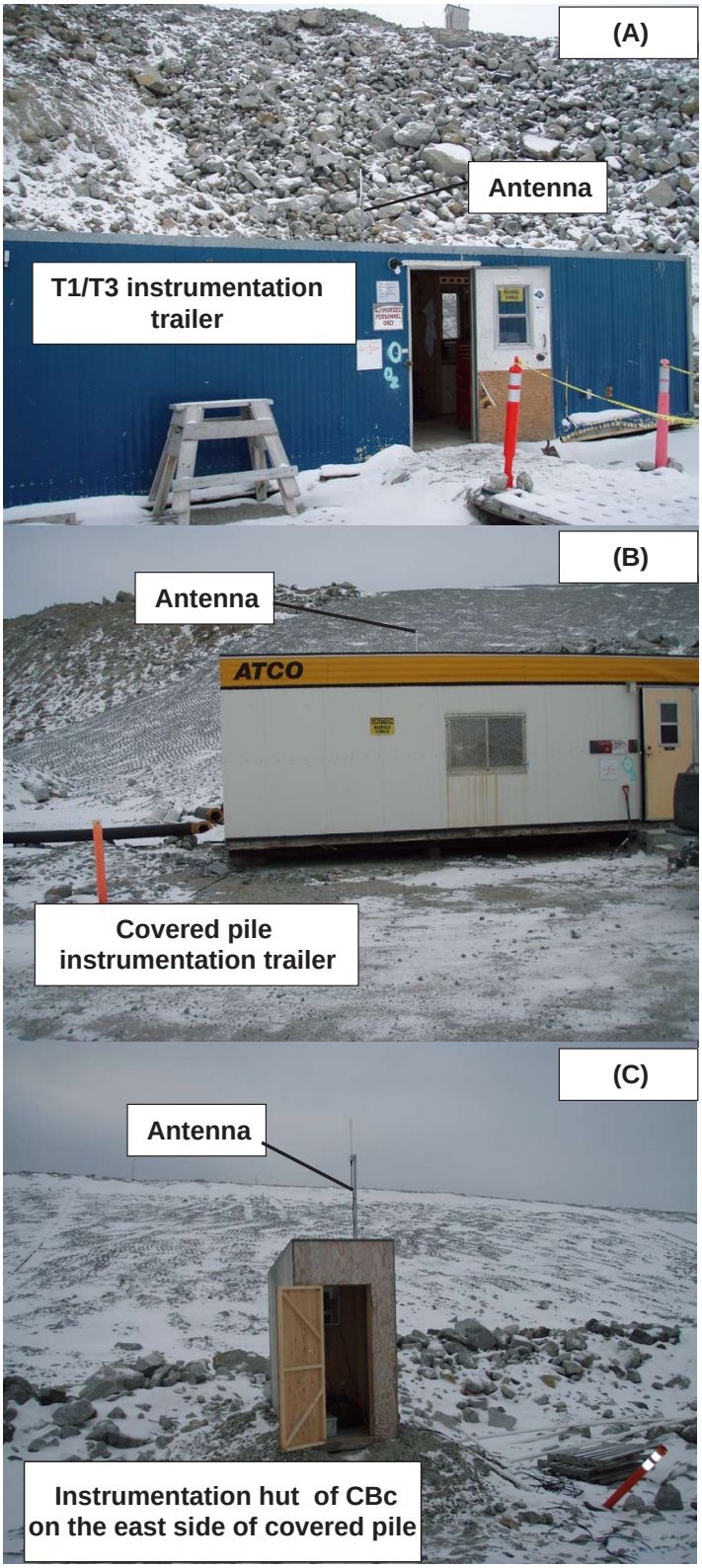

Figure D.10: Instrumentation trailers and hut (the pictures taken on Oct. 21, 2009 by Richard Amos)

D.2 Data logger programs

All programs were written in the annotated version of the language used by Edlog, the text editor for various Campbell Scientific data loggers. CBc program is similar to that of CBb excepting that CBc is only recording 72 temperature sensors.

```
;{CR23X-TD_3Bb Station - Diavik Test
;Piles Project}
;
; *** Program Information ***
; Nam Pham (University of Alberta) adaptation of Matthew
;Knezevich  Campbell (Scientific) Canada Corporation

; Date updated: July 18, 2007
;
; Flag 1 will be used for thermistor temperature data
; (which is output every 4 hours)
;
; Flag 2 will be used for daily status output
; (which is output every 24 hours)
;
; Program Description:
;
; This program has been written for use with a CR23X
; datalogger and 6 AM16/32-XT multiplexers.  Each
; multiplexer will be setted up 4X16 mode and will have
; 318 thermistors connected.
;
; The multiplexers will be numbered from 1 to 6, and
; will all be connected to the CR23X wiring panel. For
; wiring information, refer to the wiring diagrams
; that come along with this program.
;
; The thermistors are part number YSI 44007 and are 5K
; at 25 Degrees C. The thermistors will be measured using
; instruction P4 and then the Steinhart Hart equation
; will be used to calculate the temperature. The Steinhart
; Hart coefficients were determined using the spreadsheet
; calculator available on the YSI website:
;
; http://www.ysi.com/extranet/TEMPKL.nsf/
; 447554deba0f52f2852569f500696b21/
; b06d4e8ff6f77c4085256a030072cea1!OpenDocument
;
; The resulting coefficients for the Steinhart Hart equation
; were found to be:
;
; A = 0.001286798
; B = 0.000235938
; C = 0.000000094
;
; Each single ended channel of the CR23X will have a
; precision 1k resistor attached to it.  The other end of each
; of these resistors will be attached to analog ground.
;
; The excitations for the thermistors will be wired to a ;common
; excitation bus (terminal strip) which is placed in
; multiplexer enclosure.  Excitation Channel 1 from the ;CR10X
is connected to this excitation bus and is used to ;excite all of
the thermistors that are wired to AM16/32 (1,2)

; Control ports 1-6 are used for the RESET line of AM16/32
;(1..6) respectively
; and Port 7 is used to pulse clock on both AM16/32 (1..3)
; and Port 8 is used to pulse clock on both AM16/32 (4..6)

; The temperatures will be measured every hour (3600 ;seconds)
; and stored in final storage along with the time stamp every
; FOUR hour.

;NOTE:
;
; THIS PROGRAM IS USED TO RECORD ;TEMPERATURE
DATA INSIDE TI, TIII TEST PILES ;AND BEDROCK
TEMPERATURES.

*Table 1 Program
  01: 3600      Execution Interval (seconds)

1:  If time is (P92)
 1: 0        Seconds into a
 2: 14400    Second interval
 3: 11       Set Flag 1 High

; Compute the program signature the first time is run and
; once daily.

2:  If (X<=>F) (P89)
 1: 385      X Loc [ ProgSign       ]
 2: 1        =
 3: 0        F
 4: 30       Then Do

    3:  Signature (P19)
     1: 385      Loc [ ProgSign       ]

4:  End (P95)

; Every execution interval, measure the battery voltage

5:  Batt Voltage (P10)
 1: 386      Loc [ BattVolt       ]

; *** Start of instructions to measure AM16/32(1) ***

; Activate AM16/32(1) by setting Control Port 1 high

6:  Do (P86)
 1: 41       Set Port 1 High
7:  Beginning of Loop (P87)
 1: 0        Delay
 2: 15       Loop Count
    8:  Step Loop Index (P90)
     1: 4        Step
    9:  Do (P86)
     1: 77       Pulse Port 7
    10:  Delay w/Opt Excitation (P22)
     1: 1     -- Ex Channel
     2: 0        Delay W/Ex (0.01 sec units)
     3: 1        Delay After Ex (0.01 sec units)
     4: 0        mV Excitation

; The following instructions are used to determine the
; resistance of the thermistors in ohms and then be
; plugged into the Steinhart-Hart equation to determine
; a value in Degrees C.

    11:  Excite-Delay (SE) (P4)
     1: 4        Reps
     2: 20       Auto, 60 Hz Reject, Slow Range (OS>1.06)
     3: 1        SE Channel
     4: 1        Excite all reps w/Exchan 1
     5: 10       Delay (0.01 sec units)
     6: 5000     mV Excitation
     7: 1     -- Loc [ A1            ]
     8: 1        Mult
     9: 0        Offset

; Processing calculations for first bank of thermistors

    12:  Z=1/X (P42)
     1: 1     -- X Loc [ A1            ]
     2: 1     -- Z Loc [ A1            ]

    13:  Z=X*F (P37)
```

```
   1: 1     -- X Loc [ A1          ]
   2: 5000     F
   3: 1     -- Z Loc [ A1          ]

  14:  Z=X+F (P34)
   1: 1     -- X Loc [ A1          ]
   2: -1       F
   3: 1     -- Z Loc [ A1          ]

  15:  Z=X*F (P37)
   1: 1     -- X Loc [ A1          ]
   2: 1000     F
   3: 1     -- Z Loc [ A1          ]

  16:  Steinhart-Hart Equation (P200)
   1: 1        Reps
   2: 1     -- Source Loc (R)(Ohms) [ A1          ]
   3: 1     -- Destination Loc (Deg C) [ A1          ]
   4: 1.28680  A
   5: -3       x 10^n
   6: 2.35938  B
   7: -4       x 10^n
   8: 9.4      C
   9: -8       x 10^n

; Processing calculations for second bank of thermistors

  17:  Z=1/X (P42)
   1: 2     -- X Loc [ A2          ]
   2: 2     -- Z Loc [ A2          ]

  18:  Z=X*F (P37)
   1: 2     -- X Loc [ A2          ]
   2: 5000     F
   3: 2     -- Z Loc [ A2          ]

  19:  Z=X+F (P34)
   1: 2     -- X Loc [ A2          ]
   2: -1       F
   3: 2     -- Z Loc [ A2          ]

  20:  Z=X*F (P37)
   1: 2     -- X Loc [ A2          ]
   2: 1000     F
   3: 2     -- Z Loc [ A2          ]

  21:  Steinhart-Hart Equation (P200)
   1: 1        Reps
   2: 2     -- Source Loc (R)(Ohms) [ A2          ]
   3: 2     -- Destination Loc (Deg C) [ A2          ]
   4: 1.28680  A
   5: -3       x 10^n
   6: 2.35938  B
   7: -4       x 10^n
   8: 9.4      C
   9: -8       x 10^n

; Processing calculations for third bank of thermistors

  22:  Z=1/X (P42)
   1: 3     -- X Loc [ A3          ]
   2: 3     -- Z Loc [ A3          ]

  23:  Z=X*F (P37)
   1: 3     -- X Loc [ A3          ]
   2: 5000     F
   3: 3     -- Z Loc [ A3          ]

  24:  Z=X+F (P34)
   1: 3     -- X Loc [ A3          ]
   2: -1       F
   3: 3     -- Z Loc [ A3          ]

  25:  Z=X*F (P37)
   1: 3     -- X Loc [ A3          ]
   2: 1000     F
   3: 3     -- Z Loc [ A3          ]

  26:  Steinhart-Hart Equation (P200)
   1: 1        Reps
   2: 3     -- Source Loc (R)(Ohms) [ A3          ]
   3: 3     -- Destination Loc (Deg C) [ A3          ]
   4: 1.28680  A
   5: -3       x 10^n
   6: 2.35938  B
   7: -4       x 10^n
   8: 9.4      C
   9: -8       x 10^n

; Processing calculations for fourth bank of thermistors

  27:  Z=1/X (P42)
   1: 4     -- X Loc [ A4          ]
   2: 4     -- Z Loc [ A4          ]

  28:  Z=X*F (P37)
   1: 4     -- X Loc [ A4          ]
   2: 5000     F
   3: 4     -- Z Loc [ A4          ]

  29:  Z=X+F (P34)
   1: 4     -- X Loc [ A4          ]
   2: -1       F
   3: 4     -- Z Loc [ A4          ]

  30:  Z=X*F (P37)
   1: 4     -- X Loc [ A4          ]
   2: 1000     F
   3: 4     -- Z Loc [ A4          ]

  31:  Steinhart-Hart Equation (P200)
   1: 1        Reps
   2: 4     -- Source Loc (R)(Ohms) [ A4          ]
   3: 4     -- Destination Loc (Deg C) [ A4          ]
   4: 1.28680  A
   5: -3       x 10^n
   6: 2.35938  B
   7: -4       x 10^n
   8: 9.4      C
   9: -8       x 10^n

  32:  End (P95)

  ;Deactivate Am16/32(1)

  33:  Do (P86)
   1: 51       Set Port 1 Low

  ; *** End of instructions for AM16/32(1) ***


  ; *** Start of instructions to measure AM16/32(2) ***

  ; Activate AM16/32(2) by setting Control Port 2 high

  34:  Do (P86)
   1: 42       Set Port 2 High

  35:  Beginning of Loop (P87)
   1: 0        Delay
```

```
 2: 15      Loop Count

   36:  Step Loop Index (P90)
    1: 4       Step

   37:  Do (P86)
    1: 77      Pulse Port 7

   38:  Delay w/Opt Excitation (P22)
    1: 1     -- Ex Channel
    2: 0       Delay W/Ex (0.01 sec units)
    3: 1       Delay After Ex (0.01 sec units)
    4: 0       mV Excitation

; The following instructions are used to determine the
; resistance of the thermistors in ohms and then be
; plugged into the Steinhart-Hart equation to determine
; a value in Degrees C.

   39:  Excite-Delay (SE) (P4)
    1: 4       Reps
    2: 20      Auto, 60 Hz Reject, Slow Range (OS>1.06)
    3: 5       SE Channel
    4: 1       Excite all reps w/Exchan 1
    5: 10      Delay (0.01 sec units)
    6: 5000    mV Excitation
    7: 65    -- Loc [ B1          ]
    8: 1       Mult
    9: 0       Offset

; Processing calculations for first bank of thermistors

   40:  Z=1/X (P42)
    1: 65    -- X Loc [ B1          ]
    2: 65    -- Z Loc [ B1          ]

   41:  Z=X*F (P37)
    1: 65    -- X Loc [ B1          ]
    2: 5000    F
    3: 65    -- Z Loc [ B1          ]

   42:  Z=X+F (P34)
    1: 65    -- X Loc [ B1          ]
    2: -1      F
    3: 65    -- Z Loc [ B1          ]


   43:  Z=X*F (P37)
    1: 65    -- X Loc [ B1          ]
    2: 1000    F
    3: 65    -- Z Loc [ B1          ]

   44:  Steinhart-Hart Equation (P200)
    1: 1       Reps
    2: 65    -- Source Loc (R)(Ohms) [ B1          ]
    3: 65    -- Destination Loc (Deg C) [ B1          ]
    4: 1.28680  A
    5: -3      x 10^n
    6: 2.35938  B
    7: -4      x 10^n
    8: 9.4     C
    9: -8      x 10^n

; Processing calculations for second bank of thermistors

   45:  Z=1/X (P42)
    1: 66    -- X Loc [ B2          ]
    2: 66    -- Z Loc [ B2          ]

   46:  Z=X*F (P37)
    1: 66    -- X Loc [ B2          ]
    2: 5000    F
    3: 66    -- Z Loc [ B2          ]

   47:  Z=X+F (P34)
    1: 66    -- X Loc [ B2          ]
    2: -1      F
    3: 66    -- Z Loc [ B2          ]

   48:  Z=X*F (P37)
    1: 66    -- X Loc [ B2          ]
    2: 1000    F
    3: 66    -- Z Loc [ B2          ]

   49:  Steinhart-Hart Equation (P200)
    1: 1       Reps
    2: 66    -- Source Loc (R)(Ohms) [ B2          ]
    3: 66    -- Destination Loc (Deg C) [ B2          ]
    4: 1.28680  A
    5: -3      x 10^n
    6: 2.35938  B
    7: -4      x 10^n
    8: 9.4     C
    9: -8      x 10^n

; Processing calculations for third bank of thermistors

   50:  Z=1/X (P42)
    1: 67    -- X Loc [ B3          ]
    2: 67    -- Z Loc [ B3          ]

   51:  Z=X*F (P37)
    1: 67    -- X Loc [ B3          ]
    2: 5000    F
    3: 67    -- Z Loc [ B3          ]

   52:  Z=X+F (P34)
    1: 67    -- X Loc [ B3          ]
    2: -1      F
    3: 67    -- Z Loc [ B3          ]

   53:  Z=X*F (P37)
    1: 67    -- X Loc [ B3          ]
    2: 1000    F
    3: 67    -- Z Loc [ B3          ]

   54:  Steinhart-Hart Equation (P200)
    1: 1       Reps
    2: 67    -- Source Loc (R)(Ohms) [ B3          ]
    3: 67    -- Destination Loc (Deg C) [ B3          ]
    4: 1.28680  A
    5: -3      x 10^n
    6: 2.35938  B
    7: -4      x 10^n
    8: 9.4     C
    9: -8      x 10^n

; Processing calculations for fourth bank of thermistors

   55:  Z=1/X (P42)
    1: 68    -- X Loc [ B4          ]
    2: 68    -- Z Loc [ B4          ]

   56:  Z=X*F (P37)
    1: 68    -- X Loc [ B4          ]
    2: 5000    F
    3: 68    -- Z Loc [ B4          ]

   57:  Z=X+F (P34)
    1: 68    -- X Loc [ B4          ]
```

```
    2: -1      F
    3: 68    -- Z Loc [ B4          ]

   58:  Z=X*F (P37)
    1: 68    -- X Loc [ B4          ]
    2: 1000    F
    3: 68    -- Z Loc [ B4          ]

   59:  Steinhart-Hart Equation (P200)
    1: 1       Reps
    2: 68    -- Source Loc (R)(Ohms) [ B4          ]
    3: 68    -- Destination Loc (Deg C) [ B4          ]
    4: 1.28680  A
    5: -3      x 10^n
    6: 2.35938  B
    7: -4      x 10^n
    8: 9.4     C
    9: -8      x 10^n

60:  End (P95)

;Deactivate Am16/32(2)

61:  Do (P86)
 1: 52      Set Port 2 Low

; *** End of instructions for AM16/32(2) ***


; *** Start of instructions to measure AM16/32(3) ***

; Activate AM16/32(3) by setting Control Port 3 high

62:  Do (P86)
 1: 43      Set Port 3 High

63:  Beginning of Loop (P87)
 1: 0       Delay
 2: 15      Loop Count

   64:  Step Loop Index (P90)
    1: 4       Step

   65:  Do (P86)
    1: 77      Pulse Port 7

   66:  Delay w/Opt Excitation (P22)
    1: 1     -- Ex Channel
    2: 0       Delay W/Ex (0.01 sec units)
    3: 1       Delay After Ex (0.01 sec units)
    4: 0       mV Excitation

; The following instructions are used to determine the
; resistance of the thermistors in ohms and then be
; plugged into the Steinhart-Hart equation to determine
; a value in Degrees C.

   67:  Excite-Delay (SE) (P4)
    1: 4       Reps
    2: 20      Auto, 60 Hz Reject, Slow Range (OS>1.06)
    3: 9       SE Channel
    4: 1       Excite all reps w/Exchan 1
    5: 10      Delay (0.01 sec units)
    6: 5000    mV Excitation
    7: 129   -- Loc [ C1          ]
    8: 1       Mult
    9: 0       Offset

; Processing calculations for first bank of thermistors

   68:  Z=1/X (P42)
    1: 129   -- X Loc [ C1          ]
    2: 129   -- Z Loc [ C1          ]

   69:  Z=X*F (P37)
    1: 129   -- X Loc [ C1          ]
    2: 5000    F
    3: 129   -- Z Loc [ C1          ]

   70:  Z=X+F (P34)
    1: 129   -- X Loc [ C1          ]
    2: -1      F
    3: 129   -- Z Loc [ C1          ]


   71:  Z=X*F (P37)
    1: 129   -- X Loc [ C1          ]
    2: 1000    F
    3: 129   -- Z Loc [ C1          ]

   72:  Steinhart-Hart Equation (P200)
    1: 1       Reps
    2: 129   -- Source Loc (R)(Ohms) [ C1          ]
    3: 129   -- Destination Loc (Deg C) [ C1          ]
    4: 1.28680  A
    5: -3      x 10^n
    6: 2.35938  B
    7: -4      x 10^n
    8: 9.4     C
    9: -8      x 10^n

; Processing calculations for second bank of thermistors

   73:  Z=1/X (P42)
    1: 130   -- X Loc [ C2          ]
    2: 130   -- Z Loc [ C2          ]

   74:  Z=X*F (P37)
    1: 130   -- X Loc [ C2          ]
    2: 5000    F
    3: 130   -- Z Loc [ C2          ]

   75:  Z=X+F (P34)
    1: 130   -- X Loc [ C2          ]
    2: -1      F
    3: 130   -- Z Loc [ C2          ]

   76:  Z=X*F (P37)
    1: 130   -- X Loc [ C2          ]
    2: 1000    F
    3: 130   -- Z Loc [ C2          ]

   77:  Steinhart-Hart Equation (P200)
    1: 1       Reps
    2: 130   -- Source Loc (R)(Ohms) [ C2          ]
    3: 130   -- Destination Loc (Deg C) [ C2          ]
    4: 1.28680  A
    5: -3      x 10^n
    6: 2.35938  B
    7: -4      x 10^n
    8: 9.4     C
    9: -8      x 10^n

; Processing calculations for third bank of thermistors

   78:  Z=1/X (P42)
    1: 131   -- X Loc [ C3          ]
    2: 131   -- Z Loc [ C3          ]
```

```
   79:  Z=X*F (P37)
    1: 131   -- X Loc [ C3           ]
    2: 5000     F
    3: 131   -- Z Loc [ C3           ]

   80:  Z=X+F (P34)
    1: 131   -- X Loc [ C3           ]
    2: -1       F
    3: 131   -- Z Loc [ C3           ]

   81:  Z=X*F (P37)
    1: 131   -- X Loc [ C3           ]
    2: 1000     F
    3: 131   -- Z Loc [ C3           ]

   82:  Steinhart-Hart Equation (P200)
    1: 1        Reps
    2: 131   -- Source Loc (R)(Ohms) [ C3           ]
    3: 131   -- Destination Loc (Deg C) [ C3           ]
    4: 1.28680  A
    5: -3       x 10^n
    6: 2.35938  B
    7: -4       x 10^n
    8: 9.4      C
    9: -8       x 10^n

; Processing calculations for fourth bank of thermistors

   83:  Z=1/X (P42)
    1: 132   -- X Loc [ C4           ]
    2: 132   -- Z Loc [ C4           ]

   84:  Z=X*F (P37)
    1: 132   -- X Loc [ C4           ]
    2: 5000     F
    3: 132   -- Z Loc [ C4           ]

   85:  Z=X+F (P34)
    1: 132   -- X Loc [ C4           ]
    2: -1       F
    3: 132   -- Z Loc [ C4           ]

   86:  Z=X*F (P37)
    1: 132   -- X Loc [ C4           ]
    2: 1000     F
    3: 132   -- Z Loc [ C4           ]

   87:  Steinhart-Hart Equation (P200)
    1: 1        Reps
    2: 132   -- Source Loc (R)(Ohms) [ C4           ]
    3: 132   -- Destination Loc (Deg C) [ C4           ]
    4: 1.28680  A
    5: -3       x 10^n
    6: 2.35938  B
    7: -4       x 10^n
    8: 9.4      C
    9: -8       x 10^n

88:  End (P95)

;Deactivate Am16/32(3)

89:  Do (P86)
 1: 53       Set Port 3 Low

; *** End of instructions for AM16/32(3) ***


; *** Start of instructions to measure AM16/32(4) ***

; Activate AM16/32(4) by setting Control Port 4 high

90:  Do (P86)
 1: 44       Set Port 4 High

91:  Beginning of Loop (P87)
 1: 0        Delay
 2: 15       Loop Count

   92:  Step Loop Index (P90)
    1: 4        Step

   93:  Do (P86)
    1: 78       Pulse Port 8

   94:  Delay w/Opt Excitation (P22)
    1: 1        Ex Channel
    2: 0        Delay W/Ex (0.01 sec units)
    3: 1        Delay After Ex (0.01 sec units)
    4: 0        mV Excitation

; The following instructions are used to determine the
; resistance of the thermistors in ohms and then be
; plugged into the Steinhart-Hart equation to determine
; a value in Degrees C.

   95:  Excite-Delay (SE) (P4)
    1: 4        Reps
    2: 20       Auto, 60 Hz Reject, Slow Range (OS>1.06)
    3: 13       SE Channel
    4: 1        Excite all reps w/Exchan 1
    5: 10       Delay (0.01 sec units)
    6: 5000     mV Excitation
    7: 193   -- Loc [ D1           ]
    8: 1        Mult
    9: 0        Offset

; Processing calculations for first bank of thermistors

   96:  Z=1/X (P42)
    1: 193   -- X Loc [ D1           ]
    2: 193   -- Z Loc [ D1           ]

   97:  Z=X*F (P37)
    1: 193   -- X Loc [ D1           ]
    2: 5000     F
    3: 193   -- Z Loc [ D1           ]

   98:  Z=X+F (P34)
    1: 193   -- X Loc [ D1           ]
    2: -1       F
    3: 193   -- Z Loc [ D1           ]

   99:  Z=X*F (P37)
    1: 193   -- X Loc [ D1           ]
    2: 1000     F
    3: 193   -- Z Loc [ D1           ]

   100:  Steinhart-Hart Equation (P200)
    1: 1        Reps
    2: 193   -- Source Loc (R)(Ohms) [ D1           ]
    3: 193   -- Destination Loc (Deg C) [ D1           ]
    4: 1.28680  A
    5: -3       x 10^n
    6: 2.35938  B
    7: -4       x 10^n
    8: 9.4      C
    9: -8       x 10^n

; Processing calculations for second bank of thermistors
```

```
   101:  Z=1/X (P42)
    1: 194   -- X Loc [ D2          ]
    2: 194   -- Z Loc [ D2          ]

   102:  Z=X*F (P37)
    1: 194   -- X Loc [ D2          ]
    2: 5000     F
    3: 194   -- Z Loc [ D2          ]

   103:  Z=X+F (P34)
    1: 194   -- X Loc [ D2          ]
    2: -1       F
    3: 194   -- Z Loc [ D2          ]

   104:  Z=X*F (P37)
    1: 194   -- X Loc [ D2          ]
    2: 1000     F
    3: 194   -- Z Loc [ D2          ]

   105:  Steinhart-Hart Equation (P200)
    1: 1        Reps
    2: 194   -- Source Loc (R)(Ohms) [ D2          ]
    3: 194   -- Destination Loc (Deg C) [ D2          ]
    4: 1.28680  A
    5: -3       x 10^n
    6: 2.35938  B
    7: -4       x 10^n
    8: 9.4      C
    9: -8       x 10^n

; Processing calculations for third bank of thermistors

   106:  Z=1/X (P42)
    1: 195   -- X Loc [ D3          ]
    2: 195   -- Z Loc [ D3          ]

   107:  Z=X*F (P37)
    1: 195   -- X Loc [ D3          ]
    2: 5000     F
    3: 195   -- Z Loc [ D3          ]

   108:  Z=X+F (P34)
    1: 195   -- X Loc [ D3          ]
    2: -1       F
    3: 195   -- Z Loc [ D3          ]

   109:  Z=X*F (P37)
    1: 195   -- X Loc [ D3          ]
    2: 1000     F
    3: 195   -- Z Loc [ D3          ]

   110:  Steinhart-Hart Equation (P200)
    1: 1        Reps
    2: 195   -- Source Loc (R)(Ohms) [ D3          ]
    3: 195   -- Destination Loc (Deg C) [ D3          ]
    4: 1.28680  A
    5: -3       x 10^n
    6: 2.35938  B
    7: -4       x 10^n
    8: 9.4      C
    9: -8       x 10^n

; Processing calculations for fourth bank of thermistors

   111:  Z=1/X (P42)
    1: 196   -- X Loc [ D4          ]
    2: 196   -- Z Loc [ D4          ]

   112:  Z=X*F (P37)
    1: 196   -- X Loc [ D4          ]
    2: 5000     F
    3: 196   -- Z Loc [ D4          ]

   113:  Z=X+F (P34)
    1: 196   -- X Loc [ D4          ]
    2: -1       F
    3: 196   -- Z Loc [ D4          ]

   114:  Z=X*F (P37)
    1: 196   -- X Loc [ D4          ]
    2: 1000     F
    3: 196   -- Z Loc [ D4          ]

   115:  Steinhart-Hart Equation (P200)
    1: 1        Reps
    2: 196   -- Source Loc (R)(Ohms) [ D4          ]
    3: 196   -- Destination Loc (Deg C) [ D4          ]
    4: 1.28680  A
    5: -3       x 10^n
    6: 2.35938  B
    7: -4       x 10^n
    8: 9.4      C
    9: -8       x 10^n

116:  End (P95)

;Deactivate Am16/32(4)

117:  Do (P86)
 1: 54       Set Port 4 Low

; *** End of instructions for AM16/32(4) ***


; *** Start of instructions to measure AM16/32(5) ***

; Activate AM16/32(5) by setting Control Port 5 high

118:  Do (P86)
 1: 45       Set Port 5 High

119:  Beginning of Loop (P87)
 1: 0        Delay
 2: 16       Loop Count

   120:  Step Loop Index (P90)
    1: 4        Step

   121:  Do (P86)
    1: 78       Pulse Port 8

   122:  Delay w/Opt Excitation (P22)
    1: 1        Ex Channel
    2: 0        Delay W/Ex (0.01 sec units)
    3: 1        Delay After Ex (0.01 sec units)
    4: 0        mV Excitation

; The following instructions are used to determine the
; resistance of the thermistors in ohms and then be
; plugged into the Steinhart-Hart equation to determine
; a value in Degrees C.

   123:  Excite-Delay (SE) (P4)
    1: 4        Reps
    2: 20       Auto, 60 Hz Reject, Slow Range (OS>1.06)
    3: 17       SE Channel
    4: 1        Excite all reps w/Exchan 1
    5: 10       Delay (0.01 sec units)
    6: 5000     mV Excitation
```

```
 7: 257   -- Loc [ E1          ]
 8: 1       Mult
 9: 0       Offset

; Processing calculations for first bank of thermistors

 124:  Z=1/X (P42)
  1: 257   -- X Loc [ E1          ]
  2: 257   -- Z Loc [ E1          ]

 125:  Z=X*F (P37)
  1: 257   -- X Loc [ E1          ]
  2: 5000    F
  3: 257   -- Z Loc [ E1          ]

 126:  Z=X+F (P34)
  1: 257   -- X Loc [ E1          ]
  2: -1      F
  3: 257   -- Z Loc [ E1          ]

 127:  Z=X*F (P37)
  1: 257   -- X Loc [ E1          ]
  2: 1000    F
  3: 257   -- Z Loc [ E1          ]

 128:  Steinhart-Hart Equation (P200)
  1: 1       Reps
  2: 257   -- Source Loc (R)(Ohms) [ E1          ]
  3: 257   -- Destination Loc (Deg C) [ E1          ]
  4: 1.28680  A
  5: -3      x 10^n
  6: 2.35938  B
  7: -4      x 10^n
  8: 9.4     C
  9: -8      x 10^n

; Processing calculations for second bank of thermistors

 129:  Z=1/X (P42)
  1: 258   -- X Loc [ E2          ]
  2: 258   -- Z Loc [ E2          ]

 130:  Z=X*F (P37)
  1: 258   -- X Loc [ E2          ]
  2: 5000    F
  3: 258   -- Z Loc [ E2          ]

 131:  Z=X+F (P34)
  1: 258   -- X Loc [ E2          ]
  2: -1      F
  3: 258   -- Z Loc [ E2          ]

 132:  Z=X*F (P37)
  1: 258   -- X Loc [ E2          ]
  2: 1000    F
  3: 258   -- Z Loc [ E2          ]

 133:  Steinhart-Hart Equation (P200)
  1: 1       Reps
  2: 258   -- Source Loc (R)(Ohms) [ E2          ]
  3: 258   -- Destination Loc (Deg C) [ E2          ]
  4: 1.28680  A
  5: -3      x 10^n
  6: 2.35938  B
  7: -4      x 10^n
  8: 9.4     C
  9: -8      x 10^n

; Processing calculations for third bank of thermistors

 134:  Z=1/X (P42)
  1: 259   -- X Loc [ E3          ]
  2: 259   -- Z Loc [ E3          ]

 135:  Z=X*F (P37)
  1: 259   -- X Loc [ E3          ]
  2: 5000    F
  3: 259   -- Z Loc [ E3          ]

 136:  Z=X+F (P34)
  1: 259   -- X Loc [ E3          ]
  2: -1      F
  3: 259   -- Z Loc [ E3          ]

 137:  Z=X*F (P37)
  1: 259   -- X Loc [ E3          ]
  2: 1000    F
  3: 259   -- Z Loc [ E3          ]

 138:  Steinhart-Hart Equation (P200)
  1: 1       Reps
  2: 259   -- Source Loc (R)(Ohms) [ E3          ]
  3: 259   -- Destination Loc (Deg C) [ E3          ]
  4: 1.28680  A
  5: -3      x 10^n
  6: 2.35938  B
  7: -4      x 10^n
  8: 9.4     C
  9: -8      x 10^n

; Processing calculations for fourth bank of thermistors

 139:  Z=1/X (P42)
  1: 260   -- X Loc [ E4          ]
  2: 260   -- Z Loc [ E4          ]

 140:  Z=X*F (P37)
  1: 260   -- X Loc [ E4          ]
  2: 5000    F
  3: 260   -- Z Loc [ E4          ]

 141:  Z=X+F (P34)
  1: 260   -- X Loc [ E4          ]
  2: -1      F
  3: 260   -- Z Loc [ E4          ]

 142:  Z=X*F (P37)
  1: 260   -- X Loc [ E4          ]
  2: 1000    F
  3: 260   -- Z Loc [ E4          ]

 143:  Steinhart-Hart Equation (P200)
  1: 1       Reps
  2: 260   -- Source Loc (R)(Ohms) [ E4          ]
  3: 260   -- Destination Loc (Deg C) [ E4          ]
  4: 1.28680  A
  5: -3      x 10^n
  6: 2.35938  B
  7: -4      x 10^n
  8: 9.4     C
  9: -8      x 10^n

144:  End (P95)

;Deactivate Am16/32(5)

145:  Do (P86)
  1: 55      Set Port 5 Low

; *** End of instructions for AM16/32(5) ***
```

```
; *** Start of instructions to measure AM16/32(6) ***

; Activate AM16/32(6) by setting Control Port 6 high

146:  Do (P86)
 1: 46       Set Port 6 High

147:  Beginning of Loop (P87)
 1: 0        Delay
 2: 4        Loop Count

    148:  Step Loop Index (P90)
     1: 4        Step

    149:  Do (P86)
     1: 78       Pulse Port 8

    150:  Delay w/Opt Excitation (P22)
     1: 1        Ex Channel
     2: 0        Delay W/Ex (0.01 sec units)
     3: 1        Delay After Ex (0.01 sec units)
     4: 0        mV Excitation

; The following instructions are used to determine the
; resistance of the thermistors in ohms and then be
; plugged into the Steinhart-Hart equation to determine
; a value in Degrees C.

    151:  Excite-Delay (SE) (P4)
     1: 4        Reps
     2: 20       Auto, 60 Hz Reject, Slow Range (OS>1.06)
     3: 21       SE Channel
     4: 1        Excite all reps w/Exchan 1
     5: 10       Delay (0.01 sec units)
     6: 5000     mV Excitation
     7: 321   -- Loc [ F1           ]
     8: 1        Mult
     9: 0        Offset

; Processing calculations for first bank of thermistors

    152:  Z=1/X (P42)
     1: 321   -- X Loc [ F1           ]
     2: 321   -- Z Loc [ F1           ]

    153:  Z=X*F (P37)
     1: 321   -- X Loc [ F1           ]
     2: 5000     F
     3: 321   -- Z Loc [ F1           ]

    154:  Z=X+F (P34)
     1: 321   -- X Loc [ F1           ]
     2: -1       F
     3: 321   -- Z Loc [ F1           ]

    155:  Z=X*F (P37)
     1: 321   -- X Loc [ F1           ]
     2: 1000     F
     3: 321   -- Z Loc [ F1           ]

    156:  Steinhart-Hart Equation (P200)
     1: 1        Reps
     2: 321   -- Source Loc (R)(Ohms) [ F1           ]
     3: 321   -- Destination Loc (Deg C) [ F1           ]
     4: 1.28680  A
     5: -3       x 10^n
     6: 2.35938  B
     7: -4       x 10^n
     8: 9.4      C
     9: -8       x 10^n

; Processing calculations for second bank of thermistors

    157:  Z=1/X (P42)
     1: 322   -- X Loc [ F2           ]
     2: 322   -- Z Loc [ F2           ]

    158:  Z=X*F (P37)
     1: 322   -- X Loc [ F2           ]
     2: 5000     F
     3: 322   -- Z Loc [ F2           ]

    159:  Z=X+F (P34)
     1: 322   -- X Loc [ F2           ]
     2: -1       F
     3: 322   -- Z Loc [ F2           ]

    160:  Z=X*F (P37)
     1: 322   -- X Loc [ F2           ]
     2: 1000     F
     3: 322   -- Z Loc [ F2           ]

    161:  Steinhart-Hart Equation (P200)
     1: 1        Reps
     2: 322   -- Source Loc (R)(Ohms) [ F2           ]
     3: 322   -- Destination Loc (Deg C) [ F2           ]
     4: 1.28680  A
     5: -3       x 10^n
     6: 2.35938  B
     7: -4       x 10^n
     8: 9.4      C
     9: -8       x 10^n

; Processing calculations for third bank of thermistors

    162:  Z=1/X (P42)
     1: 323   -- X Loc [ F3           ]
     2: 323   -- Z Loc [ F3           ]

    163:  Z=X*F (P37)
     1: 323   -- X Loc [ F3           ]
     2: 5000     F
     3: 323   -- Z Loc [ F3           ]

    164:  Z=X+F (P34)
     1: 323   -- X Loc [ F3           ]
     2: -1       F
     3: 323   -- Z Loc [ F3           ]

    165:  Z=X*F (P37)
     1: 323   -- X Loc [ F3           ]
     2: 1000     F
     3: 323   -- Z Loc [ F3           ]

    166:  Steinhart-Hart Equation (P200)
     1: 1        Reps
     2: 323   -- Source Loc (R)(Ohms) [ F3           ]
     3: 323   -- Destination Loc (Deg C) [ F3           ]
     4: 1.28680  A
     5: -3       x 10^n
     6: 2.35938  B
     7: -4       x 10^n
     8: 9.4      C
     9: -8       x 10^n

; Processing calculations for fourth bank of thermistors

    167:  Z=1/X (P42)
     1: 324   -- X Loc [ F4           ]
```

```
    2: 324   -- Z Loc [ F4            ]

   168:  Z=X*F (P37)
    1: 324   -- X Loc [ F4            ]
    2: 5000     F
    3: 324   -- Z Loc [ F4            ]

   169:  Z=X+F (P34)
    1: 324   -- X Loc [ F4            ]
    2: -1       F
    3: 324   -- Z Loc [ F4            ]

   170:  Z=X*F (P37)
    1: 324   -- X Loc [ F4            ]
    2: 1000     F
    3: 324   -- Z Loc [ F4            ]

   171:  Steinhart-Hart Equation (P200)
    1: 1        Reps
    2: 324   -- Source Loc (R)(Ohms) [ F4            ]
    3: 324   -- Destination Loc (Deg C) [ F4            ]
    4: 1.28680  A
    5: -3       x 10^n
    6: 2.35938  B
    7: -4       x 10^n
    8: 9.4      C
    9: -8       x 10^n

172:  End (P95)

;Deactivate Am16/32(6)

173:  Do (P86)
 1: 56       Set Port 6 Low

; *** End of instructions for AM16/32(6) ***

; *** OUTPUT INSTRUCTIONS ***


174:  Data Table (P84)^17854
 1: 0        Seconds into Interval
 2: -1       When Flag 1 is High
 3: 0        (0 = auto allocate, -x = redirect to inloc x)
 4: CR23X_T13_PILE_INSIDE      Table Name

175:  Sample (P70)^2771
 1: 228      Reps
 2: 1        Loc [ A1            ]

176:  Data Table (P84)^4979
 1: 0.0      Seconds into Interval
 2: -1       When Flag 1 is High
 3: 0        (0 = auto allocate, -x = redirect to inloc x)
 4: T1andT3_BASE_GROUND       Table Name

177:  Sample (P70)^13334
 1: 79       Reps
 2: 257      Loc [ E1            ]


178:  Data Table (P84)^32443
 1: 0        Seconds into Interval
 2: -1       When Flag 1 is High
 3: 0        (0 = auto allocate, -x = redirect to inloc x)
 4: 15B_15A                  Table Name

179:  Sample (P70)^30634
 1: 25       Reps
 2: 229      Loc [ D37           ]

180:  Do (P86)
 1: 21       Set Flag 1 Low

*Table 2 Program
  02: 0.0000    Execution Interval (seconds)

*Table 3 Subroutines

End Program
```

```
;{CR10X-TD_CBb Station - Diavik Test
;Piles Project}
;
; *** Program Information ***
;
; Nam Pham (University of Alberta) adaptation of Matthew
:Knezevich  Campbell (Scientific) Canada Corporation

; Date updated: Aug 10, 2007
;
; Flag 1 will be used for thermistor temperature data
; (which is output every 4 hours)
;
; Flag 2 will be used for daily status output
; (which is output every 24 hours)
;
; Program Description:
;
; This program has been written for use with a CR10X
; datalogger and 2 AM16/32-XT multiplexers.  Each
; multiplexer will be setted up 4X16 mode and will have
; 121 thermistors connected. The frist 64 thermistors are
connectted
; AM16/32 (1) and the last 57 thermistors are connectted to
;AM16/32 (2)
;
;
; The multiplexers will be numbered from 1 to 2, and
; will all be connected to the CR10X wiring panel. For
; wiring information, refer to the wiring diagrams
; that come along with this program.
;
; The thermistors are part number YSI 44007 and are 5K
; at 25 Degrees C. The thermistors will be measured using
; instruction P4 and then the Steinhart Hart equation
; will be used to calculate the temperature. The Steinhart
; Hart coefficients were determined using the spreadsheet
; calculator available on the YSI website:
;
; http://www.ysi.com/extranet/TEMPKL.nsf/
; 447554deba0f52f2852569f500696b21/
; b06d4e8ff6f77c4085256a030072cea1!OpenDocument
;
;
; The resulting coefficients for the Steinhart Hart equation
; were found to be:
;
; A = 0.001286798
; B = 0.000235938
; C = 0.000000094
;
;
; Each single ended channel of the CR10X will have a
; precision 1k resistor attached to it.  The other end of each
; of these resistors will be attached to analog ground.
;
; The excitations for the thermistors will be wired to a common
; excitation bus (terminal strip) which is placed in
; multiplexer enclosure.  Excitation Channel 1 from the CR10X
is connected to this
; excitation bus and is used to excite all of the thermistors that
are wired to AM16/32 (1,2)

; Control ports 4-5 are used for the RESET line of AM16/32
(1,2) respectively
; and Port 6 is used to pulse clock on both AM16/32 (1,2)

; The temperatures will be measured every hour (3600 seconds)
; and stored in final storage along with the time stamp every
; four hour.


;NOTE:
;
; THIS PROGRAM WILL BE USED TO RUN CR10X ON
THE ;EAST SIDE OF COVERED PILE
; AT THIS MOMENT, THERE ARE 6 THERMISTORS
STRINGS: ;1042(10-15(7)) 1048(10-15(5))
; 1049(10-15(3)) 1050(10-15(1)) 1054(CBNORTH)
;1055(CBSOUTH) ONE THEMISTOR FOR AIR TEMP.
; STRING 1-4 IS ON TOP OF COVERED PILE DRILLED IN
2007
;
; THUS: THE OUTPUT WILL BE 10*12+1=121 REPS

*Table 1 Program
  01: 3600      Execution Interval (seconds)

1:  If time is (P92)
 1: 0        Seconds into a
 2: 21600    Second interval
 3: 11       Set Flag 1 High

; Compute the program signature the first time is run and
; once daily.

2:  If (X<=>F) (P89)
 1: 129      X Loc [ ProgSign       ]
 2: 1        =
 3: 0        F
 4: 30       Then Do

    3:  Signature (P19)
     1: 129      Loc [ ProgSign       ]

4:  End (P95)

; Every execution interval, measure the battery voltage

5:  Batt Voltage (P10)
 1: 130      Loc [ BattVolt       ]

; *** Start of instructions to measure AM16/32(1) ***

; Activate AM16/32(1) by setting Control Port 1 high

6:  Do (P86)
 1: 44       Set Port 4 High

7:  Beginning of Loop (P87)
 1: 0        Delay
 2: 16       Loop Count

    8:  Step Loop Index (P90)
     1: 4        Step

    9:  Do (P86)
     1: 76       Pulse Port 6

    10:  Delay w/Opt Excitation (P22)
     1: 1        Ex Channel
     2: 0        Delay W/Ex (0.01 sec units)
     3: 1        Delay After Ex (0.01 sec units)
     4: 0        mV Excitation

; The following instructions are used to determine the
; resistance of the thermistors in ohms and then be
; plugged into the Steinhart-Hart equation to determine
; a value in Degrees C.
```

```
   11:  Excite-Delay (SE) (P4)
    1: 4       Reps
    2: 20      Auto, 60 Hz Reject, Slow Range (OS>1.06)
    3: 1       SE Channel
    4: 1       Excite all reps w/Exchan 1
    5: 10      Delay (0.01 sec units)
    6: 2500    mV Excitation
    7: 1    -- Loc [ A1          ]
    8: 2.0138  Mult
    9: 0       Offset

; Processing calculations for first bank of thermistors

   12:  Z=1/X (P42)
    1: 1    -- X Loc [ A1          ]
    2: 1    -- Z Loc [ A1          ]

   13:  Z=X*F (P37)
    1: 1    -- X Loc [ A1          ]
    2: 5000    F
    3: 1    -- Z Loc [ A1          ]

   14:  Z=X+F (P34)
    1: 1    -- X Loc [ A1          ]
    2: -1      F
    3: 1    -- Z Loc [ A1          ]

   15:  Z=X*F (P37)
    1: 1    -- X Loc [ A1          ]
    2: 1000    F
    3: 1    -- Z Loc [ A1          ]

   16:  Steinhart-Hart Equation (P200)
    1: 1       Reps
    2: 1    -- Source Loc (R)(Ohms) [ A1          ]
    3: 1    -- Destination Loc (Deg C) [ A1          ]
    4: 1.28680  A
    5: -3      x 10^n
    6: 2.35938  B
    7: -4      x 10^n
    8: 9.4     C
    9: -8      x 10^n

; Processing calculations for second bank of thermistors

   17:  Z=1/X (P42)
    1: 2    -- X Loc [ A2          ]
    2: 2    -- Z Loc [ A2          ]

   18:  Z=X*F (P37)
    1: 2    -- X Loc [ A2          ]
    2: 5000    F
    3: 2    -- Z Loc [ A2          ]

   19:  Z=X+F (P34)
    1: 2    -- X Loc [ A2          ]
    2: -1      F
    3: 2    -- Z Loc [ A2          ]

   20:  Z=X*F (P37)
    1: 2    -- X Loc [ A2          ]
    2: 1000    F
    3: 2    -- Z Loc [ A2          ]

   21:  Steinhart-Hart Equation (P200)
    1: 1       Reps
    2: 2    -- Source Loc (R)(Ohms) [ A2          ]
    3: 2    -- Destination Loc (Deg C) [ A2          ]
    4: 1.28680  A
    5: -3      x 10^n
    6: 2.35938  B
    7: -4      x 10^n
    8: 9.4     C
    9: -8      x 10^n

; Processing calculations for third bank of thermistors

   22:  Z=1/X (P42)
    1: 3    -- X Loc [ A3          ]
    2: 3    -- Z Loc [ A3          ]

   23:  Z=X*F (P37)
    1: 3    -- X Loc [ A3          ]
    2: 5000    F
    3: 3    -- Z Loc [ A3          ]

   24:  Z=X+F (P34)
    1: 3    -- X Loc [ A3          ]
    2: -1      F
    3: 3    -- Z Loc [ A3          ]

   25:  Z=X*F (P37)
    1: 3    -- X Loc [ A3          ]
    2: 1000    F
    3: 3    -- Z Loc [ A3          ]

   26:  Steinhart-Hart Equation (P200)
    1: 1       Reps
    2: 3    -- Source Loc (R)(Ohms) [ A3          ]
    3: 3    -- Destination Loc (Deg C) [ A3          ]
    4: 1.28680  A
    5: -3      x 10^n
    6: 2.35938  B
    7: -4      x 10^n
    8: 9.4     C
    9: -8      x 10^n

; Processing calculations for fourth bank of thermistors

   27:  Z=1/X (P42)
    1: 4    -- X Loc [ A4          ]
    2: 4    -- Z Loc [ A4          ]

   28:  Z=X*F (P37)
    1: 4    -- X Loc [ A4          ]
    2: 5000    F
    3: 4    -- Z Loc [ A4          ]

   29:  Z=X+F (P34)
    1: 4    -- X Loc [ A4          ]
    2: -1      F
    3: 4    -- Z Loc [ A4          ]

   30:  Z=X*F (P37)
    1: 4    -- X Loc [ A4          ]
    2: 1000    F
    3: 4    -- Z Loc [ A4          ]

   31:  Steinhart-Hart Equation (P200)
    1: 1       Reps
    2: 4    -- Source Loc (R)(Ohms) [ A4          ]
    3: 4    -- Destination Loc (Deg C) [ A4          ]
    4: 1.28680  A
    5: -3      x 10^n
    6: 2.35938  B
    7: -4      x 10^n
    8: 9.4     C
    9: -8      x 10^n
```

```
32:  End (P95)

;Deactivate Am16/32(1)

33:  Do (P86)
 1: 54       Set Port 4 Low

; *** End of instructions for AM16/32(1) ***


; *** Start of instructions to measure AM16/32(2) ***

; Activate AM16/32(2) by setting Control Port 2 high

34:  Do (P86)
 1: 45       Set Port 5 High

35:  Beginning of Loop (P87)
 1: 0        Delay
 2: 15       Loop Count

    36:  Step Loop Index (P90)
     1: 4        Step

    37:  Do (P86)
     1: 76       Pulse Port 6

    38:  Delay w/Opt Excitation (P22)
     1: 1        Ex Channel
     2: 0        Delay W/Ex (0.01 sec units)
     3: 1        Delay After Ex (0.01 sec units)
     4: 0        mV Excitation

; The following instructions are used to determine the
; resistance of the thermistors in ohms and then be
; plugged into the Steinhart-Hart equation to determine
; a value in Degrees C.

    39:  Excite-Delay (SE) (P4)
     1: 4        Reps
     2: 20       Auto, 60 Hz Reject, Slow Range (OS>1.06)
     3: 5        SE Channel
     4: 1        Excite all reps w/Exchan 1
     5: 10       Delay (0.01 sec units)
     6: 2500     mV Excitation
     7: 65    -- Loc [ B1           ]
     8: 2.0138   Mult
     9: 0        Offset

; Processing calculations for first bank of thermistors

    40:  Z=1/X (P42)
     1: 65    -- X Loc [ B1         ]
     2: 65    -- Z Loc [ B1         ]

    41:  Z=X*F (P37)
     1: 65    -- X Loc [ B1         ]
     2: 5000     F
     3: 65    -- Z Loc [ B1         ]

    42:  Z=X+F (P34)
     1: 65    -- X Loc [ B1         ]
     2: -1       F
     3: 65    -- Z Loc [ B1         ]

    43:  Z=X*F (P37)
     1: 65    -- X Loc [ B1         ]
     2: 1000     F
     3: 65    -- Z Loc [ B1         ]

    44:  Steinhart-Hart Equation (P200)
     1: 1        Reps
     2: 65    -- Source Loc (R)(Ohms) [ B1         ]
     3: 65    -- Destination Loc (Deg C) [ B1         ]
     4: 1.28680  A
     5: -3       x 10^n
     6: 2.35938  B
     7: -4       x 10^n
     8: 9.4      C
     9: -8       x 10^n

; Processing calculations for second bank of thermistors

    45:  Z=1/X (P42)
     1: 66    -- X Loc [ B2         ]
     2: 66    -- Z Loc [ B2         ]

    46:  Z=X*F (P37)
     1: 66    -- X Loc [ B2         ]
     2: 5000     F
     3: 66    -- Z Loc [ B2         ]

    47:  Z=X+F (P34)
     1: 66    -- X Loc [ B2         ]
     2: -1       F
     3: 66    -- Z Loc [ B2         ]

    48:  Z=X*F (P37)
     1: 66    -- X Loc [ B2         ]
     2: 1000     F
     3: 66    -- Z Loc [ B2         ]

    49:  Steinhart-Hart Equation (P200)
     1: 1        Reps
     2: 66    -- Source Loc (R)(Ohms) [ B2         ]
     3: 66    -- Destination Loc (Deg C) [ B2         ]
     4: 1.28680  A
     5: -3       x 10^n
     6: 2.35938  B
     7: -4       x 10^n
     8: 9.4      C
     9: -8       x 10^n

; Processing calculations for third bank of thermistors

    50:  Z=1/X (P42)
     1: 67    -- X Loc [ B3           ]
     2: 67    -- Z Loc [ B3           ]

    51:  Z=X*F (P37)
     1: 67    -- X Loc [ B3           ]
     2: 5000     F
     3: 67    -- Z Loc [ B3           ]

    52:  Z=X+F (P34)
     1: 67    -- X Loc [ B3           ]
     2: -1       F
     3: 67    -- Z Loc [ B3           ]

    53:  Z=X*F (P37)
     1: 67    -- X Loc [ B3           ]
     2: 1000     F
     3: 67    -- Z Loc [ B3           ]

    54:  Steinhart-Hart Equation (P200)
     1: 1        Reps
     2: 67    -- Source Loc (R)(Ohms) [ B3           ]
     3: 67    -- Destination Loc (Deg C) [ B3           ]
     4: 1.28680  A
     5: -3       x 10^n
```

```
    6: 2.35938  B
    7: -4       x 10^n
    8: 9.4      C
    9: -8       x 10^n

; Processing calculations for fourth bank of thermistors

   55:  Z=1/X (P42)
    1: 68     -- X Loc [ B4           ]
    2: 68     -- Z Loc [ B4           ]

   56:  Z=X*F (P37)
    1: 68     -- X Loc [ B4           ]
    2: 5000     F
    3: 68     -- Z Loc [ B4           ]

   57:  Z=X+F (P34)
    1: 68     -- X Loc [ B4           ]
    2: -1       F
    3: 68     -- Z Loc [ B4           ]

   58:  Z=X*F (P37)
    1: 68     -- X Loc [ B4           ]
    2: 1000     F
    3: 68     -- Z Loc [ B4           ]

   59:  Steinhart-Hart Equation (P200)
    1: 1        Reps
    2: 68     -- Source Loc (R)(Ohms) [ B4           ]
    3: 68     -- Destination Loc (Deg C) [ B4           ]
    4: 1.28680  A
    5: -3       x 10^n
    6: 2.35938  B
    7: -4       x 10^n
    8: 9.4      C
    9: -8       x 10^n

60:  End (P95)

;Deactivate Am16/32(2)

61:  Do (P86)
 1: 55       Set Port 5 Low

; *** End of instructions for AM16/32(2) ***

; *** OUTPUT INSTRUCTIONS ***

; Every four hours, the  121 temperatures will be sampled.


62:  Data Table (P84)^1613
 1: 0        Seconds into Interval
 2: -1       When Flag 1 is High
 3: 0        (0 = auto allocate, -x = redirect to inloc x)
 4: TCPILE_WEST              Table Name


;THE OUTPUT WILL BE 10*12+1=121+ 1 (for extra checked,
the last one is -200C) REPS

63:  Sample (P70)^21757
 1: 122      Reps
 2: 1        Loc [ A1           ]

64:  Do (P86)
 1: 21       Set Flag 1 Low


*Table 2 Program
  02: 0.0000    Execution Interval (seconds)

*Table 3 Subroutines

End Program
```